

The background of the cover is a photograph of a large, modern building interior. The space is characterized by a massive glass facade that allows natural light to flood in, creating a bright and airy atmosphere. The structural elements of the building, including a complex network of steel beams and cables, are visible through the glass. In the foreground, a large, dark silhouette of a tree in a pot stands prominently on the right side. The floor is highly reflective, mirroring the tree and the structural elements of the building. The overall scene conveys a sense of openness and connection with nature within a modern architectural setting.

Ventilation of Large Spaces in Buildings

Analysis and Prediction Techniques

Edited by
Per Heiselberg
Shuzo Murakami
Claude-Alain Roulet

IEA

Energy Conservation in Buildings and Community Systems
Annex 26: Energy Efficient Ventilation of Large Enclosures

Ventilation of Large Spaces in Buildings

Analysis and Prediction Techniques

Edited by
Per Heiselberg
Shuzo Murakami
Claude-Alain Roulet

IEA Energy Conservation in Buildings and Community Systems
Annex 26: Energy Efficient Ventilation of Large Enclosures

ISSN 1395-7953 R9803
Aalborg University, Aalborg, Denmark

Printed in Kolding, Denmark by Kolding Trykcenter A/S

First Edition: February 1998

Edited by Per Heiselberg, Aalborg University, Aalborg, Denmark; Shuzo Murakami,
University of Tokyo, Tokyo, Japan; Claude-Alain Roulet, École Polytechnique Fédérale de
Lausannes, Lausanne, Switzerland

Cover Photo: The Elrey B. Jeppesen Terminal, Denver International Airport. Architects:
C.W. Fentress, J.H. Bradburn and Associates in Denver. Photo: Per Olaf Tjelflaat.

FOREWORD

This report is a summary of the work performed in subtask 2 of IEA Annex 26 Energy Efficient Ventilation of Large Enclosures and is based on the work of many researchers.

The report is an official Annex report and gives an overview and an evaluation of the techniques to analyse, measure and model air flows and ventilation in large enclosures as well as working examples of methods.

There have been many people involved in this report. A list of the main authors, contributors and reviewers can be found on page 13 and a list of involved research institutes and universities on page 319. One particular person I would like to address my gratefulness to is Peter Schild (NUST, Norway). He took care of our manuscript and rewrote parts of it into proper English, so that the contents were more clear and easier to follow.

On behalf of the participants I hereby want to acknowledge the members of the Executive Committee of IEA Energy Conservation in Buildings and Community Systems Programme as well as the funding bodies. The inspiration and support from the Operating Agent of Annex 26 Dr. Alfred Moser, ETH Zürich, Switzerland is also gratefully acknowledged.

Financial support for the production of this report was provided by the Department of Building Technology and Structural Engineering, Aalborg University, Denmark.

Per Heiselberg
Editor

TABLE OF CONTENTS

NOMENCLATURE	9
ACKNOWLEDGEMENT	13
CHAPTER 1. INTRODUCTION	15
1.1 MODELLING TECHNIQUES.....	18
1.2 MEASURING TECHNIQUES	18
1.3 APPLICATION OF ANALYSIS AND PREDICTION TECHNIQUES	19
CHAPTER 2. MODELS	21
2.1 INTRODUCTION.....	23
2.2 FLOW ELEMENT MODELS.....	27
2.2.1 Isothermal and Thermal Jets.....	28
2.2.2 Thermal Plumes.....	36
2.2.3 Free Convection Flows.....	39
2.2.4 Gravity Currents.....	41
2.2.5 Exhaust Flows	45
2.2.6 Interaction between Flow Elements	46
2.2.7 Summary.....	47
2.3 ENGINEERING MODELS	49
2.3.1 Fundamental Models	49
2.3.2 Zonal Flow Models.....	55
2.3.3 Coupling with Building Dynamic Thermal Models.....	62
2.3.4 Discussion and Conclusions.....	65
2.4 FIELD MODELS.....	67
2.4.1 Introduction to Field Models	67
2.4.2 Numerical Method.....	69
2.4.3 Computational Grid.....	77
2.4.4 Relative Performance of Various Turbulence Models	81
2.4.5 Treatment of Openings.....	87
2.4.6 Treatment of Walls	91
2.4.7 Solar Heat Gain Calculation	97
2.4.8 Coupled Analysis of Radiative and Convective Heat Transfer.....	102
2.4.9 Macro Analysis Based on Micro Model Simulation.....	109
2.4.10 Interactive Analysis of Macro and Micro Models.....	114
2.5 SCALE MODEL EXPERIMENTS	121
2.5.1 Similarity Criteria for Modelling Ventilation.....	121
2.5.2 Improvements in the Approximate and Partial Modelling Methods	127
2.5.3 Scale Model Design Discussion (Based on the Case Study Turnhalle München)	129
2.5.4 Conclusions	133

2.6 VENTILATION EFFICIENCY.....	135
2.6.1 Significance of Enclosure Geometry.....	135
2.6.2 The Task of Ventilation.....	138
2.6.3 Two-Zonal Model of Enclosure.....	140
2.6.4 Prediction of Ventilation Efficiency from Models.....	141
2.7 ENERGY IMPLICATIONS.....	143
2.7.1 Introduction and Basic Hypothesis.....	143
2.7.2 Enclosure Energy Balance.....	144
2.7.3 Fresh Air Flow Rate Assessment.....	146
2.7.4 Ventilation Energy Losses Assessment.....	149
2.7.5 Energy Consumed to Drive Air Movement.....	150
2.8 CONCLUSIONS.....	153

CHAPTER 3. MEASUREMENT TECHNIQUES 155

3.1 INTRODUCTION.....	157
3.1.1 Peculiarities of L.E. with Regard to Ventilation Related Measurement Techniques.....	157
3.1.2 Purpose of Chapter.....	157
3.2 REVIEW OF EXISTING MEASUREMENT TECHNIQUES.....	159
3.2.1 Relations between Measurement Techniques and Problems.....	159
3.2.2 Commonly Used Techniques for Large Enclosures.....	160
3.2.3 Special Applications of Classical Techniques.....	160
3.3 MEASUREMENT TECHNIQUES APPLIED TO LARGE ENCLOSURES.....	161
3.3.1 Airtightness.....	161
3.3.2 Air Velocity.....	167
3.3.3 Contaminant Field.....	170
3.3.4 Ventilation Performance.....	173
3.3.5 Visualisation of Air Movement.....	179
3.3.6 Temperature.....	182
3.4 CONCLUSIONS.....	187

CHAPTER 4. DEMONSTRATION OF TOOLS ON CASE STUDY BUILDINGS.. 189

4.1 OLYMPIC MOUNTAIN HALL, GJØVIK, NORWAY.....	191
4.1.1 Description of Case Study.....	191
4.1.2 Working Examples of Measurement and Analysis Tools.....	194
4.1.3 Performance of Tools and Comparison of Results.....	199
4.1.4 Conclusion and Recommendations.....	202
4.2 QUEENS BUILDING, LEICESTER, UNITED KINGDOM.....	205
4.2.1 Building Description.....	205
4.2.2 Use of Measurement and Analysis Tools.....	207
4.2.3 Performance of Tools.....	210
4.2.4 Conclusions and Recommendations.....	215
4.3 EXPERIMENTAL ATRIUM, KANAGAWA, JAPAN.....	217
4.3.1 Introduction.....	217
4.3.2 Description of the Experimental Atrium.....	219
4.3.3 Measurements.....	219
4.3.4 Analysis Tools: CFD and Zonal Models.....	221
4.3.5 Conclusions and Recommendations.....	234

4.4 FIBREGLASS REINFORCED POLYESTER FACTORY, CAEN, FRANCE237

4.4.1 *Description of the Workshop*.....237

4.4.2 *Examples of Measurement and Analysis Tools*.....239

4.4.3 *Comparisons between Models and Experiment*247

4.4.4 *Global Ventilation Efficiency of the System*247

4.4.5 *Conclusions and Recommendations*248

4.5 TURNHALLE (GYMNASIUM) MÜNCHEN, GERMANY249

4.5.1 *Introduction*.....249

4.5.2 *Experimental Investigations*.....250

4.5.3 *Application of the CFD-Tools*.....259

4.5.4 *Summary*.....266

4.6 ATRIUM GRAFENAU, ZUG, SWITZERLAND267

4.6.1 *Description of Case Study*.....267

4.6.2 *Measurements*.....271

4.6.3 *Analysis Tools*276

4.6.4 *Conclusions and Recommendations*280

4.7 POLYTECHNIC AUDITORIUM, TURIN, ITALY281

4.7.1 *Description of Case Study*.....281

4.7.2 *Measurements*.....283

4.7.3 *Analysis Tools*289

4.7.4 *Conclusions and Recommendations*294

REFERENCES..... 299

INTERNATIONAL ENERGY AGENCY 315

ANNEX 26: ENERGY EFFICIENT VENTILATION OF LARGE ENCLOSURES. 317

PARTICIPATING INSTITUTES IN ANNEX 26 319

NOMENCLATURE

TERM	SYMBOL	UNIT
Mass, flux (flow rate per unit area)	\dot{m}	$\text{kg/m}^2 \text{ s}$
Heat transfer coefficient	α	$\text{W/m}^2 \text{ K}$
Mixing coefficient	β	-
Absorptivity	α	-
Boundary layer thickness	δ	m
Coefficient of cubic expansion	β	K^{-1}
Diffusivity, mass	δ	m^2/s
Dissipation rate of turbulent kinetic energy	ϵ	J/kg s
Emissivity, radiation	ϵ	-
Heat, flow rate (power)	Φ	W
Mass transfer coefficient	β	m/s
Reflectivity, radiation	ρ	-
Relative humidity	$\bar{\omega}$	%
Shear stress	τ	N/m^2
Stefan-Boltzman constant	σ	$\text{W/m}^2 \text{ K}^4$
Temperature, celcius	θ	$^{\circ}\text{C}$
Thermal conductivity	λ	W/m K
Transmissivity	τ	-
Ventilation efficiency	ϵ	-
Viscosity, dynamic	μ	N s/m^2
Viscosity, kinematic	ν	m^2/s
Ratio of specific heat of air at constant pressure to that at constant volume	$\chi \approx 1.4$	-
Heat, flux (flow rate per unit area)	$\phi = \Phi/A$	W/m^2
Density	$\rho = M/V$	kg/m^3
Temperature, difference	$\Delta\theta, \Delta T$	K
View factor, (geometric or configuration factor)	ϕ_{12}	-
Mass concentration (substance a in substance b)	ρ_{a-b}	kg/m^3
Solar irradiation, direct	ϕ_{dn}	W/m^2
Time constant	τ_n	s
Extraterrestrial irradiance on horizontal Plane	ϕ_o	W/m^2
Solid angle of the half-space divided by 2π	Ω_o	sr
Pressure, drop	Δp	N/m^2

TERM

SYMBOL

UNIT

Solar irradiation , diffused on horizontal plane	ϕ_{sky}	W/m ²
Viscosity, eddy	ν_t	m ² /s
Area	A	m ²
Van Driest's constant	A	-
Diffusivity, thermal	$a = \lambda/(\rho c_p)$	m ² /s
Area, cross-sectional	A_c	m ²
Thermal effusivity	b	Ws ^{0.5} /m ² K
Breadth	B	m
Mass distribution	b	kg/m ²
Concentration	c	m ³ /m ³ (ppm)
Numerical constant	C_μ	-
Crack flow coefficient	c_c	-
Discharge coefficient	C_d	-
Heat capacity, specific	c_p, c_p	J/kg K
Diameter	d	m
Diffusion coefficient	D	m ² /s
Diffusion coefficient, thermal	D_T	m ² /s
Energy	E	J
Air leakage factor	f	m ³ /s m ²
Force	F	N
Frequency	f	Hz = s ⁻¹
Critical height	f_c	m
Gravitational acceleration	g	m/s ²
Slot width	h	m
Altitude of the sun	h	E
Enthalpy, specific	h	J/kg
Heat transfer coefficient	h	W/m ² K
Height	H	m
Heat transfer coefficient, surface	$h_w = \phi/(\theta_w - \theta)$	W/m ² K
Momentum flow rate	I	kg m/s ²
Leakage coefficient	k	kg/s pa ⁿ
Turbulent kinetic energy	k	J/kg
Inlet diffusor constants	$K_a, K_p, K_r, K_{sw}, K_{sp}$	
Length	L	m
Radiant density	L	W/m ² sr
Jet penetration length	l_{re}	m
Mass	M	kg
Mass, flow rate	m	kg/s
Molar mass	M	kg/mol
Crack flow exponent	n	-
Specific flow (air change rate, ach)	$n = q/V$	h ⁻¹
Pressure	p	N/m ²
Percentage of Dissatisfied	PD	%

TERM	SYMBOL	UNIT
Predicted Mean Vote	PMV	-
Predicted Percentage of Dissatisfied	PPD	%
Heat, quantity of	Q	J
Volume flow rate	q	m^3/s
Air leakage rate	q_v	m^3/s
Gas constant, molar	R	J/mol K
Radius	r	m
Source strength	S	$m^3/s, m^3/h,$ kg/s.
Temperature, absolute	T	K
Time	t	s
Turbulence intensity	Tu	%
Heat transfer coefficient, overall	U	$W/m^2 K$
Velocity	u	m/s
Voltage	U	V
Velocity, fluctuation	u', v', w'	m/s
Velocity, component in cartesian coordinates x, y, z	u, v, w	m/s
Volume	V	m^3
Width	W	m
Coordinates, cartesian	x, y, z	m, m, m
Air jet, throw ($u(X) = 0.2$ m/s)	$x_{0.2}$	m
Air jet, separation distance	x_s	m
Air jet, spread of	Y	m
Air jet, drop of	Z	m

DIMENSIONLESS GROUPS

Archimedes number	$Ar = g\beta\Delta TL/u_o^2$	
Grashof number	$Gr = g\beta\Delta TL^3/\nu^2$	
Laminar Prandtl number	σ	(Often used in numerical methods)
Nusselts number	$Nu = hL/\lambda$	
Prandtl number	$Pr = \mu c_p/\lambda = \nu/a$	
Rayleigh number	$Ra = Gr Pr$	
Reynolds number	$Re = uL/\nu$	
Schmidt number	$Sc = \nu/\delta$	
Sherwood number	$Sh = \beta L/D$	
Turbulent Prandtl number	$\sigma_h, \sigma_k, \sigma_\epsilon$	(Often used in numerical methods)

SUBSCRIPTS AND SUPERSSCRIPTS

Dissipation rate of turbulent kinetic energy	ϵ
Room, average	$\langle \rangle$
Ambient, external	a
Average value	av
Boundary, black body	b
Convective	c
Conductive	cd
Convective	cv
Exhaust, environment	e
Effective	eff
Exhaust	ex
Enthalpy	h
Room, internal	i
Turbulent kinetic energy	k
Limit	l
Maximum value	max
Initial, measuring object, occupied zone	o
Outdoor	out
Point, local, plane	p
At constant property	p, v, θ
Radiative, received, radial	r
Heat gain from sunshine	rs
Supply	s
Supply	sp
Wall, surface, wind	w

ACKNOWLEDGEMENT

The material presented in this publication has been collected and developed within IEA Energy Conservation in Buildings and Community Systems, Annex 26 Energy Efficient Ventilation of Large Enclosures. All those who have contributed to the project are gratefully acknowledged.

This report presents the condensed results of an international joint research effort conducted in 12 countries participating in subtask 2 on Models. A list of participating institutes can be found on page 319. The following lists the editors, authors and reviewers

Editors

Dr. Per Heiselberg (Chief Editor), Aalborg University, Denmark
Prof. Shuzo Murakami (Editor chapter 2), University of Tokyo, Japan
Dr. Claude-Alain Roulet (Editor chapter 3), École Polytechnique Fédérale de Lausannes, Switzerland

Authors* and Contributors

Dr. Dario Aiulfi (Cpt. 2.3), Sorane SA, Switzerland
Dr. Dominique Blay (Cpt. 2.2), ENSMA Laboratoire d'Etudes Thermiques, France
Mr. Eoin Clancy* (Cpt. 4.2), De Montfort University, United Kingdom
Dr. Serge Collineau* (Cpt. 4.4), INRS, Inst. National de Recherche et de Sécurité, France
Dr. Gian Vincenzo Fracastoro* (Cpt. 2.7, 2.3 and 4.7), Politecnico di Torino, Italy
Dr. Per Heiselberg* (Cpt. 1 and 2.2), Aalborg University, Denmark
Dr. Kazuki Hibi (Cpt. 2.4.2 and 2.4.8), Shimizu Corporation, Japan
Dr. Christian Inard (Cpt. 2.3), INSA de Lyon Centre de Thermique, France
Prof. Shinsuke Kato* (Cpt. 2.4.1, 2.4.3, 2.4.6 and 4.3), University of Tokyo, Japan
Dr. Kjell Kolsaker (Cpt. 2.3), Norwegian University of Science and Technology, Norway
Assoc. Prof. Yasushi Kondo (Cpt. 2.1 and 2.4.7), Musashi Institute of Technology, Japan
Mr. Hannu Koskela (Cpt. 3), Finnish Institute of Occupational Health, Finland
Dr. Hans Martin Mathisen* (Cpt. 4.1), SINTEF, Norway
Prof. Stanislaw Mierzwinski* (Cpt. 2.5), Silesian Technical University, Poland
Mr. Hannes Müller (Cpt. 3), Technische Universität Dresden, Germany
Prof. Shuzo Murakami* (Cpt. 2.4 and 2.8), University of Tokyo, Japan
Dr. Shinichiro Nagano (Cpt. 2.4.4), Fujita Corporation, Japan
Prof. Peter V. Nielsen (Cpt. 2.2), Aalborg University, Denmark
Dr. Raimo Niemelä (Cpt. 3), Finnish Institute of Occupational Health, Finland
Mr. Yoshiichi Ozeki (Cpt. 2.4.6), Asahi Glass Co., Ltd, Japan
Ing. Marco Perino* (Cpt. 2.7 and 4.7), Politecnico di Torino, Italy
Prof. Zbigniew Popiolek (Cpt. 2.5.2 and 2.5.3), Silesian Technical University, Poland
Dr. Dirk Müller (Cpt. 3), RWTH Aachen, Germany
Dr. Claude-Alain Roulet* (Cpt. 3), École Polytechn. Fédérale de Lausannes, Switzerland
Prof. Mats Sandberg* (Cpt. 2.6), The Royal Institute of Technology, Sweden
Dr. Alois Schälin* (Cpt. 4.6), ETH, Switzerland
Mr. Satoshi Togari (Cpt. 2.3), Kajima Technical Research Institute, Japan

Dr. Jacobus Van Der Maas* (Cpt. 2.3), École Polytechnic Fédérale de Lausanne, Switzerland

Mr. Peter Vogel (Cpt. 3), Technische Universität Dresden, Germany

Dr. Norbert Vogl* (Cpt. 4.5), RWTH Aachen, Germany

Dr. Robert Waters (Cpt. 3), Coventry University, United Kingdom

Mr. Shinji Yamamura (Cpt. 2.4.5), Nikken Sekkei Ltd., Japan

Mr. Mutsumi Yokoi (Cpt. 2.4.9 and 2.4.10), Taisei Corporation, Japan

Reviewers

Dr. Dario Aiulfi (Cpt. 4.1-7), Sorane SA, Switzerland

Mr. Karl Terpger Andersen (Cpt. 2.1-3 and 2.5-8), Danish Building Research Institute, Denmark

Dr. Joachim Borth (Cpt. 2.1-3 and 2.5-8), Sulzer Innotec AG, Switzerland

Mr. Eoin Clancy (Cpt. 3.1-4), De Montfort University, United Kingdom

Ir. Tony Lemaire (Cpt. 3.1-4), TNO Building & Construction, Netherlands

Ing. Marco Perino (Cpt. 2.4), Politecnico di Torino, Italy

Dr. Alois Schälin (Cpt. 2.4), ETH, Switzerland

Dr. Jacobus Van Der Maas (Cpt. 1 and 4.1-7), École Polytechnic Fédérale de Lausanne, Switzerland

CHAPTER 1

1. Introduction

1. INTRODUCTION

Large enclosures, for example concert halls, sports centres and ice rinks; office buildings, factory halls, atria, shopping centres or passenger terminal buildings often present unsolved problems related to energy and air flows such as unwanted thermal stratification, local overheating, draughts or uncontrolled contaminant spreading. Large enclosures are often found in unique buildings where novel ideas are tried out. Consequently, there exists no previous experience and very careful analysis of the ventilation design is advisable.

A large enclosure is defined as an enclosed ventilated air space partly occupied and containing various contaminant and heat sources. It is distinguished from other occupied rooms by the strong effect that buoyancy and temperature differences have on air motion, in particular on vertical streams of warm or cold air. Large enclosures may be complex and have partitions and openings. In large enclosures common ventilation strategies, as e.g. complete mixing, require considerable amounts of energy to move and condition enormous amounts of air. The air flow pattern should therefore be well-planned and controlled to ensure an acceptable indoor air quality in the occupied zone without the need for excessive air flow rates. This is obviously possible since the occupied zone is relatively small in large enclosures. Some designs suffer both from over-sizing of equipment and from excessive energy requirements, which are usually caused by the lack of knowledge and guidance at the design stage.

The International Energy Agency - Energy Conservation in Buildings and Community System (IEA-ECB&CS) implementing agreement initiated a joint research programme, Annex 26 "Energy-Efficient Ventilation of Large Enclosures". The objectives of Annex 26 were to increase the understanding of the physics of air motion, thermal stratification and contaminant spread in large enclosures, and to develop methods to minimize - within large enclosures - the energy consumption in the provision of: 1) good indoor air quality and comfort, 2) the safe removal of airborne contaminants and 3) the satisfactory distribution of fresh air. Annex 26 concentrated on analysing the response of the air mass in large spaces to thermal and other inputs from the building and the environment, and it aimed at reducing energy consumption by ventilation. The air flow is particularly important in large enclosures. Firstly, it provides a mechanism for relatively large scale energy transfer processes and, secondly, it has a strong relevance to thermal comfort, removal of airborne contaminants and provision of fresh air at the breathing level, which are of prime importance to comfort and productivity of the occupants. The Annex addressed problems that are related to the elements of the design procedure for a real building: 1) design, 2) construction, 3) commissioning and 4) troubleshooting. Methods to solve these problems were developed as well as measuring techniques for field measurements in large enclosures and design and analysis methods for air flow and ventilation. Better understanding of the air motion was achieved by measurements in a number of case studies.

This part of the Annex 26 final report summarizes improved and new methods for design and analysis of ventilation in large enclosures. It includes description and application of different mathematical models for simulation in the design process of thermal dynamics of building components, temperature distribution, air motion and contaminant spread in order to evaluate performance and locate problems. It also includes improved and new measuring techniques for diagnostics of large enclosure ventilation. Finally, application of both

measuring and modelling techniques on specific case studies is reported and evaluated. The report gives an overview of the different modelling and measurement methods available to analyse large enclosure ventilation. With regard to more specific information on each method references are made to scientific and technical literature.

1.1 Modelling Techniques

Techniques for design and analysis of ventilation are categorized in two main groups according to the level of modelling detail. The first group is macroscopic models which are simplified models for a first estimate and concept evaluation, such as flow element models, engineering models and zonal models. The second group is microscopic models which are detailed models for design evaluation and troubleshooting, such as computational fluid dynamics (CFD) and scale model experiments. Add to this the ventilation efficiency model which is strictly spoken a method to evaluate the ventilation performance based on the results of the macro or microscopic models or measurements in the actual building.

The different stages involved in the design process of a large enclosure can be divided into: initial design phase, building design phase, ventilation design phase, ventilation design evaluation and troubleshooting, construction phase and commissioning. At the first stages of the design process, when the architectural form of the building and the quality of the indoor environment are roughly sketched, information is rather limited. Consequently, only approximate HVAC solutions are applied based on engineering experience (such as data on existing similar buildings) and appropriately simple analytical tools (macroscopic models) are used to save design work. However, for critical or unconventional spaces suitable previous experience or engineering methods may not be available. In such cases more elaborate tools (microscopic models) may be used earlier in the design process, but only for a coarse analysis to evaluate qualitatively different design options.

At the latter stages of the design process, where the HVAC and the architectural design are better defined and more information is available, detailed analytical tools (microscopic models) can be applied to evaluate whether the proposed air flow design will work as intended or there are problems with local thermal discomfort, low IAQ, condensation etc. The performance of the ventilation system can be evaluated by a ventilation efficiency model. If the design criteria are not fulfilled the models can be used for further troubleshooting and design improvement. However, for conventionally sized enclosures such detailed analysis is rarely necessary, as ventilation techniques for such enclosures are well-established and application of simple analytical methods will often be sufficient.

Chapter 2 summarizes function, capability, output information and necessary resources for each type of modelling technique. Data requirements, expectations to results and application advantages and disadvantages are discussed. Chapter 4 shows examples of application of the techniques on different types of large enclosures

1.2 Measuring Techniques

The large volume and area to be examined in large enclosures result generally in more work, a larger number of measuring points and more material cost. Links between sensors and data loggers are long and may require either special techniques or long cables, and some measuring points might even be problematic to reach. Therefore, a careful planning of experiments is essential. First the problem should be defined, then the missing information

should be listed, and only after these preliminary steps measurements can be planned, when necessary, and measuring techniques chosen accordingly.

Analysis of non-homogeneities is important when studying ventilation of large enclosures. Temperature, velocity and concentration gradients will often be present in large enclosures and measurements should be performed at numerous carefully chosen points. Interpretation of measured data should obviously take account of the non-homogeneities.

Chapter 3 reviews existing measurement methods with special regard to their applicability to large enclosures, and a few measuring techniques developed specifically to large enclosures within Annex 26. Several of the measuring techniques were applied to case studies to gain experience in practical use, and their applicability, advantages, disadvantages and results are described in chapter 4. Many measurement methods are available for research, diagnostics, commissioning and management of large enclosures. The most important point is to use these methods advisedly, with the purpose of answering well-defined questions.

1.3 Application of Analysis and Prediction Techniques

Case study buildings serve to demonstrate measurement and modelling methods, to study problems and to develop design guidelines. On selected buildings detailed measurements were performed and modelling techniques were tested. The buildings represent typical large enclosures covering one sports arena, one gymnasium, two auditoria, two atria and one factory.

In chapter 4 analysis and prediction techniques are applied to each of these buildings. The applications contain both successful and unsuccessful examples with comparisons of results both between different models and between models and measurements. Together with the description of the methods in chapters 2 and 3 this gives the designer a basis for selection of appropriate methods for solution of specific problems and design of energy-efficient ventilation of large enclosures.

CHAPTER 2

2.1. Introduction

2.2. Flow Element Models

2.3. Engineering Models

2.4. Field Models

2.5. Scale Model Experiments

2.6. Ventilation Efficiency

2.7. Energy Implications

2.1 Introduction

This chapter describes the mathematical or physical models that the HVAC specialist can use as analytical tools for planning the indoor climate of a large enclosure.

The ultimate objective of the environmental control solution for a building is to ensure satisfactory *thermal comfort* and *indoor air quality* (IAQ) for the occupants. For industrial enclosures, this picture may be complicated by the additional need to provide optimum conditions for the industrial processes within. In addition to fulfilling these primary objectives, the environmental control solution should be energy efficient, and there are also economic, safety, acoustic, aesthetic and other considerations. Consequently, the HVAC specialist needs analytical tools to help evaluate thermal comfort, IAQ, ventilation efficiency, and energy consumption.

Nowadays, a designer can get by without a detailed understanding of some of the more elaborate mathematical models covered in this chapter, since they may be implemented in the guise of easy-to-use commercial simulation software. Nevertheless, the successful designer needs a sound appreciation of the basic theory of all the models he or she uses, together with the models' limits and merits when applied to large enclosures. This chapter aims to provide such an understanding.

Table 2.1.1 summarises the different stages involved in the design process of a large enclosure. As the environmental and architectural design of the proposed building develops, more data becomes available to the HVAC designer, who should therefore select an analytical tool, or tools, of an appropriate level of detail for each stage.

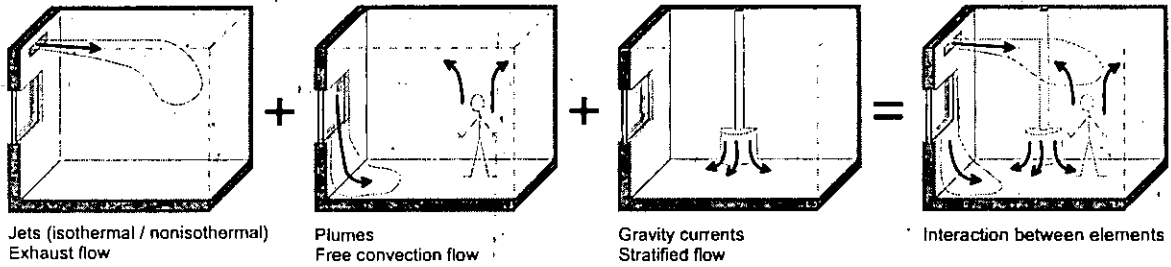
Table 2.1.1 *Design process and design tools for indoor environment of a large enclosure.*

	(1) <i>Scheme design</i>	(2) <i>Basic design</i>	(3) <i>Detailed design</i>
Matter to be planned	<ul style="list-style-type: none"> • Building shape and envelope materials. • Quality of indoor environment. • HVAC system concept. 	<ul style="list-style-type: none"> • Refinement of building layout and envelope design. • Decision of air supply outlet, air volume and supply air temperature. • Outline of operation of building and HVAC system. 	<ul style="list-style-type: none"> • Final decision of building layout and envelope material, etc. • Specification of HVAC system. • Operation and controls system of building and HVAC.
Subject to be known	<ul style="list-style-type: none"> • Rough estimate of heating and cooling loads. • Rough prediction of airflow and temperature distribution. 	<ul style="list-style-type: none"> • Accurate prediction of heating/cooling loads, with associated energy consumption and running costs. • Distribution of airflow and temperature. • Index of thermal comfort (e.g. PMV). • Regions of discomfort caused by sunshine, cold draughts at the base of windows, condensation problems, etc. • Situation of pre-cooling and pre-heating. 	
Design tool	<ul style="list-style-type: none"> • Experience and measurement data on similar existing buildings. • Simple Macroscopic models, for first estimation. 	<ul style="list-style-type: none"> • Advanced Macroscopic or possibly Microscopic model, for second estimation. 	<ul style="list-style-type: none"> • Microscopic model for design validation and 'troubleshooting'. → CFD or scale model expt.
		<ul style="list-style-type: none"> • Ventilation efficiency model. → Evaluation of ventilation performance. 	

Simplified models (macroscopic)

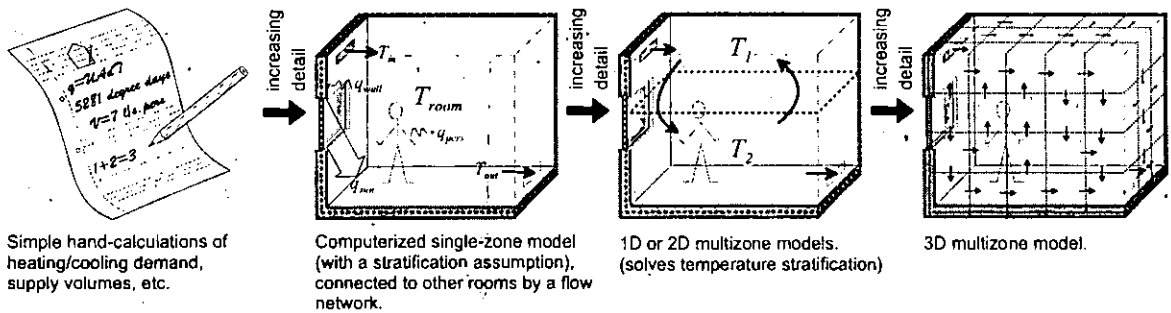
Flow Element Models

To design air distribution solution, and empirically evaluate local discomfort



Engineering Models

Computer / hand prediction of heating & cooling loads, energy consumption, airflow, thermal comfort & IAQ



Detailed models (microscopic)

For validation of final ventilation design and for troubleshooting

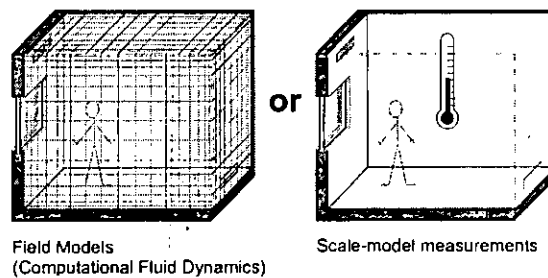


Figure 2.1.1 Overview of the different prediction tools.

In the first stages of the design process, when the architectural form and quality of the indoor environment are roughly sketched out, information on the proposed building is rather scant, so only an approximate HVAC solution is developed, based on engineering experience (such as data on existing similar buildings) and use of appropriately simple prediction tools (i.e. *macroscopic analysis*). This keeps design costs down. However, for critical or unconventional spaces, suitable previous experience or engineering methods may not be available. In such cases, more elaborate prediction tools (i.e. *microscopic analysis*) may be used earlier in the design process, but only for a coarse analysis, to qualitatively evaluate different design options.

In the latter stages of the design process for a large enclosure, the HVAC and architectural design are more highly developed, so more information is available, including the specifications of the envelope materials, positions and volumes of supply & extract openings, cooling & heating loads. There is a consequent need to use a more detailed analytical tool, or tools, to evaluate whether the proposed air diffusion design will work as intended (i.e. *microscopic analysis*). Thus the designer can examine whether there are problems with local thermal discomfort, draughts, low IAQ, condensation etc., and the performance of the ventilation system can be evaluated by a ventilation-efficiency model. If the design criteria are not satisfied, then the tool can be used for further troubleshooting. For conventionally sized enclosures, however, such detailed analysis is rarely necessary, as ventilation techniques for such enclosures are well established, so simpler analytical methods will often suffice.

Prediction tools can thus be categorised in two main groups, according to the level of modelling detail, as shown here, and illustrated in Figure 2.1.1:

- (1) *Simplified models, for first estimate and design development (macroscopic analysis).*
 - Flow element models (subchapter 2.2)
 - Engineering models (including zonal models) (subchapter 2.3)
- (2) *Detailed models, for design validation and troubleshooting (microscopic analysis).*
 - Field models (computational fluid dynamics, CFD) (subchapter 2.4)
 - Scale model experiments (subchapter 2.5)

Microscopic models (CFD and scale model experiments) can predict velocity, temperature and other flow properties throughout a whole space, with a high degree of resolution. In contrast, the simpler, macroscopic models, whilst being cheaper and quicker to use, have a much lower resolution (in the case of Zonal models) or provide an empirical picture of the flowfield driven by only individual flow elements (in the case of Flow Element models).

In addition to the above prediction tools, various appraisal methods are needed to quantify the performance of the modelled HVAC system. Ventilation efficiency models (subchapter 2.6) can be used to evaluate the results of macro- or microscopic models, or even actual buildings, with respect to ventilation performance. Another important consideration is thermal comfort, which is amply covered elsewhere [e.g. *ISO 7730*] and so is not covered here. Also the energy cost of the chosen ventilation system must be estimated (subchapter 2.7).

Table 2.1.2 summarises the function, capabilities, output and necessary computer resources for each type of ventilation analysis tool.

Table 2:1.2 : Outline of analytical models of thermal environment within a large-enclosure.

	<i>Macroscopic model</i>	<i>Microscopic model</i>	<i>Ventilation efficiency model</i>
Design stage	<ul style="list-style-type: none"> • Scheme design & basic design. 	<ul style="list-style-type: none"> • Basic design and detailed design stages. 	<ul style="list-style-type: none"> • All stages, but principally detailed design stage.
Purpose	<ul style="list-style-type: none"> • Macroscopic analysis of airflow and temperature distribution at a few typical points. 	<ul style="list-style-type: none"> • Microscopic analysis of airflow and temperature distribution in detail. 	<ul style="list-style-type: none"> • Evaluation of efficiency of HVAC system.
Available models	<ul style="list-style-type: none"> • Flow element model. • Zonal model. 	<ul style="list-style-type: none"> • CFD • Scale model experiment. 	<ul style="list-style-type: none"> • Analysis based on the results of CFD. • Analysis by experiment.
Outputs	<ul style="list-style-type: none"> • Mean temperature. • Vertical temperature distribution. • Heating & cooling load. • Flow pattern between zones. • Boundary conditions for CFD. 	<ul style="list-style-type: none"> • Detailed distribution of airflow and temperature. • Study of problems to be solved in design (troubleshooting). • Mechanism of heat transfer and airflow in real enclosures. 	<ul style="list-style-type: none"> • Distribution of ventilation efficiency index. • Mechanism of heat transfer and airflow in real enclosures.
Necessary equipment /computer	<ul style="list-style-type: none"> • Personal computer, etc. 	<ul style="list-style-type: none"> • Workstation or supercomputer for CFD. • Scale model with sensors for model experiment. 	<ul style="list-style-type: none"> • Workstation or supercomputer for CFD. • Scale model with sensors for model experiment.
CPU time	<ul style="list-style-type: none"> • A few minutes. 	<ul style="list-style-type: none"> • 10-100 hours per case for CFD. 	<ul style="list-style-type: none"> • 1-10 hours per case for CFD.
Required time for application	<ul style="list-style-type: none"> • About half day per case to input data. 	<ul style="list-style-type: none"> • About 1 week per case to input data for CFD. • 1-3 weeks per case for model experiment. 	<ul style="list-style-type: none"> • About 1 day per case to input data for CFD. • 1-3 weeks per case for model experiment.

2.2 Flow Element Models

Air distribution in ventilated rooms is a flow process that can be divided into different elements such as supply air jets, exhaust flows, thermal plumes, boundary layer flows, infiltration and gravity currents. These flow elements are isolated volumes where the air movement is controlled by a restricted number of parameters, and the air movement is fairly independent of the general flow in the enclosure. In many practical situations, the most convenient method is to design the air distribution system using flow element theory. The flow element method is very useful in situations where the air flow pattern in a room is dominated by a single flow element or by flow elements that are not interacting with each other. In normal-size enclosures this is often true, so simple calculations using Flow Element models are all that is needed to design the air distribution system. In displacement ventilation, the supply of air from a low-level device and the thermal plume from heat sources above the floor are good examples of different flow elements that do not influence each other, and where the design of the air distribution system can be based on the models of these two flow elements. In large enclosures the airflow will often consist of several flow elements occurring at the same time. The flow elements will only dominate the air distribution in small parts of the enclosure and the flow path will often be influenced by other flow elements. Therefore, in large enclosures there will be large parts of the space where Flow Element models are not able to predict the air distribution. In such cases, Flow Element models will be useful only in the first stages of the design process, to keep design costs down, and possibly to estimate the airflow conditions in specific areas of the enclosure. More detailed analytical tools (field models) will be necessary to estimate the airflow and temperature conditions in the enclosure as a whole, but the results from Flow Element models will be very useful as initial input. The results can for example give an indication of where large gradients can be expected, so that a good distribution of local grid refinement can be made for CFD calculations.

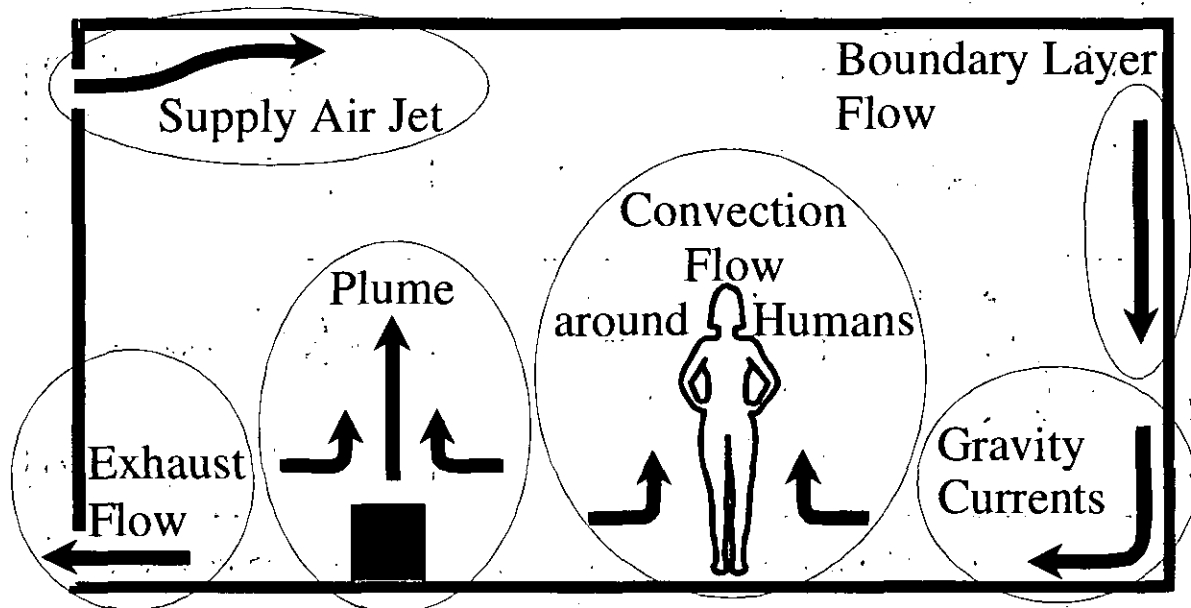


Figure 2.2.1 Examples of flow elements in ventilated spaces.

2.2.1 Isothermal and Thermal Jets

Air jets are often used to distribute the incoming air and to heat or cool the occupied zone in ventilated enclosures. In designing air distribution with jets, it is necessary to determine the jet trajectories, and the velocities and temperatures along the trajectories. This information is used to check that the jets will properly ventilate the occupied zone, with minimal discomfort. Depending on the type of air terminal device, the air jet can be characterised as a circular, plane or radial jet. In addition, the jet can be characterised as a free or wall jet depending on the location of the terminal device in relation to enclosing surfaces (Figure 2.2.2). A circular jet is generated from a circular, square or another concentrated outlet. A plane jet is generated from a slot or a row of closely spaced nozzles, while a radial jet is generated from an air terminal device that distributes the air radially. In practical situations, there can be different combinations of the above devices, which generate intermediate forms of these main jet types. Circular and radial air jets are most common, and generally the air is distributed by wall jets (along the ceiling) in small rooms, while large enclosures typically have free jets projected either vertically or horizontally into the enclosure. The work within Annex-26 has concentrated on vertical free jets.

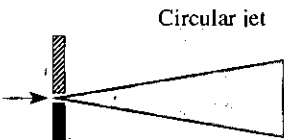
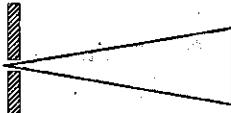
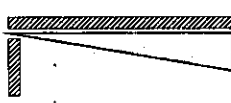
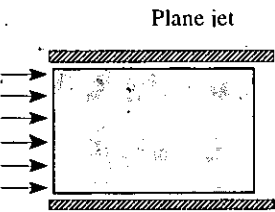
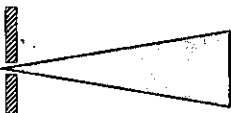

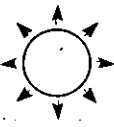

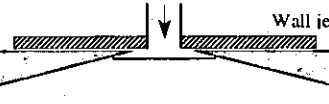
Top view	Side view	Velocity decay
<p>Circular jet</p> 	<p>Free jet</p> 	$u_x = u_o \frac{K_a \sqrt{A_o}}{\sqrt{2} x} \quad (\text{m/s}) \quad (2.2.1)$
	<p>Wall jet</p> 	$u_x = u_o K_a \frac{\sqrt{A_o}}{x} \quad (\text{m/s}) \quad (2.2.2)$
<p>Plane jet</p> 	<p>Free jet</p> 	$u_x = u_o \frac{K_p \sqrt{h_o}}{\sqrt{2} x} \quad (\text{m/s}) \quad (2.2.3)$
	<p>Wall jet</p> 	$u_x = u_o K_p \sqrt{\frac{h_o}{x}} \quad (\text{m/s}) \quad (2.2.4)$
<p>Radial jet</p> 	<p>Free jet</p> 	$u_x = u_o \frac{K_r \sqrt{A_o}}{\sqrt{2} x} \quad (\text{m/s}) \quad (2.2.5)$
	<p>Wall jet</p> 	$u_x = u_o K_r \frac{\sqrt{A_o}}{x} \quad (\text{m/s}) \quad (2.2.6)$

Figure 2.2.2 Different isothermal air jet types with corresponding velocity distribution.

Isothermal jets

A free jet is one that, in theory, flows into an infinitely large space, unhindered by obstructions. Likewise, a wall jet is one that flows along a surface bordering the space. These ideal jets,

which are not influenced by downstream conditions, can be described by boundary layer approximations which give a self-similar flow with universal flow profiles; see Rajaratnam [1976]. These conditions are important because it enables us to describe the flow in jets independently of the surrounding enclosure dimensions. It can be assumed that the initial flow momentum supplied at the air terminal device is preserved along the jet's trajectory. This leads to a simple relationship governing the velocity decay along the jet, shown in Figure 2.2.2. The constants K_a , K_p and K_r characterise the individual air terminal device. Typical values are $K_a = 3-10$, $K_p = 2-4$ and $K_r = 1-2$. The values can, as you can see, differ a great deal, and they are Reynolds-number dependent at low Reynolds numbers [Nielsen and Möller, 1985, 1987, 1988]. Therefore, it is advisable to use values measured at the actual air terminal device.

Horizontal thermal jets

Buoyancy will influence the flow in a jet if the air is supplied at a temperature different from the room temperature, as is the case when the air is used to heat or cool the space.

A horizontal projected nonisothermal free jet has a trajectory that curves downwards in the case of a cold jet (due to its higher density than surrounding air), and curves upwards in the case of a warm jet (due to buoyancy). The trajectory can be described by Equation (2.2.7) [Koestel, 1955]. The trajectory's geometrical co-ordinates, x and y , describe the curve traced out by the centre-line of the jet, i.e. the point of maximum velocity, and maximum or minimum temperature, for any given vertical cross section along the jet.

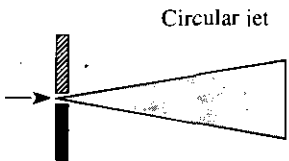
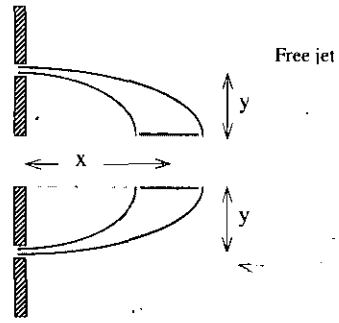
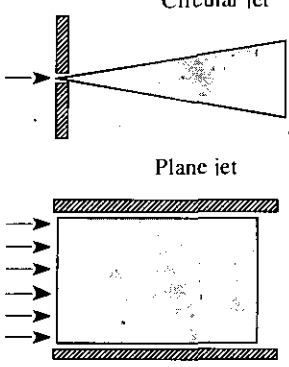
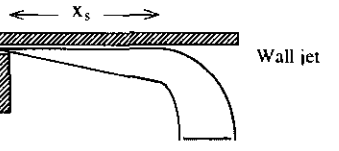
Top view	Side view	Trajectory/Penetration length
 <p>Circular jet</p>	 <p>Free jet</p>	$y = \frac{0.02 \Delta T_o A_o}{K_a u_o^2} \left(\frac{x}{\sqrt{A_o}} \right)^3 \quad (\text{m}) \quad (2.2.7)$
 <p>Circular jet</p> <p>Plane jet</p>	 <p>Wall jet</p>	$x_s = K_{sa} K_a \sqrt{\frac{u_o^2 \sqrt{A_o}}{\Delta T_o}} \quad (\text{m}) \quad (2.2.8)$ $x_s = K_{sp} K_p^2 \left(\frac{u_o^2 \sqrt{h}}{\Delta T_o} \right)^{2/3} \quad (\text{m}) \quad (2.2.9)$

Figure 2.2.3 Trajectory and penetration length of horizontal thermal jets.

Also nonisothermal wall jets are influenced by gravity. However, the Coanda effect (see page 35) prevents the flow from detaching from the surface and following the free-jet trajectory described in Equation (2.2.7), until the jet reaches a certain distance, x_s , from the

supply opening. When air-conditioning with ceiling wall-jets, a short penetration length; x_s , is undesirable, because a jet may have a high velocity and a low temperature when it flows down prematurely into the occupied zone, causing discomfort. The Coanda effect can thus be used to good effect in ventilation of large enclosures, by increasing throw length and preventing unwanted draughts in the occupied zone. A good example of this is the large jets used to ventilate the terminal hall at Kansai International Airport, Japan [Guthrie *et al.*, 1992; Guthrie, 1996].

Grimitlin [1970] and Schwenke [1976] have shown that the penetration length for a circular wall jet can be described by Equation (2.2.8) and for a plane wall jet by Equation (2.2.9); see Figure 2.2.3. The values of the constants K_{sa} and K_{sp} depend on parameters outside the jet, such as room dimensions, location of thermal load etc. [Hestad, 1976]. A value of $K_{sa} = K_{sp} = 1.5$ is valid for large rooms with an evenly distributed heat source over the whole floor area [Nielsen and Möller, 1987, 1988]. The values of K_a , K_p should be evaluated as described for isothermal jets.

The decay in centre-line velocity along a nonisothermal jet can be described by the same equation as used for the isothermal jet.

Thermal energy is preserved along a jet, in the same way as momentum, so it can be assumed that the temperature decay or increase along the jet's trajectory is proportional to the velocity decay (Equations (2.2.1 - 2.2.6) [Nielsen and Möller, 1987].

$$\frac{T_x - T_r}{T_x - T_o} \approx \frac{u_x}{u_o} \quad (2.2.10)$$

Vertical thermal jets

The velocity distribution in a vertical thermal jet depends on whether the momentum and gravity forces act in the same or opposite directions. In a jet where the forces are in opposition, the velocity decay is faster than in an isothermal jet, whilst it is slower in the reverse case. The velocity decay in a vertical circular jet is described by Equation (2.2.11) [Koestel, 1954], while Equation (2.2.12) gives an estimate for a vertical plane jet [Regenscheit, 1970]. In Equations (2.2.11) and (2.2.12) the plus sign is used when the momentum and gravity forces are in the same direction. The minus sign is used when they are in opposition.

A downward projected warm jet and an upward projected chilled jet have a limited penetration length, y_m , which corresponds to the distance where the velocity has fallen to zero. For a circular jet, the penetration length can be described by Equation (2.2.13) [Helander *et al.*, 1953], and for a plane jet it can be roughly estimated by Equation (2.2.14) [Regenscheit, 1959].

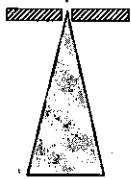
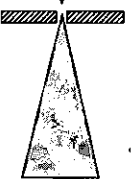
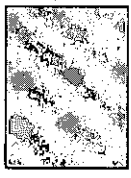
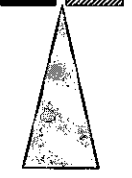
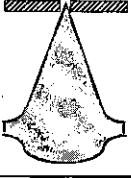
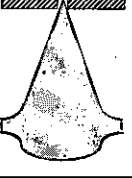

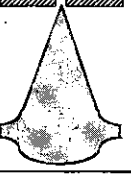
Front view	Side view	Velocity decay/Penetration length
Circular jet 		Cold jet downwards Warm jet upwards use + sign $v_y = v_o \frac{K_a \sqrt{A_o}}{\sqrt{2}} \frac{1}{y} \left(1 \pm 0.09 \frac{ \Delta T_o \sqrt{A_o}}{K_a v_o^2} \left(\frac{y}{\sqrt{A_o}} \right)^2 \right)^{3/2} \quad (\text{m/s}) \quad (2.2.11)$ Cold jet upwards Warm jet downwards use - sign
Plane jet 		Cold jet downwards Warm jet upwards use + sign $v_y = 2.5 v_o \sqrt{\frac{h_o}{y}} \pm 0.18 \sqrt{h_o \Delta T_o } \left(\sqrt{\frac{y}{h_o}} - 1 \right) \quad (\text{m/s}) \quad (2.2.12)$ Cold jet upwards Warm jet downwards use - sign
Circular jet 		Cold jet upwards Warm jet downwards $y_m = 3.33 \sqrt{\frac{K_a v_o^2 \sqrt{A_o}}{ \Delta T_o }} \quad (\text{m}) \quad (2.2.13)$
Plane jet 		Cold jet upwards Warm jet downwards $y_m = 19.2 h_o \left(\frac{v_o^2}{h_o \Delta T_o } \right)^{3/2} \quad (\text{m}) \quad (2.2.14)$

Figure 2.2.4 Velocity decay and penetration length for vertical thermal jets.

Vertical rectangular thermal jets

Very little results concerning 3D thermal free jets are available in the literature. Recently, an experimental study of 3D vertical free buoyant air jets was performed by Vialle and Blay [1996]. Decay laws were determined for 3D rectangular jets with positive buoyancy and penetration length were measured for jets with negative buoyancy. Results were obtained in the following parameter range: Jet aspect ratio: 4.4 (20 cm:4.5 cm); $0 < Ar < 0.3$; $3600 < Re < 12000$.

Jets with positive buoyancy

Several conclusions were drawn from this study. It was first found that the jet flow is not sensitive to Reynolds number but is very dependent on Archimedes number. Second, the centerline velocity and temperature decay slopes are depending on the Archimedes number defined as:

$$Ar = \frac{g\beta(T_0 - T_\infty)\sqrt{A}}{v_o^2} \quad (2.2.15)$$

Second the jet flow can be divided into three zones depending on the dimensionless distance Y .

$$Y = \frac{y}{\sqrt{A}} \tag{2.2.16}$$

where A is the inlet section area.

The three zones are defined as Zone 1 where the flow is establishing, ($Y < 2$), Zone 2 where the flow tends to behave as a plane jet, ($2 < Y < 7$), and Zone 3 where the flow tends to behave as an axisymmetrical jet, ($Y > 7$), see figure 2.2.5. Centerline velocity, and temperature decay laws are given in table 2.2.1.

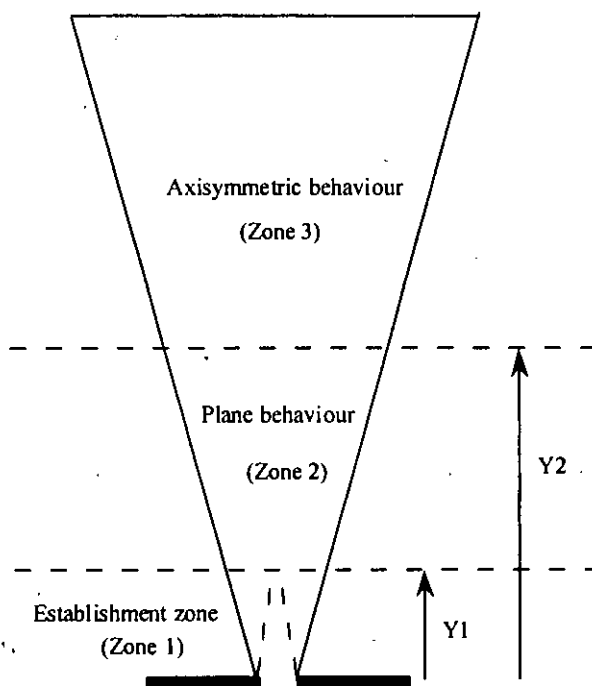


Figure 2.2.5 Side view of a rectangular vertical thermal jet with positive buoyancy.

Jets with negative buoyancy

For rectangular jets with negative buoyancy, penetration lengths were deduced from centerline velocity and temperature measurements. Results were obtained in the following parameter range: Jet aspect ratio : 4.4 (20 cm x 4.5 cm); $0.002 < Ar < 0.025$; $6000 < Re < 12000$. The penetration length is given by :

$$Y_m = 1.48Ar^{-0.5} \tag{2.2.17}$$

Table 2.2.1 Velocity and temperature decay for vertical rectangular free thermal jets.

Zone		Velocity	Temperature
Zone 1	$Y_1 = 2$ $0 < Y < Y_1$	$v = v_o$	$T = T_o$
Zone 2	$Y_2 = 7$ $Y_1 < Y < Y_2$	$\frac{v}{v_o} = \left(\frac{Y_1}{Y}\right)^{b_2}$ $b_2 = 0.28 \frac{0.22Ar + 0.07}{Ar + 0.07}$	$\frac{T - T_\infty}{T_o - T_\infty} = \left(\frac{Y_1}{Y}\right)^{b_2}$ $b_2 = 0.28 \frac{5.40Ar + 1.26}{Ar + 1.26}$
Zone 3	$Y_1 = 2$ $Y_2 = 7$ $Y > Y_2$	$\frac{v}{v_o} = \left(\frac{Y_1}{Y_2}\right)^{b_2} \left(\frac{Y_2}{Y}\right)^{b_3}$ $b_3 = 0.73 \frac{0.203Ar + 0.028}{Ar + 0.028}$	$\frac{T - T_\infty}{T_o - T_\infty} = \left(\frac{Y_1}{Y_2}\right)^{b_2} \left(\frac{Y_2}{Y}\right)^{b_3}$ $b_3 = 0.73 \frac{1.63Ar + 0.06}{Ar + 0.06}$

Behaviour of jets in confined spaces

The jets described by the Equations (2.2.1 - 2.2.17) are considered to be in an infinite isothermal medium. Depending on the room size, jets developing in real rooms are affected by wall and entrainment effects, which create substantial recirculation zones, as well as by thermal stratification.

In a deep room, an isothermal jet will have a restricted penetration length because entrainment generates a return flow in the room, so the jet gets dissolved after a certain distance. A jet can be considered to be developing freely as long as its cross section is less than 25% of the cross section of the room. The penetration length for a plane horizontal wall jet is given by Equation (2.2.21) [Nielsen, 1976]. The variation depends on the entrainment in the jet, where a high entrainment and a low K_p value give a short penetration length and a low entrainment and a high K_p value give a long penetration length [Skåret, 1976]. Equations (2.2.18 - 2.2.20) describe the penetration length of circular free, wall or corner jets, respectively [Krause, 1972].

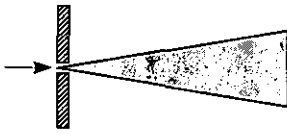
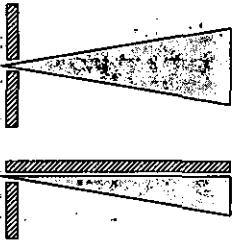
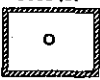

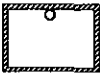


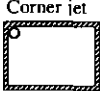
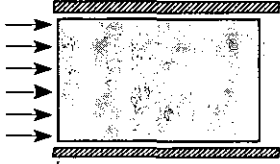
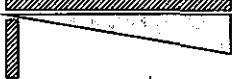
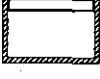
Top view	Side view	Front view	Penetration length
<p>Circular jet</p> 		<p>Free jet</p> 	$l_{re} = 3\sqrt{A}$ (m) (2.2.18)
		<p>Wall jet</p> 	$l_{re} = 4.2\sqrt{A}$ (m) (2.2.19)
		<p>Corner jet</p> 	$l_{re} = 6\sqrt{A}$ (m) (2.2.20)
<p>Plane jet</p> 		<p>Wall jet</p> 	$l_{re} = 3.0 - 5.3H$ (m) (2.2.21)

Figure 2.2.6 Penetration length of isothermal jets in deep rooms.

In a short room the jet will reach the end wall and be deflected towards the floor where it will turn 90° again and return along the floor. Experiments in conventional rooms ($L/H \approx 2-4$) with isothermal flow show that the maximum velocity in the reverse flow in the occupied zone, u_m , is a simple function of a reference velocity, u_L , which is the velocity of an undisturbed wall jet at distance L from the actual diffuser. The velocity u_L contains information on supply velocity, distance from inlet and geometrical details that influence the initial flow, such as diffuser type and distance from ceiling. The ratio u_m/u_L contains information on velocity decay in the deflected jet which is due to the end wall height and the geometry, as well as information on the velocity level in the recirculating flow which is due to the entrainment into the jet below the ceiling. For plane jet flow the ratio u_m/u_L is rather independent of diffuser dimension and room height, and is equal to 0.7. A circular jet will be deflected downwards at the end wall as a semi-radial jet, so the ratio u_m/u_L depends on the jet width compared with the width of the end wall. A small jet width ($< 0.5B$) results in a radial flow at the end wall and a ratio u_m/u_L of 0.3, while a wide jet ($> 1.6B$) corresponds to plane jet flow and a ratio u_m/u_L of 0.7 [Hestad, 1976]. New diffuser types with a specially designed semi-radial flow pattern may incorporate the sidewall regions in the important part of the jet flow and this may result in values of u_m/u_L above 0.7 in the occupied zone.

The behaviour of a nonisothermal free jet discharged into the open space is predicted rather well by the equations in Figure 2.2.3. However, Murakami *et al.* [1991] showed that it is not always possible for the equations to predict the trajectory of a jet discharged into an enclosed space. This is due to the fact that the air temperature around the jet is uniform in an open space while there is often a vertical temperature gradient in an enclosed space, as is the case in many large spaces. A temperature gradient means that the temperature in the lower region of the space differs from the temperature in the upper region. Thus the temperature difference between the jet and its surroundings is smaller in the lower region. Therefore, a

chilled air jet in an enclosure will not fall as rapidly as it would in an open space with uniform temperature. Thermal jets developing in real rooms are also, depending on the room size, affected by wall and entrainment effects [Grimtlin, 1970; Schwenke, 1975].

When calculating the penetration length of nonisothermal wall jets in confined spaces, Equations (2.2.8) and (2.2.9) can be difficult to use in practice, because different air terminal devices produce different air flow patterns in the area where the jet leaves the ceiling region [Nielsen and Möller, 1985, 1987, 1988]. Jets from some diffusers may travel a further distance Δx along the ceiling (typically about 2-2.5 m) before they flow down into the occupied zone, while other wall jets leave the ceiling very abruptly.

Ceiling-mounted obstacles can influence the development of isothermal wall jets. Obstacles of large enough dimensions can deflect the jet downwards prematurely, which can cause uncomfortable draughts and temperature differences in the occupied zone. A jet will be deflected down if the distance between the terminal and an obstacle of a given height is less than a critical distance, x_c . If the distance is equal to or greater than x_c , then the jet will reattach to the ceiling after passing the obstacle, and if the distance is more than 8 times x_c , then the wall jet will not be influenced at all by the obstacle. Room height also has an influence on the critical height, f_c , of an obstacle, because an initial deflection of a jet needs much space both in height and in the downstream direction to reattach itself to the ceiling. Figure 2.2.7 shows the critical height of an obstacle versus the distance from the diffuser for a plane wall jet [Holmes and Sachariewicz, 1973; Nielsen, 1983], and a for circular wall jet [Nielsen et al., 1987].

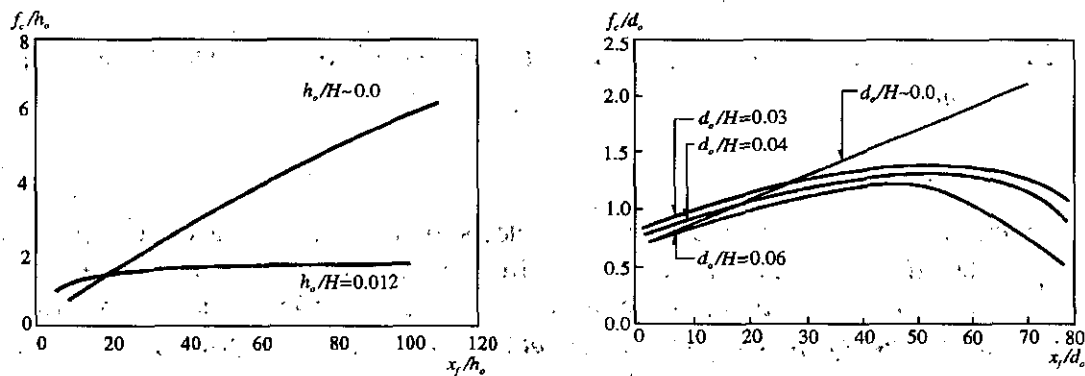


Figure 2.2.7 Critical height, f_c , of an obstacle versus distance, x_p , from the air supply terminal for (a) plane wall-jet flow and (b) circular wall-jet flow.

For nonisothermal flow, the critical height for ceiling-mounted obstacles also depends on the flow's Archimedes number in addition to the geometrical relations mentioned above. A chilled air jet will have a smaller critical height while a warm air jet will have a larger critical height of the obstacle [Söllner and Klingenberg, 1972; Nielsen, 1980].

When a plane air jet or a circular air jet is injected parallel with and close to a surface, the turbulent mixing layer on both sides of the jet entrains air from the surroundings. A lower pressure on the side closest to the surface attracts the jet towards the surface, and so a wall jet is established at some distance from the supply terminal. The effect that generates this deflection is called the Coanda effect [Jackman, 1970]. There is no reliable information about the maximum distance where this effect can occur. It depends on the jet type and the air temperature, with a large maximum distance for plane and/or warm jets and a small maximum distance for circular and/or cool jets. The deflection reduces the jet's flow

momentum; measurements made by McRee and Moses [1967] show that the final momentum can be reduced to 60-70 % of the inlet momentum, which means a reduced velocity level in the whole room.

A free jet that is injected at a certain distance and angle towards a surface will turn into a wall jet when it reaches the surface. This type of jet is called an impinging jet. The development of the wall jet will depend on the angle between the free jet and the surface. A circular free jet will continue as a circular wall jet if the angle is small, and as a radial wall jet if the angle is large ($\sim 90^\circ$). This can be expressed by a change in the factor K_a as a function of the impingement angle, as in Figure 2.2.8 [Beltaos, 1976]. Equation (2.2.2) shows the development of the wall jet after impingement, and the appropriate K_a value can be taken from Figure 2.2.8.

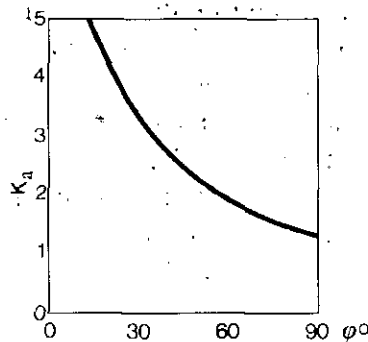


Figure 2.2.8 K_a values for an impinging circular jet as a function of the angle of impingement, ϕ .

2.2.2 Thermal Plumes

Thermal plumes are created above everyday objects such as hot surfaces, equipment and persons, and they transport heat and air upwards from the lower region of a room to the upper region. In designing air distribution systems which use this effect, such as displacement ventilation, it is necessary to determine the amount of air which is transported, and in the case of temperature gradient in the space and/or distributed heat sources, how far the air reaches into the space. Buoyancy generates an upward jet-like flow with a maximum velocity just above the source, where the flow has its narrowest diameter. Air is entrained into the plume such that the width and the volume flow increase with height.

A concentrated heat source creates a circular flow while a line source creates a two-dimensional plane flow. The volume flow in a circular plume can be described by Equation (2.2.23) [Popiolek, 1996], which is based on the analysis of experimental data of several investigators. The equation is strictly valid for $y > d$ where d is the hydraulic diameter of the heat source. However, practice shows that the equation can be used down to a height of $y \approx 2d-3d$ [Kofod and Nielsen, 1990]. The convective heat emission Φ_k can be estimated from the energy consumption of the heat source. For pipes and channels, the convective heat emission is about 70-90 % of the energy consumption. For smaller components it is about 40-60%, and for large machines and components it is about 30-50 %. The location of the virtual origin of the flow can in practice be very difficult to judge but, nevertheless, it is very important for an accurate estimate of the volume flow. It is often assumed that $y_o \approx 2d$ for

concentrated heat sources. In practical situations the position of the virtual origin of the flow can also be found on the basis of a measured (e.g. by smoke visualisation) maximum plume width at a certain distance from the heat source by Equation (2.2.22) [Popiolek, 1996]

$$y_0 = 2.6D_{\max,1} - y_1 \quad (\text{m}) \quad (2.2.22)$$

The volume flow in a two-dimensional plume from a line heat source can be described by Equation (2.2.24) [Skåret, 1986]. In this case, the virtual origin y_0 can be assumed to be 1-2 times the width of the heat source.

Influence of temperature gradient on plume development

Equations (2.2.23) and (2.2.24) are strictly only valid for homogeneous surroundings. If the surroundings have a vertical temperature gradient, the plume will have a lower velocity and volume flow compared with homogeneous surroundings, because the temperature gradient will diminish the buoyancy force. In a room with a pronounced temperature gradient, the buoyancy force will even become neutral at a certain height, y_p , but due to the momentum in the plume, it will continue a short distance until it has reached the maximum height, y_m . The flow will finally return to the height of neutral buoyancy, y_p , where it spreads out horizontally (Figure 2.2.9). Equations (2.2.25) and (2.2.26) can be used to find the values of y_m and y_p respectively [Morton et al., 1956; Mundt, 1992]. The flow rate, q_y , below height y , is only moderately influenced by the temperature gradient.


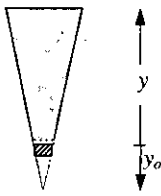
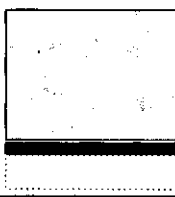
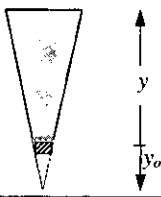
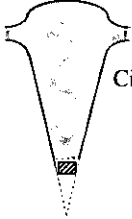
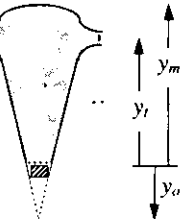
Frontview	Sideview	Velocity Decay/Penetration length
<p>Circular Plume</p> 		$q_y = 0.006\phi_k^{1/3}(y + y_0)^{5/3} \quad (2.17)$
<p>Plane Plume</p> 		$q_y = 0.014\left(\frac{\phi_k^{1/3}}{l}\right)(y + y_0)^{5/3} \quad (2.18)$
<p>Circular Plume</p> 		$y_m = 0.98\phi_k^{1/3}\left(\frac{dT}{dy}\right)^{-3/5} - y_0 \quad (2.19)$
		$y_p = 0.74\phi_k^{1/3}\left(\frac{dT}{dy}\right)^{-3/5} - y_0 \quad (2.20)$

Figure 2.2.9 Volume flow and penetration height of thermal plumes.

Interaction between thermal plumes and influence of walls

If a heat source is close to a wall, then the resulting plume will be attached to the wall due to the Coanda effect. The rate of entrainment is then less than for a free plume. The wall can be considered as a symmetry plane, such that the flow will be similar to one half of the flow in a free plume of twice the convective heat emission. If the heat source is located close to a corner, similar assumptions may be applied, and so the plume can be considered as a quarter of a plume of four times the heat emission. The volume flow in a wall plume and a corner plume can be calculated from Equations (2.2.27) and (2.2.28) [Nielsen, 1988; Kofoed and Nielsen, 1991].

If a number of heat sources are located close to each other, then their thermal plumes may be absorbed into one large plume due to the Coanda effect. The flow from identical sources is given by Equation (2.2.29). The volume flow rate at a given height above two adjacent identical heat sources will only be 26% larger than the volume flow above one of the heat sources if it is separated from the other. In other words, the flow in a merged plume from a large number of heat sources is small compared with the flow in independent plumes with sufficient space for entrainment.

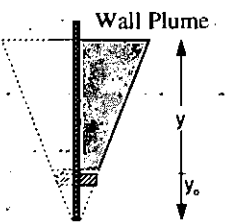

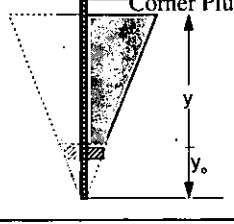

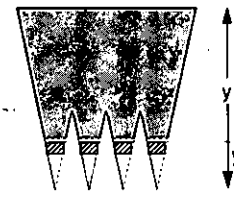

Sideview	Topview	Volume Flow
<p>Wall Plume</p> 		$q_{yw} = 0.0032\phi_k^{1/3}(y + y_0)^{3/2} \quad (2.21)$
<p>Corner Plume</p> 		$q_{yc} = 0.002\phi_k^{1/3}(y + y_0)^{3/2} \quad (2.22)$
<p>Number of Plumes</p> 		$q_{yN} = N^{1/2}q_y \quad (2.23)$

Figure 2.2.10 Volume flow in thermal plumes influenced by walls or plumes from other heat sources.

Plume development in a confined space

The development of a plume in a confined space is affected by the geometry of the space and by the airflow in the space. In a tall slender space the cross-sectional area of the plume may grow to fill the whole cross-sectional area of the space, and then the plume will continue its

vertical motion without entrainment. The height at which a confined flow is established can be calculated from Equation (2.2.30) [Milke and Mowrer, 1995].

$$y_c = 2.82\sqrt{A} \quad (\text{m}) \quad (2.2.30)$$

where A is the cross-sectional area of the space (m^2).

In spaces with a low ceiling height, the distance between the heat source and the ceiling might be too short for the plume to develop according to Equations (2.2.27 - 2.2.29). The minimum distance depends on the type and size of the heat source.

Depending on the conditions, the airflow in the space may act as a co-flow (flowing in the same direction as the plume), boosting the velocity and volume flow rate in the plume, or may conversely reduce the velocity and the volume flow rate. A case with cold downdraught along the walls and a plume in the middle of the space is an example of a space with co-flow airflow conditions [Kofoed and Nielsen, 1990].

2.2.3 Free Convection Flows

Free convection flow arises at surfaces with a temperature different from the surroundings. Surfaces with temperatures different from the room air, are usually either poorly insulated or exposed to solar radiation. The work on free convection flows within Annex 26 has concentrated on cold surfaces, e.g. windows, where the important problem is to estimate the risk of draught in the occupied zone of the enclosure caused by cold downdraught along the glazing. This work focused on estimating maximum velocity and minimum temperature in the boundary layer, as well as the implications on the resulting thermal comfort in the occupied zone. This section discusses the results of the work on boundary layer flow, while the flow in the occupied zone is discussed in section 2.2.4 (Gravity Currents). The results may in most cases be equally applied to warm surfaces, with close accuracy.

The air adjacent to, for example a cold surface, will be cooled by conduction to the surface. This results in buoyant forces, causing the layer to flow downward. This layer of air adjacent to the surface, to which the vertical motion is confined, is called the natural convection boundary layer. The thickness of the boundary layer is zero at the top of the vertical surface, and increases in the downward direction due to entrainment of room air. If the surface is placed in calm surroundings, the boundary layer flow at the top of the surface will be laminar, and at a certain distance from the top it will become turbulent. The ratio between the buoyancy and viscous (friction) forces can be expressed by the Grashof number, defined as

$$Gr_x = \frac{g\beta\Delta t_w x^3}{\nu^2} \quad (2.2.31)$$

In experimental conditions typical of building enclosures [Cheesewright, 1968; Cheesewright and Ierokipitis, 1982] the boundary layer flow is laminar for $Gr_x < 1 \times 10^9$ and fully turbulent for $Gr_x > 1.0 \sim 1.6 \times 10^{10}$. In large enclosures of considerable surface height, the flow is usually turbulent.

Free convection boundary layer flow on a vertical plane surface

The solution of the boundary layer equations for a vertical plane surface in both the laminar and the turbulent cases, after Eckert *et al.* [1951, 1959], gives equations for the maximum velocity (eq. 2.2.32), boundary layer thickness (eq. 2.2.34) and volume flow (eq. 2.2.35),

which are widely used in engineering applications. Laboratory measurements of the maximum velocity in boundary layer flows, Billington [1966], Howarth [1972], Shillinglaw [1977], and Topp and Heiselberg [1996], all show agreement with the theoretical dependence on surface height and temperature difference. However, they found lower velocity levels, i.e. values of the constant. The theoretical value of the constant [Eckert and Jackson, 1951; Eckert and Drake, 1959] was for laminar flow $k = 0.11$ and for turbulent flow $k = 0.10$, while the average values found in the measurements were $k = 0.09$ and $k = 0.07$, respectively. Table 2.2.2 shows equations for maximum velocity, average velocity, boundary layer thickness, volume flow rate, momentum flow and cooling/heating capacity of a boundary layer flow [Andersen, 1996]. In the table, the measured values are used for the maximum velocity and all the other theoretical relations are corrected according to that.

Table 2.2.2 Expressions for prediction of boundary layer flow at vertical plane walls.

	Laminar flow	Turbulent flow	
Maximum velocity (m/s)	$u_{\max} = 0.09\sqrt{H\Delta T}$	$u_{\max} = 0.07\sqrt{H\Delta T}$	(2.2.32)
Average velocity (m/s)	$u_{av} = 0.05\sqrt{H\Delta T}$	$u_{av} = 0.019\sqrt{H\Delta T}$	(2.2.33)
Boundary layer thickness (m)	$\delta = 0.048H^{1/4}\Delta T^{1/4}$	$\delta = 0.11H^{1/10}\Delta T^{1/10}$	(2.2.34)
Volume flow rate (m ³ /s)	$q = 0.0024H^{3/4}\Delta T^{1/4}B$	$q = 0.0021H^{6/5}\Delta T^{1/5}B$	(2.2.35)
Momentum flow (N)	$I = 1.9 \cdot 10^{-4} H^{5/4}\Delta T^{3/4}B$	$I = 1.2 \cdot 10^{-4} H^{17/10}\Delta T^{9/10}B$	(2.2.36)
Cooling/heating capacity (W)	$\Phi = 1.2H^{3/4}\Delta T^{5/4}B$	$\Phi = 0.64H^{9/5}\Delta T^{1/4}B$	(2.2.37)

Free convection boundary layer flow on vertical surface with obstacles

Obstacles such as horizontal glazing frames, on a vertical surface, will influence the boundary layer flow depending on the characteristics of the flow and the size of the obstacles [Heiselberg et al., 1995]. If an obstacle is only small, then the boundary layer flow will reattach (or remain attached) to the surface after passing the obstacle. However, if the obstacle is sufficiently large, i.e. it exceeds a critical width, and if the flow conditions are transient or turbulent, then it will cause the boundary layer flow to separate permanently from the surface, and mix with the room air as a jet. A new boundary layer flow will then be established below the obstacle. In this way a high surface with regularly spaced obstacles will act as a collection of repeated individual flow units stacked on top of each other. The top units supply cold air to the room above the occupied zone, and the risk of draught in this zone will only be determined by the flow conditions at the lowest part of the facade [Topp and Heiselberg, 1996].

The critical width depends on the flow conditions at the wall. Under laminar flow conditions the critical width can be very large. Under transient and turbulent flow conditions, $Gr_c = 3 \times 10^9 - 5 \times 10^{10}$, the critical width is about 0.25-0.30 m. If the size of the obstacle is

below the critical width, the boundary layer flow will not separate from the wall. A recirculation zone will arise behind the obstacle and the boundary layer flow will at some distance reattach to the wall. However, the presence of the obstacle will reduce the maximum velocity in the boundary layer.

Figure 2.2.11 shows the expected development of the maximum velocity in the boundary layer flow according to Equation (2.2.32) at a plane surface of height of 3m and 6m, respectively. Further, velocities are given for measurements on a 6m high surface with obstacles 3m up which have widths of 0.1 m and 0.3 m:

The maximum velocity in the boundary layer flow measured just before the obstacle has the expected value. Below the obstacle, a new boundary layer flow is established, so for an obstacle of width 0.3 m, which exceeds the critical width, it will develop as would be expected for a 3m high plane surface. An additional increment of the obstacle width does not reduce the velocity level further. For an obstacle of width 0.1 m, which is below the critical width, the boundary layer flow reattaches to the surface, and the maximum velocity in the boundary layer below the obstacle is higher than would be observed in a 3m high surface, but it is still below the level for a 6 m high plane surface.

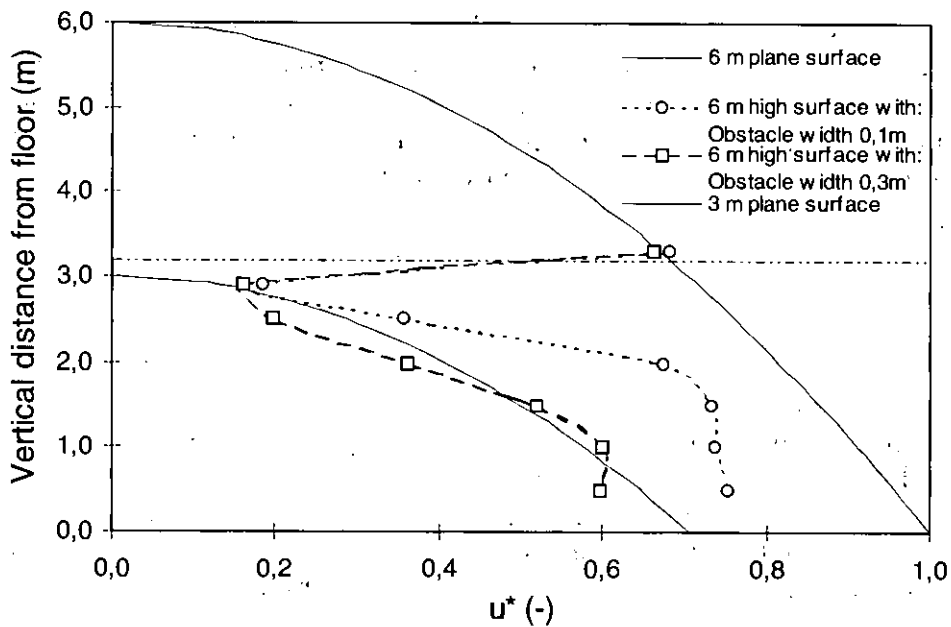


Figure 2.2.11 The measured maximum velocity in the boundary layer flow along a vertical surface with an obstacle of width above and below the critical width, respectively. Measurements are compared with the expected velocity along a plane surface with the heights of 3 m and 6 m. The temperature difference between the surface and the room was 9°C. [Topp and Heiselberg, 1996].

2.2.4 Gravity Currents

Gravity currents are primarily horizontal flows generated by small density differences, and governed by their negative buoyancy. The behaviour of a gravity current is therefore very much different from the behaviour of an air jet. For example the velocity increase above the supply velocity.

Examples of gravity currents generated within large enclosures are: airflow from low velocity devices in displacement ventilation, airflow from opening of doors to the outside or to another room where there is a temperature difference between the exterior and the interior air, and airflow along the floor from a vertical cold surface.

Wilkinson and Wood [1970] showed that a gravity current can be divided into three regions. In the first region the flow entrains fluid in a process similar to flow in a wall jet. This region is followed by a roller region after a certain distance, and the two regions together constitute what in hydraulics is known as a density jump. In the third region, downstream from the density jump, the entrainment fades. The flow in the entrainment region is called supercritical flow, and in the area with diminishing entrainment it is called subcritical flow.

It has not been possible to identify all these elements in the flow from low velocity devices and air flows induced by free convection flows at vertical walls, but the decreasing entrainment coefficient as a function of the distance or the local Archimedes number has been identified for gravity currents in rooms [Nielsen, 1994a; Sandberg and Mattsson, 1993; Heiselberg, 1994a].

Air supply from low velocity devices

In displacement ventilation, air is supplied directly into the occupied zone. The supply openings may either be mounted in the floor producing vertical free jets directed upwards, or they are located along the walls as low velocity air terminal devices. Floor-mounted diffusers must generate very high entrainment to keep the velocity level low close to the inlet. This is usually achieved by supplying a swirl to the flow [Nielsen *et al.*, 1988]. Another possibility is to adopt the whole floor as the supply area, as shown by Akimoto *et al.* [1995]. At large Archimedes numbers the cold air from a wall-mounted low velocity air terminal device accelerates towards the floor due to gravity, and it behaves like a gravity current as it progresses along the floor. This airflow influences the thermal comfort of the occupants, so it is vital to estimate the maximum velocity of the flow along the floor. The velocity level depends on the flow rate to the room, the temperature difference and the type of air terminal device, where especially the height of the device is an important parameter.

The flow from a single air terminal device will be radial partly due to the gravity effect and partly due to the construction of the device, and it will have an almost constant thickness across most of the floor. The maximum velocity, u_x , in the symmetry plane of the flow at distance x is given by Equation (2.2.38) [Nielsen, 1994a].

$$u_x = q_o K \frac{1}{x} \quad (\text{m/s}) \quad (2.2.38)$$

The parameter K (m^{-1}) is given by the diffuser design and the ratio

$$\frac{(T_{oc} - T_o)}{q_o^2} \quad (^\circ\text{C}\cdot\text{s}^2/\text{m}^6) \quad (2.2.39)$$

The temperature difference ($T_{oc} - T_o$) is between the temperature at the height of 1.1 m and the supply temperature. The ratio in Equation (2.2.39) can be regarded as a part of an Archimedes number.

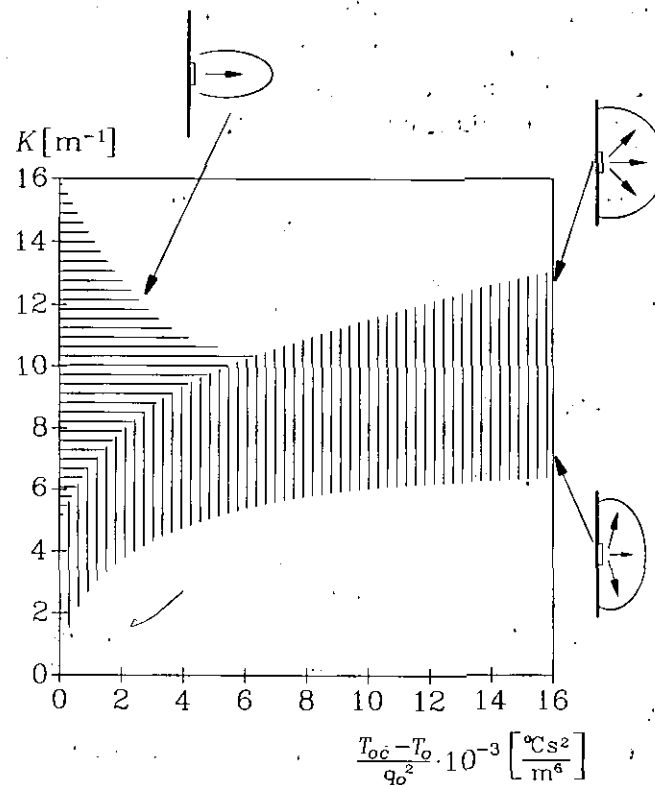


Figure 2.2.12 K -values for low velocity air terminal devices as a function of air flow and temperature difference [Nielsen, 1992, 1994a].

Figure 2.2.12 shows the parameter K versus the ratio given by Equation (2.2.39). The K -value for an air terminal unit with an axial air supply is located in the upper part of the graph. The flow is axial at small temperature differences. The gravity effects turn the flow into a radial pattern at high Archimedes numbers. The upper part of the graph is typical of air terminal devices with a radial/axial velocity distribution, and the lower part of the graph is typical of diffusers with a 'flat' velocity distribution at the diffuser surface [Nielsen, 1992, 1994a]. Figure 2.2.12 is based on diffusers with a height up to 1.0 m and an area up to 0.5 m². Equation (2.2.38) is valid for distances larger than 1.0-1.5 m from the air terminal device.

Airflow induced by convective flow along vertical walls

Free convection flows at surfaces with a temperature lower than the surroundings will produce airflow along the floor. The main concern for such flow is estimating of the risk of draught in the occupied zone and consequently the estimation of the parameters' maximum velocity and minimum temperatures in the flow.

Measurements by Heiselberg [1994a] have shown that the airflow along the floor can be divided into three different zones. The first zone is near the foot of the vertical wall, where the flow turns from a vertical boundary layer flow to horizontal airflow. In the second zone, the flow entrains room air and develops like a wall jet. Here the maximum velocity decreases and the height of the flow increases proportionally with the distance from the virtual origin of the flow. Due to buoyancy, the flow gradually changes and the entrainment rate of room air decreases. In the third zone, both the height of the flow region and the maximum velocity are constant and the entrainment rate of room air is very small.

In a two-dimensional airflow situation the Equations (2.2.40 - 2.2.43) give the maximum velocity and the minimum air temperature in the near floor region of the airflow as a function of the distance to the cold vertical wall, the height of the wall, and the temperature difference between the cold wall and the occupied zone.

$$u_{\max}(x) = 0.055\sqrt{H \cdot \Delta T} \quad (\text{m/s}), \quad x < 0.4 \text{ m} \quad (2.2.40)$$

$$u_{\max}(x) = 0.095 \frac{\sqrt{H \cdot \Delta T}}{x + 1.32} \quad (\text{m/s}), \quad 0.4 \text{ m} \leq x \leq 2.0 \text{ m} \quad (2.2.41)$$

$$u_{\max}(x) = 0.028\sqrt{H \cdot \Delta T} \quad (\text{m/s}), \quad x > 2.0 \text{ m} \quad (2.2.42)$$

$$T_{\min}(x) = T_r - (0.30 - 0.034x)\Delta T \quad (\text{K}) \quad (2.2.43)$$

The expressions are valid for conditions at the cold vertical surface corresponding to Grashof numbers between $1.12 \times 10^{10} - 3.85 \times 10^{10}$, which means that the boundary layer flow at the surface is in the fully turbulent region. The expressions should be used with caution considering that the room geometry influences the development of the flow along the floor. The experiments were performed in a room which was 7 m deep. In a three-dimensional situation, the velocity at the symmetry plane of the airflow along the floor is approximately the same as in the ideal two-dimensional situation. These expressions were compared with measurements of draught in a real atrium, as part of Annex-26; see Section 4.6.3.

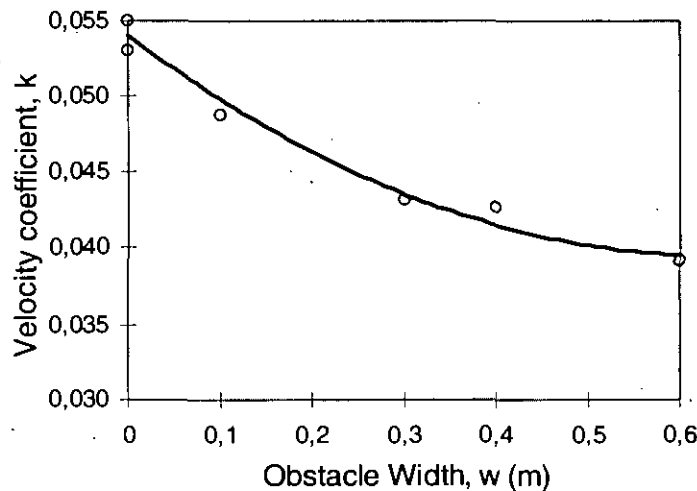


Figure 2.2.13 Maximum velocity in the occupied zone, expressed by the coefficient k , as a function of obstacle width for a 6 m high vertical surface with a horizontal obstacle positioned at 3 m height. The temperature difference between the surface and the room was 9°C. [Topp and Heiselberg, 1996].

The presence of an obstacle on a wall will reduce the maximum velocity in the boundary layer flow and the velocity level in the occupied zone. The larger the obstacle is, the larger the reduction in the velocity level will be. Figure 2.2.13 shows the reduction of the maximum velocity in the occupied zone as a function of the obstacle width expressed by the reduction in the constant, k , in Equation (2.2.40). The constant is reduced from $k = 0.055$ for

a plane surface to $k = 0.040$ for a surface with an obstacle with the width of 0.6 m. The velocity level in the occupied zone found by Equation (2.2.40) and a constant of 0.040 corresponds to the velocity level in the occupied zone caused by a 3m high surface. Therefore, an increase in the obstacle width will not give a further decrease in the velocity level in the occupied zone.

The velocity will only be reduced close to the wall ($x < 1.0-1.5$ m) where the level and consequently the risk of draught is highest, while there is almost no reduction in the velocity level further from the wall, ($x > 2.0$ m).

2.2.5 Exhaust Flows

The air movement in the vicinity of a return opening is called a potential flow. Air moves in a virtually straight line towards the opening (sink) from all directions. This contrasts with the situation near a supply opening, where the jet flow is highly directional due to the conservation of momentum. Consequently, the velocity at a given distance from an extract opening is much lower than the maximum velocity of a supply jet of the same volume flow.

Naturally, momentum flow is also preserved at an extract opening. A wall jet flow which passes near an extract grille will only be slightly deflected because the return grille generates small velocities compared with the velocity in the wall jet. The air that is removed by the return grille will mainly be mixed room air because the jet has a high entrainment and, therefore, contains a high fraction of recirculated room air. Short-circuiting of air is therefore avoided even in cases with a short distance between the supply and extract, for isothermal flow.

Although the extract opening has only a small influence on the velocity level in the room, it may have large influence on the ventilation effectiveness. In order to prevent short-circuiting, the extract must have a high location if the room is ventilated by chilled jets and a low location if the room is heated by a warm air system. Extract openings can also be used to control the pressure distribution in a room or in a building. It is possible to keep contaminated air in a part of a building by extracting enough air in that region to control the pressure distribution. For example, this principle can enclose a catering section in a large room.

An extract opening in a plane surface will, in case of isothermal surroundings, generate a velocity, u_x , at a distance x from the opening as given by Equation (2.2.44). The equation shows that the velocity will be very small at a short distance from the opening.

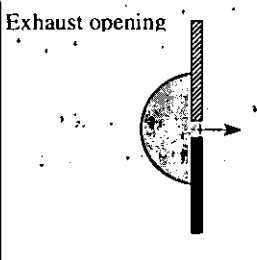
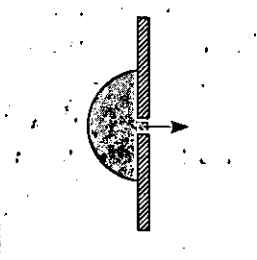
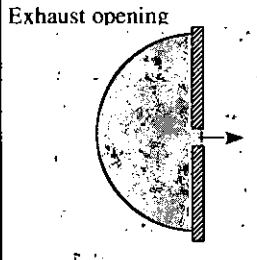
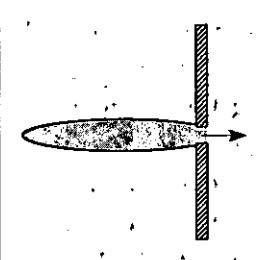
Top view	Side view	Velocity distribution
Exhaust opening 		Isothermal surroundings $u_x = \frac{q_E}{A_E + 2\pi x^2} \quad (\text{m/s}) \quad (2.2.44)$
Exhaust opening 		Surroundings with thermal stratification

Figure 2.2.14 Velocity distribution in front of an exhaust opening in case of isothermal surroundings and surroundings with temperature stratification.

When a temperature gradient is present, the flow in front of an exhaust opening will change, as illustrated in Figure 2.2.14 [Skistad, 1994]. Horizontal air movement will be more pronounced than vertical air movement, because the flow must act against the buoyancy forces in the latter case. This effect can be used as a flow element in industrial areas. Skistad [1993] showed how it is possible, by the correct location of the exhaust openings, to divide a large ship building hall with displacement ventilation into a contaminated part and a part with clean air. Combined heat and contaminant sources often generate a layer of contaminated air in a tall room with a vertical temperature gradient, and it is therefore very efficient to locate the exhaust opening close to this height.

2.2.6 Interaction between Flow Elements

In large enclosures, which often have a complicated geometry, different flow elements occur at the same time, and they may influence each other's flow path. The resulting airflow pattern in the enclosure depends on the individual strength of each element and on the way they act together. It is therefore necessary, during the design of the air distribution system, not only to determine the jet trajectories but also to take into account all sources of air movement, in order to assess whether the interaction between the flow elements changes the flow paths of individual elements, and to estimate if this affects the overall airflow pattern and efficiency of the ventilation system.

In a series of scale model experiments, it was investigated how different flow elements such as horizontal air jets, thermal plumes and free convection flows interact with each other in a large enclosure [Heiselberg, 1994b]. The main emphasis was put on the pathway of chilled horizontal free air jets, and whether the convective flows from both distributed and concentrated heat sources affected the pathway of the jet and the air flow pattern in the enclosure as a function of the location of the heat source and as a function of the heat supplied by the source.

The experiments showed that the penetration depth and the paths of cold jets in enclosures were not influenced by the presence of distributed heat sources, e.g. a heated floor or a heated part of the floor, and were only slightly influenced by the presence of concentrated heat sources. In the latter case the air jet entrained the warm air from the plume above the heat source giving higher temperatures in the jet and therefore it did not fall as rapidly as expected.

As regards the overall flow in the enclosure, the experiments showed that at low Archimedes numbers for the jet, the airflow pattern in the enclosure was determined by the supply air jet. At higher Archimedes numbers, where the strength of the jet was smaller, the pathway of the jet was still independent of the type and location of the source. However, the experiments showed that the airflow pattern in the enclosure was increasingly determined by the convective flows from the heat sources. This means that the thermal comfort and the risk of draught in the occupied zone, because of low temperatures and high velocities in the supply air jet, can be estimated from traditional jet theory, while the air quality and the ventilation effectiveness in the occupied zone depend also on the type, location and strength of the heat sources.

2.2.7 Summary

Flow elements are isolated volumes of the enclosure where the air movement is controlled by a restricted number of parameters, and the air movement is fairly independent of the general flow in the enclosure. This subchapter contains a selection of the most important models for flow elements. The development of these semi-empirical models is based on comprehensive measurement work and experience, but they are often constrained to simplified geometrical and physical conditions. Therefore, Flow Element models give very good predictions in cases that closely match the experimental conditions, while it can be difficult to apply them and get accurate predictions in cases that differ. The greatest assets of these models are that they are easy and fast to use, they require only a few input parameters, and they do not need any investment to use. To apply the models on a particular case, it is necessary first to define the geometrical and physical conditions, to find the appropriate model, to estimate the input parameters and to calculate the results using a pocket calculator or a spreadsheet program. However, at the same time this is the models' greatest disadvantage. Many of the models are only applicable under certain conditions, and together with the limited requirements to the input parameters, the results will not give very detailed information on the airflow conditions but only on the level of a few key parameters of the flow.

Conventionally sized enclosures typically have simple geometry and physical conditions, and the airflow is usually dominated by a single flow element or by flow elements that do not interact with each other. Therefore, an analysis of the airflow by Flow Element models is sufficient in the design of the air distribution system.

Large enclosures on the other hand, often have very complicated geometry and physical conditions, and the airflow is often driven by several flow elements. Flow elements dominate the airflow only locally in relatively small regions of the enclosure and their flow paths are often influenced by other flow elements. In such cases, Flow Element models are useful only in the first stages of the design process, to keep design costs down, and possibly to estimate the airflow conditions in specific areas of the enclosure. More detailed analytical tools (field models) are necessary to estimate the airflow and temperature conditions in the enclosure as a whole. However, Flow Element models are still a very useful guide for comparison and as input when using more advanced models.

2.3 Engineering Models

Achieving energy-efficient ventilation of large enclosures requires not only a deep understanding of the factors governing indoor airflow but also the interaction between the airflow and the thermal behaviour of the building and its environment. Engineers need rapid and accurate solutions to these complex problems, so a wide range of practical engineering tools have been developed, with yet more under development, in response to this demand.

Engineering models are therefore the design engineer's main workhorse. They are typically tailored to fulfil specific design tasks, so there exists a diverse collection of models, ranging from back-of-the-envelope calculations to elaborate computer models describing very complex problems. Although the simpler models, early on in this subchapter, only require a calculator or a spreadsheet program, the majority must be implemented as computer programs. There is an abundance of such software available commercially, too much to mention them all here; anyhow most are based on the same theory described here. All the models covered here were employed to analyse the case studies in Annex-26; many of them are new developments. Their performance in these case studies is documented in Chapter 4.

Engineering models can be likened to lego; an advanced model can be constructed from a collection of simpler specialised engineering submodels. For example, the TRNSYS implementation on page 62 was a combination of the fundamentals of a model for natural ventilation (Section 2.3.1) and a multizone flow model (Section 2.3.2) coupled with a building thermal dynamics solver (Section 2.3.3).

This subchapter is aimed at a wide engineering public; the models here are described in-depth in referenced technical papers or publications.

2.3.1 Fundamental Models

Natural ventilation

The general features of natural ventilation of large enclosures can be described with models derived from the Bernoulli equation. The air pressure distribution across the building envelope can be estimated from the geometry and the wind characteristics (wind pressure) and from the inside-outside temperature differences (stack pressure). Natural ventilation is driven by these wind and stack pressures, constrained by the leakage characteristics of the envelope. It is important for us to be able to predict natural ventilation flow rates, both to estimate energy loss, and to enable natural ventilation control. The ventilation heat loss rate is determined from the natural ventilation rate and the inside-outside temperature difference.

Typical ventilation problems involving natural convection are: preventing overheating in summer, removing smoke during and after fire (i.e. smoke control) and predicting airflow following door-openings. Figure 2.3.1 illustrates the shift in the neutral pressure level (NPL, the level at which the inside-outside pressure difference is zero), when an exhaust is opened near the top of the building.

Basic principles of the model

The Bernoulli equation (which is based on the conservation of energy) is used to calculate air velocities in ventilation openings, while the law of mass conservation applied to an enclosure allows us to calculate the mass flows. The hydrostatic pressure difference caused by the stack effect is

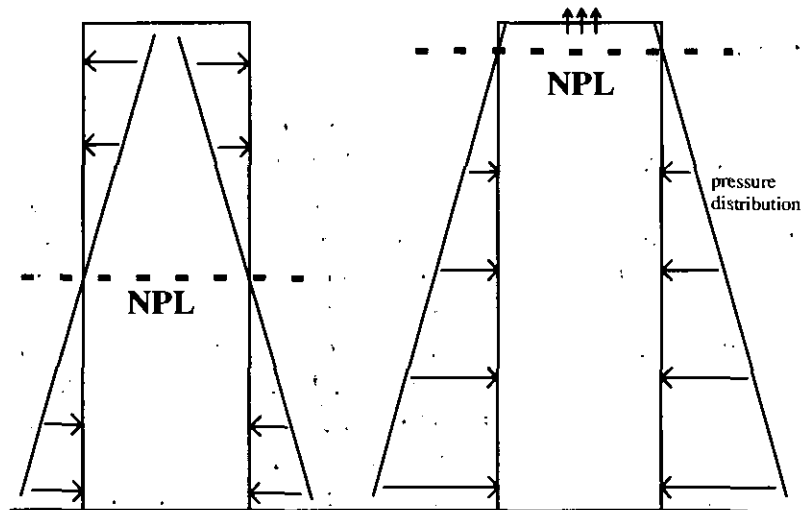


Figure 2.3.1 The typical stack pressure distribution around a heated enclosure. In a building with uniform leakage distribution (left), with an exhaust opening near the top (right).

$$\Delta p_s = (\rho_e - \rho_i)g(z - z_n) \quad (2.3.1)$$

where z_n is the height of the NPL (neutral pressure level). Using the ideal gas law, the air densities and air temperatures are related by $\Delta\rho/\rho = \Delta T/T$, where T is given in degrees Kelvin. The expected stack velocity in an opening at distance $(z - z_n)$ from the NPL follows from the Bernoulli equation:

$$u = \sqrt{\frac{2\Delta p_s}{\rho_e}} = \sqrt{2g(z - z_n)\frac{\Delta T}{T_e}} \quad (2.3.2)$$

At any location on the building envelope, the pressure differential is the sum of the pressure resulting from wind and the stack pressure:

$$\Delta p = \Delta p_s + \Delta p_w \quad (2.3.3)$$

The mass air flow rate through an opening of area A , submitted to a pressure difference Δp , and in which air flows in only one direction, is calculated with Bernoulli's equation as:

$$\dot{m} = \rho C_d A \sqrt{\frac{2\Delta p}{\rho}} \quad (2.3.4)$$

The discharge coefficient, C_d , is determined experimentally and is related to both the contraction of the streamlines near the opening and to turbulent pressure losses. The value for a sharp rimmed orifice is 0.63, which is a useful reference value, knowing that the discharge coefficient C_d depends on the Reynolds number of the opening geometry, and on the cross-sections before and after the opening [Idelchik, 1994].

If several openings are ventilated in series, an effective opening area, A_{eff} can be defined and used for A in (2.3.4):

$$\left(\frac{1}{A_{eff}}\right)^2 = \left(\frac{1}{C_{d1}A_1}\right)^2 + \left(\frac{1}{C_{d2}A_2}\right)^2 + \dots + \left(\frac{1}{C_{dn}A_n}\right)^2 \quad (2.3.5)$$

This expression assumes that there is no interaction between the flows through successive openings. The opening geometries found for inlets and outlets of large enclosures are often pivoting windows for which little data is available [Baturin, 1972; Warren, 1986].

In the case of a pivoting window opened at a medium angle, the effective opening area is calculated with Equation (2.3.5), taking two openings in series (Figure 2.3.2) [Phaff *et al.*, 1980]. The first opening is $A_1 = (H-d)W$ (when frame indent width $g=0$, Figure 2.3.2) and the second opening is the sum A_2+2A_3 .

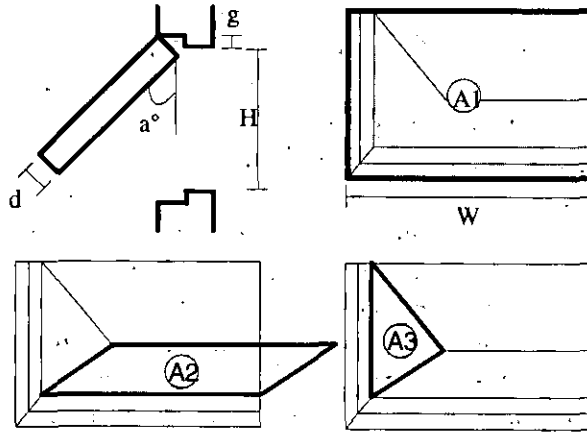


Figure 2.3.2 Areas A_1 , A_2 and A_3 to be considered for the calculation of the effective area of a top-hung window.

For a large enclosure with two openings that are separated vertically by distance H , the position of the NPL can be calculated using Equation (2.3.2) for each opening and applying the principle of mass conservation. When there is temperature stratification, and the indoor temperature variation is $T_i(z)$, it is convenient to define (1) the mean value \bar{T}_i , calculated over the full height H , (2) the mean temperature T_i , calculated over the distance between the NPL and the top opening, and (3) the mean temperature T_b , calculated over the distance between the NPL and the bottom opening. It is a characteristic of stratification that T_b is always smaller than or equal to T_i .

The distance, h , between the centre of the top opening and the NPL (Figure 2.3.3), can be expressed as

$$h = \frac{H}{1 + \left[\left(\frac{C_{d2}A_2}{C_{d1}A_1} \right)^2 \left(\frac{T_e}{\bar{T}_i} \right) \left(\frac{T_b - T_e}{T_i - T_e} \right) \right]} \approx \frac{H}{1 + \left[\left(\frac{C_{d2}A_2}{C_{d1}A_1} \right)^2 \left(\frac{T_e}{\bar{T}_i} \right) \right]} \quad (2.3.6)$$

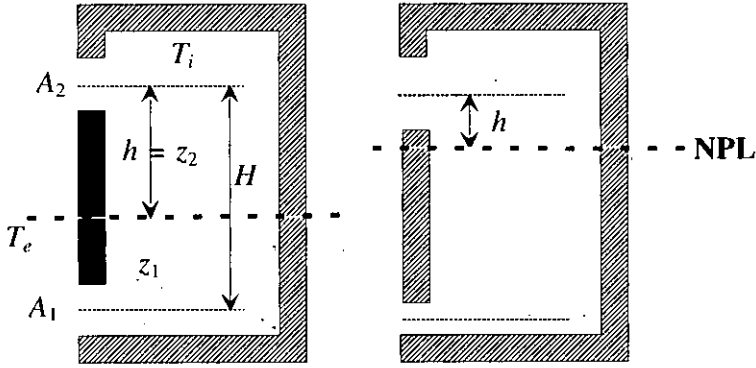


Figure 2.3.3 Determination of the neutral level, when located between two openings.

Where the third term corresponds to the case without stratification. The mean air temperatures T_i and T_b depend themselves on height h but they can be approximated in two iterations. As a first estimate, T_i and T_b are calculated using the third term of Equation (2.3.6) for h , after which these values are inserted in the second term.

Equation (2.3.6) shows that the neutral level tends to move towards the largest opening. If one opening is much larger than the other, or if there is only one opening, the position of the neutral level will be in the opening, and a bidirectional flow will occur at the opening, as in Figure 3.3.2

Temperature stratification within the enclosure (i.e. $T_b < T_i$) causes the neutral level to move upwards, and this has a positive effect on ventilation since fresh air can enter the building at a higher level. The latter effect becomes important when the 'vertical temperature difference', $T_i - T_b$, becomes larger than the horizontal temperature difference, $T_b - T_e$, as is frequently the case during warm weather.

Combining the formula for the position of the neutral level (Equation 2.3.6) and Bernoulli's equation (Equation 2.3.4), the mass flow rate due to the stack-effect through an enclosure with two openings is approximated with:

$$\dot{m} = \rho_i A_2 C_{d2} \sqrt{\frac{2gh(\bar{T}_i - T_e)}{T_i}} = \rho_i A_2 C_{d2} \sqrt{\frac{2gH(\bar{T}_i - T_e)}{T_i \left[1 + \frac{T_e}{T_i} \left(\frac{C_{d2} A_2}{C_{d1} A_1} \right)^2 \right]}} \quad (2.3.7)$$

For bidirectional flow through a single large opening of width W and height H , we get similarly:

$$\dot{m} = \frac{1}{3} \rho_e H W C_d \sqrt{\frac{gH(\bar{T}_i - T_e)}{T_e}} \quad (2.3.8)$$

For the infiltration of air through small openings or cracks, an empirical relationship is used:

$$\dot{m} = C_c \Delta p^n \quad (2.3.9)$$

where C_c and n are coefficients determined by experiment ($0.5 \leq n \leq 1$) but in most cases, $n \approx 0.6$. Air leakage characteristics of building components can be found in the databases of the AIVC [Orme et al., 1994] and of ASHRAE [Colliver et al., 1994].

Once the mass flow rate is known, the ventilation heat loss rate or cooling power is given by

$$\Phi = c_p \dot{m} (T_i - T_e) \quad (2.3.10)$$

The assumption that the internal heat gain, including solar gain, is transferred to the air and is removed by ventilation forms the basis for a simple engineering model that can be used for the sizing of ventilation openings of a large enclosure [Schaelin et al., 1996].

Although the above model is suitable for hand calculations, it is best implemented in a small computer program. Below is a summary of the computer model's input and output parameters, and its case-study applications in Annex-26.

Input parameters

- Distribution of ventilation openings over the building envelope, including size, geometry, vertical position and the discharge coefficient of each opening; it is often possible to group openings and to reduce the data to a simple two-opening configuration
- Vertical air temperature distribution
- Outdoor air temperature

Output parameters

- Neutral pressure level
- Flow direction in each opening, including bidirectional flow
- Velocities and mass flow rates in the openings
- Ventilation heat loss rates

Applications : comparison with experimental data

This model was used to calculate the natural ventilation rates for the De Montfort University Auditorium (subchapter 4.2), the Grafenau-Zug atrium (subchapter 4.6) [Schaelin et al., 1996], the Swissair Hangar [Van der Maas and Schaelin, 1995], and to calculate infiltration rate in the Japanese Experimental Atrium (section 4.3.4) [Schild, 1996].

Applications : comparison with CFD

Comparison with case studies of the De Montfort University Auditorium (subchapter 4.2) and the Grafenau-Zug atrium (subchapter 4.6).

Discussion of the limits of application

The enclosure is treated as a single zone with temperature stratification, and wind effects are neglected. The uncertainties in the calculation are closely related to the uncertainties in the input parameters, which are the discharge coefficients and the air leakage characteristics. The latter is important when the equivalent leakage area is comparable with the size of the ventilation openings (see for example subchapter 4.6). The overall results correspond with the predictions of the multizone air flow model COMIS (Annex 23).

Contaminant concentration and the decay equation**Basic principle**

The law of mass conservation is applied to a contaminant released in a ventilated volume to obtain a first order differential equation. Time-integration gives a solution for the time-dependent concentration $c(t)$ in an enclosure of volume V , which is called the decay equation [Jones, 1994]. If initially (at time $t=0$), the concentration is c_0 , the source strength S and the ventilation rate Q , then :

$$c(t) = c_0 \exp(-\varepsilon n(t-t_0)) + (c_b + \frac{S}{\varepsilon \cdot Q}) \cdot [1 - \exp(-\varepsilon n(t-t_0))] \quad (2.3.11)$$

where $n=Q/V$, and ε is the ventilation efficiency. It is assumed that the ventilation air contains pollutants of background concentration c_b . When the contaminant is CO_2 released by N people, the source strength $S=qN$, where q is the volume of carbon dioxide produced by breathing per person. All quantities are in SI units.

The model can be applied as long as the variables c_0 , n , c_b , S , Q and ε are constant and uniformly distributed throughout the volume. When there is a change in one of the variables at time t_0 , instantaneous values are stored and used as new initial values of the variables in Equation (2.3.11). Therefore t is replaced by $t-t_0$, when $t > t_0$.

It is in principle possible to consider non-uniform spatial distribution of supply air and pollutant sources by dividing the volume into subvolumes over which the ventilation efficiency ε is constant.

Input parameters

The time variation of the contaminant sources, the ventilation rate and the ventilation efficiency inside the considered volume. Also, the concentration in the ventilation air and the initial concentration of the contaminant are needed.

Output parameters

The variation of the concentration of each contaminant with time, averaged over the considered volume.

Applications : comparison with experimental data

In order to evaluate the performance of the decay equation, the model was applied to the Auditorium of the Polytechnic in Torino by calculating the transient history of the CO_2 concentration and comparing with the measurements. Using a ventilation efficiency of $\varepsilon = 0.5$, the agreement between simulated and experimental results was excellent (see subchapter 4.7).

Applications : comparison with CFD

The model was compared with CFD applied to the Auditorium of the Polytechnic in Torino. The overall agreement was good (subchapter 4.7).

Discussion of the limits of application

The model is simple and robust because it is based on the definitions of the basic parameters. It is limited by the fact that the ventilation efficiency must be known in advance and by the assumption that ε is uniform throughout the considered volume. The latter is equivalent to saying that complete mixing takes place making the contaminants spread evenly throughout the space. The decay equation can be applied to parts of large enclosures that can be considered uniform as regards ventilation rate and pollutant release. Alternatively, the model could be

improved upon by using the two-zone model assumption, as explained in Section 2.6.3, though Equation (2.3.11) would then have to be replaced by two coupled equations.

2.3.2 Zonal Flow Models

The last decade or so has seen substantial progress made in modelling the thermo-convective field in enclosures [Allard and Inard, 1992]. This work has aimed to go beyond the isothermal flow model which is appropriate for dimensioning purposes but not appropriate for comparing systems with respect to thermal comfort, energy saving and indoor air quality. One important area of development has been multizone flow models, which are now used in building design with reasonable confidence.

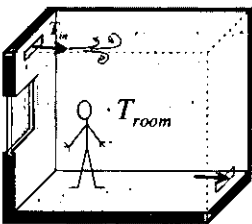
The main principle of zonal models is to split the indoor air volume into several macro-volumes of an assumed (usually uniform) temperature distribution, and to solve the mass- and energy balances in each zone in order to compute the temperature and flow fields. The main problem to be addressed with zonal models is the prediction of air mass flow (and to a lesser extent heat flux) between the macro-volumes.

A first approach was to establish the indoor air flow pattern using specific laws in each zone for flow elements such as jets and thermal plumes. Although good results can be obtained [Inard and During, 1994], its application is limited due to constraints on the air flow pattern.

Therefore, a second approach was proposed [Dalcieux et al., 1992; Wurtz and Nataf, 1994] which is based on the computation of a pressure field with a 'degraded' momentum equation which allows one to link air mass flow between zones with a pressure difference. It is obvious that this method has an application field larger than the first one but the performance was poor for high momentum driving flows. A zonal model with a larger application field and with good accuracy was obtained by coupling these two approaches into a three-dimensional zonal model.

The zonal models used to study the case-study buildings in Annex 26, were of varying complexity and these are presented below as single-zone, one-, two- and three-dimensional zonal models.

Single-zone models



This is by far the commonest and simplest zonal model used in HVAC design today. Most dynamic building models (page , section 2.3.3) treat each room as a single zone. The single-zone assumption, which implies that the airflow in the enclosure is fully mixed, can *not* be applied to most large enclosures. Only in rare cases where a large enclosure *is* fully mixed, maybe due to natural circulation or draughts, will a single-zone model be as accurate as multizone models when predicting air temperature or heating/cooling load, as was observed in two cases in subchapter 4.3.

Attempts have been made to improve the accuracy of single-zone models when applied to model thermal stratification, by using an assumed temperature gradient. One example, the 'linear temperature stratification model' [Kolsaker and Mathisen, 1992], implemented in FRES (page , section 2.3.3), has proven to be closer to reality for the lower zone than a basic single-zone model, but it still shows clear differences for large atria because the model is developed from measurements of pure displacement ventilation.

1D multizone models

Basic principles of the model

When the airflow is similar to piston flow or displacement ventilation, the interaction between the air and the walls is simply described by a succession of zones *along a single ventilation flow path*. In each zone, three models are thermally coupled (Figure 2.3.4): an airflow model, a heat transfer model and a thermal storage model for the wall [Van der Maas and Roulet, 1993; Van der Maas and Maldonado, 1996].

In each zone, the requirement for heat energy conservation in the air node implies that the convective heat gain equals the heat loss by heat transfer, while the heat conservation at the surface temperature node(s) implies that the heat gain by convection and radiation equals the heat loss by heat conduction.

The airflow model, might for example be the two-opening natural ventilation model described in section 2.3.1. Heat transfer is calculated using a prescribed convective heat transfer coefficient and a heat transfer surface area.

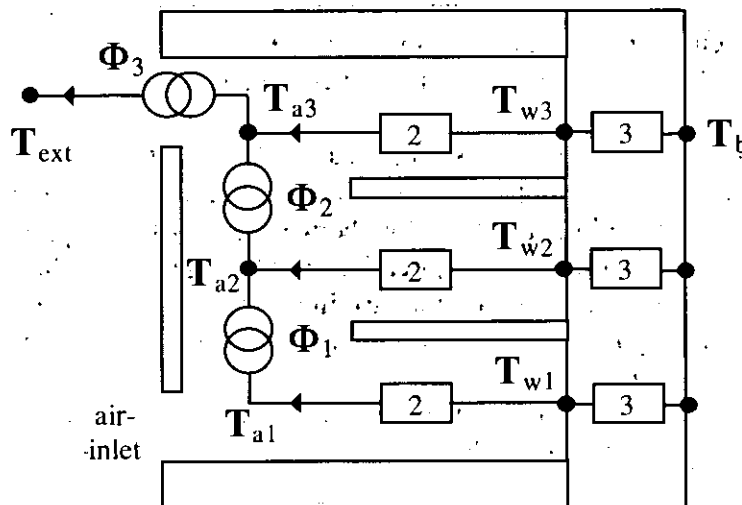


Figure 2.3.4 Multizone cooling model with three zones. (2) are the heat transfer resistances and (3) is the dynamic wall resistance (thermal storage model). The air flow pattern is limited to a single flow path, between inlet and outlet. The heat sources Φ_i represent the combined effect of internal heat gain and ventilation heat loss.

If an enclosure or a zone m is subject to a sudden increase or decrease of convective internal heat flow $\Phi(m)$ (e.g. by opening a window or switching on a heater), the density of heat flow rate at the internal surfaces of the envelope increases by:

$$\varphi = \frac{\Phi(m)}{A(m)} \tag{2.3.12}$$

The thermal storage model can be based on a simple solution of the equation of heat for a semi-infinite medium submitted to a heat flow step function which amplitude is φ [Carslaw and Jaeger, 1959]. The surface temperature, T_w , then varies with the square root of the time:

$$T_w(t) - T_w(0) = \Delta T_w(t) = \frac{2\phi}{b} \sqrt{\frac{t}{\pi}} = \phi R_{dyn} \quad (2.3.13)$$

In this equation, the thermal effusivity, b , is the material characteristic of importance for this model. It is related to other properties by:

$$b = \sqrt{\lambda \rho c} \quad (2.3.14)$$

where λ (W/m·K) is the thermal conductivity of the material, ρ (kg/m³) its density, and c (J/kg·K) the heat capacity. Thermal effusivity is hence expressed in Ws^{0.5}/m²·K. It represents the capacity of the material to quickly absorb large amounts of heat. Heavy and thermally conductive materials have a large thermal effusivity, while insulating materials do not. Thermal effusivity varies over about two orders of magnitude for non-metallic construction materials (from 20 for fibreglass to 2000 Ws^{0.5}/m²·K for concrete).

When there are several materials in the zone, each having a thermal effusivity b_k and covering a surface A_k , an average thermal effusivity is estimated from:

$$b_m \equiv \frac{\sum_{k=1}^n A_k b_k}{\sum_{k=1}^n A_k} \quad (2.3.15)$$

This quantity can also be measured on site [Van der Maas and Roulet, 1993]. The summation should only include those walls which have a time constant which is long compared to the time scale over which the simulation is made.

Any variation of the density of heat flow rate $\Phi(t)$ can be represented by a series of step functions. The variation of the surface temperature of the heat-storing wall is then represented by a sum of solutions like Equation (2.3.12), in which the time t is the time spent since the start of each step.

Input parameters

Common to all zones:

- Single flow path (single inlet and exhaust) air flow parameters (see section 2.3.1)
- Ventilation time schedule (transient)

For each zone:

- Heat gain schedule including solar gains (radiative and convective fraction)
- Convective heat transfer coefficient
- The heat exchanging surface area
- Thermal inertia characterised by the mean thermal effusivity of the zones
- The mean initial temperature of the structure
- External air temperature

Output parameters

Time variation of:

- Air temperatures
- Mean surface temperatures
- Ventilation heat loss rate

Applications : comparison with experimental data

The model has been implemented in a computer program for use as a predesign tool [Florentzou *et al.*, 1996]. A similar single-zone model was used to model the thermal response of the Gjøvik Mountain Hall (subchapter 4.1) [Van der Maas and Kolsaker, 1996] and the De Montfort Auditorium (subchapter 4.2), [Aiulfi and Van der Maas, 1996].

Discussion of the limits of application

The flow model is suitable for displacement, or piston flow type ventilation where a single flow path is defined, from one inlet to one outlet. An enclosure with back-flow between zones, e.g. due to downdraught along walls, requires a 2D or 3D zonal model. However, because there is no radiative coupling between zones, the prediction of temperature stratification in a large space is not reliable. The thermal mass effect depends in the first place on the available surface area for heat transfer between the air and the massive surfaces and in the second place on the surface temperature response. The modelling of the surface temperature response is based on the assumption that the wall behaves as a semi-infinite medium. Whether this assumption is justified depends on the relevant time scale and on the thickness of the heat storing medium. For the evaluation of instantaneous overheating problems, the relevant time scale is of the order of a few hours, and concrete walls of a few centimetres thick play an important role in heat storage. For heat storage over a whole day, only surface areas with thick (>8cm) externally insulated concrete walls are significant and need consideration.

2D multizone models

Basic principles of the model

Unlike 1D zonal models, 2D models can capture the effect of mixing between zones, which is caused by e.g. downdraught, thermal plumes or supply jets. The most basic form of 2D zonal model is the 'two-zone model' (Section 2.6.3), which has a very simple formulation, based on a mixing coefficient, β . The two-zone model is best suited to enclosures with a well defined temperature stratification height, as in large halls in the metallurgical industry, but for other large enclosures it may be better to subdivide the enclosure into more than two zones, such as the model described below.

The proposed model is a time-dependent model for predicting the vertical temperature distribution in a large indoor space such as an atrium [Togari *et al.*, 1993; Arai *et al.*, 1994]. In this model, it is assumed that the horizontal temperature distribution in the large space is uniform except for the regions around the supply air jets and adjacent to the walls. Based on this assumption, the space is vertically divided into zones (see Figure 2.3.5). The main components of air movement in a large space are assumed to be the airflow along the vertical wall surfaces and the supply air jets.

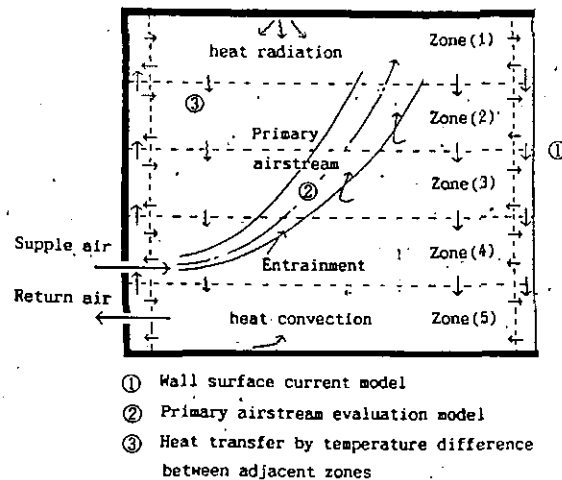


Figure 2.3.5 Schematic of the model used by Togari, (1993) to predict vertical temperature stratification. The space is subdivided into five stacked zones.

Input parameters

The model consists of four parts:

(1) The first is the 'wall surface current model' for evaluating ascending or descending natural convection currents generated by heat flow along the walls using the boundary layer analysis on a flat plate [Eckert and Jackson, 1951].

(2) The second is the 'primary air stream evaluation model' that handles the air streams discharged from outlets as nonisothermal free jets. The path of the supply air jets and the volume of air entrained from each zone are evaluated by means of the free jet theory [Koestel, 1955].

(3) The third is the 'heat transfer factor' C_b , for evaluating the heat transfer generated by the temperature difference between vertically adjacent zones. A value of $C_b = 2.3 \text{ W/m}^2$ has been used [Togari et al., 1993; Arai et al., 1994; Takemasa et al., 1996].

(4) The model also includes a calculation method which treats separately heat radiation and convection on the wall surfaces.

Output parameters

Using these methods, the vertical temperature distribution is calculated by solving a heat-balance equation and an airflow-balance equation in each zone at each time step. Thermal conduction via the surrounding walls is calculated by a one-dimensional progressive finite difference method. The model can also be applied for example, when the space is affected by transmitted solar radiation.

Applications : comparison with experimental data

Subchapter 4.3 reports the comparison between the calculated and measured vertical temperature distributions in a low-rise atrium [Takemasa et al., 1996]. The calculated values were fairly close to the measurement results.

Applications : comparison with CFD

Comparison with CFD was made by Kondo and Miwa [1992].

Discussion of the limits of application

It is difficult to apply the model to regions where a supply wall-jet plays an important role, because supply air streams are assumed to be free jets in the model.

3D multizone models

Basic principles of the model

The indoor air volume is split into isothermal zones assuming a three-dimensional Cartesian grid. For each zone, the mass and energy balances are written. In order to evaluate the air mass flows, two zone types are used: (1) a standard zone or (2) a flow element zone. Figure 2.3.6 illustrates the used zone types. Each standard zone is assumed to have a uniform temperature and pressure; the mass air flow between two zones i and j is computed in a different way when considering a vertical or a horizontal frontier [Inard et al., 1996]. For a vertical frontier:

$$\dot{m}_{ij} = K\rho_{ij}A_{ij}(P_i - P_j)^n \tag{2.3.16}$$

and for a horizontal frontier,:

$$\dot{m}_{ij} = K\rho_{ij}A_{ij}\left[P_i - P_j - \frac{1}{2}(\rho_i h_i + \rho_j h_j)g\right]^n \tag{2.3.17}$$

In cooled, heated or ventilated enclosures the driving flows are jets, thermal plumes or boundary layers. So, in order to represent such flows as well as possible, flow element models based on an integral analysis are included in the model. At present, models have been included for:

- horizontal nonisothermal wall jets
- thermal wall plumes issued from heat sources
- thermal boundary layers

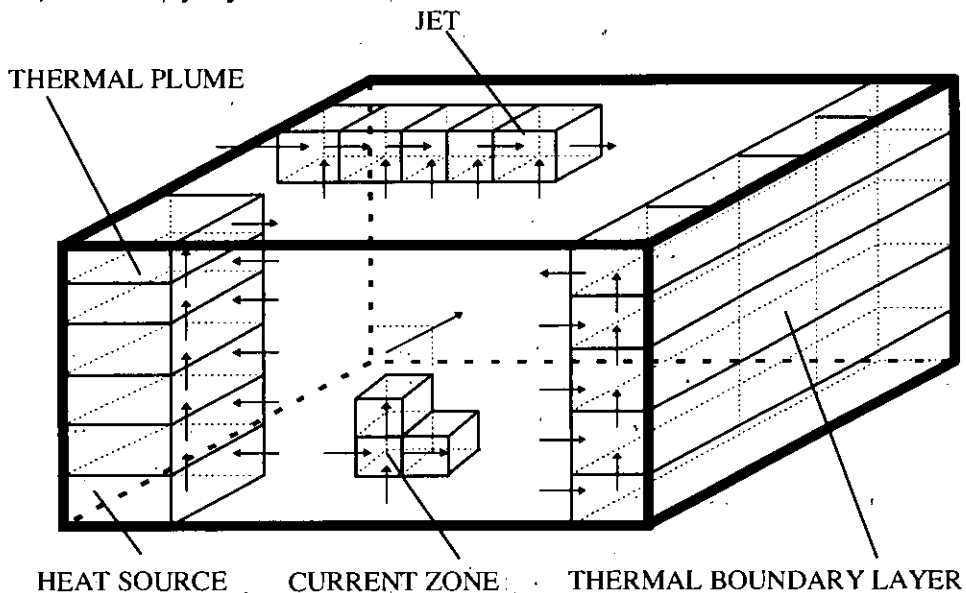


Figure 2.3.6 3D zonal model: Qualitative presentation of the used zone types.

So, for zones with flow elements, specific laws are used in order to compute air mass flows between two zones. For example, these laws could be:

- Horizontal nonisothermal linear wall jets [Rajaratnam, 1976]:

$$X_s = 0.74b_o Ar_o^{-2/3} \tag{2.3.18}$$

$$Ar_o = \frac{g\beta\Delta T_o b_o}{U_o^2} \quad (2.3.19)$$

$$\dot{m}(x) = 0.25\dot{m}_o \left(\frac{x}{b_o}\right)^{\frac{1}{2}} \quad (2.3.20)$$

- Thermal wall plumes originating from a linear heat source [*Liburdy and Faeth, 1978*]:

$$\dot{m}(z) = 0.009\Phi(z)^{\frac{1}{3}}(z - z_o) \quad (2.3.21)$$

- Thermal boundary layers [*Allard et al., 1990*]:

$$\dot{m}(z) = 0.004\Delta T^{\frac{1}{3}}z \quad (2.3.22)$$

In the future, flow element models for free thermal plumes and vertical nonisothermal jets will be included. The solution of the nonlinear system of equations based on mass and energy balances for each zone, provides the pressure and temperature fields. Furthermore, considering a pollutant as a passive scalar, concentration fields can also be computed.

Input parameters

- Mesh description: number of zones and dimensions
- Boundary conditions at inner surfaces: temperature, convection coefficient
- Supply/exhaust openings: locations, dimensions, temperature, flow rate (supply openings)
- Flow element zones:
 - Jets*: location, type, entrainment constant, penetration length constant
 - Thermal plumes*: location, heating power, entrainment constant, virtual origin, Stanton number, Froude number
 - Thermal boundary layer*: location, entrainment constant
 - Pollutant sources*: location, source concentration

Output parameters

- Temperatures
- Pressures
- Concentrations
- Convective heat fluxes

Applications : comparison with experimental data

The model was applied to the Experimental atrium (subchapter 4.3) and the Fibreglass factory (subchapter 4.4) [*Inard et al., 1996*].

Applications : comparison with CFD

The comparison was made for to the Fibreglass factory case study (subchapter 4.4).

2.3.3 Coupling with Building Dynamic Thermal Models

Airflow in large enclosures depends critically on the thermal boundary conditions such as surface temperatures and heat fluxes at the surfaces bordering the space. For the calculation of detailed air flow fields, surface temperatures are usually needed as input parameters. To

calculate these strongly time-dependent surface temperatures, a building dynamic thermal model can be used. However, because of the heat transfer between the wall surfaces and the air, the airflow model and the building thermal model must be coupled.

The various approaches that have been used in the Annex-26 to solve this problem for large enclosures, are presented in this section.

Program TRNSYS

Introduction

TRNSYS is a transient simulation program that allows the simulation of different energy systems coupled with the dynamics of buildings. Each building can be separated into different zones where each zone is coupled with the adjacent ones by conduction through walls and by mass transfer through ventilation openings.

Many different energy systems can be modelled (e.g. solar collector, energy storage system). The ability to simulate HVAC systems coupled with building dynamics is fundamental in order to predict and analyse energy consumption of a building before it is built or retrofitted.

The program is modular and can accept new subroutines. This means that special models representing e.g. a new component, can be incorporated without difficulty. For example, to analyse the energy performance of displacement ventilation in comparison with mixing ventilation, a very simple zonal model was developed with TRNSYS.

A special version of COMIS (the Multizone air infiltration program of Annex 23), was developed to run with TRNSYS, to couple both airflow and thermal simulation models. This coupled model was then used in Annex-26 case-studies.

Basic principles of the building model

The building model is a component of the TRNSYS program that models the thermal behaviour of a building with up to 25 thermal zones. The temperature of the air in each zone is assumed fully mixed. The model determines the energy balance by solving the following equations: For each zone i , the net heat gain to the air, Φ_i , is expressed as:

$$\Phi_i = \Phi_{surf,i} + \Phi_{inf,i} + \Phi_{v,i} + \Phi_{g,c,i} + \Phi_{cplg,i} \quad (2.3.23)$$

where

- $\Phi_{surf,i}$ = Net heat transfer by convection from all inside surfaces
- $\Phi_{inf,i}$ = Air infiltration heat gain
- $\Phi_{v,i}$ = Ventilation heat gain
- $\Phi_{g,c,i}$ = Internal convective gain
- $\Phi_{cplg,i}$ = Gains due to convective flows from all adjacent zones

Energy transmission

The walls are modelled according to the transfer-function concept [Mitalas and Arseneault, 1974], where each wall is subdivided into layers to solve one-dimensional heat transfer. The long-wave radiation exchange between surfaces within the zone and the convective heat flux from the inside surfaces to the zone air, are calculated using a method called 'star network' [Seem, 1987]. Simple area ratios are used to calculate view factors between surfaces, so that the radiation model is not geometrical.

The different types of wall that can be defined are: (1) external walls, (2) internal walls, and (3) walls between zones. The temperature of the wall surfaces can be fixed. The

internal walls play a role in solar- and internal gains distribution, and their mass contributes to thermal storage (As both its surfaces are in the same zone, there are no conduction losses associated with the wall!).

A window is considered as a wall with no thermal mass, it is partially transparent to short-wave solar radiation, but opaque to long-wave internal radiation exchange and gains. Windows can only be placed on the outer walls or roof.

Solar radiation and distribution

The total solar gains to any zone i are given by :

$$\Phi_{\text{sol-}i} = \sum A_s I_{t,s} \tau_s \quad (2.3.24)$$

where

- Σ = summation over the windows of zone i
- A_s = Surface of the window
- $I_{t,s}$ = The solar radiation incident upon the surface
- τ_s = The overall transmittance of the surface

The transmittance of the surface is normally calculated by a separate subroutine taking into account the type of glass, the incident angle and the type of (internal or external) solar shading device. The incident solar radiation is distributed over the surfaces according to absorptance-weighted area ratios. Only windows can have non-zero transmittance.

Other subroutines

Separate TRNSYS subroutines calculate :

- The solar radiation incident upon the window surface
- The effect of shading devices including overhangs, wingwalls and solar protection devices
- Air movements between adjacent zones
- Air infiltration
- Ventilation (natural or mechanical and air conditioning)
- Internal heat gains
- Heating or cooling
- Daylighting and artificial lighting

Typical inputs

- Surface orientation and window properties (absorptance, transmittance)
- Surface and wall compositions as well as absorptance for short-wave radiation
- Infiltration losses
- Air exchange rate and supply temperature for mechanical ventilation
- Climatic data (hourly values)
- Internal heat gains
- Air temperature set points (if applicable for heating or cooling)

Standard output parameters

- Air temperature of each zone
- Sensible energy load (if applicable, for heating and cooling)
- Total convective heat transfer between the zone surfaces and the air
- Infiltration heat gain

- Ventilation heat gain
- Gain due to convective coupling with adjacent zones
- Internal convective gains
- Change in internal sensible energy of zone air since beginning of simulation
- Humidity of zone air
- Latent energy load (if applicable, -humidification, +dehumidification)
- Net latent energy gains
- Total solar energy entering through windows
- Total short wave radiation absorbed by all inside surfaces and separately by all outside surfaces
- Optional outputs include surface temperatures and heat fluxes

Application of TRNSYS

In the framework of Annex 26 the program has been applied to evaluate displacement ventilation in large enclosures and the importance of temperature stratification for the natural ventilation of atria.

Further, the coupling of TRNSYS with COMIS [Dorer and Weber, 1994] enabled the study of energy consumption for the auditorium of the De Montfort University (subchapter 4.2) [Aiulfi and Van der Maas, 1996], with either a natural or mechanical ventilation system. The energy consumption for the latter included the energy for heating and cooling, and the electricity to run the fans.

Program FRES

Basic principles of the model

- *Building constructions:* Walls have 2 internal nodes and 2 surfaces as standard, with the option for more than two nodes
- *Windows:* One-layer equivalent inner glass, no thermal mass
- *Rooms:* Full radiation model. Linear radiative heat transfer is default, with the option for non-linear heat transfer. No option for detailed view factors. Constant convective heat transfer film coefficients as standard, with some nonlinear correlations available (option). Thermal mass is considered for room air. Internal load according to time schedules. Local heating and cooling
- *Four room types:* Stratified (a linear temperature stratification model), Active (single fully-mixed zone), Inactive, and Outdoor
- *Ventilation system:* Rotating heat exchanger, heating coil, wet (or dry) cooling coil, fans, and vapour humidifier. Simple models. Fixed component positions
- *Air flow:* Specified separately as 'air paths' following closed circuits with individual time schedules
- *Control:* Ideal control of limited heat sources and cooling sources with individual thermostat setpoints. Heating/cooling sources are local or central (coil heat input)
- *Short-wave radiation:* Solar data calculated according to ASHRAE using cloudiness factors. No heat absorbed in outer opaque surfaces (and no option for sol-air temperature). Windows modelled according to the ASHRAE standard. Absorption in inner surface of windows considered. All transmitted radiation is considered diffuse.

Simple two-step calculation of distribution to room surfaces. Back transmission through windows considered. Window facades between rooms may be defined

- *Climatic data:* Temperature, humidity and cloudiness. Automatic generation of single 24 hour period (Sinus) for temperature and humidity. Climatic file with a special format for single years, available for many sites in Norway, and a few sites in other countries
- *Solution method:* One-dimensional finite difference method for the building constructions, solved with an implicit Euler using 1 hour time step for the whole model. Complete direct solution method partly utilising matrix sparseness

Model requirements (input and output parameters)

- *Wall input :* Area, heat resistances and capacities, film coefficients, emissivities
- *Windows input:* Heat resistance, film coefficients, total transmission, direct transmission
- *Room input:* Volume, internal loads, max. heating and cooling, thermostat setpoints.
- *Model output:* Temperatures, surface heat flows, solar heat load, internal heat load, utilities. Single values may be requested for further post processing
- *Graphical presentation:* Specialised presentations of thermal comfort, temperatures, loads and energy use

Applications: Comparison to experimental data

The linear stratification model has been compared to the ELA atrium reference case study and to the Gjøvik rock cavern (subchapter 4.1) [Van der Maas and Kolsaker, 1996].

Discussion of the limits of application

FRES is a tool especially intended for studying the performance of a building with limited HVAC utilities in a certain climate. Design of installed cooling is one of the main purposes of the program. The limited geometry input makes it hard to forecast the correct solar heat load for complex and even simple geometries. The one-hour time-step makes it unsuitable for analysing control systems, and also detailed studies over shorter periods than 24 hours.

2.3.4 Discussion and Conclusions

The engineering models presented in this chapter have been applied successfully to several large enclosures, so the following conclusions can be drawn.

- It is often possible to use simple airflow models to provide answers to specific questions, such as natural ventilation design
- Sound engineering judgement is needed to determine which model is most appropriate to study a specific problem, and to apply the model successfully
- Temperature stratification in large enclosures can be predicted with some zonal models but the result depends very much on the definition of the zones and the way zone input data are provided
- Temperature stratification is closely related with the distribution of both heat gain and thermal mass and requires the use of a building thermal model

A continued effort is needed to demonstrate the application of these models to practical design cases and to compare the predictions with on-site measurements.

2.4 Field Models

2.4.1 Introduction to Field Models

Computational Fluid Dynamics (CFD) programs are described as field models, or microscopic models, as they predict velocity, temperature and other flow properties throughout a whole space, with a high degree of resolution. In contrast, simpler, macroscopic models have a much lower resolution (in the case of zonal models) or provide an empirical picture of only individual elements of the flowfield (in the case of flow element models).

This subchapter reviews aspects of the CFD (field model) technique of particular importance to modelling airflow in large enclosures, and provides some guidance for its use. CFD is a large software system composed of many subsystems, and hence its use demands an insight into topics such as HVAC, computational mathematics, fluid dynamics and turbulence statistics. The successful application of CFD to HVAC design requires a high degree of specialised knowledge and sound engineering judgement based on experience. However, we have targeted this subchapter not at CFD specialists, but at non-specialists, such as air-conditioning engineers/researchers, designers and architects. Therefore, complete details of the CFD technique cannot be given here, only an overview. We hope this introduction to CFD will enlarge the scope of its routine application to indoor environmental engineering. For additional reading on CFD applied to indoor airflow, we suggest Awbi [1991, 1989], Jones and Whittle [1992], and Murakami and Kato [1987, 1989, 1991].

Historical development of field models

The technique of applying Computational Fluid Dynamics (CFD) to HVAC design has matured greatly in the last few years. CFD has become a powerful tool for the design of indoor climate control. Today, user-friendly CFD programs are available, including versions tailored for building environmental design. CFD is particularly useful when it is coupled with the simulation of solar- and long-wave thermal radiation, as well as heat conduction through walls.

Although basic research into applying it to room airflow problems started about 20-25 years ago, it is only in the last decade that CFD has become practical for real design applications. This advance has been aided by the rapid evolution of computer technology. Further advances in computer hardware and software technology, combined with the decreasing costs of computing, will undoubtedly make CFD a more accessible and attractive design tool in future. The past, present and expected future stages of this remarkable development of CFD are given below:

Past stage: Basic research

- 2D (two-dimensional) isothermal laminar flow simulation for a room with simple geometry, under steady-state conditions
- 2D isothermal turbulent flow simulation
- 2D nonisothermal turbulent flow simulation

Present stage: Practical application of CFD to real HVAC design

- 3D nonisothermal turbulent flow analysis
- As above but for rooms of complex geometry or for large enclosures

- As above but coupled with radiative and conductive heat transfer simulation (i.e. wall heat transfer depends on external ambient conditions, internal convection and radiation exchange)

Future stage: Current areas of research and development

- Interactive analysis by microscopic simulation (CFD) and macroscopic simulation (flow network model)
- Thermal comfort analysis, with a computational thermal mannequin, by CFD coupled with radiative and conductive heat transfer simulation
- Time-dependent analysis by LES (Large Eddy Simulation)
- Simulation of fire and smoke movement

Micro vs. macro models

The two main types of computational methods for modelling airflow in enclosures, macro (i.e. zonal) and micro (i.e. CFD) simulation, are founded on the same principles. In both methods, the space is divided into smaller control volumes (cells), and the airflow is calculated numerically by applying the laws of conservation of mass, energy, etc. on each cell. But the similarity ends here.

Theoretical basis of macro models and their limitations

Macro (i.e. zonal) simulation is based on the conservation laws of mass (continuity equation) and energy (Bernoulli's equation). Macro modelling uses far larger cells than does micro modelling. Representing the flowfield in this way, with very large cells, means that the small-scale variations within the cells are not resolved, and their contribution to the large scale properties are ignored, or somehow replaced by empirical relationships that are strictly valid only in specific cases. Three-dimensional fluid motion is characterised only by the volume flow rate through each cell. Therefore, the correspondence between the model's predictions and reality depends critically on the accuracy of the modelling assumptions (such as total pressure drop coefficient for flow past constrictions). And, of course, the fine scale motion within the cells cannot be analysed.

Theoretical basis of micro models

Micro or field models (i.e. CFD) are based on the conservation laws of mass (continuity equation), energy (internal-energy equation) and momentum (Navier-Stokes equations), collectively called the governing equations for fluid flow. Micro models use far smaller cells than do macro models, such that the flow properties can be assumed to be uniform in each cell, or if they are not uniform, they can be interpolated with a simple linear function.

If the assumption of uniform/linear cell properties is strictly preserved, micro models founded on the basic governing equations can give very accurate results. This modelling approach is called DNS (Direct Numerical Simulation, or Direct Navier-Stokes Simulation), and is described on page 81 (Turbulence modelling theory). Admittedly, this approach requires cells of minute size, and is thus computationally far too intensive to be feasible for room airflow problems.

Practical micro simulation therefore uses larger cells than for DNS. To compensate for the larger cells, some form of statistical turbulence modelling must be implemented in the governing equations to capture the effect of subcell turbulence. Various kinds of turbulence models have been developed.

Problems peculiar to modelling large enclosures with CFD

There exist many difficulties in simulating the flowfield in large enclosures with CFD. Large enclosures are more difficult to model than conventionally sized enclosures. These difficulties are due mainly to the following two factors:

- (1) the large size of the enclosure
- (2) the flowfield is very complicated

(1) The large size of the enclosure

When the space is large, we are forced to conduct a simulation with larger computational cells (i.e. a coarser grid) due to limited computing capacity. For example, a large room of 10m×10m×10m is discretised into an array of 100×100×100 (=10⁶) computational cells. One cell would be 10cm wide, which is rather too large to model the turbulent flow field accurately. Using a coarse grid also causes various types of numerical errors, as will be discussed later. The most important point in contriving simulations is therefore to balance the requisite prediction accuracy and the computer resources needed to achieve that accuracy.

Moreover, as a result of the large size, the airflow is typically predominantly thermally-driven, since the momentum of supply jets diminishes with throw distance, whilst the momentum of buoyant plumes increases with height. This is augmented by the fact that large enclosures typically have a high degree of thermal coupling with the external environment (i.e. large area of external walls). Also, due to the large size, radiative absorption by water vapour in the space might become significant. It is therefore especially important to accurately model surface/air heat transfer processes, such as natural/mixed convection, solar radiation, long-wave thermal radiation transfer (infrared), heat transfer through external walls, and structural heat storage. The accurate prediction of natural convection in CFD is difficult. All these processes have been studied in Annex 26.

(2) The flowfield is very complicated

The complicated flowfield in a large enclosure is characterised by the following phenomena:

- An elliptic flow composed of separation, reattachment, circulation, etc.
- Anisotropic, highly three-dimensional flow
- Nonisothermal flow, sometimes with pronounced thermal stratification. Typically, the airflow in large enclosures is predominantly buoyancy-driven

Accurate prediction of such a turbulent flowfield is very difficult. The popular $k-\epsilon$ turbulence model sometimes fails to give reasonable results in the simulation of such flowfields. One aim of Annex-26 has therefore been to evaluate the accuracy of different CFD models in relation to these points, by comparison with experimental data from case study buildings.

2.4.2 Numerical Method

All variants of CFD (field model) methods are based on the governing equations for fluid flow (sometimes referred to as the Navier-Stokes equations), which have been known for over 150 years. These equations are derived from the fundamental laws of conservation of mass, energy and momentum. The governing equations are highly nonlinear and coupled so they cannot be solved using analytically mathematics unless extreme simplifications are imposed, and the solution would therefore be unreal. Instead, the equations must be solved numerically by discretising them into a set of algebraic equations to be solved by computer. There are many CFD methods, the oldest of which is the vortex method which assumes inviscid flow.

However, for a given ventilation problem, the computational result should be the same irrespective of the CFD method used, provided that the same treatment is given to turbulence, boundary conditions, and discretisation (i.e. grid size and numerical integration).

The choice of numerical procedure to reach the solution of the system of equations is very important, especially when modelling large enclosures, as it can be slow or difficult to achieve a solution if the wrong method is chosen. It is therefore important for the CFD user to have insight into the characteristics of computational methods and computational grid systems as well as the processes occurring in the physical flowfield.

The governing equations for fluid flow

To give the reader an insight into the complexity of solving a ventilation problem, and for the sake of completeness, the governing equations are given below, in simplified form, and using tensor notation. The most significant simplification here is the Boussinesq approximation, which assumes that the fluid is incompressible, i.e. the variation in density is neglected. This approximation is valid for small temperature variations, which is reasonable for room airflow. The governing equations are characterised as a set of transient, coupled and nonlinear, elliptic, partial differential equations of second order. Turbulence modelling requires the solution of additional transport equations not shown here.

Continuity equation :

$$\frac{\partial u_i}{\partial x_i} = 0 \tag{2.4.1}$$

Energy transport equation :

$$\rho c_p \left\{ \underbrace{\frac{\partial \theta}{\partial t}}_{\text{transient term}} + \underbrace{\frac{\partial}{\partial x_i} (u_i \theta)}_{\text{convection term}} \right\} = \Gamma \underbrace{\frac{\partial}{\partial x_i} \left(\frac{\partial \theta}{\partial x_i} \right)}_{\text{diffusion term}} + \underbrace{S}_{\text{source term}} \tag{2.4.2}$$

Momentum (Navier-Stokes) transport equations (3 equations, for x,y,z directions) :

$$\underbrace{\frac{\partial u_i}{\partial t}}_{\text{transient term}} + \underbrace{\frac{\partial u_i u_j}{\partial x_j}}_{\text{convection term}} = - \underbrace{\frac{1}{\rho} \frac{\partial P}{\partial x_i}}_{\text{pressure gradient}} + \underbrace{\nu \frac{\partial}{\partial x_j} \left(\frac{\partial u_i}{\partial x_j} + \frac{\partial u_j}{\partial x_i} \right)}_{\text{diffusion term}} - \underbrace{g \beta \Delta \theta \delta_{i3}}_{\text{buoyancy term}} \tag{2.4.3}$$

where

x_i = spatial coordinate components ($i=1,2,3$: x,y,z directions)

u_i = velocity vector components

ρ = density

c_p = specific heat capacity

θ = temperature

Γ = thermal conductivity

S = heat source

ν = viscosity

- β = coefficient of volumetric expansion
 δ_{ij} = Kronecker delta

The most basic 3-D nonisothermal airflow problems (i.e. laminar airflow), therefore require 5 governing equations to be solved: the continuity equation (conservation of mass), the energy equation, and the three Navier-Stokes equations (conservation of momentum in x , y and z coordinate directions).

Methods of discretisation

A wide variety of discretisation methods can be used to represent the governing equations in computational fluid dynamics. They fall into four categories:

- (1) finite difference method
- (2) finite volume method (FVM)
- (3) finite element method (FEM)
- (4) spectral method.

The field of computational structural dynamics (i.e. structural/mechanical component design) makes use of one predominant discretisation method, the finite element method (FEM). In contrast, the field of computational fluid dynamics makes use of many discretization methods, though the finite volume method (FVM) is the most widely adopted, as it balances computational efficiency with flexibility of grid shape.

The finite difference method is computationally efficient, though its application is limited to orthogonal grids. On the other hand, FVM and FEM have the advantage, from their original formulations, that the grid can more easily be adapted to any boundary shape, using unstructured grids. The computational efficiency of FEM has recently been improved by adopting the same approach as the MAC procedure used in the finite difference method (see page 73). The finite volume method, which is similar to the finite difference method, can be applied with a body-fitted coordinate (BFC) grid or even an unstructured grid system, and thus has the advantages of both the finite difference and finite element methods. The spectral method is not widely used for ventilation applications, and will not be discussed further.

(1) Finite difference method

This method is widely used in CFD as it is computationally efficient. In order to discretise the partial derivatives of the governing equations, a flowfield variable (e.g. temperature, velocity etc.) can be expressed in terms of a Taylor's series expansion about the point defined by the derivatives in Figure 2.4.1.

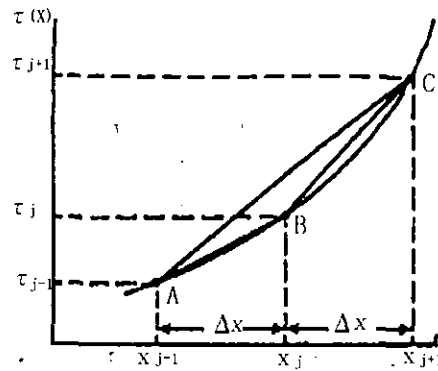


Figure 2.4.1 Derivatives used in a Taylor's series expansion.

The concatenated Taylor's series at point $j+1$ is

$$T_{j+1} = T_j + \frac{\partial T_j}{\partial x_j} \Delta x + \frac{\partial^2 T_j}{\partial x_j^2} \frac{\Delta x^2}{2} + \text{higher order terms} \quad (2.4.4)$$

If the second order and higher terms are discarded, a finite difference approximation of the temperature gradient in the above figure becomes:

$$\frac{\partial T_j}{\partial x} = \frac{(T_{j-1} - T_{j+1})}{2 \cdot \Delta x} \quad (2.4.5)$$

In the finite difference method, various levels of accuracy can be achieved by including higher order terms from the Taylor's series in the computational scheme. But incorporating higher order terms slows down the computation.

(2) Finite volume method (FVM)

This method is very similar to the finite-difference method. In the finite volume method, the algebraic difference equations are formulated by applying the conservation laws (of mass, energy or momentum) directly to a small control volume. The finite volume method is therefore based on an *integral approach* (i.e. control-volume formulation) as opposed to the finite difference method which uses a more indirect, *differential approach*. Although the finite volume method is essentially the same as the finite difference method, it has the advantage, as does the finite element method, of the flexibility of the boundary shape of the computational cells, as the conservation laws are maintained irrespective of shape. The finite difference approach is limited to orthogonal cell shape.

(3) Finite element method (FEM)

The finite element method is formulated to minimise the weighted residual over the flow field. As this method uses an unstructured grid, consisting of cells of different topologies (e.g. triangles or quadrilaterals for a 2D mesh), very complex geometries can be handled easily. Traditionally, the finite element method has been more computer-intensive than both the finite difference and finite volume methods. However, the situation has been improved by the introduction of a technique similar to the MAC method (which is explained later). One

advantage over the finite volume or difference methods is that FEM enables one to easily estimate numerical errors due to grid size, so it is easier to implement a solution-adaptive grid.

Methods of solving the system of equations

To solve the flowfield, the strong coupling of the transport equations dictates the use of an iterative procedure. Before the calculation can start, an initial estimate of the flow field must be given, as well as steady or dynamic boundary conditions for heat and mass transfer at walls etc.

Various strategies have been developed for solving the system of discretised governing equations. They differ in the way time differences and spatial differences are treated, as well as in the solution technique for velocity and pressure. The most important aspect is the treatment of the convection terms in the transport equations, which introduce a strong nonlinearity to each equation. Much research on the discretisation of the convection term has been done for the finite difference and finite volume methods, and has resulted in a number of different numerical interpolation schemes, described in the next section (Numerical scheme for the convection term).

A major challenge is how to calculate the pressure term in the governing equations and ensure that the continuity equation is satisfied. Various computational strategies have therefore been developed to treat the pressure term. Two common strategies are described below; the MAC procedure for the finite difference method, and the SIMPLE procedure for the finite volume method.

CFD is not only based on spatial integration of the transport equations, but also on transient integration. For practical design purposes, it is sufficient to simulate steady-state (i.e. stable) conditions, in which case the 'fully-implicit' iterative method is used as it has the advantage of being very stable. If, however, a dynamic solution of the flowfield is being pursued, then time-dependent analysis using 'explicit' or 'semi-implicit' iterative methods are usually preferable. The MAC procedure is a time-dependent method, whilst SIMPLE can be used for either steady-state or time-dependent solution.

For low velocity buoyancy-affected flow, which can be encountered in large enclosures, the solution may be divergent, or very many iterations may be needed to achieve a steady-state solution. Such instabilities during the iteration process are often due to the choice of numerical procedure or interpolation scheme (for the convection terms), due to the chosen turbulence model, or just due to poor control of solver parameters (such as underrelaxation coefficients) by the CFD operator. Nevertheless, sometimes the flow is naturally oscillatory. Previous research has indicated that the characteristic frequencies of turbulent fluctuations decrease with increasing strength of buoyancy-driven flow. If such periodic fluctuations are of a large scale, it may be inappropriate or even impossible to achieve a steady-state solution by means of time-averaged CFD analysis. In such cases, a transient CFD simulation should be carried out. However, unequivocal recommendations of general validity can hardly be given here due to the complexity of the equations and the immense number of interlinked numerical operations. The choice of adequate measures for optimising the efficiency of the numerical procedure is not only a question of flow type but may even be case dependent [Jacobsen 1993].

MAC

The Marker And Cell (MAC) method originated from the Los Alamos Research Institute in 1965. With this method, a transport equation for pressure (the Poisson equation) is mathematically derived from the transport equations for mass and energy. Most of the

computation time is consumed in an iterative procedure to solve the Poisson equation. This iterative procedure involves time-marching that is not completely satisfied by the continuity restriction. The major advantage of the MAC method is that the error is not cumulated, but is self-adjusted by the iterative procedure.

The MAC method has since been improved by many new techniques concerning Poisson equation treatment. This has culminated in a new iteration scheme for the Poisson equation called SOLA (SOLution Algorithm) or HSMAC (Highly Simplified MAC). In this procedure, velocity and pressure are corrected simultaneously to satisfy the continuity equations. The finite element method's solution procedure has also been improved using similar ideas. As the MAC procedure involves explicit time integration, it is simple, and thus computationally fast. It has been widely used for unsteady time-marching problems up to now.

SIMPLE

The Semi-Implicit Method for Pressure-Linked Equations (SIMPLE) [Patankar, 1980] was developed in 1972 specifically with nonisothermal fluid flow problems in mind. It involves a simultaneous iterative procedure for solving velocity and pressure, in a similar way to SOLA, but the convection and diffusion terms in the momentum and pressure transport equations are neglected at the pressure iteration stage. More recently, the SIMPLER (SIMPLE-Revised) method has been developed, in which the momentum equation is solved in two stages; with or without the pressure term. SIMPLE is more complicated than the MAC method.

SIMPLE was originally developed for steady-state solution only, using a semi-implicit time-integration scheme. Since then, the applicability of SIMPLE has been extended by the development of time-dependent solution capability. This method has been extended with the finite volume method, and has been widely adopted in commercial CFD codes with the unstructured grid system. Compared to other more elaborate methods (e.g. SIMPLER and PISO), SIMPLE is characterised by less computing effort but lower convergence rate for each iteration. The benefit of applying more advanced methods diminishes with increasing flow complexity. Flow in large enclosures is strongly buoyancy-affected. The velocity-temperature coupling due to the buoyancy term in the momentum equation is mainly responsible for slow convergence and the velocity-pressure coupling which is extensively accounted for by the SIMPLER and PISO methods is thus of less importance [Jacobsen, 1993].

As mentioned above, the most challenging aspect of solving the governing equations is the treatment of pressure. In the early days of the finite element method, a direct approach was used, by solving the momentum and the continuity equations in the same large matrix, but now, computational efficiency has been vastly improved by the development of the 'penalty method' or methods similar to MAC.

Numerical scheme for the convection term

The treatment of the nonlinear convection term is a notorious source of instability when solving the flowfield. In the early days of CFD, an oscillation of the solution appeared at high velocities (high cell-Reynolds-numbers), which had no physical meaning, and a stable solution could not be achieved. To solve this oscillation problem, the 1st order 'upwind difference' interpolation scheme was introduced. This is the simplest of all interpolation schemes, and despite its limited accuracy, especially for low velocity flow, it is still widely used today because of its superior stability. Since then, many more finite difference interpolation schemes have been suggested with various orders of approximation. In principle they all originate from the Taylor's series. They fall into two groups:

- Central difference (2nd order, 4th order...)
- Upwind difference (1st order, 3rd order, QUICK ...)

Upwind difference schemes (i.e. schemes of odd order) suffer from varying levels of 'numerical dissipation', an unphysical numerical error that erodes gradients in the flow field.

Central difference schemes (i.e. schemes of even order) do not suffer from numerical dissipation. However, as was mentioned above, they suffer from numerical oscillation at high cell-Reynolds-numbers such as flow round a corner, or flow near the air extract opening.

The strengths of the 1st order upwind and 2nd order central difference schemes have been combined in the HYBRID scheme [Spalding, 1972]. This scheme switches between the upwind scheme for convection-dominated flow, and the central difference scheme for diffusion-dominated flow.

For all the schemes, the discretisation process introduces a numerical 'truncation error' attributed to the limited order of accuracy of the interpolation scheme. Accuracy can be improved simply by applying approximations of higher order accuracy. Lately, a large number of higher order variants have been suggested following the increasing available computer speed, notably QUICK (Quadratic Upwind Interpolation for Convective Kinematics) [Leonard, 1979]. All of these high-order schemes are computationally slower than the 1st order upwind scheme. Moreover, the numerical procedure's ability to reach a converged solution is severely deteriorated for higher order schemes. Matsuo *et al.* [1992] tested several advanced higher order schemes in laminar airflow and demonstrated their advantages in terms of prediction accuracy. Leschziner [1992] also advocated the use of higher order schemes, but common to both authors is the recognition of the severe inherent stability problems which may cause numerical oscillations and breakdown of the calculations [Jacobsen, 1993].

The task of choosing an appropriate interpolation scheme for a particular study is therefore akin to choosing a turbulence model as discussed in Section 2.4.3. The choice involves a trade-off between the accuracy of the scheme and the cost in terms of computation speed and stability, when a tolerable grid refinement is applied [Jacobsen, 1993].

Computational accuracy and error estimation

The accuracy of CFD predictions depends on the method used to discretise the governing equations, the grid resolution, and of course the boundary conditions. When translating the governing equations into a form that can be solved numerically with CFD, they are usually discretised by truncating a Taylor series expansion. This introduces a truncation error which is larger for coarser grids. Moreover, in regions of the flow field where the flow is oblique to the grid lines and when there is a nonzero gradient of the dependent variable in the direction of the flow, local 'false diffusion' or 'numerical dissipation' occurs. The magnitude of this unwanted additional diffusion depends upon the scheme used to discretise the convection term, and may also be reduced by refining the grid. Grid refinement is dealt with in the section 2.4.3. *Computational Grid*.

Theoretical estimation of errors

When an exact steady-state solution is known to exist, error estimation methods can be used to evaluate two sorts of numerical error in computation grids of different coarseness. One is the 'truncation error', which is due to the coarseness of finite-differencing, and the other is the 'solution error' which incorporates all the numerical errors mentioned above, and is the

difference between numerical solution and exact solution. Solution errors from the finite difference/volume methods can be estimated well by Richardson extrapolation, which gives an estimate of the exact solution. The truncation error is calculated in a similar way. [Caruso *et al.*, 1985 and 1986; Murakami *et al.*, 1988; Scheuerer, 1993].

What level of accuracy is acceptable?

The purpose of CFD in indoor environmental design is to evaluate quantitatively (1) indexes of thermal comfort, and (2) indexes of indoor air quality. Thus the degree of accuracy that is demanded of a CFD simulation is dictated solely by the 'permitted tolerance' in these two requirements. In other words, if a high degree of thermal comfort or ventilation efficiency is demanded for a specific enclosure, then the CFD simulations should be of correspondingly high accuracy. This principle is illustrated in Figure 2.4.2 which shows a curve of Predicted Percentage of Dissatisfied (PPD) versus operative temperature for a typical winter indoors situation. If the enclosure's design specification demands 10% PPD, then a CFD calculation of accuracy $\pm 2.3^{\circ}\text{C}$ is permissible. However, if only 20% PPD is required, then the requisite accuracy is reduced to $\pm 3.9^{\circ}\text{C}$, which is well within the capabilities of CFD. A summer situation would have a smaller design tolerance though, since lighter clothing makes the bell-shaped PPD curve narrower.

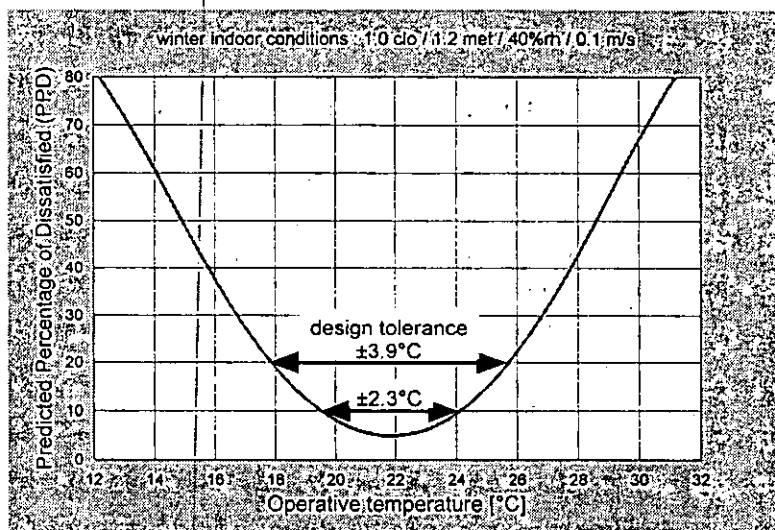


Figure 2.4.2 PPD versus operative temperature - winter indoor conditions.

Which numerical method is recommended for practical use?

When choosing between two CFD methods, it is not very meaningful to consider solution accuracy alone without also considering the execution time and consequently the computational efficiency. One must strike a balance between accuracy and speed.

Concerning the numerical scheme for the convection term, as mentioned above, the central difference scheme suffers from unphysical numerical oscillation and the 1st order upwind scheme suffers from unphysical diffusion, therefore the use of a higher order approximation is recommended, especially 3rd order upwind schemes such as QUICK. When you need a steady-state solution, SIMPLE is recommended due to its shorter calculation time.

2.4.3 Computational Grid

Types of grid structure

Numerous types of computational grid structures have been used. They can all be broadly classified in the following categories:

- Structured grid
 - ↳ orthogonal grid
 - ↳ general-coordinates grid
- Unstructured grid

Additionally, there are grid techniques to enhance computation efficiency (such as multigrid, composite grid, adaptive grid). These can be implemented with any of the above types of grid structure. They are described later.

When modelling large enclosures, it is most efficient to refine the grid only locally, in regions of large gradients, in particular near walls, supply jets and outlets. Storage and CPU requirements are thus typically reduced by a factor of 10-100 compared to a uniform fine-resolution grid, without sacrificing accuracy.

Orthogonal grid

Figure 2.4.3 shows an example of a 2-D orthogonal grid system. In this method the grid cells are aligned in rows running parallel to the coordinate axes. For room airflow applications, as well as most other applications, an orthogonal grid based on the Cartesian coordinate system (x, y, z coordinate axes) is used, as shown in the figure, though it is also possible to construct orthogonal grids based on spherical or cylindrical coordinate systems (e.g. for pipe flow).

As explained in section 2.4.6 (Treatment of walls), it is essential to use a fine grid near boundary surfaces in order to more accurately bridge the flowfield with the boundary conditions for flow and heat transfer. An orthogonal grid with nonuniform grid spacing should be used in such cases, as illustrated in Figure 2.4.3, such that cells of different sizes can be used in different regions of the flow field (e.g. cells must be very small near boundaries and around jets, but can be larger in the core of the space). A major disadvantage of this grid system is that such refinement of the grid (e.g. around a supply opening) is propagated along grid lines to other parts of the flow field where such grid refinement is not needed, which leads to a high number of cells, and is computationally expensive.

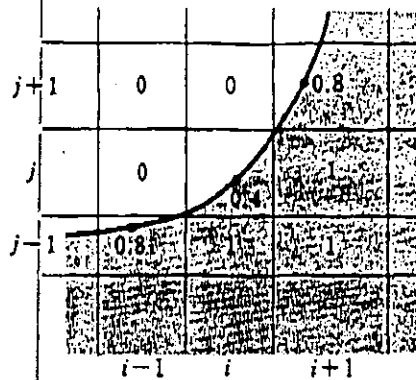


Figure 2.4.3 An orthogonal grid with nonuniform grid spacing.

As illustrated, in cases involving complex boundary geometry or a curved flowfield, it is difficult to fit the grid onto non-orthogonal boundaries, such as angled roofs or curved walls. A simple way round this is the approximation method (Figure 2.4.3), that adjusts the physical quantity in the boundary cell according to the boundary surface area and space volume in the cell, though this method is not accurate.

An orthogonal grid is mostly used with the finite difference method, though it can equally be used in the finite volume and finite element CFD methods. However, the last two CFD methods lend themselves to other, better, grid methods. The finite difference method, using a Cartesian orthogonal grid, is quite satisfactory in the case of square geometry often encountered in simple building enclosures. In such cases, the orthogonal grid method is preferred over other grid methods, as grid generation is easy and it is computationally faster than the other methods.

General-coordinates grid

Figure 2.4.4 shows an example of 2-D general coordinate grid system. In this method, also known as the Boundary-Fitted Coordinate (BFC) method, the grid lines are curvilinear, such that the grid can be made to fit complex boundary surfaces. This is achieved by mapping regular computational space (e.g. in the figure the grid is 7 cells by 13 cells) onto the complex physical space, by means by a mathematical transformation (coordinate mapping). This technique is mainly used in the finite difference method, though it can also be used with the finite volume and finite element methods. This method can generate a smooth grid. However, BFC has the disadvantage that the mathematical manipulation needed for coordinate mapping (to relate the physical space to the computation space) is computationally demanding. Moreover, generating BFC grids for problems with complex 3-D geometry (e.g. Figure 2.4.4) is significantly more time consuming than generating orthogonal grids.

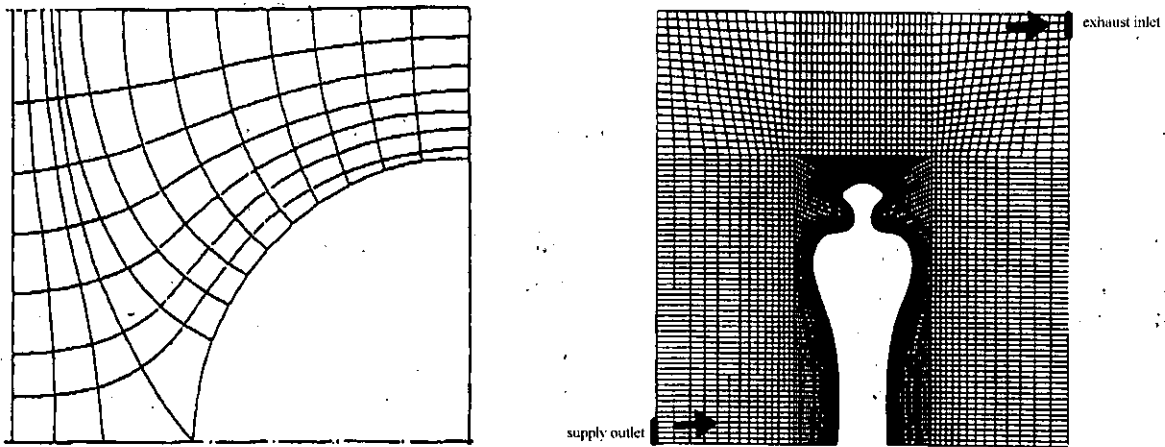


Figure 2.4.4 (left) An example of 2-D general coordinate grid system, (right) Multiblock BFC grid for airflow around a person.

Unstructured grid

Figure 2.4.5 shows an example of 2-D unstructured grid system. Whereas structured grids consist of topologically identical cells ordered in rows and columns, unstructured grids have no such restriction, and topologically different cells may be used together in the same mesh. This grid method can be used for both finite volume and finite element CFD methods. The example (Figure 2.4.5) shows a mesh constructed using triangular and quadrilateral elements. Unlike structured grids, which have simple ordering of rows and columns of nodes in computer memory, the unstructured grid must be managed in computer memory with a look-up table that includes the node number, physical node coordinates, and nodal connectivity. This implies a higher memory consumption per cell. Like BFC grids, grid generation is a complicated task. However, automatic grid generation software has been developed that can vastly simplify this task.

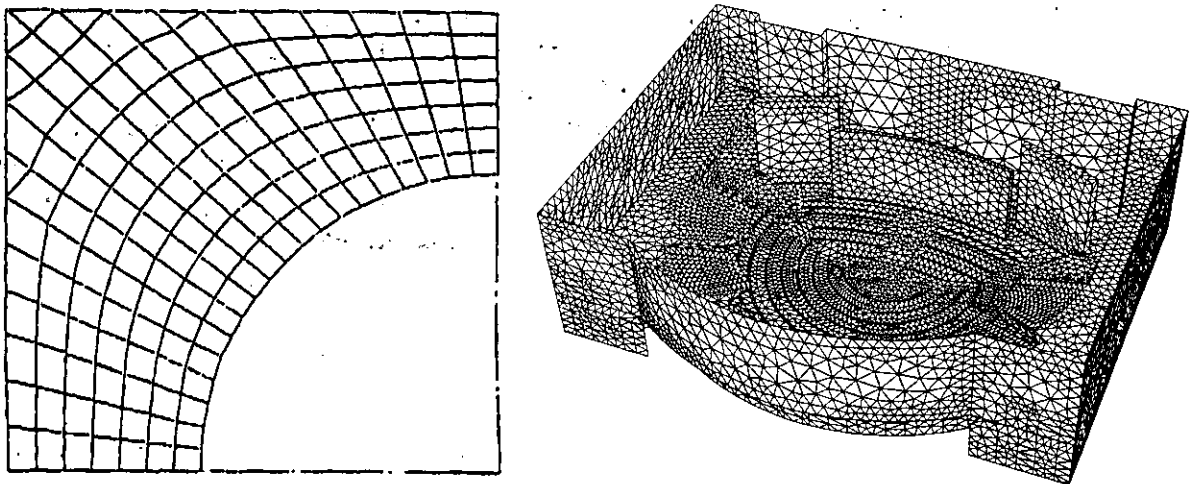


Figure 2.4.5 (left) An example of 2-D unstructured grid system, (right) Unstructured grid of the inside surfaces of the 'Reichstag' building, Berlin (ceiling removed), done with a commercial finite-volume CFD code.

Enhanced grid techniques

Multigrid

The multigrid method can significantly shorten computing time. It is a general asymptotic optimal method to solve elliptic PDEs, so CFD is one of many applications. The principle of the method is that a hierarchy of superimposed computational grids of increasing refinement is used, often just two. The refined grids are constructed by further subdividing the coarsest grid. This results in a solution that is as accurate as the finest grid used, while convergence is achieved much faster than if only the finest grid was used, since the solution is propagated quickly using the coarse grid. The idea exploits the good smoothing properties of standard iterative methods (using local averaging) such that the successively refined meshes reduce the error components that are considered to be oscillative on each mesh. This is done using the correction problem idea, which relies on nested iteration. The fine grid calculations are performed to compute the changes to the solution at each node. These changes are then transferred to the nodes of the coarse grid. The transferred changes are then propagated on the coarse grid and henceforth create the coarse grid corrections. These corrections are then interpolated back to the fine grid nodes. The technique was used by ETH (see Subchapter 4.3).

In practice, it has been shown that for large scale problems, no other solution method is more efficient, not only for strongly elliptic cases, such as heat conduction, but also for the Navier-Stokes equations. Moreover, unlike conventional grids, the multigrid methods has an inherently built-in truncation error estimate, which makes it an effective error control method.

Just as for adaptive gridding methods (below), multigrid refinement can be applied locally in regions of high gradients, using a local error indicator. This is called the adaptive multigrid method.

Solution-adaptive gridding methods

Adaptive gridding methods improve computational efficiency; they also reduce the number of man-hours needed to set up case models. The solution-adaptive grid method can be utilised with any of the above grid structure methods, though it is best suited to general-coordinate and unstructured grid systems. With this method, the computational grid is automatically adjusted as the CFD simulation progresses. An estimate of 'local computational error' is calculated for each cell; regions of the grid with a high local error are refined, and regions with a low local error are coarsened, thereby achieving uniform computational accuracy throughout the flow domain. For many practical problems, the regions that need to be refined are extremely small compared with the overall computational domain. Various types of solution-adaptive grid method have been developed, each achieving local grid refinement in different ways. However, none have yet been implemented in a commercial software package; this is still an active area of research. None were used in Annex-26.

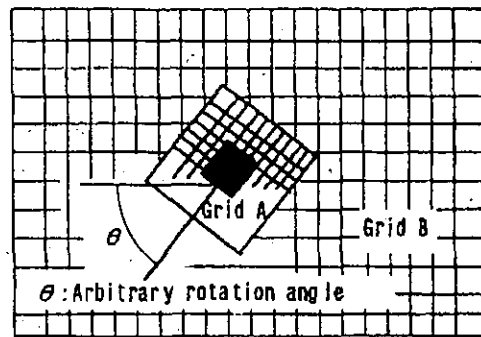


Figure 2.4.6 The principle of composite grid.

Composite grid

A composite grid consists of two or more computational grids which overlap each other, each with a different level of grid refinement. The physical quantities in the cells of each grid are affected by the nearby cells of the overlapping grids in a way such that the accuracy of the solution on the coarse grid is improved by the overlapping grid with the finest level of grid refinement. This allows one to optimise the grid to improve computational efficiency. Figure 2.4.6 illustrates the principle of composite grid; the coarse grid (Grid B) occupies the whole flowfield domain, whereas the overlapping fine grid (Grid A) occupies only a small region of the flow domain where a high grid resolution is needed locally. Figure 2.4.7 shows an example of a composite grid using a BFC grid system.

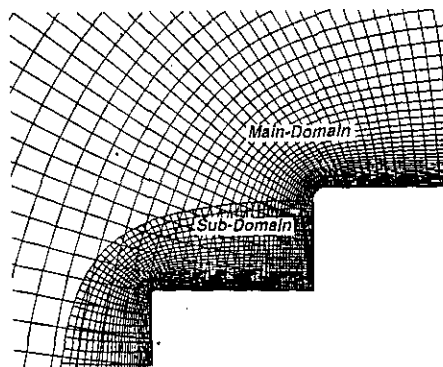


Figure 2.4.7 An example of a composite grid using a BFC grid system.

2.4.4 Relative Performance of Various Turbulence Models

Turbulence modelling theory

The direct solution of turbulent flow using DNS (Direct Numerical Simulation), as mentioned on page 68 (Theoretical basis of micro models), has a serious limitation, namely that it needs a very fine grid system to resolve the Kolmogorov microscale (of order 1mm), the concept of which comes from Kolmogorov's experiments on turbulence statistics. The resulting number of cells for modelling an entire room may be of the order of 10^{14} , which combined with the correspondingly minuscule time step needed, is impossible for today's computers. In order to overcome this obstacle, various types of turbulence models have been proposed that can function with larger (hence fewer) cells. Turbulence modelling is intended to simulate the

averaged flowfield (coarse graining) rather than the original flowfield. Since small turbulent eddies are not resolved by the coarse grid, they have to be modelled empirically as uniform turbulence parameters in each cell.

There are two types of coarse graining (averaging); time averaging and space averaging. These types of averaging and their associated turbulence models are illustrated in Figure 2.4.8, which includes DNS though it uses no averaging (no turbulence model). For a flowfield that has steep fluctuations in its flow variables, the averaged fluctuations in the flowfield will naturally be less steep, so when applying a turbulence model, a relatively coarse grid can be used with certain accuracy. The small eddies neglected by the coarse graining have been indirectly incorporated in the simulation through the turbulence model.

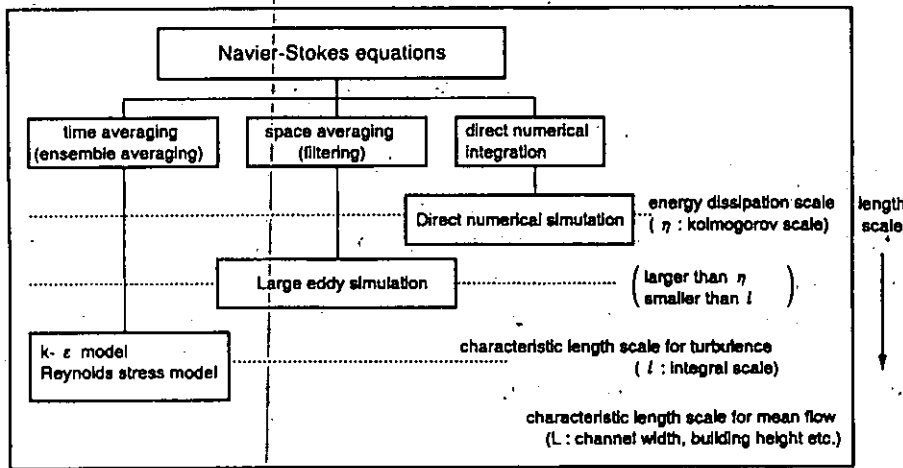


Figure 2.4.8 The concept of different turbulence models.

Turbulence models based on Reynolds-averaged equations

The time-averaged forms of the governing equations are called the Reynolds equations. These equations express only the movements of large-scale eddies. Since the flowfield contains only larger eddies, numerical analysis can be conducted with a rather coarse grid. Most CFD simulations in the field of engineering have been based on this type of modelling, partly because of limited computer performance. The most famous and most widely used is the 'k-ε two equation turbulence model' hereafter the 'k-ε model' [Launder and Spalding, 1972; Murakami et al., 1988]. However, it has become clear that the model possesses some shortcomings. The highest precision version of the Reynolds-averaging approach is the Differential Second-moment Closure Model (DSM), also known as the Reynolds Stress Model (RSM). The use of DSM and its simplified version, the Algebraic Stress Model (ASM), is becoming more routine every year. Notable applications are by Launder et al. [1975], Rodi [1976] and Murakami et al. [1990].

Improvements to the k-ε model

Of the traditional k-ε turbulence model's many weaknesses, its main weakness in large enclosure simulations is that it cannot model laminar (low-Reynolds-number) flow; it was originally developed for analysing only fully turbulent flow. This degrades accuracy especially when modelling large enclosures with pronounced thermal stratification. There are two causes of near-laminar flow in the core of a large enclosure:

- Stable thermal stratification attenuates turbulence in the vertical direction, due to the stabilising effect of buoyancy forces. Likewise, unstable stratification amplifies turbulence
- Much of the volume in large enclosures is almost stagnant with little turbulence

To account for these two effects, the traditional k - ϵ model can be extended to analyse low-Reynolds-number flow as well, and the k and ϵ equations should include buoyancy terms. Many so called ‘low-Reynolds-number’ k - ϵ models have been proposed; they were originally developed for the analysis of near-wall behaviour, but later versions have been extended to free flows. The disadvantage of adding buoyancy terms is that it may become slow or impossible to get a steady solution.

Chen *et al.* [1990] studied different options for turbulence modelling for buoyant turbulent flow in a cavity with k - ϵ turbulence models. They reported that a low-Reynolds-number k - ϵ turbulence model, with buoyancy source terms in the k and ϵ equations, was the most accurate option tested. Though adding buoyancy source terms had little effect on velocity or temperature, it did greatly affect turbulent kinetic energy, which is important in itself, because turbulence affects the sensation of draught.

Chikamoto *et al.* [1992] have developed a low-Reynolds-number model that more elaborately captures the damping effect of stable thermal stratification. The model’s predictions corresponded well with measurements of an experimental atrium, though they observed that the model may benefit from further refinement. Their model managed to achieve stable convergence, whereas the traditional k - ϵ model incorporating buoyancy terms did not.

Turbulence models based on space filtering

Another method of coarse graining is ‘space filtering’. The degree of averaging can be adjusted easily by changing the width of the filter.

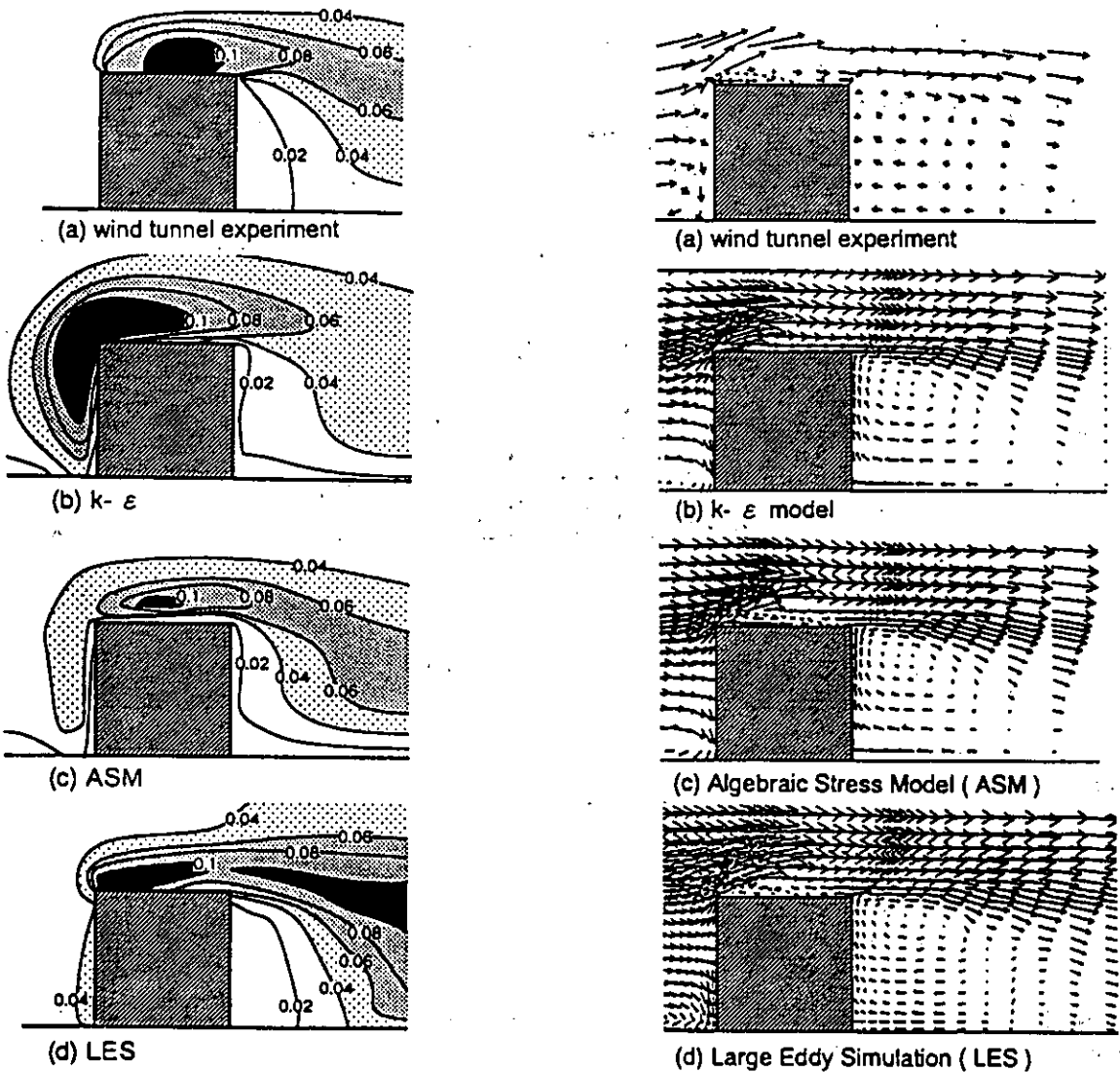
This type of modelling is called Large Eddy Simulation (LES), since turbulent eddies smaller than the width of the filter (i.e. eddies of subgrid scale) are not analysed directly, and eddies larger than the filter width are simulated directly, being of resolvable scale [Smagorinsky, 1963; Deardorff, 1970; Schumann, 1975; Moin *et al.*, 1982; Murakami *et al.*, 1987]. With LES, the effect of small eddies neglected by filtering is modelled by incorporating a subgrid-scale eddy viscosity. Since Reynolds averaging is not applied to the transport equations solved with LES, the scale of resolved eddies is usually much smaller than that of the k - ϵ model, DSM or ASM. Thus, LES predicts a time-dependent flowfield with small fluctuations. Consequently the effect of modelling the subgrid-scale eddies on the overall turbulence structure of the flowfield is relatively small, compared to that of the k - ϵ model. In fact, LES succeeds in reproducing the properties of highly anisotropic flowfields, as demonstrated in Figure 2.4.9. In recent years, a high-precision version of subgrid-scale modelling has evolved, called Dynamic Subgrid-scale modelling.

Choice of turbulence model

The well known k - ϵ turbulence model has been used very widely, yielding many successful results in different engineering applications. Originally the k - ϵ model was developed in the field of mechanical engineering for analysing simple turbulent flows, such as channel- or pipe flow. For such flows, the k - ϵ model has provided very accurate results. However the k - ϵ model reveals some shortcomings when applied to anisotropic, nonisothermal flow, such as

room airflow, as the $k-\epsilon$ model is based on the assumption of isotropic turbulence. Two illustrative examples are given here (Figures 2.4.9 and 2.4.10) to show the relative performance of the various turbulence models described above.

Figure 2.4.9 shows the results of wind tunnel experiments and simulations of the flowfield around a building model. The three turbulence models $k-\epsilon$, ASM and LES were compared. All the models showed similar results for the velocity vectors, as shown in 2.4.9(2). However, the small reverse flow on the roof was not reproduced by the $k-\epsilon$ model, which is a rather serious error. The reason why the $k-\epsilon$ model produced this error can easily be understood by considering Figure 2.4.9(1). In the case of the $k-\epsilon$ model, the value of turbulence energy k was overestimated greatly at the frontal corner. This large k value produced large eddy viscosity, ν_t , such that the reverse flow on the roof was negated by this large value of ν_t . This overestimation of k in the impinging region is one fundamental shortcoming residing in model's assumption of isotropic turbulence.



(1) Turbulence energy, k

(2) Velocity Vector Field

Figure 2.4.9 Flow field and turbulence energy around a building (modelled with k - ϵ , ASM and LES).

Figure 2.4.10 shows an analysis of a nonisothermal flow in an enclosure. The enclosure has a cooling jet emanating from the left wall and a heated right wall. Some differences between the results of the k - ϵ model, DSM and ASM appeared around the centre-line of the cooling jet. The distributions of temperature around the centre line are less steep in the case of DSM and ASM (Figure 2.4.10(3)). As shown here, the results of DSM and ASM correspond better to the experiments than do those of the k - ϵ model.

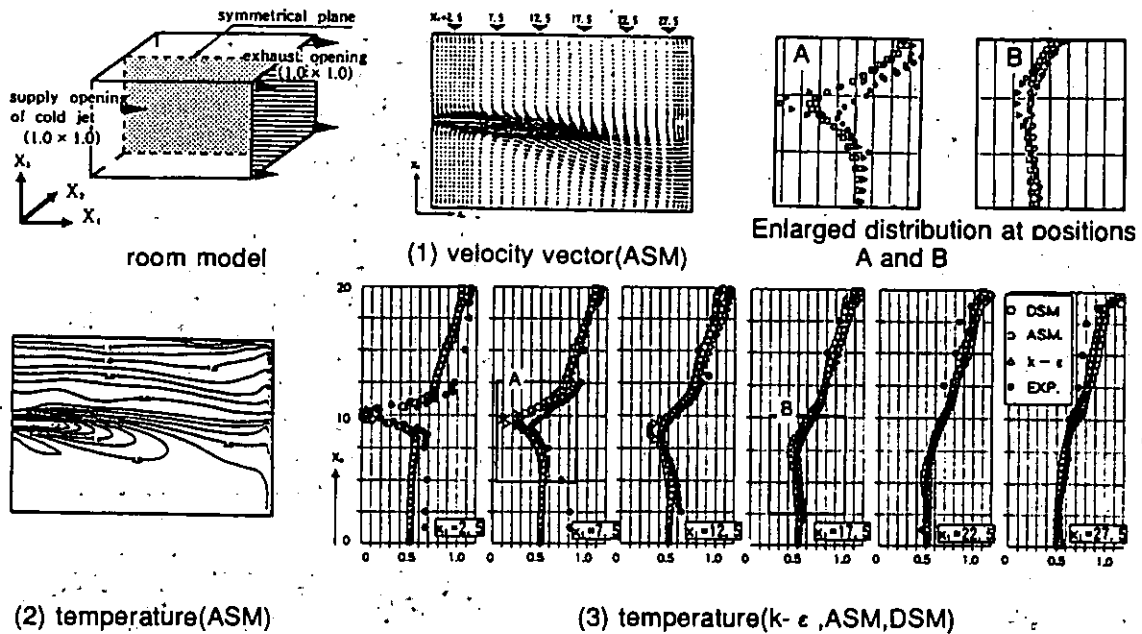


Figure 2.4.10 Velocity and temperature fields in a room with cooling (modelled with $k-\epsilon$, DSM and ASM).

In conclusion, the results given by the $k-\epsilon$ model are a little inferior to those of DSM or ASM (compared in Figure 2.4.10) and clearly inferior to those of LES (compared in Figure 2.4.9). Due to the $k-\epsilon$ model's shortcomings when applied to such flow, it is recommended that DSM or LES be used instead, to achieve predictions of higher accuracy.

The relative merits of the various turbulence models when applied to various flow fields, are summarised in Table 2.4.1. As a rule, increased predictive accuracy of a turbulence model requires increased computer resources (memory and CPU time). Thus, the choice of turbulence model for a particular application depends upon the required accuracy and the available computing resources. LES is the most promising model for application to air-conditioning engineering. The weak point of LES is the disproportionate computing time, and the vast data storage required, both of which are considerably larger than what the $k-\epsilon$ model requires. While the $k-\epsilon$ model solves the time-averaged flowfield, LES produces a long sequence of instantaneous (time-dependent) flowfields which must be stored for results analysis. However, this problem will be overcome to a certain degree by future advances in computer hardware technology.

Table 2.4.1 Comparison of various turbulence models for practical modelling of different types of flow in an enclosure.

Turbulence model	Standard $k-\epsilon$	Low-Re-# $k-\epsilon$	Standard DSM (ASM)	Low-Re-# DSM (ASM)	LES (standard)	LES (dynamic)
wall boundary condition	wall function	non-slip	wall function	non-slip	-	-
1. Simple flows (channel flow, pipe flow, etc.) (local equilibrium is valid)	○	○	○	○	○	○
2. Flow with streamline curvature 1) weak curvature 2) strong curvature (flow around bluff body)	○ ●, ⊙	○ ●, ⊙	○ ○(⊙)	○ ○(⊙)	○ ○(⊙)	○ ○
3. Impinging flow	●, ⊙	●, ⊙	⊙, ○	⊙, ○	○	○
4. Low-Reynolds-no. flow field	●, ⊙	⊙, ○	●, ⊙	⊙, ○	⊙, ○	○
5. Non isothermal flow 1) weak stratification 2) strong stratification	○ ●, ⊙	○ ●, ⊙	○ ○	○ ○	○ ⊙	○ ○
6. Convective heat transfer at wall	●, ⊙	○	●, ⊙	○	⊙, ○	○
7. Unsteady flow or diffusion 1) highly unsteady 2) vortex shedding	● ●	● ⊙	● ○	● ○	○(⊙) ○	○ ○
8. Jet 1) normal 2) swirl	○ ●	○ ●	○ ○	○ ○	○ ○	○ ○

○ : functions well ⊙ : insufficiently functional ● : functions poorly

2.4.5 Treatment of Openings

Treatment of supply openings

The airflow in a space is driven by forced convection due to mechanical ventilation, and by natural convection due to differing wall surface temperatures, infiltration airflow through cracks and large openings. So in order to accurately predict the flow field inside a space dominated by forced convection, it is important to reproduce precisely of the jet stream from each inlet.

The two main factors which influence the accuracy of jet modelling are grid resolution and the accuracy of prescription of the inflow boundary conditions, as shown in Figure 2.4.11. The jet goes through a mixing process, entraining the surrounding air and mixing with it. The large velocity gradient which is formed in this mixing region, produces much turbulence. The jet's diffusion pattern therefore greatly depends on the velocity gradient and the accompanied turbulence. The accuracy of predicting this pattern nearly entirely depends on the accuracy of reproducing the velocity gradient, which is subject to the local grid size. In the jet region the grid size must therefore be very fine. An example of grid division is shown in Figure 2.4.12. As can be seen in the figure, the grid size in the jet and the surrounding airflow greatly affects the turbulence energy distribution, which in turn has a significant influence on the prediction of the jet diffusion pattern. In order to correctly model the inlet flow from a complicated

opening, detailed measurements should ideally be made of 3-D velocity components for a real opening. A good example of such measurements was done in the Fibreglass factory case-study on induction type diffusers using a 3-D ultrasonic anemometer (see Subchapter 4.4). The measurements should include turbulence intensity. However, if this has not been measured then the inlet turbulence boundary conditions can be estimated from Awbi [1991].

The above-mentioned local grid refinement is computationally expensive in the case of large enclosures, since the resulting number of computational cells may become prohibitively high, particularly if the grid system is orthogonal. One way forward is to use a more advanced grid system (i.e. curvilinear or unstructured) or a local composite grid around the supply jet. These grid methods improve computation efficiency, as the grid cells can be collectively arranged at desired locations and so the total number of cells can be minimised. The increasing use of the composite and unstructured grid systems is expected.

Further difficulty is encountered when modelling real supply terminals, as the incoming airflow invariably has a complicated structure. To simulate an outlet having complicated configuration with narrow fins, an approach shown in Figure 2.4.13 has been devised. In the case of a supply terminal with a grille or perforated panel, or anemostat-type outlet, the properties of the airflow cannot practically be represented by grid division. Instead, a very simple approach is to prescribe the average velocity and flow direction derived from experiments and turbulent statistics. A better approach, advocated by Nielsen [1992], is to prescribe the flow in the supply jet at some distance from the opening, by using either (1) the Box Method, or (2) the Prescribed Velocity Method. An added advantage of these two methods is that they reduce the need for local grid refinement around the developing jet, thus the need for an advanced grid system is partly eliminated. The two methods cannot strictly be used in transient simulations involving dynamic boundary conditions, though. Both methods must be implemented by writing extra program code for incorporating in the CFD software.

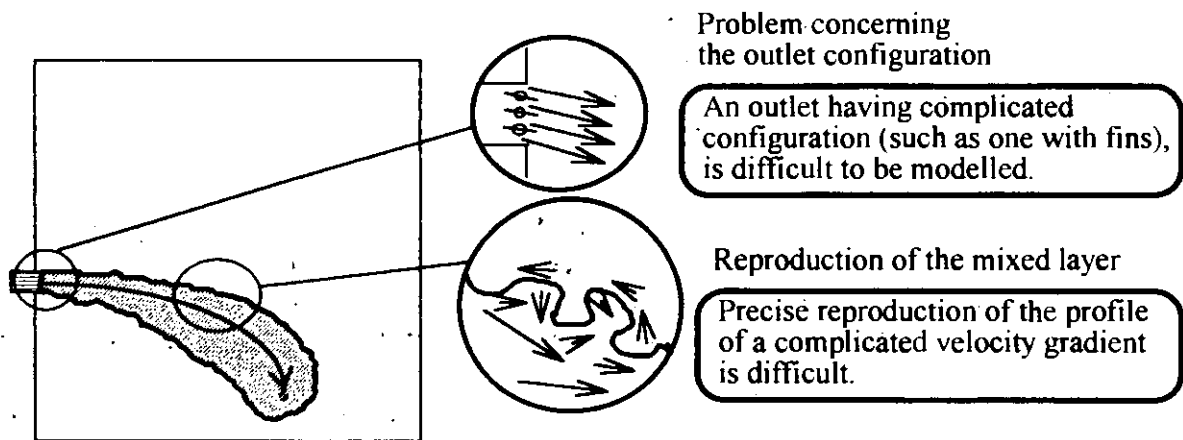


Figure 2.4.11 Problem concerning of the treatment opening.

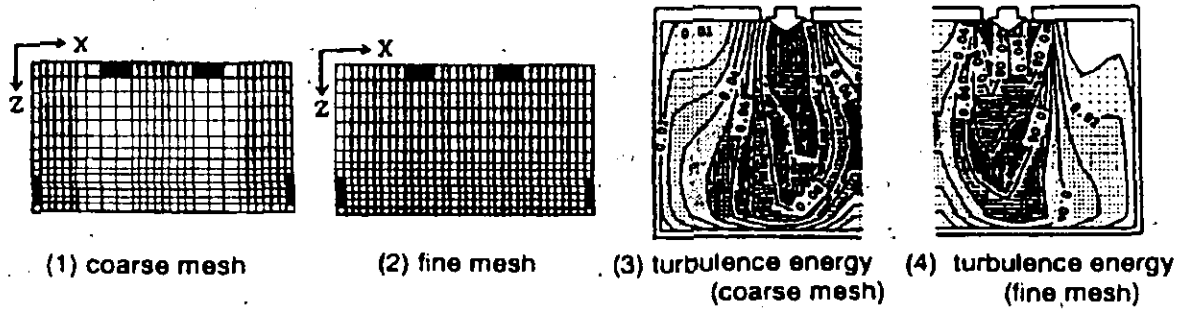
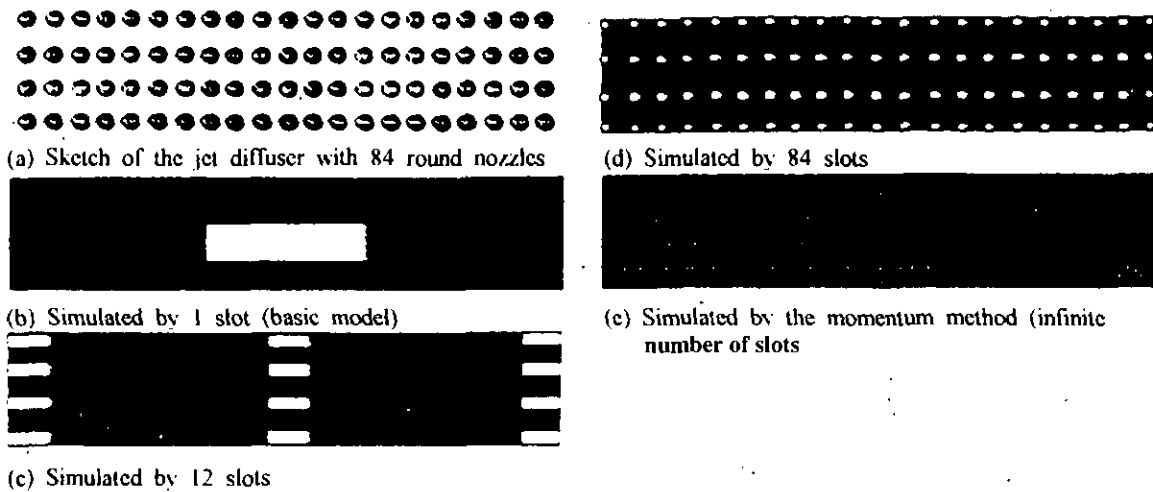


Figure 2.4.12 Effect of grid discretisation on turbulence energy k around supply jet.



The diffuser (a) simulated with the simple-rectangular slot model (b),(c),(d) and the momentum method (e)

Figure 2.4.13 Example for modelled supply openings.

Treatment of exhaust openings

The airflow through outflow openings has practically no effect on the enclosure's airflow pattern. Consequently, the local grid size has little effect on the accuracy of enclosure's airflow distribution. Nevertheless, outflow boundary conditions can have a significant influence on the convergence and stability of the numerical procedure.

At outlets, one can assume a zero gradient normal to the opening, for all the flow variables (*Neumann* boundary conditions). Alternatively, for steady-state simulations, faster convergence is achieved if the CFD code is set up to calculate the exit temperature and velocity by calculating the energy and mass balances of the whole flow field (*code-balanced Dirichlet* boundary condition). If the modelled enclosure has multiple outlets, each with a known flow rate, and if the simulation is a steady-state one, then fastest convergence is achieved if all but one outlet are defined with a prescribed exit velocity (*Dirichlet* boundary condition), and the last outlet with a *Neumann* or *code-balanced Dirichlet* boundary condition for velocity. The application of this *Dirichlet* type outlet is undesirable in transient calculations with Large Eddy Simulation, since it actually slows convergence and may even cause

simulation errors to propagate upstream. It should be noted that inappropriate definition of the outflow boundary conditions often causes problems, such as decreasing accuracy, slowing convergence and reducing stability. The treatment of outflow boundary conditions is still subject to ongoing research.

It is not always correct to assume that the outlet flow streamline area is equal to the physical area of the outlet. As shown in Figure 2.4.14, the abrupt compression of airflow as it enters the inlet may affect the indoor streamline. Likewise, the same effect occurs at an outlet where the airflow abruptly expands. One solution to this problem is to use a local composite grid, in which models the duct which is connected to the inlet. An example of an analysis of the airflow in the supply jet by means of the Fortified Solution Algorithm is presented in Figure 2.4.15.

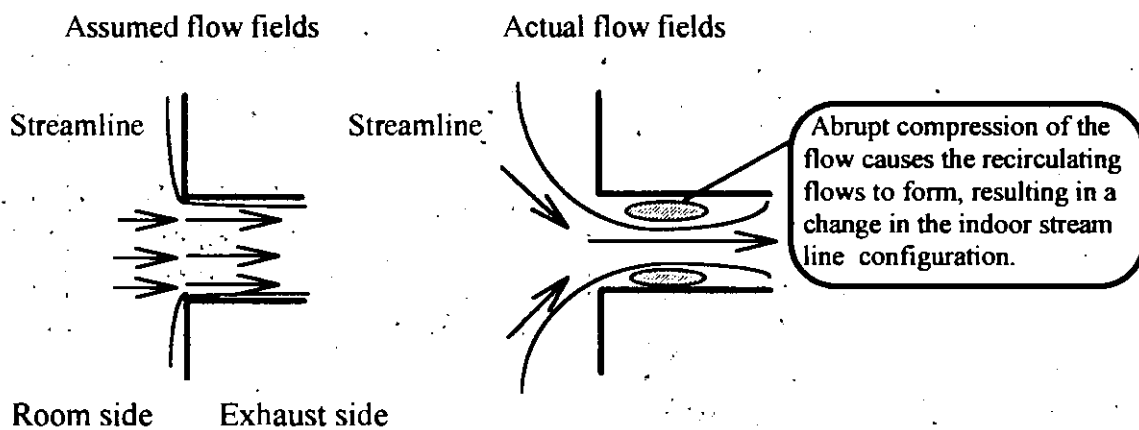


Figure 2.4.14 Condition of streamline at exhaust opening.

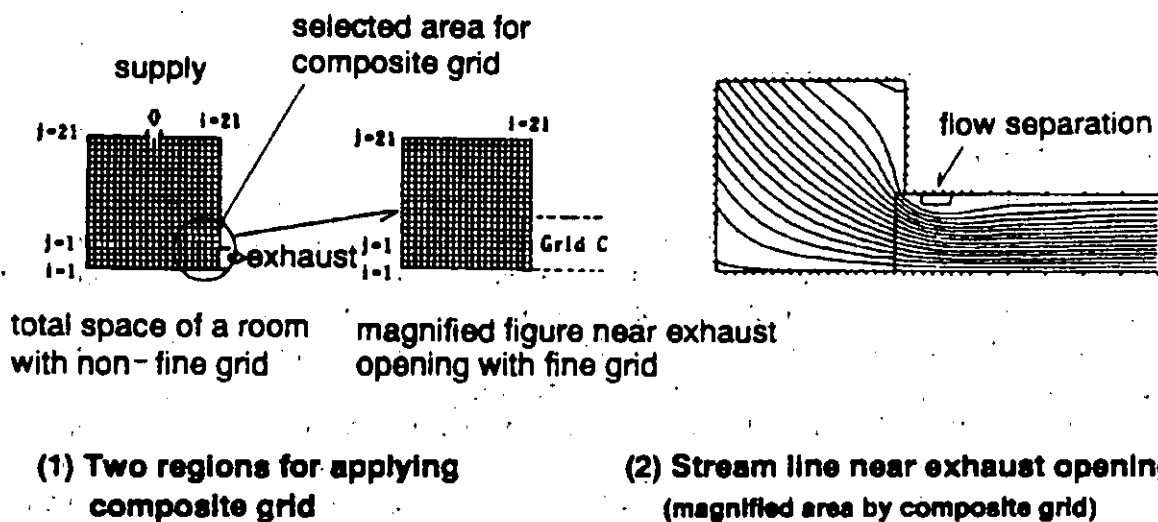


Figure 2.4.15 Composite grid system applied for room air flow.

Special treatment for natural ventilation

Natural ventilation (by infiltration & exfiltration) can significantly influence the flowfield in large enclosures, as the stack effect is particularly strong in these high spaces. Natural ventilation (driven by wind or the stack effect) is harder to model than mechanical ventilation, partly because it is pressure-dependent, and because of the wide distribution of leakages. Simplified boundary conditions must therefore be used. The simplest way of modelling infiltration/exfiltration is to estimate first the flow rates by hand-calculation, and then impose them in the CFD code just as for mechanical ventilation. Alternatively, the CFD code may be set up to calculate infiltration flow rates by itself. For this, the CFD code must be provided with the external ambient air temperature and density. The program then calculates the internal static pressure at each opening, by integrating vertically from the floor to the height of each opening, and then uses an empirical expression to calculate the flow rate through each opening and the neutral height. Awbi [1991] gives a fuller account of infiltration modelling.

2.4.6 Treatment of Walls

Wall boundary-layer flow

Accurate boundary conditions, and an accurate method of bridging them with the flow field, are a prerequisite to achieving an accurate solution of the airflow in the core of the enclosure. Accurate evaluation of surface temperature distribution, combined with accurate estimation of convective heat transfer coefficient, are therefore essential for correct assessment of convective heat transfer. This is particularly true when modelling large enclosures, as the airflow may be dominated by natural convection boundary-layer flow. Underestimation (or overestimation) of convective heat transfer will inevitably result in under-(or over) evaluation of temperature throughout the space and will further adversely affect the velocity distribution in the whole space. (Here we use 'wall' to mean all surfaces facing the enclosure, including the floor and ceiling).

Figure 2.4.16 illustrates the concept of near-wall flow (boundary layer flow). In an air-conditioned enclosure, a steep velocity gradient is formed next to each wall, due to friction, with zero velocity at the wall surface. These are described as forced-convection boundary layers. Further, where the wall surface temperature is high (e.g. due to incident solar radiation) or low (e.g. due to heat loss through glazing), the influence of temperature becomes predominant, and a thin layer of rising or falling buoyant air develops along walls. These are described as natural-convection boundary layers. In either case, the boundary layer is typically only several millimetres thick. Nevertheless, it is very important that the loss of velocity and the heat transfer mechanism in these thin layers be accurately dealt with in CFD. In addition, heat transferred by natural convection is accumulated in the upper part of the enclosure and stable stratification is observed. This is one of the special features of large enclosures. The effect of stratification on these layers therefore needs to be captured in the analysis.

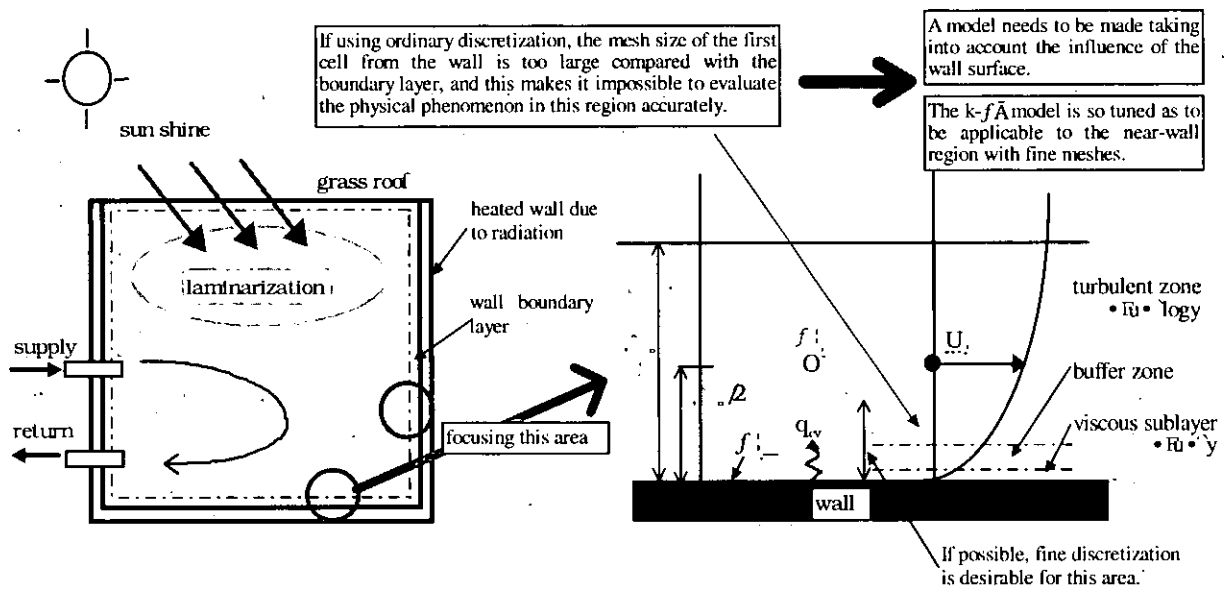


Figure 2.4.16 Concept of Flow Field in Large Enclosure.

Here, we will first describe the treatment of the boundary layer in the vicinity of the wall. There are two ways of modelling them in CFD. One is to employ a low-Reynolds-number turbulence model, together with a very fine grid near the wall (approx. 50-60 rows of cells within the thickness of the boundary layer) so that the boundary layer can be modelled in detail. The other approach is the 'wall-function' method, which is simpler and computationally more efficient. In this method, a coarser near-wall grid can be used (the near-wall cell extends out into the turbulent region of the boundary layer), and the velocity and temperature in the near-wall cell is calculated by way of 'universal' functions (not truly universal though). The former method is more accurate, but the extra computing costs are prohibitive in the case of 3D analysis of large enclosures. The latter method's accuracy depends on the suitability of the chosen 'universal' wall functions for the particular flow field studied.

The wall-function method

In this method, a universal function that bridges the wall surface and the first row of near-wall cells, is derived from experimental results, and is given as one of the wall boundary conditions. Velocity and other variables are defined at grid points indicated in Figure 2.4.16. As this method dispenses with using many rows of cells within the wall boundary layer, it has major advantages. For instance: (1) it is not limited by computer power, and (2) it is relatively easy to incorporate empirical results into the wall functions (such as surface roughness). Because of these merits, this method has been widely adopted, and is subject to considerable research [originally Spalding, 1967 and Patankar and Spalding, 1970]. Some typical analysis examples, utilising this method, will be introduced in the next few paragraphs.

Velocity boundary condition

For determining velocity boundary conditions, a component tangential to the boundary plane and one normal to it, need to be defined. A normal component is generally taken as zero at the wall surface, while a tangential component is often given as a shear stress τ_w at the wall surface, as above. However, there are relatively few cases where the analysis of indoor flow fields is significantly affected by the value of shear stress τ_w , except in wall jet simulations and

other special cases. There are two main types of wall function, depending on the assumed velocity profile: (a) log-law method, and (b) power-law method.

(a) *Log-law method*

The log-law method is the most widely used boundary condition technique in CFD analysis. Launder and Spalding [1974] developed a generalised wall function (Equation 2.4.6) assuming that the near-wall velocity profile is logarithmic, regardless of the Reynolds number (since the profile is different for extremely high or low Reynolds numbers). The function therefore bridges the wall surface (zero velocity) and the near-wall cell (velocity U_1).

$$\frac{U_1}{\tau_w / \rho} (C_\mu^{1/2} k_1)^{1/2} = \frac{1}{\kappa} \ln \left[\frac{h_1 E (C_\mu^{1/2} k_1)^{1/2}}{2 \nu} \right] \quad (2.4.6)$$

where

- U_1 = velocity in the first cell from the wall surface.
- κ = von Kármán constant
- C_μ = numerical constant
- τ_w = shear stress at wall surface
- E = 9.0
- k_1 = turbulence energy in the first cell from the wall surface
- ρ = density

The above equation is so devised as to induce a friction velocity stress (Reynolds stress) τ_w at the wall surface, from the mean velocity U_1 and k_1 in cell adjacent to the wall. This formula is intended for relatively smooth wall surfaces. For air flow affected by rough wall surfaces, the wall functions proposed by Sakamoto *et al.* [1976] may be applied.

The general log-law function given above is based upon the assumption that the streamwise pressure gradient is zero. It cannot, therefore, be expected to provide reasonable solutions in cases involving highly complicated near-wall flow fields, such as reverse flow, separation and reattachment. For analysis of such cases, Chieng and Launder [1980] proposed a log law wall function in which a viscous sublayer was taken into account in determining the boundary conditions for velocity U and they also assumed the statistic values of U , k , ϵ etc. in the viscous sublayer. While theirs is currently the most elaborate wall function method, it should be remembered that as far as this method is predicated on turbulent boundary layers, the method does not always provide highly accurate solutions.

Fortunately, new wall functions have recently been developed that are suitable for natural convection boundary flow: Yuan, Moser and Suter [1993, 1994] divided the natural convection boundary layer into inner and outer sublayers as did George and Capp [1979], Tsuji and Nagano [1989]. The inner sublayer covers the region from the wall to the point of maximum velocity in the boundary layer, and the outer sublayer covers the remainder of the boundary layer. These wall functions were evaluated in CFD simulations of the Experimental Atrium case-study (see Subchapter 4.3). Yuan [1995] gives a detailed description of the wall functions. The proposed velocity wall function for natural convection as follows (Equations 2.4.7 - 2.4.12):

$$U^{**} = \min\{f_i, f_o\} \quad (2.4.7)$$

$$f_i = 1.41y_i^{**} - 3.11y_i^{**2} + 2.38y_i^{**3} \quad y_i^{**} \leq 0.53 \quad (2.4.8)$$

$$f_i = 0.228 \quad y_i^{**} > 0.53 \quad (2.4.9)$$

$$f_o = 0.228 \quad y_o^{**} < 0.005 \quad (2.4.10)$$

$$f_o = -0.458 - 0.258 \ln y_o^{**} - 0.02425 \ln^2 y_o^{**} \quad 0.005 \leq y_o^{**} \leq 0.1 \quad (2.4.11)$$

$$f_o = 0.0 \quad y_o^{**} \geq 0.1 \quad (2.4.12)$$

where

U^{**} = dimensionless streamwise velocity ($=U^*R^4$ where $U^*=U/U_q$ and U_q is a velocity scale based on heat flux)

y_i^{**} = dimensionless distance for the inner sublayer ($=y^*R^2$)

y_o^{**} = dimensionless distance for the outer sublayer ($=y^*R^6$)

R = dimensionless parameter

y^* = dimensionless distance normal to the wall

(b) Power law method

This method is based on the assumption that the velocity gradient in the region immediately adjacent to the wall to the first cell from the wall is 1/7 in non-dimensional form. [Murakami, 1985].

$$\frac{\tau_w}{\rho} = \left(v_t \frac{\partial U}{\partial y} \right)_{y=0} = \frac{1}{7} v_t \frac{U_1}{(h_1/2)} \quad (2.4.13)$$

where v_t = eddy viscosity.

Although this expression disregards the viscosity effect of the wall, it is frequently used as a practical technique for CFD analysis of indoor airflow. However, since the range of application of this method is subject to restriction by the Reynolds number (unlike the log-law method) it does not always accurately evaluate the physical behaviour of near-wall turbulent flow.

Thermal boundary condition

As has already been mentioned, the wall boundary conditions for temperature are crucial to the accuracy of analysing natural convective flows driven by wall heat transfer.

Thermal boundary conditions may be given directly, in the form of wall heat flux, or it may be given in the form of wall surface temperature. If surface temperature is to be prescribed, the convective heat transfer coefficient must be correctly evaluated. As for the velocity boundary condition, applying a low-Reynolds-number $k-\epsilon$ turbulence model, together with a fine grid near the wall, generally gives precise results, though this approach is often ruled out by limited computing capacity, especially for 3-D analysis. Consequently, it is currently considered more practical to use the wall function method, or simplest of all, to prescribe a fixed convective heat transfer coefficient at the wall.

The application of a general log law wall function for temperature (Equation 2.4.14, after Launder and Spalding [1974]) in the same manner as for velocity (Equation 2.4.6) results in inaccurate prediction of the convective heat transfer coefficient, and hence wall heat flux $u^* \theta^*$, where θ^* = friction temperature = $q_w / (\rho c_p u^*)$; or wall surface temperature θ_w (whichever is not set as the boundary condition). The calculated heat transfer coefficient is not independent of grid spacing. Prompted by this shortcoming, a variety of tuning methods have been proposed for the temperature wall function. Neitzke has compared a few of them [1996]. For instance, Yuan, Moser and Suter [1993, 1994] have taken the Prandtl number ($Pr = \nu/\alpha_c$) as parameter for a convective flow that takes place where there exists a solid wall which has definite the wall surface temperature and the heat flux distribution, and using this parameter they have tuned the log-law by obtaining the temperature gradient from the wall (Equations 2.4.15 - 2.4.17).

Another approach, by Murakami *et al.* [1990] was to use a wall function for convective heat transfer coefficient (h_c , Equation 2.4.18) instead of temperature. Here h_c is evaluated by reference to the temperature in the near-wall cell, θ_1 . This simple method has yielded satisfactory results in cavity flow simulation. In the work conducted for Annex-26, many other similar studies have been conducted using a prescribed fixed value of h_c .

$$\frac{(T_1 - T_w) C_p \rho C_\mu^{1/4} \cdot k_1^{1/2}}{q_w} = \frac{\sigma_h}{\kappa} \ln \left[\frac{E \cdot h_1 (C_\mu^{1/2} \cdot k_1)^{1/2}}{\nu} \right] + \sigma_h \frac{\pi/4}{\sin(\pi/4)} \left(\frac{A}{\kappa} \right)^{1/2} \left(\frac{\sigma_{h,L}}{\sigma_h} - 1 \right) \left(\frac{\sigma_h}{\sigma_{h,L}} \right)^{1/4} \quad (2.4.14)$$

$$T^* = y^* \quad y^* < 1 \quad (2.4.15)$$

$$T^* = 1 + 1.36 \ln y^* - 0.135 \ln^2 y^* \quad 1 \leq y^* \leq 100 \quad (2.4.16)$$

$$T^* = 4.4 \quad y^* > 100 \quad (2.4.17)$$

$$u^* \theta^* = \frac{h_c}{C_p \cdot \rho} (\Theta_w - \Theta_1) \quad (2.4.18)$$

where

- T_1 = mean temperature of the first cell from the wall
- T_w = mean temperature of the wall surface
- q_w = heat flux at the wall surface
- C_p = specific heat at a definite pressure
- σ_h = Prandtl number for turbulent flow
- $\sigma_{h,L}$ = Prandtl number for laminar flow = 0.9
- E = wall surface roughness (=9.0)
- A = Van Driest's constant (26, in case of smooth surfaces)
- T^* = dimensionless temperature
- y^* = dimensionless distance normal to the wall
- $u^* \theta^*$ = convective heat flux
- Θ_w = wall surface temperature
- Θ_1 = temperature of the first cell of the wall

Boundary conditions for turbulence

Boundary conditions must also be provided for each transport equation in the chosen turbulence model. In the case of the k - ε turbulence model, boundary conditions must be given for k and ε . Generally in indoor airflow analysis, the flow field is not greatly affected by the wall boundary conditions for k . However, the flow field is significantly influenced by the boundary condition for ε . In particular, if non-slip boundary conditions are used (i.e. wall functions are not used), ε at the wall must be given, which is particularly problematic, and failure to obtain realistic solutions is often experienced.

Viscosity due to the wall surface is not considered if k is assumed in a non-slip condition. Leschziner *et al.* [1987] proposed a method which takes account of the effect of the viscous sublayer and gives a dissipation taken in the transport equation for k in the near-wall cells in the form of a mean volumetric value.

The value of ε increases in the near-wall region. When ε is given by the wall law $\varepsilon_1 = C_\mu^{3/4} \cdot k^{3/2} / (k^{3/2} \cdot h_{1/2})$, ε tends to be underestimated because the computation results are substantially affected by fineness/coarseness of the grid near the wall. To alleviate this tendency, Murakami, Kato & Nagano [1988] proposed a method in which ε is given as a mean(integrated) value at the center of the first cell from the wall.

Near-wall low-Reynolds-number turbulence models

The 'universal' wall function method described above is based on the assumption that the velocity and temperature distributions of all wall boundary layers are the same as a simple forced convective boundary layer. But there are many types of flow for which this assumption is not acceptable. It is particularly inappropriate in the case of a large enclosure where the flow is laminarised by the effect of thermal stratification. Generally, for indoor airflow, the field of boundary condition as a whole is more greatly affected by the temperature distribution than by the velocity distribution.

On the other hand, low-Reynolds-number turbulence models (described in section 2.4.3) can in most cases more accurately predict surface heat transfer since they can be applied to model the inner region of the boundary layer, with a non-slip boundary condition (i.e. zero velocity at the wall surface). The chosen low-Reynolds-number turbulence model should ideally be one which can capture the effect of anisotropic turbulence (especially such damping of the turbulence component normal to the wall caused by the echo effect), the effect of anisotropic characteristic of ε etc., and of course, a very fine near-wall grid is necessary. Since the standard (i.e. high-Reynolds-number) k - ε model is a basic turbulence model, developed for simulating turbulent flow apart from the wall surface, some modifications have been made to this model by the use of damping function, f_μ , for computation of the turbulent viscosity, ν_t , and by the use of f_1 and f_2 for the production and dissipation terms (source terms) of the k and ε equations. Following the initial proposal to modify f_μ , f_1 and f_2 by Jones & Launder [1972], a variety of similar proposals have been made and consequently these empirical factors have now been improved [e.g. Reynolds, 1976]. A variation proposed by Murakami, Kato and Chikamoto [1993, 1994] also models laminarisation of flow due to buoyancy forces (such as in a thermally stratified space), as well as laminarisation due to viscous forces (such as near walls).

2.4.7 Solar Heat Gain Calculation

The distribution of solar radiation on the inside and outside surfaces of a large enclosure has a fundamental influence on the flow field and temperature distribution. This calculation is equally important for simpler zonal models, and is not limited to CFD analysis.

Solar gain calculation for coupled analysis of convective and radiative heat transfer.

The analysis of the indoor climate of a large enclosure with glazed facades consists of two main steps. The first step is precalculation of the absorbed solar radiation (short-wave radiation, visible part of the spectrum). Second is the actual CFD (or zonal) analysis of the indoor airflow, coupled with long-wave thermal radiation analysis, possibly including solution of heat conduction through walls and their heat storage (next subchapter, page 102). In this second step the heat transfer phenomena of convection, conduction and long-wave radiation must be solved simultaneously by coupled simulation, as they are essentially interrelated. The solar radiation analysis, however, is conducted independently of this last step, as it is unaffected by surface temperature.

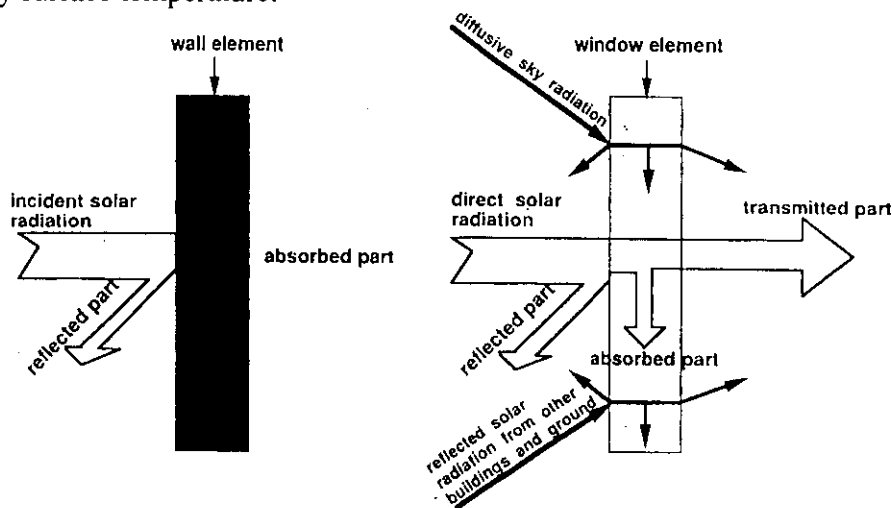


Figure 2.4.17 Incident solar radiation on a wall and a window surface.

Calculation of absorbed solar radiation

For large glazed enclosures, a significant amount of the incoming solar radiation may pass out again. Moreover, the distribution of the absorbed solar radiation depends on the reflective-transmissive properties of the different surfaces and their geometry. Thus a solar distribution computing program must be used, to analyse a geometric model of the building. In the program, all the surfaces enclosing and surrounding the space are divided into small surface patches, each treated independently. Often, the surface patches do not coincide with the wall boundary-cells used in the CFD analysis of the room airflow; they are typically larger in area.

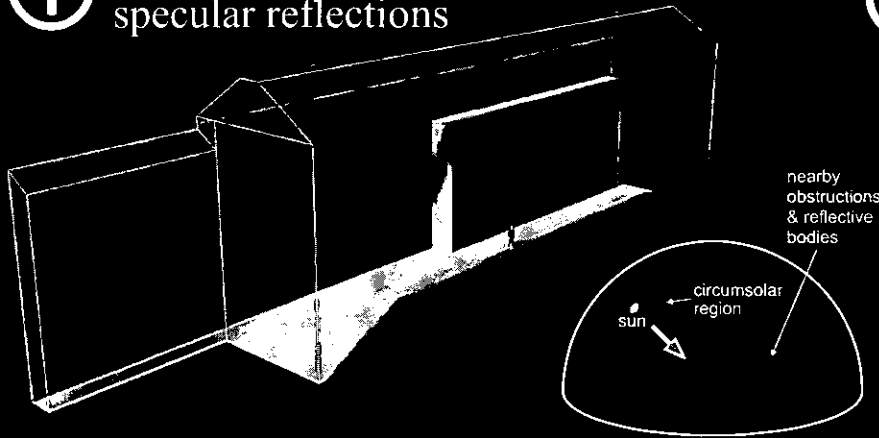
The incident solar radiation on a building consists of three main components: direct, sky-diffuse, and ground-reflected diffuse radiation, as shown in Figure 2.4.17. The magnitude of these can be derived from meteorological data (many weather stations measure solar radiation), or can be estimated empirically from relations that take account of global location of the building (latitude, longitude), time (month, day, hour, minute) and air clarity and cloudiness. A comprehensive account of solar radiation calculation is given in Duffie and Beckman [1991] or Siegel and Howell [1992].

The short-wave absorptivity of the inner surfaces of a building is usually not so high. It is less than 0.3 for most non-glass surfaces in buildings. It is therefore important to model the multiple internal reflections in some way, as they have a large influence on the solar gain distribution. The distribution of this short-wave 'surface radiant emittance' on the surfaces in the enclosure, is calculated by a so-called radiation analysis, which will be described later. The reflected component of the incident solar radiation for each surface patch gives that patch's radiant emittance, whilst the absorbed component leads to a rise in surface temperature (cf. Figure 2.4.17).

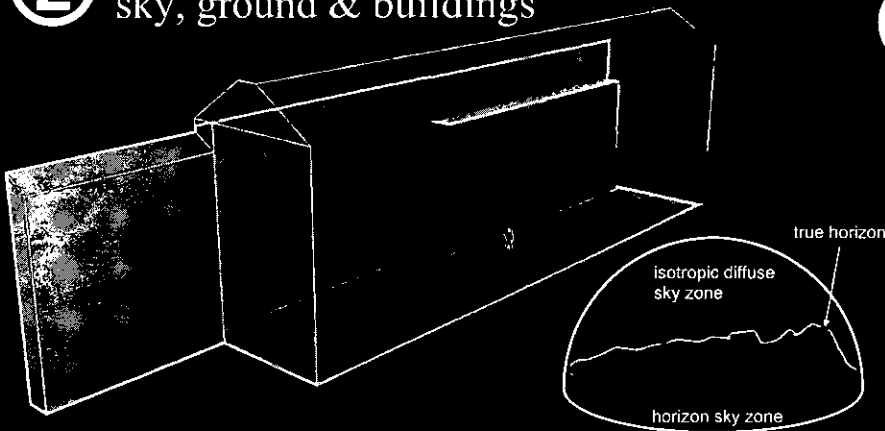
The procedure for calculating absorbed solar radiation can be broken down into four main steps, as illustrated in Figure 2.4.18. This procedure, with two others, was demonstrated in CFD simulations of the Experimental Atrium case-study (Subchapter 4.3). Detailed descriptions of similar solar radiation simulation procedures are given in references such as Kato *et al.* [1995], Li *et al.* [1992], Off *et al.* [1994], Omori *et al.* [1990, 1994], Ozeki *et al.* [1992], and Schild [1996].

4 steps to accurately calculate absorbed solar radiation

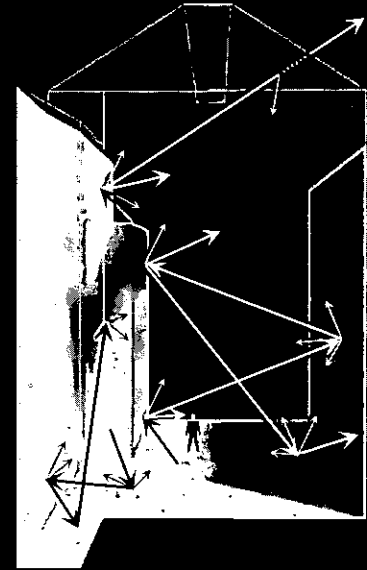
① absorbed beam radiation & specular reflections



② absorbed diffuse radiation from sky, ground & buildings



③ absorbed diffuse & specular inter-reflections of surface radiosity from steps ①+②



④ final solution = ①+②+③

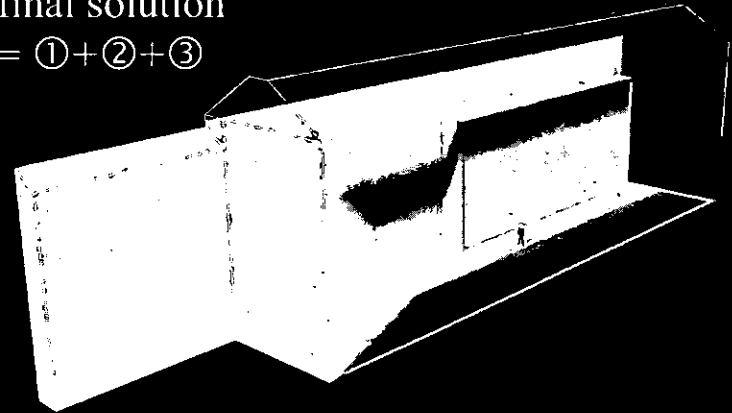


Figure 2.4.18 The four steps in calculating absorbed solar radiation.

Computation of direct solar radiation

The incident direct solar irradiance on an inside wall surface depends on the glazing transmittance and whether the direct solar radiation is obstructed by other walls or roofs (cf. Figure 2.4.17). The existence of obstructions is determined by tracing straight lines from the surface patches towards the sun, by means of a computer program. If a traced ray intersects a window and is not intersected by any intervening opaque walls or roofs (including the walls and roofs of the other buildings), then the originating wall patch receives direct solar radiation (Figure 2.4.19). The short-wave transmittance and reflectance of glass or other transmissive surfaces depends on the angle of incidence, and this should be included in the solar radiation simulation, if these properties are known.

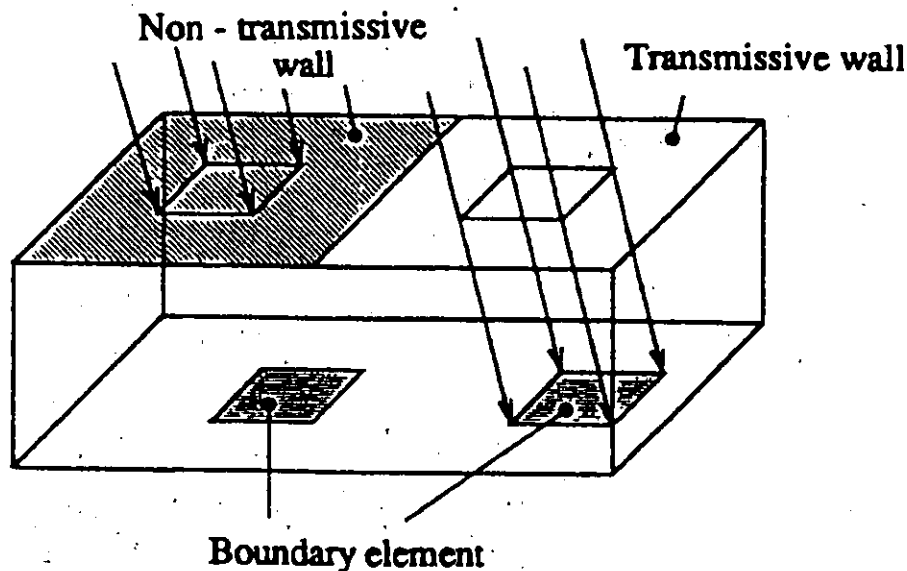


Figure 2.4.19 The direct solar radiation reaching the boundary elements.

Computation of diffuse radiation

Incident diffuse radiation from the sky dome (sky-diffuse radiation) and from the ground and other buildings (ground-reflected radiation) should also be considered. As diffuse radiation is somewhat less intense than direct radiation, we can safely apply some simplifications in its calculation, without significantly affecting the accuracy of the solar gain calculations. The most common simplifications are the use of an isotropic sky model, and an overall albedo (reflectance) for the ground and surrounding buildings. Another simplification is to treat the window as a plane light source in the enclosure (i.e. translucent glass). This requires only the calculation of the view factors between the window and the ground and sky. Thus the apparent radiant emittance of the window is also given by the sum of the incident direct, sky-diffuse and ground-reflected diffuse radiation incident on the window (cf. Figure 2.4.17).

Computation of multiple reflections

The surface-reflected radiation is normally assumed to satisfy Lambert's cosine law, i.e. specular (mirror) reflections are negligible compared to isotropic diffuse reflections. Starting with the resultant radiant emittance of the surface patches from the computation of direct and diffuse radiation, the short-wave multiple reflections in the enclosed space are solved using a radiation analysis method such as the Zone Method [Hottel, 1967], the Radiosity Method

[Cohen and Greenberg, 1985], Gebhart's Absorption Factor Method [Gebhart and Ithaca, 1959], a Monte Carlo Method [Siegel and Howell, 1992] or ray tracing [Dunne *et al.*, 1995]. Monte Carlo statistically models the basic physical process at photon level, and is therefore the most accurate, and can handle any level of geometric complexity. It can additionally model specular reflections, not only diffuse like the other methods. If the geometry is not too complicated then the other methods are accurate whilst requiring less calculation than Monte Carlo. Gebhart's method (and of course other zone methods such as Hottel's) is a good method for considering the effect of multiple reflection. Generally speaking, the zone methods, including Gebhart's Absorption Factor Method, are more accurate than iterative methods such as the Radiosity Method. These same methods are also used to precalculate the long-wave radiation exchange factors for the CFD-coupled simulation. The above methods, excluding Monte Carlo, rely on separate calculation of surface view factors (shape factors), details of which are also found in the above references, though a good overview is given by Emery *et al.* [1991].

Total absorbed solar radiation

Finally, the total absorbed solar radiation on each surface patch is simply the sum of the absorbed solar radiation.

Examples

Figure 2.4.21 shows an example of the solar radiation analysis of a large glazed enclosure (atrium) in summer [Murakami, 1992]. The atrium space, shaped like a big ship with glass walls, is shown in Figure 2.4.20. It is built in Tokyo, as part of an international conference centre. The length, height and width of the space is about 200m×65m×32m. Neighbouring buildings were accounted for in the direct solar radiation calculations. In this case, between 11am and 3pm no buildings shaded the atrium. The large structural framework (beams) under the ceiling was considered in the calculations, as they have a considerable effect on the solar radiation distribution. The small-scale structural components such as glazing frames and columns, which would not have such great influence on the radiant simulation, were neglected. The total number of surface patches for the radiation simulation was about 10000.

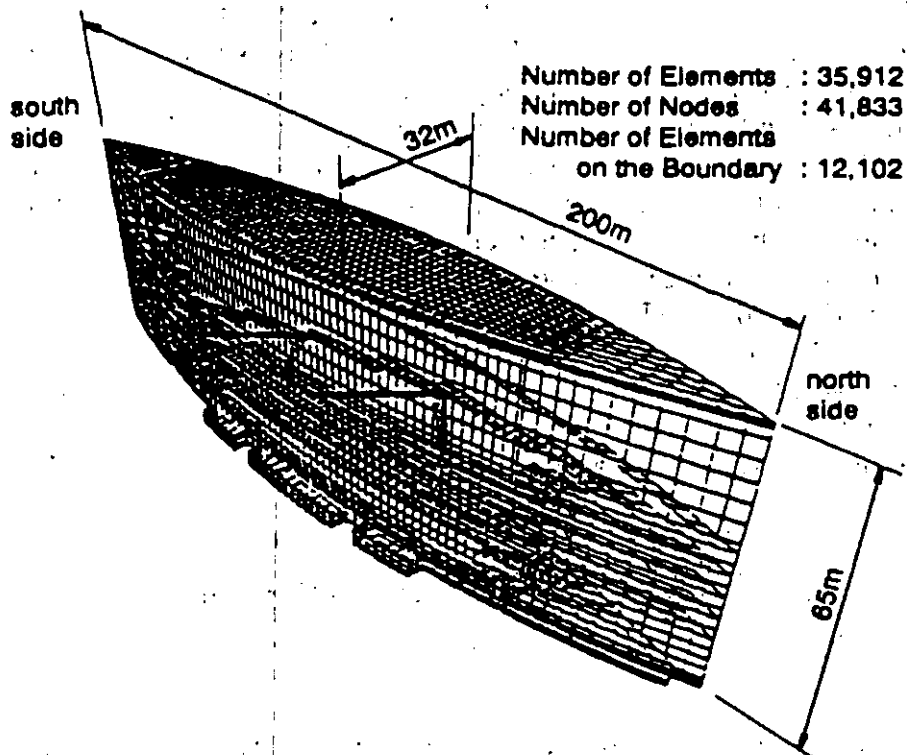


Figure 2.4.20 Shape of atrium and finite element mesh system.



Figure 2.4.21 Distribution of solar radiation absorbed.

2.4.8 Coupled Analysis of Radiative and Convective Heat Transfer

When the airflow and heat transfer in a room is studied, it is vital to consider surface heat transfer by both natural convection and long-wave thermal radiation (infrared radiation). Both these phenomena are governed by surface temperature, so a coupled analysis of radiation and convection heat transfer is needed. In a large indoor space, the ceiling's surface temperature may be affected by pronounced thermal stratification, such that the radiative heat flux from the ceiling to other surfaces is very large. Similarly, in an atrium, where the floor and walls are heated by solar radiation, the absorbed heat is redistributed to other surfaces by long-wave radiation. The long-wave redistribution of solar radiation in this way is very important in analysis of an atrium. Such a situation is shown in Figure 2.4.22.

Figure 2.4.23 outlines the procedure of coupled analysis of radiation and convection. In this simulation, the view factors and Gebhart's absorption factors [Gebhart & Ithaca, 1959] for mutual radiation analysis between surfaces, must be precalculated before the airflow analysis. The view factors for a space with complex geometry can be calculated by a Monte

Carlo method etc., as described on page 101. Moreover, another characteristic of the coupled simulation is to calculate the surface temperature of each wall by the heat balance equation composed of convection, conduction and radiation (see Figure 2.4.23). The two case studies described below, illustrate the practical application of coupled analysis:

In a large enclosure, gas absorption and reemission of infrared radiation cannot be neglected; since the distance between the walls of the enclosure is quite large. Carbon dioxide and water vapour can considerably affect the radiation field, and hence airflow, in a large enclosure if the concentration of those gases is quite high. In a sophisticated simulation, gas absorption and reemission of infrared radiation might be considered. As the absorptive-emissive properties of gases is highly wavelength-dependent; a line-by-line calculation method should ideally be used, which is very computer-intensive [Schenker and Keller, 1995]. Simpler faster approaches to gas radiation modelling have been suggested [Parthasarathy et al., 1996], though none were tested in Annex-26.

Case study 1: Local air-conditioning in hall by seat-integrated supply jets

Here, coupled analysis was carried out for concert hall seating with integrated air outlets for local air-conditioning [Kondo et al., 1993]. As shown in Figure 2.4.24, the conditioned air is supplied upwards from an opening at the top of the seat back, and it is intended to maintain a comfortable microclimate only in the zone of occupancy. The exhaust openings are located in the ceiling as well as in the floor under each seat. Heat from lighting etc. which builds up in the upper part of the hall is effectively removed by the ceiling-mounted exhaust openings. The floor-mounted exhaust returns air to the ventilation plant for recirculation.

Figure 2.4.25 shows the simulation model in which the condition of supply air and heat load from the human body and the lighting are included. The computational grid is not shown here. The view factors and the radiation absorption factors of the surface elements was calculated first, and then the coupled analysis of radiation and convection was carried out. The simulated area is the partial space cut out of the hall as in Figure 2.4.24; the symmetrical plane is treated as a 'free slip' plane for airflow and to be a mirror for radiation.

Figure 2.4.26 shows some results of temperature distribution. In order to study the effect of mutual radiation between walls, the results simulated with and without the radiative heat transfer are compared. Thermal stratification appears to be excessive when the radiation is disregarded and the temperature difference between the upper part and the lower part is overestimated. On the other hand, in the case of the coupled analysis of convection and radiation, the temperature of the upper area is about 38°C and the vertical temperature difference is half of that compared to the case without radiative heat transfer. The radiative heat transfer between object surfaces makes the surface temperature tend to uniformity. Figure 2.4.27 shows the heat balance of convection and radiation for each object surface. For example, the ceiling surface receives 41 Watts of heat from adjacent hot air, by convection, and this is transmitted to other object surfaces as radiative heat flux. In the region close to the surface received this radiation from the ceiling, the temperature distribution tends towards uniform. Moreover, the detail of the radiation, i.e. what ratio of the radiative heat flux from one wall is received by another object, can be calculated by referring to the absorption factor between specific objects. For instance, of the radiative heat leaving the ceiling surface (41 W), 29% reaches the human body, 24% the seat, and 44% the floor.

In a space such as mentioned above, where the thermal stratification is pronounced, the radiative heat transfer plays very important role and has an effect not only on the surface

temperature of the object but also on the air temperature. Note: the result shown in this section is part of a more extensive study which included model experiments.

Case study 2 : Floor standing air diffuser system

Here is presented the numerical simulation of an air-conditioning system with floor-mounted air diffusers. A vertical distribution of air temperature is formed in this system, and the supply air temperature can be raised while the level of comfort is kept in the same as a conventional fully-mixed ventilation system. This system can therefore reduce energy consumption. The simplified model as shown in Figure 2.4.28 is analysed here [Nagase et al., 1994]. The internal heat load is modelled as cubic shaped objects set in the office space that covers floor area 10m² and the lighting heat goes to the ceiling surface. Figure 2.4.29 shows calculation results. In order to see the influence of radiation, the results of interactive analysis of convection and radiation is compared with the result by the simulation without regard for radiation. From the simulated temperature distribution (Figure 2.4.30), the vertical temperature difference in the case of the interactive analysis is smaller than that in the result without radiation. The reason for this is that the radiative heat transfer between the ceiling and other object surface is captured only in the coupled analysis. Therefore the heat in the near region of the ceiling is transmitted to the floor side by radiation and this radiative heat has a tendency to make the temperature distribution uniform. In the interactive analysis, the air temperature near the floor rises due to the mutual radiation. As the result of this effect, temperature difference between the supply cool air and the surrounding air becomes higher and the throw of the supply jet is shortened than the results without radiation effect. Figure 2.4.31 shows the vertical distribution of concentration when the pollutant is assumed to be generated from the surface of the internal heat load models. The concentration distribution has little difference between with and without radiation effect, because there is no transportation mechanism corresponding to the radiative heat transfer.

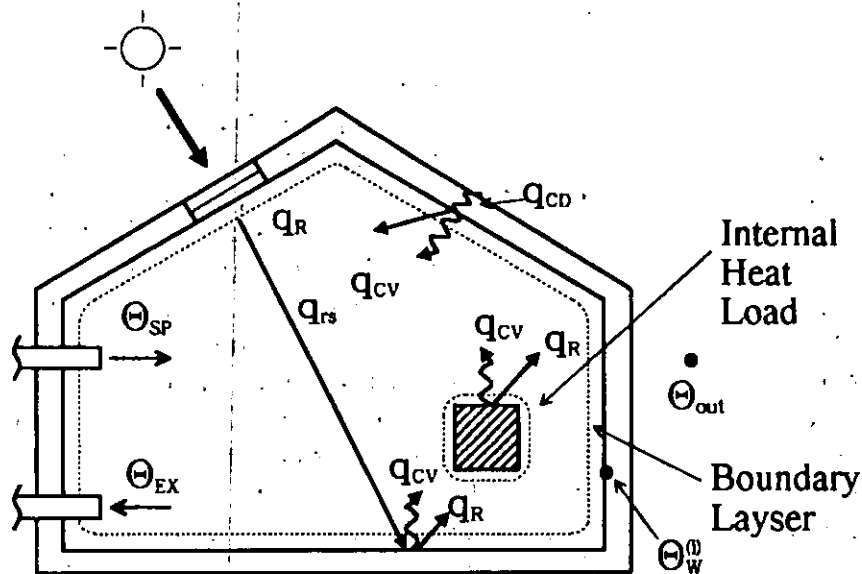


Figure 2.4.22 Radiation and Convection in a Room.

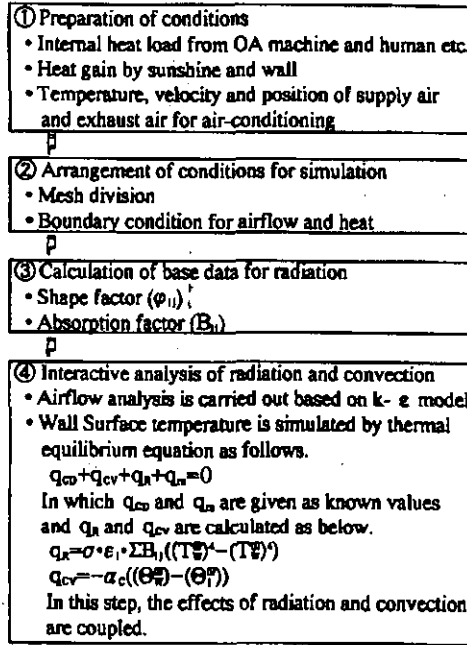


Figure 2.4.23 Procedure of Interactive Analysis of Radiation and Convection.

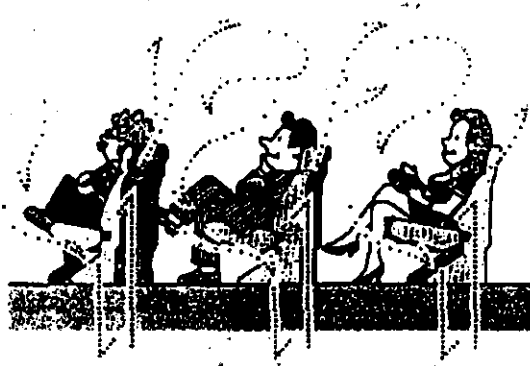


Figure 2.4.24 Local Air-conditioning by Seat-Mounted Supply Jet in Hall.

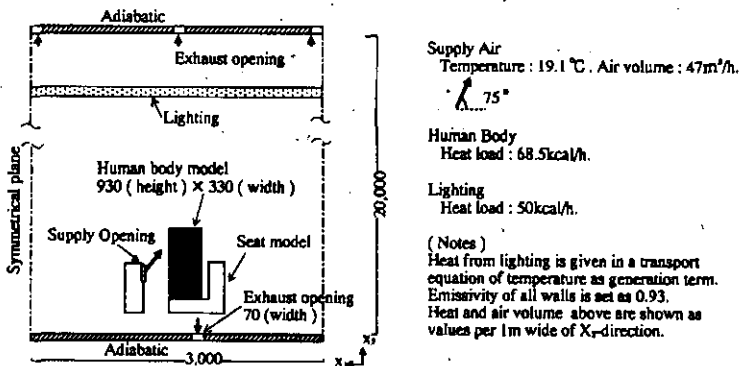


Figure 2.4.25 Two Dimensional Room Model Analysed(Unit:mm).

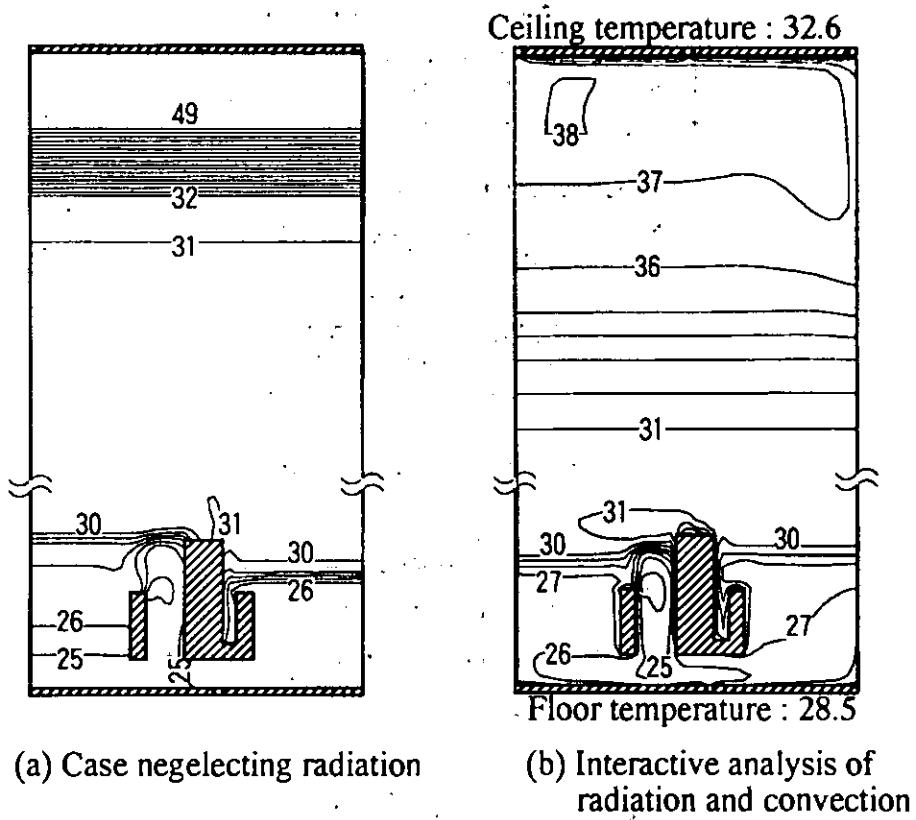


Figure 2.4.26 Results of Temperature (Unit: °C).

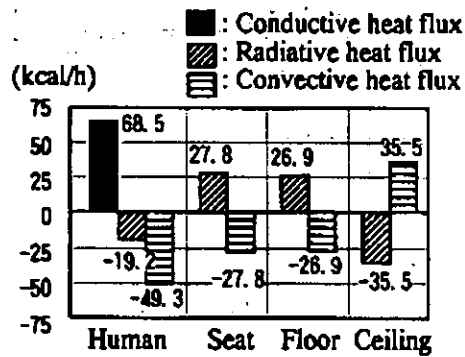
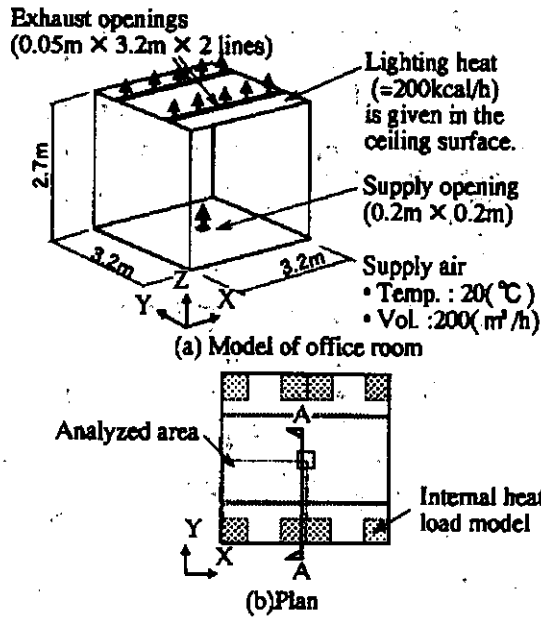


Figure 2.4.27 Balance of Radiation, Convection and Conduction for each Object. Surface (Flux into object surface is show as positive).



(Notes)
Internal heat load is assumed to be generated from 8 cubic objects (0.5m × 0.5m × 0.5m), and total heat generation rate is 400kcal/h (50kcal/h per a cubic). Pollutant generation from cubic objects is supposed to be 1×10^{-3} [m³/m³·s] per a cubic and the concentration of supply air is 400 ppm.

Figure 2.4.28 Simulation Model for Floor-Mounted Air Diffuser System.

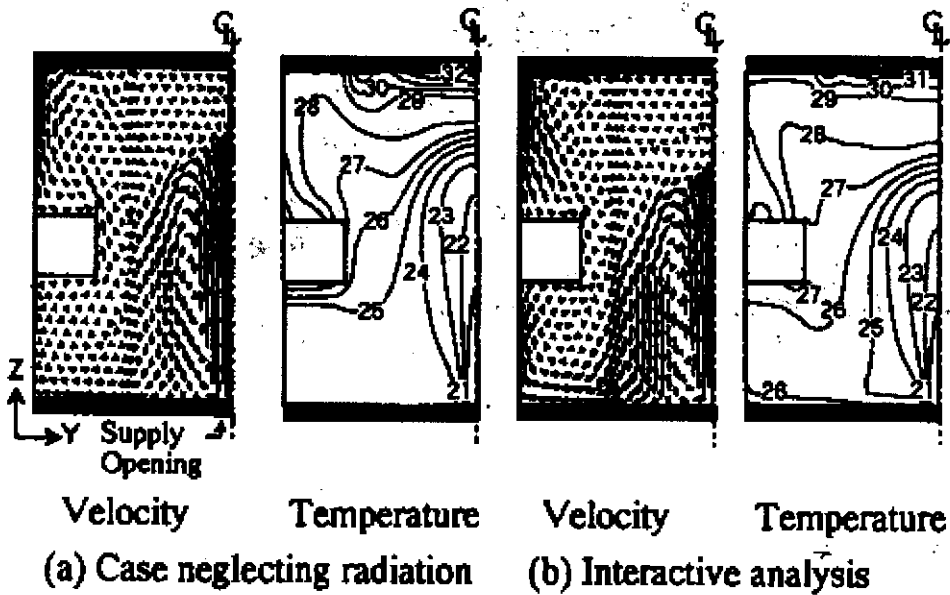


Figure 2.4.29 Simulation Results (Section A-A).

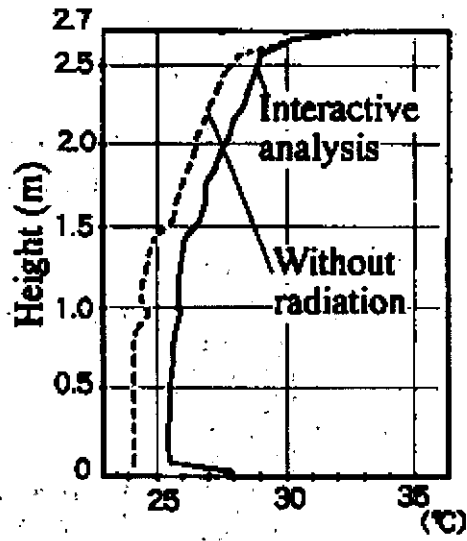


Figure 2.4.30 Vertical Temperature Distribution.

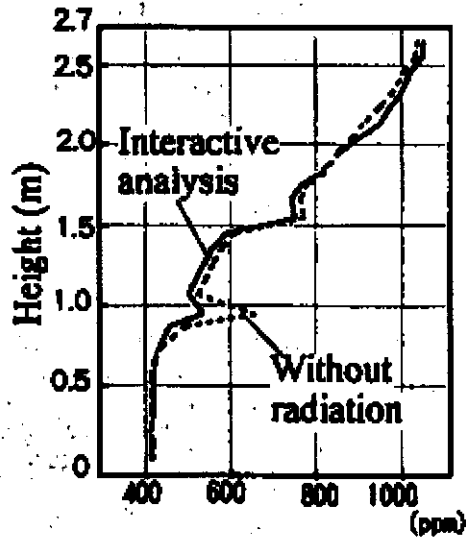


Figure 2.4.31 Vertical Concentration Distribution.

2.4.9 Macro Analysis Based on Micro Model Simulation

Significance of macro analysis

CFD (i.e. micro model) simulation gives detailed information on velocity and temperature throughout the space, but this is sometimes too much! It is not always easy to comprehend the macroscopic flow of mass and heat in a large enclosure from the results of micro simulation only. A technique to solve this problem is described here.

The macroscopic behaviour of a computed flow field can be examined by means of macro analysis of the flow field solved by micro-simulation. In other words, macro analysis is a method of making the results of a micro simulation more comprehensible. Knowing the macroscopic behaviour of the flow field, we can intuitively understand the fundamental transportation structure in the enclosure, which is very helpful for HVAC design. The interaction between micro-simulation and macro-analysis is shown in Figure 2.4.32 [Murakami *et al.*, 1994].

Figure 2.4.33 shows some cases of large enclosures where macroscopic analysis has played a large role in the HVAC design process.

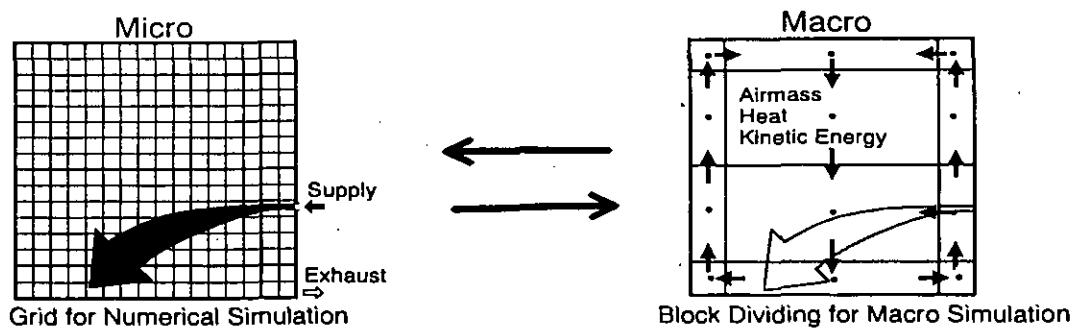
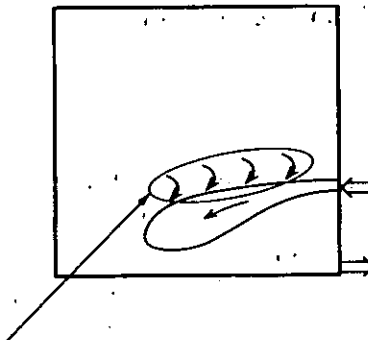
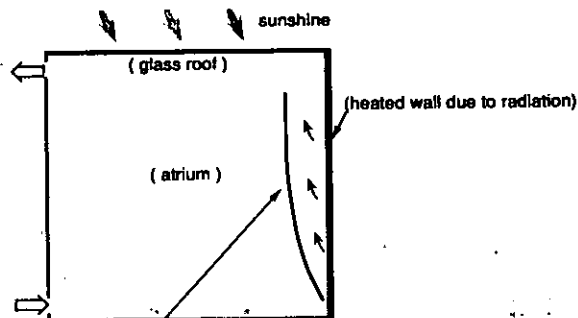


Figure 2.4.32 Interactive analysis by micro-simulation and macro-analysis.



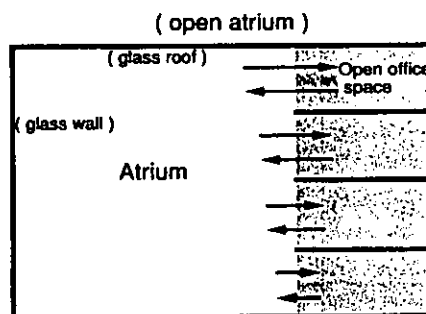
How much air and how much heat is induced by the supply jet ?

(a) Airmass induced by supply airflow



How much air and how much heat is transported by rising streams due to buoyancy ?

(b) A ascending current within an atrium



How much air and how much heat is transported between Atrium and open office spaces ?

Is it transported by convection or by turbulent diffusion ?

(c) Airmass and heat transport between an atrium and open spaces

Figure 2.4.33 Macro-analysis within large enclosure.

Concept and method of macro analysis

In macro analysis, the space is subdivided horizontally and vertically into medium-size control volumes (hereafter 'blocks'). The blocks are considerably larger than the computational cells used in micro simulation. For instance, the space may be divided into a 3×3×3 matrix thus: near-wall upper block, near-wall middle block, near-wall lower block, centre upper block, and so on.

Next, the physical properties of each block are evaluated by integrating the values of each term of the continuity equation, the temperature transport equation and the total kinetic energy transport equation, within each block. This gives us the mass balance, the heat balance and the total kinetic energy balance in the blocks, from which the macroscopic behaviour of airflow rate, heat transport, the total pressure loss etc. between the blocks can be evaluated. This macro-analysis may prove itself to be of great use in developing new principles for air-conditioning and ventilation systems.

Case Study 1 : Macro analysis of airflow and heat transport within a model atrium

This is an example of macro analysis of airflow and heat transfer by means of micro simulation of an experimental atrium (Figure 2.4.34). The indoor climate within the atrium, under cooling conditions, was analysed with CFD using the standard $k-\epsilon$ turbulence model, as well as being measured.

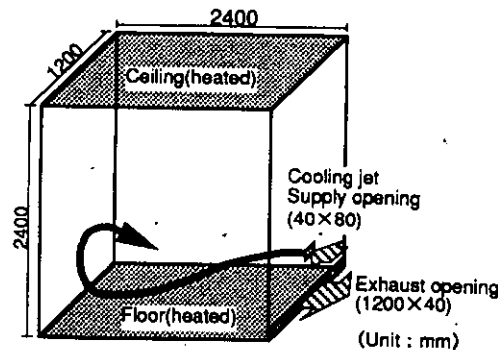


Figure 2.4.34 Model atrium space used for simulation and experiment.

The simulated velocity field is shown in Figure 2.4.35. The simulated velocity field seems to reproduce the experimental results fairly well, though the measured flow field is not shown here. The velocity in the lower part of the space is high due to the air supply. Natural convection airflow is observed near the wall due to the temperature difference between the air and the wall surface, which is mainly derived from radiation from the ceiling or floor. The velocity in the upper part of the space is extremely low due to damping by thermal stratification, except for near the wall surface.

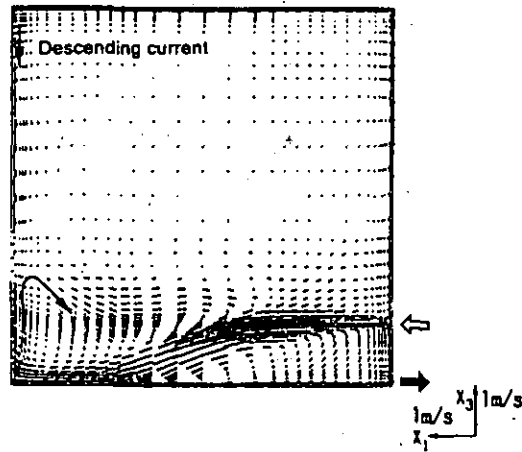


Figure 2.4.35 Distribution of velocity vectors (micro-simulation, centre section).

In order to analyse the macroscopic behaviour of air and heat transport within the space, the block model in Figure 2.4.36 was used. As shown in Figure 2.4.37, a descending current is observed in blocks $b \sim f$ in the centre zone, while ascending currents are generated in the blocks near the wall surface (blocks $f \sim b$ of zones $W1$ and $W2$). A large airflow rate, 3 to 10 times larger than the supplied air volume, is observed in the lower part of the space (blocks $d \sim e$ of centre zone) where supply/exhaust openings are located. The airflow rate is extremely small between the blocks in the upper part of the space (e.g. between blocks a & b of centre zones, approximately $1/10$ of the supply airflow rate).

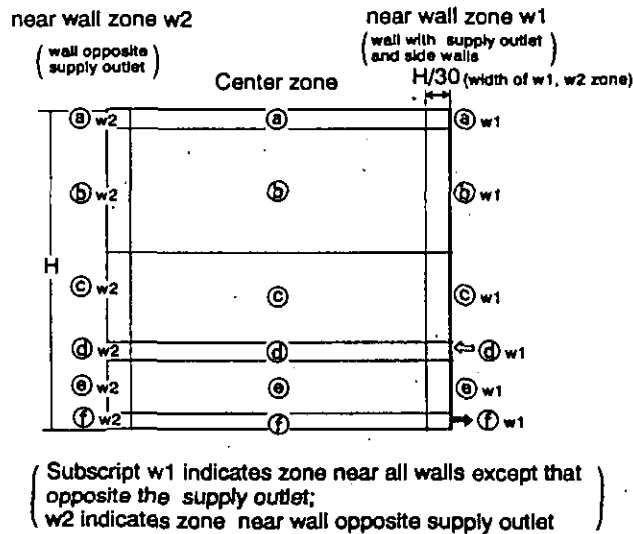


Figure 2.4.36 Block dividing for macro-analysis (subscript w1 indicates zone near all walls except that opposite the supply outlet ; w2 indicates zone near wall opposite supply outlet).

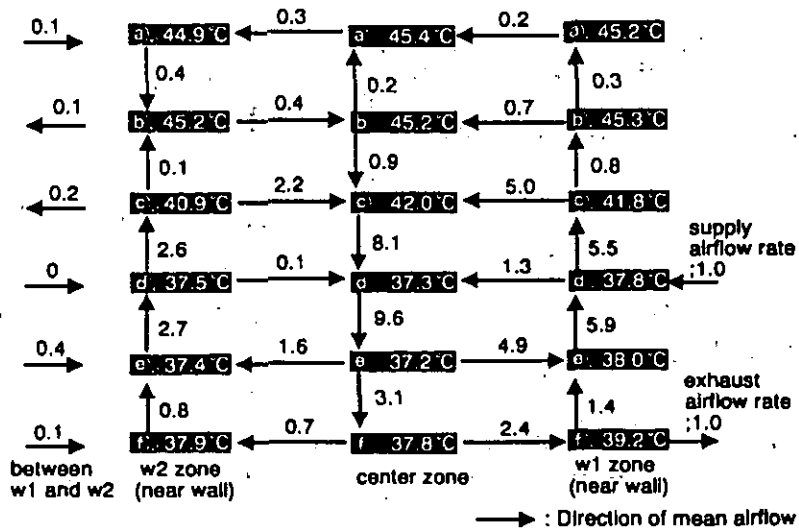


Figure 2.4.37 Air movement between blocks (normalised by supply airflow rate).

Case Study 2 : Determination of the optimum placing of tracer gas sampling points

Some measurement techniques used to obtain ventilation efficiency parameters require the injection of a tracer gas followed by the sampling of air at a number of points in the space.

However, it is physically difficult to sample the air at a large number of points, so the sampling points must be strategically selected such that the results are representative of the air movement and distribution characteristics of the whole space.

To this end, it was decided to explore the suitability of CFD as a modelling tool to provide knowledge of the air movement characteristics of the buildings under investigation. The result of the CFD analysis was converted to a multizonal representation which was then subjected to successive simplification. At each level of simplification, the ventilation efficiency parameters within each zone were obtained, and the results from each simplification level were compared, in order to determine the effect of reducing the number of sampling points. Although this investigation is still at an early stage of development, the indications are that a preliminary analysis is a good guide to the optimum placing of tracer gas sampling points, [Brouns et al., 1994].

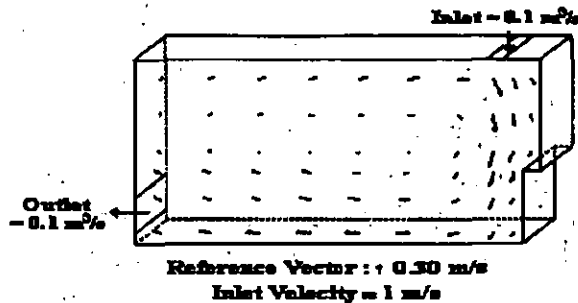


Figure 2.4.38 CFD representation of the velocity field for the 57-zone model.

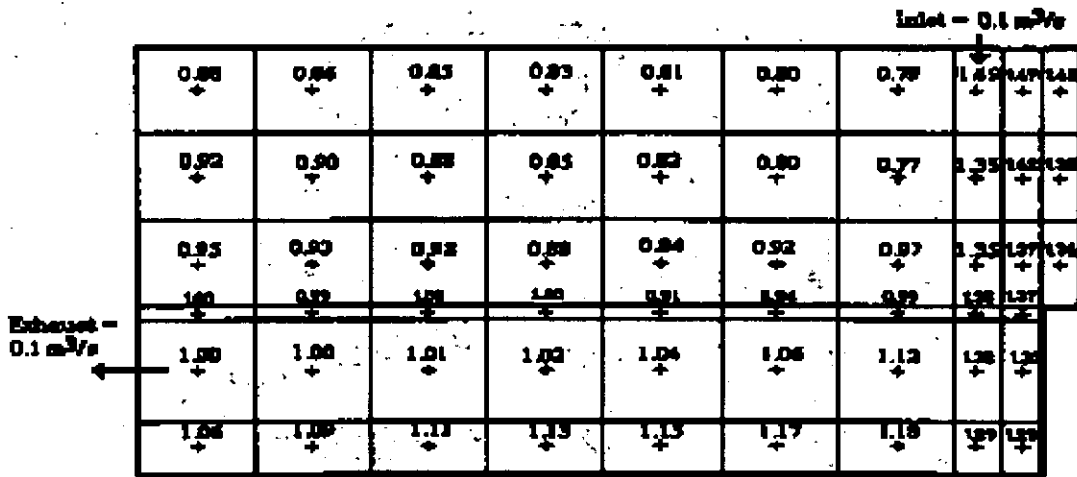


Figure 2.4.39 Local Air Change Index Contours, 57-zone model.

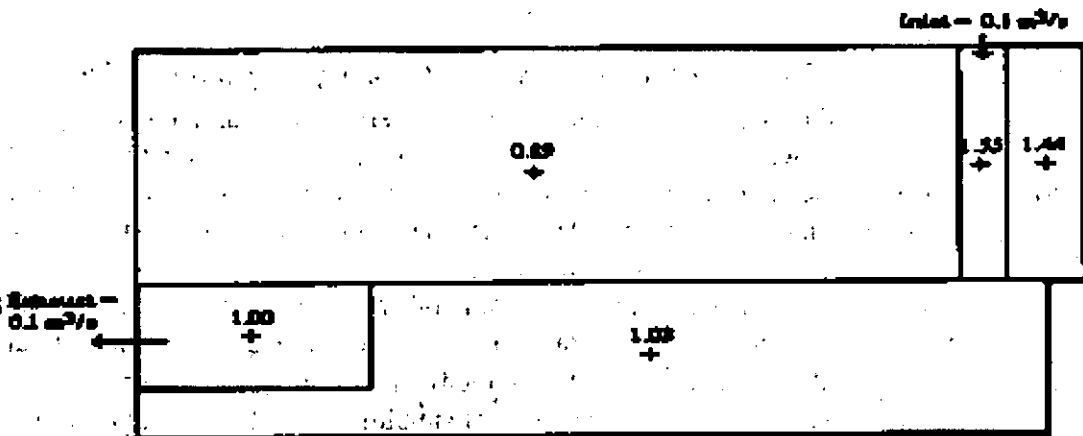


Figure 2.4.40 Values of Local Air Change Index, 5-zone model.

2.4.10 Interactive Analysis of Macro and Micro Models

Advantages of interactive analysis

The two categories of numerical methods for simulating airflow and heat transfer in buildings, macro analysis (i.e. zonal models); and micro analysis (i.e. CFD) each have their own advantages and disadvantages in practical use.

In macro analysis, each space (or zone within the space) is represented by a nodal point as shown in Figure 2.4.41 and the transport of mass, heat or contaminants between the points, along network paths, is predicted. It is therefore a simple and fast method, yet it can handle complex models, such as the simultaneous analysis of all rooms in a building with a central HVAC plant, with structural thermal storage and convective, conductive and radiation heat transfer, etc.

In micro analysis, the spatial distribution of velocity and temperature is resolved in considerably more detail, usually for only one room (Figure 2.4.4I). However, boundary conditions which are implicitly related to the rest of the building, such as walls shared with

adjoining rooms are not known, and it is computationally costly to implement dynamic boundary conditions, with thermal storage, etc.

Consequently, the advantages of both methods can be exploited by interactive analysis where the boundary conditions for the micro simulation are given from the results of macro simulation. These two prediction methods are here used interactively [Kato *et al.*, 1990; Axley, 1988; Schälin *et al.*, 1992].

The technique of 'macro analysis based on micro simulation' described in the previous section, has a role in connecting macro and micro simulations, even though it is not a method of simulation itself (but rather a method of post-processing of the final results). The interaction between these three methods is shown in Figure 2.4.42 [Murakami *et al.*, 1994].

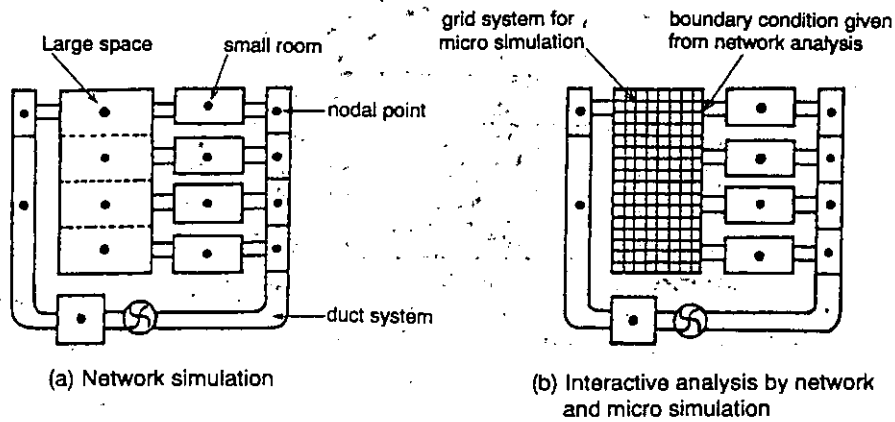


Figure 2.4.41 Whole building analysis by network model including large space analysis with micro model.

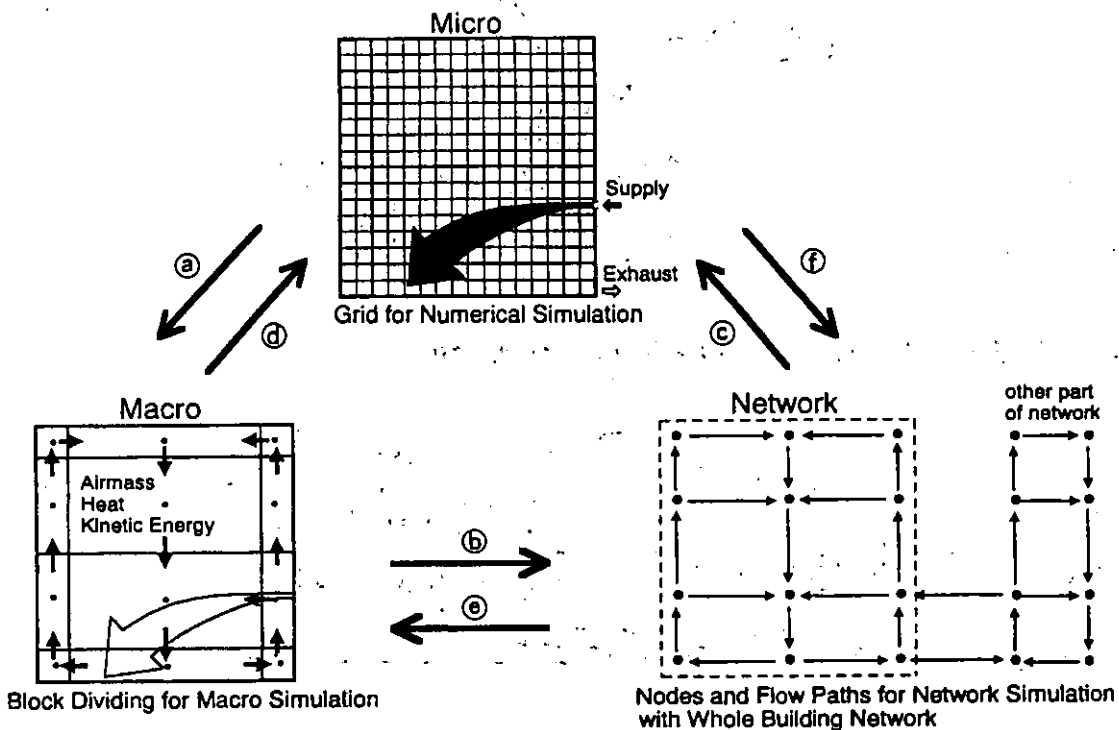


Figure 2.4.42 Interactive analysis using micro, macro and network simulation.

Case Study 1 : Linking CFD with a multizone model

Zonal models are commonly used for calculating airflow and contaminant spread in the rooms of a building and between the building and outdoors. Usually a whole room is modelled as only one calculation node, with the assumption of homogeneously mixed conditions within the room, whereas in reality temperature and contaminant concentrations vary in space. The exchange with the neighbouring nodes via flow paths is then a function of the local values of these variables. Detailed knowledge can be obtained from CFD analysis of the air flow pattern within the room at the expense of far higher computation cost.

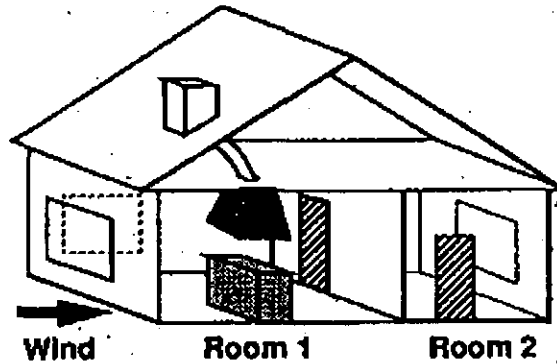


Figure 2.4.43 (a) Example house with two rooms. The left room with internal details shown is the one chosen for the CFD calculation.

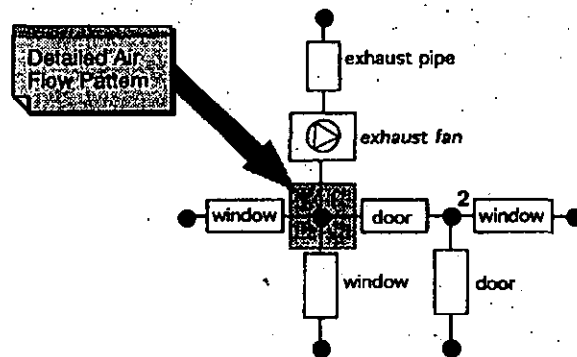


Figure 2.4.43 (b) Multizone network of the whole building.

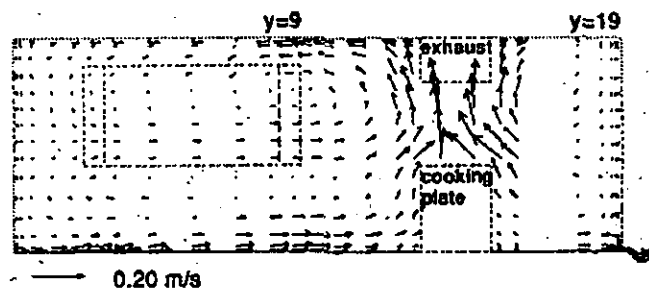


Figure 2.4.44 CFD-predicted flowfield.

The method is demonstrated in an example case with air infiltration/exfiltration, ventilation and contaminant spread, shown in Figures 2.4.43 and 2.4.44. This method, called

method of detailed node values, promises to improve the zonal model predictions with few additional CFD computations.

Case Study 2 : Numerical study of an atrium by micro-macro simulation

To predict the indoor climate within an atrium, two numerical simulation methods are applicable. One is a rough study by using a macro model [Togari et al., 1993, Refer to Note] and the other is micro simulation based on a turbulence model. Each method has its limitations. For instance, the former method cannot provide the detailed data of the flow and temperature fields whereas the latter method has a drawback in that it is difficult to determine proper boundary conditions concerned with heat transfer at wall surfaces. The results of simulations on indoor climate within an enclosure by these two methods are shown, (Figures 2.4.45-2.4.48).

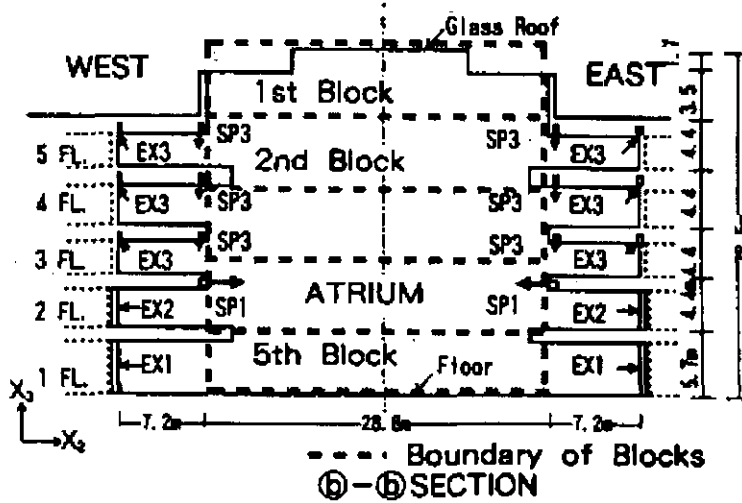


Figure 2.4.45 Atrium analysed by micro and macro simulation.

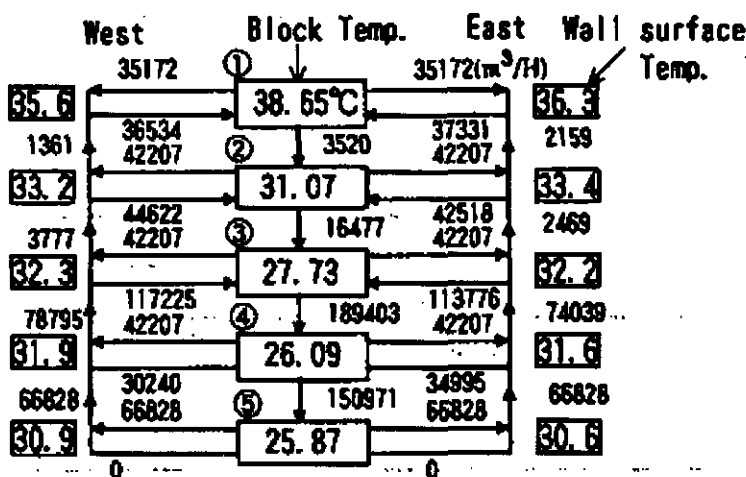


Figure 2.4.46 Results of macro-simulation at the steady states.

Note .

This macroscopic model is a simplified model for predicting vertical temperature distribution in a large space [Togari *et al.*, 1993]. In this model, the space is vertically divided into a number of zones. The ascending and descending currents along the vertical wall generated by convective heat-flow to the wall are evaluated. When the space is air-conditioned, the path of the supply air jet and the air volume entrained from each zone are evaluated. Next, by solving the equations of airflow balance and that of heat balance in each zone, the vertical temperature distribution can be calculated. This calculation model has a useful feature that can be incorporated into dynamic thermal analysis.

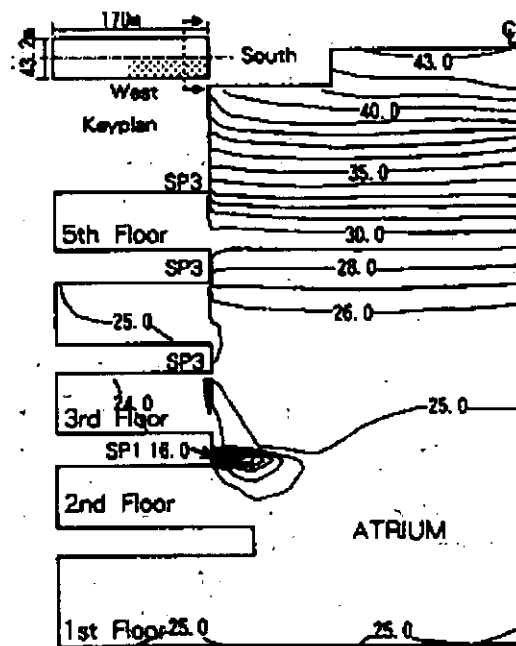


Figure 2.4.47 Temperature distribution - ($k-\epsilon$ turbulence model).

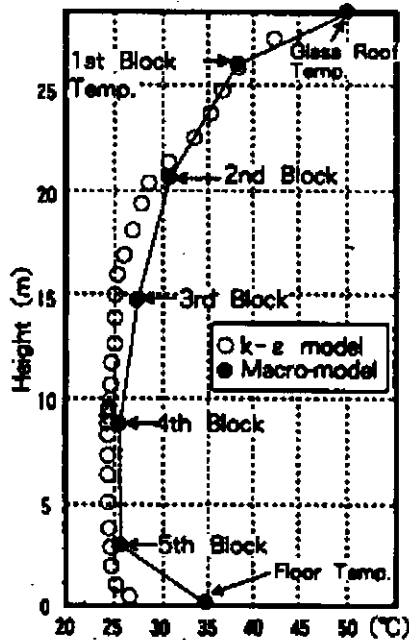


Figure 2.4.48 Comparison between results of macro-model and that of the $k-\epsilon$ model.

Coupled analysis for treatment of dynamic boundary conditions

Structural thermal capacity can have a large influence on the environment in an atrium. Ozeki et al. [1994] reported that the predicted mean room air temperature in a very large atrium changed significantly when they switched from a steady-state micro analysis (with boundary conditions based on zero thermal capacity) to a dynamic micro simulation incorporating thermal capacity. The swings in room air temperature were damped (peak temperature was 4°C lower) and delayed significantly (by 3 hours). The difference was due to the thermal capacity of the solid walls and floor.

Other researchers have also coupled dynamic macro and micro models, to evaluate the ventilation performance of conventional enclosures [Peng and van Paassen, 1994; Aasem et al., 1994; Holmes et al., 1990]. Holmes et al. found that operating the models in coupled mode, with 1 second time steps, revealed important transient airflow features caused by the HVAC controls such as temperature change of inlet jet, which could not be revealed when operating the codes separately. The computational overhead of the dynamic macro model was only 0.5%, the run time being dominated by the heavy computational requirements of the transient micro analysis. Both Holmes et al. and Peng et al. concluded that unless such detailed transient analysis of HVAC controls performance is necessary, a significant reduction in the computational effort may be possible by using a long integration time step. For example, Ozeki et al. [1994] used 10 minute time steps. This is justified because the time constant of the airflow in an enclosure is shorter than the thermal time constant of the surrounding surfaces. Alternatively, a more efficient method is to operate the two models in sequence, and perform a quasi steady-state micro analysis at the moment when the most severe design conditions occur.

2.5 Scale Model Experiments

Scale models of indoor ventilation enable one to visualise the airflow and measure air temperature and mean velocity at any point in the space. Scale modelling of ventilation aerodynamics has a long tradition. Despite the recent introduction of CFD modelling, scale model experiments are still considered a useful and sometimes necessary tool in ventilation design, especially for designing air distribution in large enclosures.

Scale models in water are often used. Density gradients may be obtained either by heating or by adding a saline solution (brine), or a less dense alcohol/water mixture. These methods are useful for evaluating buoyancy-induced airflow, but cannot correctly model surface heat exchange. Moreover, water models are generally less turbulent than the real airflow they simulate. These problems can be overcome by using air as the modelling fluid.

It is assumed that similarity of the mean velocity fields is achieved when the flow in the real enclosure and its scale model are both fully turbulent. This assumption means that the effect of some physical phenomena, e.g. fluid viscosity, is neglected in the modelled system, which results in approximate similarity and hence *approximate modelling*. In a programme of complex model tests, it is possible to separate the aforementioned *approximate modelling* regions and regions of boundary conditions simulation. This *partial modelling* approach makes use of the principle that similar external actions result in similar reactions both in the model and in the real enclosure.

Achieving thermal and airflow similarity in a scale model is especially tricky in the case of large enclosures. One of the many aims of the Annex-26 research work was therefore to look into these problems, and develop improved techniques for scale modelling of large enclosures. Improving scale modelling of large enclosures involves, above all, finding the conditions needed to get a Reynolds-number-independent-flow pattern in the model, as well as defining a similarity criterion that characterizes the flow's turbulent structure and finding ways in which this structure can be replicated in the model. In some model cases, e.g. when predicting air change efficiency in a ventilated space, turbulence similarity is required since irregularities in the airflow are determined not only by the mean velocity field but also by the irregularity and randomness of the real turbulent motion. Improving scale model experiments also requires careful selection of the model construction and measurement methods.

All these problems have been considered in connection with modelling of the Annex 26 case study building 'Turnhalle München' (page 129).

2.5.1 Similarity Criteria for Modelling Ventilation

It is useful to distinguish three regions of a large enclosure that can be treated separately and differently in a scale model experiment (Figure 2.5.1) [Kato *et al.*, 1988; Baturin and Elterman, 1974; Mierzwinski, 1987].

- **Region 1** is the inner space of the enclosure except the boundary layer flows adjacent to the walls and internal obstacles. The air movement in the space is treated as fully turbulent. This region is mainly of interest in model experiments as a region of air distribution processes
- **Region 2** contains surfaces such as external walls, partitions, equipment, persons etc., with inner boundary flows. In this region, the problem is to model heat transfer from surfaces to the enclosure's interior

- **Region 3** is the area surrounding the building. Here, the modelling problem includes heat transfer from the atmosphere and surrounding objects through the outside boundary layer to the external walls, and air mass transfer through the openings into the enclosure, e.g. by natural ventilation

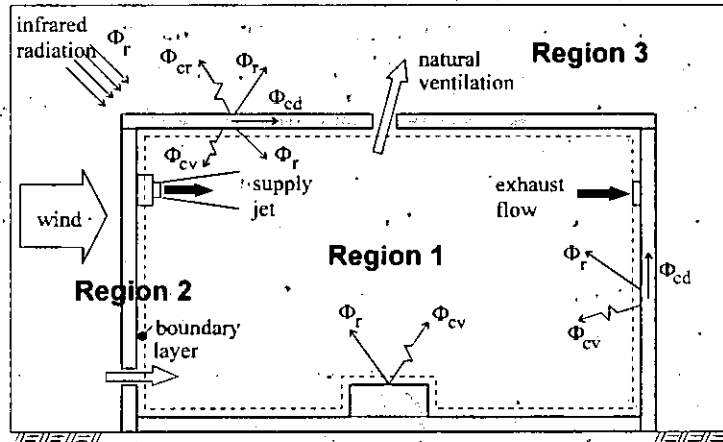


Figure 2.5.1 Illustration of the physical phenomena influencing airflow in enclosures, showing the three separated modelling regions. Φ_r , Φ_{cv} , Φ_{cd} = radiative, convective and conductive heat flow rate, respectively.

To achieve similarity between a real full-scale enclosure and its small-scale model, the following criteria must be met:

- Geometric similarity (length-scale)
- Physical similarity (time-scale & force-scale), which consists of :
 - ↳ similarity of governing equation for the modelled phenomena of heat and mass transfer
 - ↳ similarity of boundary conditions

Flow conditions for a real enclosure and its scale model are completely similar if all the relevant 'similarity-determining criteria' (i.e. dimensionless numbers) are equal for both. When these similarity criteria are met, then airflow properties such as velocity, at equivalent points in the enclosure and its model are related by simple scaling factors.

It is actually impossible to achieve true equality of all the relevant dimensionless numbers simultaneously in all three regions mentioned above. It is therefore necessary to choose, according to the experiment's objective, which part of the whole flow process is of special interest, and in which region physical simulation is acceptable (e.g. simulation of the heat and mass fluxes as substitute boundary conditions). This *partial modelling* approach can greatly simplify the modelling process. The objective of scale modelling of ventilated enclosures is usually to determine the airflow pattern in the enclosure (Region 1) under given boundary conditions determined by the HVAC system and building construction (Region 2) and outdoor climate (Region 3).

Air distribution process - Region 1

Region 1 comprises forced and convective nonisothermal airflow where mechanical and thermal similarity ought to be fulfilled. Therefore, when modelling the air distribution process

under steady-state conditions, the laws of conservation of mass, momentum and energy dictate that the following dimensionless numbers are used to indicate similarity for the velocity and temperature fields:

- Reynolds number (Re), which is a qualitative ratio of the effects of *inertia* over *viscosity*, for forced fluid flow, a high number indicating turbulent flow
- Archimedes number (Ar), which characterizes the ratio of *buoyancy forces* over *inertia*, for forced fluid flow, a high number indicating highly buoyancy-affected flow
- Prandtl number (Pr), which is a physical property of the fluid. It is the ratio of the fluid *viscosity* over *thermal conductivity*, a low number indicating high convection

$$\text{Re} \equiv \frac{uL}{\nu} \quad \text{Ar} \equiv \frac{\beta g L \Delta T}{u^2} \quad \text{Pr} \equiv \frac{\nu}{\alpha} \quad (2.5.1)$$

The modelling fluid in scale models of large enclosures is usually air. Hence the Prandtl-number equality is fulfilled automatically. But comparison of the above formulae shows that it is not possible to achieve similarity between an enclosure and its scale model with both Ar and Re at the same time, when using air as the model fluid. Some interesting methods have been suggested to avoid this difficulty by way of the substitute assumption. e.g.:

- $u_F = u_M$ in a cross-section of the real enclosure and its model, a reference velocity, corrected Ar-number after Nerval and Probert [1977]. ($F \equiv$ Full-scale $M \equiv$ Model)
- The so-called 'critical Ar-number' for nonisothermal flow, which is larger for large rooms. This enables a compromise between 'Ar-number similarity' and 'Re-number similarity' in a given model [Zhang et al., 1992]

Such assumptions divert the course of the modelling experiment from physically self-governing flow similarity to substitute controlled flow in the model.

The *approximate modelling* method [Baturin and Elterman, 1974; Mierzwinski, 1987] involves approximating the physical meaning of the modelled phenomena. The method is based on the property of flow that, as the Reynolds-number increases, the level of turbulence increases asymptotically to a stable fully-turbulent state where the mean flow and turbulence patterns are preserved (self-preserving, [Reynolds, 1974]) since the role of viscosity in the energy spectrum becomes insignificant. Such fully turbulent flow is described as being Reynolds-number independent.

The length and velocity scales of the mean motion can then be used to reduce cross-stream profiles of the time-mean axial velocity, along different sections in an enclosure, to a common form by means of suitable scaling functions. Profiles and flow patterns with this characteristic are described as self-similar [Reynolds, 1974]. In other words, at sufficiently high Re-numbers, the flowfield becomes asymptotically self-similar because of its independence from molecular viscosity.

Thus, for a physically reasonable simplification of the scale model, the main challenge is to identify the lowest Reynolds-number, the threshold-Re-number, Re_t , above which the flow in the model becomes Re-number independent. Then, for approximate modelling of a space in which turbulent flow (jets and forced or natural convection) occurs, it is sufficient to maintain in a model (M) the same Ar and Pr-numbers as in the full-scale object (F) and Re and Gr-numbers over their threshold levels:

$$Ar_M = Ar_F \quad Pr_M = Pr_F \quad \& \quad Re_M \gg Re_t \quad \text{or} \quad (Gr Pr)_M \gg (Gr Pr)_t \quad (2.5.2)$$

Choosing a threshold Reynolds-number, Re_t , in a scale model experiment has a bearing on the selection of the geometrical scale factor S_L of the model (where $S_L < 1$), which in turn affects the model's accuracy in connection with reproducing the self-similarity of parameter profiles and turbulence structure.

A consequence of this opportunity to neglect molecular viscosity when flow is turbulent, is that Re is not included among the similarity criteria. Instead, a similarity criterion for turbulent flow patterns must be introduced. From analysis of the Reynolds-averaged momentum equation (Section 2.4.3) [Kato *et al.*, 1988; Szűcs, 1980], the Reynolds stress, $\rho \cdot \overline{u_i' u_j'}$, and the turbulent heat flux, $c_p \rho \cdot \overline{u_j' \Delta \Theta}$, could represent the initial range and character of a turbulent flow. This character can be expressed by eddy kinematic viscosity, ν_t , and eddy thermal diffusivity, a_t , or by the turbulence Reynolds number, Re_t , and turbulence Prandtl number, Pr_t , respectively.

For experimental scale modelling, the nondimensional Kármán number can be used to characterize similarity of the boundary flow structure. The Ka criterion [Szűcs, 1980] expresses the ratio of the turbulent stress to the square of a reference mean-velocity at the boundary:

$$Ka \equiv \frac{\overline{u_i' u_j'}_b}{(\overline{u}_b)^2} \quad (2.5.3)$$

A consequence of this similarity is equality of the Reynolds stress relation at corresponding points in two similar systems.

$$\frac{\overline{u_i' u_j'}}{\overline{u_i' u_j'}_b} = idem \quad (2.5.4)$$

Turbulent flow has to be treated as a stochastic process and the quantities indicated by the Ka criterion as expected values. Both mean velocity and velocity fluctuation have to be measured. However, there is a problem of choosing which cross-section in the supply jet should be considered as the representative mixing layer flow. This choice of cross-section is very important because it is representative of the flow structure similarity for the whole volume in the model (Region 1). It seems it should be the initial cross-section in the self-preserving region of the supply jet. In this region the supply jet is characterized by fully-developed self-preserving turbulence, where its shape and self-similar profiles of the mean axial velocity are settled. However, the distance between the supply opening and the self-preserving region depends significantly on the turbulence intensity in the supply opening. This is because the self-preserving region is preceded by the developing region of the jet (its initial part with a core of constant velocity, and a transient part) where the flow structure is gradually transformed from the state found in the supply opening to fully developed turbulence.

In a fully developed supply jet, the mean axial velocity profile contains the encoded shear-stress distribution, i.e. the Ka criterion. The required Ka criterion can therefore be measured on the basis of an experimental model of the supply jet. Similarity of the mixing layer flow structure can in practice be characterized by means of the coefficient of axial velocity decay, K , and the position of the jet virtual origin x_s :

$$u_x = K \sqrt{\frac{I_s}{\rho (x + x_s)}} \quad (2.5.5)$$

where

- I_s = axial momentum in jet flow at the outlet
- u_x = centreline velocity at the distance x from the outlet
- x = distance from opening, in axial direction along the jet
- x_s = distance from the virtual origin of the jet to the opening

Thus, when constructing the supply nozzle in the scale model, information is acquired regarding the required turbulence structure in the self-preserving region of the jet and the distance between this region and the supply opening whose shape and fittings in the real enclosure are known. It is possible to change this distance in the model by additional turbulence generation at the nozzle.

The above approach to the problem is based on the studies connected with the case study building 'Turnhalle München'. However they have not yet been sufficiently advanced to define detailed construction guidelines.

Modelling scales for air distribution

Based on the equality of the Archimedes numbers in the full-scale space and in its model, $Ar_F = Ar_M$, the following relation between the scale factors of the representative parameters can be derived:

$$S_u = S_L^{0.5} S_{\Delta\theta}^{0.5} \quad (2.5.6)$$

where the scale factors of the representative velocity, length and temperature difference, are respectively:

$$S_u = \frac{u_M}{u_F} \quad S_L = \frac{L_M}{L_F} \quad S_{\Delta\theta} = \frac{\Delta\theta_M}{\Delta\theta_F}$$

In the *approximate modelling* method, two of the three above-mentioned scales may be selected freely. But there are some practical limitations. The size and cost of the model depends on the length scale, and its selection should fulfil the condition $Re_M > Re_l$. The choice of the temperature-difference scale, $S_{\Delta\theta}$, should not make it impossible to carry out the experiment under laboratory conditions (i.e. feasible temperatures of the air and the surfaces in the model). The velocity scale, S_u , should enable sufficiently accurate measurements of the mean velocity and velocity fluctuations, since among other things, accurate measurements of the mean velocity and velocity fluctuations are necessary in the supply jets, to determine the Kármán number. There will usually be a need to modify the initial turbulence of supply jets in the model by means of turbulence-generating artefacts in supply openings.

Section 2.5.2 (page 127) discusses some connections between the threshold Re_l number and the real Re number in the model at the selected scale factor S_L .

Similarity of boundary conditions - Regions 2 and 3

Similarity of mechanical velocity field boundary conditions (i.e. openings, etc.) may be fulfilled through geometric and velocity similarity. Similarity of thermal boundary conditions for region 1 may create:

- Similar surface temperature distribution of surfaces and
- Similar distribution of convective and radiative heat flow rates inside the enclosure

The temperature distribution and heat flux at the boundary of Regions 1 & 2 depends on the heat and mass transfer with Region 3 and heat exchange inside the enclosure by convection and radiation. There are two modelling problems related to this:

- Heat transport from Region 3 to the building by forced convection and short- or long-wave radiation (wind, sun, atmosphere, surroundings, etc.) are complex and their distributions are to a certain extent random
- For heat transport in the boundary layer close to the walls of the enclosure, the following relation holds true:

$$-\lambda \frac{\partial \Theta}{\partial \mathbf{n}} = (h_{wcv} + h_{wr})(\Theta_w - \Theta_i) \quad (2.5.7)$$

where

$$h_{wcv} = f(\text{Re}, \Delta\Theta)$$

\mathbf{n} = the direction normal to the wall

• The Re-number here in the boundary layer flow is mostly smaller than Re_t . Thus, the flow cannot be treated as Re-number-independent, so there is no similarity of the convection due to heat transfer at the wall. It is therefore difficult to model the inside surface temperature and at the same time maintain similarity of the convective and radiative heat distribution.

It is therefore best to *simulate* the thermal boundary conditions for Region 1 in the model based on the heat balance for the enclosure (Region 2) and on an assumed heat transfer through the walls from Region 3 to Region 1. Thus the heat balance should be known for the full-scale space.

From the heat conservation law applied to the enclosure surrounded by the outer wall surfaces, the heat balance can be obtained in an integrated form as follows:

$$\Phi_i = \Phi_{cv} + \Phi_r - \Phi_a \quad (2.5.8)$$

where

Φ_i = net heat gain to the indoor air

Φ_{cv} & Φ_r = convective and radiative heat gains respectively

Φ_a = heat loss through walls

By dividing Equation (2.5.8) by Φ_i , relations for heat flow rates can be obtained whose values should be the same in the full-scale space and its model:

$$\frac{\Phi_{cv}}{\Phi_i} = idem \quad (2.5.9)$$

$$\frac{\Phi_r - \Phi_a}{\Phi_i} = idem \quad (2.5.10)$$

The construction, thermal insulation and long-wave emissivity of the walls in the model should be connected with the assumed simulation range and method.

2.5.2 Improvements in the Approximate and Partial Modelling Methods

Selection of threshold Reynolds number

In order to reduce the cost of model tests, we try to make scale models as small as possible. However, this decreases the Reynolds number, Re_M . This raises the following questions:

- What should be the threshold Reynolds number, Re_l , to maintain the self-similarity of the flow patterns in the model and the real building?
- Is the selected Re_l number at supply openings valid for the entire modelled ventilation process?

With regard to the above questions, the following three flow areas can be observed in Region I:

- *Jet flow self-similarity of the mean flow appears when $Re_{Mb} > Re_l$ at the boundary*
The problem of Reynolds number independence of a round air jet flow was tested by Soehrich in four enclosure models of similar shape but of different sizes [Mierzwinski, 1987]. In round jets we can observe a quasi-stabilisation of the mean velocity profiles at $Re = 2500 \sim 4000$ and of the normalised turbulent shear stresses, $\overline{u'_i u'_j} / u_{sm}^2$, at $Re > 6000$ depending on the model size. The above-mentioned numbers can be treated as threshold Re numbers, Re_l , related to the boundary conditions.
- *Secondary-flows have low mean velocities, high turbulence intensity, and the contribution of dissipation and viscosity forces may have an influence*
Self-similarity of secondary flows and flows in areas of mixing is not evident. As the model's length scale is reduced, regions of intermediate and smaller elements of turbulence increase. Turbulence intensity increases up to 100% and higher. In this flow area, stabilisation of the velocity profiles and normalised turbulent stresses was not observed in the model tests up to $Re = 10000$ (Re related to the supply opening) [Mierzwinski, 1987]. Thus, it may be expected that the modelled velocity distribution in the secondary-flow areas is less accurate than in jets.
- *Free convection flow, particularly a plume self-similarity of the mean flow can be observed only at some distance from the heat source*
- Self-similar turbulent free-convection flows are Grashof-number independent. The threshold Grashof number can be described as $(Gr Pr)_l = 1.0 \times 10^6$ to 3.3×10^8 depending on the source shape. In conditions where the flow is Gr-number-independent, the

convective heat transfer coefficient does not depend on the heat source dimensions and hence on the model size either.

$$Gr \equiv ArRe^2 \equiv \frac{gL^3\beta\Delta T}{\nu^2} \quad (2.5.11)$$

Problem of fulfilling the Kármán criterion

The above-discussed stabilisation of nondimensional velocity and shear stress profiles in different models occurs at different parameter levels according to the model size and to the spectral density of the turbulent motion. In small-scale models that are constructed on the basis of Archimedes-number equality, supply openings have to be equipped with special turbulizers to fulfil the Kármán criterion. Preliminary tests by Mierzwinski et al. [1996] indicate how a supply-air outlet should be constructed in models.

When similarity requirements: $Re_M > Re_l$, $Ka_M = Ka_F$ are not fulfilled, the flow patterns in the model will be deformed by the error of the method.

Partial modelling

A physical scale-model encompassing the entire complex process of ventilation may be too complicated, or may introduce similarity approximations that are too inexact. In such cases, it is sensible to divide the complex system of flow and heat transfer phenomena into subsystems and partial processes. The modelling can be partitioned in different ways. Conception and construction of partial models should be selected according to the objective of the measurements. Building on the discussion from Section 2.5.1, the following aspects of partial modelling can be separated:

- Functional division into subsystems, e.g. Region 1 of the air distribution modelling and Regions 2 and 3 of boundary conditions simulation. This division may facilitate analysis of different ventilation system concepts, synthesis of partial test results, and relating the experiment to numerical methods.
- Geometric separation of a part of the subsystem and implementation of partial models of various sizes, e.g. separation of a part of the ventilation area in Region 1 for turbulence structure tests. The problem of simulation of the influence of the enclosure's cut-off regions should be considered as additional boundary conditions

Visualisation and measurement methods

Methods for airflow visualisation and measurements of airflow parameters and thermal boundary conditions are of great importance for the accuracy of the scale model test results. Similar measurement techniques are used in both scale models and real enclosures (Chapter 3).

The first stage of the tests is flow-pattern visualisation by means of smoke or larger airborne particles, and forms a background for detailed measurements of parameter distributions in the analysed air flow pattern.

In model tests, it is of particular interest to observe the whole parameter field. To achieve this, quantitative visualisation methods have been developed, such as measurement of the velocity field using digital image processing.

In order to measure air velocity and turbulence parameters, thermoanemometers and laser anemometers are used. In secondary and mixing flows, due to velocity reduction, there are high requirements for velocity measurement: mean velocity ranges from 0.05 to 1 m/s, high spatial resolution, and accuracy better than typical accuracy for spherical probes ($10.05u \pm 0.05$ | m/s). The type and characteristics of the anemometer sensors (hot-wire, omnidirectional, reversal) should be chosen suit to the measurement task. It is advisable to make measurements at many points of the flow field, with computer interpretation of the signals.

To measure age-of-air and contaminant migration, the tracer gas technique is used. It is necessary to improve the measurement equipment as much as possible, as far as discharging the tracer gas, measuring concentration and sampling automation are concerned.

For air and wall temperature distribution, measurement thermocouples are used. For identification of thermal boundary conditions in model tests, thermography and heat flux measurement methods are useful. The ammonia absorption method with photometric evaluation [Vogel, 1995] (Section 3.3.5) can be used to measure the local values of heat and mass transfer coefficient over entire wall surfaces.

Accuracy of scale model experiments

When estimating the accuracy of scale model tests of nonisothermal ventilation flow, the following two types of error may be separated:

- *Errors of the modelling method which include:*
 - a) Error of the method of simplified modelling, relative to modelling where full physical similarity is maintained
 - b) Errors resulting from the lack of fulfilling turbulent flow self-similarity conditions.
- *Errors of physical parameter measurements*

The error related to simplified modelling of nonisothermal airflow, when Archimedes numbers are equal, results from the lack of complete similarity of turbulent flows in the full-scale space and its model. It is particularly difficult to evaluate this error theoretically and it cannot be determined by comparison with an ideal model since we are not able to construct a scale model in which complete physical similarity would be maintained. Neither are we able to divide the error value into the values corresponding to (a) or (b) above. Therefore, it is only possible to estimate modelling errors by comparing the results of ventilation measurements carried out in situ and in a model.

2.5.3 Scale Model Design Discussion (Based on the Case Study ‘Turnhalle München’)

Description of the enclosure and the scope of tests

This case study involved measuring and modelling the air distribution in the ‘Turnhalle München’ gymnasium (THM), where air heating is used. Using the above enclosure as an example, the problems related to scale modelling of the air distribution are discussed.

Figure 2.5.2 shows the enclosure and the location of the ventilation openings. The data regarding the heat balance of the enclosure and supply jet parameters are assumed on the basis of in-situ measurements in winter [Richter et al., 1996] and on numerical studies [Renz et al., 1995].

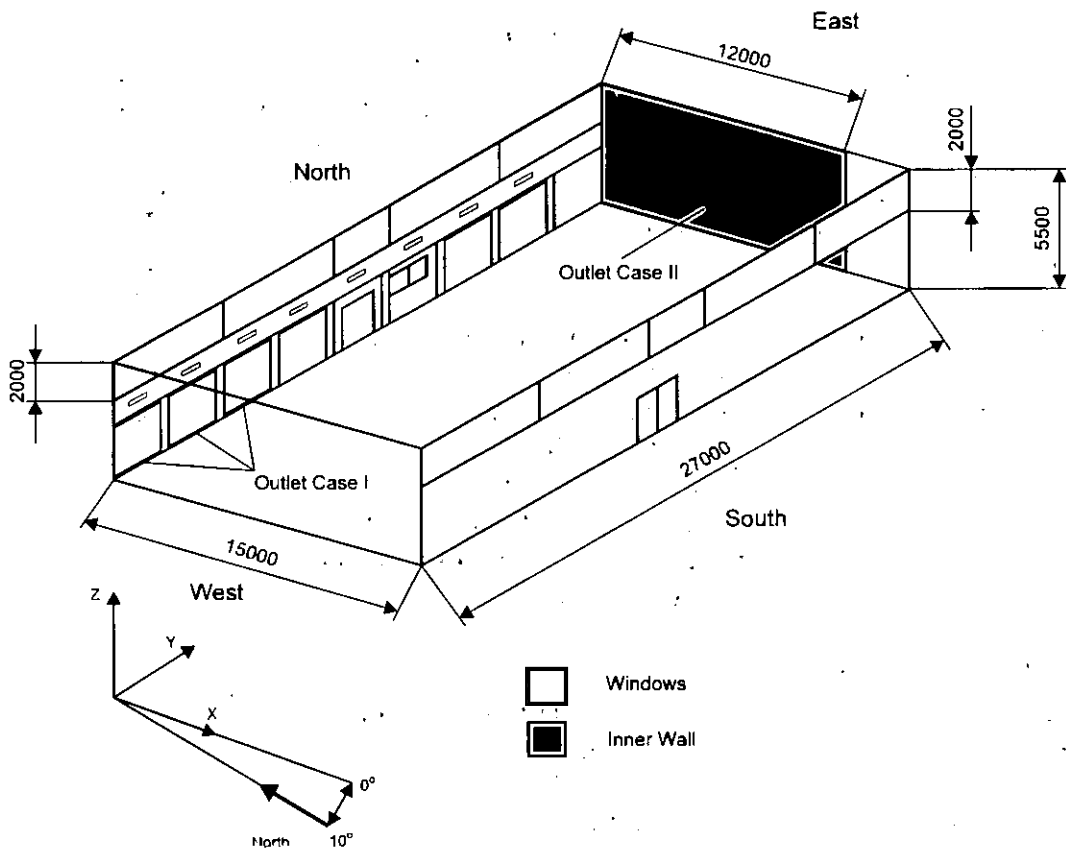


Figure 2.5.2 “Turnhalle München” dimensions.

The input data for designing the scale model are as follows:

- enclosure dimensions: 15 × 27 × 5.5 m
- supply opening dimensions: 8 openings 0.9 × 0.03 m
- exhaust opening dimensions: 3 openings 2.54 × 0.05 m
- case II: 1 opening 0.354 × 0.354 m
- air velocity in supply openings: 3.7 ~ 5.2 m/s
- total flow rate of supply air: 1.13 m³/s
- supply / exhaust air temperature 19.3 / 6.9 °C, ΔΘ = 2.4 K
- outdoor air temperature: +2°C

Selection of modelling scale factors

Air is used as the modelling fluid. When using the *approximate modelling* principle, two of the scale factors of length, temperature difference and velocity should be selected and the third one calculated based on Archimedes-number equality $Ar_M = Ar_F$ and Reynolds-number-independence of the flow (see Section *Modelling scales for air distribution*, page 125).

The modelled space is characterized by a low air change rate (about 1.8 h⁻¹) and low value of Reynolds number for supply flows, $Re_{Fs} = 20240$. Thus, the requirement of high length scale factor of the model is difficult to fulfil. This is illustrated in Table 2.5.1 which shows that when $Re_{Ms} > Re_l = 2500 \sim 6000$ (see Section *Selection of threshold Reynolds number*, page 127), the length scale in the model, S_L , should not be less than 1:4 and also that it is favourable to have the temperature difference scale $S_{\Delta\Theta} > 1$.

Table 2.5.1 Reynolds number Re_{Ms} and air velocity u_{Ms} in supply openings of the model at different length scales S_L and temperature difference scales, $S_{\Delta\theta}$.

S_L (assumed)	$S_{\Delta\theta}$ (assumed)	S_u (Eqn. 2.5.6)	Re_{Ms}	u_{Ms} [m/s]
0.5	1	0.707	7080	3.7
0.5	3	1.224	12350	6.4
0.25	1	0.5	2540	2.6
0.25	3	0.866	4370	4.5
0.15	1	0.387	1110	2.0
0.15	3	0.671	2020	3.5
0.1	1	0.316	640	1.6
0.1	3	0.548	1110	2.8
0.1	10	1.0	2020	5.2

However, taking into account the area of the laboratory rooms and the cost of the model construction, it is possible to separate issues requiring precise experimental analysis from general qualitative observations in the research programme. Precise analyses (e.g. local air distribution, characteristics of supply openings, flow structure) may be carried out using the *partial modelling* method in partial models at a higher length scale.

For some qualitative observations (e.g. air distribution at different location of ventilating openings) a small scale model of the whole enclosure may be required. In the relatively simple case of THM, it could be a model with the following scale factors: $S_L = 0,15-0,1$ and $S_{\Delta\theta} = 3-10$. It is worth noting that the velocity scale factor, S_u , increases together with $S_{\Delta\theta}$. The value $S_u > 0.5$ is reasonable for model tests owing to the technical capabilities of velocity measurement in models.

Table 2.5.2 lists the sets of required modelling scale factors for Turnhalle München, to illustrate the above problems of designing and implementing a scale model.

Table 2.5.2 Sets of modelling scale factors.

Physical quantity	Symbol	Calculation formula	Scale factors at $S_{\Delta\theta} =$			Remarks
			1	2	3	
Length	S_L	(page 125)	0.252	0.15	0.10	
Temperature difference	$S_{\Delta\theta}$	(page 125)	1	3	10	
Velocity	S_u	$S_L^{0.5} S_{\Delta\theta}^{0.5}$	0.5	0.67	1.0	
Volume flow rate	S_q	$S_L^{2.5} S_{\Delta\theta}^{0.5}$	0.031	0.015	0.01	
Mass flow rate	S_m	$S_L^{2.5} S_{\rho} S_{\Delta\theta}^{0.5}$	0.031	0.015	0.01	$S_{\rho} = 1$
Heat flow rate	S_{ϕ}	$S_L^{0.5} S_{\rho} S_{\Delta\theta}^{1.5}$	0.031	0.045	0.1	$S_c = 1$
Time	S_T	$S_L^{0.5} S_{\Delta\theta}^{-0.5}$	0.5	0.29	0.1	
Air change rate	S_z	$S_L^{-0.5} S_{\Delta\theta}^{0.5}$	2.0	3.46	10	

Simulation of thermal boundary conditions

The temperature distributions at the surfaces of walls in THM, measured in winter [Richter *et al.*, 1996] show differences in the range of several degrees K. Thus, heat exchange due to radiation as well as the condition expressed in Equation (2.5.10) can be neglected in the enclosure heat balance (Equation 2.5.8). Therefore, there is no need to modify the radiative coefficients of walls in the model (e.g. covering with aluminium foil).

Simulation of heat loss through the walls to the environment may therefore be limited to the conditions expressed by the Equation (2.5.9). Heat loss through walls is expressed by the formula:

$$\Phi = A U (\Theta_i - \Theta_a) \quad (2.5.12)$$

which can be transformed into

$$C_U C_{\Delta\Theta} = S_\phi S_L^{-2} \quad (2.5.13)$$

where

$$C_U = \frac{U_M}{U_F} \quad \text{and} \quad C_{\Delta\Theta} = \frac{(\Theta_i - \Theta_a)_M}{(\Theta_i - \Theta_a)_F} \quad (2.5.14)$$

Factors C_U and $C_{\Delta\Theta}$ should be treated only as scale conversion factors since the heat transfer coefficient, U , is not subject to univocality conditions (see Equation 2.5.7) and the air temperature difference $\Theta_i - \Theta_a$ may be influenced independently of $S_{\Delta\Theta}$ for Region 1. Equation (2.5.5) implies that for simulation of buoyant plumes on the border of Region 1, it is possible to select alternative sets of the model wall insulation and of air temperature differences inside the enclosure and in the model surroundings - according to the technical conditions of the laboratory. This is illustrated by the following example.

The heat losses measured in THM indicate the following values of overall heat transfer coefficients:

walls:	$U_F = 0.5 \text{ W/m}^2\text{K}$
luxfer tiles:	$U_F = 1.2 \text{ W/m}^2\text{K}$

In the case with the model scale factors: $S_L=0.15$, $S_{\Delta\Theta}=3$, the heat flow rate scale factor is $S_\phi=0.045$. By introducing $C_{\Delta\Theta}=0.5$ to Equation (2.5.11) (which is realistic in a laboratory) the conversion factor $C_U=4$ may be obtained, which results in the following values of overall heat transfer coefficients for the model walls:

walls:	$U_M = 2 \text{ W/m}^2\text{K}$
luxfer tiles:	$U_M = 4.8 \text{ W/m}^2\text{K}$

To achieve this, a row of plexiglass windows, 3 mm thick, may be constructed in the THM model. The external walls may be made of similar plexiglass plates, placed in three layers at the distance of 5–10 mm from each other. Transparent walls will enable airflow visualisation in the model.

Model rig conception

Figure 2.5.3 shows the conception of the THM model and its location in a laboratory enclosure. Table 2.5.3 lists the characteristic parameter values.

Table 2.5.3 Values of characteristic parameters for THM and its scale model when $S_L=0.15$, $S_{\Delta\theta}=3$:

Physical quantity	Symbol	Unit	Real bldg. (THM)	Scale model	Remarks to the model
Ambient air temperature	Θ_a	$^{\circ}\text{C}$	+2	+20	optional
Temperature difference	$\Theta_i - \Theta_a$	K	16	8	$C_{\Delta\theta}=0.5$
Internal air temperature	Θ_i	$^{\circ}\text{C}$	+18	+28	
Temperature difference	$\Theta_s - \Theta_e$	K	2.4	7.2	$C_{\Delta\theta}=3$
Supply air temperature	Θ_s	$^{\circ}\text{C}$	+19.2	+31.6	
Exhaust air temperature	Θ_e	$^{\circ}\text{C}$	+16.8	+24.4	
Overall heat transfer coefficient	U_{wall}	$\text{W}/\text{m}^2\text{K}$	0.5	2.0	$C_U=4$
Overall heat transfer coefficient	U_{window}	$\text{W}/\text{m}^2\text{K}$	1.2	4.8	$C_U=4$

The planned scale model experiments involve measurement of air velocity and temperature fields, heat flux at the walls and air flow visualisation. Methods and measurement equipment used are covered in *Visualisation and measurement methods*, page 128, and in Chapter 3.

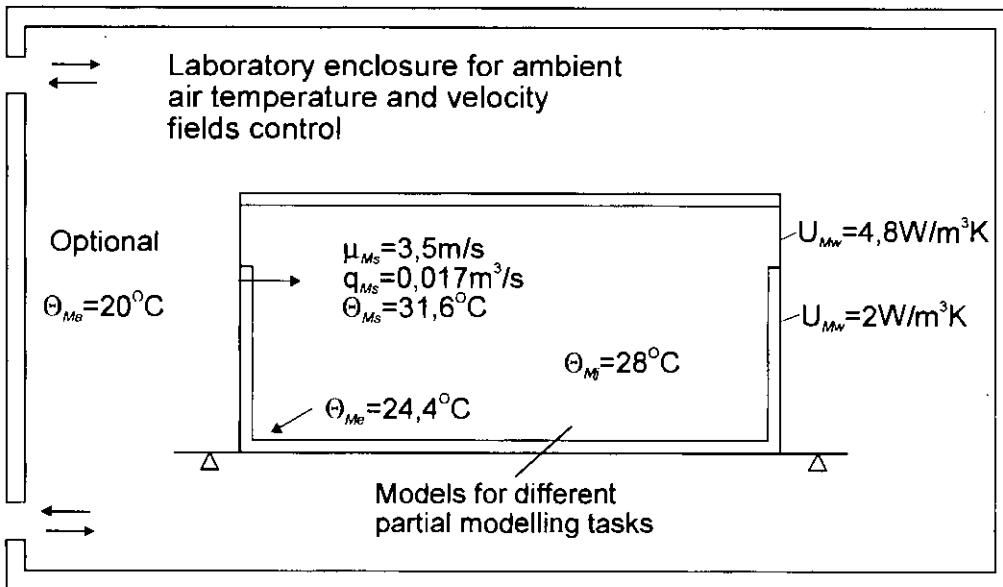


Figure 2.5.3 Conception of the measurement stand for scale modelling of air distribution in THM, complete with figures from Table 2.5.3 as an example.

2.5.4 Conclusions

Scale modelling is useful in the prediction and analysis of air distribution and indoor climate in large enclosures, though it requires a thorough approach to model design and experimentation. Some general remarks are:

- When constructing the model, the following factors are crucial:
 - a) Choice of the model length scale S_L so as to ensure airflow within the self-similarity range ($Re_M > Re_l$)

- b) Proper simulation of boundary conditions
- c) Choice of the temperature difference scale $S_{\Delta\theta}$ so as to maintain relevant thermal boundary conditions in the model and the required accuracy of air velocity measurement
- d) Practical design of the model so as to permit flow pattern visualisation and field measurements in it in a convenient way
- The more the model size and flow parameter values are related to those in the full-scale enclosure, the smaller the error of the approximate modelling method is, and the more reliable the tests results are
- In order to reliably predict ventilation processes in large enclosures from scale model tests, it is advisable:
 - a) To sensibly differentiate between those problems that require precise quantitative analysis with the use of partial modelling methods, from those problems for which qualitative observations in small models but of the whole space may be sufficient
 - b) To carefully determine the properties and effects of aerodynamic factors which influence the tested process at the boundaries

2.6 Ventilation Efficiency

Ventilation efficiency consists of a number of concepts, or indices, that can be used to evaluate various aspects of ventilation performance during stationary or transient conditions, either locally or globally in an enclosure. These concepts are based on field variables such as concentration, temperature, etc. Therefore, one cannot say that there is a specific ventilation efficiency model, because *any* model, be it physical or computational, that provides information on field variables, can be used to assess ventilation performance. The reliability with which ventilation performance can be assessed therefore depends on the reliability of the model or measurements used to gather information about the state in the ventilated space.

Ventilation is *effective* when it 'produces a desired effect', i.e. provides occupants with air of good quality. However, good air quality can be achieved without the ventilation being efficient; ventilation is *efficient* only when it is 'effective whilst wasting little energy'. The connection between energy efficiency and ventilation efficiency is that an efficient system with respect to e.g. contaminant control requires a lower air change rate to meet the IAQ requirements of the enclosure's occupants, and thereby uses less energy to transport and climatize air. Moreover, as regards temperature control, a more efficient system requires a smaller temperature difference between supply and the occupied zone, so less energy is required to meet comfort requirements. Furthermore, an efficient system can make do with a smaller plant.

To create efficient ventilation in large enclosures, one should exploit the fact the occupied zone is small in relation to the enclosure's total volume, and that the flow is typically stratified. This subchapter therefore starts with a discussion of the significance of enclosure geometry on ventilation efficiency; then the various concepts are discussed.

Continuous development of measurement and calculation methods has led to a growth in the number of ventilation efficiency indices. Contemporary overviews of definitions and their application are found in Sutcliffe [1990], Brouns & Waters [1991], Sandberg [1992] and Liddament [1993].

2.6.1 Significance of Enclosure Geometry

The size and geometry of an enclosure in relation to the scales of the air motion, has implications on the type of flow that is generated and the possibility to use the volume above the occupied zone as a buffer for heat and contaminants. To characterise the geometry, it is convenient to introduce two nondimensional aspect ratios (see also Figure 2.6.1).

The width to height ratio

$$A_w = \frac{W}{H} \quad (2.6.1)$$

The length to height ratio

$$A_L = \frac{L}{H} \quad (2.6.2)$$

Atria are examples of enclosures dominated by height, so A_w can be much less than one. Large enclosures are generically characterised as spaces where the occupied zone is much smaller than the total volume of the enclosure. It is therefore not energy efficient to climatize

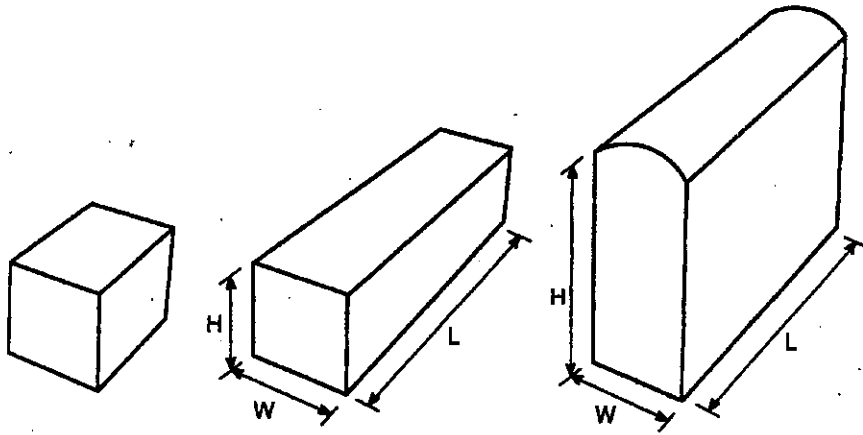


Figure 2.6.1 Different shapes of enclosures.

the whole volume uniformly by fully-mixed mechanical ventilation. Instead, one should strive to create non-uniform conditions by climatizing only the occupied zone and exploiting the non-occupied part of the enclosure as 'storage' for rising heat and contaminants. Whether this can be done depends on whether the occupied zone can be 'isolated' sufficiently from the remainder of the enclosure. Such isolation can be achieved by exploiting the properties of stratified flow. Stratification is built up by air currents flowing vertically through air of graduated temperature and finding their level of neutral buoyancy, i.e. the level where the density of the air stream is equal to the density of the ambient air at that height. There are two main categories of sources of buoyant air currents: a *point* heat source and a source with a *continuous input or loss of heat over its height* (Figure 2.6.2). The air stream from a point source rises until it finds its level of neutral buoyancy where, after a small overshoot, it falls back on itself and spreads out horizontally. In boundary layer flow along a surface with a continuous input or loss of energy along its height, stratification will force the outer region of the boundary layer to be gradually 'peeled off' into the ambient air (detraining flow). This occurs because the boundary layer has a temperature gradient normal to the wall, and at any given height, the outermost region of the boundary layer will have reached the level where its density is just higher (or lower, if it is a cold wall) than the ambient density at that level. Therefore in the bulk of stratified flow, the air motion occurs horizontally, whereas vertical convection currents are driven by plumes and boundary layers along the walls.

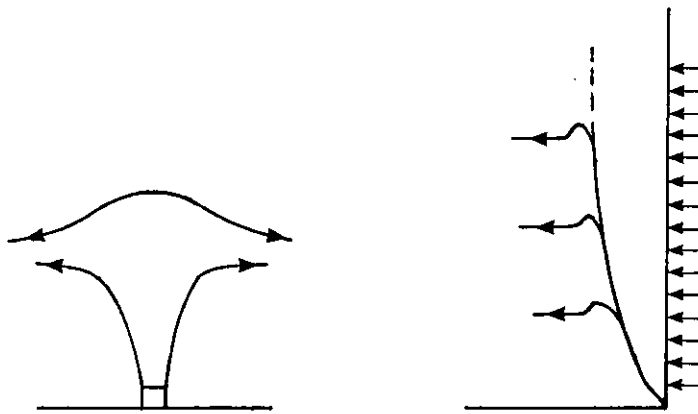


Figure 2.6.2 Sketch of built up of stratified flow in enclosures. Isolated point source (left), source with continuous input of heat along its height (right).

Stratification also introduces a natural frequency of oscillation, the Brunt-Väisälä frequency:

$$N = \sqrt{g\beta \frac{dT}{dz}} \quad (\text{s}^{-1}) \quad (2.6.3)$$

where β is the coefficient of volumetric thermal expansion.

Sensors used in systems for demand-controlled ventilation must filter out this inherent frequency.

A decisive factor influencing how the occupied space can be isolated from the remainder of the enclosure, is the shape and extent of the occupied zone. In case (b) in Figure 2.6.3, it is difficult to isolate the occupied space from the main volume because there will always be transport by horizontal airflow. In case (a) transport of contaminants from the unoccupied region to the occupied zone can occur by breakthrough of air along the walls. Whether breakthrough occurs depends on the temperature difference between the walls and the air, as shown in Figure 2.6.4.

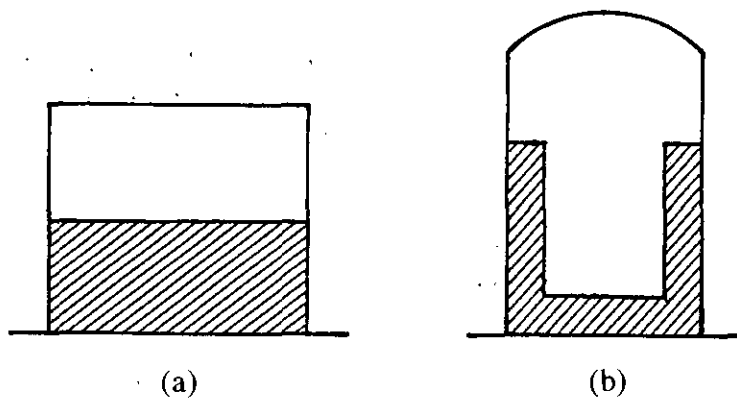


Figure 2.6.3 Different shapes of the occupied zone (hatched area).

One general prerequisite for energy efficient ventilation is source control. This has implications not only for plant size but also because it is easier to achieve efficient ventilation when the load is small. Source control of heat is particularly important because there is always transport of heat by radiation exchange between surfaces, so one cannot obstruct heat transfer between different zones.

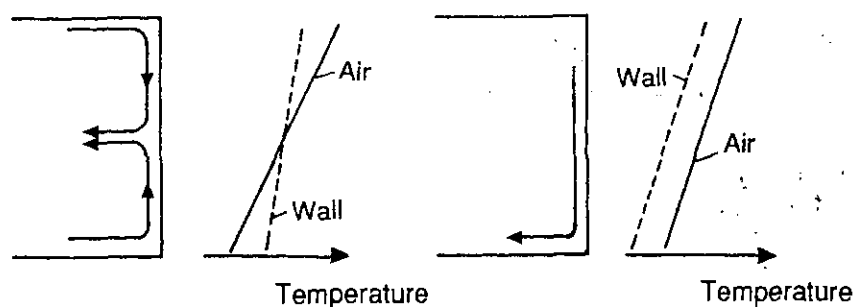


Figure 2.6.4 Temperature distribution and corresponding air flow pattern.

2.6.2 The Task of Ventilation

- Provide fresh air (oxygen)
- Contaminant control
- Temperature control
- Moisture control

Contaminant control

Given the nominal load in the space, \dot{m} [kg/s], the design load in the occupied zone, taking into account the contaminant removal effectiveness in the occupied zone, ϵ_o^c , is

$$\frac{\dot{m}}{\epsilon_o^c} \quad (2.6.4)$$

where the contaminant removal effectiveness in the occupied zone, ϵ_o^c , is defined as

$$\epsilon_o^c \equiv \frac{\text{Concentration in the extract}}{\text{Concentration in the occupied zone}} = \frac{C_e}{\langle C \rangle_o} \quad (2.6.5)$$

The removal effectiveness can be either greater or less than 1.0 depending on the properties of the contaminant and the airflow pattern, which in turn depends on:

General

- Type of supply air terminal
- Velocity at the supply air terminal
- Momentum flow rate (i.e. flowrate times the velocity) at the supply air terminal
- Geometry of the room
- Location of the supply terminal and proximity to room surfaces. Mutual location of supply and extract air terminal and the 'flow distance'¹ between them
- Movement of objects in the space
- Obstacles
- Steady or intermittent load

Additional factors in the case of nonisothermal air supply

- Supply temperature higher (positive buoyancy) or lower (negative buoyancy) than the ambient buoyancy flux (flow rate times the reduced gravity²)
- Location of heating or cooling load
- Co-flow, i.e. flow from supply air terminal and natural convection currents are in the same direction
- Opposing flow, i.e. flow from supply air terminal and natural convection currents are in opposite directions
- U-value of room surfaces

¹ The distance a fluid particle starting at the supply device will travel before it reaches the extract air terminal.

² Reduced gravity $g' = g\beta\Delta T$ where β is the volume expansion coefficient and ΔT is a temperature difference

Temperature control

Another task of the ventilation is to maintain thermal comfort in the occupied zone. Heat can be regarded as just another contaminant. Thus one can use an analogous concept to contaminant removal effectiveness, where the source is a heat source and concentration is replaced by temperature. Given the nominal load in the space, P [Watts], the design load in the occupied zone, taking into account the heat removal effectiveness in the occupied zone, ϵ_T , is

$$\frac{P}{\epsilon_T} \tag{2.6.6}$$

where the heat removal effectiveness in the occupied zone, ϵ_T , is defined as

$$\epsilon_T = \frac{T_s - T_e}{T_s - \langle T \rangle_o} \cdot 100 \% \tag{2.6.7}$$

Just as for contaminants, the standard design assumption for fully-mixed ventilation is to assume uniform conditions throughout the volume, i.e. that the temperature is the same everywhere and equal to the temperature of the air leaving the enclosure. Thus the set-point space temperature is equal to the temperature in the extract. However, in large enclosures, a temperature gradient will lead to a deviation between the temperature in the occupied zone and the set-point temperature which according to usual design practice is measured in the extract duct. This temperature gradient can either be favourable or unfavourable (Figure 2.6.5).

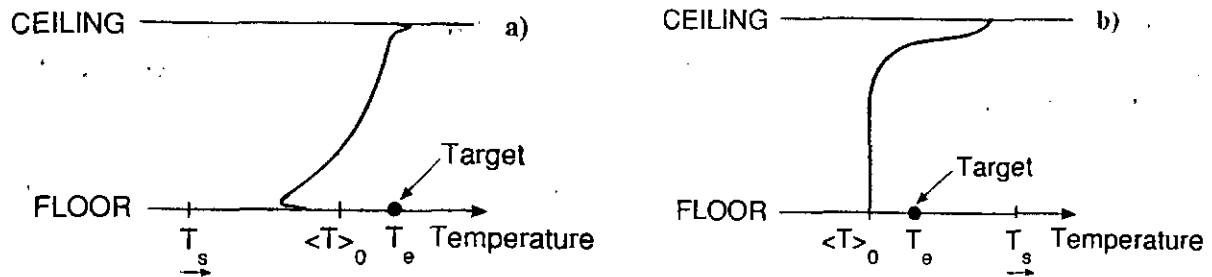


Figure 2.6.5 (a) Favourable temperature gradient (cooling), (b) Unfavourable temperature gradient (heating).

A small temperature difference between the supply and the occupied space implies a high degree of utilisation of the supplied energy. Therefore a favourable temperature gradient ($\epsilon_T > 100\%$) means that the supply temperature can be lowered when heating and raised when cooling. For conditions with an unfavourable temperature gradient ($\epsilon_T < 100\%$) the supply air temperature must be raised when heating and lowered when cooling to meet the required temperature in the occupied space.

Age distribution and air-exchange efficiency

Knowledge of the local mean age of air, $\bar{\tau}_p$, provides information about the distribution of supplied ventilation air. One can also define the mean age of air, $\langle \bar{\tau}_p \rangle$, in the whole enclosure of volume, V , and from this information one can calculate the air exchange efficiency, ϵ .

$$\varepsilon = \frac{\tau_n}{2\langle\bar{\tau}_p\rangle} \cdot 100\% \quad (2.6.8)$$

where the nominal time constant is defined as

$$\tau_n = \frac{V}{q_v} \quad (2.6.9)$$

The upper limit is 100%. The air exchange efficiency is a global quantity based on the whole volume of air in the enclosure and is therefore of limited value when the occupied zone constitutes a minor fraction. In such cases where the occupied zone occupies only a minor part of the total volume, it is recommended to use the distribution of the local mean age.

2.6.3 Two-Zone Model of Enclosure

This is the simplest model that can model the effect of stratification on ventilation efficiency. Transport of contaminants between zones occurs by convection, with velocity field U (laminar, transitional or turbulent), and by molecular diffusion (diffusion coefficient D_c). The *instantaneous flux* vector, \mathbf{q}_c of contaminants is

$$\mathbf{q}_c = UC - D_c \nabla C \quad (2.6.10)$$

In an enclosure as shown in Figure 2.6.6, the most natural reference flux is the ventilation flow rate divided by the horizontal area. In each zone the mixing is assumed to be uniform, whereas the mixing between the zones is expressed by βq_v where β may vary from no mixing ($\beta=0$) to complete mixing in the whole space ($\beta \rightarrow \infty$). The mass balance equation for the two-zone system is

$$V_1 \frac{d}{dt} C_1 = -(1+\beta)q_v C_1 + \beta q_v C_2 + \dot{m}_1 \quad (2.6.11)$$

$$V_2 \frac{d}{dt} C_2 = +(1+\beta)q_v C_1 - (1+\beta)q_v C_2 + \dot{m}_2 \quad (2.6.12)$$

The total contaminant load is $\dot{m} = \dot{m}_1 + \dot{m}_2$. Efficient ventilation is obtained if one can create an air flow pattern where a large fraction of the total load is effectively transported to the upper zone whilst keeping the exchange coefficient β as low as possible. This is the principle of displacement ventilation.

The concentration in the lower zone (zone 1) due to the load \dot{m}_2 in the upper zone is

$$C_1 = \frac{(\text{Load in zone 2}) \cdot (\text{Transfer probability from zone 2 to 1})}{\text{Purging flowrate in zone 1}} = \frac{\dot{m}_2 \cdot \beta}{q_v (1+\beta)} \quad (2.6.13)$$

For a zonal model to represent a large enclosure with complicated geometry, it may be necessary to subdivide the enclosure into more than two zones. However, this requires information about an additional number of exchange coefficients, β , which can be obtained

experimentally by using multi-tracer gas techniques or from predictions by using a combination of macro-micro models. Multizone models are dealt with in Etheridge and Sandberg [1996] and the combination of macro-micro modelling is dealt with in Murakami et al. [1994].

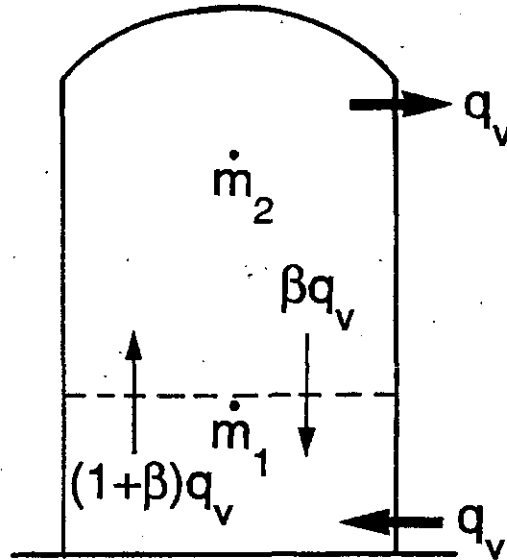


Figure 2.6.6 Two-zonal model of enclosure.

2.6.4 Prediction of Ventilation Efficiency from Models

Regardless of type of computational model, the various measures of ventilation efficiency can be obtained in exactly the same way as they are from experimental measurements (see Section 3.3.4). For example, if one wants to predict the local mean age of air, one can use the decay or step-up tracer-gas techniques, which means that one prescribes uniform concentrations as initial conditions. Unlike experimental tracer-gas measurements, there is no problem of achieving uniform initial concentrations in a computational model. Furthermore, in computations the tracer gas is ideal in the sense that it is passive, so it can be added after the flowfield has been computed. The decay and step-up techniques are transient techniques, so one must reproduce the correct time-evolution of concentration. This can take a fairly long time in CFD simulations with a fine grid. An alternative to transient techniques is to use the steady-state concentration distribution obtained with uniformly distributed contaminant sources throughout the computational domain. This approach is the computational equivalent of the homogeneous emission technique described in Section 3.3.4. In CFD calculations this is done with a source strength that is proportional to the volume of each computational cell.

Example

Figure 2.6.7 shows the local mean age recorded on the first floor of a library [Stymne et al., 1996]. The local mean age was recorded with the homogeneous emission technique employing a passive tracer gas technique. Other examples can be found in Koskela et al. [1995] and Nimelä et al. [1995].

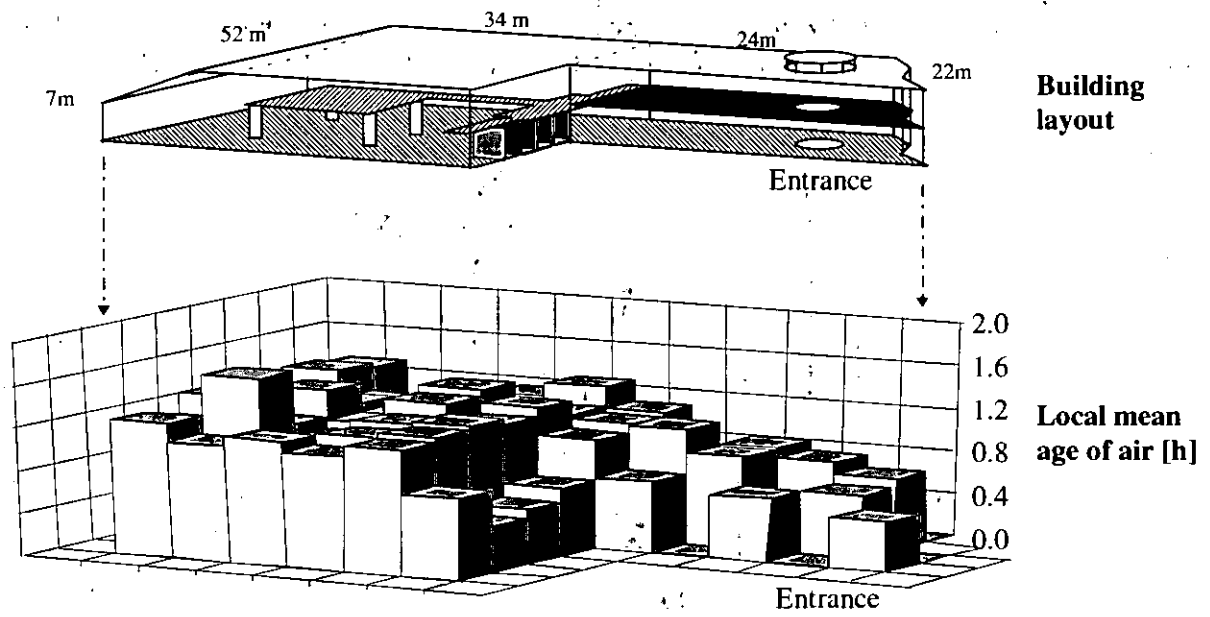


Figure 2.6.7 Distribution of the local mean age in the first floor of a library.

2.7 Energy Implications

2.7.1 Introduction and Basic Hypothesis

This subchapter outlines a procedure to determine the energy implications of the ventilation solution for a large enclosure. The procedure is based on the following hypotheses:

- Calculations are performed in steady-state conditions
- All the time-dependent quantities are given suitable mean values over the integration time period, t
- In the case of intermittent or variable occupancy, the integration period may be corrected by adopting the procedure suggested by ASHRAE Standard 62 [1990]
- All the quantities that actually show a spatial distribution are considered as mean values over the volume (the effect of the space distribution is only taken into account by means of ventilation or thermal efficiencies)
- Ventilation and thermal efficiencies apply to the whole space and not only to the occupied zone, nor only to the breathing zone
- Local extraction systems (hoods) are not considered, though they achieve the highest ventilation efficiencies
- The integration time is one month (i.e., 30 days)

Figure 2.7.1 shows the conceptual schematic of the ventilation plant:

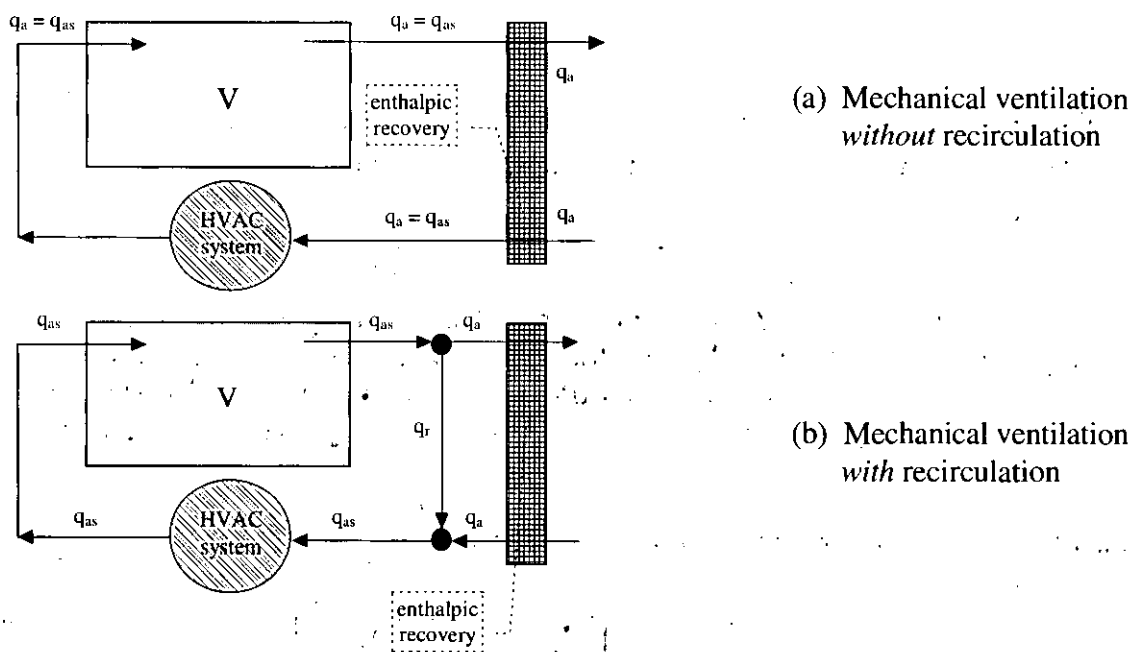


Figure 2.7.1 Schemes of ventilation systems.

2.7.2 Enclosure Energy Balance

A large enclosure is an open thermodynamic system that exchanges energy and mass with the outdoor environment. A simple illustration of the main energy flows involved in this phenomenon is shown Figure 2.7.2.

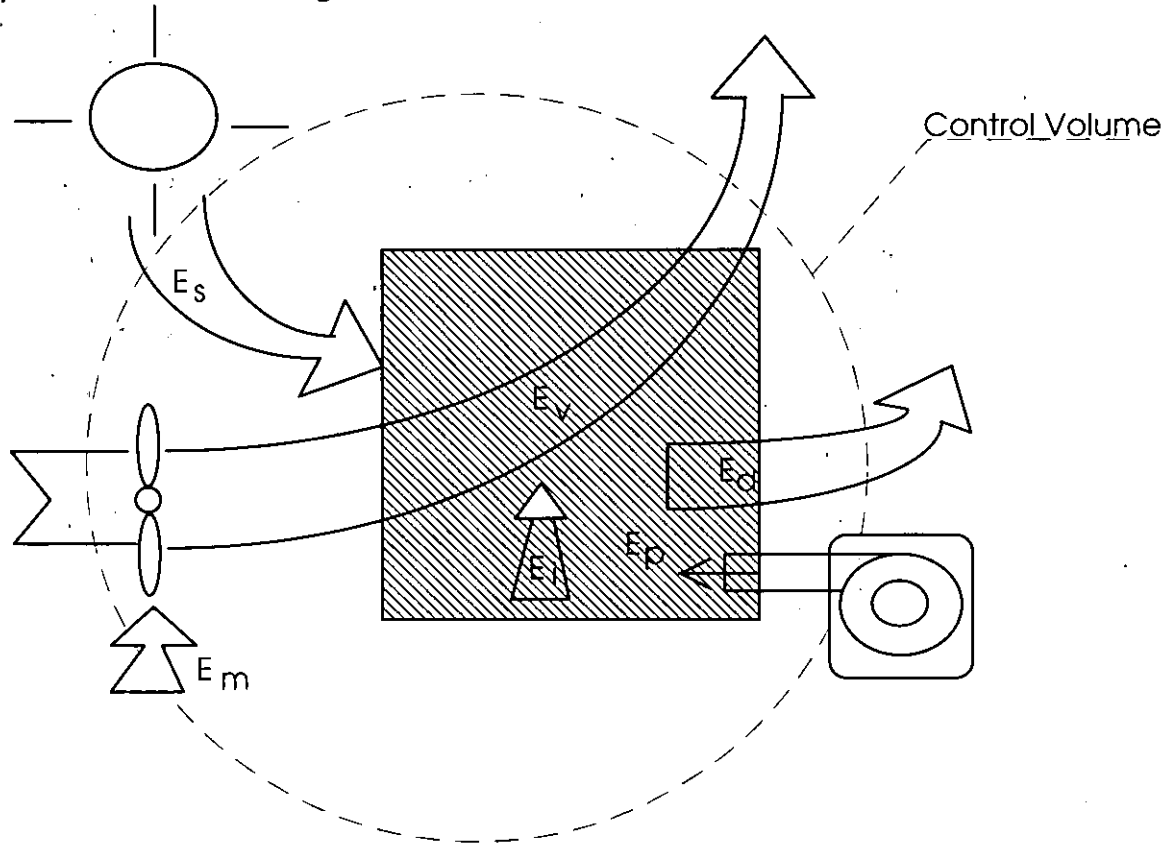


Figure 2.7.2 Enclosure energy balance.

The energy balance for the enclosure in steady-state condition is:

$$E_p = E_d + E_v + E_m - E_i - E_s \quad (2.7.1)$$

E_p is positive for heating and negative for cooling, and represents the total energy that has to be employed for the thermo-hygrometric control of the ambient. E_d is transmission loss or gain, E_v is energy gain or loss by ventilation, E_m is energy use for moving the air, E_i is internal production and E_s is solar heat gain. Let us now separately examine the right-hand side terms of Equation (2.7.1).

Transmission energy losses through the envelope (E_d) :

$$E_d = \int_0^t \dot{E}_d(t) \cdot dt = \int_0^t \left[\sum_k \dot{E}_{dw_k}(t) + \sum_j \dot{E}_{dg_j}(t) \right] \cdot dt \quad (2.7.2)$$

where k and j are the number of the different envelope components and E_{dw} and E_{dg} are transmission loss through walls and ground respectively.

The integral in Equation (2.7.2) may be solved by introducing suitable mean values of the various quantities over the integration period $[0, t]$:

$$E_d = t \cdot \bar{U} \cdot A_{env} \cdot (\bar{T}_i - \bar{T}_o) \quad \text{or} \quad E_d = t \cdot \bar{U} \cdot A_{env} \cdot i \cdot (\bar{T}_{sp} - \bar{T}_o) \quad (2.7.3)^3$$

where \bar{U} overall heat transfer coefficient of the envelope, A_{env} overall envelope area, \bar{T}_i indoor air temperature, \bar{T}_o outdoor air temperature, \bar{T}_{sp} set-point temperature, i night temperature set-back factor and t time.

Internal energy production (people, appliances) (E_i)

$$E_i = \int_0^t \dot{E}_i(t) \cdot dt = \int_0^t [A \cdot N(t) \cdot \varphi_o + \varphi_i(t) \cdot V] \cdot dt \quad (2.7.4)^5$$

where N is no. of people per unit floor area, A floor area, φ_o specific heat gain from people, φ_i specific internal gain from non-occupant sources and V enclosure volume.

Integration of Equation (2.7.4) yields:

$$E_i = t \cdot (\bar{N} \cdot \varphi_o + a) \cdot A \quad (2.7.5)$$

where

$$a = \frac{1}{t} \cdot \int_0^t \varphi_i(t) \cdot \frac{V}{A} \cdot dt = \bar{\varphi}_i \cdot \frac{V}{A} \quad (2.7.6)$$

$$\bar{N} \cdot \varphi_o = \frac{1}{t} \cdot \int_0^t N(t) \cdot \varphi_o \cdot dt \quad (2.7.7)$$

Solar energy entering through the envelope (E_s)

$$E_s = \int_0^t (\dot{E}_{op}(t) + \dot{E}_{tr}(t)) \cdot dt = \int_0^t \left[\sum_m \varphi_m \cdot C_m \cdot A_{op,m} + \sum_n \varphi_n \cdot C_n \cdot A_{tr,n} \right] \cdot dt \quad (2.7.8)$$

where \dot{E}_{op} is solar power through the opaque envelope, \dot{E}_{tr} is solar power through transparent envelope, φ is solar irradiance and the C coefficients take into account the effects of shading, optical transmission of glasses etc. Hence:

$$E_s = t \cdot A_{eq} \cdot \bar{\varphi}_{th} \quad (2.7.9)$$

³Particular care must be taken in the use of the available various mean data (for example meteorological). The averaging time, in fact, could be different from the integration period.

⁵The value of φ_o is actually a function of time, as the metabolic rate depends on human activities; moreover we may consider this quantity to be constant over the time and evaluate its magnitude as a function of the enclosure type (theatre, auditorium, gymnasium....).

where A_{eq} is equivalent horizontal solar opening and $\bar{\phi}_{th}$ is total solar irradiance on the horizontal plane.

Ventilation energy losses (E_v)

This is the energy for the thermo-hygrometric treatment of the ventilation air, that is, to bring the ventilation air from the outdoor conditions (T_o, x_o) to the indoor conditions (T_i, x_i). E_v is equal to the net enthalpy flow:

$$E_v = \int_0^t \dot{E}_v(t) \cdot dt = \int_0^t \rho \cdot q_a \cdot [h_i(t) - h_o(t)] \cdot dt \quad (2.7.10)$$

where h_i is indoor air enthalpy, h_o is outdoor air enthalpy and q_a is fresh air flow rate.

Energy for moving the ventilation air (E_m)

This is the energy needed to transport ventilation air to and from the enclosure. E_m is zero if natural ventilation systems are used. For mechanical ventilation systems E_m may be written as:

$$E_m = \int_0^t P_m \cdot dt \quad (2.7.11)$$

$$P_m = \frac{q_{as} \cdot \Delta p}{\eta}$$

where P_m is power absorbed by the fans, q_{as} is supply air flow rate and η is overall efficiency of fan.

From this simplified energy analysis of an enclosure, it follows that whenever a certain amount of ventilation is needed, two energy consumption terms appear: E_v and E_m . Indeed these energy fluxes may be reduced by adopting suitable ventilation and air-distribution strategies. However, the first term, at least, is always present.

As stated by Equations (2.7.10 and 11) the magnitudes of E_v and E_m are directly linked to the fresh air flow rate, whose *a-priori* assessment is therefore needed to calculate the energy consumption.

2.7.3 Fresh Air Flow Rate Assessment

In general, there are two main independent reasons to ventilate an enclosure:

- The removal of the pollutant load, to ensure acceptable IAQ
- The removal of the (positive or negative) heat load, to ensure acceptable indoor climate

However, in practice, the first reason is usually the most constraining one, and determines the actual value of the air change rate, \bar{n} . The second reason, in fact, overrides the first only when the thermo-hygrometric treatment of the enclosure is performed by means of ventilation air and no recirculation is performed. Nevertheless, this is not an energy-efficient ventilation system and hence should be avoided whenever possible. In any case, the procedure should start with the assessment of the driving load by means of both the pollutant-determined air-change rate (ach) and the thermally-determined ach calculation.

Pollutant-constrained ventilation

The ventilation volume required to control a certain pollutant load, i.e. to keep the contaminant concentration below its threshold limit, is, in general, given by:

$$n = \frac{q_p}{\varepsilon \cdot V \cdot \Delta c_{sp}} \quad (2.7.12)$$

where Δc_{sp} is the upper limit for satisfactory pollutant concentration, determined by IAQ factors or by safety purposes in case of pollutants that pose a health risk: $\Delta c_{sp} = \langle c_{sp} \rangle - c_b$, q_p is pollutant flow rate and ε is ventilation efficiency.

For pollution emitted by the occupants, Equation (2.7.12) may be rewritten as :

$$n_o = \frac{N \cdot A \cdot q_o^s}{\varepsilon \cdot V \cdot \Delta c_{sp}} \quad (2.7.13)$$

where q_o^s is pollutant produced by occupants.

Remembering that many standards specify a value, q_a^s , of ventilation rate per person (a typical value is 8 l/s.pers.), it follows that:

$$n_o = \frac{q_a^s \cdot N \cdot A}{\varepsilon \cdot V} \quad (2.7.14)$$

ASHRAE Standard 62 suggests that in case of peak occupancies with a residence time less than 3 hours, N should be determined on the basis of average occupancy for the system operation duration, provided that its value is not less than one-half of the maximum.

For non-occupant pollutant sources:

$$n_p = \frac{N_s \cdot A \cdot q_p^s}{\varepsilon \cdot V \cdot \Delta c_{sp}} \quad (2.7.15)$$

where q_p^s is pollutant produced by sources

Thermally-constrained ventilation

When the conditioning of the enclosure is performed by means of ventilation air, the supply air flow rate should not only dilute and remove the contaminant produced inside the enclosure, but it should also carry a suitable thermal flow in order to balance the energy gains and/or losses.

For these systems the 'extra power' $\Delta \dot{E}$ needed to treat the air from the indoor (T_i, x_i) to the supply (T_s, x_s) conditions (in order to balance the heat gains/losses due to solar radiation, internal loads and transmission losses and the moisture internal production) is:

$$\Delta \dot{E} = \rho \cdot q_{as} \cdot (h_s - h_i) = \rho \cdot q_{as} \cdot [(x_s - x_i) \cdot r_0 + c_p \cdot (T_s - T_i)] \quad (2.7.16)$$

where h_s is supply air enthalpy, h_i is indoor air enthalpy, x_s is moisture content in supply air, x_i is moisture content in indoor air, c_p is specific heat capacity of air at constant pressure, T_s is supply air temperature and T_i is indoor air temperature.

Hence the thermally driven air change rate (ach) is given by:

$$n_h = \frac{|\Delta \dot{E} - \dot{E}_l|}{\rho \cdot V \cdot c_p \cdot \Delta T_{\max} \cdot \epsilon_T} \quad (2.7.17)$$

where \dot{E}_l is the power due to the latent heat, $\Delta \dot{E}$ is the amount of the extra-energy flow needed to control the moisture internal production and $\Delta T_{\max} = T_{s,\max} - \langle T_{i,sp} \rangle$ is the maximum recommended temperature difference between supply air and indoor air.

The amount of $\Delta \dot{E}$ may be determined from the energy balance of the enclosure.

Design air change rate

Once the values of n_o , n_p and n_h have been calculated, the highest value among them will represent the design value, n_d :

$$n_d = \text{Max}[n_o, n_p, n_h] \quad (2.7.18)$$

Knowledge of n_d allows one to identify the class of the enclosure (O, P or H) and to determine the fresh air flow rate.

For systems without recirculation.(see Figure 2.7.1a):³

$$q_{as} = q_a = n_d \cdot V = \begin{cases} n_o \cdot V & \text{for "O - type" bldgs.} \\ n_p \cdot V & \text{for "P - type" bldgs.} \\ n_h \cdot V & \text{for "H - type" bldgs.} \end{cases} \quad (2.7.19)$$

For systems with recirculation (see Figure 2.7.1b), i.e., where the extra amount of air, needed for thermal purposes, is recirculated:

$$n_d = n_p \quad \text{or} \quad n_d = n_o$$

and

$$q_{as} = n_h \cdot V \geq q_a \quad q_a = n_d \cdot V = \begin{cases} n_o \cdot V \\ n_p \cdot V \end{cases} \quad (2.7.20)$$

while the recirculated air flow rate may be written as :

$$q_r = q_{as} - q_a = (n_h - n_d) \cdot V = \begin{cases} (n_h - n_o) \cdot V \\ (n_h - n_p) \cdot V \end{cases} \quad (2.7.21)$$

2.7.4 Ventilation Energy Losses Assessment

Once the total amount of fresh air volume flow rate has been determined, by means of the equations above, the ventilation energy loss may be calculated using Equation (2.7.10). By

³ Not recommended, unless recirculation is not practicable.

³ Not recommended, unless recirculation is not practicable.

introducing suitable mean values and assuming $c_{p,w} \cdot \Delta(T \cdot x) \approx 0$, this relation may be rewritten as:

$$E_v = t \cdot \rho \cdot \bar{q}_a \cdot [(\bar{x}_i - \bar{x}_o) \cdot r_0 + c_p \cdot (\bar{T}_i - \bar{T}_o)] = t \cdot \rho \cdot \bar{n} \cdot V \cdot t \cdot [(\bar{x}_i - \bar{x}_o) \cdot r_0 + c_p \cdot (\bar{T}_i - \bar{T}_o)] \quad (2.7.22)$$

or, if the ventilation system is fully balanced and a heat recovery unit is present:

$$E_v = t \cdot \rho \cdot \bar{n} \cdot V \cdot t \cdot (1 - \varepsilon_r) [(\bar{x}_i - \bar{x}_o) \cdot r_0 + c_p \cdot (\bar{T}_i - \bar{T}_o)] \quad (2.7.23)$$

where ε_r is the recovery efficiency.

Applying these relations, however, particular care must be taken in the assumption of the mean values, in fact: t is the integration period, over which the energy consumption is calculated, \bar{n}' is the average value of n over t . Hence, $(\bar{n}' \cdot V \cdot t)$ represents the total volume of air treated by the ventilation plant, while the values in square brackets are the values of indoor and outdoor temperature and moisture content, averaged over the whole integration period t . This last quantity may be expressed as the product of the daily operating time of the ventilation system, τ , and the total number of days over which the analysis is performed: $t = \tau \cdot d$.

The daily operating time is given by:

$$\tau = \tau_d + \Delta\tau \quad (2.7.24)$$

where τ_d is the actual daily operating time, $\Delta\tau$ is the *lag* or *lead time*, determined according to ASHRAE Standard 62, in order to take account of transient effects and $\Delta\tau$ is positive in the case of *lead* time and negative for *lag* time.

In fact, when the enclosures are occupied only for a quite short period of time and when the only relevant pollution sources are due to the occupants, then the operation of ventilation system may be delayed, using the volume capacity in order to dilute the pollutants.

In this case the actual operating time of the system, to be used for the calculation of ventilation losses, will be:

$$\tau = \tau_d - \Delta\tau \quad (2.7.25)$$

where

$$\Delta\tau = \frac{V}{q_a} \quad (2.7.26)$$

is the *lag time*, which may be calculated by means of Equation (2.7.26) or using suitable diagrams [see ASHRAE Std. 62, 1990].

On the other hand, in case of pollutants generated within the enclosures by sources independent of human occupancy, ventilation should commence before occupancy starts, and hence the actual operation period of the ventilation system will be:

$$\tau = \tau_d + \Delta\tau \quad (2.7.27)$$

where

$$\Delta\tau = \frac{V}{q_a} \cdot \ln \left(\frac{\frac{c_0 \cdot q_a}{q_p} - 1}{X} \right) \quad (2.7.28)$$

is the *lead time*, which may be calculated by means of Equation (2.7.28) or using suitable diagrams [see *ASHRAE Std. 62, 1990*], c_0 is initial pollutant volume concentration and X is the fraction above the final steady state concentration level.

With these assumptions, it is then possible to write

$$\bar{n}' \cdot V \cdot t = V \cdot d \cdot \bar{n} \cdot \tau \quad (2.7.29)$$

where \bar{n} is now the average value of n over τ , and d is the number of days.

The connection between \bar{n} and n_d is not straightforward and depends on the ventilation system type:

- For constant air flow rate systems, without recirculation, it held: $\bar{n} = n_d$
- For variable fresh air flow rate systems the value of \bar{n} may differ significantly from the design value and it depends on: the average degree of occupancy for the "O"-type enclosure, the average pollution production rate for "P"-type enclosure and the average heat load conditions for "H"-type enclosure

2.7.5 Energy Consumed to Drive Air Movement

Energy consumed by the fans for moving the air through the ducts is given by Equation (2.7.11) which, integrated introducing suitable mean values, becomes:

$$E_m = \bar{P}_m \cdot t_m = \frac{\bar{q}_{as} \cdot \Delta\bar{p}}{\bar{\eta}} \cdot t_m = \frac{\bar{n} \cdot V \cdot \Delta\bar{p}}{\bar{\eta}} \cdot t \quad (2.7.30)^4$$

where \bar{P}_m is the electrical power absorbed by the fan and t_m is the operation time of the fans.

Furthermore, the pressure losses along the circuit are given by the sum of distributed, Δp_d , and accidental (fittings, sudden changes in diameter, valves, etc.), Δp_c pressure losses

$$\Delta p = \Delta p_d + \Delta p_c \quad (2.7.31)$$

Considering that the ventilation systems are usually designed in order to keep a constant the mean velocity value, u , of the air inside the ducts, this relation may be rewritten, as:

$$\Delta p = \rho \cdot \frac{u^2}{2} \left(\bar{f} \cdot \frac{L}{D} + \xi_{tot} \right) \quad (2.7.32)$$

⁴ The value to be assigned to the air flow rate, q_a or q_{as} , depends on the ventilation system type. In case of recirculation the air flow rates that circulates in the various parts of the plant may not be the same.

where L is the length of the duct, D is the hydraulic diameter and ϵ_{tot} is the total friction loss factor.

The friction factor \bar{f} for fully developed turbulent flow may be related only to the relative roughness of the duct ($e_r=e/D$) by the equation:

$$\bar{f} = a_1 \cdot e_r + b_1 \quad (2.7.33)$$

The equivalent length, L , of the circuit may be related to the characteristic length of the enclosure, $L_c = 4V/A_{env}$:

$$L = a_2 \cdot L_c + b_2 \quad (\text{or perhaps } L = a_2 \cdot L_c) \quad (2.7.34)$$

The total friction loss factor may be written as

$$\xi_{tot} = c_1 \cdot \bar{\xi} \cdot L = a_3 \cdot L \quad (2.7.35)$$

where c_1 is the number of obstacles per unit length, $\bar{\xi}$ is the average friction loss factor and a_3 is the average friction loss factor per unit length.

In these hypotheses, remembering Equations (2.7.30. & 32), it is possible to write:

$$E_m = \frac{\rho \cdot \frac{u^2}{2} \left(\bar{f} \cdot \frac{L}{D} + \xi_{tot} \right)}{\bar{\eta}} \cdot \bar{q}'_{as} \cdot t_m \quad (2.7.36)$$

The duct hydraulic diameter may be written as a function of the average cross section area \bar{A}_c :

$$\bar{D} = a_4 \cdot \bar{A}_c^{0.5} = a_4 \cdot \left(\frac{\bar{q}'_{as}}{u} \right)^{0.5} \quad (2.7.37)$$

The air volume flow rate may be determined according to the different criteria (n_o , n_p , n_h) shown in section 2.7.3 (Equations (2.7.19 and 20)).

Hence Equation (2.7.36) becomes:

$$E_m = \frac{\rho \cdot \frac{u^2}{2} \left[\bar{f} \cdot \frac{L}{a_4 \cdot \left(\frac{\bar{q}'_{as}}{u} \right)^{0.5}} + \xi_{tot} \right]}{\bar{\eta}} \cdot \bar{q}'_{as} \cdot t_m \quad (2.7.38)$$

where \bar{q}'_{as} is the average value of the supply air flow rate over the integration period t_m .

However, it is frequently preferable to express ξ_{tot} as a fictitious equivalent length, L_f , that gives the same pressure losses due to accidental causes. Using this assumption,

introducing the corrected daily operation period, τ_m , of the fans, it is possible to rewrite Equation (2.7.38) as:

$$E_m = \frac{\rho \cdot \frac{u^2}{2} \cdot \left[\frac{\bar{f} \cdot \frac{L + L_f}{a_4 \cdot \left(\frac{\bar{q}_{as}}{u} \right)^{0.5}}}{\bar{\eta}} \right] \cdot \bar{q}_{as} \cdot t_m}{\bar{\eta}} \quad (2.7.39)$$

and

$$E_m = \frac{\rho \cdot \bar{f} \cdot L_{tot}}{2 \cdot a_4 \cdot \bar{\eta}} \cdot \tau_m \cdot d \cdot u^{2.5} \cdot \bar{q}_{as}^{0.5} = \frac{\rho \cdot \bar{f} \cdot L_{tot} \cdot V^{0.5}}{2 \cdot a_4 \cdot \bar{\eta}} \cdot \tau_m \cdot d \cdot u^{2.5} \cdot \bar{n}^{0.5} \quad (2.7.40)$$

where \bar{q}_{as} is now the average value of supply air flow rate over the corrected operation period, τ_m . Note that the integration period $t_m = d \cdot \tau_m$, may substantially differ from that used for energy ventilation losses assessment. If, for example, a lag time $\Delta\tau$ is used and the thermal control of the enclosure is performed by means of ventilation air, then during time $\Delta\tau$, no ventilation losses are present, as the outdoor air flow rate is zero and total recirculation occurs, but the fans are operating for moving the recirculated air. Therefore the integrating period t_m of Equation (2.7.40) must coincide with the actual daily operation time of the fans multiplied by the number of days (over which the analysis is performed).

2.8 Conclusions

In summary, this chapter describes the various design tools for analysing the indoor climate and ventilation/energy performance of large enclosures.

The characteristics of these modelling tools, such as the resources needed, the type of information given, the accuracy and limitations, differs for each model. Hence, they complement each other, because they can fulfil different roles in the HVAC design process. This is illustrated in Table 2.8.1, which reviews the characteristics of the different model types, and compares their advantages and disadvantages. This table (together with Tables 2.1.1 and 2.1.2) is a useful guide to help the designer or HVAC engineer choose the appropriate modelling tool for each stage of the building design process.

One final word; these modelling tools generally yield best results only when in competent hands, and are thus no substitute for sound human engineering judgement and experience.

Table 2.8.1 Comparison of performance of the different model types.

		Flow element model	Zonal model	Field model (CFD)	Scale model experiment	Ventilation efficiency
Outline of the model		<ul style="list-style-type: none"> Each element of flow-field, i.e. supply jet, thermal plume, boundary layer etc. is analysed individually. Entire flowfield is examined by combination of these flow elements. 	<ul style="list-style-type: none"> Entire space is subdivided into a few zones. Balance of air flow rate, heat flux, etc., are analysed, so zone-mean values of velocity, temperature and concentration are given. 	<ul style="list-style-type: none"> Space is subdivided into many small cells. Total number of cells is about 10^4–10^5. Discretized transport equations of velocity, temperature, concentration are solved with finite difference method. 	<ul style="list-style-type: none"> Indoor climate of large enclosure is measured using scale model of the space. The similarity condition between real scale and model scale is important. 	<ul style="list-style-type: none"> Ventilation effectiveness for supplying fresh air and exhausting contaminants is analysed using results given from various the models on the left.
How to apply	Macro / Micro	Macro	Macro	Micro	Micro	-
	Analysis of time-dependent phenomena	difficult	possible	possible	impossible	-
	Limits or disadvantages	<ul style="list-style-type: none"> Only the region of flow element is analysed. 	<ul style="list-style-type: none"> Detailed distribution can't be predicted, i.e. only low resolution. 	<ul style="list-style-type: none"> A great number of cells are required for analysing a large enclosure. 	<ul style="list-style-type: none"> Its very difficult to satisfy similarity conditions accurately. 	
Input		<ul style="list-style-type: none"> Definition of type of flow element. Empirical constants for supply jet, etc. Temperature of supply air, wall surface, etc. 	<ul style="list-style-type: none"> Zone dividing. Boundary conditions at walls. Position of supply and exhaust openings etc. Property of supply jet etc. 	<ul style="list-style-type: none"> Grid layout. Boundary conditions for velocity and heat flux etc. 	<ul style="list-style-type: none"> Property of supply jet for simulating the Archimedes number. Boundary conditions for interior heat source and wall surface temperature etc. 	<ul style="list-style-type: none"> Room air velocity distribution or exchange coefficient between zones Positions of contaminant sources Position and volume of fresh air supply
Output		<ul style="list-style-type: none"> Continuous (not discrete) distributions of velocity and temperature for each flow element. 	<ul style="list-style-type: none"> Mean temperature, mean pressure and mean concentration for each zone. 	<ul style="list-style-type: none"> Fine-detailed distribution of velocity and temperature throughout space Wall surface temperature when radiation simulation is coupled. 	<ul style="list-style-type: none"> Space distribution of velocity and temperature. Number of measuring points are limited due to cost of experiment. 	<ul style="list-style-type: none"> Evaluation of ventilation efficiency Distribution of concentration
Program in public domain?		?	✓	✓	-	✓
Advantage		<ul style="list-style-type: none"> Very simple; suitable for hand-calculations. 	<ul style="list-style-type: none"> Practice is rather simple, and fast on a computer. Analysis of time dependent phenomena is possible 	<ul style="list-style-type: none"> Very detailed analysis is possible Presentation using computer graphics is very realistic & useful. 	<ul style="list-style-type: none"> Measurement of physical phenomena is reliable. Very realistic data. 	
Disadvantage		<ul style="list-style-type: none"> Can not be applied where flow elements interfere with each other. 	<ul style="list-style-type: none"> Prediction accuracy becomes lower when the flowfield is complicated. 	<ul style="list-style-type: none"> Design of grid layout takes many man-hours. Long computation time and much memory. 	<ul style="list-style-type: none"> Requires a very large amount of time, money, and work. 	

CHAPTER 3

3.1. Introduction

3.2. Review of Existing
Measurement Techniques

3.3. Measurement Techniques
Applied to Large Enclosures

3.4. Conclusion

3.1 Introduction

3.1.1 Peculiarities of Large Enclosures with Regard to Ventilation-Related Measurement Techniques

Large enclosures are addressed by Annex-26 for two main reasons, the first one being obvious and resulting in the second one:

- Large enclosures have a large volume and a large envelope area
- The physical properties of the air is usually not homogeneous within large enclosures

These are also the two main causes of difficulties encountered when measuring ventilation in large enclosures.

Peculiarities resulting from size

The large volume and area to be examined generally means a larger amount of work, larger number of measurement points and more material cost. The use of some tracer gases can be much too expensive, so only tracers naturally generated within the volume (e.g. CO₂) or those that can be detected at trace concentrations (e.g. PFTs) are affordable. For some experiments, the required instruments could be very large. For example, huge fans were developed to measure the air tightness of large enclosures.

Large size can also be an advantage. For example, neutrally buoyant balloons, easier to prepare than neutrally buoyant bubbles, could be used in large enclosures, since their size remains relatively small. Facilities never encountered in small enclosures, like cranes and trucks, could be used in industrial premises for scanning. In tall enclosures the stack effect, which pressurises the envelope, can be used, together with known openings, to easily assess the air tightness.

Peculiarities resulting from non-homogeneity

The analysis of inhomogeneities is an important consideration when studying the ventilation of large enclosures. There can be large spatial variations in air temperature (hence density), velocity and contaminant concentration. Therefore, several measurement points are needed and must be thoughtfully positioned, which makes measurement more complicated.

Measurement techniques that assume that the measured zone is homogeneous cannot be used in large enclosures. If such measurements are required (e.g. age of the air, or air change rate), some corrections should be applied. A good example is presented below [Stymne *et al.*, 1992].

Interpretation of measured data should obviously take account of the inhomogeneities. Multizone concepts can be used for this purpose.

3.1.2 Purpose of Chapter

The intention here is not to describe all possible measurement techniques; such descriptions are available in the literature [Roulet and Vandaele, 1992; Charlesworth, 1988]. Therefore, only a brief summary is given here. The purpose of Chapter 3 is rather to present measurement techniques especially developed for large enclosures. Some of these techniques were developed within the framework of Annex 26.

3.2 Review of Existing Measurement Techniques

3.2.1 Relations between Measurement Techniques and Problems

Obviously, measurements should be performed only when there is a defined purpose. Hence, the purpose or problem should first be defined, and the missing information should be listed. Only then can the measurements be planned, and measurement techniques chosen accordingly.

For each problem encountered in the ventilation of large enclosures, measurement techniques can be useful in the quest of a solution. Table 3.2.1, which resulted from a discussion within Annex-26, tries to summarise these relations.

Table 3.2.1 Variables related to some problems encountered in large enclosures, and related measurement techniques.

Problem	Measurable variables	Measurement method
Draughts	Velocity Turbulence ¹ Temperature	Anemometry ² Thermometry ³
Thermal radiation	Radiant temperature	Radiometer Comfort meter
Overheating	Temperature Comfort	Thermometer Comfort meter
Specific contaminants	Contaminant concentration	Analyser Samplers / dosimeters (passive and active)
Simulation of contaminant spread	Concentration Removal efficiency	Tracer gas, smoke
Infiltration	Leakage parameters Leak detection	DC pressurisation ⁴ Stack pressurisation Thermography Smoke detection
Correct ventilation	Specific air flow rate Age of the air Airflow visualisation	Tracer gas, uniform concentration ⁵ Tracer gas, homogeneous emission Smoke, balloons

Notes in Table 3.2.1:

1. A distinction should be made between turbulence, which is a random variation in velocity, with a slowly varying average velocity, and intermittence, where the turbulence can change together with the average velocity.
2. Directional anemometry should be used, like LDA and field techniques.
3. The size of large enclosures may lead to mapping problems, because of the large number of measurement points required.
4. DC pressurisation may be technically or economically impossible for leaky large enclosures, because of the fan size required.
5. There are specific problems linked with measurements in large enclosures. Mixing the tracer is one, which could be minimised by the use of constant concentration techniques.

3.2.2 Commonly used Techniques for Large Enclosures

This section summarises the information received from different experts within IEA.

Information was collected on the techniques used at least once by some laboratories to analyse large enclosures, as well as on techniques under development for that purpose. Table 3.2.2 summarises this information, without mentioning the classical techniques such as those used to measure temperatures, meteorological data, etc.

Table 3.2.2 *Measurement techniques used by some institutes for analysing ventilation-related problems in large enclosures.*

Country	Institute	Technique	Applied to:	Ref.
Finland	Turku Regional Institute for Occupational Health	CO concentration in 3 locations + exhaust	Garage	Koskela <i>et al.</i> 1992
Finland	Vanuatu Institute for Occupational Health	Multitracer gas, marking gas flows of interest	Industry hall	Niemelä <i>et al.</i> , 1986 and 1987
Switzerland	LESO-PB, EPFL, Lausanne	Tracer gas on an optimised grid Pulse pressurisation Stack pressurisation	Auditorium, Industry hall Under dev. Large encl.	Roulet <i>et al.</i> , 1991 Zamboni <i>et al.</i> , 1992 Fürbringer <i>et al.</i> , 1994
Netherlands	TNO, Delft.	Contaminant concentration Pulsed smoke emission and stereo photography	Several	van Beukering <i>et al.</i> , 1973 Crommelin <i>et al.</i> , 1980 and 1989
UK	BRE, Garston	Flow Visualisation with neutral buoyant balloons	Atria	Seager
USA (IL)	CES, University of Illinois, Effingham	Evaluation of Particle Image Velocimetry	Farms, Barns	
Germany	Rheinisch-Westfälische Technische Hochschule, Aachen	Laser Doppler Anemometry, Laser-sheet anemometry, Laser holography	Intend to develop for large encl.	
Sweden	NSIB, Gävle	Age of air, Homogeneous emission	Laboratory	Stymne <i>et al.</i> , 1992
Germany	IKE, Uni. Stuttgart	Tracer gas, "Belastungsgrad"	Industry hall	Dittes, 1983

3.2.3 Special Applications of Classical Techniques

The use of expensive tracer gas can be cut by either using a tracer generated by normal use of the enclosure (e.g. CO₂ in assembly halls, auditoriums, etc. or CO in garages) [Koskela *et al.*, 1992] or by using the tracer at the lowest detectable concentration at the sampling locations [Niemelä *et al.*, 1986 and 1987; Roulet *et al.*, 1991]. These techniques have severe limitations however, since the flow rate of tracer gases naturally generated within the enclosures is generally not well known, and non-homogeneity still poses a problem if standard techniques are used.

Visible tracers, like smoke or balloons, are very useful and are often used for qualitative observations of airflow in large enclosures. However, further development will be required, especially of image analysis, to obtain reliable quantitative data from these tracers.

Contaminant concentrations, (as well as tracer gas concentration) usually fluctuate with time. Crommelin *et al.* [1980] noted that the distribution of these fluctuations is lognormal. Knowledge of this temporal property allows one to minimise the number of measurements.

3.3 Measurement Techniques Applied to Large Enclosures

3.3.1 Airtightness

Stack-effect method for high rise buildings

This simple method of estimating the air leakage distribution in tall buildings is based on the pressure distribution induced in buildings by the stack effect [Tamura and Wilson, 1966]. Up to three parts can be estimated separately: the ground floor, top floor and intermediate floors.

The basic idea is to take advantage of the stack effect, which pressurises the building, and to plan different experiments in order to obtain three independent equations for the different leakages that are being estimated [Hajakawa and Togari, 1990].

The building should be tall and the temperature difference between indoors and outdoors should be large enough such that the pressure difference between inside and outside induced by the stack effect outweighs the pressure due to wind. This pressure difference will reach 30 Pa if the product of the height by the temperature difference surpasses 700 K·m. The technique can be performed only under windless conditions.

The leakage of the building can be divided into three parts:

- Leakage through the ground level including the entrance door (suffix g)
- Leakage through the top level including the roof (suffix t)
- Leakage through the intermediate floors (suffix r)

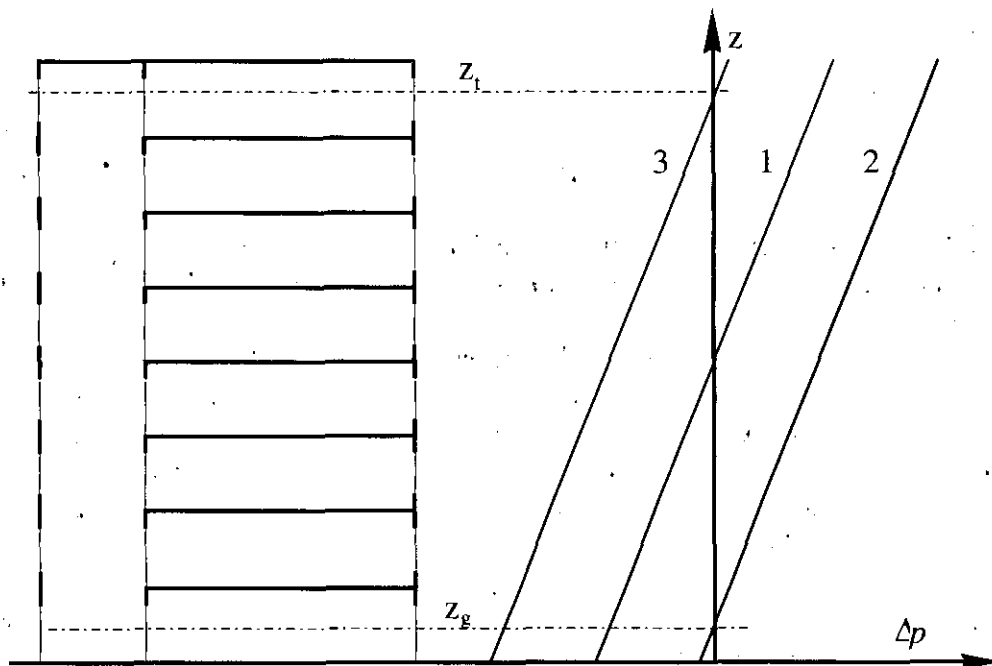


Figure 3.3.1 The building is represented to the left. To the right, the pressure distributions for the three experimental cases are given: 1) closed building envelope; 2) ground floor door open; 3) top level window(s) open.

If the building has all its internal doors open as well as the staircase and/or the lift shaft, and if the temperature does not vary too much throughout the building, then there is only one

neutral plane, at height z_0 . The pressure difference, Δp , caused by the stack effect at any height in a given building configuration is then:

$$\Delta p(z) = \int_{z_0}^z g \Delta \rho(\zeta) d\zeta \quad (3.3.1)$$

where

$\Delta \rho$ = difference in density of air between inside and outside

g = gravitational acceleration (about 9.81 m/s²)

If the temperatures are homogeneous, Equation (3.3.1) gives:

$$\Delta p(z) = \Delta \rho g (z - z_0) \quad (3.3.2)$$

From the law of ideal gases:

$$\rho = \frac{M p}{R T} \quad (3.3.3)$$

Combining (3.3.2) and (3.3.3) gives:

$$\Delta p(z) = \frac{M p}{R} \left[\frac{1}{T_i} - \frac{1}{T_e} \right] g (z - z_0) \quad (3.3.4)$$

The leakage mass flow rate through the building envelope is approximated by a generic power-law equation:

$$\dot{m} = \rho C \Delta p^n \quad (3.3.5)$$

where C and n are empirical coefficients. C is an indicator of the area of leakage.

Assuming that the value of exponent n is the same for all the leaks (e.g. 0.6), there are three unknowns, the leakage coefficients C_g , C_r and C_t . To estimate these coefficients, three measurement cases are performed where the pressure differences, the temperatures at various heights in the building and some flow volumes are measured. This enables the solution of three equations. The first equation is given by the conservation of mass with a closed envelope. The two other equations are obtained by mass conservation with a large opening at the bottom or the top of the building, respectively. In these last two cases, the airflow through these openings is measured. The relations are as follows:

All openings closed: In this case, the neutral plane is somewhere at the mid-height of the building and, by conservation of the mass of air, we have:

$$\rho_g C_g \Delta p(z_g)^n + \int_{z_{rb}}^{z_n} d(\rho_r C_r \Delta p(z_r)^n) + \rho_t C_t \Delta p(z_t)^n = 0 \quad (3.3.6)$$

where

- ρ_g = density of air at ground level
- ρ_r = density of air at intermediate floors
- ρ_t = density of air at top level

Entrance door open: The airflow through the open entrance door (or any other large opening on the ground level), \dot{m}_g , is measured, for example by measuring the air speed at several locations across the opening and integrating over the whole opening:

$$\rho_g \dot{m}_g + \int_{z_b}^{z_t} d(\rho_r C_r \Delta p(z_r)^n) + \rho_t C_t \Delta p(z_t)^n = 0 \quad (3.3.7)$$

Windows open at the top level: The airflow through these windows, \dot{m}_t is measured. We have similarly:

$$\rho_g C_g \Delta p(z_g)^n + \int_{z_b}^{z_t} d(\rho_r C_r \Delta p(z_r)^n) + \rho_t \dot{m}_t = 0 \quad (3.3.8)$$

The neutral plane is now close to the top level.

Assuming that n is 0.6, or $2/3$, which is typical, then Equations (3.3.6) to (3.3.8) can easily be solved to estimate C_g , a global C_r and C_t . If the temperatures are not uniform inside or outside, then Equation (3.3.1) should be used instead of Equation (3.3.2). The system is then more complex but can still be solved. The most important condition to observe during the measurement is the absence of wind.

The main advantage of the method is that it does not require the use of sophisticated equipment. The minimum required equipment is:

- 1 anemometer, 0-5 m/s
- 2 differential manometers, 0-50 Pa
- 3 air temperature thermometers
- 1 accurate tape measure

This minimum equipment can be complemented by more differential manometers and thermometers. These additional instruments are used to verify the linearity of the pressure distribution through the building.

Tracer gas equipment may also be used to measure the airflow through the openings. Note that a perfect mixing of the tracer gas is essential and especially difficult to achieve in large openings.

Neutral pressure level (NPL) method

A simplification of this method was recently developed, taking advantage of the modelling of airflow through large openings [van der Maas *et al.*, 1992 and 1994]. The stack effect method is used as mentioned above, but the net air flow rate is obtained by measurement of the position of the neutral level in the opening. For this, the opening should be large enough (or the rest of the envelope airtight enough) to find the neutral level within it, and the prevailing wind should not add a significant pressure to the envelope of the building.

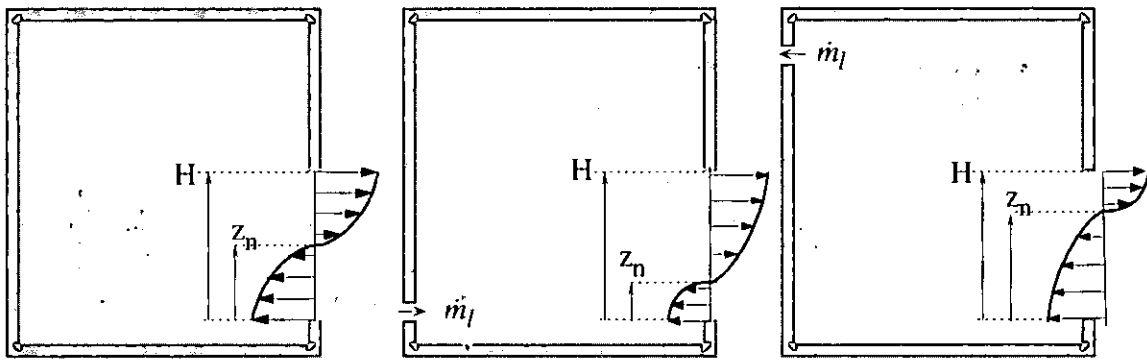


Figure 3.3.2 Air flow rate by convection through a large opening. Left: airtight enclosure. Centre and right: leaky enclosures.

If an airtight enclosure with temperature T_i is connected to the external environment (temperature T_o) by a single large opening of height H , width W , and area $A = H \cdot W$, a bi-directional airflow occurs in the opening by natural convection. Warm indoor air leaves through the top half of the opening, and cold outside-air enters through the bottom half (Figure 3.3.2 left).

From Bernoulli's equation and mass conservation, it can be shown that the mass flow rate through the upper or lower half of the opening is:

$$\dot{m}_A = \frac{1}{3} C_d \rho_o A \sqrt{\frac{g H \Delta T}{T_o}} \quad (3.3.9)$$

where

C_d = discharge coefficient of the opening (typically 0.6)

ρ_o = density of outdoor air (assumed to be the cold zone at absolute temperature T_o)

g = gravitational acceleration (9.81 m/s²)

ΔT = indoor-outdoor temperature difference

If the enclosure is airtight then the neutral level, z_n , is near the mid-height of the opening; $z_n = \frac{1}{2}H$. But if some air enters or leaves the enclosure through another opening or through leaks, the neutral level will be lower or higher, respectively. Using mass conservation, and assuming that $T_i > T_o$, the net leakage mass flow rate is given by:

$$\dot{m}_l = 2\sqrt{2}\dot{m}_A \left[\left(\frac{T_o}{T_i} \right)^{\frac{1}{2}} \left(1 - \frac{z_n}{H} \right)^{\frac{1}{2}} - \left(\frac{z_n}{H} \right)^{\frac{1}{2}} \right] \cong 2\sqrt{2}\dot{m}_A \left[(1-a)^{\frac{1}{2}} - a^{\frac{1}{2}} \right] \quad (3.3.10)$$

where $a = \frac{z_n}{H}$.

Equations (3.3.9) and (3.3.10) allow one to assess the leakage air flow rate by measurements of the location of the neutral level (using a ruler and a smoke puffer) and of the indoor and outdoor air temperatures at the neutral level.

The accuracy of this method decreases dramatically if the neutral level is too close to the mid-height of the door. In such a case, the door should be left ajar, leaving a narrower rectangular aperture. Conversely, if the leakage flow rate is larger than $2\sqrt{2}\dot{m}_A$, the flow

through the large opening becomes unidirectional, so the neutral level method cannot be applied. In this case, either enlarge the opening, or measure the air flow rate directly by a velocity traverse across the opening or by tracer gas technique. This technique was used on the Annex-26 case study building Grafenau Zug (Section 4.6.2)

Pulse pressurisation

During and after injection of a puff of air in an enclosure, the evolution of the air pressure with time depends on the volume of the enclosure and on its leakage characteristics. The time dependence can be found by writing an energy balance for the enclosure, assuming that the energy losses are due only to leakage.

The limits of application of this method are not well known, as it is still under development. An obvious limitation is that the pressure drop due to leakage is delayed by the transit time of sound pressure waves across the enclosure. Another one is technical; the quantity of air delivered to the enclosure in about one second should be more than one thousandth of the volume of the enclosure, in order to get a measurable pressure pulse.

The pressurisation equipment is a compressed air container equipped with a mass flow controlled valve. The instruments needed are a manometer able to follow the evolution of pressure with time, and fast recording equipment.

By time derivation of the law for adiabatic relaxation, the following model is obtained which relates the variation of pressure to the variation of air flow rate and leakage coefficients:

$$\frac{d(\Delta p_i)}{dt} = A \left[\dot{m}_s(t) - C \cdot (\Delta p_i - \Delta p_e)^n(t) \right] \quad (3.3.11)$$

where

$$A = \frac{\chi p_o}{V_o} \text{ is constant}$$

$$\chi = \text{ratio of specific heat of air at constant pressure to that at constant volume.} \\ \chi \approx 1.4$$

$$p_o = \text{reference pressure}$$

$$V_o = \text{volume of the enclosure [m}^3\text{]}$$

$$\Delta p_i = \text{internal pressure differential [Pa]}$$

$$\Delta p_e = \text{external pressure differential [Pa]}$$

$$\dot{m}_s = \text{mass flow rate of the source of air [kg/s]}$$

$$C = \text{leakage flow characteristic}$$

$$n = \text{leakage exponent } (0,5 \leq n \leq 1)$$

Knowing V , $p(t)$ and $\dot{m}_s(t)$, the nonlinear differential Equation (3.3.11) can in principle be solved to obtain the leakage coefficients C and n . There are various ways to do this, several of which were tested in Annex-26. One appeared to be too sensitive to noise, and provided random results. Another turned out to be far too stable, always giving the same result, irrespective of C and n ! The inverse problem theory [Tarantola, 1987; Fürbringer et al., 1994] gave a robust solution, which was found to be correct on simulated experiments. It is as follows:

Integrating Equation (3.3.11) and using finite differences, one gets a vectorial function whose norm can be calculated. The model linking the measured quantities and the leakage coefficients is then:

$$d = \sum_{i=1}^{n-1} \left(\Delta p_{i+1} - \Delta p_i - \frac{A \Delta t}{2} \sum_{j=i}^{i+1} (\dot{m}_{Sj} - C \Delta p_j^n) \right)^2 = 0 \quad (3.3.12)$$

The technique involves giving each quantity in (3.3.12) an assumed probability density. Then the collective maximum likelihood of the whole set of quantities is evaluated, taking account of the model linking them. The measured quantities, \dot{m}_S and Δp , are given a normal distribution which centres on the measured values and with an appropriate standard deviation⁷. The exponent n is given a uniform distribution between 0.5 and 1; and C is likewise given a distribution between 0 and a maximum value. These probability densities (ρ_M) represent the information *a priori* on parameters, in the space M of these parameters. Since $d = 0$ in Equation (3.3.12), the probability density ρ_D represents the information on the true value of d . The information *a posteriori* is a new ensemble of parameters, $\{M\}$. Assuming that the probability densities of individual quantities are independent of each other, the probability density of this ensemble is in the space $M \cup D$:

$$\sigma(M, d) = \rho_M \rho_D \quad (3.3.13)$$

The best estimate of C and n is at the point in $[C, n]$ space that has the highest probability (Figure 3.3.3). A numerical searching technique is used to find the co-ordinates of this maximum, and hence the values of C and n for the enclosure.

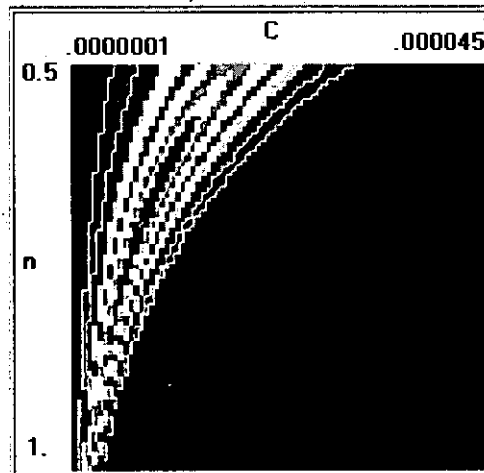


Figure 3.3.3 Isolines representing the probability density of the leakage coefficients C and n (result of an experiment).

This technique was tested by Sherman & Modera [1988], using the decaying part of the function, after slamming the door of a 25 m³ cabin. For this relatively small volume, reproducible results were obtained that agreed with pressurisation tests. More recently, measurements at LESO on a scale model seemed to show a systematic bias between results of this dynamic method and of static pressurisation. Development of this method is still required, but its future application to large enclosures is doubtful.

⁷ In fact, ρ_M is the product of the distributions of all variables, in the space of the measured quantities.

3.3.2 Air Velocity

Measurement of air velocity in large enclosures is difficult because mean velocities and often turbulence quantities have to be measured at several points throughout a large volume, with difficult accessibility, particularly to points at high level. Also, measurements take a long time since the airflow is normally characterised by low velocities, high turbulence levels and in most cases by an unsteady behaviour. The use of known and new measuring techniques both need special attention.

Many different measuring techniques are available, such as thermal anemometers, Laser-Doppler anemometers, particle-image anemometers and ultrasonic anemometers. These are dealt with in the next few pages.

Thermal anemometers

Basic principle: A thin electrically heated element (film or wire) is cooled by the airflow being measured. The heat transfer from the element is a function of the air velocity, the temperatures of the surface and the air. With regard to control, there are three basic types of anemometers: (1) the constant-current anemometer (CCA), (2) the constant temperature anemometer (CTA), and (3) the constant temperature difference anemometer (CTDA). To take account of the effects of the probe geometry, of natural convection induced by heated surface and of the air turbulence, a calibration is normally carried out in specially designed calibration equipment. Standard probes for ventilation airflow measurements are of spherical or cylindrical shape with a diameter of 2 to 3 mm. The velocity range is from 0.10 to 20 m/s.

Advantages: The thermal anemometer technique is widely used in ventilation. The measuring system is relatively simple and easy to operate. There is a wide variety of different systems ranging from standard versions for mean velocity and turbulence levels up to sophisticated versions for comfort measurements including the use of temperature, radiation, and humidity probes.

Disadvantages: The thermal anemometer technique is a point measuring technique; this means that the information on mean velocity, turbulence, and in most cases temperature, is evaluated at a single point within the room. A typical measuring time for one point is about 2 to 10 minutes. To get complete information on the airflow pattern within a large enclosure, this method is very time consuming. Measurements in a large enclosure with unsteady airflow, for example due to solar radiation effects, is not feasible even when several probes at different positions are used simultaneously.

The probe and the probe-stand can themselves disturb the airflow at the measuring point, especially in highly three-dimensional low-velocity airflow, as is the case in large enclosures. At very low air velocity, natural convection driven by heat from the anemometer becomes significant. At a velocity of 0.10 m/s, the heat transfer by forced convection and the heat transfer by natural convection driven by the heated surface of a probe at 60°C, are of the same order of magnitude. For turbulence measurements with three-dimensional velocity fluctuations, the natural convection effects can not be calibrated. In an experimental investigation in a ventilated room with a mixed air flow system, large discrepancies have been found between different commercial low velocity thermal anemometers. The simultaneously measured turbulence intensities at a mean velocity of 0.10 m/s ranged from 35 % up to 70 %

(mean value 55 %) compared with the value from the Laser-Doppler anemometer of 40 %. Radiation may also affect the accuracy of the measurements.

Price: Depending on the system, the price ranges from \$1000 for simple scalar velocimetry to \$15 000 for comfort-data measurements.

Laser-Doppler anemometer (LDA)

Basic principle: Two laser beams intersect within a measurement volume, producing a fringe pattern. When a small tracer particle of the airflow crosses the fringe pattern, light is scattered. From the detected frequency of the scattered light during the flight of the particle across the fringe pattern, one component of the particle velocity can be evaluated from straightforward geometrical considerations. The system can be extended to two and three-component measurements. Depending on the optics and the data acquisition, a large range of velocities from a few mm/s up to several 100 m/s can be measured.

Advantages: LDA devices do not need calibration. If the system is operated correctly, the results are free from systematic errors. The technique is non-intrusive. The distance between the optical probe, which may be connected to the laser light source by an optical fibre, and the measuring point, depends on the size of the measurement volume to be realised. Typical distances in large enclosures could range from 0.2 to 5 m. The size of the measurement volume depends on the optical configuration and is in any case small enough for applications in ventilation. The frequency response depends on the size of the tracer particles used and is uncritical for ventilation applications.

Disadvantages: The LDA technique is a point measuring technique, with the same associated disadvantages as mentioned above for thermal anemometry. In large enclosures it is often a problem to provide tracer particles such as oil droplets, water droplets, solid particles, in appropriate quantities.

The worst disadvantage, apart from cost, is the complexity and weight of the equipment. The set-up of the optical system and the evaluation of the data cannot be carried out by merely following a manual, but needs a skilled operator. Large enclosures require high-powered lasers (>1 W), so an effective water cooling-system must be provided.

Price: LDA systems are expensive. Depending on the complexity of the system, from simple one-component to three-component velocity measurements, and depending on the laser power and data acquisition, the price ranges from \$50 000 to \$150 000.

Particle-image velocimetry (PIV)

Basic principle: Particle-image velocimetry is derived from the well known qualitative laser light-sheet technique. It involves measuring the displacement of markers that travel with the airflow, either as streaks on a single frame taken by long exposure times or by multiple sequential frames taken with short exposure times. The displacement of the markers (particles, bubbles or even balloons) must be small enough to represent a good approximation of the actual velocity. Commercial systems are available that record the particle images in a plane of the flowfield, illuminated by either white light or by a laser system. The appropriate two-velocity components are evaluated by image processing software. To obtain the third velocity

component, several extensions have been proposed, such as stereo photogrammetry or using more than one laser to create parallel laser sheets of different colours (Figure 3.3.4).

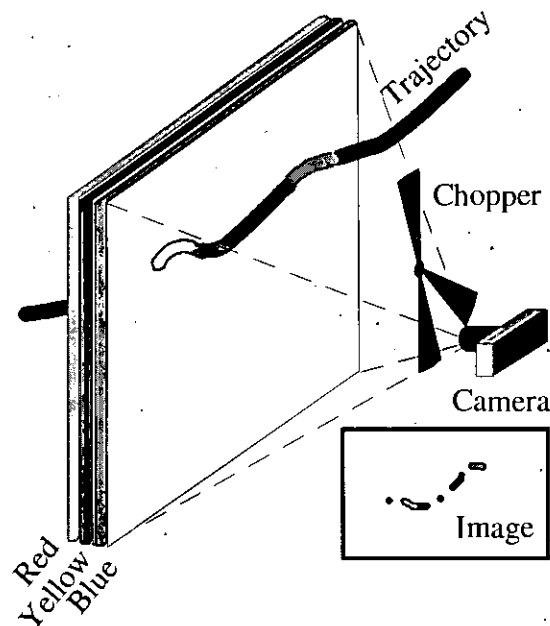


Figure 3.3.4 One possibility to get 3-D information on velocity of particles

Advantages: The PIV technique is a plane measuring technique which allows the simultaneous evaluation of the two velocity components throughout one plane of the flow field. New methods that measure the third velocity component within this plane are currently under development. This would allow the measurement of all three velocity components in a given plane simultaneously. No calibration is needed. An accuracy of 5 to 10 % is estimated for the two-component technique. The PIV technique is non-intrusive.

Disadvantages: The two-component PIV technique has so far been mostly used in small scale applications. For laboratory measurements of ventilation, measuring areas of several square meters have been realised recently. However, for measurements within large enclosures, new systems will have to be developed. The maximum allowable measuring area depends on the size of the tracers (e.g. helium-filled bubbles), on the light intensity (laser power), and on the resolution of the detecting medium (photocamera, CCD-chip). Furthermore, bubbles are difficult to concentrate within an illuminated plane of a large enclosure and the control of neutral buoyancy in large enclosures is critical.

Only snapshots of velocity fields can be evaluated. The evaluation of mean velocities and turbulent quantities, which has to be based on large numbers of such snapshots, is beyond the capabilities of standard computer systems at present.

Price: PIV systems for large enclosures are not available commercially. The price of the equipment may be comparable to that of the LDA system.

Ultrasonic anemometers

Basic principle: The technique is based on the measurement of the travelling time of a sound wave between an emitter and a receiver, which is affected by the direction of the air velocity. This measuring principle is well known in meteorology and has been introduced in ventilation only recently. The velocity, is a mean value for the measurement volume of a typical dimension of about 50 mm and ranges from a few mm/s up to 10 m/s.

Advantages: Commercial systems are able to measure all three velocity components simultaneously and to evaluate mean velocities and turbulence intensities. The measuring system is relatively simple, easy to operate and, once properly calibrated at the factory, needs no further calibration. Unlike thermal anemometers, the output from the probes is linear, even at low speed. There is no influence of temperature. The air temperature can be evaluated simultaneously from the same signal.

Disadvantages: The ultrasonic anemometer is an intrusive point-measuring technique, the disadvantages of which have been discussed for thermal anemometers.

Price: Ultrasonic systems costs between \$15 000 and \$25 000.

3.3.3 Contaminant Fields

Purpose of measurements

The concentration of airborne contaminants in large spaces is characterized by large spatial and temporal variation. Description of concentration fields depends heavily on the purpose of measurements. The aim of measurements can be divided roughly into three categories:

- exposure assessment
- performance evaluation of ventilation or other control technologies
- model verification

Traditionally, in occupational exposure assessment, air samples are taken in the breathing zone with a sampling device carried by a person. Instead, area samples are taken at a few fixed sampling sites in order to describe concentration levels in the general room atmosphere.

When contaminant dispersion and removal is explored in detail, concentration must be measured at a large number of points in the space. In recent years the development of CFD models has created a need to measure concentration distributions with narrow spatial resolution for the purpose of verification. Also, the recording of the evolution of concentration is necessary. For model verification, the concentration field of the zone of interest or in the entire large enclosure should be described.

Personal monitoring

Personal monitoring focuses on the inhaled exposure of a person during the time period of interest. The air sample is taken in the breathing zone, i.e. near the person's nose in such a way that normal work procedure can be continued during sampling. Breathing zone monitoring is performed in spaces with strong localised sources, e.g. in industrial work spaces.

It is worth noting that the person's work practice often influences the breathing zone concentrations.

Passive samplers, adsorbing contaminants into a material which is analysed later in a laboratory are often used for this purpose. Active sampling and on site analysis may also be used for control. Sampling may for example be done by a small battery-operated dosimeter with a sampling tube slung over the bearer's shoulder towards the breathing zone.

Monitoring at fixed points

Monitoring at fixed points, or area sampling, is usually conducted to evaluate general concentration levels in the area of interest. The area samples collected in the zone of occupancy may reflect personal exposure in buildings where contaminant sources are rather homogeneously distributed. However, the measurements are often focused to detect the influence of changes in ventilation configurations or processes. The location of sampling points are selected with respect to contaminant sources, permanent working sites and ventilation configuration. For practical reasons, the number of fixed sampling sites in large open rooms is seldom more than twelve. The duration of sampling depends on the time scale of the process or the activity in the space. In exposure estimation, the sampling period is the same as that of breathing-zone monitoring.

For this purpose, passive or active sampling may be used. Continuous analysers coupled with scanning valves on one end and to a data logger on the other hand, allow multi-channel continuous monitoring.

Concentration mapping

In CFD calculations, thousands of grid points are used. Obviously it is not feasible to measure concentration at so many points in existing buildings or even in a full-scale test. Nevertheless, in order to produce sufficient data for model verification, a large number of measurement points are needed. In practice, only a limited number of measurement points can be selected. Their locations should therefore be chosen carefully. Roulet *et al.* [1991] describe a systematic approach for selecting sampling points in a room. The selection of the sampling points should also take account of room geometry, available instruments, professional experience of the measurers, as well as labour and cost. The choice of sampling points is discussed further on page 175.

After the measurements, a concentration map can be made by interpolating between the experimental points, using a certain algorithm [Collineau *et al.*, 1995]. (Figure 3.3.5). Concentration mapping can be performed both in full-scale laboratory mock-ups and in real buildings. Laboratory tests give more detailed and accurate results. On the other hand, field measurements, although being difficult to conduct, give information on real conditions.

The measuring system is basically the same for laboratory and field measurements. Instrument control and data logging is best done with computer, as this reduces errors and work and enables statistical sampling [Koskela *et al.*, 1990]. If statistics of concentration variation is desired, a number of fast gas/contaminant analysers or sensors must be used for measurement. The output of these can be sampled by the computer or data logger. The second possibility is to use a single analyser with a multiplex unit connected to several sample tubes. This system is usually too slow for statistical sampling, but it has other advantages: there is no need for inter-calibration of analysers and a more sophisticated analyser can be used.

Steady state

Steady-state conditions are required for measurements when analysed points cannot be sampled at the same time, but are scanned sequentially. This can be achieved in laboratory measurements, but not in the field. Because of this, the results of field measurements include both spatial and temporal variation. There are numerous factors causing temporal variations: changes in production, contaminant sources with varying intensity, temperature or location, changes in supply air flow pattern, movements in the space, outside conditions, opening of doors, etc. The effect of these factors must be minimised by selecting the proper time to measure, when the conditions are approximately stable. The performance of a ventilation control system has to be checked, because variation of, for example temperature difference between the supply and room air, can cause a major change in the airflow pattern. Monitoring of air temperatures and contaminant generation rate is recommended during the traversing. The effect of temporal variations can be estimated by carrying out repeated measurements.

Sampling period and measurement grid

The number of measurement points is restricted by the averaging or scanning time needed in each position and the duration of steady-state conditions. Averaging time should be long enough to cover short-scale variations of concentration. An averaging time of 3 minutes is recommended for air velocity measurements (ISO), and should also be appropriate for concentration. The error in the mean value and standard deviation depends on the number of samples taken during the averaging period. Some analysers have a long time-constant, which can be due to a large sampling volume. This causes low-pass filtering or averaging to the measured concentration and has to be taken into account in the selection of the sampling period.

The traversing measurement can be started when the concentration in the space is sufficiently close to the steady-state value. This depends on the nominal time constant of the enclosure. After three time-constants from the beginning of steady-state conditions, the concentration reaches 95% of its steady-state value.

A full 3D measurement grid can be realised only in full-scale laboratory tests with an automated traversing system. In field conditions the traversing must be done in one or several vertical or horizontal planes. A vertical plane can be traversed by a measurement carriage fitted with a mast that has sampling tubes or probes at several heights. The location of the traversing plane and measurement positions has to be selected taking into account the locations of contaminant sources, supply devices, occupied areas, and obstacles in the space. It may be wise to take measurements symmetrically in relation to important locations, especially if the measurement results will be compared to simulations. The steepest concentration gradients are found near contaminant sources and supply openings. The measurement grid should be most dense in these areas.

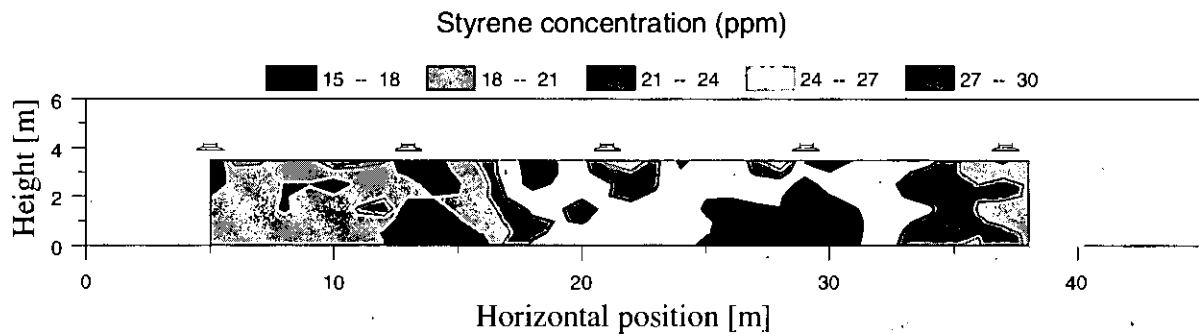


Figure 3.3.5 Contour diagram presentation of concentration distribution in a vertical plane.

Data presentation

The concentration traversing results are recorded in the format

$X, Y, Z, Value1, Value2, \dots$

where X , Y and Z are the co-ordinates of each measurement point in relation to the selected reference point in the enclosure, and $Value1$, $Value2$, etc. are measured concentrations or statistical parameters of concentration. There are several methods and software products to present this kind of data. One common method for presenting results in one plane is a contour diagram (Figure 3.3.5). If the data is not regularly spaced, an interpolation must first be performed. Extrapolation outside the measured region is not recommended because it may produce unrealistic values and lead to wrong conclusions.

3.3.4 Ventilation Performance

Ventilation performance parameters

The parameters that are of greatest interest in assessing the ventilation performance of a large enclosure are some or all of the following:

- *Fresh air exchange rate (or specific flow)*
This may be expressed as the nominal time constant
- *Air change efficiency*
In a large enclosure, the distribution of fresh air is of particular concern, and so the parameters that are most useful are:
 - local mean age of air
 - local air change index

The room mean age of the air and the air change efficiency itself are unlikely to be required, as there are no relevant criteria for them, and their values are not necessarily meaningful in a large enclosure.

- *Contaminant removal effectiveness*
It is probable that the effect of a contaminant on occupants and the effectiveness of contaminant removal is important at specific locations in the occupied zone, but not throughout the entire space. The most useful parameters are therefore:

- local air quality index
- dosage index
- transfer index

The contaminant removal effectiveness for the whole space is unlikely to be required.

Definitions of these parameters may be found in Sütcliffe [1990], Brouns & Waters [1991], and Liddament [1993].

Suitable measurement techniques for large enclosures

Measurement is most easily accomplished by tracer gas methods, the theory and practice of which is described in detail by Roulet and Vandaele [1992]. There are no new techniques for large enclosures, so it is necessary to consider the effect that the size and function of such enclosures may have on the application of existing techniques. Experience suggests that size-related measurement difficulties become evident when the internal volume of an enclosure is greater than approximately 5000m³, and become progressively pronounced for larger sizes. The problems of large enclosures may be summarised as follows:

Difficulty of injecting sufficient tracer: If there is insufficient tracer, then concentrations may be too low to be measured. This is particularly troublesome with the pulse and decay methods, which require the measurement of concentration as it falls to low levels. For the pulse method, it may be very difficult to inject a sufficiently large quantity of tracer in a short time. The only solution is to use a combination of tracer gas and detection system that can operate at very low concentrations. The most commonly used tracers are sulphur hexafluoride and the perfreons [Roulet and Vandaele, 1992, Table 5.13]. Some tracers, for example the halons, have a very high ozone depletion potential, and the quantity required for successful measurements in a large enclosure may pose an unacceptable risk to the atmosphere.

Difficulty in distributing the tracer: The seriousness of this problem depends on the method and the parameter being measured. It is not a problem for pulse, step-up and decay methods, provided that the tracer can be injected into the supply duct. Consequently it should always be possible to measure air change rate and local mean age if the supply duct is accessible. Also, the decay method will still give a reasonable measure of the nominal time constant when the initial and subsequent distribution is non-uniform. However, when measuring contaminant removal effectiveness parameters, it is necessary to imitate contaminant release in the space, and it is often difficult to achieve a realistic distribution in the zone of release. The constant emission technique assumes a uniformly distributed release of tracer throughout the whole space, and this may be difficult to achieve in large volumes.

Time span of the measurements: There are three considerations. The first concerns the time available for measurements; this may be limited by the owner/occupier or by the resources of the investigator. The second concerns the time scale of changes in the ventilation, caused by either the weather conditions or the occupancy and usage of the space. Measurements to assess the ventilation performance during normal operating conditions are particularly difficult for highly intermittent operation with high occupancy levels, such as in sports halls and auditoria. The third concerns the time constant of the air movement processes, which may be long compared with smaller spaces. Transient methods are preferable if the measurement time is restricted, but even so, such measurements become unreliable if the time available is

significantly less than twice the time-constant of the air movement. The homogeneous emission method is ideal for long time scales, but is not likely to be satisfactory where there is short term intermittent operation.

Number and positioning of injection and sampling points: Some sampling positions are determined by the requirement to obtain ventilation parameters at specific locations (e.g. close to occupants). Others need to be chosen to give a satisfactory image of the variation of ventilation parameters throughout the enclosure. The positioning of sampling points can be assisted by the use of prior knowledge, either from velocity measurements or from modelling studies, as described by Brouns and Waters [1994]. Access to some parts of a large enclosure may be particularly difficult.

Identification of ventilation and air distribution paths: The method of ventilation and air distribution is often very complex. Although the majority of large enclosures are ventilated either partly or wholly by mechanical means, there is often a high proportion of uncontrolled air movement through doors, roof vents and other leakage paths. Also, there may be several local systems within one enclosure. This makes it difficult to identify inlet and extract paths for the ventilating air, which in turn limits the choice of tracer gas technique and the parameters which can be measured. Furthermore, modern control systems often adjust supply and recirculation rates in response to several parameters, including air quality and energy consumption rate, creating continuously variable ventilation regimes.

Temperatures gradients: In many large spaces there can be significant spatial temperature variations. This may affect the analysis. Roulet and Compagnon [1989] have published equations that do not require the assumption of isothermal conditions. However, the errors due to this assumption must be viewed in the light of the many other errors and uncertainties in large enclosures, so it may be reasonable to ignore the effect of temperature on tracer measurements, except where temperature gradients are particularly severe.

There are five main types of tracer gas measurement methods: decay, step-up, pulse, constant emission, and constant concentration. The methods are not wholly independent; for example, the step-up and constant concentration methods can both be followed by a decay test. Nevertheless they are described separately here.

The tracer decay method

Measurement of the nominal time constant: Tracer gas is injected into the enclosure and artificially mixed to a uniform concentration. The mixing fans are left on, and the tracer gas concentration is allowed to decay. The resulting decay is continuously monitored at a convenient point. The decay is exponential, with a time constant equal to the required nominal time constant of the enclosure. However, it is not normally possible to achieve an initial uniform concentration, nor to leave the mixing fans on throughout the decay process. In such a case, the law governing the tracer decay will consist of the summation of a series of exponential terms. As time progresses, one of these terms will become dominant, with a time constant corresponding to the dominant eigenvalue of a multizone model of the enclosure. This dominant time constant can always be found, regardless of the initial uniformity of tracer concentration or lack of mixing, provided the decay continues long enough for the effect of the other exponentials to die out. Unfortunately, this time constant is not necessarily the same as the nominal time constant. On the other hand, if either the air entering the space or the air

leaving the space is well distributed, then it may be shown from multizone theory that this time constant is very close to the nominal time constant. If however the ventilation inlets and extracts are not uniformly distributed, such as in displacement systems, the difference between the two time constants may be significant. Nevertheless, the dominant time constant usually gives a good estimate of the nominal time constant, regardless of the distribution of tracer throughout the space, provided that (1) the decay has continued long enough for the transient exponentials to die out, and that (2) gross spatial variations in the tracer concentration are countered by measuring at several points, and taking the average concentration.

Measurement of local mean age of air, and local air change index: The derivation of these parameters from a tracer decay experiment depends heavily on achieving an initial uniform concentration throughout the whole of the enclosure. Because this is difficult to achieve, the tracer decay method is not recommended.

Measurement of local air quality index: The decay is preceded by a step-up process (see next section, page 176), in which tracer gas is injected at the position or positions at which a contaminant would be released. Artificial mixing must not be used, and the injection continues until an equilibrium but non-uniform distribution is achieved. When equilibrium is reached, injection stops, the decay in concentration is monitored, and the decay curves used to obtain the local mean ages of contaminant, $\bar{\tau}_p^c$, and the local air quality index, ϵ_p^c , from:

$$\bar{\tau}_p^c = \int_0^{\infty} \frac{C_p(t)}{C_p(0)} dt \quad ; \quad \epsilon_p^c = \frac{\tau_n}{\bar{\tau}_p^c} \quad (3.3.14)$$

Note that it is often difficult to continue the initial injection long enough to approach the necessary equilibrium concentrations before commencing the decay.

Total dosage index and transfer index: These cannot be derived from the decay curves.

Tracer step-up method

Measurement of nominal time constant, local mean age of air, and local air change index: Tracer gas is injected into the supply air duct at a constant rate. It is assumed that the tracer and the air are fully mixed in the supply duct to produce a steady concentration, C_s , at the inlet. If C_s cannot be measured, the equilibrium concentration within the enclosure may be used instead. As high order transients die out, the concentration at all points tends towards a simple exponential of the form:

$$C_p(t) = C_p(\infty) (1 - e^{-t/t_c}) \quad (3.3.15)$$

Ignoring the first part of the measured data, the rest may be fitted to this equation to give an estimate of both $C_p(\infty)$ and the dominant time constant, t_c , which is needed for the end correction terms. All measurement points, including the exhaust, should give $C_p(\infty) = C_s$ and the same value of t_c . The nominal time constant may be taken as t_c , or it may be measured by a subsequent decay experiment. The local mean ages of air and the local air change indices are then found from:

$$\bar{\tau}_p = \int_0^{\infty} \left(1 - \frac{C_p(t)}{C_s} \right) dt \quad ; \quad \epsilon = \frac{\tau_n}{\bar{\tau}_p} \quad (3.3.16)$$

Measurement of local air quality index, dosage index, and transfer index: Tracer is injected at a steady, continuous rate at a point in the space. The equilibrium values for the concentration at each monitoring point must be estimated from the measurements. We may use the simple exponential equation to estimate $C_p(\infty)$ and the time constant, t_c . All monitoring points, including the exhaust, should give the same value of t_c (which is needed for end corrections), but *different* values of $C_p(\infty)$. The nominal time constant may be taken as t_c , or it may be measured by a subsequent decay experiment. The local mean ages of contaminant is given by:

$$\bar{\tau}_p^c = \int_0^{\infty} \left(1 - \frac{C_p(t)}{C_p(\infty)} \right) dt \quad (3.3.17)$$

The local air quality index may be obtained from the ratio of the steady-state concentrations, or from the ratio of time constants:

$$\epsilon_p^c = \frac{C_e(\infty)}{C_p(\infty)} \quad ; \quad \epsilon_p^c = \frac{\tau_n}{\bar{\tau}_p^c} \quad (3.3.18)$$

If it is not possible to monitor the exhaust concentration, then $C_e(\infty)$ may be estimated from the tracer injection rate and the air flow rate, and the latter may be estimated from the nominal time constant. The total dosage index at a point p due to tracer released at point n (which is equal to the transfer index from n to p) may be found directly from the measured equilibrium concentrations and the tracer injection rate, q_n :

$$D_p = T_{pn} = \frac{C_p(\infty)}{q_n} \quad (3.3.19)$$

Tracer pulse method

A measured pulse of tracer is injected suddenly into the supply duct, or into a selected zone of the space. In a large enclosure, it is unlikely that the pulse will contain sufficient tracer to produce measurable concentrations over the necessary measurement period.

Measurement of nominal time constant: Under conditions of complete uniform mixing, this is identical to the decay method, and the nominal time constant can be determined from the resulting tracer concentration decay curves. If uniform mixing is not fully attained, then, just as for the decay method, an estimate of the nominal time constant can be obtained by measuring the dominant time constant from the steady-state part of the decay curve.

Measurement of local mean age of air, and local air change index: Assuming it was possible to inject into the inlet duct, and that an estimate of τ_n is available, the equations for local mean age and local air change index are:

$$\bar{\tau}_p = \frac{\int_0^{\infty} t C_p(t) dt}{\int_0^{\infty} C_p(t) dt} ; \quad \epsilon_p = \frac{\tau_n}{\bar{\tau}_p} \quad (3.3.20)$$

Measurement of local air quality index, dosage index, and transfer index: This requires a short pulse of tracer gas to be injected at a point in the enclosure. The local mean ages of contaminant at the sampling positions may then be found from:

$$\bar{\tau}_p^c = \frac{\int_0^{\infty} t C_p(t) dt}{\int_0^{\infty} C_p(t) dt} ; \quad \epsilon_p^c = \frac{\tau_n}{\bar{\tau}_p^c} \quad (3.3.21)$$

The total dosage index and the transfer index are given by:

$$D_p = \int_0^{\infty} C_p(t) dt ; \quad T_{pn} = \frac{D_p}{V_{cn}} \quad (3.3.22)$$

The local air quality index, in the case of a pulse test, may also be found from:

$$\epsilon_p^c = \frac{V_{cn}}{Q \cdot D_p} \quad (3.3.23)$$

where V_{cn} is the volume equivalent of contaminant released by the pulse at point n , and the Q is the total fresh air flow rate, which may be found from τ_n , which in turn may be found from the final part of the decay of the pulse test.

End corrections: The integrals in the above formulae are evaluated in two parts. The first is found directly from the measured concentration readings by integrating up to, and including, the final reading. The second, unmeasured part, is treated as an *end correction* and is evaluated on the assumption that the remaining concentration decay, after the final reading, follows a single exponential decay constant, t_c . If the end correction is a large fraction (i.e. more than 30%) of the first, measured part of the integral, then the results are unreliable. It is therefore essential to measure sufficiently far into the time evolution of the tracer concentrations. Although there is no definitive criterion, satisfactory results are achieved when monitoring lasts for about two time constants. Circumstances often force the experimenter to make do with a shorter time series, but provided that the end corrections are small, these may still produce acceptable results. This is also true when estimating the supply concentration, C_s , or the equilibrium concentration, $C_p(\infty)$ in a step-up test.

Constant injection method

The constant injection method is essentially the same as the step-up method, with the difference that measurements are taken only when tracer concentrations have reached their

equilibrium values. A variant of this method that is of particular interest is the Homogeneous Emission Technique due to Stymne, Sandberg and Holmgren [1992]. In this method, tracer is emitted uniformly throughout the space, or at least in each zone or well mixed region, and allowed to come to a steady concentration. This is believed to require a time lapse of about 4 time constants. The local mean age of the ventilating air at any point is then given by:

$$\bar{\tau}_p = \frac{C_p(\infty)}{w} \quad (3.3.24)$$

where w is the tracer source strength per unit volume.

If the zones or regions are of different volume, and the tracer emission rate in each zone is proportional to the zone's volume, then the local mean age is given by:

$$\bar{\tau}_p = k C_p(\infty) \quad (3.3.25)$$

where k is a constant.

This method is particularly attractive for tests over a long period of time. If the exhaust concentration is also monitored, the method should also give the local air quality index for a uniformly distributed contaminant.

Constant concentration method

The constant concentration method maintains a constant concentration within each zone of the building by continuously adjusting the tracer injection rate. If conditions are stable with respect to time, this is similar to the constant injection method, but reveals the fresh air supply rate to each zone rather than the local mean age of air. It is most suitable for buildings with rooms of small volume, though it has been used in small factory units. It is unlikely to be useful in large enclosures.

3.3.5 Visualisation of Air Movement

Quantitative flow visualisation

Methods applicable to airflow in large enclosures are briefly described below.

Required materials:

- Lighting system: standard or laser
- A tracer to diffuse the light from the lighting system: metaldehyde flakes, helium-filled soap bubbles or balloons
- Recording system: photographic or video camera

Three-dimensional approaches are:

- Stereophotogrammetry using two or more cameras [Scholzen *et al.*, 1994]
- Illumination with parallel different-coloured light sheets

Velocity can be measured using various techniques:

- Tracking of particles or balloons in time [*Alexander et al., 1994; Maas et al., 1993*] (Lagrangian approach)
- Streak photography (Eulerian approach)
- Correlation techniques on one double exposed frame or two consecutive frames. (standard PIV techniques, commercially available for 2D)

These techniques should be adapted to the size of the enclosure. Small particles or bubbles provide dense velocity information, but only for a small field of about $2 \times 2 \times 0.1$ m. Balloons allow one to cover large rooms, but provide only a few tracks.

2D PIV measurement equipment is available commercially. These systems are only suitable for small areas. 1995 prices vary from \$22 000 to several \$100 000. It is impossible to use these commercial systems, without major modifications, in large enclosures particularly with low air velocities, because the lighting, particle seeding and recording systems have to be adapted to the larger dimensions (see also section 3.3.2).

Automatic velocity field processing is possible with digital imaging techniques. On-line measurements are possible only in special cases (commercial 2D PIV). Generally the analysis requires at least some minutes, or much more when handling photographic film or video tapes.

Visualisation in scale models

Scale models are often used for the visualisation of air flow patterns in large enclosures. In principle, scale models should be built and used in such a way that the most important nondimensional numbers (Reynolds, Froude, etc) are conserved. In practice however, it is not always possible to conserve all nondimensional numbers, especially for nonisothermal conditions with heat transfer. It is then up to the expert to use good engineering judgement!

Scale models in water are often used. Density gradients may be obtained either by heating or by adding a saline solution (brine). Temperature fields can be visualised by adding tiny spheres containing cholesteric liquid crystals to the water. Density fields are made visible by adding a colour together with the saline solution. These methods are useful for studying flow patterns, but cannot correctly model surface heat exchange. Moreover, water models are generally less turbulent than the real airflow they simulate.

The ammonia absorption method [*Krückels, 1969*] is a measuring technique in which mass transfer results in a chemical reaction that causes a colour change on the enclosure surfaces. This technique is used to research problems of heat and mass transfer in air under the conditions of forced convection. The technique involves covering the walls with sheets with a thin wet layer (filter paper or gel) containing an aqueous solution of $MnCl_2$ and H_2O_2 . The reacting gas NH_3 , is added to the main air stream in a short pulse and at a low concentration. The air stream and the ammonia must be mixed well. Ammonia is absorbed by the wet layer according to the local partial concentration differences and a reaction takes place in which MnO_2 is one product. While the original coating is bright, MnO_2 is dark, so the observed colour intensity is a measure of the local mass transfer rate. As a result of the reaction in the moistened layer, the ammonia concentration on the enclosure surfaces is zero ($\rho_{NH_3}=0$ kg/m³). This means that the analogous temperature field has a constant surface temperature ($T_{wall} = \text{constant}$). A photometric method is used to find the local distribution of heat and mass transfer coefficients. There are two types of photometric evaluation: the transmission method or the reflectance method. It is necessary to perform a calibration to get a correlation between the colour (transmutation coefficient) and the mass transfer. Circular disks (diameter

$d=30\text{mm}$) are the best way to perform such a calibration [Krüger, 1984]. The Sherwood number, Sh , for the stagnation point of a circular disk is calculated by

$$Sh_{d,S} = 0,756 Re_d^{0,508} Sc^{0,36} \quad (3.3.26)$$

Using Equation (3.3.26) it is possible to get the mass distribution of NH_3 by

$$b_{NH_3} = \frac{Sh_d \cdot D_{NH_3-Air} \cdot \rho_{NH_3-Air} \cdot V_{NH_3}}{d \cdot \dot{V}_{Air}} \quad (3.3.27)$$

where V is volume and \dot{V} is volume flow rate.

The mass distribution correlates directly to the colour distribution. Thus the calibration equation is determined by a linear regression of the mass distribution and the transmissivity τ of the form

$$b_{NH_3} = c_1 + c_2 \ln(\tau) \quad (3.3.28)$$

After the calibration, we can calculate the mass and the heat transfer coefficient on the measuring sheets. The starting point is the integration of the equation for the mass transfer by a short NH_3 pulse over a measuring time Δt

$$\int_{t_0}^{t_0+\Delta t} \dot{m}_{NH_3} dt = \int_{t_0}^{t_0+\Delta t} \beta_{NH_3} (\rho_{NH_3,\infty} - \rho_{NH_3,wall}) dt \quad (3.3.29)$$

The NH_3 concentration on the wall $\rho_{NH_3,wall}$ is zero. Finally, we can find the equation for the mass transfer coefficient by:

$$\beta_{NH_3} = \frac{b_{NH_3} \cdot \dot{V}_{Air}}{\rho_{NH_3} \cdot V_{NH_3}} \quad (3.3.30)$$

Using the analogy between heat and mass transfer, the heat transfer coefficient can be calculated by:

$$\alpha = \frac{b_{NH_3} \cdot \dot{V}_{Air} \cdot \lambda}{\rho_{NH_3} \cdot V_{NH_3} \cdot D_{NH_3-Air}} \left(\frac{Pr}{Sc} \right)^n \quad (3.3.31)$$

Consequently we can calculate the heat and mass transfer coefficients by using the calibration and measuring values.

The evaluation of the colour distribution of the measuring foils is done by a special system of digital picture processing. For this method, the coloured measuring sheets have to be mounted together with the calibration disks in a bank of light. The different transmission, caused by the colour distribution, is registered by a CCD-camera.

The intensity of light, measured as grey values GRV, under the bank of light is not uniform, so it is necessary to correct the recorded images. The images can be corrected by a calibration picture [Rüdiger and Vogel, 1993], according to Haberäcker [1991]:

$$\text{GRV}(x, y) = \text{GRV}_0(x, y) \cdot K(x, y) \quad (3.3.32)$$

with

$$K(x, y) = \frac{\text{GRV}_{\text{Max}}}{\text{GRV}(x, y)} \Bigg|_{\text{image for the correction}} \quad (3.3.33)$$

Figure 3.3.6 is an example of a measured distribution of heat transfer coefficient. The heat transfer coefficients are related to the temperature difference between the temperature of the intake air and the wall temperature.

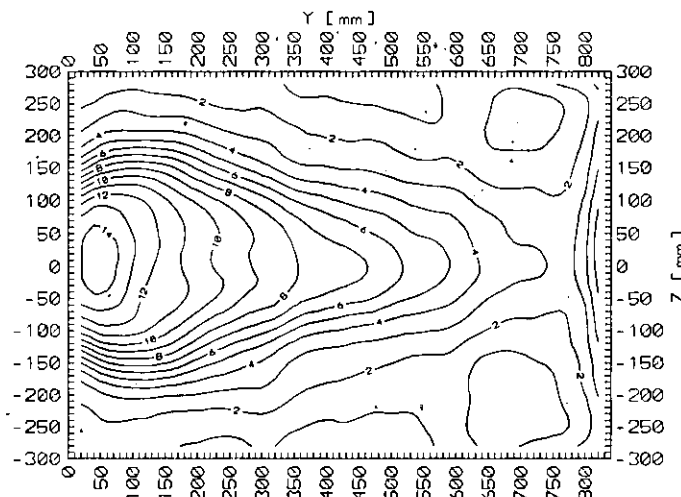


Figure 3.3.6 Distribution of heat transfer coefficient [W/m²K] for forced convection at the ceiling of the model at an air change rate of 75 h⁻¹. [Müller and Vogel, 1994].

3.3.6 Temperature

Temperature measurement in rooms can be divided into two fields of application. On the one hand is the acquisition of the wall temperature distribution and on the other hand is the measurement of the three-dimensional air temperature field. A variety of different methods may be used for these two purposes. But the application of the temperature measuring techniques in large enclosures is connected with particular characteristics. In general, varying outdoor conditions prevent the occurrence of steady-state conditions. That is why the temperature field should not only be recorded with a high spatial resolution but also in a short measuring time. Furthermore, a number of methods are unsuitable for the application in large enclosures, because they entail extensive technical effort and high investments.

For this reason, only the application of thermography for the wall temperature measurement and thermocouples for air temperature measurement, are touched on here. Both conventional methods are implemented by modern system components and data post-processing [Müller and Vogel, 1994].

Thermography

Thermography utilises the emitted radiation in the infrared spectrum of a body to determine its temperature without contact. The emitted radiant density L_b of a black body is given by:

$$L_b = \frac{\sigma}{\Omega_o \pi} T^4 \quad (3.3.34)$$

The emissivity ε is the ratio between the radiant density of an arbitrary body L and a black body L_b :

$$\varepsilon = \frac{L}{L_b} \quad (3.3.35)$$

The radiation detector receives, besides the radiation from the measuring object, radiation from the environment:

$$L_r = \varepsilon L_{b,o} + (1 - \varepsilon) L_e \quad (3.3.36)$$

Because the environmental temperature in rooms is in the same range as the wall temperature, not only the emissivity but also the environmental temperature substantially affects the conversion of radiant density into temperatures [Glückert, 1992].

In contrast to pyrometry, which measures an average radiant density, thermography records a radiant density distribution. Moreover, thermography provides a two-dimensional temperature distribution at the walls.

The surface emissivity can be calculated from a local surface temperature measurement (e.g. with a thermocouple) and the received radiant density from the thermocamera. Another approach is to partially coat the measuring surface with varnish with known emissivity and to compare the radiation from the original with the coated surface.

Generally, one local determined emissivity is applied to the whole infrared picture. Errors occur if this local emissivity varies over the measuring object. In most cases there is also no co-ordinate transformation which maps picture points onto object points.

These two limitations are solved by carrying out image post-processing*. Since the thermography system is used for temperature measurement in rooms with plane rectangular walls, the co-ordinate transformation can be reduced to a simple picture rectification. Objects recorded by the camera are distorted according to a central projection. Figure 3.3.7 shows a geometric method to relate a picture point P to a point in the wall plane by repeated bisection.

* The presented algorithm is implemented in a self-made image post-processing software

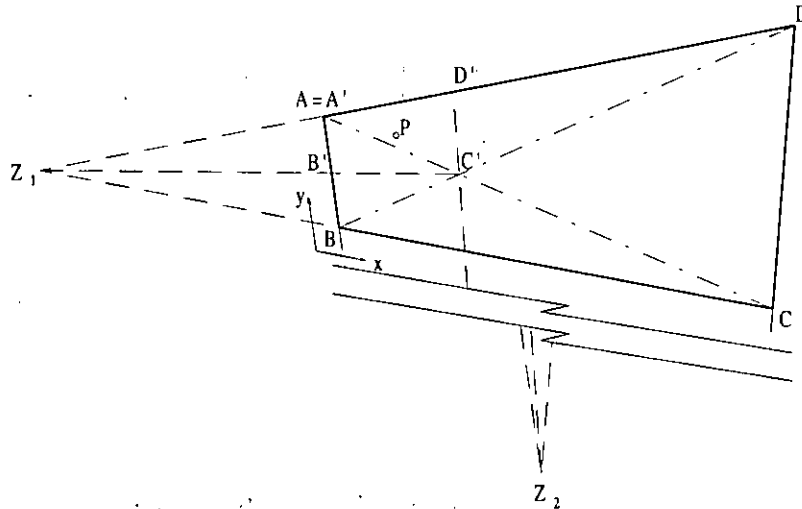


Figure 3.3.7 Rectification of a plane rectangular wall using a simple geometric bisection method.

For the rectangle $ABCD$ in the wall plane, the wall and the picture co-ordinates are known. The intersection of the two diagonals defines an additional point. The two connecting lines between this point and the projection centres Z_1 and Z_2 split the region into four subregions. The algorithm determines then which subregion ($A'B'C'D'$) contains the considered point P . Afterwards, the process of bisection is restarted and continued until the subregion reaches the picture resolution. Because a lot of picture points have to be mapped, sophisticated programming reduces the computing costs per pixel.

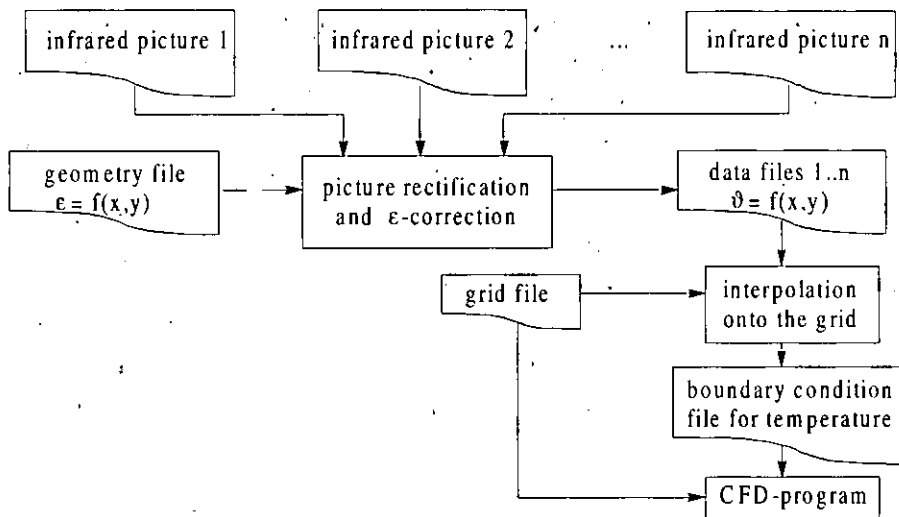


Figure 3.3.8 Structure of the infrared picture processing.

The advantages of this method are that neither the camera position nor the camera orientation are needed. Only four picture points forming a rectangle in the wall plane have to be identified by their wall co-ordinates.

If required, local emissivities for different regions (e.g. windows) can be read in from an external geometry file. These emissivities can be obtained by the methods mentioned above. Finally, the corrected temperatures are available in dependence on the wall co-ordinates.

The temperature data can also be used as boundary conditions for numerical computations. An interpolation onto the underlying grid seems to be sufficient (see Figure 3.3.8).

Figure 3.3.9 shows the original infrared picture of an inside wall of a gymnasium (case 'Turnhalle München') [Richter et al., 1994]. Picture rectification and emissivity correction described above lead to Figure 3.3.10.



Figure 3.3.9 Original infrared picture with corner points A, B, C and D for rectification.

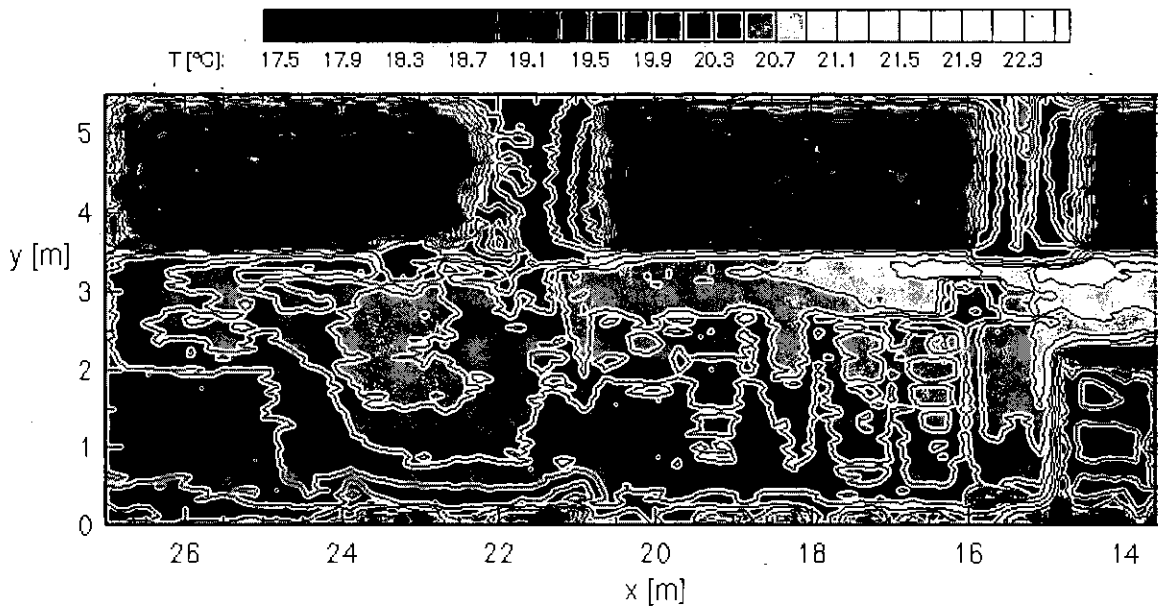


Figure 3.3.10 Resulting picture with isolines after rectification and ϵ -correction from Figure 3.3.9.

The applied camera is equipped with only one infrared sensitive element and generates its pictures using a two-dimensional reflector scanner with a resolution of 300x200. This results in lower costs than in alternative systems [Stahl and Miosga, 1986]. The lower picture repetition frequency of approximately 2 Hz seems to be sufficient for this application and should not be viewed as a disadvantage.

Thermocouples

Methods for direct measurement of a two-dimensional air temperature distribution (e.g. holographic interferometry [Hauf *et al.*, 1991]) involve high technical effort and high cost. They are therefore unsuitable for the practical investigation of large enclosures. Because of this, the temperature field is constructed from a number of single measurement points.

Thermocouples utilise the Seebeck effect, in which a closed circuit made of two materials generates a thermoelectric voltage depending on the materials and the temperature difference at the junctions [Michalski *et al.*, 1991].

The application of multiplexers (MUX) with cold-junction compensation (CJC) allows the connection of a great number of thermocouples. Thus with CJC the reference junction is placed at the multiplexer connecting strip and its temperature θ_0 is measured by a resistance thermometer. The thermoelectric voltage is amplified and via an analogue-to-digital converter (ADC) read into a computer (Figure 3.3.11).

For higher accuracy, the multiplexer and amplifier must have the same temperature θ_0 , because they are made of different materials. Therefore, all these devices are held at the same temperature. The ADC is equipped with difference inputs causing noise reduction. Its 16 bit resolution in connection with a polynomial function for the conversion of thermoelectric voltages into temperatures gives an uncertainty in θ_0 of $\pm 0.1^\circ\text{C}$ for iron-constantan thermocouples. The advantage of the iron/constantan couple is its high thermal sensitivity.

To measure air temperature, the thermocouples are protected from radiation in polished metal tubes and mounted at desired distances on portable bars. In any case, the development of a reference temperature (e.g. for intake air) should be recorded during the whole measuring process to check the constant boundary conditions and to apply a suitable correction.

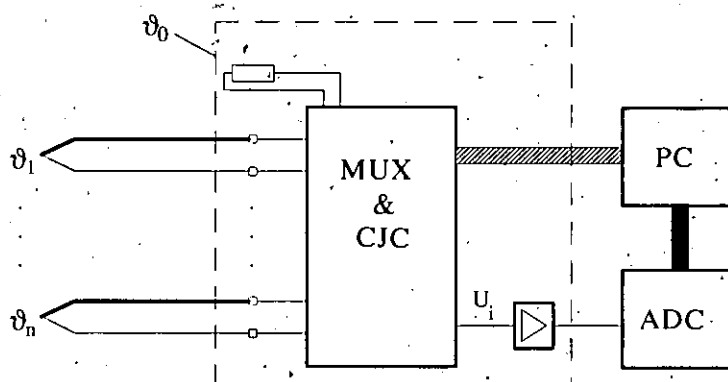


Figure 3.3.11 Measuring chain for temperature acquisition.

It is only after having followed this preliminary procedure that the instruments can be installed and measurements taken. This procedure looks tedious but it is necessary to ensure that the required results are accurate and are obtained at a modest cost.

3.4 Conclusions

Even though constant improvement is possible through further research and development, many worthy measurement methods are now available for commissioning, diagnosis, management and research of large enclosures. The most important point is to use these methods mindfully, for the purpose of answering a well defined question. Because of the dimensions of large enclosures, measurements still present several problems:

- The number of measurement points may be large
- The links between sensors and data loggers are long and may require either special techniques (IR or radio transmission, battery powered single channel data loggers, etc.) or a large amount of cables (e.g. 2 km of cables were used for 10 temperatures, 2 humidity and standard meteorology measurements in a 60 000 m³ hall)
- The accessibility of some measurement points may be problematic, due partly to height
- In general, measurements are expensive

Therefore, a careful planning of the experiments is essential. An appropriate procedure is [Roulet, 1992]:

1. Define the problem to be solved. If there is no problem, no measurement need be performed!
2. List the questions to be answered to solve the problem.
3. List the measurements required, if any, to answer these questions.
4. Define the method which will be used to interpret the measurements in order to get the required information with the required accuracy (and not better, accuracy is expensive!). Perform preliminary error analysis.
5. Define the conditions in which the measurements will be performed; in particular define the best location of measurement points.
6. Choose the appropriate instruments.

Item 4 is placed before item 5, and *not* after having performing the measurements!, because the chosen interpretation method may have an influence on the number and location of measurement points.

CHAPTER 4

- 4.1. Olympic Mountain Hall,
Gjøvik, Norway
- 4.2. Queens Building, Leicester,
United Kingdom
- 4.3. Experimental Atrium,
Kanagawa, Japan
- 4.4. Fibreglass Reinforced
Polyester Factory, Caen,
France
- 4.5. Turnhalle (Gymnasium),
München, Germany
- 4.6. Atrium Grafenau, Zug,
Switzerland
- 4.7. Polytechnic Auditorium, Turin,
Italy

4.1 Olympic Mountain Hall, Gjøvik, Norway

4.1.1 Description of Case Study

Site data

The Mountain Hall at Gjøvik, Norway, is an underground ice rink stadium that was constructed in time for the Winter Olympic Games in 1994. The site is approximately 226m above sea level, and is at latitude 61° north.

Layout

Figures 4.1.1 to 4.1.4 show the layout of the rock cavern and HVAC system. The main cavern, with a maximum span of 91m, is the world's largest spanning man-made cavern in public use.

Main steel ceiling

The stadium hall has a ceiling of corrugated galvanised steel that is fixed to the curved rock ceiling. The main function of the steel ceiling is to protect against water dripping from the rock ceiling onto the ice rink or the spectators. Much of the steel ceiling is hidden from view by a suspended reflective ceiling over the rink. About 60% of the surface area of the ceiling is covered by acoustic absorbing panels.

Suspended ceiling

A few metres below the main steel ceiling hangs a suspended horizontal steel structure that supports the air exhaust ducts, cable ladders and catwalks for maintenance of floodlights, etc. From the underside of this structure is slung aluminium-coated reflective sheets that reduce the radiative heat loss from the ice.

Floor

The hall's floor sits directly on rock. Aside from the ice-rink, the floor construction is a reinforced concrete slab on a layer of crushed stone and a diffusion barrier.

Ice rink

The ice rink floor is made of (from the surface and down):

- Reinforced concrete (15 cm thick) with embedded freezing coils
- Styrofoam insulation
- Double-layer diffusion barrier
- Levelling with on-site rock material (bottom layer)

Walls

End walls and walls at level $z = 9-11$ m are sprayed with shotcrete.

Main technical specifications

- Width / length / height of excavated cavern 61 × 91 × 25 m
- Volume of stadium hall 114 000 m³
- Gross floor area 14 910 m²
- Ice rink (gross area) 160 m²
- Seating for spectators 5200
- Max. number spectators + participants 5800

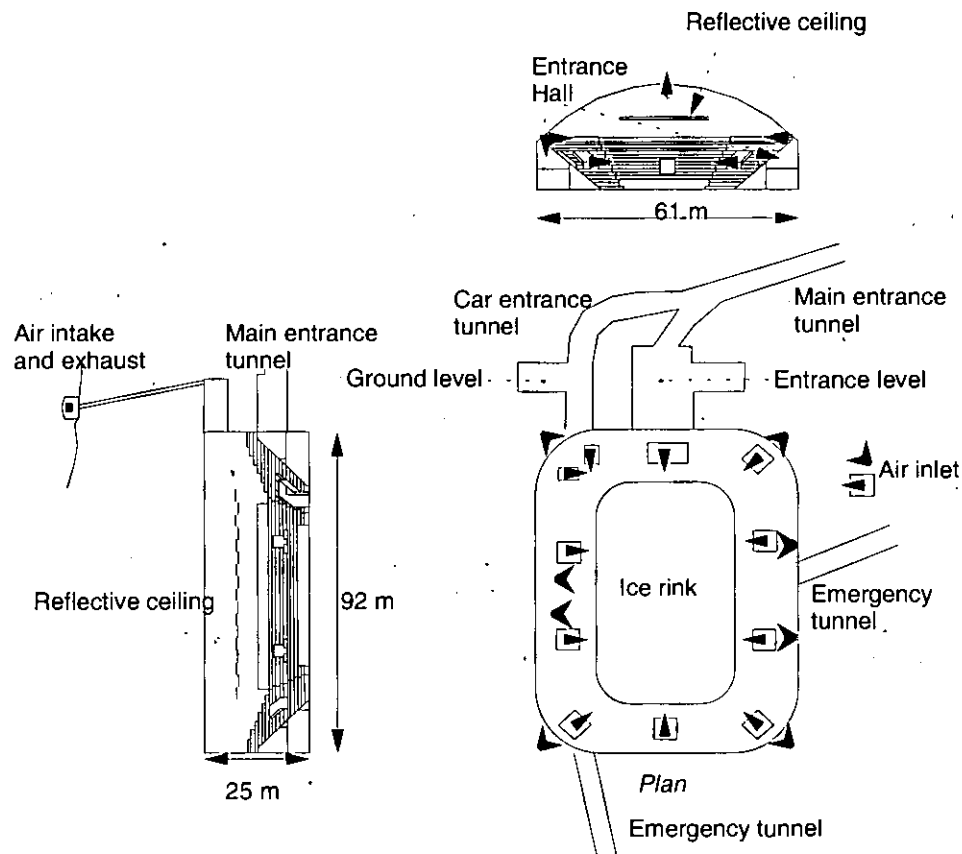


Figure 4.1.1 Layout of the mountain hall.

Principle of operation of the ventilation system

Figure 4.1.2 shows a layout of the ventilation system. The ventilation is balanced such that the inlet flow rate equals the extract air flow rate. The system is a VAV-system with an airflow rate ranging from 25 000 to 160 000 m³/h.

The capacity of the ventilation system has been designed based on 5200 spectators with an occupation time of 3 hours, plus sports participants and officials, and an illumination level at the ice surface of 1600 lux. The design temperature in the hall is 10°C to 16°C depending on the level of use.

The ventilation system has the following functions:

- Provide sufficient fresh air for good air quality in the main hall, offices, changing rooms, etc.
- Control the relative humidity in the main hall to prevent build-up of hoarfrost on the ice surface
- Control the temperature in the hall during all conditions of use
- Provide smoke-free escape routes in case of fire

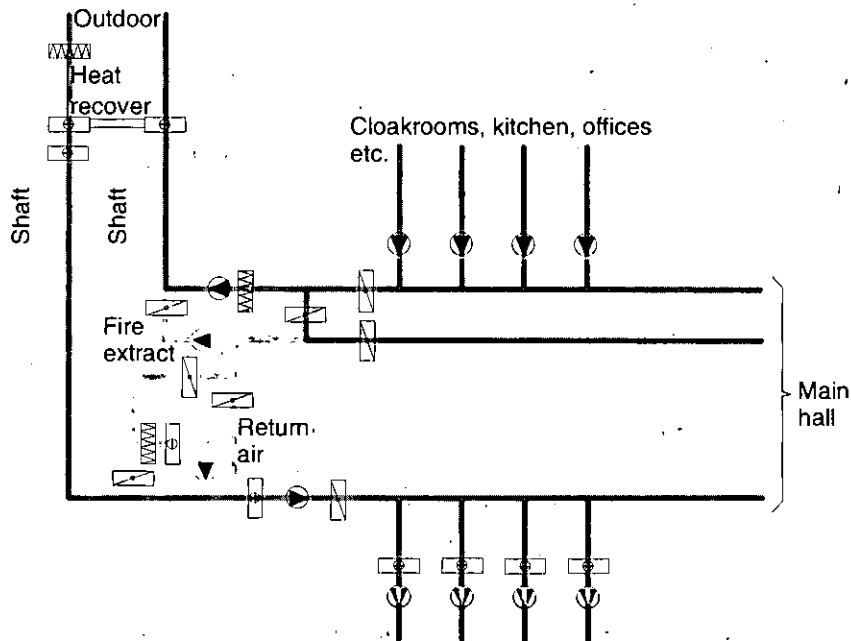


Figure 4.1.2 Simplified layout of the ventilation system.

The ventilation plant is divided in two main systems:

- Ventilation system for main hall (stadium)
- Ventilation system for offices, changing rooms, a restaurant etc., divided in four subsystems

The fresh air intake and air exhaust are located on the top of the mountain. Four shafts (two supply shafts, two extract shafts), each 1.80 m in diameter, are drilled 32 metres almost vertically down to the ventilation plant room located at ceiling level at the north end of the main hall.

In the plantroom at the top of the shafts (i.e. on the top of the mountain), the fresh air is preheated by a heat recovery coil and a directly oil-fired heat exchanger, before being supplied down the shafts to the main ventilation system.

The air is supplied to the public corridor that loops around the stadium under the stands (on the second floor), and from here it flows through the entrances into the hall. The extract air is exhausted through a duct system at ceiling level. In principle, it is a displacement ventilation system that supplies air at entrance level and at the top of the stands. The heat from the spectators and lighting results in buoyant upward airflow that removes heat and pollutants from the occupied space.

This ventilation strategy is therefore also used for smoke control during a fire, as it ensures that the lower part of the main hall and the escape routes (corridors) are smoke-free.

Ventilation system for offices, changing rooms, restaurant, etc.

This system is independent from the main hall system, and thus is of little relevance here. Offices, changing rooms, etc. all have a set temperature of 20-22°C.

4.1.2 Working Examples of Measurement and Analysis Tools

Measurements

Both long-term and short-term measurements in the Gjøvik Mountain Hall have been carried out, with the intention of using the results to verify design tools for air quality, safety and energy consumption. The short term results shown here are mainly from measurements taken during a set of ice-hockey matches in November 1993.

To determine the hall's energy consumption, continuous measurements have been taken of air flow rates and air temperatures.

Equipment

For the continuous long-term measurements, the BMS, of type Simatic S5-135U and a PC with IGSS OS32 software, were used. Temperature was measured with PT100 elements. Air flow rates in the main supply and exhaust ducts were found by measuring the dynamic pressure. The pressure difference between the inner and outer radius of bends gives the air flow rates in ducts to special areas (changing rooms, etc.) within the cavern. For this, a Huba differential pressure transmitter type 650 was used.

Measurement positions

Figures 4.1.3 and 4.1.4 show sections of the hall with the measurement positions marked. Positions A to G are columns placed in the tribunes. Position K is a column hanging down from a high-level catwalk, 16.4 metres above the ice surface.

Parameters

The following measurements were made:

Temperature

- A string of sensors, K, hung from the ceiling above the ice surface
- Short multi-sensor columns, A to G, standing in the tribunes
- Surface temperatures

Air velocity

- Columns C and D on the tribunes

Airflow pattern

- Tracer gas sample tubes on columns A to G and just inside the barrier surrounding the ice rink, as well as in supply and extract ducts
- CO₂ same positions as for tracer gas
- Smoke tests

Measurement results are shown in Figures 4.1.5 to 4.1.10. The location of measurement positions is shown in Figures 4.1.3 and 4.1.4. Figure 4.1.4 also shows the observed airflow pattern from smoke tests above the occupied area.

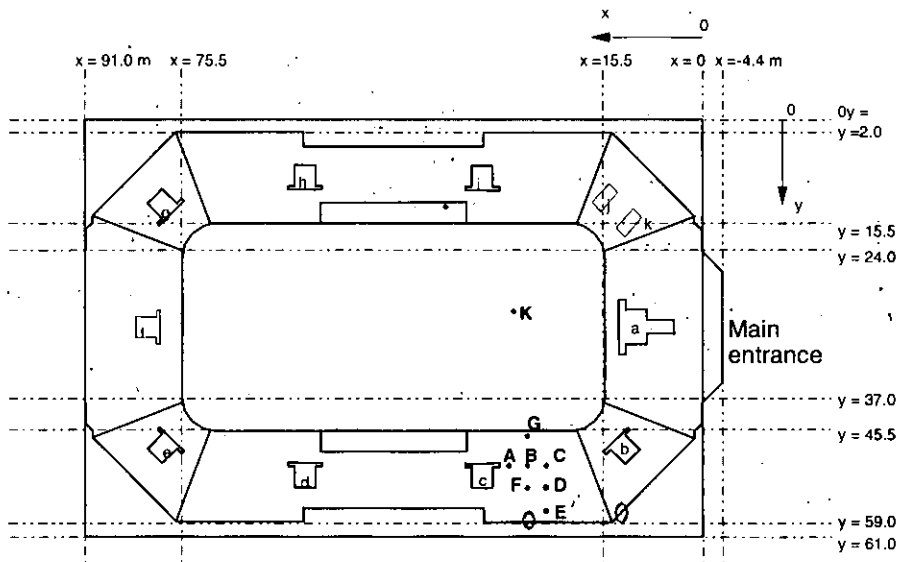


Figure 4.1.3 Plan view with measurement positions.

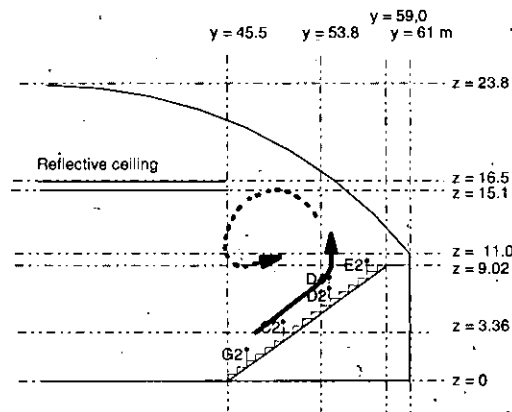


Figure 4.1.4. Section with measurement positions G, C, D and E shown together with the observed airflow pattern.

From Figure 4.1.5 it can be seen that the supply air temperature is higher than the extract air temperature when the cavern is unoccupied, due to some short-circuiting. During the match, the extract air temperature rises above the supply temperature, so the short-circuiting stops and the displacement system then works efficiently. The ventilation system was not run at full capacity during the tests, which can also be seen from Figure 4.1.5. This causes the CO₂ concentration to reach quite high levels that can be seen from Figure 4.1.6

Tracer gas measurements were also carried out during the matches; the results can be seen in Figures 4.1.8 and 4.1.9. The pulse-injection method was used, with SF₆ supplied in the ventilation duct. As can be seen from Figure 4.1.8, the measurement period was too short to reach steady-state concentration. However, some conclusions can still be drawn: The supply of air is best in the lower part of the tribunes, indicating that the system works as a displacement system. However, in the rink the air supply is poor due to the high transparent barrier surrounding the rink. From the air velocity measurements shown in Figure 4.1.10 it

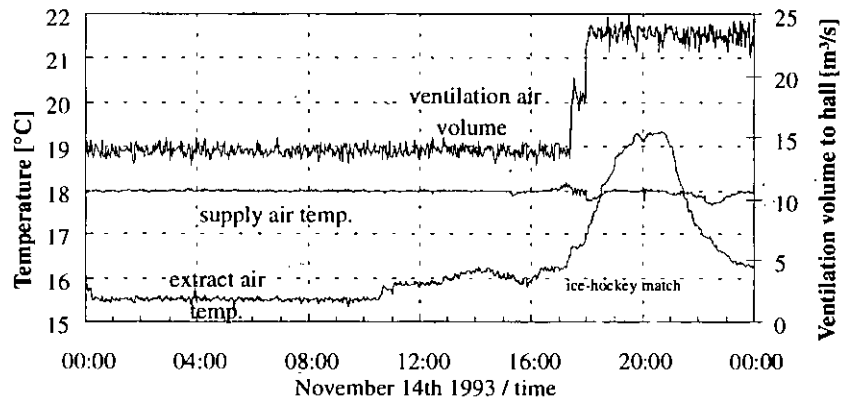


Figure 4.1.5 Temperatures of November 14.

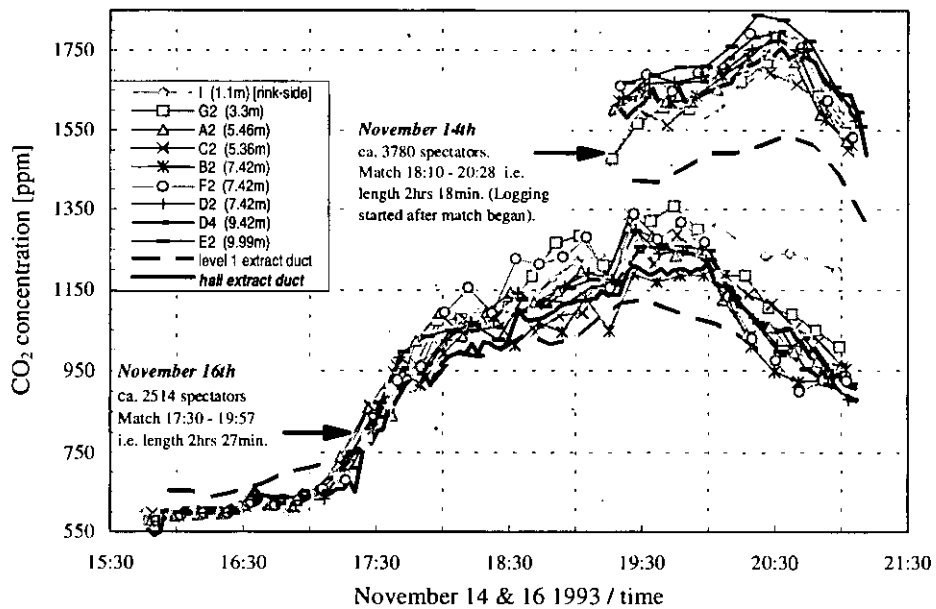


Figure 4.1.6 CO₂ concentration, 14 and 16 November, showing all measurement points during both matches.

can be seen that the velocities vary both with time and position, but most of the measurements are within the comfort range:

The temperature measurements in Figures 4.1.5, 4.1.7 and 4.1.12 show a temperature stratification when the arena is occupied.

The air velocities indicated in Figure 4.1.10 are within the comfort range.

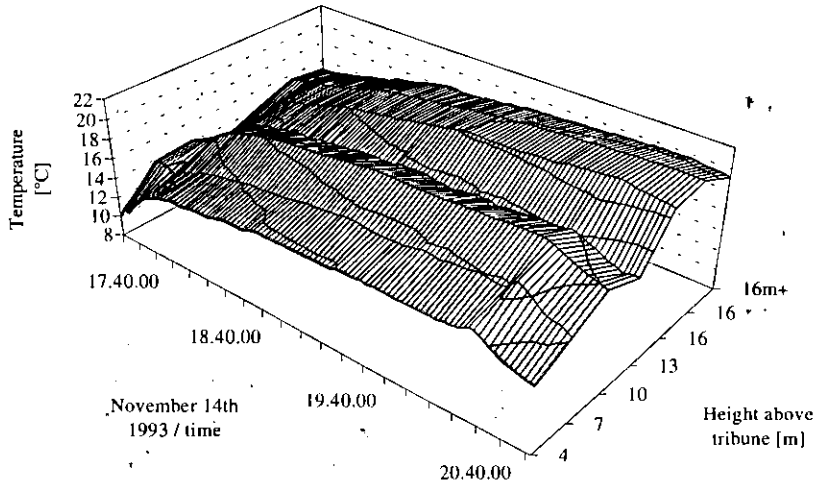


Figure 4.1.7 Temperatures, column K, see Figure 4.1.3.

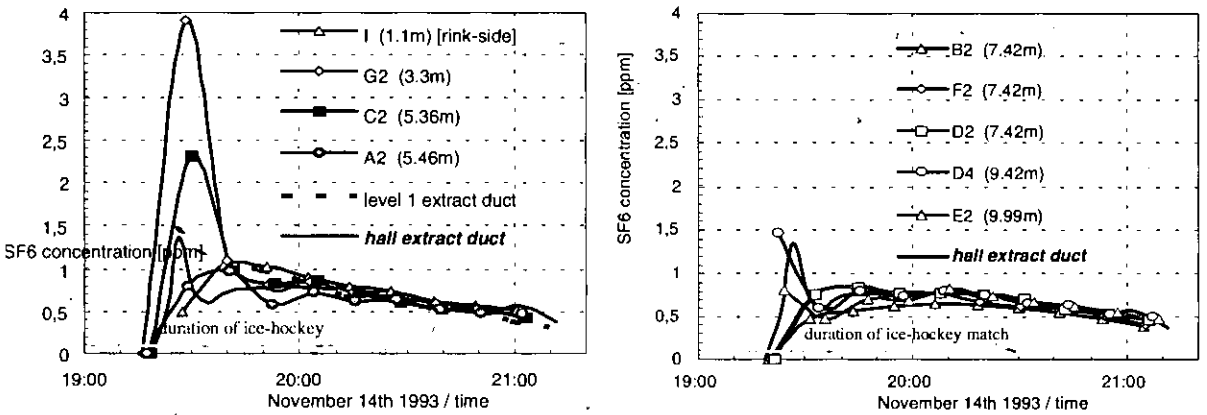


Figure 4.1.8 SF₆ concentration : (left) below 7m (right) above 7m.

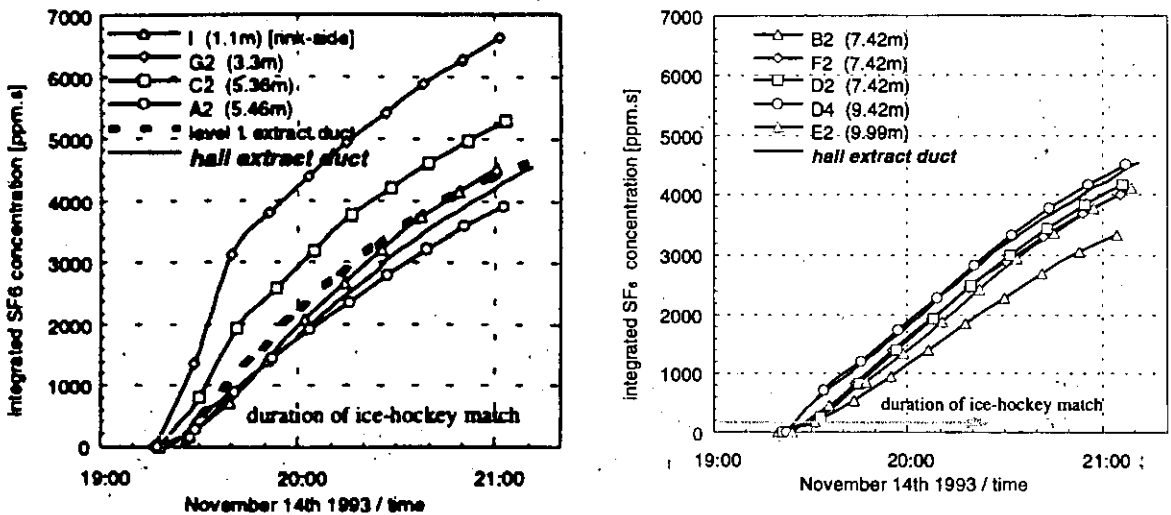


Figure 4.1.9 Time-integrated SF₆ concentration : (left) below 7m (right) above 7m.

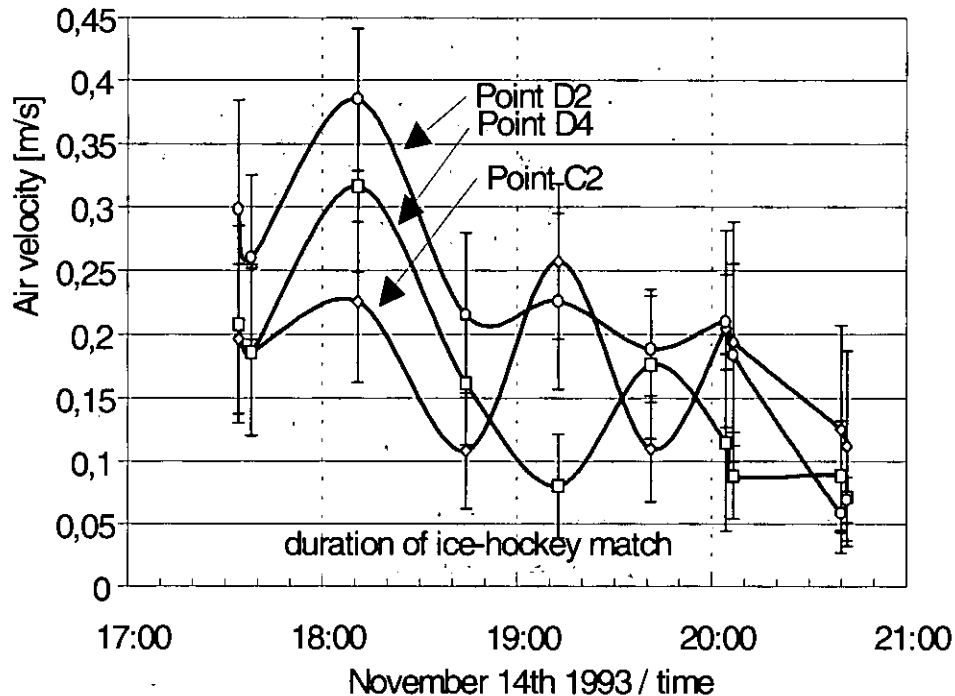


Figure 4.1.10 Measured air velocities, column D and C.

Analysis tools

CFD simulations were carried out using the program KAMELEON-II. This program uses the finite-volume method with a 3-D Cartesian coordinate grid. It includes the $k-\epsilon$ turbulence model and a radiation model (See description in subchapter 2.4).

Calculations of energy use for heating and ventilation have been carried out. This was done by using the building simulation program FRES, which is described in subchapter 2.3. Some results are shown in this document.

Since FRES is intended to be a simple-to-use tool for building design consultants, the standard version has certain limitations. Two of them are:

- A wall must consist of exactly two surface nodes and two internal nodes
- Climatic data is the only data that may be input from external files. Internal loads, for instance, may only be varied using time schedules

For the rock hall simulations, a special version of FRES was developed to overcome these limitations. The main difference between a building and a rock hall is the outer walls. This new version of FRES has four internal nodes to represent the wall, with the finest grid near the surface. The rock is modelled as a homogeneous solid material, about 20 metres thick, and the bedrock temperature is fixed to 8°C. Figure 4.1.14 shows the distance between the nodes. The wall is assumed flat, a consideration that must also be taken into account.

4.1.3 Performance of Tools and Comparison of Results

Figure 4.1.11 shows the CFD-predictions at a section through the cavern at $x=23,65\text{m}$. Figure 4.1.12 shows a comparison between measured and simulated temperatures at some points. The simulated temperatures are 1.5°C lower than the measurements. The simulated airflow pattern is quite similar to that which was observed in the measurements, though the calculated velocities are higher than the measured values. The measured velocities are about 0.2m/s with peaks of up to 0.3m/s , while the simulations show results around 0.35m/s in the upward direction. We can think of two possible reasons for this discrepancy: The computational cell size was very large, roughly one metre in each direction, with no refinement near surfaces. Also, the standard $k-\epsilon$ turbulence model does not treat the damping effect of thermal stratification.

The DTM (Discrete Transfer Model) radiation model was used in the CFD simulations. An error in this model affected the results from this simulation.

Using a radiation model like DTM adds a new level of complexity to the CFD code. There are several additional parameters to solve, which requires significant computing time. It may be difficult to find the correct balance between too few and too many radiation calculations. A CFD code with a radiation model therefore needs a more experienced user than the simpler simulation models.

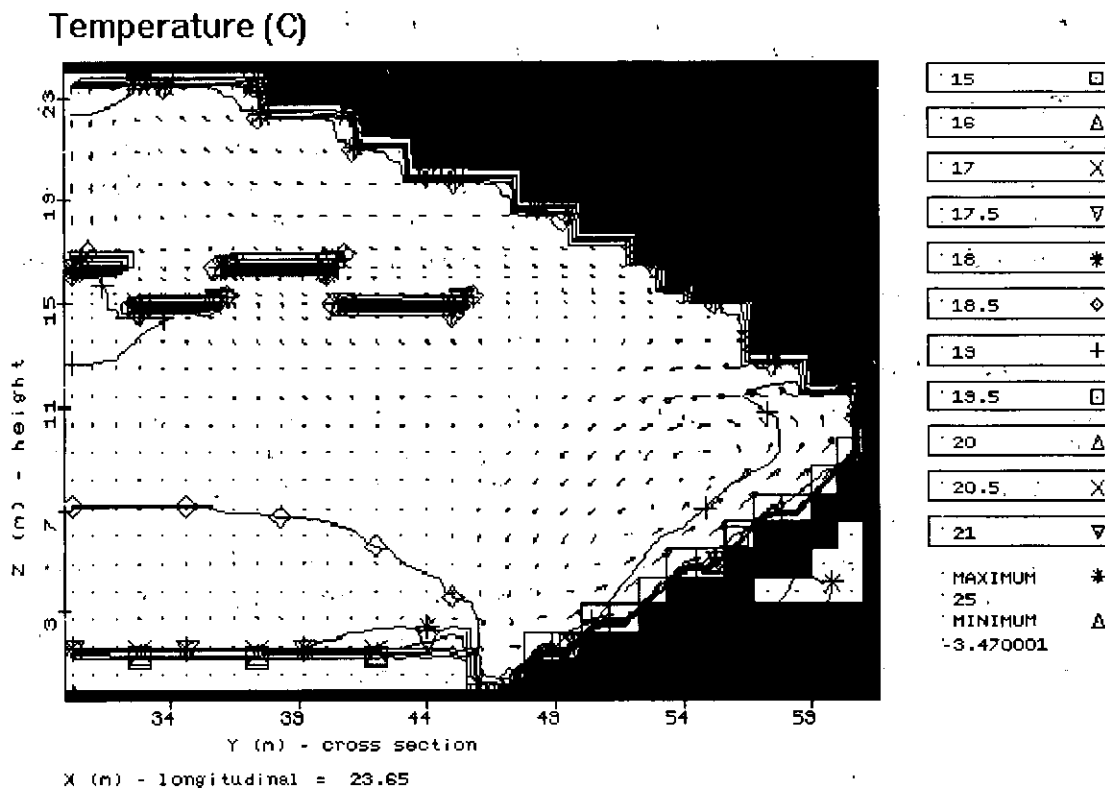


Figure 4.1.11 Simulation results from CFD-simulations at time 19:00 14 November 1993. $X=23,65\text{ m}$ (close to measurement positions shown in Figure 4.1.3).

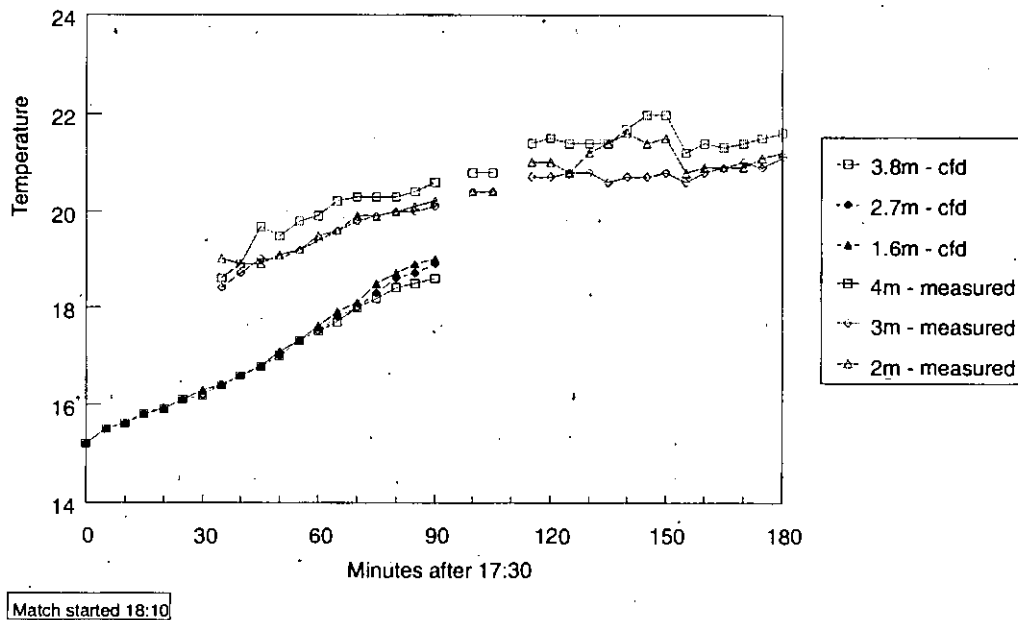


Figure 4.1.12 Comparison between temperature measurements and CFD simulations for 14 November 1993.

Two sets of simulations were done using FRES: The first set simulated a short period in November 1993 using measured temperatures and heat loads as input data. A data reader was added to FRES to achieve this. The second set used measured data from the whole of 1994, i.e. outdoor temperature, supply air temperature, airflow rates, ice temperatures and heat input from light (light is approximated from assumed activity level). Heat from spectators was omitted since it was not measured, and has little influence on the annual energy use.

First set of simulations

Figure 4.1.13 shows the predicted temperatures and input heat flows. The curves show that the extract temperature is quite similar, but generally too low. The largest discrepancies are seen during peak loads of spectators and lighting during ice-hockey matches. The way the hall was described obviously resulted in a too lightweight model.

Furthermore, since the stratification model in FRES was not used in these simulations, the temperature close to the ceiling was underestimated during peak loads. Another simplification was that a model for the reflective ceiling was not included, causing the simulated air temperature to be lower than the real temperature.

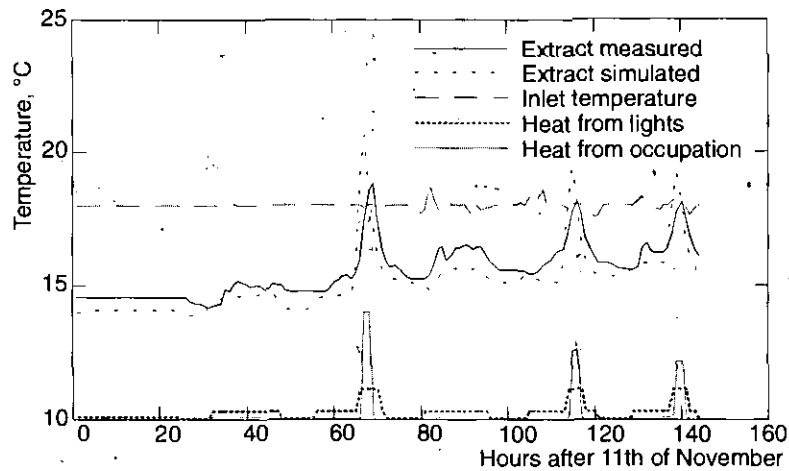


Figure 4.1.13 Simulation results from using FRES compared with measurements from November 1993. The rock was directly exposed to the room air.

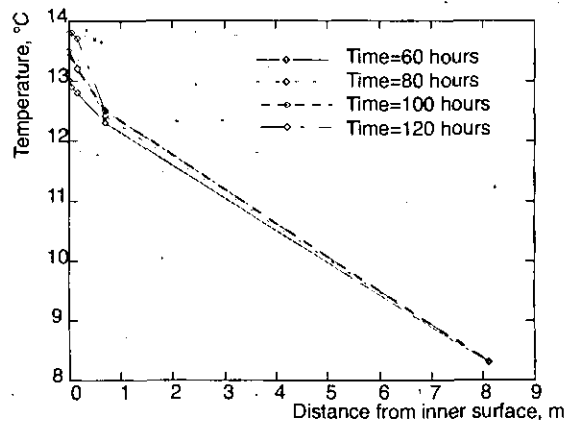


Figure 4.1.14 Temperature profile in rock simulated with FRES.

Figure 4.1.14 shows the simulated temperature profile in the rock wall. The simulated temperature agrees reasonably well with measurements. However, the accuracy could have been improved by using spherical coordinates.

Second set of simulations

Figure 4.1.15 compares the predicted air temperature in the rock cavern with an ordinary building of equivalent size, based on weather data from 1994. Both cases use the same measured supply air temperature and airflow rate, so the energy for heating the fresh air is obviously equal in the two cases. However, the extract air temperature is different because of different heat loss, as can be seen from the graphs. If the ordinary building had been heated to the same temperature as the rock cavern, then an extra theoretical heat source would be necessary, related to the difference between the two temperature levels. For the way the Gjøvik rock cavern was used in 1994, this difference represents an energy saving of approximately 110 MWh compared to an ordinary building.

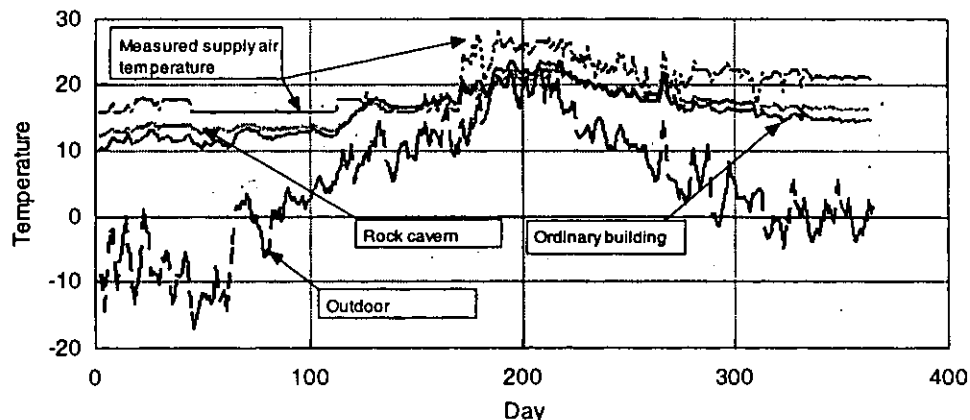


Figure 4.1.15 Comparison of simulated extract air temperatures in an ordinary building and the rock cavern. Measured values for supply airflow rate and supply temperature.

Table 4.1.1 compares the different ways of operating the rock cavern’s heating system. As can be seen, the temperature of the supply air greatly influences the energy use. Table 4.1.1 also shows that the energy use was much higher in 1994 than planned. This is probably due to extended periods with ice in the arena and a higher air temperature than envisioned.

Table 4.1.1 Comparison between different ways of heating. One year values.

Supply air temperature:	heated to 8°C	heated to 18°C	as measured	heated to 18°C
Activities:	as measured	as measured	as measured	No ice or other activities
Calculated heat loss to ice (convective and radiative) [10 ³ kWh]	790	1020	1070	0
Total calculated energy use [10 ³ kWh]	690	1770	2040	1070

Comparison between FRES and LESOcool

A comparison using simplified building simulation models was carried out with FRES and LESOcool [van der Maas and Kolsaker, 1996]. The models are described in section 2.3.2. Both models calculate the air outlet temperature, and both showed reasonable results, taking into account the uncertainties in the input parameters. The FRES model behaved slower than LESOcool and the measurements. However, this difference lies within the expected range of accuracy for simplified models, with temperatures deviating only about 1°C from measurements at the end of the ice-hockey match. The FRES model used in the LESOcool comparison was much simpler than the model used in the other simulations of the cavern (e.g. Figure 4.1.15), which exhibited a quicker response than the measurements.

4.1.4 Conclusion and Recommendations

When the hall is occupied, the ventilation works as a displacement system. However, when it is empty, the supply air short-circuits somewhat to the extract, causing the ventilation efficiency to drop and thus increasing energy consumption for ventilation and heating. A more efficient solution for when the arena is vacant, would be to separate the heating and ventilation

systems. Air jets could then be used to mix the air, or heat sources could be placed in the lower part of the arena.

The energy calculation program FRES seems to be reasonably accurate. The calculations showed that the increase in space temperature compared to the original design intention results in a considerable increase in energy consumption.

The experience gained from the CFD calculations was that care must be taken if reasonably accurate results are to be obtained for all parts of the space. A very fine computational grid is essential, together with accurate modelling of boundary conditions for heat and mass transfer.

4.2 Queens Building, Leicester, United Kingdom

4.2.1 Building Description

Building architecture and form

The Queens Building at De Montfort University, Leicester is a three storey building housing the Department of Mechanical and Manufacturing Engineering. It contains lecture theatres, classrooms, laboratories and offices. Almost all of the building is naturally ventilated; this is facilitated by the use of large chimneys or stacks which use the buoyancy of the indoor air to 'pull' fresh air through openings in the facades into the building. Warmer, stale air is then discharged via the chimney exits. Extensive use is made of daylighting using skylights.

The school contains two lecture theatres which have self-contained natural ventilation systems. In the theatre under investigation, outside air enters adjacent to a lightly used road into three plenums via modulated control dampers (see Figure 4.2.1). It disperses within voids underneath the seating and enters the room via vertical grilles positioned at ankle height. Air leaves the space via two large openings near the base of two stacks (the height of each stack above ground level is 18.5 m). Outlets are positioned at the top of each stack in the form of eight windows. Intake and outlet positions can be varied by the operation of motors controlled by the building management system (BMS). A 'punka' type of ceiling fan is installed in one of the stacks with the intent to stimulate ventilation in the event of flow stagnation. Heating in winter is provided by finned tubes (connected to a low pressure hot water circuit) placed within the seating void adjacent to the vertical grilles.

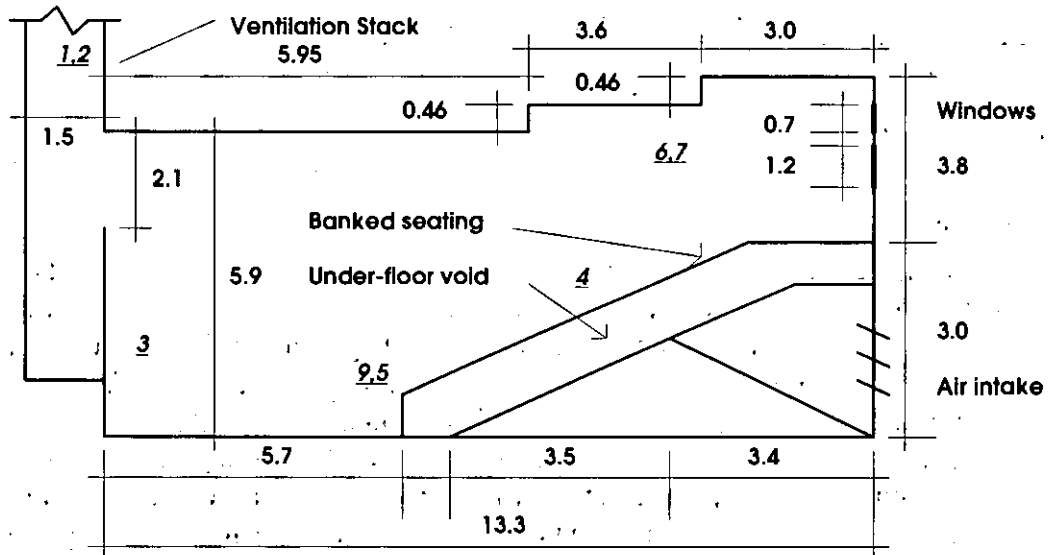
Building controls

During an occupied period, if the average internal temperature exceeds a set point (e.g. 19°C), and if it is greater than the outside temperature, the inlets and outlets will open. Otherwise the openings will close to minimum positions which are determined by the carbon dioxide sensor in the room (located in one of the stacks); i.e. 10 % open with a CO₂ concentration of 350 ppm and 100 % open when the CO₂ concentration is equal to or greater than 1000 ppm.

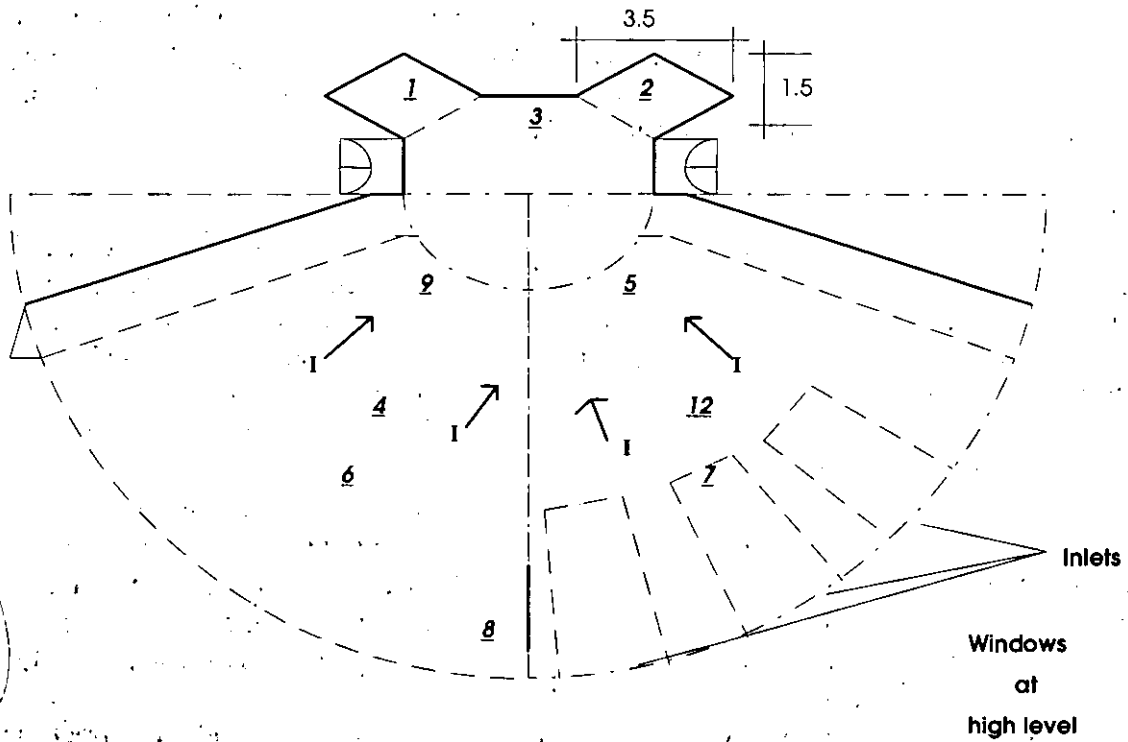
A mixing valve plus actuator varies the flow rate to the heating circuit and is controlled using the average room temperature.

The fans (one in each theatre) are started if the average internal temperature is 3°C above the room set-point and greater than the external temperature plus 2°C (provided the inlets/outlets are open and if it is not raining). When the space is unoccupied, in winter the openings close, and in summer they open at night to pre-cool the room to a set temperature (summer is assumed to occur when the minimum outside temperature is greater than 13°C; based on temperatures recorded for the previous 24 hours).

In the event of a fire, the room inlets and stack outlets fully open and the extract fan is switched on. External air (not internal) humidity is monitored and recorded, but is not used by the control system.



Section through theatre



Plan (all dimensions in metres)

Figure 4.2.1 Section and plan of theatre 1.10 showing location of injection and sampling points. (Room area = 187 m^2 , room volume = 870 m^3).

4.2.2 Use of Measurement and Analysis Tools

Purpose of measurements

The experimental objectives were as follows:

- To determine the ventilation performance of the ventilation system as installed, i.e. whether sufficient volumes of fresh air are being provided and if the air is well distributed in occupied zones
- The objective estimation of thermal comfort within occupied areas

Note: that the two points above are achieved for different internal occupancy heat gains and external conditions (variable external air temperatures, wind speeds and directions).

Equipment and methodology

Tracer gas measurement

Hardware used comprised two injection units, a sample unit, an interface unit and an infra-red two-channel gas analyser (which output a 0-to-1 Volt signal for gas concentrations from zero to 50 ppm). Sulphur Hexafluoride (SF_6) gas was injected directly into the space via mixing fans at points indicated in Figure 4.2.1. Sampling tubes were placed in both stacks, and at seven points within the auditorium. A thermistor was attached to the end of selected sampling lines so that air temperatures of particular zones could be recorded.

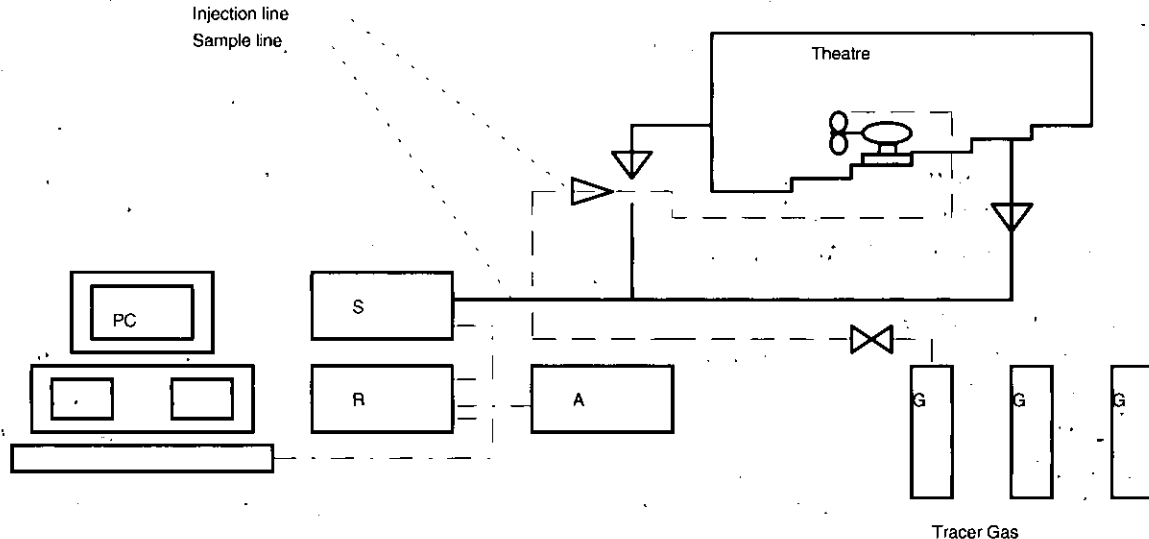


Figure 4.2.2 Schematic diagram of tracer gas injection and sampling system.

Legend:	S	sampling
	A	analyser
	R	Rexagan unit
	PC	personal computer
	Gas	SF_6 , SF_6 in N_2 , N_2

The positions of injection and sampling points are indicated in Figure 4.2.1. Six sample tubes were fed into the infra red gas analyser. 12 sampling connections were available with a cycle period of 2 minutes. The sampling frequency was doubled by using two of the equipment channels for every zone sampling-point.

Carbon dioxide (CO_2) emissions were measured using the secondary channel of the same gas analyser. If the number of occupants was recorded, the variation in CO_2 concentrations could be used to calculate infiltration rates, assuming constant emission from occupants and steady-state conditions (i.e. constant surface and air temperatures); i.e. air change rates could be found using the constant emission technique. When the room became unoccupied, infiltration rates were found using the decay technique. A plot of the variation of CO_2 levels with time for a maximum occupancy level of 50 is shown in Figure 4.2.3

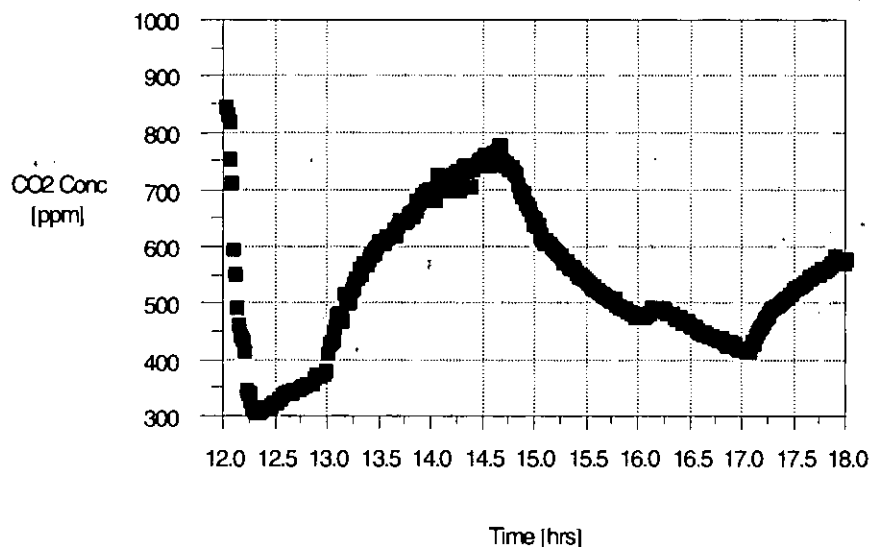


Figure 4.2.3 Carbon dioxide concentrations v. time on 19 January 1995; maximum occupancy level = 50; (Air-change rate $n = 14.5$ (/h) from 12:00 to 12:18; Infiltration rate $n = 0.3$ (/h) from 15:00 to 16:00).

Air velocity recording

Air velocities were measured using low velocity omnidirectional hot wire probes and a hand-held thermistor-based anemometer. Four probes were placed in each stack (which allowed flow rates to be calculated easily), and at positions in the first and fourth rows on either side of the theatre 0.5 metres from inlet grilles.

Velocity probes were mounted only in the stacks for most runs, while spot checks of room air velocities were made using a hand-held anemometer.

Measurement periods were similar to those used for the tracer gas monitoring, in this case 16 to 75 minutes. Velocity directions were periodically checked using a hand-held smoke generator and/or by viewing the movements of strips of paper suspended across the inlet to each stack. Flow directions could also be determined from the probe temperatures; if the external temperature was considerably less than the room temperature, a sharp drop in the stack temperature would indicate that downflows were occurring.

Experimental procedure

A Binos infra-red gas analyser was used to measure both SF₆ and CO₂ concentrations. The primary channel detected SF₆ concentrations from 0 to 50 ppm while the secondary channel measured CO₂ concentrations from 0 to 5000 ppm. Initially, zeroing and calibration of the instrument was performed using N₂ and 50 ppm SF₆ in N₂ respectively. Tracer gas was then discharged directly into the space via four injection points for a period of about 3 minutes. Four 'desk-top' mixing fans were operated at injection points together with two additional fans on adjacent rows to facilitate adequate mixed throughout the space. Fans were run for about 15 to 20 minutes.

Once a reasonably uniform concentration was reached, inlets and outlets were set in the desired positions (i.e. 50, 75 or 100% of the maximum settings) via the Building Management System (BMS) computer, which corresponded to effective areas of 2.25, 3.37 and 3.91 m² respectively. Casual heat gains from occupants of up to 5 kW were simulated by using 100 W electric filament light bulbs; these loads were placed in the first 4 rows (nearest the lecturers position). This load represented a typical level of occupancy; loads of up to 15 kW are planned in measurements at a later stage.

When the room is in use, actual occupancy levels are monitored by visual inspection. Two infra-red detectors have been installed and produce a voltage output if movement occurs a few metres away from the sensors. The historic records of the sensors can be viewed via the BMS terminal and allow an observer to monitor whether the space is occupied or not but gives no indication of the number of people present. A more methodological method (of recording occupancy levels) is being reviewed, i.e. the use of a compact wide angle camera (which can record time and date) mounted at high level near the fire exit door on the left hand side of the space.

CO₂ levels in each stack, in the left hand and right hand side of the theatre and at high level on each side were monitored over periods lasting several hours. Intakes and outlets are opened for short periods (5 to 10 minutes); air change rates can be determined if the number of occupants is known. Infiltration rates were found from the CO₂ decay rates once the room was vacated.

Data on ambient air temperatures and humidities are recorded via the building management system (BMS). External temperatures were also logged using two thermistors connected to a stand-alone recorder. Wind speed and direction are logged on top of an adjacent building using a dedicated recorder and data is downloaded to a portable computer at monthly intervals. BMS data at each point is sampled and stored every 15 minutes. Readings collected over a seven day period was periodically transferred to a floppy disc via a dedicated BMS personal computer located in the building manager's office. A facility had been provided within the BMS to allow the automatic controls to be overridden; thus allowing researchers to have independent control of intake and outlet angular positions and hence effective areas.

Data analysis

Data were obtained for gas concentrations, injection times and periods and this allowed air-change rates to be determined. Air change rates were found from gas concentration values and corresponding times; i.e. average local values were calculated by dividing the areas of the concentration curves versus time, into the initial concentrations.

Local air-change rate at point p :

$$n_p = \frac{C_p(0)}{\int_{t=0}^{t=\infty} C_p(t) dt} \quad (4.2.1)$$

An average room air change rate could then be calculated for particular internal and external conditions (Equation 4.2.2, where N is the number of measuring points). When a series of air-change values had been estimated, under different conditions, they could then be used to check how air-change rates varied with temperature and size of opening.

$$n = \frac{1}{N} \sum_{p=1}^N n_p \quad (4.2.2)$$

4.2.3 Performance of Tools

Tracer gas decay method

The decay method and the equipment used, allowed the relative fresh-air distributions on either side of the room, in the occupied zones and at high level (see Table 4.2.1.) to be found. Local air change rates due to infiltration could be estimated much more accurately than those generated when the vents were open (with effective areas greater than 2.24 m³). The method became too inaccurate when air change rates exceeded 20 ac/h (above which direct measurement of stack velocities should be used to find global flow rates).

Velocity measurement

- Ventilation flow rates could be estimated more accurately if the air velocities in the stacks exceeded approx. 0.3 m/s. The manufacturer gives an error of less than $\pm 10\%$ at velocities above 0.25 m/s (flows perpendicular to transducer axis). However the errors due to the nature of the flow, i.e. degree of flow turbulence and flow profiles, are likely to be more significant. Above 0.3 m/s, flows were likely to be less turbulent and more unidirectional
- A total of 24 low velocity sensors was available. However, the distances from the measurement points to the logging equipment meant that only 15 sensors could be used in practice (two lengths of cable were required for sensors mounted adjacent to inlet grilles on the fifth row and in the right-hand stack). Thus only 7 sensors were available for measuring room air speeds
- It was difficult to mount and access sensors positioned in the stacks. Rigid sensor supports were required and temporary cable supports were needed

Results*Conditions in the space during 'summer' (minimum external temperature greater than 13°C)*

- Stable room air temperatures (20 to 23°C) and ceiling slab temperatures (22 to 24°C) (due to the heavyweight nature of the building). See Figure 4.2.7
- Apparent effectiveness of pre-cooling of exposed brick and concrete surfaces. (Night venting was used to pre-cool exposed concrete slabs within the space)
- Low room air velocities: Generally inlet and room air velocities not directly opposite an inlet plenum have been low (less than 0.3 m/s on average)
- Much higher room air velocities were recorded on the right-side than on the left-side (since the 3 intake openings (to the outside) are located adjacent to the right-side of the space only (see Figure 4.2.1))
- High wind-induced ventilation rates (a minimum of 3 ac/h but generally much higher than this value; i.e. in excess of 4 m³/s or 13.6 ac/h have been observed). These flow rates occur even though the external temperature may be equal to, or greater than, the average internal air temperature
- Some data obtained from June to August 1995 suggests that particular outlet configurations of the stacks (i.e. windward vents closed and leeward vents closed) can enhance global flow rates through the space

Conditions found during 'winter' (average external temperatures less than 5 oC)

- High temperature differences (i.e. 21–6 = 15°C) produced large flow rates; i.e. 22 ac/h and above (wind speeds were generally relatively low when measurements were taken)
- Very low inlet air temperatures were recorded (e.g. down to 7°C with speeds above 0.5 m/s with external air temperatures of 3~4°C). Such conditions will rarely occur in practice, i.e. if the heating is switched off and if occupancy levels are high (greater than 100 people)

'Mid-season' conditions (average external temperature equal to ~10 oC)

The points above, for winter, were also applicable assuming an average internal temperature of about 21°C and an outside temperature of ~10°C. Very good agreement was achieved between flow rates measured using stack-mounted velocity probes and values calculated using the CIBSE Guide stack formula [CIBSE Guide A, Table A.4.4], see Figure 4.2.6; i.e.

$$Q_B = C_d A_B \left(\frac{2gh_a(T_i - T_o)}{\frac{T_i + T_o}{2} + 273} \right)^{0.5} \quad (4.2.3)$$

General comments

Due to the location of intakes (to the outside), the local air change rates were generally significantly higher on the right hand side (rhs) of the theatre than on the left hand side (lhs). (Inlet openings are arranged asymmetrically and are positioned on the rhs of the space).

Similar flow rates were found at the '75%' and '100%' opening settings (corresponding to opening areas of 3.37 and 3.91 m² respectively).

The temperature differences between low and high level zones was generally about 2°C, with little variation occurring with changes in flow rates. The depth of the warmer high level zone appeared to decrease with increase in air-change rate, and greater temperature fluctuations were observed at high level than at low level (i.e. ~0.5°C and 0.2°C respectively).

There was no evidence that bidirectional flows were taking place within each stack (the overall height is ~18.5 m and the internal cross-sectional width and breadth are 3.5 m, and 1.43 m respectively); temperatures measured using velocity probes indicated the same values. These temperatures also provided useful information on flow directions through the stacks; if there was a significant difference between inside and outside temperatures, then a sharp drop in temperature would indicate that air was flowing down a chimney while a rapid rise in temperature would demonstrate that rising flows were occurring.

It was found that individual velocity values and hence flow rates within each stack were approximately the same over a given time period (see Figure 4.2.5).

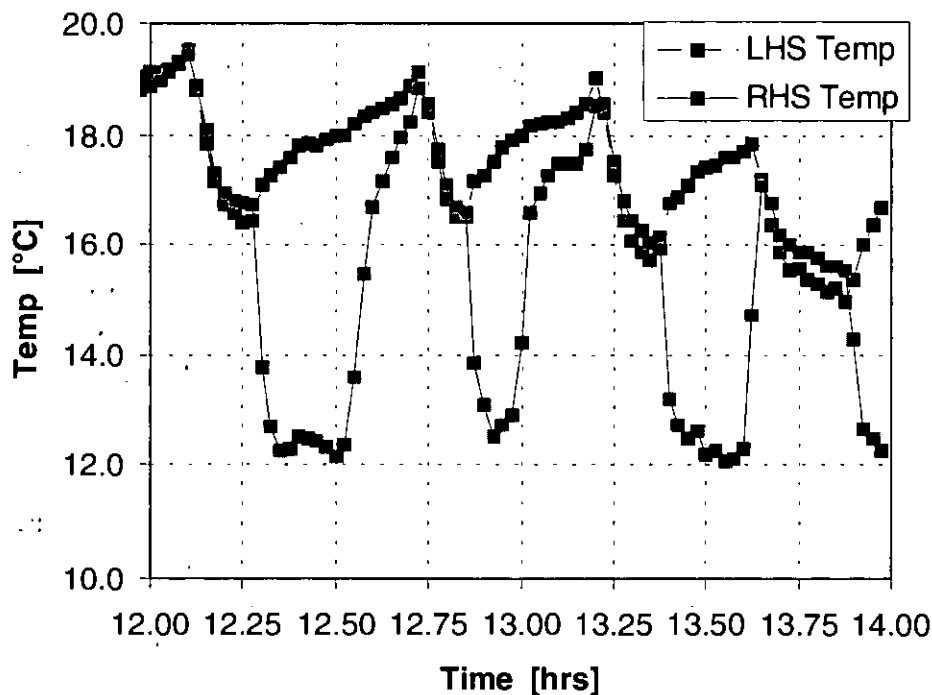


Figure 4.2.4 Temperatures of stack air at a height of 9.25 m above floor level (lhs Stack and rhs Stack); external temperature = 4.9 to 6.1°C.

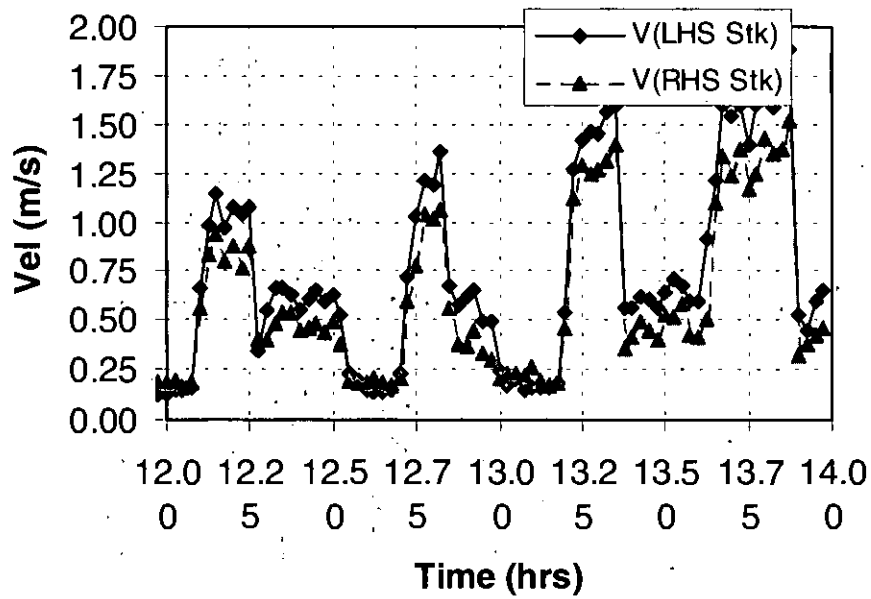


Figure 4.2.5 Velocities of air in lhs and rhs stacks at a height of 9.25 m above floor level.

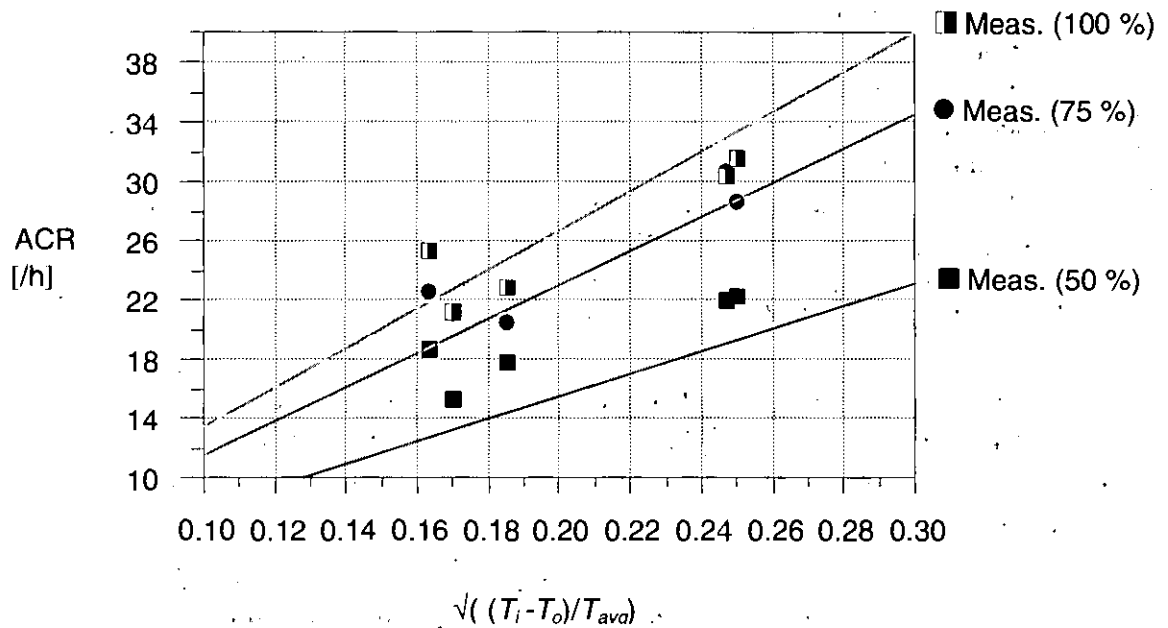


Figure 4.2.6 Measured and calculated air change rates v. $\left(\frac{T_i - T_o}{T_{ava}}\right)^{0.5}$ for different opening settings ("winter" and "mid-season" conditions).

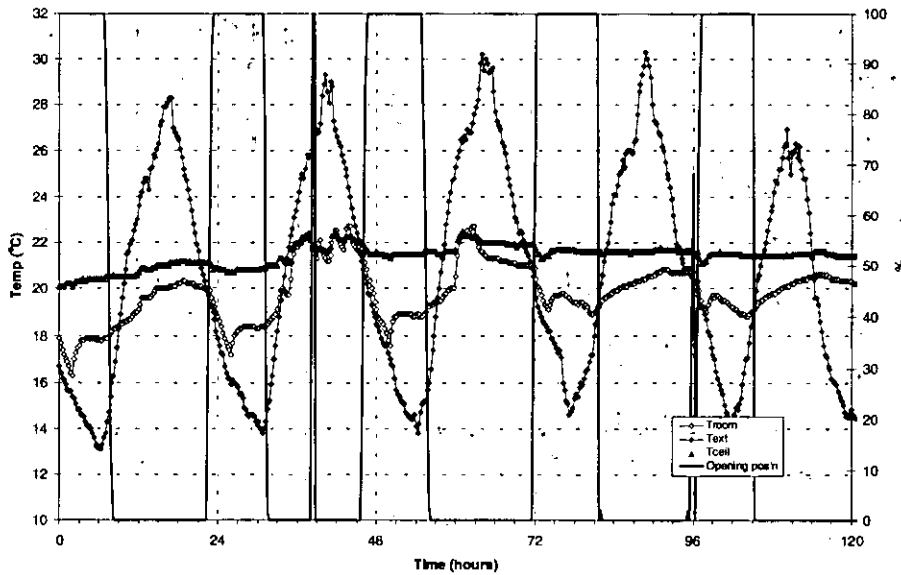


Figure 4.2.7 Average room temperatures, external and ceiling slab temperatures and relative opening positions for "summer" external conditions.

Advantages of the ventilation system as designed

- Large savings in energy (both for heating and that used in electrical power) and in plant maintenance can and are being realised. Hence large running cost savings are being achieved comparable to an equivalent air-conditioned auditorium. The statement on energy use is based on published figures for the annual gas and electricity consumption of the entire building
- When the design and installation is sufficiently rigorous and thorough, the system can run completely under automatic control with minimal periodic maintenance

Problem areas with the ventilation system as designed

- *Uneven distribution of fresh air*

Generally, much higher local air-change rates have been measured on the right hand side of the theatre. This is partly due to the layout of the space and the positions of the inlets (i.e. only one half of the end wall (or curved surface) is external). See Table 4.2.1

- *Relatively high air velocities in occupied areas*

High air velocities (> 0.5 m/s) in occupied areas (at ankle height, adjacent to inlet grilles), and low air temperatures ($< 10^{\circ}\text{C}$) when inlets are fully open ('winter' external conditions). When outside air temperatures are 10°C or below, the stack effect generates high inlet velocities via inlet plenums and grilles; the heat transfer rate from the underfloor heating coils is insufficient to prevent low air temperatures when flow rates are high (~ 5.9 m³/s). Much of the incoming air bypasses the coils, which would produce occupant discomfort in areas adjacent to the inlet plenums. However, under normal operation, the openings will only remain open for a relatively short period (until the control conditions are satisfied, see section *Building controls*, page 205)

- *Occurrence of down-flows in stacks*

When stack outlets move to their closed positions, down-flows can occur. Discomfort can be produced for a short period if the external temperature is much less than the room temperature (i.e. less than say 10°C with an average internal temperature of 20°C). This problem has been partially overcome by limiting the travel of the outlet actuators if the low level stack air temperatures are less than 12°C. The actuator motors, which provide the power to open and close the outlets, are run in sequence. The consequence of this is that, if the vents are initially open, the left hand side openings will start to close before those on the right hand side, thus causing a temporary higher flow resistance through one stack. This results in downflows in one stack with upflows occurring simultaneously in the other (see Figures 4.2.4 and 4.2.5)

- *Maintenance of adequate ventilation rates with high occupancy levels*

Further commissioning of control system components is required in order to get the ventilation to operate as designed

- *Relatively high dust levels*

Dust accumulation has been observed at the base of the stacks and within the inlet plenums. The reduction in the rate of deposition would be difficult to avoid as filters cannot be used to remove dust since they introduce excessive pressure drops into the system. Air quality problems may occur if such dust is suddenly dispersed into the room in high enough concentrations following a rapid increase in inlet velocities

4.2.4 Conclusions and Recommendations

Conclusions

- There are likely to be large uncertainties in the measurements due to relatively small number of points used. Ideally at least two samplers should operate simultaneously, thus allowing more gas samples to be obtained over a given time period
- Air speed and direction need to be measured at the same time. Room air speeds are difficult to monitor when the room is occupied
- Equipment is intrusive and visible, and considerable amounts of time are required to route and position tubing, sensors and associated wiring. Ensuring safety of personnel can be difficult when installing sensors at high level
- It would be relatively expensive to obtain and site a large number of surface temperature sensors. Hence interpolation methods are required to allow calculation of intermediate wall and ceiling temperatures. This could then be verified using spot measurements.

Recommendations (use of experimental equipment and techniques)

- Ensure that sufficient and appropriate sensing equipment is inserted when the building is being constructed (as part of a building management system)

This should include the following:

<u>Sensor type</u>	<u>Accuracy</u>	<u>Minimum number per 1000 m³</u>
Air temperature	±0.2 °C	4 (shape dependent)
Surface temperature	±0.2 °C	(depends on ceiling area)
Velocity (shielded hot-wire)	±0.05 m/s	(4 per 2.5 m ² (duct cross section))
CO ₂ (Infra-red etc.)	±50 ppm	1 plus tubing array and local pump per duct.
Infra-red (occupancy)	±2 % of full	1 per door scale reading

- Carry out periodic recalibration of sensors and associated equipment (hence there should be a routine procedure for gaining access to high-level areas; the methods used may coincide with those used by the building maintenance personnel)
- Isolate the area(s) under examination so that uncontrollable influences are minimised (i.e. lock access doors) such that ventilation areas are fully under the operators control

Table 4.2.1 Local air change rates for “winter” and “mid-season” external conditions. Point 1 = lhs stack; point 2 = rhs stack; point 6 = lhs (high level); point 7 = rhs (high level).

Run	Opening Settings (%)	Heat Load (OC) (kW)	Air change rates (/h)						Avg ACR (/h)	Stack		Avg. Temp.		Wind Speed / Dim (m/s)
			1	2	LHS R	RHS R	6	7		Velocity (m/s)	ACR (1/h)	Internal (°C)	External (°C)	
1	50	5	12.2	12.3	21.3	28.6	15.6	12.1	17.0	1.4	22.3	21.2	3.3	L /
	75	5	33.4	38.2	28.0	40.0	32.0	21.4	32.0	1.7	28.2	20.5	3.2	L /
	100	5	37.2	42.1	38.9	49.9	30.8	20.0	36.5	1.8	29.5	19.8	4.4	L /
2	50	5	23.6	22.9	28.8	32.9	18.0	19.5	24.3	1.3	21.9	19.5	2.2	L /
	75	5	30.8	29.7	41.9	51.9	30.8	25.9	35.2	1.8	29.0	19.7	4.3	L /
	100	5	22.8	22.7	34.7	84.5	27.0	21.0	35.5	1.7	28.2	19.5	4.7	L /
3	50	5	23.4	18.4	16.7	23.1	13.1	19.2	19.0	1.3	20.5	17.3	4.9	M /
	75	5	29.0	29.6	37.1	79.4	38.1	23.0	39.4	1.5	24.7	16.9	5.0	M /
	Infiltration	5	1.1	1.2	1.1	1.1	1.1	1.1	1.1	1.1		18.2	5.2	M /
4	Infiltration	var												
		var	0.3	0.2	0.2	0.2	0.2	0.2	0.2			19.8	9.3	H /
		var	0.1	0.1	0.1	0.1	0.1	0.1	0.1			20.2	9.5	H /
5	Infiltration	var												
		var	1.2	1.3	0.9	1.1	1.1	1.2	1.1			20.7	5.7	M /
		var	0.5	0.4	0.3	0.4	0.5	0.4	0.4			20.3	5.5	M /
6	50	var	9.9	10.3	22.2	21.3	8.8		14.5			20.2	8.0	H /
	Infiltration	var	0.3	0.3	0.3	0.3	0.3		0.3			21.5	7.4	H /
7	50	5	21.0	22.3	24.2	26.1	7.6	11.1	18.7	1.1	17.9	19.9	10.0	M /
	75	5	17.0	20.0	24.0	22.5	16.9	13.8	19.0	1.3	20.7	19.2	9.2	M /
	100	5	16.0	17.6	20.5	48.1	17.4	12.8	22.1	1.4	22.7	18.8	9.2	M /
8	50	5	15.1	17.6	22.5	43.6	11.2	9.8	20.0	0.9	15.3	20.4	12.0	7.7
	75	5	20.9	20.6	26.8	44.7	30.2	18.8	27.0	1.3	22.1	20.8	11.6	5.4
	100	5	22.7	18.8	18.9	19.2	17.3	20.3	19.5	1.3	21.8	20.4	11.6	6.7
9	50	5								0.9	15.5			M
	50	5	20.5	22.4	25.4	36.4	13.6	7.2	20.9	1.1	18.8	19.0	11.3	M
	75	5	17.2	22.1	25.9	70.1	21.2	14.8	28.5	1.4	23.0	18.8	10.9	M
	100	5	19.0	10.9	27.2	45.8	24.4	15.6	23.8	1.5	24.2	18.0	11.1	M

4.3 Experimental Atrium, Kanagawa, Japan

4.3.1 Introduction

Solar radiation, outdoor temperature, wind, and envelope properties all exert a strong influence on the indoor environment in atria, due to the large area of glass. Atria can therefore experience large spatial and temporal variations in temperature and airflow, which makes them difficult to model. A measurement programme lasting over two years has been carried out in a purpose-built full-scale experimental atrium in Yokohama, Japan (Figure 4.3.1). Since it was built for experimental purposes, no one was permitted to enter the atrium. Measurements could therefore be carried out undisturbed, and uncertainties such as adventitious air exchange caused by people going in and out, were greatly reduced in comparison with atria in common use.

Detailed measurements were made of the indoor environment (air velocity, turbulence, air and surface temperatures etc.). Measurements were also made of the boundary conditions affecting the indoor thermal environment, such as envelope material properties, leakage areas and weather conditions [Hiramatsu *et al.*, 1996]. This data is intended for validating mathematical analysis methods, including CFD and macroscopic models, which are now extensively used to predict the indoor environment of atria during design. The modelling results of some participants in IEA Annex-26 are presented in the next few pages.

Convective heat transfer is an important component of the energy (heat) balance in atria. The accuracy of the predicted convective heat transfer in the CFD models is examined in detail here. The predicted vertical air temperature distributions from both CFD models and zonal models are also investigated by comparing their results with those of the experiment.

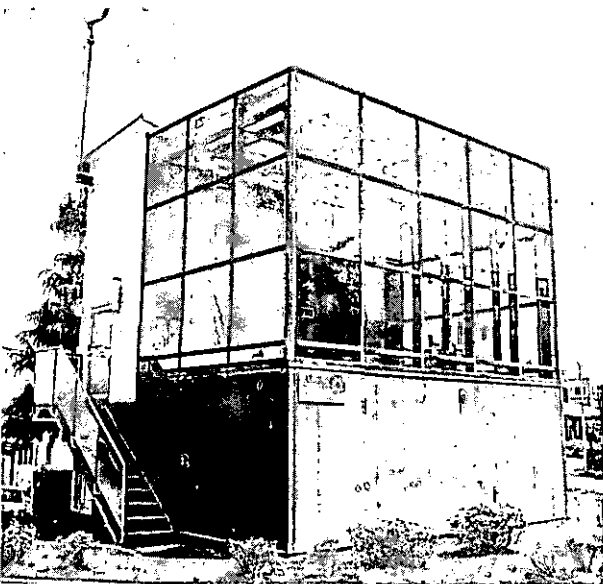


Figure 4.3.1 The experimental atrium.

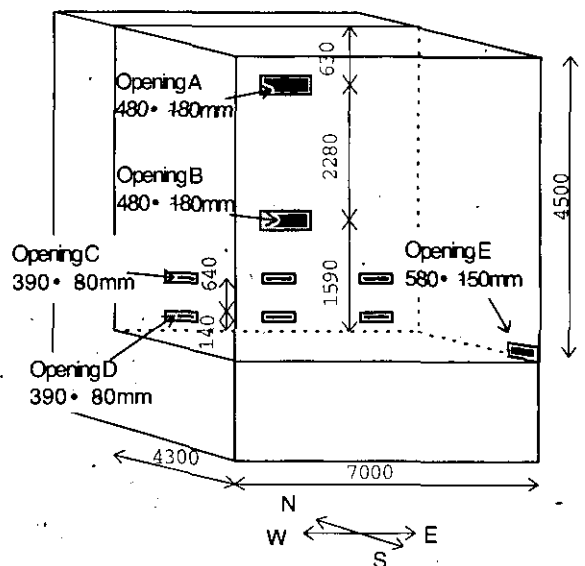


Figure 4.3.2 Configuration of experimental atrium.

Table 4.3.1 Thermophysical properties of the envelope materials.

	Thermophysical properties			
	Short-wave		Long-wave emissivity inside / outside	Overall thermal conductivity [W/m ² K]
	absorptance inside / outside	transmittance		
glass A	0.19 / 0.33	0.37	0.30 / 0.84	116
glass B	0.46 / 0.69	0.16	0.51 / 0.84	116
floor (black)	0.91 / -	0	0.95 / -	0.36
floor (white)	0.20 / -	0	0.90 / -	0.36
wall (black)	0.98 / -	0	0.95 / -	0.27
wall (white)	0.20 / -	0	0.90 / -	0.27

Table 4.3.2 Positions of the air supply and exhaust openings for cooling and natural ventilation conditions (see Figure 4.3.2 for locations A to D).

	type	supply	exhaust
Cooling	I	A	B
	II	B	A
	III	C	D
Natural ventilation	IV	B	A
	V	E	A

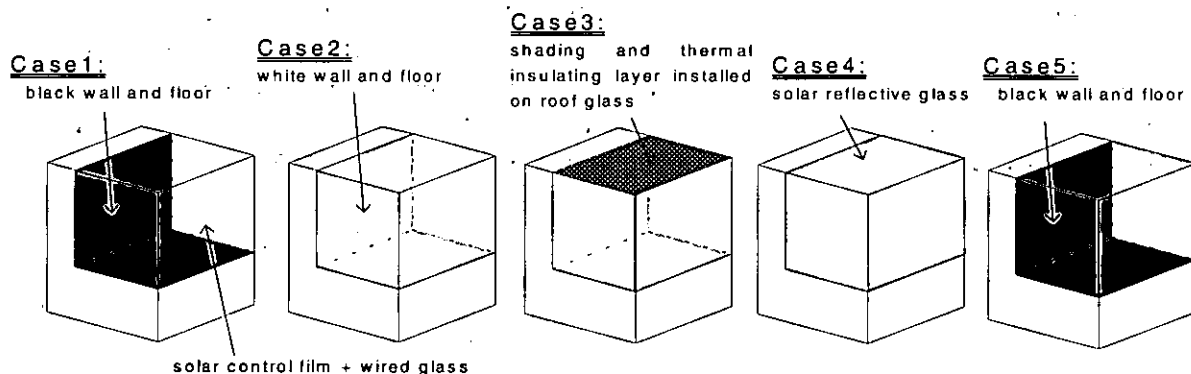


Figure 4.3.3 Illustration of the different measurement conditions.

Table 4.3.3 Measurement conditions.

Case	1	2 (a)	2 (b)	3 (a)	3 (b)	4	5
Ventilation type (see Table 4.3.2)		(1) <i>nc</i> (2) <i>c</i> -Type I (3) <i>c</i> -Type I (4) <i>c</i> -Type III (5) <i>nv</i> -Type IV		(1) <i>nc</i> (2) <i>c</i> -Type I (3) <i>c</i> -Type II (4) <i>c</i> -Type III (5) <i>nv</i> -Type IV		(1) <i>nc</i> (2) <i>nv</i> -Type IV (3) <i>nv</i> -Type V	
<i>nc</i> : natural convection (no cooling) <i>c</i> : air conditioning (cooling) <i>nv</i> : natural ventilation	<i>nc</i>		<i>nc</i>		<i>nc</i>		<i>nc</i>
Measurement period	Feb '94	Apr & Aug '94	Apr '94	May - Aug '94	May '94	Nov '94 - Apr '94	Aug '95
Fine days / Measurement days	1 / 3	13 / 22	2 / 6	14 / 37	4 / 6	13 / 29	6 / 10
Colour of floor and north wall	black			white			black
Glass type ¹ (see Table 4.3.1)			A			B	
Heat storage		x	✓	x	✓	x	
Shading and thermal insulating layer installed on roof glass ²		x		✓		x	

¹ Bricks (thickness 60 mm, area 17 m², thermal capacity 1550 J/K) are laid on the floor.

² 100mm thick polystyrene board, sandwiched between 12 mm plywood, is used as a sunshade and thermal insulation.

4.3.2 Description of the Experimental Atrium

The atrium faces south. It has three glazed facades (south, west, and east), a glazed roof and two insulated surfaces (north wall and floor). Table 4.3.1 lists the thermal properties of the envelope materials. The atrium can be ventilated by either a mechanical cooling system or by natural ventilation, both of which have different possible configurations of inlets and outlets. Figure 4.3.2 and Table 4.3.2 denote the locations of the supply and exhaust openings of the different systems. Further details are given by Hiramatsu et al. [1996].

Steel glazing-frames account for about 10% of the glazed facade area. The internal steel support structure (columns & beams) and protruding glazing frames, occupy 0.34% of the space volume. The total area of steel frame exposed in the space equals 240% of the floor area. The quantity of frames used is typical for this type of building, and was neither intentionally increased nor reduced.

4.3.3 Measurements

During the two year measurement programme, different configurations of ventilation, materials, shading etc., were studied (Figure 4.3.3 and Table 4.3.3). In each case, the measurements included: (1) solar radiation, (2) solar radiation after transmission through each glass wall, (3) outside temperature, (4) wind velocity and direction, (5) indoor air temperature at many points in the space, (6) surface temperature at some points on each wall, inside & outside, and of steel frames, (7) air velocity vectors and turbulence intensity at many points in the space. The measurements were time-integrated and logged hourly.

Vertical temperature distribution

Cases with no ventilation (Figure 4.3.4): (Case 1, Case 2(a-1), Case 3(a-1), Case 4(1) and Case 5).

In these cases, the main mechanisms of heat loss were conduction through walls and leakage infiltration driven mostly by stack effect. Natural convection results in well-mixed indoor air, hence the vertical temperature difference was relatively small. The floor and the north wall were heated by solar radiation while the glass walls acted as cooling surfaces. In Case 4(1), which had glass of high absorptance for solar radiation, the surface temperatures of the glass were higher. Here, the air recirculation in the space was depressed, and the vertical temperature difference was a little larger than in the other cases.

Cases with air conditioning, i.e. cooling (Figure 4.3.5): (Case 3(a-2), Case 3(a-3), and Case 3(a-4)).

When the cooled air was supplied at high level (type I, opening 'A' in Figure 4.3.2), the indoor air was well mixed. However, it was not as uniform as was observed in the natural convection cases above. In the cases where the cooled air was discharged at low level (type III, three type 'C' openings in Figure 4.3.2), the airflow became stagnant in the space above the supply openings, and highly stable temperature stratification was observed.

Cases with natural ventilation (Figure 4.3.6): (Case 2(a-5) and Case 3(a-5)).

Since the ventilation opening area was small in comparison with the south facade area, and since observations were made on calm (not windy) days, the air exchange rate was not so large. In the case with no shading layer on the roof glass, Case 2(a-5), natural ventilation reduced the indoor temperature by about 5°C relative to having no ventilation. In the case with a shading layer on the roof, (Case 3(a-5)), the indoor temperature was not reduced so

much by the ventilation. The air exchange rate in this case was lower than in the former case, in line with the reduction in solar gain.

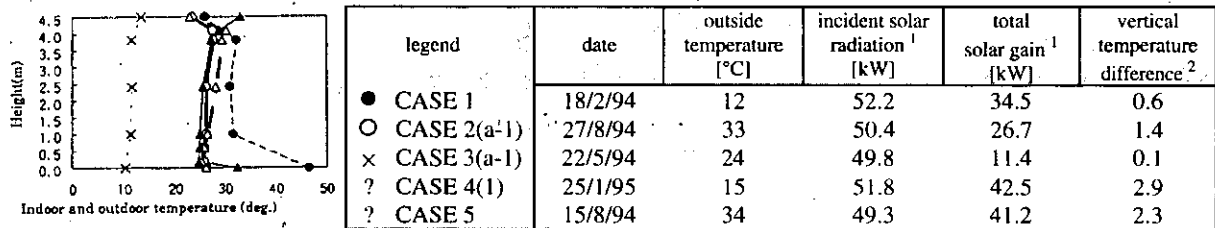


Figure 4.3.4 Cases without ventilation (only infiltration by leakage) : Vertical temperature profile at centre of room at 13:00 hrs.

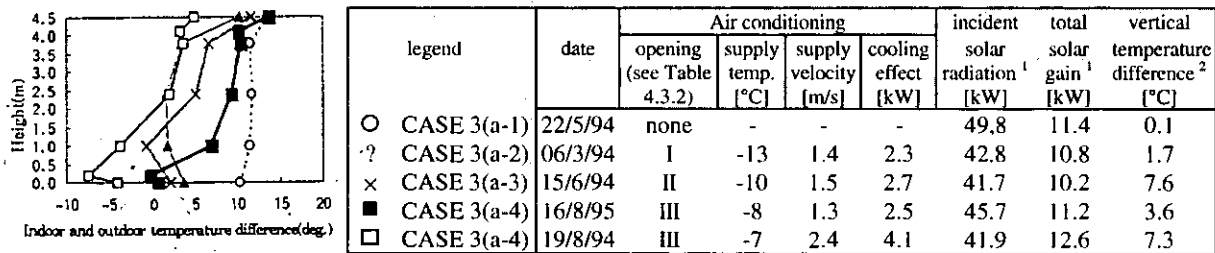


Figure 4.3.5 Cases with air conditioning : Vertical temperature profile at centre of room at 13:00 hrs. (Case 3(a-1) which has no ventilation, is added for comparison).

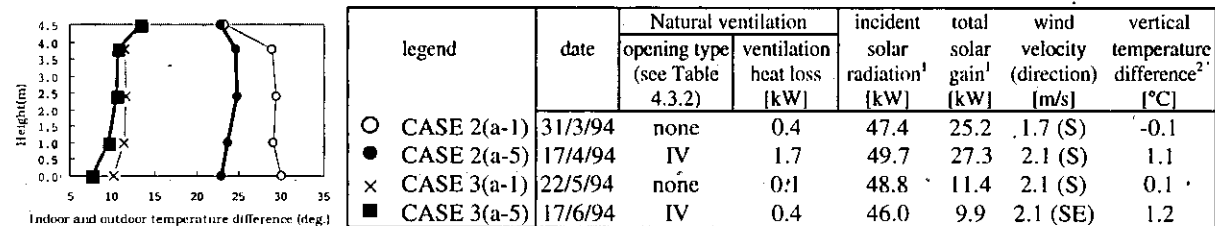


Figure 4.3.6 Cases with natural ventilation : Vertical temperature profile at centre of room at 13:00 hrs. (Cases 2(a-1) and 3(a-1), both without ventilation, are added for comparison).

Energy (heat) budget

The energy (heat) budget of the indoor air was estimated from the measured temperature of the air and the surfaces facing the enclosure, and the air exchange rate. Figure 4.3.7 shows the heat budgets for the three types of ventilation. The vertical axis corresponds to estimated heat gain (loss) to the indoor air by infiltration and convective heat transfer from the steel frames. The horizontal axis corresponds to estimated heat gain (loss) by convective heat transfer from the four walls, ceiling and floor. When the heat gain from the steel frames is included, the data points closely fit the best-line, which is at about 45°, indicating a strong proportional relationship. So it is clear that heat gain from the steel frames strongly influences the indoor

¹ Calculated value from measured solar radiation (horizontal global radiation and sky radiation), assuming diffuse interreflection between indoor surfaces. To account for the frames, the solar gain to the north wall and floor includes the shading factor of the glazing frames, and the solar gain to the glazing is estimated by adding the solar gain of the glass and that of the frames.

² Difference between the air temperatures at 1.0m and 3.8m above the floor.

temperature. The steel frame's impact is reduced when the incident solar radiation entering the enclosure is reduced by low transmittance glass (Cases 4 and 5) or by shading (Case 3).

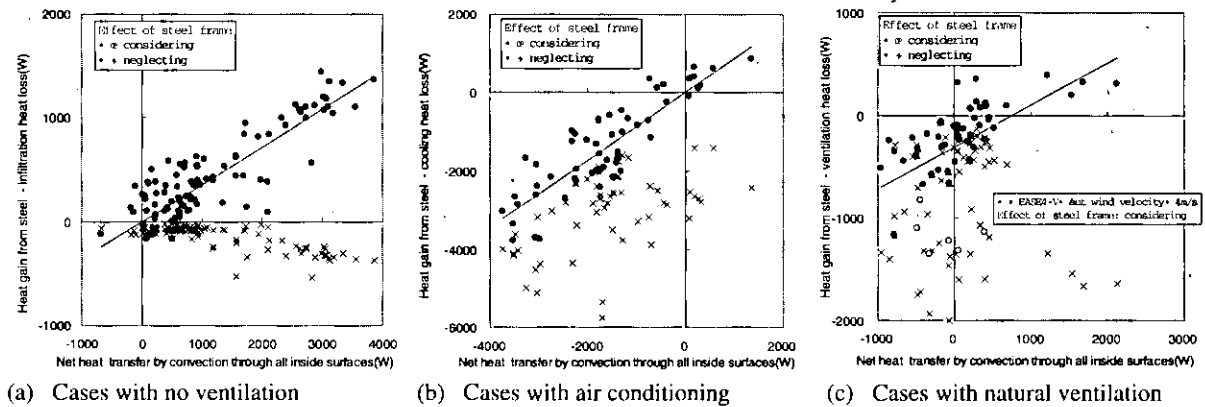


Figure 4.3.7 Effect of the steel glazing frames on the space heat balance (measured at 13:00 and 14:00 hrs).

Summary of experiments

When there is no cooling, the vertical temperature difference is relatively small, because the indoor air is mixed well by natural convection driven by the solar heated floor and cool glass walls. When there is cooling and the supply openings are positioned close to the floor, highly stable temperature stratification is observed, because vertical air flow is greatly suppressed in the space above the supply opening. Natural ventilation driven by the stack effect, is effective when there is no shading device on the roof. It was shown that the convective heat transfer from the steel frames is a major source of heat gain to the space.

4.3.4 Analysis Tools : CFD and Zonal Models

CFD and zonal model simulations of the airflow and temperature distribution of the experimental atrium were carried out on the basis of the experimental data. The aims of the computations were to ascertain: (1) how the simplification of the CFD boundary conditions, such as heat gain from frames, affect predictions, (2) how the CFD simulation method, such as the computational grid, affect prediction results, (3) how accurate is the convective heat transfer from the walls predicted from the viewpoint of energy calculations, (4) how zonal models perform in predicting the vertical temperature distribution of large enclosures.

Two purely natural convection cases (no ventilation, but with some infiltration) with flow characterised by high Rayleigh numbers (Case 1 and Case 2(a-1)), and two cases of air-conditioning with different positions of the supply, and exhaust openings (Case 2(a-2) and Case 2(a-4)), were simulated by Annex-26 participants, using both CFD and zonal models. In the next section, the numerical results are compared with the indoor climate measurements.

CFD

Table 4.3.4 lists the participants in Annex-26 who modelled the atrium with CFD. Comparison between the results of the different participants enabled us to evaluate the performance of the different CFD methods.

Table 4.3.4 Working groups and CFD modelling.

Name	Country	CFD includes [†]	Case no. [‡]	CFD model	Boundary Conditions	Grid	Heat gain from steel frames	Output
Mr. Frank Off (IET)	CH	① ② ③ ④	1 2(a-3)	Standard <i>k-ε</i> (TASCflow)	Standard wall functions	35 × 47 × 35 33 × 49 × 41	✓	Time-dependent velocity, air & surface temperature
Prof. Erik Olsen (CTH)	S	①	1	Standard <i>k-ε</i> (non-commercial)	Standard wall functions	21 × 21 × 21	✗	Velocity & air temperature
Mr. Peter Schild (NTNU)	N	① ② ③ ⑤	1 2(a-1)	Standard <i>k-ε</i> (CFX Flow3D)	Standard wall functions	19 × 26 × 19	✓	Solar insolation, velocity, air & surface temperature, infiltration flow rate, convective heat transfer rate & coefficient
Dr. Marco Citterio (ENEA)	I	①	1 2(a-1) 2(a-3) 2(a-4)	Standard <i>k-ε</i> (Phoenix 2.1)	Standard wall functions	22 × 33 × 22 22 × 35 × 30 22 × 42 × 35	✓	Velocity, air temperature, convective heat transfer rate & coefficient
Dr. Markus Rösler Mr. Volker Fischer (TUD)	D	① ② ③ ④	2(a-1)	Standard <i>k-ε</i> (ResCUE)	New wall functions for natural convection	22 × 28 × 20	✓	Time-dependent Velocity, air & surface temperature
Mr. Yoshiichi Ozeki (ASAH)	J	①	1 2(a-1) 2(a-3) 2(a-4)	Standard <i>k-ε</i> & Low-Re <i>k-ε</i> (non-commercial)	Standard wall-functions & no-slip	43 × 48 × 43 43 × 52 × 55 42 × 62 × 46	✓	Velocity, air temperature, convective heat transfer rate & coefficient. Also time-dependent results

† ① Solution of convective heat transfer (nonisothermal CFD)
 ② Long-wave radiation coupled with CFD simulation
 ③ Solar insolation calculation
 ④ Time-dependent calculation with heat storage in walls
 ⑤ Automatic calculation of infiltration

§ Case 1 Natural convection (i.e. no ventilation) & black walls
 Case 2(a-1) Natural convection & white walls
 Case 2(a-3) Air conditioning without thermal stratification
 Case 2(a-4) Air conditioning with thermal stratification

Simulation cases

Four cases were chosen for simulation (Case 1, Case 2(a-1), Case 2(a-2) & Case 2(a-4)). Cases 1 and 2(a-1) had no ventilation (just natural convection and some infiltration), and black or white walls, respectively. Cases 2(a-2) and 2(a-4) had air conditioning (cooling), and a well-mixed state or thermally stratified state, respectively. Table 4.3.4 summarises the simulations carried out by each participant. All groups carried out steady-state simulations, at 14:00 hrs in each case. Additionally, time-dependent CFD simulation of one whole day was done by TUD, ASAH, and IET who used the multigrid method to accelerate solution.

Different CFD models used

Different CFD software codes, commercial as well as research codes developed by the participants, were used. Either the Finite Element Method or the more common Finite Volume Method of discretization was used. As for the turbulence model, the standard *k-ε* model was used. The low-Reynolds-number *k-ε* model was also used by ASAH to compare its performance with that of the standard one. It was expected to more accurately predict convective heat transfer from inside surfaces to the room air, since it allows a very fine near-wall grid to be used.

The three groups IET [Off et al., 1996], NTNU [Schild, 1996] and TUD [Fischer and Rösler, 1995, 1996] used CFD codes that were coupled with conjugate heat transfer models that could calculate boundary conditions automatically by solving conduction through the walls (also heat storage for IET and TUD) together with solar and long-wave radiation. NTNU additionally coupled an air-infiltration model with the CFD code. These coupled codes are recent research developments. No-one considered gas radiation.

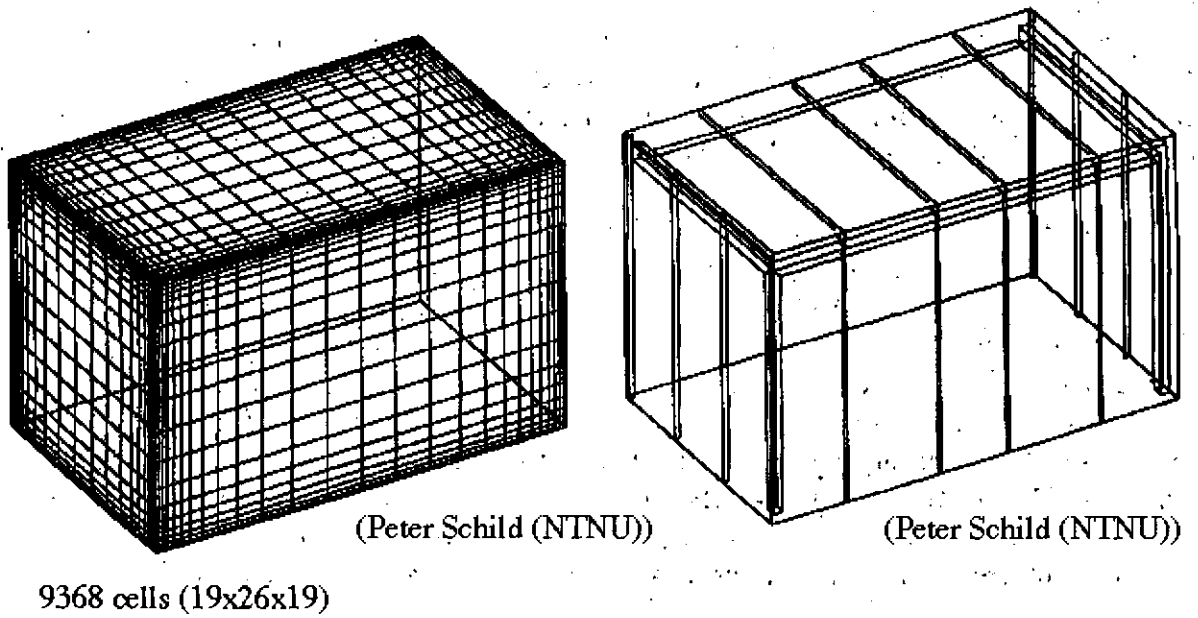


Figure 4.3.8 Example of computational grid and simplified modelling of steel frames in the CFD flow field. See Figure 4.3.10 for the geometric model in the two-band radiation analysis.

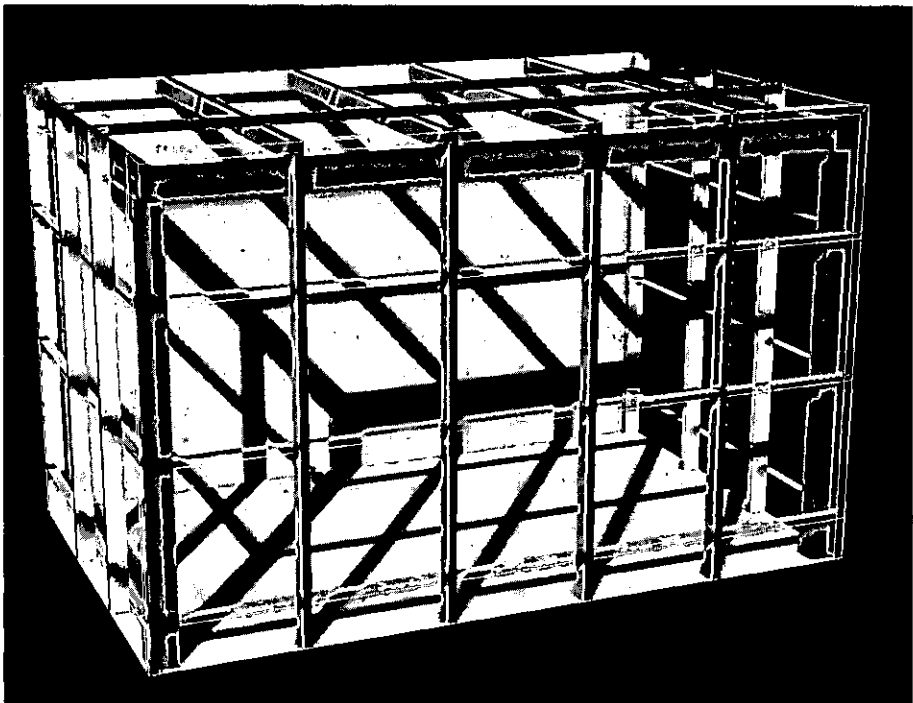


Figure 4.3.9 Example of solar radiation calculation [Schild, 1996].

Grid system and near-wall treatment

The presence of obstacles in the flow domain (i.e. steel frames) was considered by ENEA and NTNU. NTNU modelled all of the frames geometrically exactly in the boundary condition calculations (solar & long-wave radiation etc., Figure 4.3.10), but simplified the frames in the CFD grid whilst maintaining correct heat gain (Figure 4.3.8). Other groups neglected such obstacles.

Different grid systems were used by the different groups, though most used standard structured grid systems. Near-wall grid resolution also varied, according to the simulation conditions and the turbulence model used. ASAH used a fine grid system with the low-Reynolds-number k - ϵ model, and a so-called 'no-slip' wall condition for temperature and flow. The remaining groups used coarser grid systems with the standard k - ϵ model, and with log-law wall functions. The log-law wall functions used were almost invariably of the traditional forced-flow type, and are not strictly applicable to natural convection flow in the atrium. However, TUD used a new wall-function for natural convection [Yuan *et al.*, 1992, see also Section 2.4.5]. They could thus achieve predictions of convective heat transfer of reasonable accuracy, but without the burden of using a fine grid, as with a low-Re k - ϵ model.

Boundary conditions

Most groups made use of the experimentally measured surface temperatures for the boundary conditions in their CFD simulations. Three different methods were used for imposing these surface temperatures in the CFD analysis:

- A uniform surface temperature is given for each wall boundary. The imposed value for each wall is the plane-average of the measured surface temperature
- A uniform temperature was given on 9 areas of each wall boundary, one area corresponding to each measurement point
- Wall surface temperature distribution is given for the wall boundary by a linear interpolation of the measurement data between measurement points

As mentioned earlier, three groups (IET, NTNU and TUD) calculated their boundary conditions with a conjugate heat transfer model coupled to the CFD code (requiring only data on solar radiation, outside air temperature, wind, material properties etc.). These three groups therefore did not have to resort to applying the experimentally-determined surface temperatures as boundary conditions, as the other groups did.

The heat gain from the obstacles inside the computational domain (steel frames) was also considered by most of the participants' simulations. The surface temperature of the obstacles (the steel frames) and the prescribed convective heat transfer coefficient were used to manually calculate the convective heat gain from them. The heat gain from the frames was then imposed as a uniform heat source throughout the whole computational domain. However, three groups (IET, NTNU and TUD) distributed the heat sources more realistically, according to the positions of the frames.

For modelling of infiltration / exfiltration in the atrium, two methods were tried:

- Infiltration / exfiltration was modelled in a simple way, merely as a uniform heat sink throughout the whole computational domain

- Infiltration / exfiltration was modelled as a source / sink in each individual near-wall cell, under the assumption that each surface was uniformly porous. The effect of the incoming infiltration air on the momentum field was ignored

Almost all groups used the first method, hand-calculating the infiltration by empirical methods. NTNU tried both methods, and in addition, coupled an infiltration model with the CFD code to calculate infiltration automatically. This was a multizone stack-effect model, using leakage areas determined from pressure tests of the atrium's facades, as input data. This model was thus self-governing; the infiltration flow rate varied concurrently with the temperature field in the atrium.

Results

Air velocity and temperature distributions were obtained by all of the CFD modelling participants for the Japanese experimental atrium. Some groups also analysed the distribution of the convective heat transfer coefficient and flux. The results are documented in Figures 4.3.10 to 4.3.15.

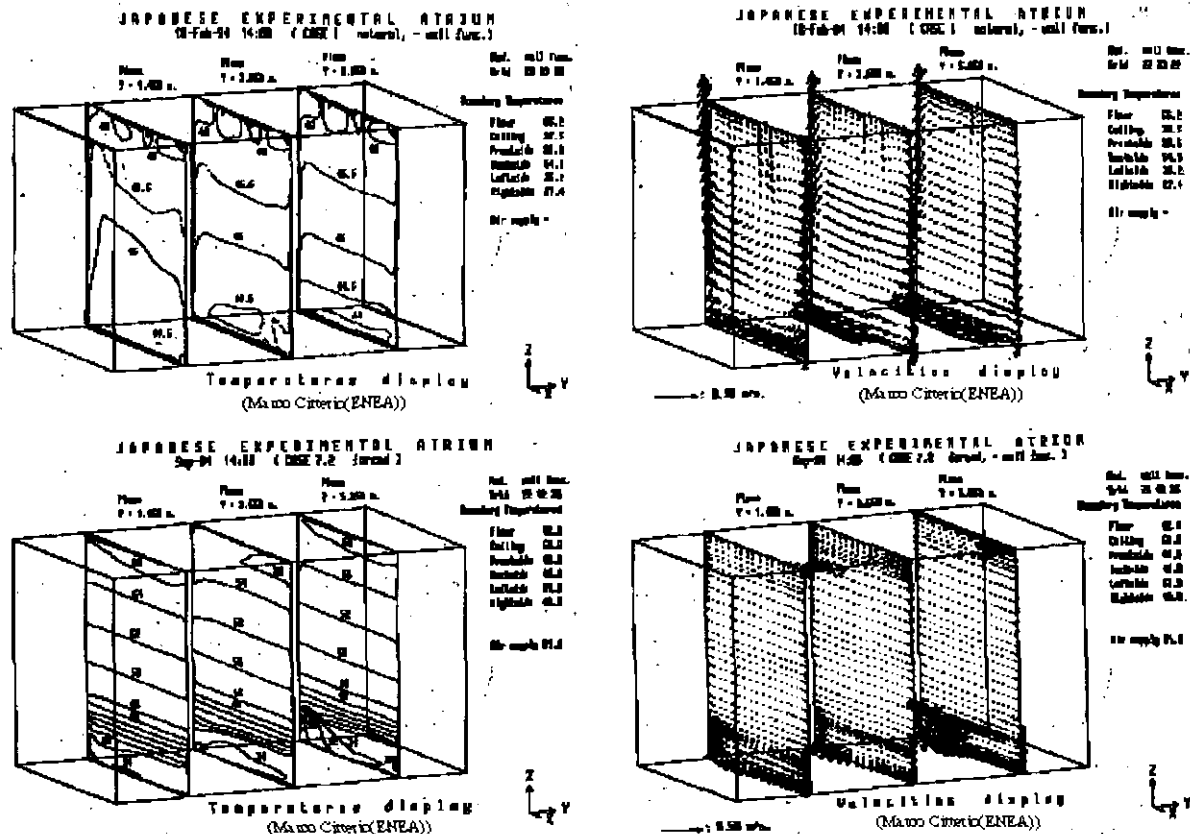


Figure 4.3.10: Examples of CFD predictions of temperature and velocity fields.

In the two natural convection cases, a gentle recirculation flow in the space was observed (Figure 4.3.10). This recirculation was driven by the sun-heated north wall and cooler east and south glass walls. In the air-conditioning (cooling) cases, a stratified air-temperature distribution with a vertical difference of 6–8°C was accurately predicted by all of the turbulence models. On the whole, small changes in the boundary conditions had little influence on the mean flow pattern in the room. Even if the geometry of the steel frames was

resolved in the CFD grid, and even if the wall temperature was given by interpolation instead of uniformly, the obtained flow and temperature distributions were not much different from that of the simplified CFD models. However, none of the predictions fitted the measurement data perfectly.

The temperature gradient obtained by the low-Reynolds-number k - ϵ model in the near-wall region is steep compared with the standard k - ϵ model (Figure 4.3.11). The boundary layer obtained by the low-Reynolds-number k - ϵ model is also thinner, as illustrated by a steeper near-wall velocity gradient (Figure 4.3.11). The space-averaged temperature is affected by the simulated convective heat transfer rate at the walls and by the amount of infiltration and heat gain from the steel frames. The latter two factors, heat loss/gain by infiltration and from the frames, had a significant influence on the predicted energy balance and hence air temperature. This suggests that it is critically important that the chosen boundary conditions impose a correct energy balance, whereas small cosmetic changes to the boundary conditions, that do not affect the energy balance, do not significantly improve the prediction of the airflow pattern and spatial temperature distribution in the space.

Figure 4.3.12 shows the convective heat transfer rate predicted by the different groups. Table 4.3.5 gives the associated heat transfer coefficients. The dependence of grid refinement on the convective heat transfer coefficients is observed in traditional log-law wall functions. The convective heat transfer rate was generally underestimated with coarse grids.

On the whole, the degree of correspondence between simulation and the experiment was fairly good (Figures 4.3.14 and 15). The discrepancies in the space-averaged temperature in the simulations is due mainly to the different assumptions concerning infiltration and heat gain from the steel frames, which account for most of the thermal mass in the atrium. Accurate estimation of these factors is therefore necessary to predict airflow and temperature distributions in any computer simulation of atria. The simulations are not entirely to blame; the measured values had a scattered tendency. It is reasonable to assume that the measured air temperature was affected a small amount by radiation from the sun and from hot steel frames, an error that was obviously not duplicated in the CFD calculations.

As mentioned earlier, coupled CFD analysis, incorporating a two-band radiation model, was carried out by IET, NTNU and TUD. For all three research laboratories, the predicted space temperatures were about as accurate as the predictions of the other laboratories. This is a very good result in itself, considering the added difficulty of calculating boundary conditions from basic weather data etc. The evident discrepancies between the coupled simulations and the experiment may be due to a combination of reasons. One reason is that the thermal mass, especially the collective storage effect of the steel frames, is very large, and was difficult to address accurately. NTNU stressed the need for accurate treatment of the frames in the solar radiation calculations, as more than a quarter of the internal solar gain was absorbed by frames in the atrium even though the glazing frames covered only 10% of the facade. The shading effect of the frames therefore cannot be neglected (Figure 4.3.9). Finally, the measurement data, such as material properties, obviously had an element of uncertainty, and the room temperature was slightly affected by radiation from the sun and hot steel structure.

Figure 4.3.13 shows an example of the time-dependent results of IET, TUD and ASAH, for which the solar radiation simulation, the coupled simulation with CFD and the long-wave radiation simulation were performed over a whole day. Though the computation cost (CPU time and memory/disk requirements) was huge, the detailed physical features that occurred in the space were carefully analysed.

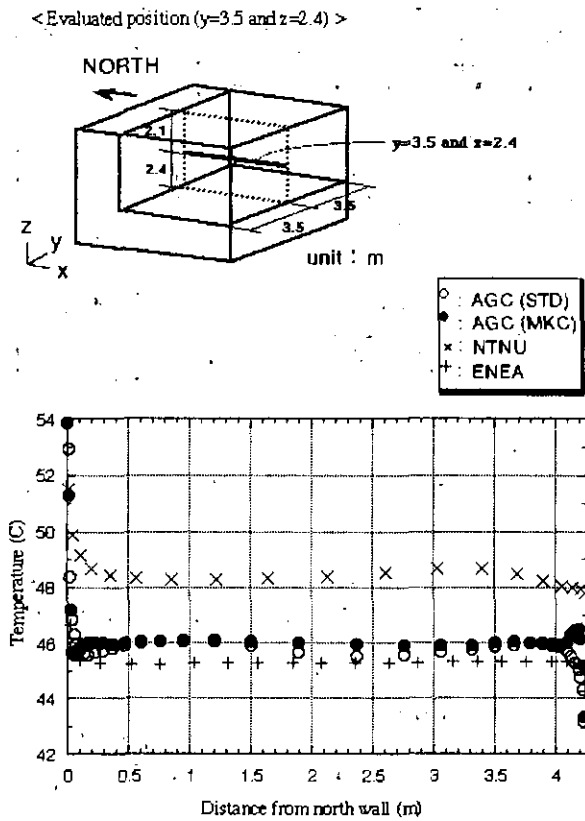


Figure 4.3.11a Air temperature profile across enclosure at y=3.5, z=2.4m (Case 1).

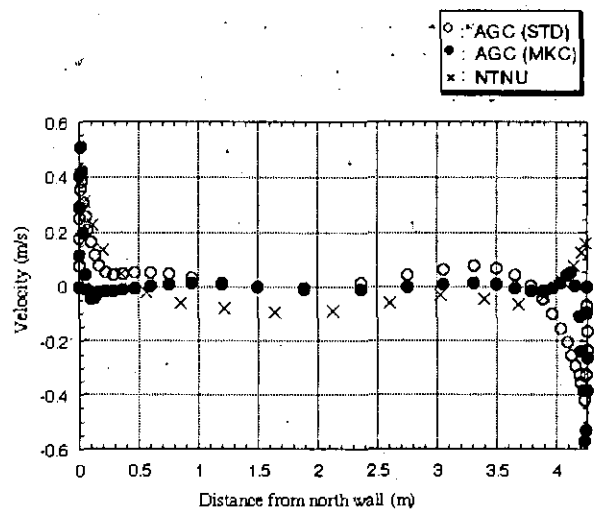


Figure 4.3.11b Velocity profile across enclosure, at y=3.5, z=2.4m. (Case 1).

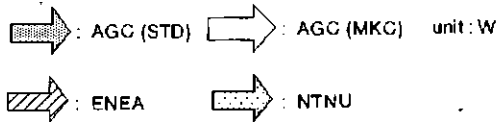
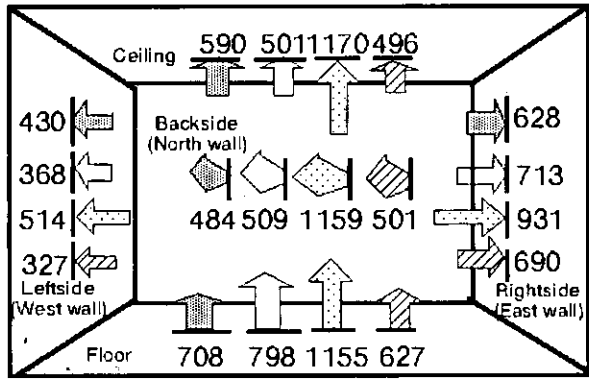
Table 4.3.5 Predicted convective heat transfer coefficients [W/m²K].

(a) Assuming the air temperature about 5cm from the wall as the heat transfer air temperature

case	Case 1				Case 2(a-1)					Case 2(a-4)		
	AGC (std. k-ε)	AGC (MKC)	ENEA	NTNU	AGC (std. k-ε)	AGC (MKC)	ENEA	NTNU	TUD	AGC (std. k-ε)	AGC (MKC)	ENEA
Front glass	1.5	1.2	1.6	2.3	1.6	1.4	1.9	2.2	3.4	1.1	1.5	5.9
Right glass	1.9	2.0	2.3	2.6	1.6	1.8	2.0	2.7	3.5	7.2	6.7	2.3
Left glass	2.3	1.9	1.9	2.7	1.7	1.4	1.5	1.8	2.9	5.8	6.0	2.7
Roof glass	2.3	1.7	1.8	2.6	2.0	1.2	2.0	2.3	2.7	6.3	5.6	16.8
Floor	2.5	2.5	2.1	2.6	2.5	2.7	1.7	2.2	3.0	8.2	8.6	4.7
Back wall	2.0	1.8	1.9	3.0	1.6	1.5	0.9	2.1	2.6	7.4	6.2	0.7

(b) Assuming room bulk air temperature (volume-weighted average) as the heat transfer air temperature

case	Case 1				Case 2(a-1)					Case 2(a-4)		
	AGC (std. k-ε)	AGC (MKC)	ENEA	NTNU	AGC (std. k-ε)	AGC (MKC)	ENEA	NTNU	TUD	AGC (std. k-ε)	AGC (MKC)	ENEA
Front glass	1.2	1.1	1.7	2.4	1.4	1.4	1.7	2.4	3.6	1.5	2.0	6.9
Right glass	1.8	2.0	2.0	2.5	1.5	1.8	1.8	2.6	3.4	7.1	6.5	2.5
Left glass	2.1	1.8	1.7	2.7	1.6	1.4	1.4	2.7	2.9	5.1	5.7	1.7
Roof glass	2.3	1.9	1.9	2.9	1.8	1.2	3.0	2.6	4.2	5.8	5.1	5.2
Floor	2.6	3.0	2.1	2.6	4.0	5.8	2.3	2.5	6.9	8.4	8.8	6.1
Back wall	1.7	1.8	1.6	2.9	1.3	1.6	0.8	2.0	2.4	7.3	6.1	0.7
Bulk temp.	45.6°C	45.7	45.2	48.6	46.0	46.2	45.4	46.6	44.5	48.4	48.3	47.3



< Heat loss at south wall >

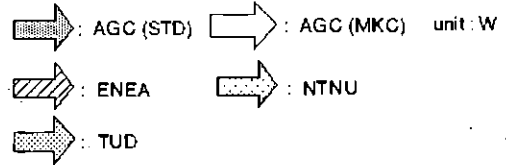
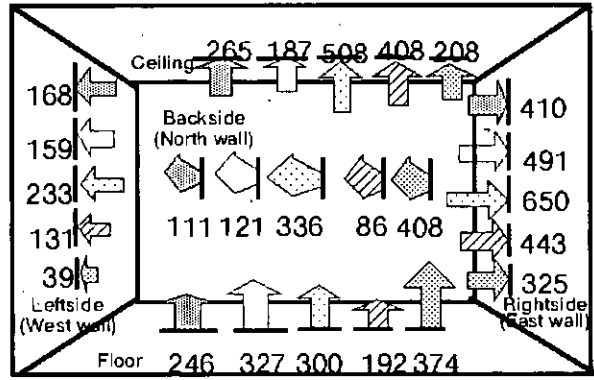
- 216W (AGC (STD)) , • 203W (AGC (MKC))
- 554W (NTNU) , • 300W (ENEA)

< Heat gain from steel frame >

- 688W (AGC) , • 2041W (NTNU)
- 688W (ENEA)

< Infiltration >

- -1570W (NTNU)



< Heat loss at south wall >

- 292W (AGC (STD)) , • 290W (AGC (MKC))
- 467W (NTNU) , • 346W (ENEA)
- 230W (TUD)

< Heat gain from steel frame >

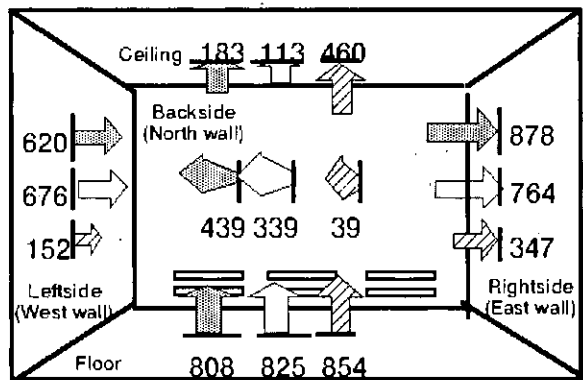
- 1051W (AGC) , • 1854W (NTNU)
- 1052W (ENEA) , • 348W (TUD)

< Infiltration >

- -737W (NTNU)

Figure 4.3.12a Predicted convective heat transfer rate for Case 1 (no ventilation).

Figure 4.3.12b Predicted convective heat transfer rate for Case 2(a-1) (no ventilation).



: AGC (STD) : AGC (MKC) unit: W
 : ENEA

- ◁ Heat loss at south wall ▷
 - 13 W (AGC (STD)) , • 23 W (AGC (MKC))
 - 146 W (ENEA)
- ◁ Heat gain from steel frame ▷
 - 2101 W (AGC) , • 1868 W (ENEA)
- ◁ Heat load of air conditioning ▷
 - 2969 W (AGC (STD)) , • 2892 W (AGC (MKC))
 - 1950 W (ENEA)

Figure 4.3.12c Predicted convective heat transfer rate for Case 2(a-2) (air cond.).

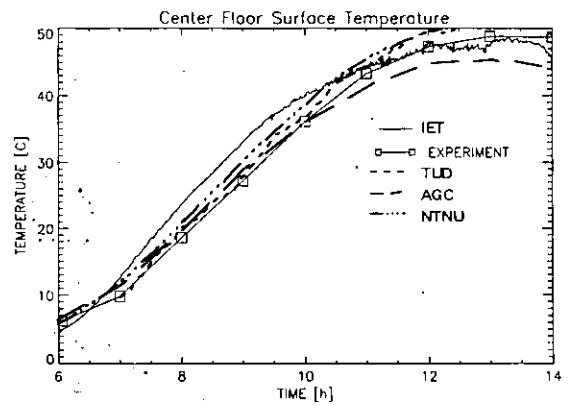
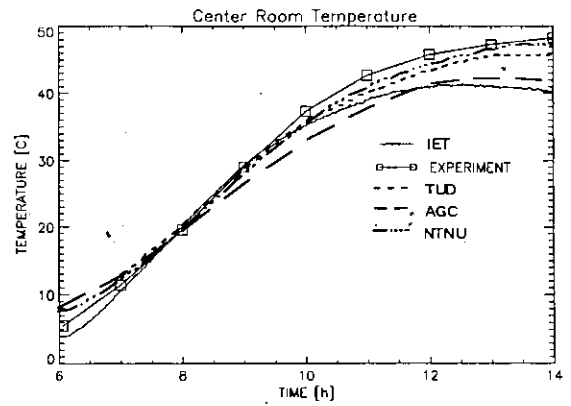
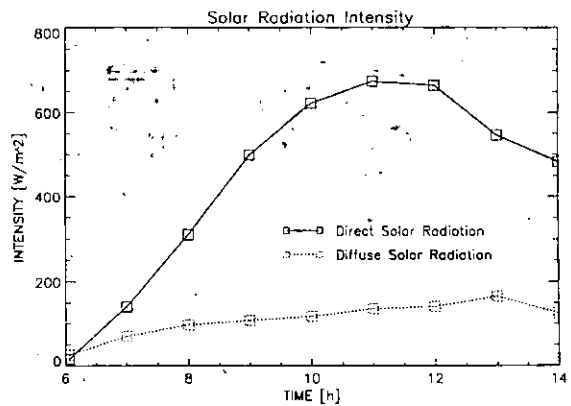


Figure 4.3.13 Example of time-dependent CFD analysis of IET, TUD and ASAH, and single-zone analysis of NTNU.

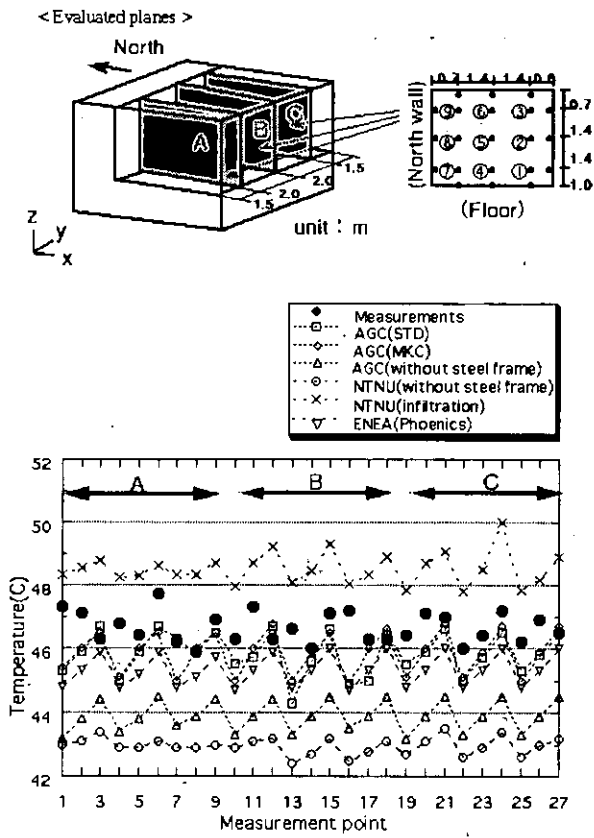


Figure 4.3.14a Predicted vs. measured air temperature distribution for Case 1 (no ventilation, black walls).

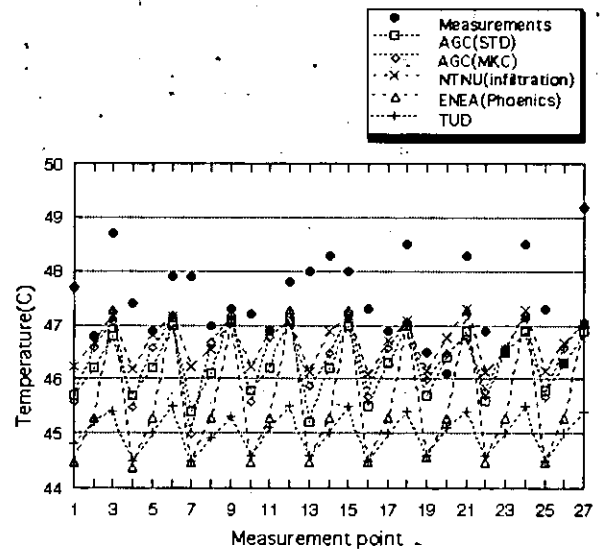


Figure 4.3.14b Predicted vs. measured air temperature distribution for Case 2(a-1) (no ventilation, white walls).

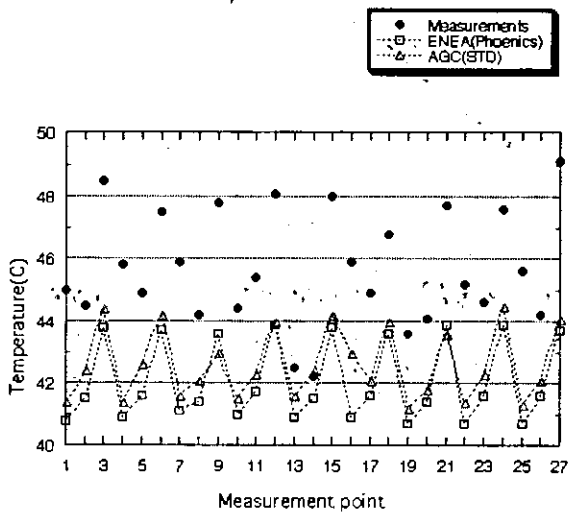


Figure 4.3.14c Predicted vs. measured air temperature distribution for Case 2(a-2) (air conditioned, fully mixed).

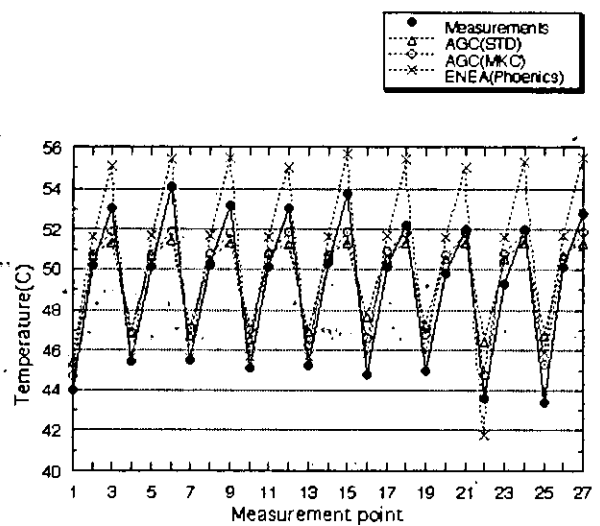


Figure 4.3.14d Predicted vs. measured air temperature distribution for Case 2(a-4) (air conditioned, thermally stratified).

< Evaluated planes >

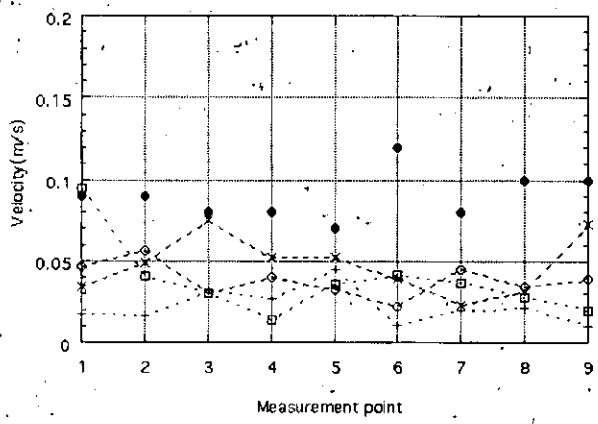
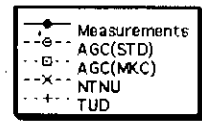
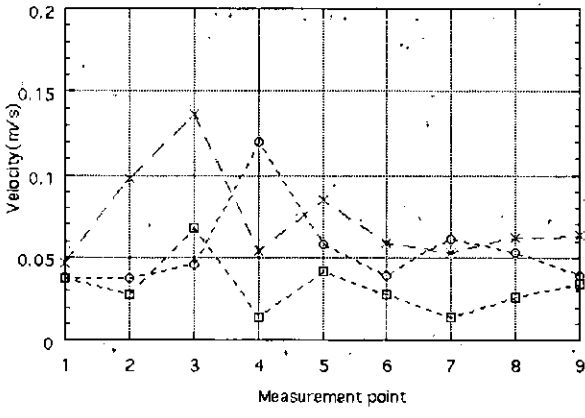
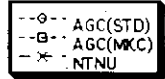
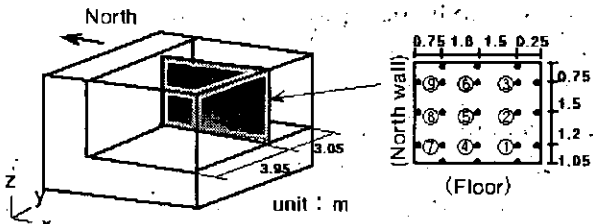


Figure 4.3.15a Predicted and measured air velocity for Case 1 (no ventilation, black walls).

Figure Figure 4.3.15b Predicted and measured air velocity for Case 2(a-1) (no ventilation, white walls).

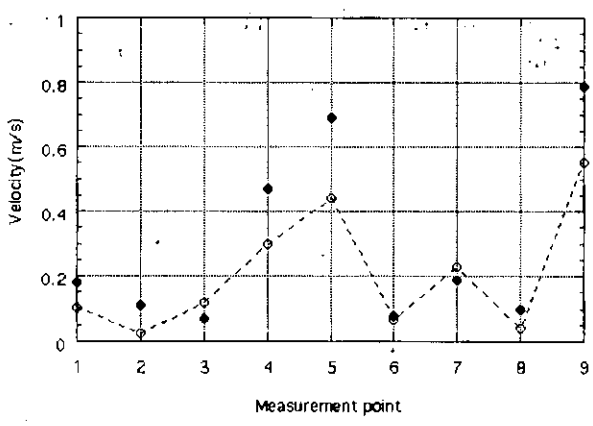


Figure 4.3.15c Predicted and measured air velocity for Case 2(a-2) (air conditioning, fully mixed).

Zonal models

A zonal model is one in which the room volume is subdivided into a few macro-volumes (zones), far fewer than in CFD. Mass and thermal balances are estimated for each zone to calculate the indoor air temperature field. This requires significantly fewer calculations than CFD. Several participants in Annex-26 performed zonal model simulations.

NTNU used a single-zone model coupled with their aforementioned model for conjugate heat transfer and infiltration, that feeds on weather, geometry & materials data. The time-dependent predictions of room bulk temperature were as accurate as the CFD predictions, though only for the cases with fully-mixed airflow (see Figure 4.3.13). Single-zone models are not discussed further here, as they are only suitable for fully-mixed airflow.

Three kinds of multizone model were tested. They all behaved similarly, so only the results of INSA [*Inard, 1996*] are reported here. This model captured the behaviour of the supply jet and agreed well with the experiments. All three are covered by Ozeki and Kato [*1996*].

Simulation case

Case 2(a-4) was chosen for simulation. In this case, air-conditioning (cooling) was used and the indoor air was thermally stratified.

Calculation conditions

The 3-dimensional simulation domain was subdivided into $4 \times 3 \times 10$ and $4 \times 3 \times 9$ zones. The measured inner surface temperature, air supply temperature and air flow rates were given as boundary conditions. Fixed convective heat transfer coefficients were used: $3 \text{ W/m}^2\text{K}$ at the floor & roof; and $1.5 \cdot \Delta T^{1/3}$ at vertical walls. Heat gain from the steel frames was distributed according to their position in the thermal balance equation. No adventitious air leakage (infiltration) was considered.

Results

The calculation results were obtained for every hour of the measurement day. Figures 4.3.16 and 17 show the predicted vertical temperature distributions and the comparison between the simulation and the experiment. The multizone model functioned very well in predicting the thermal stratification of the air. The success was due in part to the use of realistic convective heat transfer coefficients.

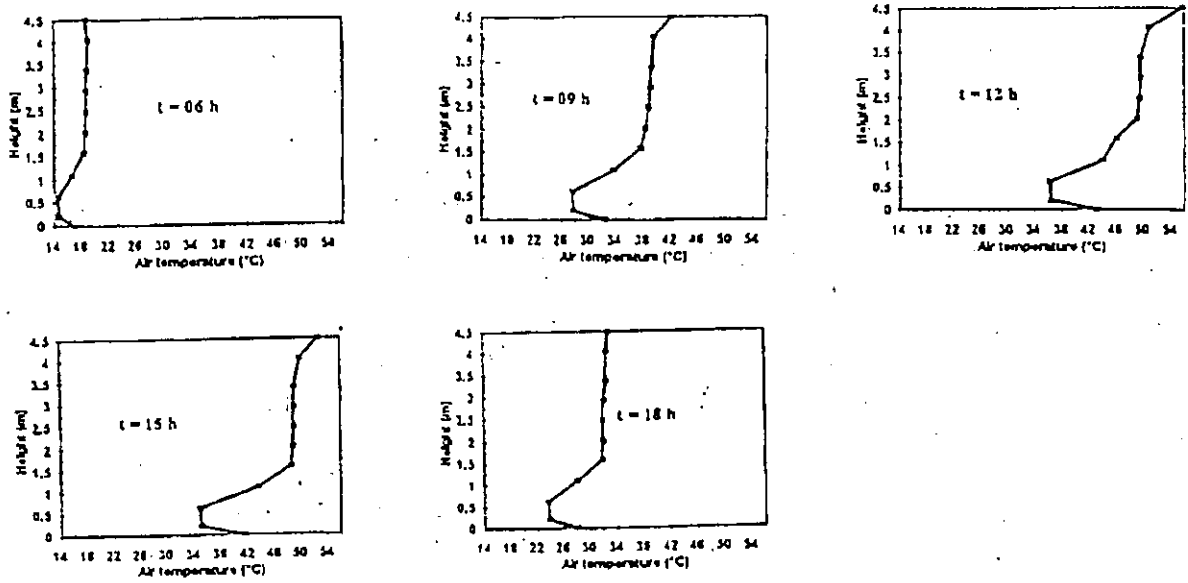


Figure 4.3.16 Vertical temperature profile predicted by 3D zonal model.

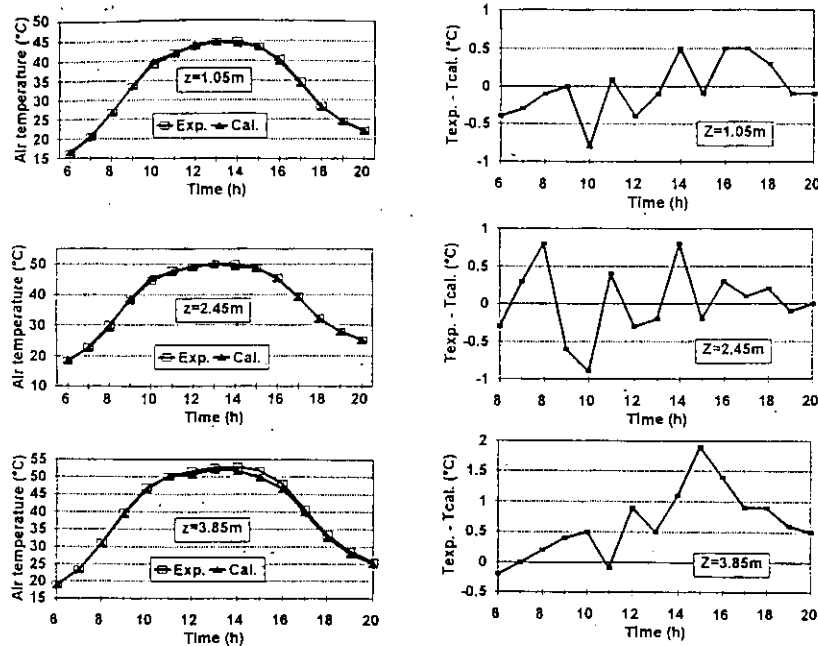


Figure 4.3.17 Time-dependent zonal model predictions vs. measurements of air temperature at three different heights in the atrium..

Performance of tools and comparison of results

CFD

Convective heat transfer rate: The convective heat transfer rate predicted by the different researchers was scattered over a rather wide range. When the traditional log-law type wall function is applied, the predicted heat transfer rate is affected by the coarseness of the near-wall grid. These wall functions are not strictly meant for flow where there is buoyancy-driven heat transfer. New wall functions for natural convection, used by TUD, worked very well, but

were not completely independent of near-wall grid size. TUD had to do some preliminary tests before every new situation to optimise the near-wall grid and hence get reliable heat transfer coefficients. NTNU used the same principle as a stop-gap to better predict convective heat transfer with log-law wall functions [Nui and van der Kooi, 1992]. The low-Reynolds-number type k - ϵ model, which does without any wall-functions, presumably gave the best prediction of wall heat transfer. However, it requires significantly more computation time and is difficult to use in practical applications. Therefore, the k - ϵ turbulence model with a finer grid, and the new wall functions covered in Section 2.4.5, is probably the best bet for practical design use at the current time.

Simplification of boundary conditions: Steel frames can make up an enormous total surface area in large glazed enclosures, and so strongly affect the temperature field. In the case of the Japanese experimental atrium, the surface area of the steel structure is about two and a half times the floor area. This is larger than the combined area of the floor and the north wall, which are the two opaque surfaces. It should therefore be noted that occasionally the solar gain to the steel structure, and the structure's thermal capacity, must not be neglected in atrium design.

Coupled simulation analysis with CFD: The solar radiation analysis satisfactorily reproduced the solar insolation of the large glazed enclosure. The structural frames are a considerable source of solar heat gain to the space, so simplifying the shading effect of the steel structure, affected the simulation results significantly. Solar radiation analysis should therefore accurately resolve their shading effect.

In an enclosed space, heat transfer occurs by both convection and radiation. Coupled simulation by two-band radiation (short & long-wave) and CFD is therefore crucial to correctly analyse heat transfer in all enclosures with windows, not only atria.

The coupled infiltration model performed well, despite being simple. For this atrium, the natural ventilation (no ventilation) cases had a significant amount of infiltration. As the airflow was well-mixed, it was quite satisfactory to assume that the infiltration heat loss was uniform throughout the space.

Zonal models

The multizone models reproduced thermal stratification very satisfactorily, including the model that captured the effect of the jet stream momentum. Not surprisingly, single-zone predictions of surface temperatures and bulk air temperature in the two natural convection cases, were as accurate as the CFD predictions [Schild, 1996]. This is fortuitous however, as these cases had fully mixed airflow. The single-zone model would be expected to perform less well in predicting the energy balance in cases where there are temperature or airflow gradients in the space, such as the air-conditioned case with thermal stratification.

4.3.5 Conclusions and Recommendations

Measurements

A long term observation (about two years) was made of the indoor climate of an experimental full-scale atrium (the Japanese experimental atrium for the IEA Annex-26 collaborative study). The structural steel frames and glazing frames considerably affect the thermal environment. The affect of the factors on the indoor thermal environment and on the heat budget have been analysed in detail.

Analysis tools: CFD and zonal models

CFD used with a suitable turbulence model, such as the k - ϵ model, can be a reliable prediction tool. Simplifications to the boundary conditions that affect the space heat balance, generally result in incorrect prediction of indoor climate. However, small-scale changes in boundary conditions do not greatly affect the qualitative characteristics of the flow field and temperature distributions.

The traditional log-law type wall function can not reliably calculate convective heat transfer. Instead, when a coarse grid is used, it is preferable to use prescribed convective heat transfer coefficients in place of wall functions. It is not so easy to specify the appropriate value of convective heat transfer coefficient for various situations, but reasonable correlations have been developed for this purpose [see Section 2.4.5]. For more accurate analysis, the k - ϵ turbulence model with a finer grid, and possibly new wall functions that are valid for natural convection flow, is probably the best bet for practical design use at the current time. A great wish for the future is that new *universal* wall-functions (i.e. for forced/mixed/natural convection), that are amply grid-independent, will be developed. Promising work on this task has already been done by Neitzke [1996].

The multizone models satisfactorily reproduced the vertical temperature distribution in the large atrium even when the air was thermally stratified. For zonal models, it is also important to specify rational values of convective heat transfer coefficient.

4.4 Fibreglass Reinforced Polyester Factory, Caen, France

4.4.1 Description of the Workshop

Introduction

This case-study enclosure is a workshop for the production of fibreglass reinforced polyester, located in Normandy. This new facility has been used since May '94 for the production of polyester components of various shapes and sizes. The process is carried out manually by spreading styrene resins over moulds, so workers are potentially exposed to styrene vapour.

Site and location

Located 48°31 N and 0°33 E, the building is surrounded by agricultural fields and shrubs in a relatively flat area. The main ventilated workshop is adjacent to the office building as well as to an older moulding workshop.

Building form

The overall dimensions of the workshop are 35m×6m×42m, with an internal volume of 8820 m³ (Figure 4.4.1). The new workshop communicates with the older one through two large openings (size 4m×4m). There are no major doors to the outside.

Building services

The ventilation system

The ventilation system has been designed according to two main criteria: the extraction of styrene and temperature control. As a matter of fact, a uniform temperature of about 20°C is needed for the chemical reactions to occur in styrene resins. Moreover, styrene concentrations within the enclosure must remain below the maximum exposure limit (50ppm in France).

A mixing ventilation principle has been chosen to complete these goals. No heat recovery system has been introduced. The actual design was made according to dilution calculations with a safety ratio of 4 regarding styrene, so that the theoretical fresh air flow rate equals 70000 m³/h (42000 m³/h for extraction). This corresponds to an air change rate of about 8 volumes per hour. As the building is overpressured, the residual flow rate supplies the adjacent workshop through the two large openings.

Fresh air is supplied by 20 identical spherical inlet units located 4m over the floor. 24 exhaust grilles are located at floor level. The air is supplied by two independent fans (10 inlets per fan) and heated in two air handling units.

The heating system

The two air handling units are located on the roof of the building. They are controlled by two indoor sensors located on opposite walls of the building, one for each system.

Specific features

The main pollution sources are located on moulding tables. There are about 40 in the whole space. Styrene emission is regarded as difficult to estimate since it relies more on the mould area than on the total amount of styrene used and since fabrication requires moulds with

various shapes and sizes at the same time. Total styrene emission was estimated at 3.75 kg/h for the whole workshop.

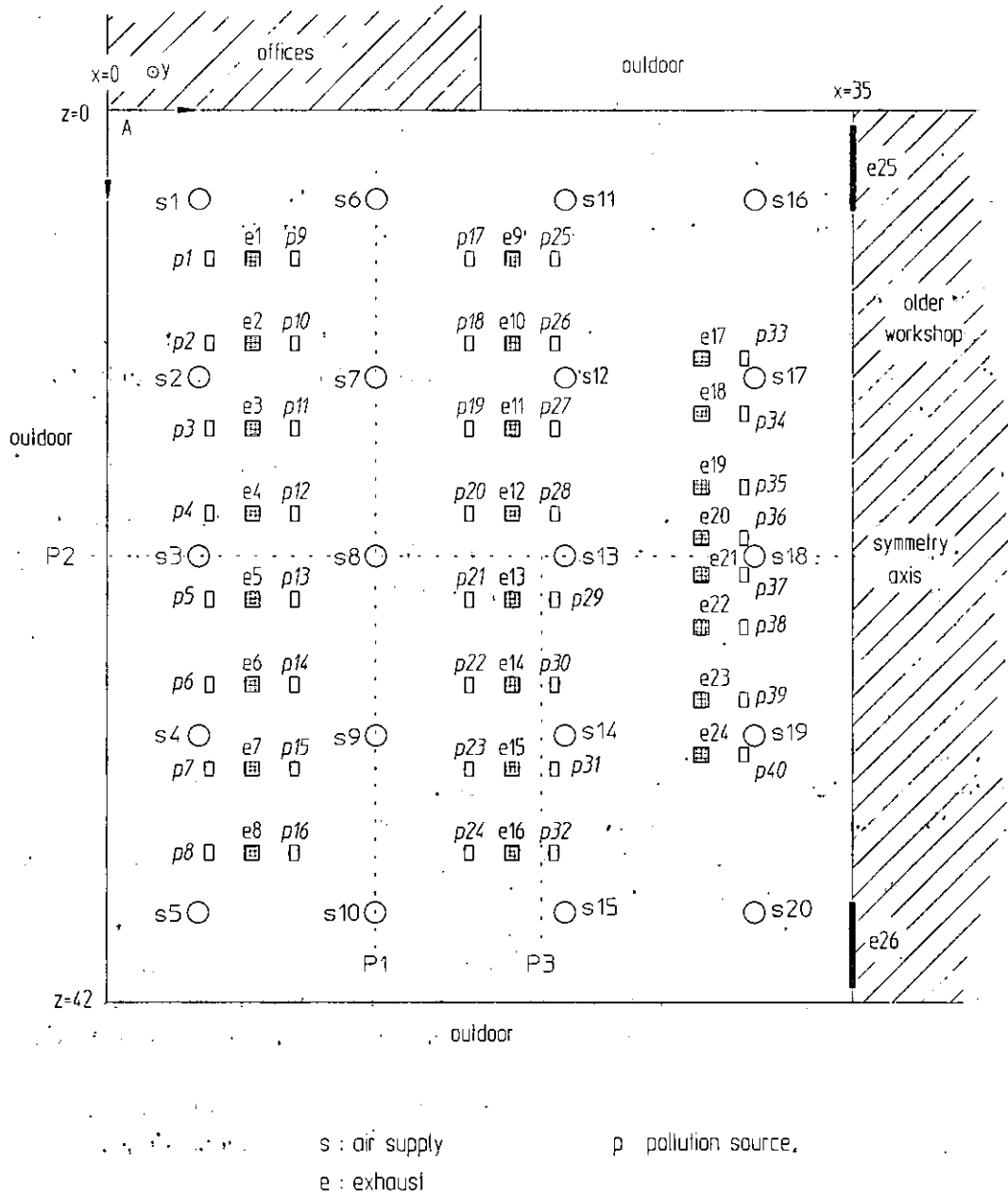


Figure 4.4.1 Plan of the polyester workshop.

4.4.2 Examples of Measurement and Analysis Tools

Measurements

No reliable energy performance data are available for the building. However, considering the flow rates and differences between outdoor and indoor temperature, heating costs must be high, since there is no heat recovery.

Measurements including styrene concentration, air temperature, omnidirectional and vectorial velocities (joint measurement campaign by FIOH and INRS) were made in the bulk of the workshop. Sections of the building were investigated by moving a mast equipped with all sensors on the same profile [Koskela et al., 1996a]. Two sections of the building are described here (vertical sections P1 and P2 in Figure 4.4.1): one in a corridor in between the moulding tables and along with a supply duct including 5 inlets (Figure 4.4.2); the second in the symmetry plane of building very near the moulding tables and across the two supply systems (2 supplies for each one) (Figure 4.4.2).

The first part of the measurement campaign concerned the boundary conditions of the ventilation system. The total fresh air and extract flow rates were estimated to be 46600 m³/h and 36100 m³/h respectively. Mass balance is achieved by airflow through the two large openings of about 7000 m³/h and 3500 m³/h respectively. This gives 5 air changes per hour.

The ventilation system seems to comply with the two main objectives given by the building designer. As a matter of fact, temperature gradients stay within a 1~2 degree range. As regards styrene concentrations, they remain mostly in a 20~30 ppm interval, except in some regions where very large moulds were used (Figure 4.4.3). As far as velocity fields are concerned, no clear flow pattern can be extracted from the measurements. Air jets resulting from the inlets can interact with each other and seem to have an erratic behaviour from one terminal device to another. Moreover, velocity profiles are complex and vary from one device to another (Figure 4.4.4). Finally, omnidirectional velocities are generally over 0.2~0.3 m/s, which means that the ventilation system is working as designed.

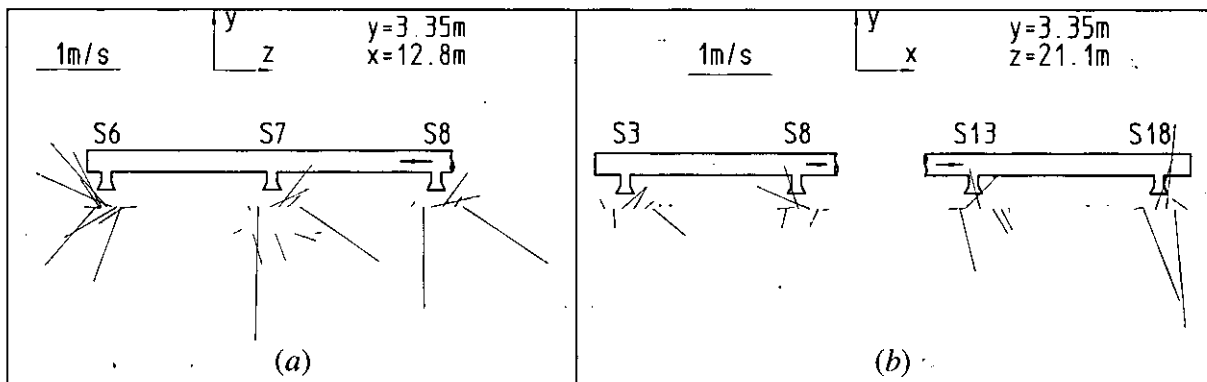


Figure 4.4.2 Examples of air velocity vectors as measured on site (a) P1; (b) P2.

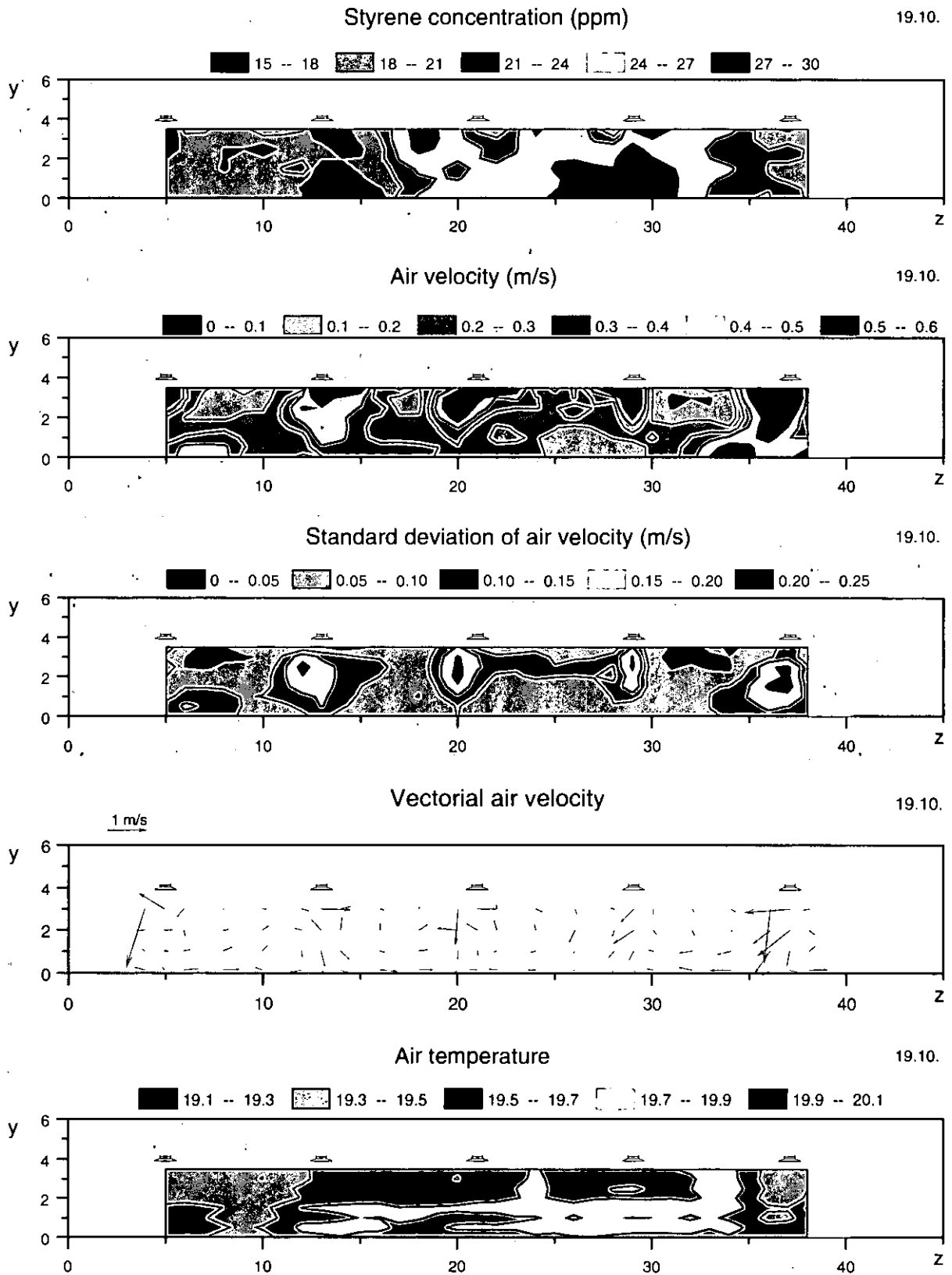


Figure 4.4.3 Measurement results in section $x=12.8\text{m}$ (units: concentrations in ppm of styrene; velocities in m/s; temperature in $^{\circ}\text{C}$).

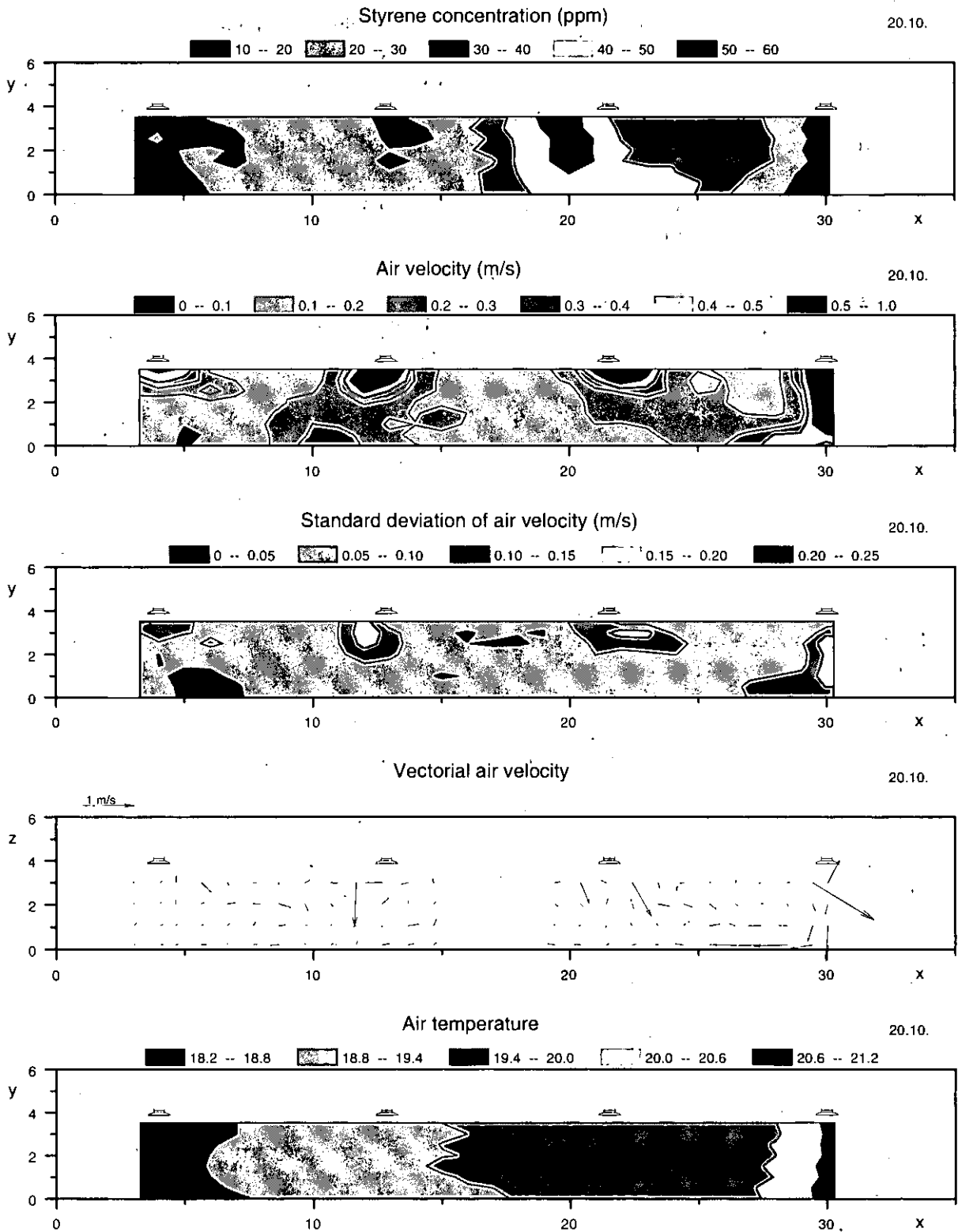


Figure 4.4.4 Measurement results in section $z=21m$ (units: concentration in ppm of styrene; velocities in m/s; temperature in °C)

Analysis tools

Assumptions

Due to the geometrical complexity, simulation tools were applied with some extra assumptions. Firstly, velocity profiles at supply devices were supposed to be isotropic around anemosthats (45° angle with vertical axis) and zero in the middle of them. Measured flow rates are available for each inlet. A symmetry plane $z=21\text{m}$ can be imposed, since flow rates through the large openings are low compared with the total fresh air volumes. No furniture or other obstacles, apart from ventilation ducts, were included in the occupied zone.

The styrene is supposed to be emitted at the 40 working places at the total flux of 3.75 kg/h. Two configurations are considered:

- Uniform flux over the 40 sources
- Fluxes weighed by estimated mould sizes. (The pollutant sources in each of the five north-south rows in Figure 4.4.1 had coefficients 1, 1, 4, 4 and 0.5 respectively)

Simulation attempts

Below is listed the two kinds of numerical simulations that were used. Table 4.4.1 presents a digest of these simulations including some basic characteristics.

- Zonal model (1 attempt)
- CFD model based on $k-\varepsilon$ turbulence model (4 examples)

Computed styrene concentration (Figure 4.4.5) and velocity (Figure 4.4.6) fields were gathered for vertical sections P1, P2 and P3. Emphasis was given to sections P1 and P2, for which measurements are available. The zonal model could only give information on concentration, whereas the CFD codes provided both velocity and pollutant concentration fields. Results were also presented for a horizontal plane, P4, which is the plane 1.5 m above the floor, i.e. at breathing level, of concentration (Figure 4.4.7) and age-of-air fields (Figure 4.4.8).

Table 4.4.1 Summary of simulations.

Author	Index	Simulation	Code	Symmetry plane	Grid points	Boundary conditions	Inlet velocity profiles	Global removal efficiencies.	
								uniform	weighted
J. Heikkinen (VTT, Finland)	F1	CFD (k-ε)	CFDS-Flow3D (CFX)	no	127000	measured	as specified	0.96	1.14
S. Collineau (INRS, France)	F2	CFD (k-ε)	EOL-3D	yes	88000	measured	as specified	1.02	1.17
C. Inard (INSA, France)	F3	Zonal model	SAMIRA	no	10750	measured	radial jet model	1.26	-
T. Lemaire (TNO, Netherlands)	F4	CFD (k-ε)	WISH3D	no	189000	measured	as specified	-	1.28
P.O. Tjelflaot (NTNU, Norway)	F5	CFD (k-ε)	Kameleon II	yes	63000	theoretical	porous surface cells	1.13	-

Influence of the symmetry hypothesis

In the CFD calculations, no significant asymmetry was detected in the velocity fields in sections P1 or P3. As regards styrene concentrations (Figures 4.4.5a), the flow rate difference between the two openings has a locally limited effect; for example, pollutant removal is better

at pollution sites p25, p26 & p33 (Figure 4.4.1) than on the other side of the workshop. However, this difference is no longer detectable in the region $x < 17\text{m}$ in the CFD calculations. Finally, the zonal model (F3) proved to be more sensitive to asymmetry than the CFD models; the concentration field in plane P1 was strongly asymmetrical.

Comparison between simulation models

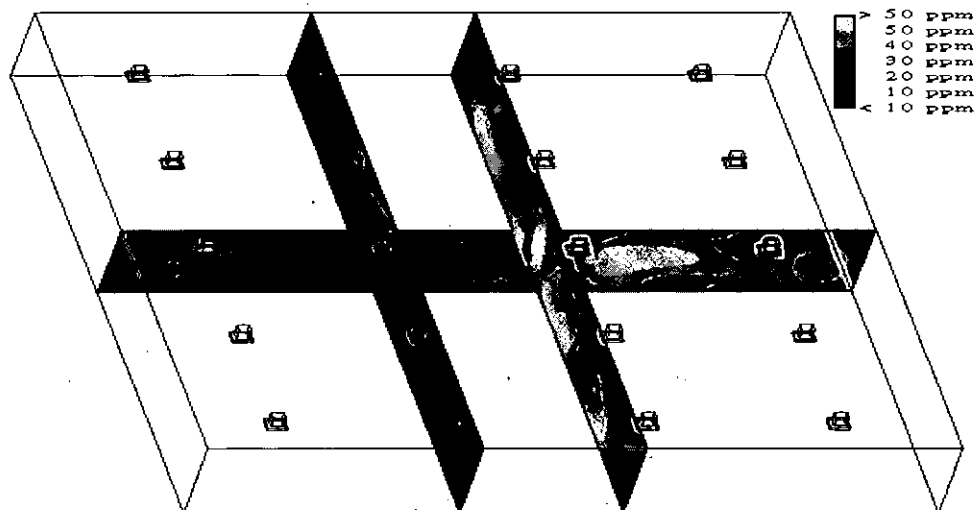
In a factory like this, which has efficient mixing ventilation, the level of styrene concentration depends mostly on the ventilation flow rate. This is why the models agreed with each other on this topic. In model F1 the most polluted area is larger than in the others. These differences may arise from the modelling of sources, either pointwise or surface-averaged.

As far as mean velocities are concerned, all CFD simulations agreed on very small values in the volume of the workshop except in the near vicinity of air jets.

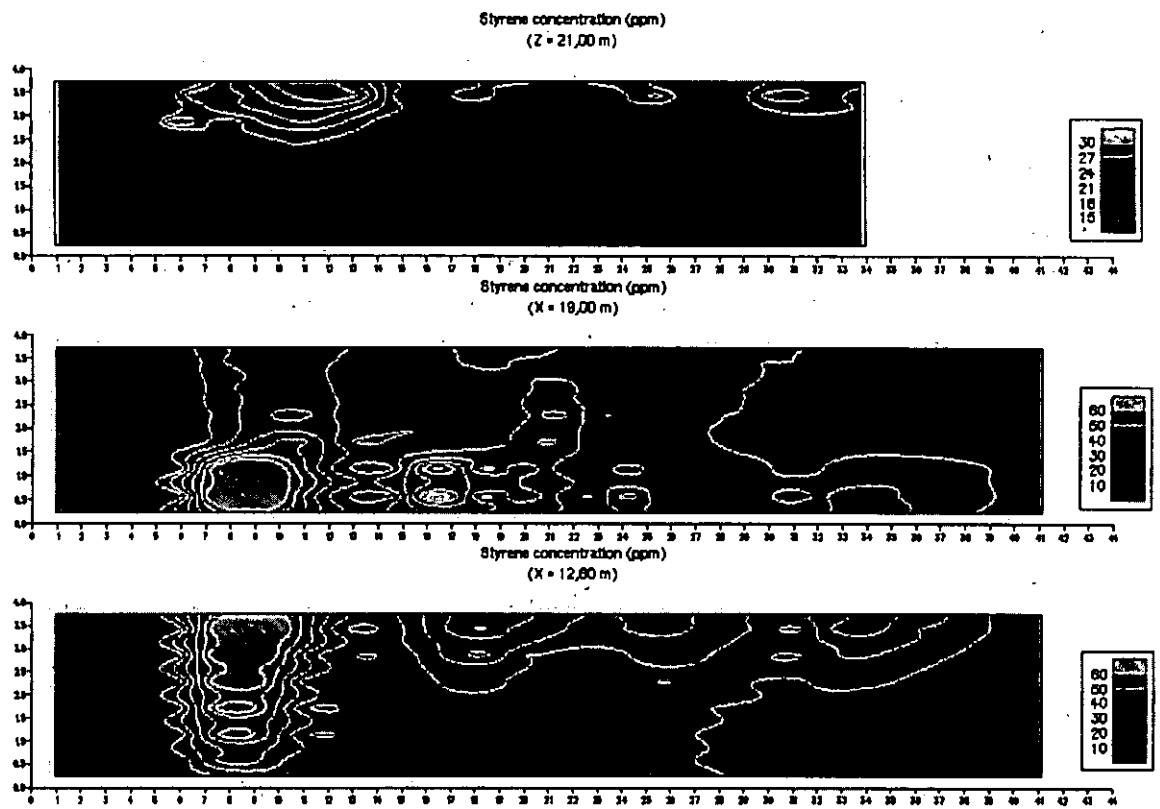
Finally, all the CFD calculations agreed with each other about the occurrence of upward air motion taking with it styrene vapour.

Main conclusions taken out of simulations

- Mixing ventilation induces very complex flows
- Upward air motion between jets lead to pollutant dispersion in the upper part of the workshop
- Horizontal pollutant dispersion occurs at breathing level (Figure 4.4.7)
- Actual flow rates are sufficient to dilute styrene vapour below the TWA
- The flow rate difference between the two openings has a locally limited effect
- Velocities in the bulk of the workshop are very low (typically $< 0.1\text{ m/s}$)
- No clear influence of the grid size can be detected from the CFD calculations



(a)



(b)

Figure 4.4.5 Concentration fields (ppm of styrene) in sections P1, P2 or P3 for (a) F1 (weighted sources) and (b) F4 (weighted sources).

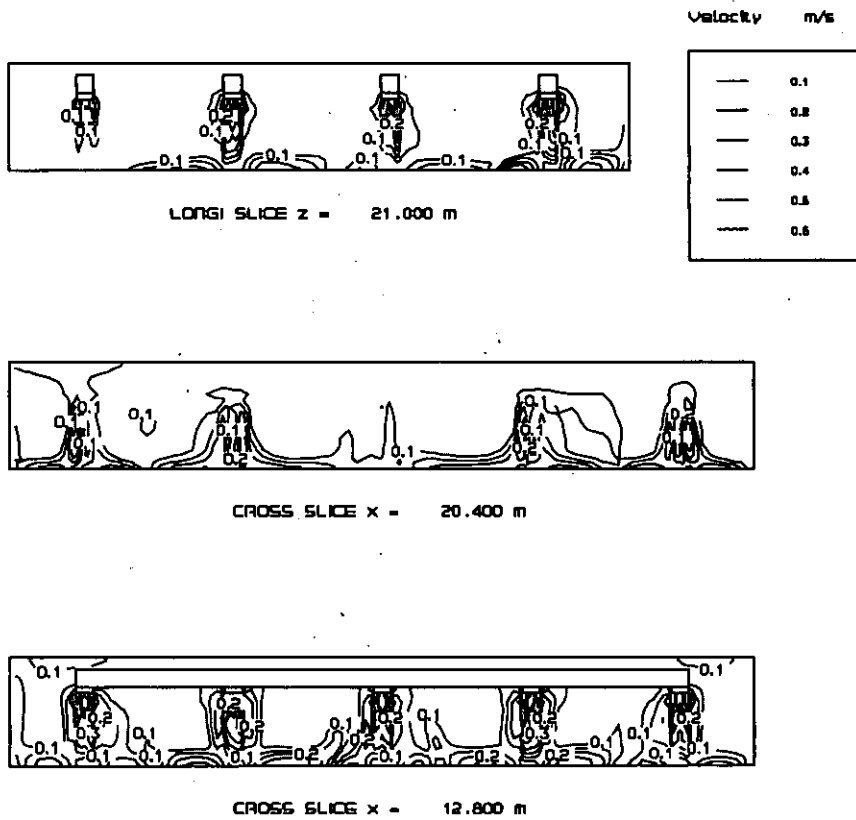
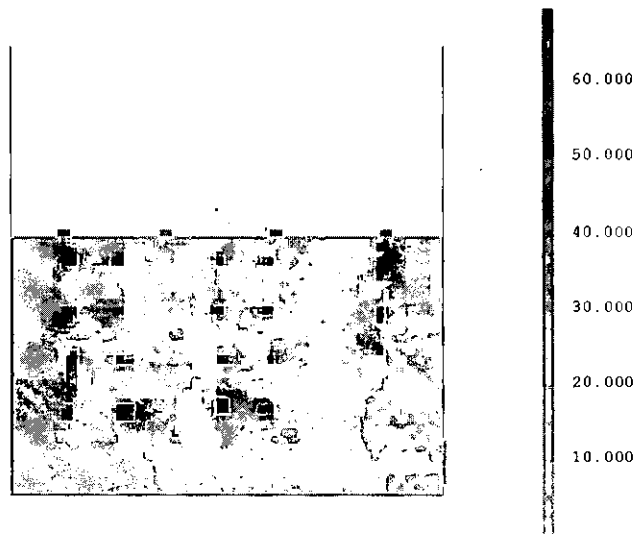
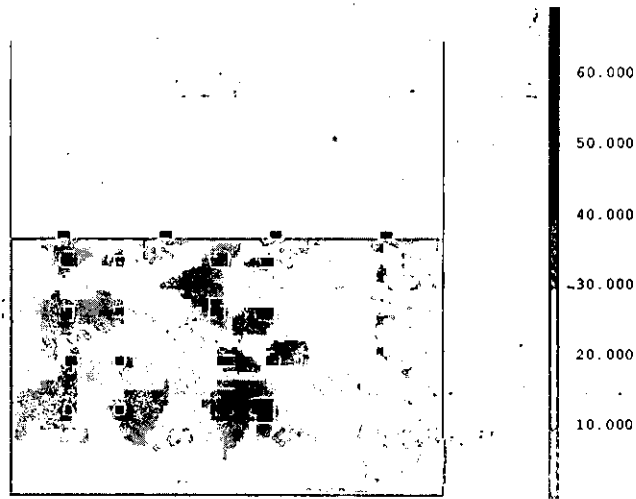


Figure 4.4.6 Velocity vector fields (m/s) in sections P1, P2 or P3 for F4.



EOL 3D - INRS

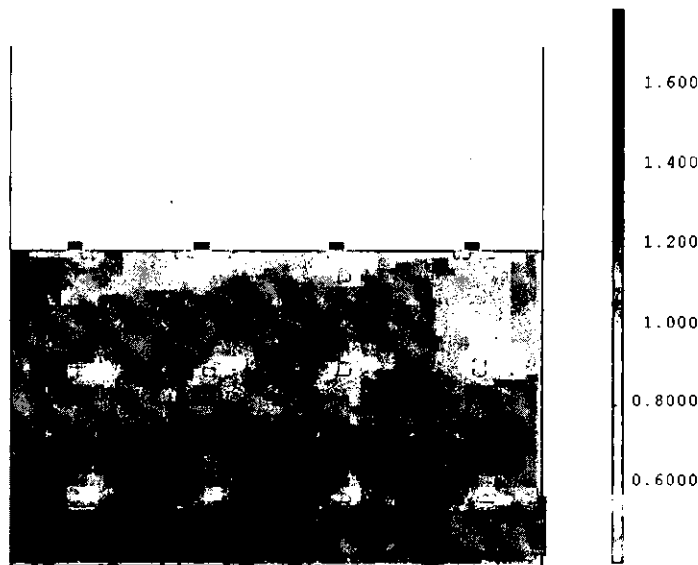
(a)



EOL 30 - IHRS

(b)

Figure 4.4.7 Styrene concentration in P4 plane according to F2 (a) uniform sources and (b) weighted sources.



EOL 30 - IHRS

Figure 4.4.8 Age of air normalised by the nominal time (11mn) at breathing level (P4) for F2..

4.4.3 Comparisons between Models and Experiment

It would be unrealistic to expect a perfect match between the measurements and simulation results, considering the experimental uncertainties and the simplification of the numerical models. However, we intend to compare the interpretations from both approaches:

First of all, the orders of magnitude of styrene concentration agree well in the bulk of the workshop, as a result of dilution. Furthermore, the concentration peaks in plane P2 were well predicted by the CFD models (one between s3 and s8, and another around s13).

As for velocity, the main message from the simulations was the small but significant regions of upward flow between supply diffusers. In spite of the sparsely located measurement points, these upward flows were detected by ultrasonic anemometry, as seen in Figure 4.4.3 and somewhat less in Figure 4.4.4.

Finally, the CFD models seem to underestimate mean velocities; according to simulations, they predicted velocities below 0.1 m/s in most of the workshop except close to the supply diffusers. This discrepancy may be partly due to the hot sphere anemometers, which tend to overestimate mean velocities [Koskela *et al.*, 1996b].

4.4.4 Global Ventilation Efficiency of the System

Numerical simulations can provide other indicators related to contaminant capture and air quality. Among them, we present computed age of air (Figure 4.4.8) and global contaminant removal efficiency, defined below. The calculated global contaminant removal efficiencies are shown in Table 4.4.1.

$$\varepsilon^c \equiv \frac{C_e}{\langle C \rangle_o} = \frac{\overline{C}_{\text{perfect mixing}}}{\overline{C}_{\text{mean}}} \quad (4.4.1)$$

The observed patterns of age of air from the CFD simulations (Figure 4.4.8) are characteristic of good mixing. At breathing level, the normalised age of air mostly ranges from 0.8 to 1.4. Overventilated regions are limited to where the supply jets penetrate the breathing zone, whereas 'underventilation' is detected in the opposite corner of the wall with the large opening.

The global contaminant removal efficiency enables us to compare a ventilation system with perfect mixing. In this factory, the models almost unequivocally indicated that the air diffusion is better than perfect mixing (Table 4.4.1). This may be due to overpressure in the space, which displaces some air horizontally towards the two openings. The weighted source assumption leads to higher efficiencies than the uniform source hypothesis. This comes from the fact that, in the *weighted* case, sources are concentrated in the middle of the workshop in a well ventilated area; whereas, in the *uniform* case, styrene sources create larger contaminated regions (Figure 4.4.7).

Finally, attempts to compare CFD concentration fields with styrene exposure estimated by passive sensors carried by operators, were not very successful. This is because concentration gradients are high near sources, and a slight misplacement of a source leads to significant differences between both approaches. Moreover, because of the operator movements, exposure measurements do not match local concentration values, since they are averaged not only in time but also in space.

4.4.5 Conclusions and Recommendations

Mixing ventilation is not suitable in general when pollutants are involved. In this factory, the designer had to compromise between indoor air quality and heating aspects. Dilution leads to low exposure, but contaminant extraction is not controlled at all. In this case, general ventilation could have been coupled with local extract near to the pollution sources, in order to minimise the fresh air flow rate (and thus heating cost) and pollutant dispersion. Moreover, supply air diffusion could have been optimised:

- General ventilation could have been coupled with a local extraction equipment, in order to minimise the fresh air flow rate (and thus heating cost) and pollutant dispersion
- Ventilation principle should be connected with process stages, for example: one zone for preparing the mould, one for spreading resins and one for drying. It implies wall separations between zones even if flexibility remains a key criterion since mould size and shape keep changing
- Confined and local extracts would improve ventilation efficiency, reduce exposure levels and decrease the needed fresh air flow rate (and thus heating cost)

Moreover, suggestions for the improvement of the installation include:

- Optimisation of supply air and duct installation
- Wall separations between working positions
- Financial opportunity of investing in heat exchangers

All these hypotheses contain potential pitfalls either on energy efficiency or on pollutant removal.

Numerical tools are generally not up to modelling such a case which has a highly complex ventilation flow field and enclosure geometry. Nevertheless, it was possible to detect the main features of the airflow pattern. As a matter of fact, the numerical simulations did not add much to our knowledge of mixing ventilation. It was nevertheless able to underline some items such as possible upward flows and unexpected complexity of the flow. However, this case shows that CFD simulation is technically feasible, though a large amount of information is needed to implement it accurately. Numerical simulation may be more pertinent for a very demanding working environment, where the flow pattern itself proves to be critical.

4.5 Turnhalle (Gymnasium) München, Germany

4.5.1 Introduction

The building Turnhalle München was selected as a case study building despite of its rather simple geometry (Figure 4.5.1). The simple geometry and the well-defined inlet devices make it easy to measure the air velocities at the inlets, the temperature and velocity distribution in the enclosure, and the temperature distribution at the walls. This detailed data is suitable for verifying CFD codes applied predicting the air movement in large enclosures.

Three different sets of boundary conditions were chosen for the numerical investigations of this case study building. These three categories are relevant to different stages in the design process:

- Case Ia. Isothermal boundary conditions
- Case Ib. Nonisothermal boundary conditions with two different Rayleigh numbers
- Case II. Measured boundary conditions

The building

The geometry of this gymnasium is quite simple. The enclosure is cuboid in shape, as seen in Figure 4.5.1. The eight inlet supplies are spread along the north wall. Each inlet is formed as a simple slot of height 30 mm and width 900 mm. The gaps under the three doors at the north wall are usually used as outlets, but during the measurements the location of the outlet device has been moved to the east wall. The air was sucked out of the gym hall into the adjacent room. This was the only way to ensure that there was no mixing of supplied air with outlet air. This was a necessary requirement for the tracer gas measurements

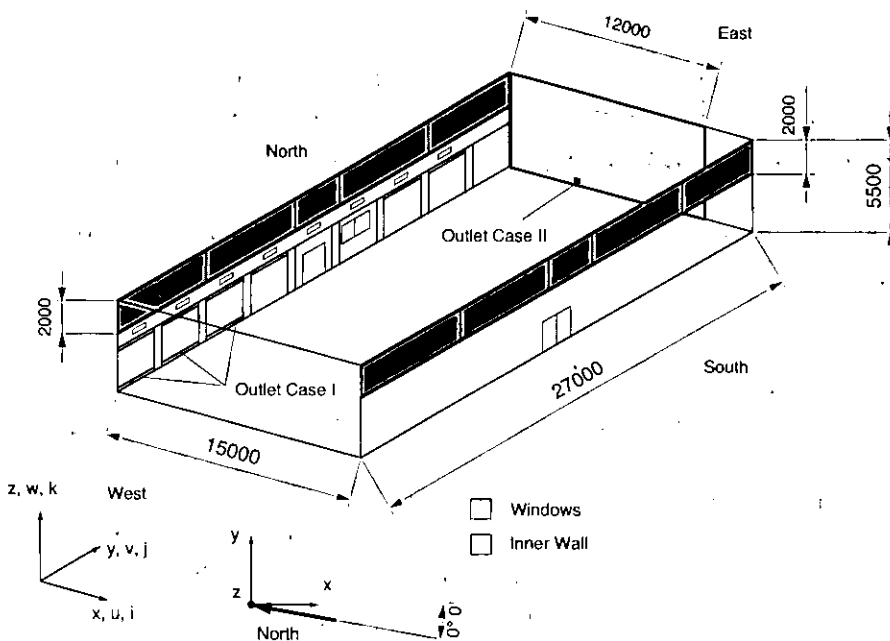


Figure 4.5.1 Dimensions of the 'Turnhalle München'.

Measurement tools

The following measurement tools were applied to provide data for Case II:

Table 4.5.1 Applied measurement tools in Turnhalle München.

Object	Method	Country	Work Group
Temperature distribution in the enclosure	Thermocouples	D	TUD
Temperature at the inlet devices	Thermocouples	D	TUD
Temperature distribution at the walls	Infrared Camera	D	TUD
Velocity and turbulence parameter at the inlet devices	Hot wire anemometers	D	TUD
Velocity distribution in the enclosure	Particle-image-velocimetry (PIV) in two dimensions	D	RWTH
Mean age of the air in the enclosure	Tracer gas	D	RWTH
Flow pattern in the enclosure	Smoke injection 3D Analysis	D	TUD
Flow pattern in the enclosure	Smoke injection 2D Analysis using a laser sheet Method	D	RWTH

4.5.2 Experimental Investigations.***Measurement of velocity and temperature distribution (TUD)******Introduction***

After the first test measurements in November 1993, two measurement campaigns were undertaken in the summer and winter of 1994. The reference data-set was generated from the results of measurements taken in December 1994 and contains the following data:

- Boundary conditions including wall temperature distribution and conditions of intake air
- Air temperature field in the hall
- Field of velocity magnitudes

Measurement technique

Mean velocities and turbulence intensities were calculated from 7 simultaneously-sampling hot wire probes (10 μm diameter, 3 mm pin distance). All anemometers were connected to a PC for data logging and data processing via an analogue to digital converter.

Only velocity magnitudes could be measured with the single wire probes. In preliminary investigations the following relation between the measured velocity magnitude, c and the velocity components was found:

$$c = \sqrt{0.04u^2 + v^2 + w^2} \quad (4.5.1)$$

where

u = velocity component parallel to the wire

v, w = velocity components normal to the wire

As described in Section 3.3.6, infrared thermography was used to measure the wall temperature, and thermocouples for the air temperature field.

Measurement procedure

At first, the velocity profile over each inlet was measured. The outlet flow rate was adjusted to the inlet flow rate. Simultaneously, the temporal development of a reference inlet air temperature and velocity was recorded for the conversion of the measured boundary conditions to the time of the field measurement.

The field measurement was carried out within 1.3 hours. This relatively short interval was necessary to prevent changing boundary conditions due to varying outdoor conditions. The constant wall temperature distribution at the beginning and at the end of the measuring period was checked by thermography. The air temperature was measured at $6 \times 9 \times 15$ points (x, y, z directions respectively) and velocity magnitudes at $6 \times 5 \times 14$ points. Due to the short measuring period, the mean velocities and turbulence intensities at each point were calculated from a short signal of only 7 seconds.

Results

The ventilation flow rate, which varies from 4.2 to 6.6 m/s at the inlets, results in an air change rate of 1.8 h^{-1} . The inlet air has a turbulence intensity of 5~6 % and the inflow angle, measured in the x, y -plane relative to the normal direction, varies among the inlets from -30° to 0° . Furthermore, the inlet air temperature oscillates with a time period of 8 minutes caused by the two-point controlled heating system. Despite the enclosure's simple geometry, the flow field shows a strongly three-dimensional flow pattern with periodical fluctuations. The time period of the long-period fluctuations is approximately 2.0~2.5 min.

Except for the regions near inlets, the velocity magnitudes are less than 0.5 m/s and no large structures can be found in the velocity field. One of the reasons for this result might be the small time-scale for the measurements. Figure 4.5.2 shows a velocity signal near the floor. It can be seen that the mean velocity magnitude calculated from a 7 s long signal changes with time. From this point of view, the integration time should ideally be several minutes but this is not feasible for field measurements in large enclosures.

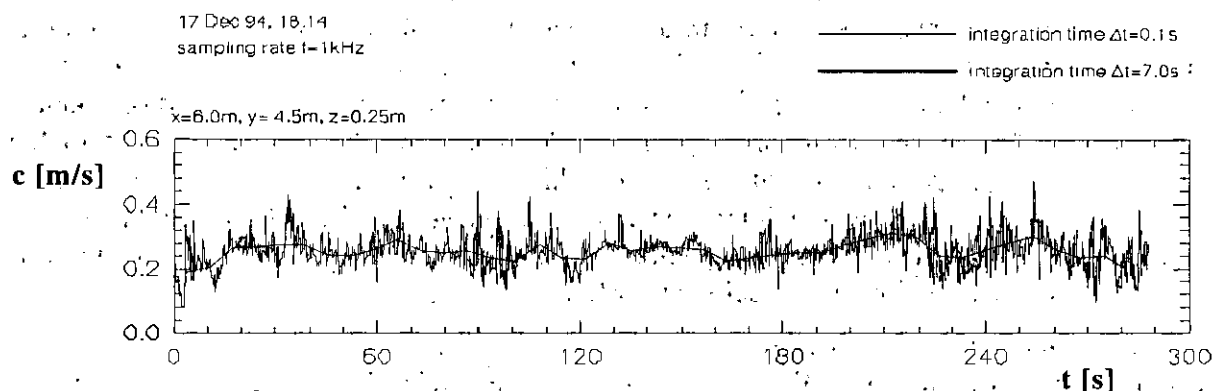


Figure 4.5.2 Velocity signal with different integration times for mean value determination.

The air temperature field gives more information about the flow pattern, because the temperature can be used as a tracer (Figure 4.5.3). Colder air from the small side walls flows on the warmer floor to the middle of the hall and is warmed up. The warmest region is in the middle of the hall but nevertheless the temperature difference to the coldest air in the hall is only 1.6 K. The warm jets near the inlets are not resolved by the coarse measuring grid.

While observing the temperature, the oscillations of the inlet air can be recognised with the same fluctuation time but smaller amplitude.

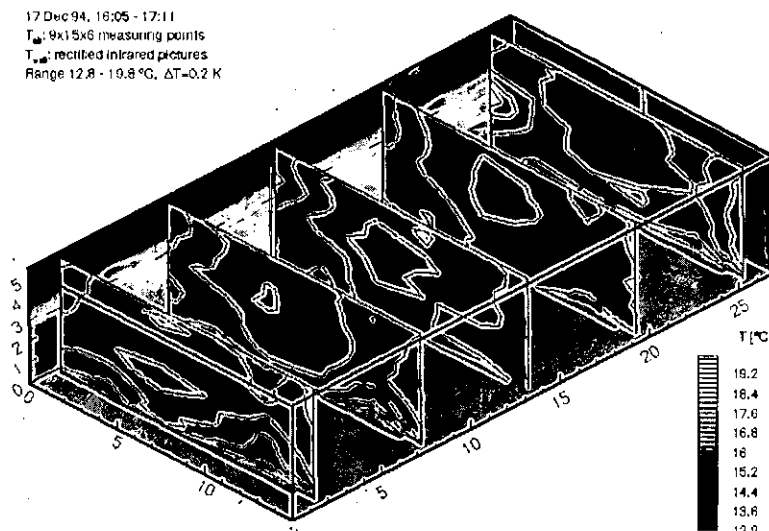


Figure 4.5.3 Air temperature field.

PIV-measurements of airflow (RWTH)

Measurement technique

The PIV system uses a light sheet from an argon ion laser and helium-filled soap bubbles as tracer particles. These tracer particles have almost the same density as air and due to their low mass they follow the airflow quite accurately. A digital camera records these tracer particles as they pass the pulsed laser light sheet. On a computer each picture can be used to determine the two dimensional velocity vector components of up to fifty points placed randomly in the approximately two square meter sized measurement plain. All the velocity vectors from one picture are measured simultaneously, which makes it possible to get an overview of the different flow conditions at one plain in the room at different times. By applying a global coordinate system, many measurement plains can be linked together to get a picture of the airflow in a whole cross section of the room. This gives a good impression of the airflow condition if steady-state flow conditions exist or if the changes of the airflow conditions over time in every measurement plain are negligible. All the measurements in the cross section can be used for an interpolation of a velocity vector field.

Location of the airflow measurements

The measuring plane for the PIV measurements is located under the second air inlet normal to the y-axis (i.e. $y=4.5$ m). The section extends from the floor to a height of three meters. The measurements for this cross section were taken in twelve planes, six sets at an equal distance along the floor, at two different heights (Figure 4.5.4).

Results of the airflow measurements

Many pictures of every plane were taken with the digital camera to get an impression of the airflow changes. These pictures show an airflow with small changes in direction and magnitude directly under the air inlet ($0 < x < 2$ m) and also further away from the air inlet ($8 < x < 15$ m). The airflow between these two approximately steady-state flow planes showed a very unstable behaviour. The variation of the magnitude of every flow vector ranged from zero to maximum velocity and also the flow direction varied over the full range. To explain these results, the airflow was visualised with a smoke experiment with smoke emitted at the air inlet. This experiment showed that the airflow develops huge vortices in the region $3 < x < 8$ m, see Figure 4.5.5. These vortices were caused by airflow coming from the air inlet which was stopped by airflow from the opposite direction in the middle of the cross section.

Three general airflow regions were observed in this cross section. The first region located under the air inlet shows an upward airflow being entrained by the fast jet leaving the air inlet. The second region starts at the wall opposite the air inlet and has a stable airflow moving towards the inlet. The third region is the mixing zone where air from the inlet meets air from the second region. This mixing region leads to an almost perfect mixing of supplied and old air in the room. This result agrees with the tracer gas measurement performed at the same time, and discussed later. An interpolation of the velocity vector field for this cross section is shown in Figure 4.5.4. This interpolation is performed with zero velocity boundary conditions at both walls and the floor of the room. Furthermore, this interpolation neglects the vortex located in the mixing zone and shows only the mean flow direction in this region. The corresponding visualisation of the airflow with smoke is shown in Figure 4.5.5, which clearly shows the returning air from the opposite wall after 120 seconds.

Conclusion

The PIV system is capable of measuring the airflow in large rooms. Measurements can be taken not only in steady airflow but also under highly unsteady flow conditions. For the interpretation of unsteady airflow regions, a smoke experiment is recommended because this kind of experiment provides a helpful overview of the complete airflow situation in the room.

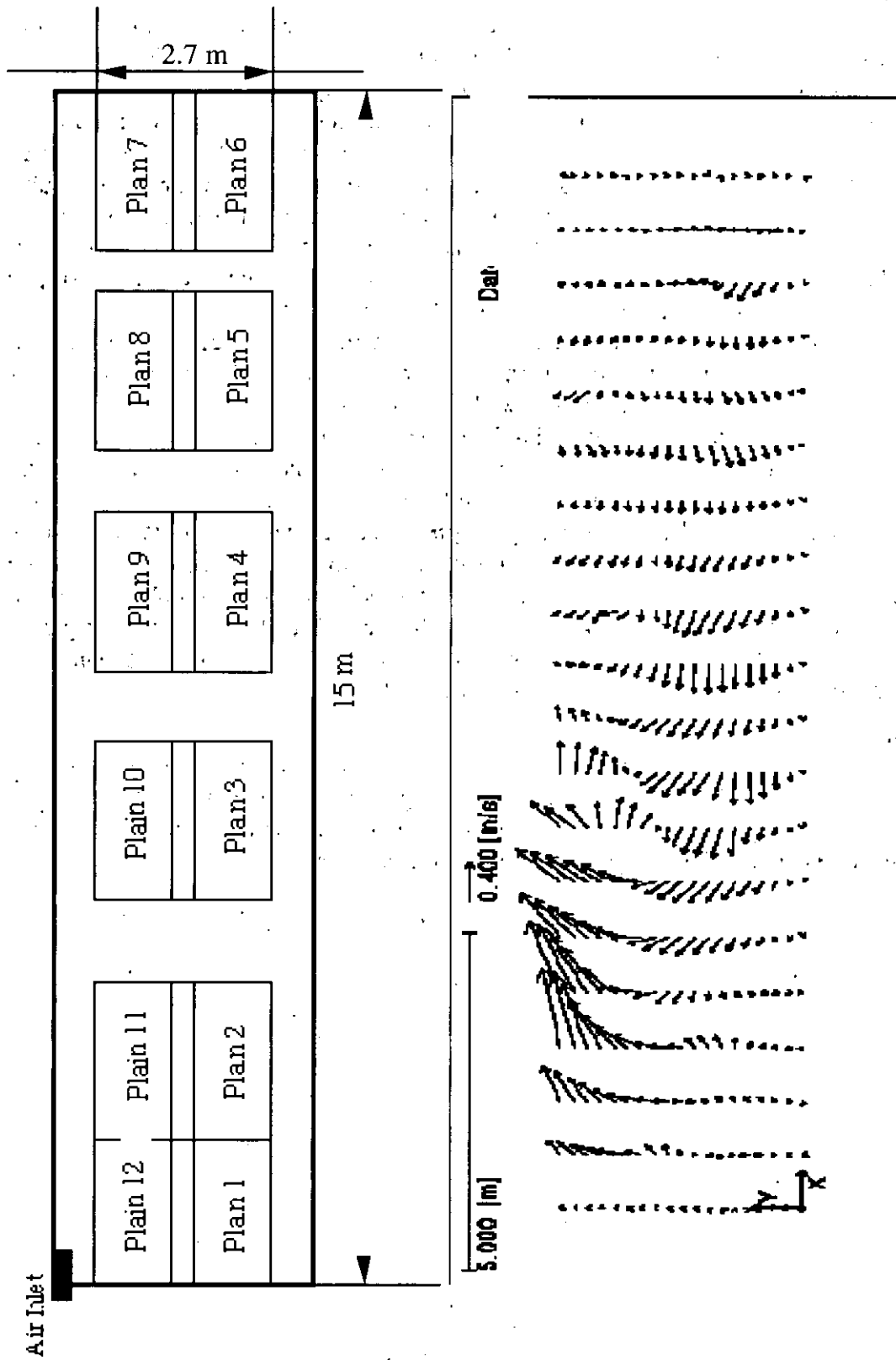


Figure 4.5.4 Velocity field in the cross section.

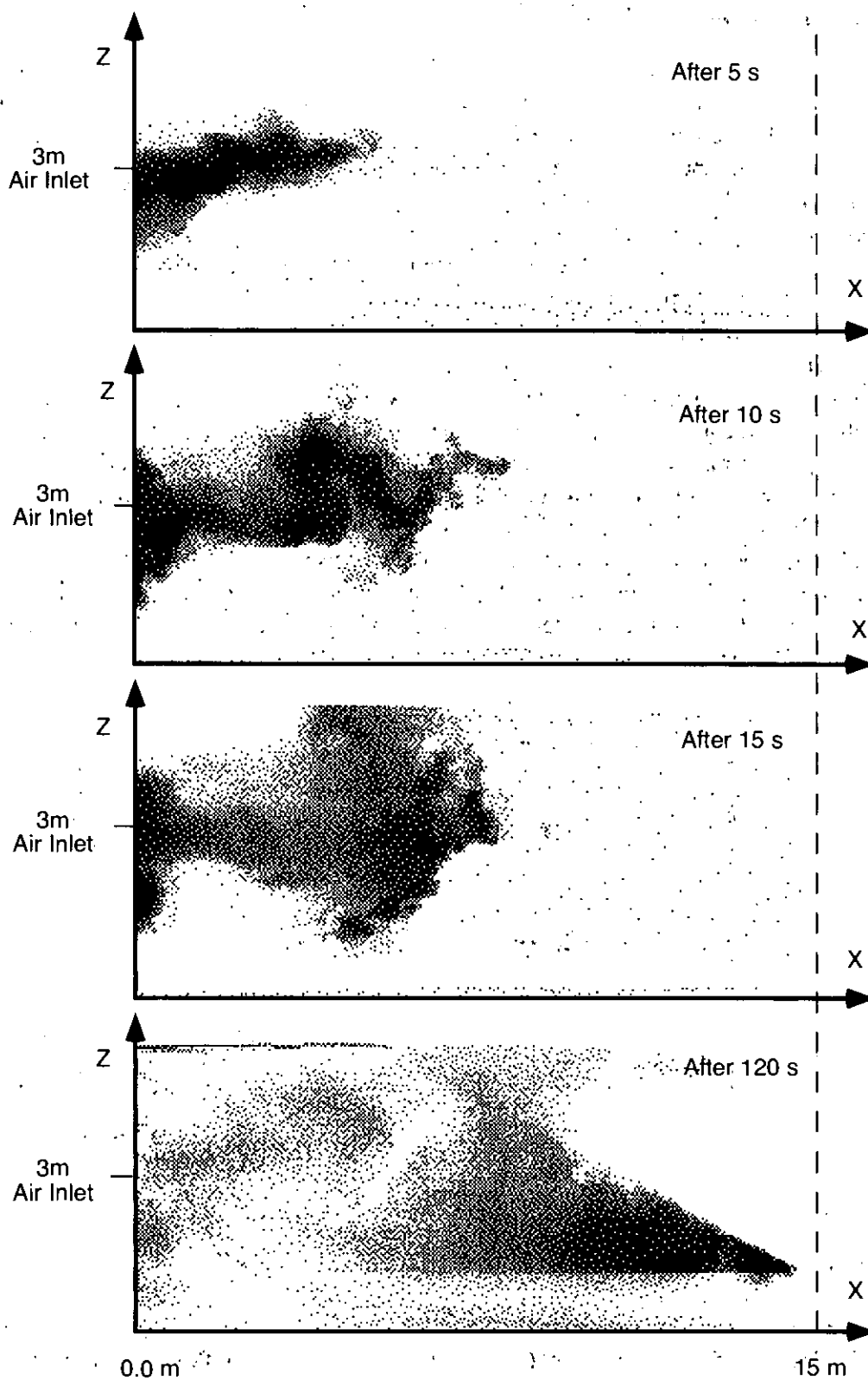


Figure 4.5.5 Smoke experiment in the cross section.

Tracer gas measurements (RWTH)

Measurement strategy

Working with three tracer gases SF₆ ($c_{max} = 3$ ppm), N₂O (20 ppm) and C₃H₈ (40 ppm) in parallel, the supply and exhaust air flows, the air exchange efficiency of the inlets 1–5, 6–8 and of all inlets 1–8 and the ventilation effectiveness with respect to one passive contaminant source (mixture of C₃H₈ and He) at $x = 11.25$ m, $y = 20.25$ m, $z = 1.5$ m (Figure 4.5.6) were determined by using the system of Brüel & Kjær. (Type 1302 and Type 1303, sampling time for one probe ~ 100 s, i.e. a sufficient data sampling rate of 3.4 values/ τ_n , where τ_n = nominal time constant of the room). The age-of-air and the age-of-contaminant were measured twice at five points in the middle of the room ($x = 7.5$ m, $y = 13.5$ m, $z = 1, 2, 3, 4, 5$ m, position 2) by means of a cyclic sequence of the step-up and the step-down method. One sampling point was always in the exhaust duct. The respective steady-state concentration distributions additionally were measured at $x = 7.5$ m, $y = 6.75$ m, $z = 1, 2, 3, 4, 5$ m (position 1) and $x = 7.5$ m, $y = 20.25$ m, $z = 1, 2, 3, 4, 5$ m (position 3) by taking the arithmetic mean of 6–10 probes sampled within 60–100 min. Perfect mixing of the tracer and the supply / exhaust air was achieved by using perforated tubes for dosing, by placing two mixing fans into the empty air filter chamber before the supply ventilator and by inserting a frame with three layers of 0.8 mm mesh screen in the supply duct. A total of two cyclic sequences was carried out, each lasted about 8 h. Parallel measurements of the boundary conditions showed almost identical conditions for both periods.

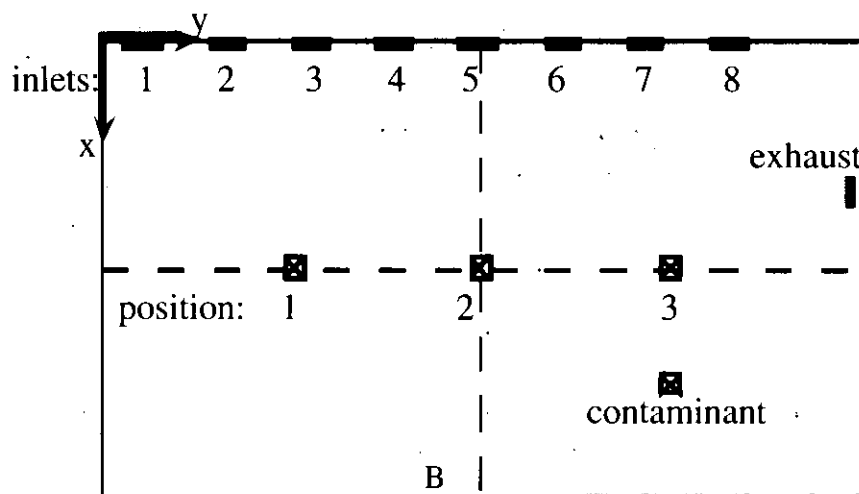


Figure 4.5.6 Location of sampling and dosing points.

Airflow measurements

The measurements confirmed the existence of a slight overpressure in the hall (total supply air flow rate 3900 m³/h and exhaust flow rate 3800 m³/h) corresponding to $n = 1.8$ h⁻¹ or $\tau_n = 34$ min. Inlets 1–5 accounted for 60 % of the total supply air flow. These results are in good agreement with the hot wire measurements.

Measurements of air exchange efficiency and ventilation effectiveness

The standard deviation of the supply concentration among the inlets 1–5, 6–8 and 1–8 was less than ± 5 % of the mean value. The corresponding values of the steady state concentrations

measured at positions 1, 2, 3 and the exhaust (including the measurement with the contaminant source) were within the range $\pm 5\% \sim \pm 10\%$ of the respective local mean values.

The step-up and the step-down method gave identical results when the tracer was dosed into all inlets 1–8. The step-up results were unreliable when the tracer was dosed into the inlets 1–5 or 6–8 and even useless when the tracer was dosed into the room as a contaminant. This is because the concentration difference between the ‘source’ of the tracer (i.e. the supply inlets 1–5, 6–8 or the contaminant source) and the room/exhaust are higher than in the following step-down test. In combination with the unsteady airflow conditions in the hall, this results in unsystematic fluctuations in the concentration curves during the whole step-up test. With a step-down test these large fluctuations and differences only exist at the start at $t=0$. Summing up the step-down method is the most reliable one, the step-up method can only give the same results if the total or large portions of the supply air flow are marked with a tracer.

Figure 4.5.7 shows the local portion of the supply air flow from the inlets 1–5 or 6–8 with respect to the total supply air flow 1–8 expressed as the ratio of the mean local and mean supply concentration $c_p / c_{s,i}$. It can be seen that the portion of the inlets 1–5 is slightly higher in the lower regions of the hall than in the upper regions, the reverse holds for the inlets 6–8. Theoretically the sum of both ratios must equal 1, the measured values were in the range 0.99~1.01, i.e. a very good agreement. For a balanced ventilation system the global portion of the supply air flow of the inlets i can be calculated from $\langle c_i \rangle / c_{s,i} = (\tau_{e,i} / \tau_e)(\tau_{e,i} / \tau_{s,i})$.

Figure 4.5.8 shows that the air exchange in the hall as a whole is somewhat better than in a perfect mixing situation, where the inlets 1–5 more or less displace the supply air towards the exhaust, which is impaired by the inlets 6–8 having a high amount of short-circuit air ($\tau_e = 31$ min, $\tau_{e,1-5} = 36$ min, $\tau_{e,6-8} = 26$ min). The supply air from inlets 1–5 arrives ‘early’ in the lower regions of position 2 and ‘late’ in the upper regions, the reverse holds for inlets 6–8. Both effects cancel out each other when all inlets 1–8, or the weighted sum of 1–5 and 6–8, are regarded resulting in an almost uniform distribution of ϵ_p at position 2. The explanation for both figures is that an air vortex across the whole y,z -plane with a counter-clockwise rotation must exist, if the hall is viewed from position ‘B’ in Figure 4.5.6. This is in agreement with the measured wall surface and air temperature field and the fact that the hall is in a heating mode. The air from inlets 1–5 is already supercooled when it arrives at inlets 6–8, so the warmer air from inlets 6–8 tends to rise towards the ceiling.

The results of the passive contamination source did not reveal any further details about the air flow pattern and yielded the same explanations as mentioned before (Figures 4.5.9 and 4.5.10). The global air quality index (steady-state) was calculated as $c_e(\infty) / \langle c \rangle = \tau_e / \tau_e^c$ with $\tau_e^c = 24$ min.

Conclusions

Although the airflow in the hall was unsteady; all of the performed tracer gas measurements gave reproducible and conclusive results about the structure of the air flow pattern in the y,z -plane. The applied measurement strategy turned out to be successful and recommendable for further field studies.

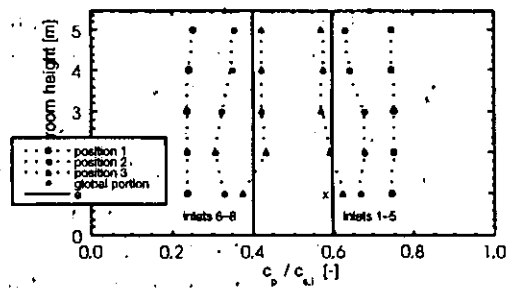


Figure 4.5.7 Local and global portion of the different supply-air flows at positions 1-3.

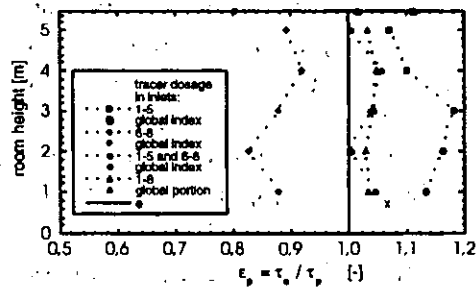


Figure 4.5.8 Local and global air change index of the different supply air flows at position 2.

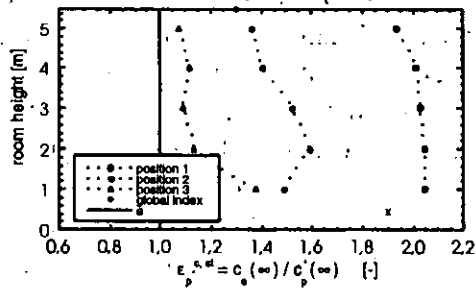


Figure 4.5.9 Local and global air quality index (steady state) of the contaminant at positions 1-3.

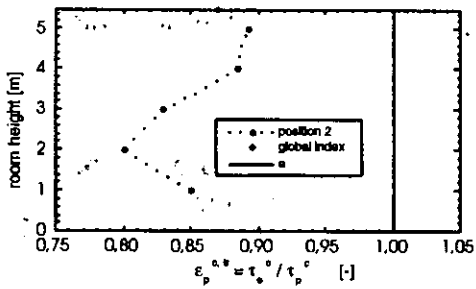


Figure 4.5.10 Local and global air quality index (transient) of the contaminant at position 2.

4.5.3 Application of the CFD-Tools

The participating groups are listed in table 4.5.2.

Table 4.5.2 Work groups applying CFD tools on Turnhalle München.

Country	Work-Group	Abbrev.
Switzerland	ETH-Zürich	IET
Switzerland	SULZER Innotec	SULZER
Germany	TU Dresden	TUD
Germany	RWTH Aachen	RWTH
Finland	VTT, Technical Research Centre of Finland	VTT
Sweden	Chalmers Univ. of Technology, Thermo and Fluid Dynamics	CTH
Netherlands	TNO Buildg. & Constr. Research Dept. of Indoor Env.	TNO

Three test cases were defined with a different quality of boundary conditions. These test cases relate to different stages of the design process. All boundary conditions were time-independent. The following results are computed with different CFD codes, either commercial codes or codes developed by the participants (see Table 4.5.3).

The coarsest grid was used by the TUD group mainly to save computing time. This was necessary because the explicit solver needs a very small time step and the time scale of the problem is quit big. All other grid sizes are almost the same, except the one of Sulzer who used a finer grid in the k -direction and TNO who choose a fine grid in the i and j directions. All CFD codes used boundary-fitted coordinates except TNO who used Cartesian coordinates. All participants used the so-called standard k - ϵ turbulence model for their calculations.

Table 4.5.3 Information's about the used CFD-codes.

Work Group	CFD Code	Used solver	Grid size (I x J x K)
IET	TASCflow	implicit, stationary	30×75×37 *
SULZER	Star CD	implicit, time-dependent	38×109×27
TUD	non-commercial	explicit, time-dependent	26×74×18
RWTH	FLUENT	implicit, time-dependent	36×71×27
RWTH2	FLUENT	implicit, time-dependent	40×79×47 (Case b)
VTT	CFDS Flow3D (CFX)	time-dependent	35×74×29
CTH	non-commercial	time-dependent	26×87×42
TNO	non-commercial		52×68×42

* local grid refinement at the inlets

Test case Ia: Prescribed isothermal boundary conditions. All inlets have the same velocity direction and magnitude. Inlets and Outlets at the north wall.

The computed flow field is dominated by the eight inlet jets. The outlet device (see Figure 4.5.1) is placed in a corner of the enclosure and thus the flow field is forced to asymmetry. In fact the flow field is very unstable and shows a non-stationary flow pattern. The same behaviour could be seen in the results of the numerical simulations.

As mentioned before, the defined boundary conditions were stationary, though only one of the participants (IET) reached a convergent stationary solution. All other calculations show a highly unsteady behaviour. As an example of the time-dependent behaviour of the flow field, the history of two monitoring points at different heights ($z=1\text{m}$ & $z=3\text{m}$) at the centre of the enclosure can be seen in Figure 4.5.11. The upper monitoring point has the same height as the inlet devices and the big amplitudes of this plot are caused by the upward & downward swaying oscillation of the inlet jet.

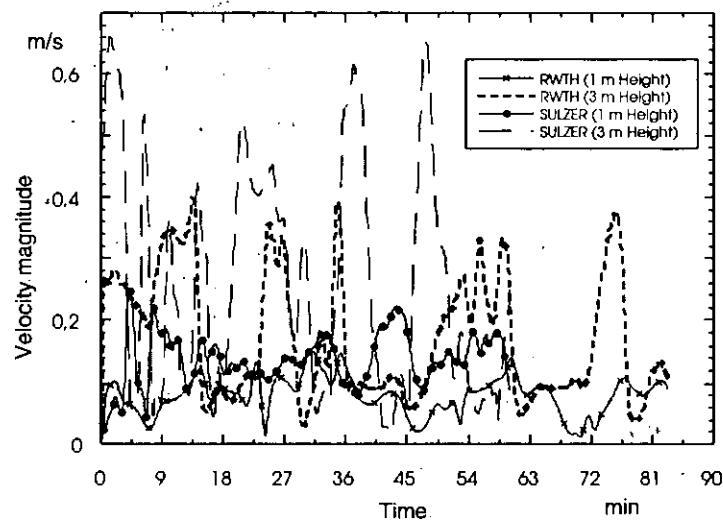


Figure 4.5.11 Calculated time history of the velocity magnitude at two monitor points in the centre of the enclosure (RWTH, SULZER).

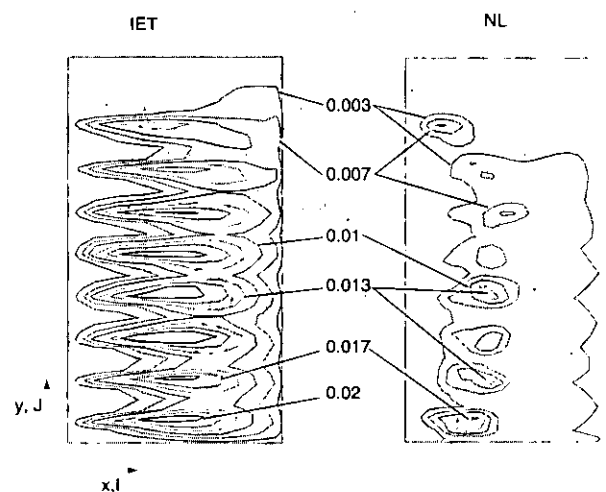


Figure 4.5.12 Lines of constant turbulent kinetic energy ($z=3.5\text{m}$).

The calculations by the RWTH group and by Sulzer show an oscillation time-scale of about 10 to 20 minutes. The stability of the solution can be related to the predicted amount of turbulent kinetic energy or the effective viscosity. The stationary solution of IET predicted the highest level of kinetic energy and the results of TNO gave the lowest value of kinetic energy. The fields of the turbulent kinetic energy of these two participants are shown in Figure 4.5.12 at a height of 0.5 m above the inlet devices ($z=3.5$ m). A small recirculation zone is located in the region opposite to the outlets ($y = y_{max}$) in IET's flow field (see Figure 4.5.13). This recirculation zone is much bigger in TNO's flow field; it fills almost half of the room and it has an influence on the three inlet jets in this zone. These three inlet jets link to one big jet. The results of all other participants are somewhere between these two extremes.

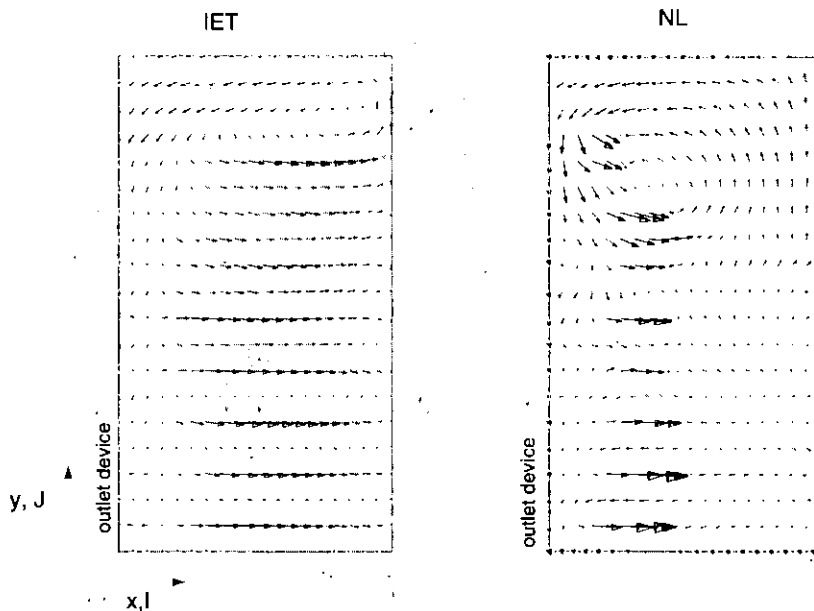


Figure 4.5.13 Velocity vectors ($z= 3.5$ m).

Another main difference in the predicted flow fields is the vertical expansion of the jets. In the most unstable solution (TNO) all inlet jets are attached to the ceiling. In the other results the jets stay almost horizontal. The result of RWTH shows a strong deflection of the jet to the floor. This also can be seen in the other solutions in a less strong way.

Discussion

It is difficult to compare all results, because of the dominating time-dependency of the numerical solutions for the flow field. The compared results of TNO, VTT, TUD are just snapshots of this unstable three-dimensional flow field. Even if an average over time of the flow field is calculated it is still difficult to compare the results, because the time duration (RWTH: 80 min) of the simulation is too small for the long time-scale of the motion (see Figure 4.5.11). The rms. velocity values calculated by RWTH have the same order of magnitude as the mean values. If the real flow field also has a time scale of about 10 to 20 minutes like in the simulation, it would be difficult to get reliable measurements, because the necessary time for small statistical errors measurements would be a few hours. During this time the boundary conditions would change.

Test case Ib: Prescribed nonisothermal boundary conditions, All inlets have the same velocity direction and magnitude. The temperatures of the inlets are 30 °C and the temperatures of the walls are 20 °C. Inlets and outlets along the north wall.

Buoyancy effects due to the temperature difference between the warm jets and the surrounding air causes a more stable flow field than in test case Ia. The calculated flow patterns are all independent in time. The flow fields have approximately the same pattern as before, but the warm inlet jets are attached at the cold ceiling. Nevertheless there is a difference by a factor of 2 in the predicted maximum turbulent kinetic energy within the flow fields of the various participants. The temperature distribution in the centre of the enclosure (Figure 4.5.14) agrees very well. The predicted heat losses through the various walls are listed below in Table 4.5.4.

Table 4.5.4 Heat losses through the walls (in Watts).

	TNO	VTT	RWTH	RWTH2	CTH	SULZER	TUD
turb.-Mod	$k-\epsilon$	$k-\epsilon$	$k-\epsilon$	LR+buoy.	$k-\epsilon$	$k-\epsilon$	$k-\epsilon$ +buoy.
Wallf.	std.	std.	std.	std./*	std.	std.+ buoy	std.
Wall x-	-850	-990	-801	-1089	-818	-979	-1080
Wall x+	-857	-1012	-772	-965	-930	-1015	-1199
Wall y-	-425	-510	-459	-329	-282	-519	-229
Wall y+	-594	-492	-382	-399	-349	-519	-339
Wall z-	-1039	-507	-1480	-528	-1590	-1064	-898
Wall z+	-2931	-2910	-2148	-4029	-2540	-3472	-2076
Total	-6696	-6421	-6042	-7339	-6509	-7552	-5821

* wall-function at the floor and at the x-wall, full Low-Reynolds treatment at the ceiling, sublayer model at the other walls

The calculated heat fluxes show no clear tendency between the groups as long as the standard $k-\epsilon$ model and standard wall functions are used. The overall heat flux lies in the range of 7000 Watt $\pm 8\%$. The scatter for specified surfaces is definitely higher. The hot air jet will cause stratification effects, so buoyancy-extended turbulence models should be used.

The main heat loss is at the ceiling (wall z+). Thus the calculation of the heat flux through the ceiling is most critical, and shows the largest differences between the participants. Two participants (RWTH2 and Sulzer) used a different treatment at the ceiling. Sulzer used a modified wall function taking into account additional buoyancy effects. RWTH2 modelled the boundary layer at the ceiling using the Launder-Sharma model including Yap-correction. The heat fluxes at the ceiling, calculated by these two participants, indicate that thermal instabilities in the boundary layer are increasing the heat transfer, and therefore the heat flux predicted by standard log-law wall function is too small.

Figure 4.5.14 shows numerically predicted vertical temperature profiles in the centre of the enclosure. A stratified temperature distribution is observed in the core region, so the profiles are representative for the whole core region. Additionally this plot shows the results from measurements in a scale model (1:10) performed by the Department of Heating, Ventilation and Dust Removal Technology, Silesian Technical University (STU), Poland (See Section 2.5.3). They agree very well.

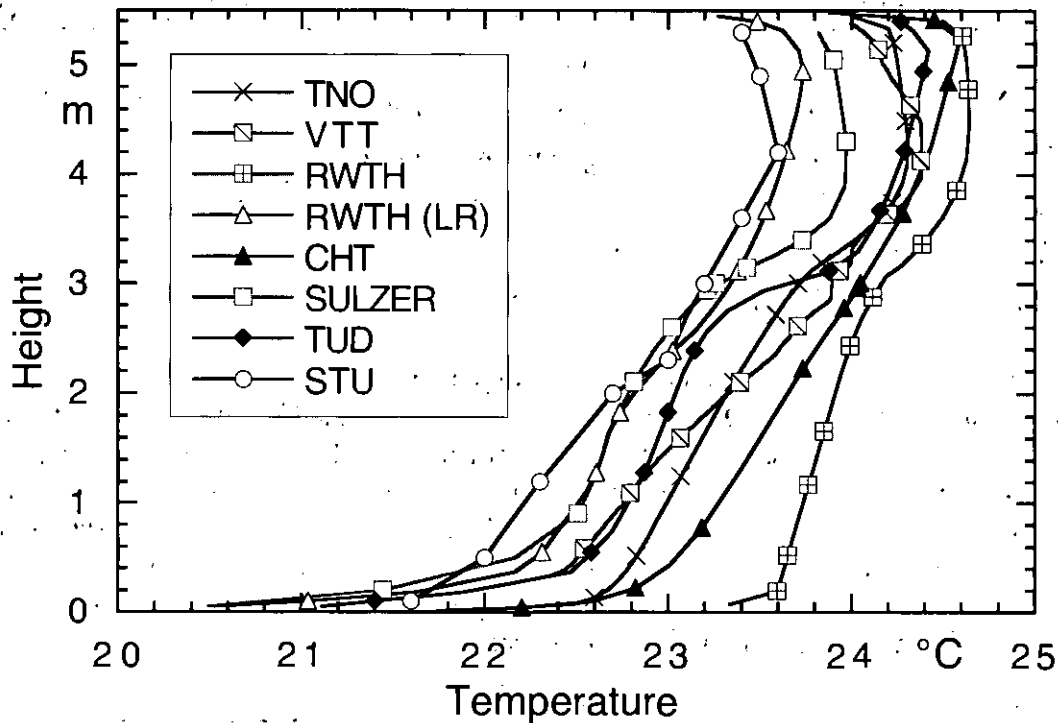


Figure 4.5.14 Temperature profiles in the centre of the enclosure.

Discussion

The results of all participants show the attaching of the inlet jets at the ceiling due to buoyancy effects. Consequently the heat loss through the ceiling has a major influence on the temperature distribution in the core region. In the near wall region, wall functions usually are applied, which give an empirical description of this region based on the similarity solution of isothermal flow along a flat plate. In this case, buoyancy effects are important near most of the walls, so the heat flux predicted by wall functions is very sensitive on the y^+ values near the walls.

Test case II: Measured boundary conditions. Each inlet has a different velocity direction and magnitude. The distribution of the temperatures at the walls are defined. Inlets on the north wall, outlets on the east wall.

Because of the modified outlet and temperature boundary conditions, it was necessary to generate a new grid system for these calculations. Also in this case, the standard $k-\varepsilon$ turbulence model was used by all participants. The number of cells varied from 74 592 (VTT) to 193 116 (IET), as seen in the Table 4.5.5.

Table 4.5.5 Information about the used CFD codes.

Work Group	CFD Code	Used solver	Grid size (I x J x K)
IET	TASCflow	implicit, time-dependent	42×121×38
TUD	non-commercial	implicit time-dependent	42×77×27
RWTH	FLUENT	implicit, time-dependent	42×81×24
RWTH2	FLUENT	implicit, time-dependent	54×93×36
SULZER	Star CD	implicit, time-dependent	38×109×27
VTT	CFDS Flow3D (CFX)	time-dependent	36×74×28

As reported in the description of the measurement results, the flow field is unstable. The temperature difference between the inlet air and the walls is not sufficient to stabilise the flow, unlike test case Ib. The simulations done by RWTH and VTT show a strongly time-dependent behaviour whereas IET predicted a stationary flow field. Figure 4.5.15 shows a history plot of the time-dependent velocity at a point in the hall. The results of VTT show nearly the same instabilities, with large fluctuations as in test case Ia. The remarkable difference between the two results of RWTH (grid size 41×80×23 : 76 000 cells and 52×90×33 : 160 000 cells) demonstrates that these solutions are not independent of the grid size.

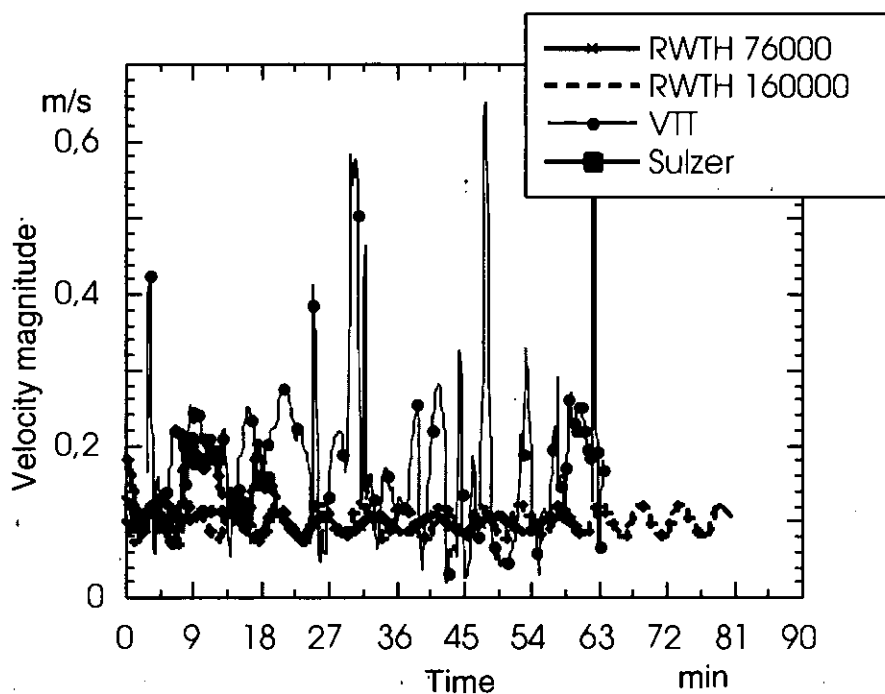


Figure 4.5.15 Velocity history in the centre of the hall ($x = 7.5$ m, $y = 15.5$ m, $z = 3$ m).

The flow structures of these predictions look quite similar. In the west side of the enclosure, a big swirl driven by the tilted inlet jets can be found. Due to the unsteady flow behaviour, no quantitative comparison can be made.

The following table shows the calculated heat fluxes through the different walls of the building. The predictions of the total heat loss are in close agreement (2200 atts $\pm 10\%$) but

are too low compared to the value evaluated from an energy balance between the inlet and outlet flows.

Table 4.5.6 Heat losses through the walls (in Watts).

	IET	VTT	SULZER	RWTH	RWTH2	TUD
turb.-Mod	$k-\epsilon$	$k-\epsilon$	$k-\epsilon$	$k-\epsilon$	$k-\epsilon$	$k-\epsilon$
Wallf.	std.	std.	std.+ buoy.	std.	std.	std.
Wall x-	-474	-264	-421	-259	-278	-286
Wall x+	-1491	-1110	-1284	-913	-1116	-963
Wall y-	-340	-316	-256	-240	-273	-217
Wall y+	-149	-138	-129	-118	-119	-141
Wall z-	-62	-177	-66	-267	-250	-178
Wall z+	44	-178	-203	-189	-165	-254
Total	-2474	-2183	-2359	-1986	-2115	-2039

The influence of grid refinement and the range of y^+ near walls is not so important in this case, as can be seen by the results of RWTH and RWTH2. The predicted total heat losses are in the range 2000 to 2500 Watts. The largest heat flux was predicted by IET, who got y^+ values of about 25.

The next plot shows the air temperature over the room height in the middle of the hall. All calculated temperatures are in very close agreement (17.7 ± 0.3 °C) but are definitely higher than the measured air temperatures. A detailed analysis showed that there was obviously an appreciable amount of cold air infiltrating through the ceiling, which explains the differences between the measured and predicted heat fluxes and temperature profiles. The results from a scale experiment (STU) is in good agreement with the measurements.

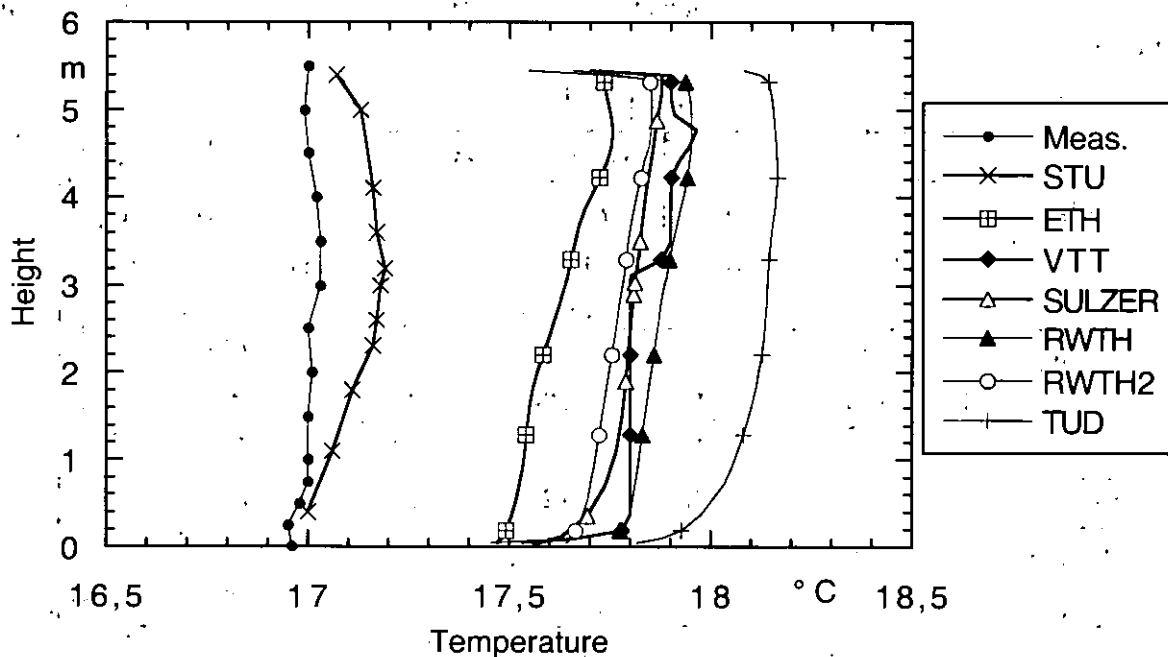


Figure 4.5.16 Temperature profiles at the centre of the enclosure.

4.5.4 Summary

Large enclosures are characterized by buoyancy-driven flows and by low air velocities and often unstable flow. The Turnhalle München, although of medium size, shows all these flow characteristics.

Two simple test cases, an isothermal and a nonisothermal test case, were simulated first. All CFD-codes, except one, predicted unsteady flow fields, which makes a quantitative comparison very difficult. The nonisothermal test case results in a stable, but highly three-dimensional flow pattern. Predicted results based on standard $k-\epsilon$ turbulence model equations and standard wall functions are in acceptable agreement as long as the grid size and the grid distribution are similar.

The agreement was even better for the real test case Turnhalle München. However, probably due to infiltration of cold air, large discrepancies with the measurements were observed for both the heat fluxes and the temperature profiles.

The successful application of CFD codes to the simulation of large enclosures depends crucially on the use of accurate boundary conditions. However, the available CFD codes are suitable for airflow predictions, though special care must be taken to ensure sufficient grid refinement and distribution. Improvements are still needed with the buoyancy extensions in the turbulence equations and with wall-function formulations.

4.6 Atrium Grafenau, Zug, Switzerland

4.6.1 Description of Case Study

General

'Grafenau' (Figure 4.6.1a) is a large office building that was completed in 1993. The first of two planned additional wings on the west side was completed in November 1995.

The building contains three atria of interest to Annex 26. All three face south; they are 26 m high, and have floor areas of 320, 320 and 640 m² respectively. Figure 4.6.1b shows an inside view of the largest atrium. One of the two smaller atria, atrium 'East' (320 m²), which is the right-most atrium in Figure 4.6.1a, was subject to detailed measurements.

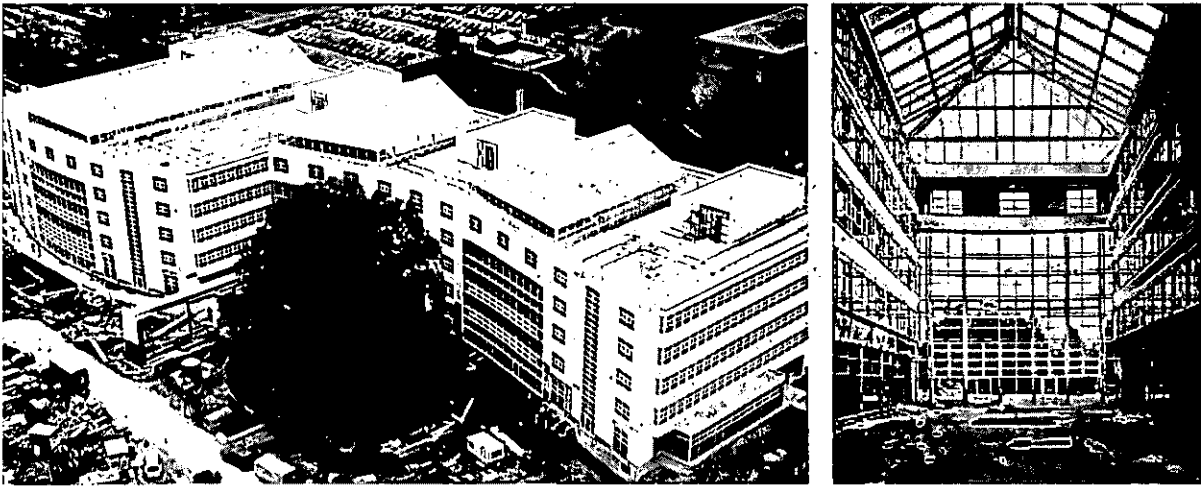


Figure 4.6.1 (a) Left: View of whole building, south side.
(b) Right: Inside view of largest atrium, before completion.

Site and location

Located 46°10' N and 8°30' E, the building is situated in the centre of the small town Zug (30 000 inhabitants), 22 km south of Zurich, halfway to Lucerne, and only about 150 m from the shore of the Lake Zug, circled on map to the right.

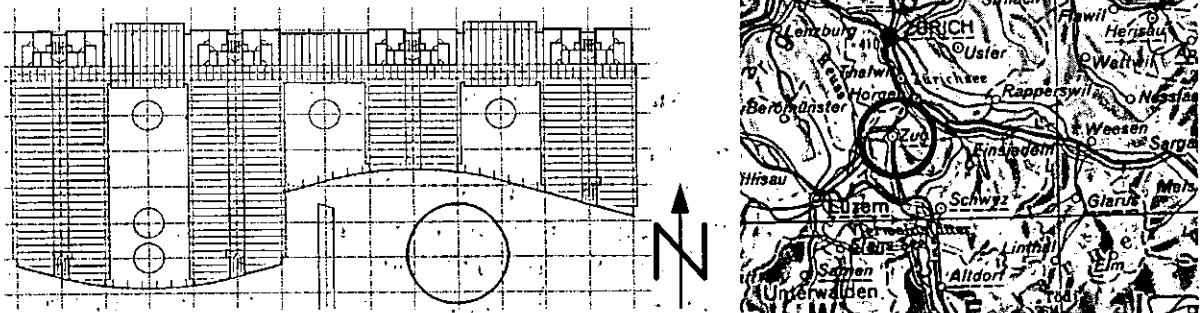


Figure 4.6.2 Above: Plan of Grafenau building, Zug.
Right: Map of location.

Building services

The building is designed as a demonstration building for energy-conservation, so the building's control system is more extensively equipped with measuring points than usual, with financial support from the Swiss Federal Office of Energy (BEW). It contains over 30 permanent monitoring points: outside air temperature (on the roof), temperature in all atria at six levels near an inside office facade.

Ventilation and heating

Each building wing has its own ventilation system on the roof with a heat recovery wheel of efficiency 79%. The offices have a constant ventilation rate. In conference rooms the air change rate can be increased by a factor of 2 on demand. Air supply in the offices is of displacement type. There is a small evaporative cooling system for some conference rooms. An oil/gas boiler system supplies the additional heating required.

In summer, fresh air is taken from outside (on the north facade). In the intermediate season, 70% pre-heated air is taken from the atrium, if the following conditions are fulfilled:

- Heat recovery power is over 70% of maximum before use, and over 20% of maximum during use of atrium air
- No heating in the atrium, and atrium temperature is over 10°C

The air change rate in the atria is about 5 ach (outside air) when atrium air is used for the ventilation system, or in natural ventilation in summer with open roof openings, and about 1 ach when the atrium roof vents are closed. Fresh air can enter the atrium by natural convection through intakes in the north facade at first floor level. When the atrium temperature drops below 10°C, it is heated by the hot-water heated convectors shown in Figure 4.6.5c. This is however very rare; in the winter of 1994/95 the heating was used only one day!

Shading of the atria

The atria roofs have each 3 groups of sun-shade awnings facing east, south and west, which are controlled separately by individual sensors. The sun shading is mounted inside, 1m below the glass roof, and has following properties: 71% reflectance, 5% absorptance, 24% transmittance (for visible light and total energy).

The atria are shaded in summer as soon as the atrium temperature reaches a threshold value, and during winter nights if the outside temperature is below -10°C. In addition, the windows of the offices have blinds (also towards the atria) which are centrally controlled. The control can be locally overridden by the occupants. The blinds have the following properties: 71% reflectance, 4.4% absorptance, 24.6% transmittance (for visible light and total energy).

Glazing

The glazing in the atrium roofs and facades has a U-value of 2.8 W/m²K including the frames, a reflectance of 14%, and a transmittance of 80% for sunlight.

Description of atrium 'East' (Annex 26 case study)

This atrium is roughly rectangular in shape, except for the glass facade which is slightly curved. See Figure 4.6.3 for the ground plan and Figure 4.6.5a for an outside view. At ground level in the atrium there are two inside buildings, an exhibition hall and a cafeteria, and a tree, all of which are shown in Figures 4.6.3 and 4.6.4. The three atria are connected at ground level by an open passage 3.5 m high and about 4 m wide. On the 4th floor, the office wings are connected by a gallery in the facade of the atria, shown in Figure 4.6.1b.

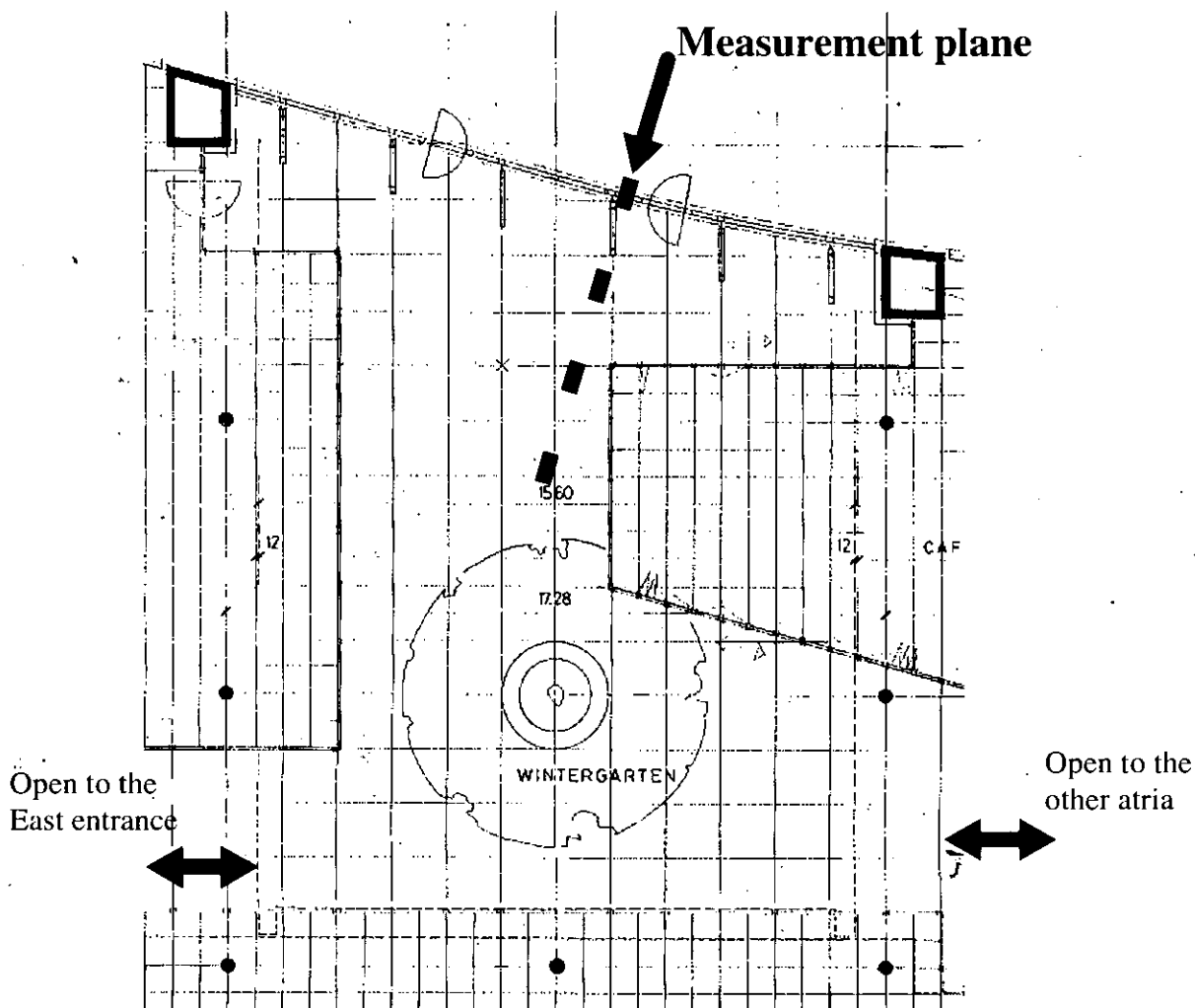


Figure 4.6.3 Ground floor plan of atrium 'East', showing location of measurement plane.



Figure 4.6.4 Atrium "East". Left: Inside view from back to front, through cafeteria building, still empty. Right: Inside view from front to back with cafeteria building and tree.

Facade structure

The glass facade is not at all a smooth surface, but has quite a complicated frame structure. This can be seen in Figure 4.6.5; the atrium heating system is integrated with this structure. Figure 4.6.6 shows a drawing with some details. The height of the glass facade to the gallery is 14.4 m.

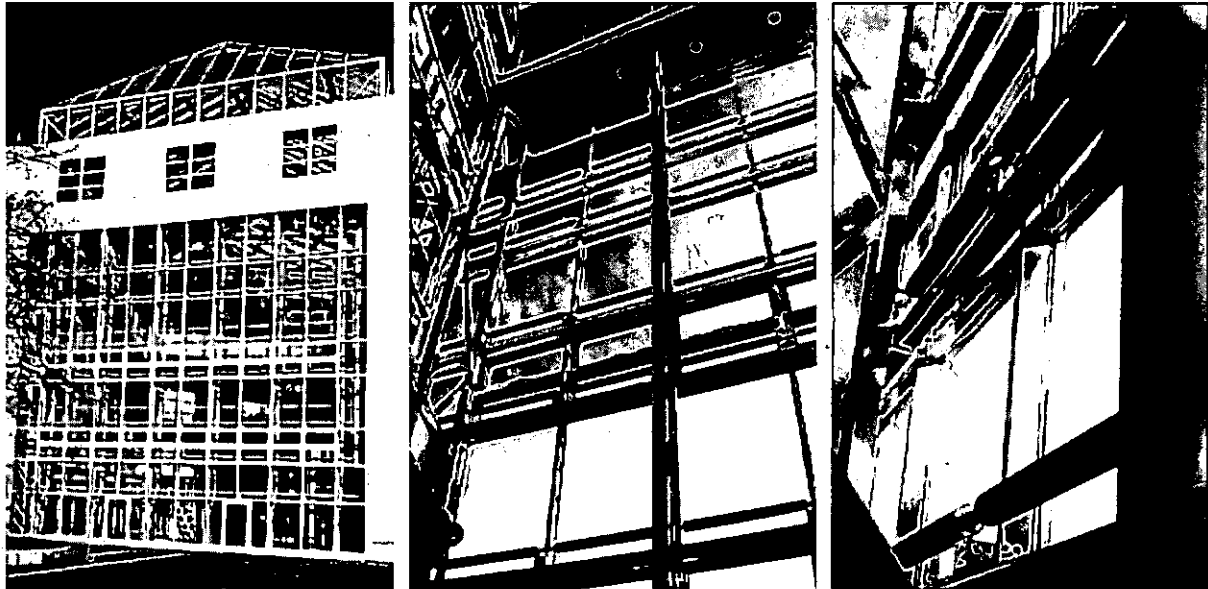


Figure 4.6.5 (a) Left: Outside view of atrium glass facade. (b) Middle: Inside view of part of glass facade with structure. The gallery is visible on top. (c) Right: Details of structure with heater elements.

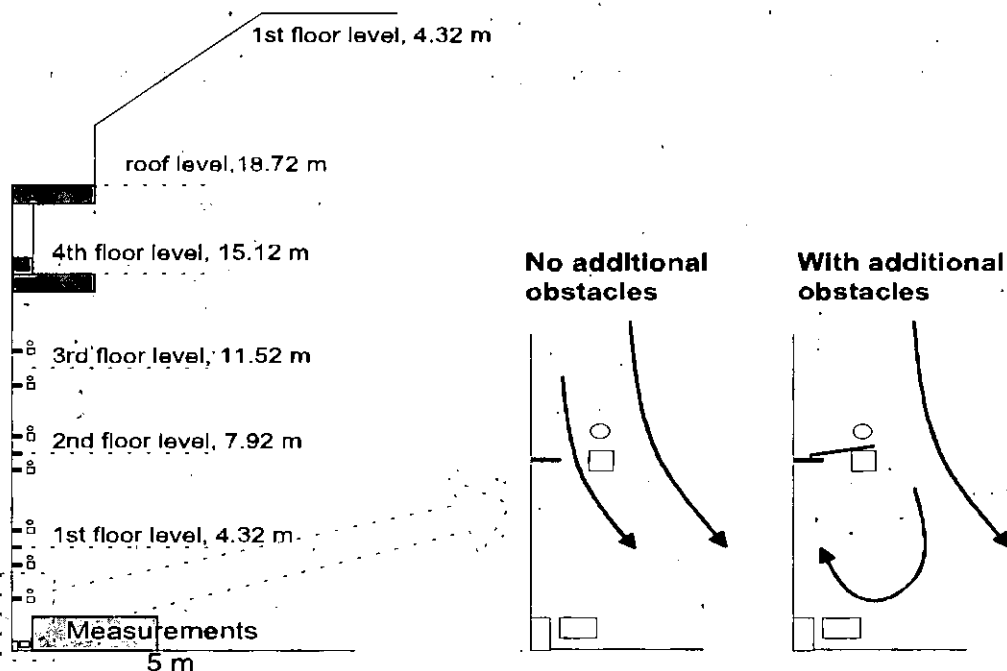


Figure 4.6.6 Details of facade with obstacles (part of structure and heater elements). In some experiments the cold air downdraught has been inhibited by adding additional obstacles.

Measurement location

For the downdraught measurements (air velocity and temperature) a plane perpendicular to the glass facade was selected; the choice was not free because of the two inside buildings of height of 3-4 m. In addition the glass temperature was measured at heights of 2 m and 10 m as well as the atrium air temperature at a distance of 6 m from the facade at a height of 1.1 m.

Figure 4.6.3 shows the measurement plane in the atrium, while Figure 4.6.6 shows the location of the measurement points.

4.6.2 Measurements

Following experiments are described here in some detail:

- Permanent monitoring with 30 temperature probes, every 5 minutes, all year
- Additional temperature and velocity measurements near the glass facade
- Envelope permeability by stack pressurisation

Permanent monitoring

Figure 4.6.7 shows examples of the atrium temperatures on a winter and a summer day. Such data is monitored all year round [Pauli and Ruch, 1994].

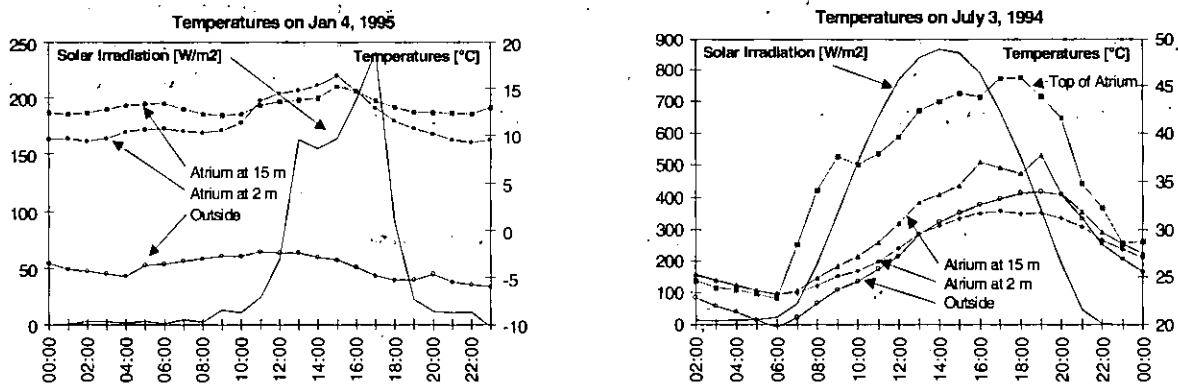


Figure 4.6.7 Examples of permanently monitored measurements. Left: Temperatures in one atrium in winter. Right: Temperatures in one atrium in summer.



Figure 4.6.8 Computerised equipment with 3 omnidirectional anemometers used for measurements.

Additional temperature and velocity measurements

General

The main goal of the additional measurements was to investigate cold air drafts, primarily for comparison with model predictions. As only a limited amount of work was available for the Annex-26 measurements, it was decided to choose a simple situation on a cold winter day without direct sunshine, without ventilation or people.

- Outdoor air temperature
- Surface temperature inside, atrium air temperature 1.1 m above floor
- Air velocity and temperature profiles near floor at several distances from facade
- In addition, the flow pattern was visualised by smoke and captured on video

Measurement dates

1 st day	Dec 19, 1994	cloudy, some rain, outdoor temp. 5 °C
2 nd day	Jan 12, 1995	cloudy, some snow, outdoor temp. 1 °C
3 rd day	Jan 31, 1996	cloudy, outdoor temp. -2 °C

The most detailed results were obtained on the last measurement day when new computer-controlled equipment was used (see Figure 4.6.8), which can scan a plane of 2m×1.2m with 3 simultaneously monitoring omnidirectional hot-wire anemometers. The flow direction was determined by smoke release and the flow pattern was captured on video.

The data collected on the 2nd day (one year earlier) showed velocities that were about 30% smaller, and smaller temperature differences within the atrium.

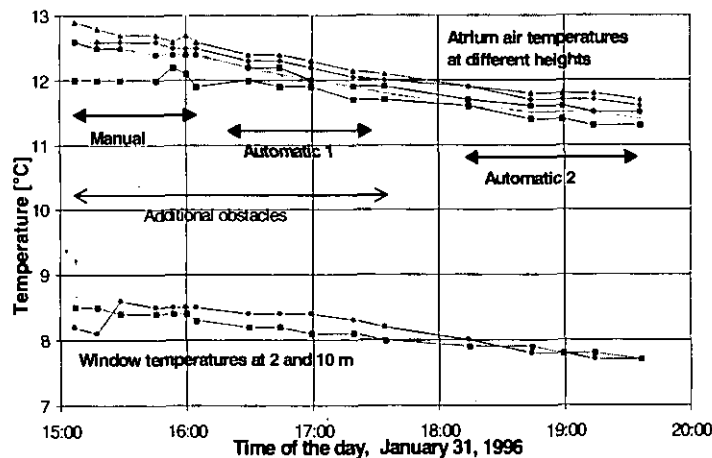


Figure 4.6.9 Temperature data on 3rd measurement day, Jan 31, 1996, for some monitoring points in the atrium. The terms “manual” and “automatic” refer to the measurement sets.

The atrium temperatures were measured along a column in the centre of the atrium, and with the sensors connected to the building control system, close to the office walls. Figure 4.6.9 shows temperature data for several locations in the atrium. It is surprising to see that all the inside temperatures decrease by 1°C within 4 hours, while the outside temperature increases by 1°C in the same period, followed by a sudden decrease by 1°C at 8pm. This data agrees with manual measurements taken inside the atrium and outside.

The facade frame structure consists of a series of metal bars (see Figure 4.6.5). During part of the experiments, these 'native' obstacles were enlarged by placing 37 cm wide cardboard over the bars, such that the air had to flow around the enlarged obstacles (Figure 4.6.6). This was done over a height of 8 m and a width of 9 m in the facade. The following data sets were taken:

Data set	Facade obstacles
Manual	Enlarged
Automatic 1	Enlarged
Automatic 2	No extra

Figure 4.6.10 shows a comparison of the first 2 sets for the same situation, but not taken at the same time (see Figure 4.6.9). It can be seen that :

- The data collected manually and by the automated setup agree well
- The velocity boundary layer along the floor, due to the atrium facade downdraught, has a thickness of roughly 1m. Highest velocities are found close the floor (~10 cm). Above 1m, velocities are below 0.1 m/s
- In the case of the enlarged obstacles, air velocities are slightly higher at a distance of 3m, but up to 30% lower closer to the facade (1m or less), close to the floor. It was observed from smoke visualisation that there was a small back recirculation in this case. These results are qualitatively sketched in Figure 4.6.6
- Temperatures are about 0.5°C lower at the floor, due to the downdraught, but otherwise show nothing particular

Smoke visualisation

In addition to the measurements, smoke visualisation was performed in the measurement area and in the upper half of the atrium near the glass facade. The smoke distribution was visually observed and recorded on video. Surprisingly, the smoke pattern is clearly visible on video.

Without additional obstacles, the smoke distribution for the above measurement situation showed a steady downdraught along the facade followed by a distribution along the floor in the measurement area. In the case of additional obstacles, a recirculation zone near the lower corner was observed, as sketched in Figure 4.6.6. The air velocity was around 0.3 m/s.

On the 2nd day, the following additionally observations were made: Smoke that was released from half way along the gallery, at a height of 15m, showed that downdraught velocities up there were quite small (0.1~0.2 m/s). Later, smoke released at one end of the gallery, about 2-3 m from an inside office wall. Instantly the smoke flowed upwards (instead of downwards). At the same time, it was noted that a person entered the building through a door quite far away, so this event influenced the flow pattern that far. This demonstrates that the downdraught driving forces are quite small.

In addition, a second experiment was performed with the facade heaters turned on (we assumed that after about half an hour, constant conditions would be achieved). The flow pattern was then reversed. The air flowed steadily but quite strongly upwards along the facade, and of course also through the gaps in the facade's metal structure. Air velocities were around 1 m/s. Along the floor air is entrained towards the near-facade updraft, at velocities of about 0.4 m/s. At a height of 1.5 m however, the air was still and appeared stratified.

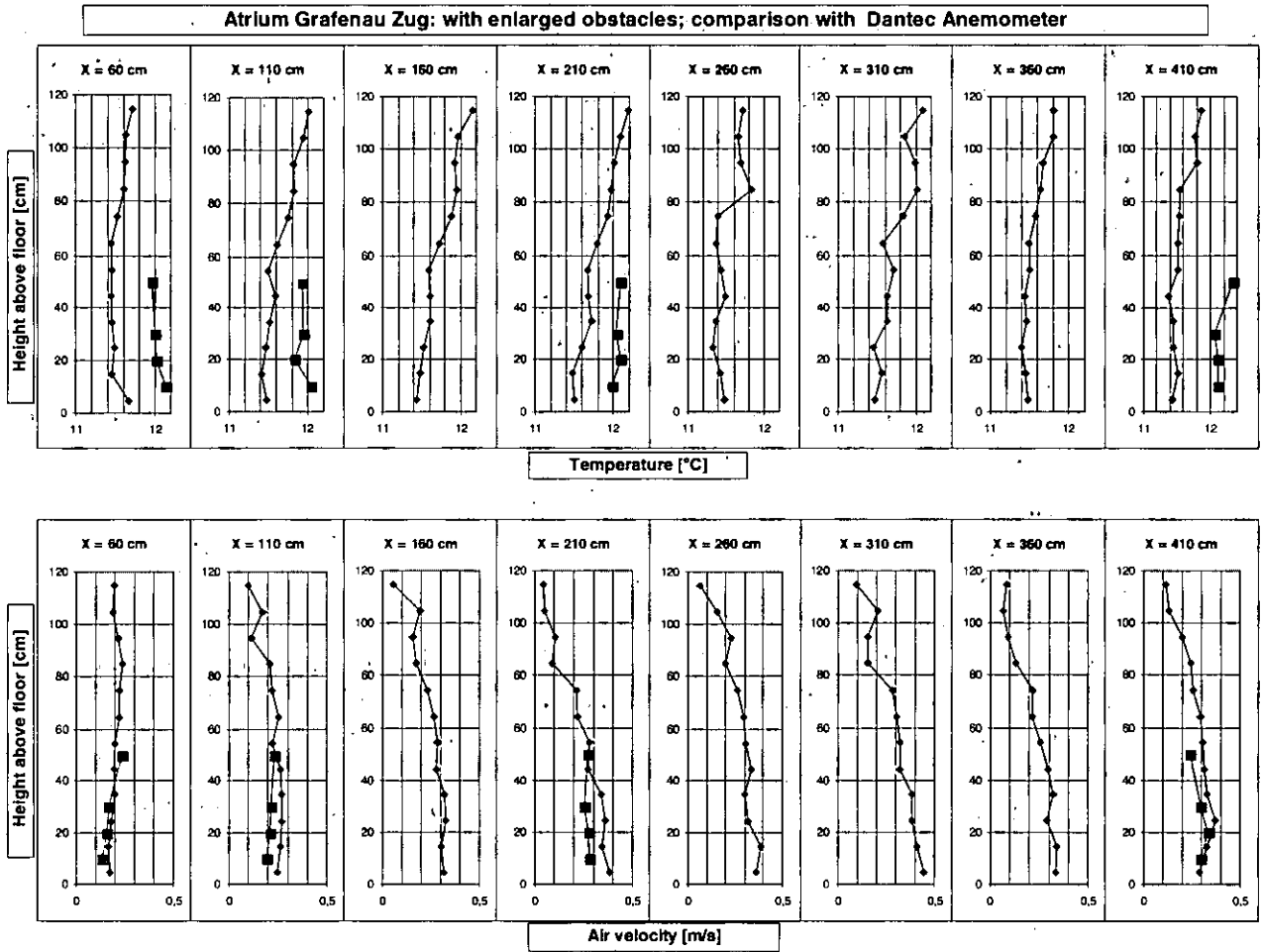


Figure 4.6.10 Automated and manual measurements, both with enlarged obstacles in facade. (a) Above: Temperature values, (b) Below: Velocity values. The additional 4x4 data points show the values measured manually by a Dantec velocimeter; the agreement is very good bearing in mind that the Dantec measurements were collected one hour earlier.

Envelope permeability by stack pressurisation.

The air leakage characteristics of the East atrium (8000m³) were determined by van der Maas using the stack pressurisation method, Section 3.3.1 [Hajakawa and Togari, 1990; Roulet and Müller, 1996]. The stack pressure variation with height was calculated from the inside-outside air temperature difference, measured during the experiment along a column in the centre of the atrium. For a given temperature difference ΔT and a height z from the neutral pressure level (NPL), the stack pressure difference equals [Roulet and Müller, 1996]:

$$\Delta p \approx \frac{z\Delta T}{30} \tag{4.6.1}$$

The NPL is the height where the inside-outside pressure difference is zero and could be observed when it is level with a door opening, by visualising the bidirectional velocity profile with smoke. With a temperature difference of 13 K ($T_{in}=10^{\circ}C$, $T_{out}=-3^{\circ}C$) and a height of 25 m, the maximum stack pressure in the experiments was 11 Pa.

The theoretical stack-flow velocity follows from the Bernoulli equation $\Delta p = \frac{1}{2} \rho u^2$. The air velocity was measured in the door or window opening and using a velocity coefficient of (0.8 ± 0.1) the position of the NPL was estimated. The observed stack velocities were less than 3 m/s.

The experiments were performed with an outside wind speed of less than 1 m/s, so the pressure variations due to the wind were negligible ($\ll 0.6$ Pa), and stable velocity profiles were observed in door and window openings.

For a configuration with two openings, a top opening A_t , and bottom opening A_b , at a distance H , the distance, h , between the top opening and the NPL is given by [Roulet and Müller, 1996; ASHRAE, 1985]:

$$h \approx \frac{H}{1 + (A_t/A_b)^2} \tag{4.6.2}$$

In a first measurement campaign the three atria were not disconnected; the air velocity in an open door ($A_b=1.9$ m²) was high (>2 m/s) corresponding to an airflow rate in excess of 2 m³/s. The top leakage area A_t was estimated to be 3 ± 0.5 m². It was found out later that roof windows in the central atrium were not closed and the open window area was indeed about 3 m².

In the second measurement campaign, the East atrium was separated from the other atria by closing the 4m×5m passageway, using a wooden frame, plastic sheet and tape. The NPL was then found to be 1.6 m above the floor when two doors were open ($A_b=3.8$ m²), and 20.5 m above the floor on the opening of a roof vent ($A_t=1.8$ m²) with the doors shut. With the roof vents shut, and by varying the size of the bottom opening, A_b , and measuring the air velocity in the opening for each case, the top leakage area A_t at height $H=21$ m from the floor was found to be 0.5 ± 0.1 m². Further, using the roof vents as the known opening A_t , the data was found to be consistent with a leakage area at ground level of $A_b=0.1 \pm 0.03$ m². When the plastic sheet was removed, the apparent leakage area at ground level increased to $A_b=0.4 \pm 0.1$ m².

The air infiltration in winter, related to these leakage areas, is plotted in Figure 4.6.11 as a function of temperature difference.

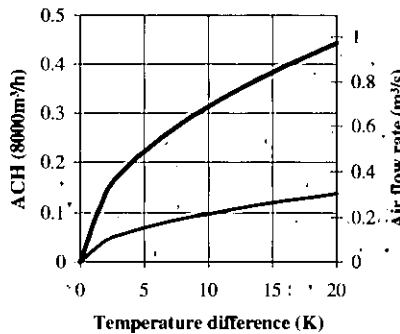


Figure 4.6.11 Air infiltration rate as a function of temperature difference for a leakage area of $A_t=0.5$ m² at 21 m, and ground leakage area $A_b=0.1$ m² (bottom curve) and $A_b=0.4$ m² (top).

4.6.3 Analysis Tools

Overview of model applications

- Draught model (P. Heiselberg)
- Natural ventilation model (D. Aiulfi)
- Thermal zonal model (J. van der Maas)
- CFD modelling to the whole of atrium 'East' (A. Schälin)

Draught model (P. Heiselberg)

Heiselberg (Section 2.2.4) [Heiselberg, 1994] has investigated draught along a cold vertical wall and found a simple empirical relationship between maximum velocity in the occupied zone vs. distance from the wall, as a function of wall height and temperature difference between the wall and the room.

For the 2nd measurement day, the maximum air velocity in the occupied zone at a distance of 1~5 m from the facade was very similar to Heiselberg's model, but the velocity closer than 1.5 m was quite different (see Figure 4.6.12). For the 3rd measurement day, the model's predicted velocities were considerably lower, even if one took the full atrium height of 26 m into account.

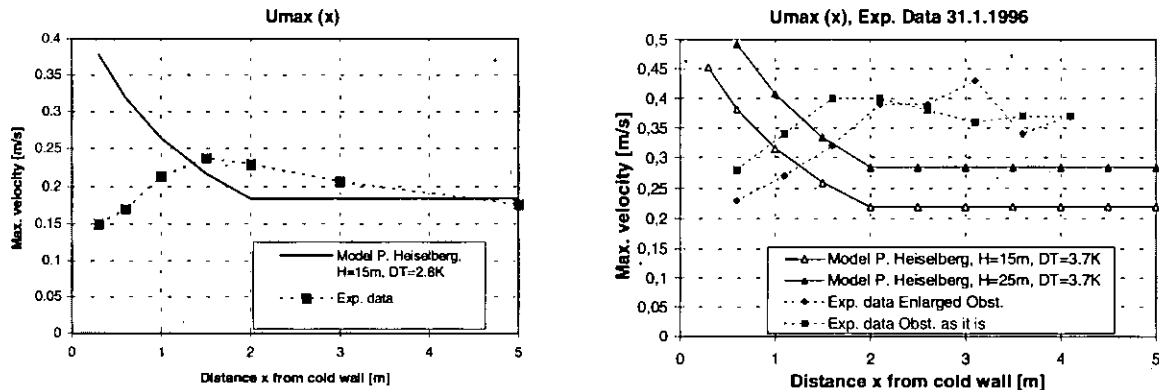


Figure 4.6.12 Prediction of model P. Heiselberg and comparison to measurement data. Left: Data for 2nd day, Jan 12, 1995. Right: Data for 3rd day, Jan 31, 1996.

Discussion

Possible reasons for discrepancies are:

- The facade in the case of the Grafenau atrium shows a lot of structure which inhibits the evolution of a 'nice' boundary layer flow. New work by Heiselberg including the effect of obstacles in the cold facade (Section 2.2.3) [Heiselberg et al., 1995] shows that velocities at distances >2 m from the wall are similar to the case without obstacles, but velocities close to the wall are smaller, and almost only determined by the lowest part of the wall (2.16 m in our case)
- The flow in the Grafenau atrium is disturbed by the inside buildings; the draught air is compressed into the space between the two inside buildings. The numerical simulation supports the existence of this effect (see Figure 4.6.17)

Natural ventilation (D. Aiulfi)

This simple model is based on the same principles of the natural ventilation model presented in Section 2.3.1. The model is based on the same principles as used for stack pressurisation (Equations 4.6.1 and 4.6.2). In addition, hourly solar heat gain is calculated, with and without shading devices.

The model [Aiulfi, 1995] is intended as a design tool to decide the necessary opening area, its type and location, such that natural ventilation by the stack-effect will be sufficient to prevent overheating in the space. Wind will normally increase the overall air exchange rate, and because the critical situation for overheating is a hot and sunny summer day without any wind, wind is not taken into account in the design. Further, the thermal inertia of the atrium has not been taken into account, so a steady-state condition is assumed. This is a conservative assumption, as overheating will usually be overestimated when thermal mass is neglected. However, many atria are lightweight spaces, so such a model will then slightly overestimate the necessary opening area, thus providing a safety margin for the designer.

In the case of the atrium Grafenau Zug a typical hot sunny day has been simulated. Figure 4.6.13 shows the calculated exhaust air temperature for two assumptions :

- Fully mixed airflow in the space
- Linear temperature stratification. The stack flowrate is calculated assuming a linear air temperature variation between inlet and outlet.

In both cases, the exhaust air temperature is calculated from the conditions of energy and mass conservation.

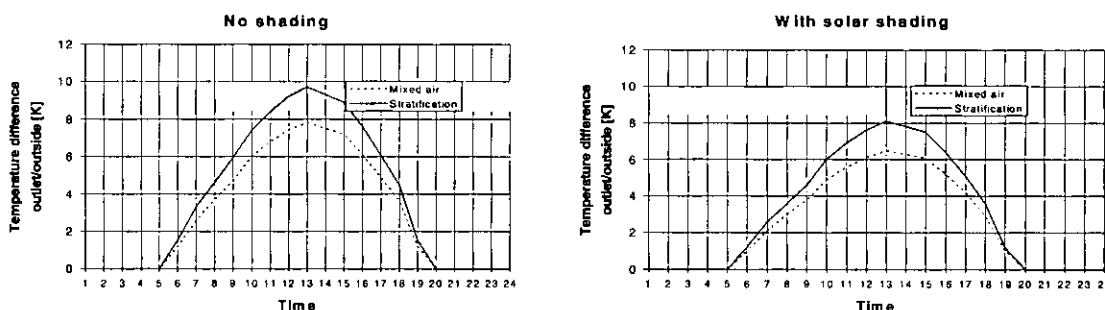


Figure 4.6.13 Predicted overheating in atrium for the two assumptions “Mixed air” and “Stratified air”. Left: No shading. Right: With solar shading devices.

Internal solar shading devices as well as all the openings are used. It was found, if ideal mixing or a linear temperature stratification are assumed, the maximum air temperature difference between outside air and exhaust air is about 6 to 8°C with an air exchange of 75 000 m³/h and 59 000 m³/h, respectively. 59 000 m³/h corresponds to 7 ach, for a volume of 320m²×25m = 8 000 m³.

The temperature rise, measured over a whole summer, was also found to range between 5 to 8°C, depending on the typical day conditions such as wind. Similar calculations have been performed on other atria which confirm the validity of this simple model for design purposes.

In order that the warm air flows out through the highest openings, the design aims at a high position of the neutral pressure level (NPL). From Equation 4.6.2 it follows that for a two-opening configuration, the surface area of the exhaust openings should be significantly

larger than the inlets. The designer should be aware that the air velocity at the inlets is high and that they should be positioned so as not to cause discomfort.

CFD modelling (A. Schälin)

At the IET, CFD calculations using the program TASCflow have been performed for the winter, where comparison with the detailed measurements was possible. The calculation was done using the standard $k-\varepsilon$ turbulence model in conjunction with grid-independent wall functions for natural convection flow [Yuan *et al.*, 1994].

The 3rd measurement day was simulated. To estimate the temperature boundary conditions (inside surfaces of atrium walls and roof) a simple 4-zone thermal model was used. For the glass facade, the experimental value of 8°C was used (see Figure 4.6.9).

Figure 4.6.14 shows the computation model of the atrium with 97 200 cells. The geometry was modelled in a realistic way including the gallery on the 4th floor, the inside buildings at floor level and the roof details. The frame-structure of the glass facade was not taken into account in this model, but the differences in velocities are small (5%), as confirmed by a 2-dimensional calculation.

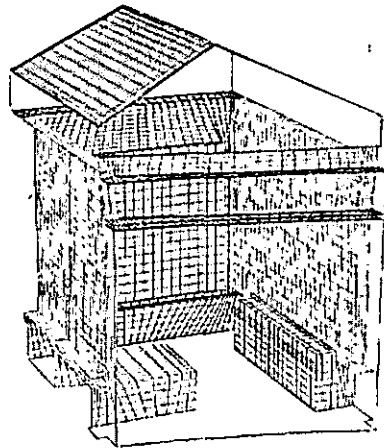


Figure 4.6.14 Grid model of atrium.

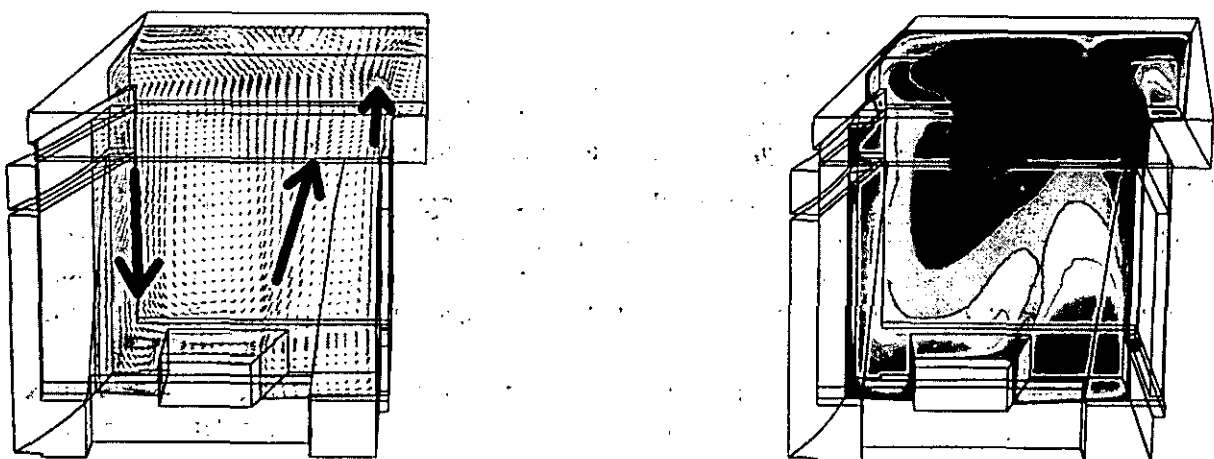


Figure 4.6.15 Left: Velocity profile in a plane perpendicular to the cold facade. Right: Temperature distribution in a plane perpendicular to the cold facade. The temperature range is between 11.5 and 12.5 °C.

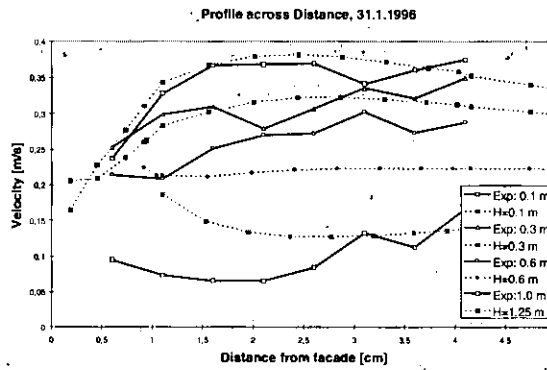


Figure 4.6.16 Comparison between experimental values and CFD results: All the values are magnitudes of the velocity vectors in the measurement plane. Solid lines show measured values, dotted lines show calculated values.

Figure 4.6.15 shows the resulting velocity and temperature distribution respectively in a vertical plane. The measurement plane is about 3 m closer to the viewer than this selected plane which crosses the inside cafeteria building.

Air rises along the rear office wall, which is about 18°C, and is falls along the glass facade. The maximum velocity along the glass facade is about 0.5 m/s. The calculated velocity distribution in the whole occupancy zone on the atrium floor (Figure 4.6.15) do not exceed 0.4 m/s. The highest velocities are found close to the floor (at a height <0.3 m) about 2 m from the facade.

Figure 4.6.16 shows the most interesting comparison between the measured field data and the CFD calculation, along 4 lines at different heights in the measurement plane. The agreement is very good, specially close to the floor: The numerical values are higher at a height of 1 m close to the facade, which can be attributed to the missing glazing frame obstacles in the CFD model.

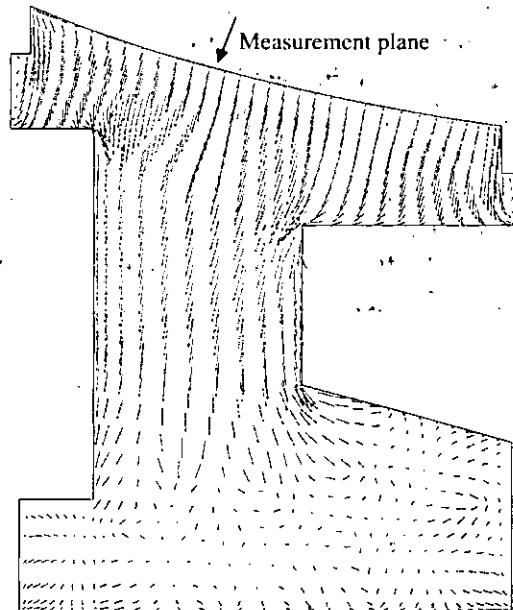


Figure 4.6.17 Velocity distribution in a plane just 0.3 m above the floor in the atrium. It shows the compression of the air flow between the 2 inside buildings.

Figure 4.6.17 shows the compression of the airflow between the 2 inside buildings. This may partly explain the discrepancy between the measured data and Heiselberg's downdraught model. In this case, the predictions of the CFD model are a bit better than that model.

4.6.4 Conclusions and Recommendations

Modelling

Airflow models of different levels of complexity have been applied to this 8000 m³ atrium in order to show their suitability as design tools. The models have been used to predict stack flow ventilation rates, overheating problems, downdraughts along a glazed facade, and local air velocities. Overall, the predictions compare well with the measured air velocities and temperatures, proving that, these models can be used as design tools for the ventilation of atria, if applied with care.

Practical experience in use of the atrium

People are quite happy with the concept of natural ventilation in the atria. The temperatures are reasonable all year round: In summer the atria is considered 'cool', and in winter one can use the cafeteria 'garden' in the atrium at outdoor temperatures below 10°C. The cold downdraught is not felt to be too uncomfortable. The facade heating is very rarely used, and is usually only run on special occasions, like exhibitions or concerts, to maximise comfort.

Important contributors to the good indoor climate are the intelligent control of the shading and the ventilation, as well as some architectural features: The atria roofs are higher than the other building parts. The warm air can therefore be effectively removed by opening the roof vents, even enabling flow enhancement by wind. In winter, and especially in the intermediate season, warm air from the atrium can be added to the office ventilation air by intakes in the roof area. When it is very cold outside, the roof openings are closed, and the atrium is shaded at night to reduce heat loss by radiation.

The office occupants complain about glare from direct sunlight when the sunshades in the atria are open to let the air warm up in the intermediate season, because they do not have local sun blinds. Information on how and why the whole concept works should therefore be spread better to the building's occupants.

Optimizing the building control is very important but also very time-consuming. Without a long-term study of the behaviour of the whole system and measuring all the relevant parameters, it is hardly possible to find an optimum trade-off between all the requirements (heat buffer, adding air to the ventilation, sun shading and preventing solar glare).

4.7 Polytechnic Auditorium, Turin, Italy

4.7.1 Description of Case-Study

This case study enclosure is one of the largest auditoria (1750 m^3) at the Polytechnic of Torino, Italy, used for first and second year students. It has a capacity of about 350 seats arranged in 17 rows divided into two groups by a longitudinal main passage, and it has been recently equipped with a CO_2 -controlled mechanical ventilation plant (DCV system). The room, whose longitudinal section and plant view are shown on Figures 4.7.1 and 4.7.2, has a stepped floor sloping down from the main entrance to the teacher's desk. The ceiling is shaped in large steps and, with a small portion of the two lateral walls, is the only boundary wall facing outdoors. All the other walls separate the auditorium from other indoor spaces. A total of ten fixed windows are located in the upper part of the two lateral walls, but solar radiation is usually shaded by heavy curtains.

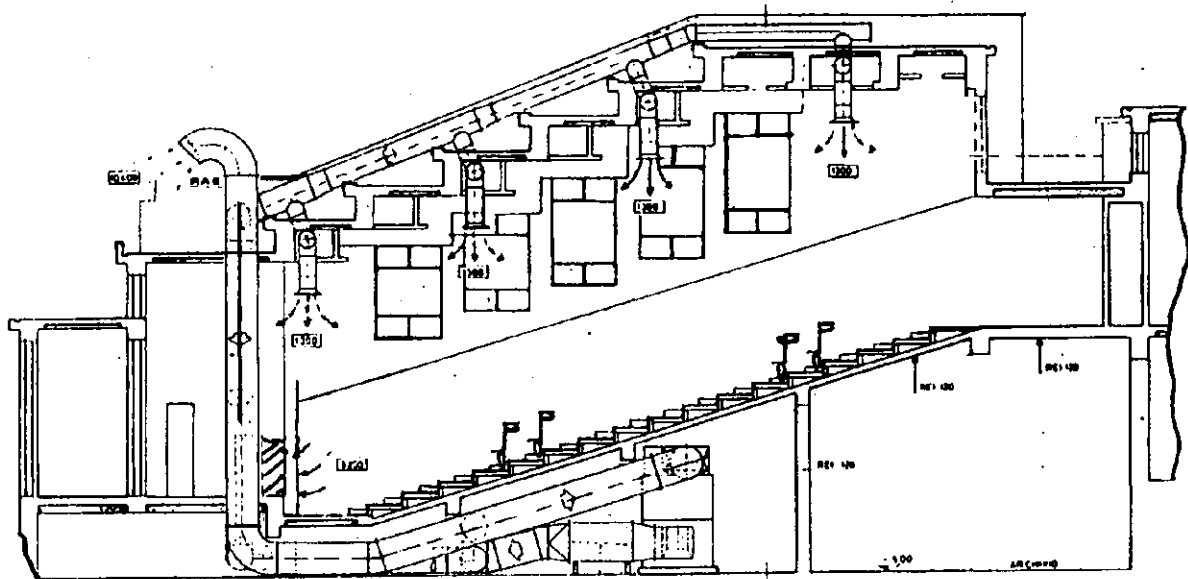


Figure 4.7.1 Longitudinal section.

The supply air is distributed by means of 8 circular inlet grilles located about 1 meter below the ceiling. These diffusers are of the variable geometry type, with 6 helicoidal blades generating a turbulent flow. The jet shape (i.e. penetration length, opening angle, swirl...) is set by changing the angle of attack of the blades; its control is based on the temperature difference between the supply air and the exhaust air. The polluted air is exhausted by two grilles located in the lower part of the auditorium, near the teacher's desk. The ventilation and air conditioning system is placed in a technical room below the auditorium; the air treatment is centralised. There are two fans, one for supply air and one for exhaust air, that generate a balanced and constant volume flow rate of $10\,400 \text{ m}^3/\text{h}$ (nominal design value). A system of conjugate dampers allows the adjustment of the recirculation rate. It is possible to vary the fresh air volume flow rate from a minimum 'base' value to the total amount of supply air, depending on the occupancy load, that is, on the CO_2 air content detected by a sensor located in the exhaust duct.

- Sampling points Cases N° 4 to 7 and 15 to 18
- Sampling points Cases N° 1, 2 and 10
- Sampling points Case N° 3

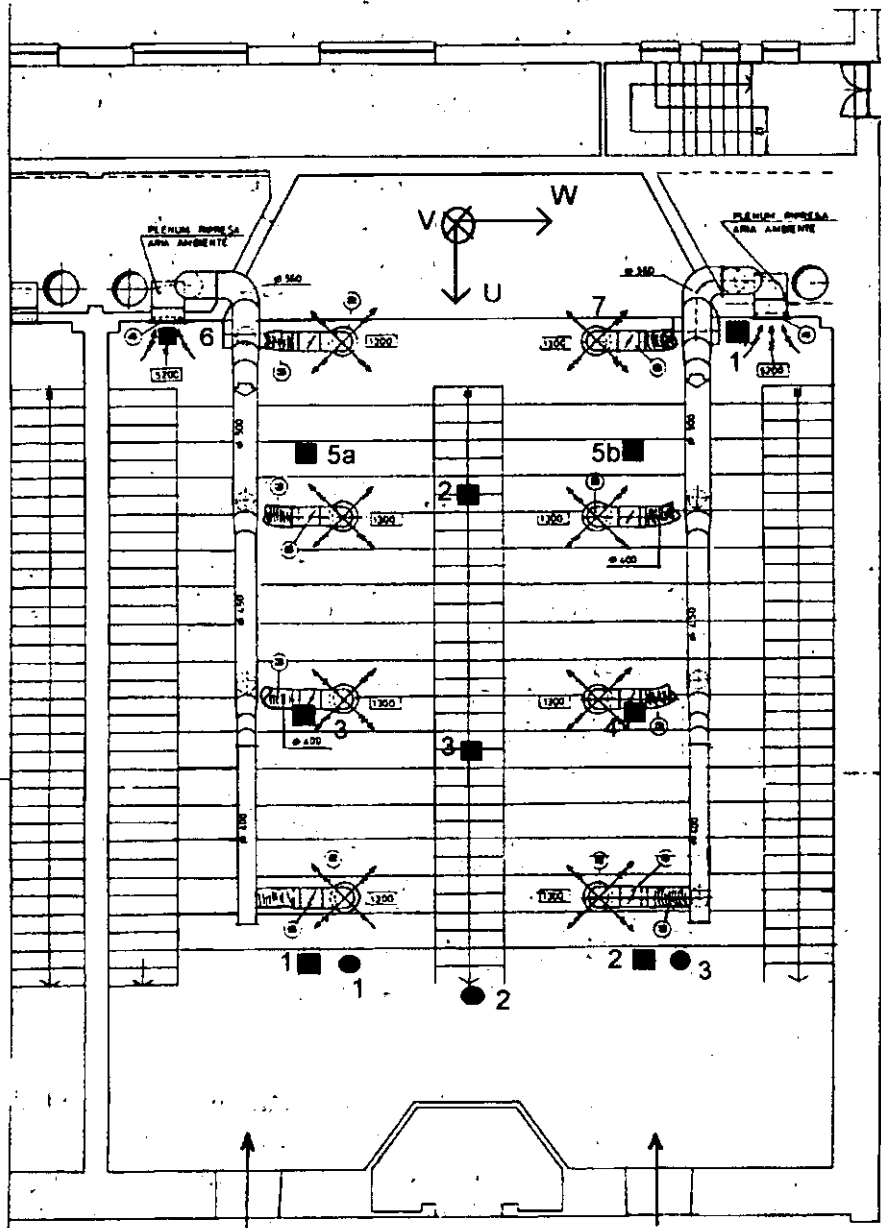


Figure 4.7.2 Plan view and location of sampling points.

Table 4.7.1 Summary table of the auditorium main features and the ventilation system.

Auditorium size (approx.)	21.8 × 16 × 5.5 (height)
Volume	1750 m ³
Nominal volume flow rate	10400 m ³ /h
Ventilation system	<ul style="list-style-type: none"> • Balanced • Constant volume, variable fresh air rate • Low velocity • Cooling and heating only
Heat recovery	enthalpic

During winter, the supply air can be preheated by means of hot water (80°C); the system is equipped with an enthalpic heat recovery unit also performing a certain degree of humidification of the inlet air. During summer, time the supply air is cooled by means of well-water, and, since its temperature is constant at about 15° C, the control of the thermohygro-metric conditions of the air is limited in range. Two series of filters ensure sufficient particle uptake.

4.7.2 Measurements

Four types of measurements were been performed (A, B, C and D), each for a number of different configurations and operating conditions. Measurement types and features are summarised in Table 4.7.2 (for more details on measurement methods and procedure see Chapter 3). For all types of measurements, a photoacoustic gas analyser was employed to measure tracer gas and contaminant concentrations.

Table 4.7.2 Summary table of measurements.

Aim of measurement campaign	Code	Measurements performed
<i>IAQ</i>	A	<ul style="list-style-type: none"> • CO₂ concentration • Water vapour content • TOC (Total Organic Carbon) concentrations (Cases 6 & 7) • Location of relevant contaminant sources • Air temperature
<i>Mechanical ventilation flow rates</i>	B	<ul style="list-style-type: none"> • Fresh air supply rate • Total air supply rate • Recirculated air rate
<i>Ventilation parameters</i>	C	<ul style="list-style-type: none"> • Local mean age of the air • Local air change index • Air change efficiency • Dosage index due to unit pulse of contaminant • Local mean age of the contaminant • Contaminant removal effectiveness
<i>General air movement pattern</i>	D	<ul style="list-style-type: none"> • Air velocity measurement

Indoor climate equipment monitored the air temperature. For B- and C-type measurements different tracer gas methods were applied (see Table 4.7.3).

When the tracer gas SF₆ was used, in order to avoid buoyancy problems, it was injected into the supply air in the plantroom, just upstream of the centrifugal fan, to achieve good mixing with the air. In addition, its maximum concentration was kept below 90 ppm vol.

Type D measurements were taken with an ultrasonic anemometer. Table 4.7.4 summarises all the measurements performed, showing the general features of the various cases. The location of the sampling points is shown in Figure 4.7.2.

Table 4.7.3 Summary of used tracer-gas methods.

Method	Method code	Type of gas
Constant-emission	a1	SF ₆
	a2	SF ₆ and N ₂ O
Step-down	b	SF ₆
Pulse	c	SF ₆
Step-up	d	SF ₆

Table 4.7.4 Measurements summary.

Case	Type & method	No. of occ.	Vent. system	DCV	Fresh air supply	No. of samplg. points
1	A -	55	on	on	-	2
2	A -	33	off	-	nat.vent.	3
3	A -	200	on	off	100 %	3
4	A -	114	on	on	-	6
5	A -	145	on	on	-	6
6	A - ¹	194	off	-	nat.vent.	6
7	A - ¹	200	on	off	100 %	6
8	B a1	-	on	off	100 %	-
9	B a2	-	on	on	38.2 %	-
10	C b	33	off	-	nat.vent.	3
11	C c	-	on	off	100 %	1 (exh.)
12	C a1	-	on	off	100 %	2 (exh.; inlet)
13	C b	-	on	off	100 %	2 (exh.; inlet)
14	C b	110	on	on	-	6
15	C b	145	on	off	100 %	6
16	C b	43	on	off	50 %	6
17	C b	194	off	-	nat.vent.	6
18	C b	200	on	off	100 %	6
19	B a1	-	on	off	100 %	-
20	B a1	-	on	off	100 %	-
21	C b	-	on	off	100 %	1(exh.)
22	C d	-	on	off	100 %	6
23	C b	-	on	off	100 %	1(exh.)
24	D -	-	on	on	-	-

(A) IAQ measurements

These measurements were performed in order to assess the IAQ and the thermo-hygrometric indoor environment. Different conditions have been investigated, with 2 or 6 sampling points. In the last case, air samples were taken at six different locations throughout the room using

¹ TOC concentrations are available

vertical plastic tubes. A platinum resistance thermometer, installed inside an aluminium radiation shield, was used to measure the air temperature.

Figure 4.7.3 shows an example of the monitored concentrations of CO₂ for some of these experimental investigations. It is possible to see that natural ventilation (case 6 in Table 4.7.4) does not allow an effective control of the IAQ, while, when the ventilation plant is switched on (case 7), after a short period of time the CO₂ concentration is reduced to about 1000 ppm. Another measurement, performed with DCV on (case 5), showed that the system was able to keep a steady CO₂ concentration of about 1000 ppm.

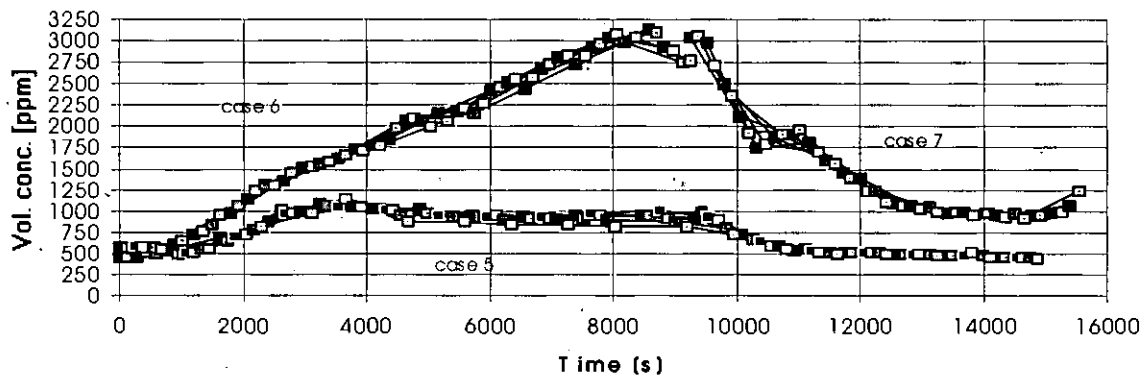


Figure 4.7.3 CO₂ concentration - Cases 5, 6 and 7.

Figure 4.7.4 reports the Total Organic Carbon concentration versus CO₂ concentration for cases 6 (squares) and 7 (circles); as the occupants are the only internal pollutant source, it is possible, knowing the production rate of CO₂, to determine the production rate of TOC per person. The resulting value is: $Q_{TOC} = 0.051$ l/h per person. The good correlation ($r^2 = 0.91$) between CO₂ and TOC concentrations confirms that CO₂ as a good indicator of IAQ when pollution is mainly generated by people.

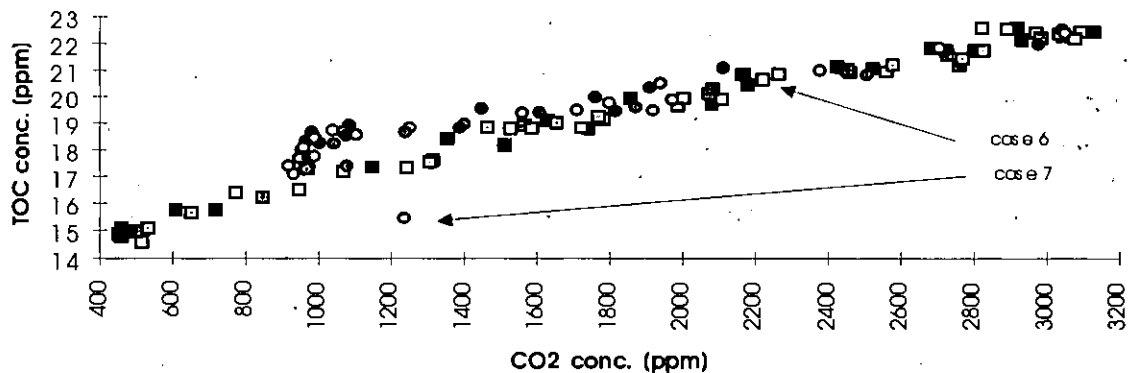


Figure 4.7.4 TOC concentration versus CO₂ concentration - Cases 6 and 7.

(B) Mechanical ventilation flow rates

Measurements were made in the plantroom in order to verify the magnitude of the air flow rates these values allow to check the nominal plant performances for the system

commissioning, and provide boundary conditions for the CFD simulations. The influence of plant maintenance and the effect of time on the system performances were investigated.

Different methods, a_1 and a_2 in Table 4.7.3, were used. The measurement error on flow rates results from both the error produced by the gas meter ($\pm 1.8\%$) and that of the gas monitor ($\pm 1.0\%$), and may therefore be estimated at around 3%. Results are summarised in Table 4.7.5.

Table 4.7.5 Air flow rate measurements (m^3/h).

Case	Filters status	Supply air (S)	Exhaust air (E)	Fresh air (F)	Recirculated air (R)
8	new	10700	10700	10700	0
9	new	9700	9700	3700	6000
19	aged	5000	5250	-	0
20	aged	7000	7400	-	0

Nominal condition values (cases 8 and 9 in Table 4.7.4) were in good agreement with the design flowrate of $10\,400\ m^3/h$. The difference between the two cases probably relates to the increased accidental pressure drops when the air is partially recirculated and enthalpic recovery is used. Results related to aged filters seem rather low air flowrates, with unbalancing between supply and exhaust.

(C) Ventilation parameters

A number of ventilation and air change indices have been measured to assess the ventilation plant performances. Different methods have been adopted in order to check their reliability and the easiness of development. For all the performed cases, the tracer gas (SF_6) was injected in the supply duct. When a starting uniform concentration was required (method b in Table 4.7.3), some minutes of forced total air recirculation ensured satisfactory indoor air mixing. For multi-point measurements, samplings were taken at six locations by means of an automated apparatus for multi-point sampling.

Analyses have been done on either natural ventilation (cases 10 and 17 in Table 4.7.4) or mechanical ventilation (cases 12-16, case 18 and cases 21-23). Some measurements were repeated, with the same boundary conditions, on different days in order to assess the reliability of the methods (for example, cases 15 and 18, cases 17 and 10).

Figure 4.7.5 shows, for cases 15 and 18 (method b Table 4.7.3), the measured values of the local and global air change index. It is possible to see that the value of *global air change index* is less than 1; this indicates a condition of partial short-circuiting of the supply air. Table 4.7.6 shows the corresponding local air quality index values and the local mean age of the air.

For natural ventilation (case 17), an air change rate value of $0.43\ h^{-1}$ was measured, with local mean age of air between 130 and 152 minutes. A measurement performed for

similar conditions (case 10), showed comparable τ_p values in the central (point 2, Figure 4.7.2) and upper part (point 3, Figure 4.7.2) of the auditorium, while a large difference was detected in the lower part (point 1, $\tau_p=320.8$ min).

For cases 21, 22 and 23, a procedure made of sequential step-up and step-down measurements (methods *b* and *d* in Table 4.7.3) was used. All the measurements were done in the plantroom and hence they only give information about mean values. The obtained data is summarised in Table 4.7.7.

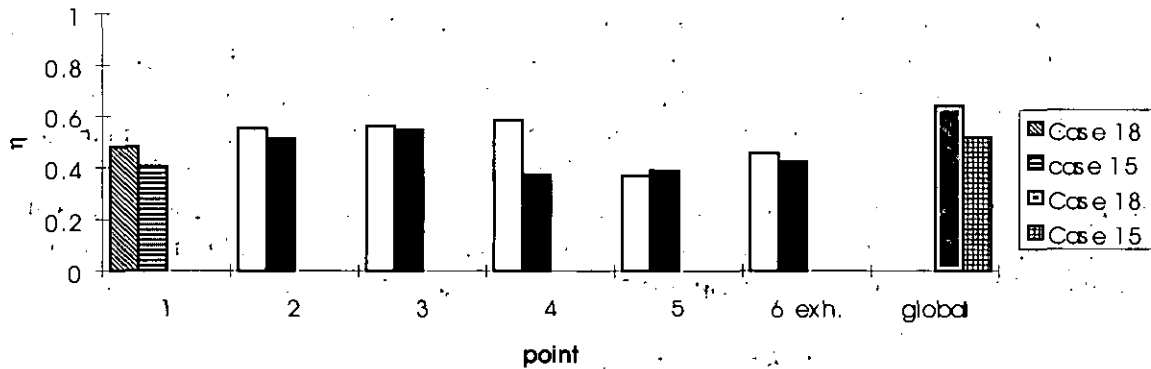


Figure 4.7.5 Air change indices - cases 15 and 18.

Table 4.7.6 Mean ages of the air, local air quality index (defined as: C_{exh}/C_p). Table 4.7.7 Cases 21, 22 and 23.

Point ²	case 15	case 18
air quality index		
1	0.90	0.98
2	0.91	0.99
3	0.91	0.98
4	0.92	1.03
5	0.96	0.98
6 (exh.)	1	1
ages of the air (τ_p [min.])		
1	20.5	24.3
2	17.8	19.3
3	17.5	18.0
4	16.9	26.6
5	26.7	25.4
6 (exh.)	21.6	23.4

Case	Mean age at the exhaust [min]	Global mean age [min]
21	27	30
22	20	22
23	36	41

It is interesting to see that the first two measurements show quite comparable results, while quite larger values are found in the second step-down (case 23), performed at the end of the daily operation period of the plant. The increase in the age of air during the operating period is due to the progressive filters' obstruction and to their saw-tooth-shape pressure-flow

²Point numbers refer to Figure 4.7.2.

rate characteristic. The decrease over time of the supply air flowrate was also confirmed by some measurement performed in the supply ducts (method *a1* Table 4.7.3).

(D) Air flow pattern inside the enclosure

The general airflow pattern inside the enclosure was been investigated using an ultrasonic anemometer that allows the simultaneous measurement of the three velocity components with a sampling frequency of 4 Hz. Measurement conditions were: nominal supply air flow of 9000 m³/h, no occupancy, isothermal air flow rate.

The velocity profile along a vertical line below the air diffuser (point 7 in Figure 4.7.2) and along three horizontal axes (between points 1-2, 3-4, and 5a-5b in Figure 4.7.2) was analysed. For the vertical profile, samples were taken at 25 cm intervals starting at 1.5 m above the floor. These results are shown in Figure 4.7.6, where the velocity components (see Figure 4.7.2 for the reference co-ordinate system) and magnitudes are plotted. It is possible to see that the decay of the jet centreline velocity is not sufficient to assure acceptable air velocity in the occupied zone (0.8 m/s). Horizontal profiles, instead, have pointed out a quite uniform velocity distribution with low velocities (velocity magnitudes between 0.1 and 0.35 m/s).

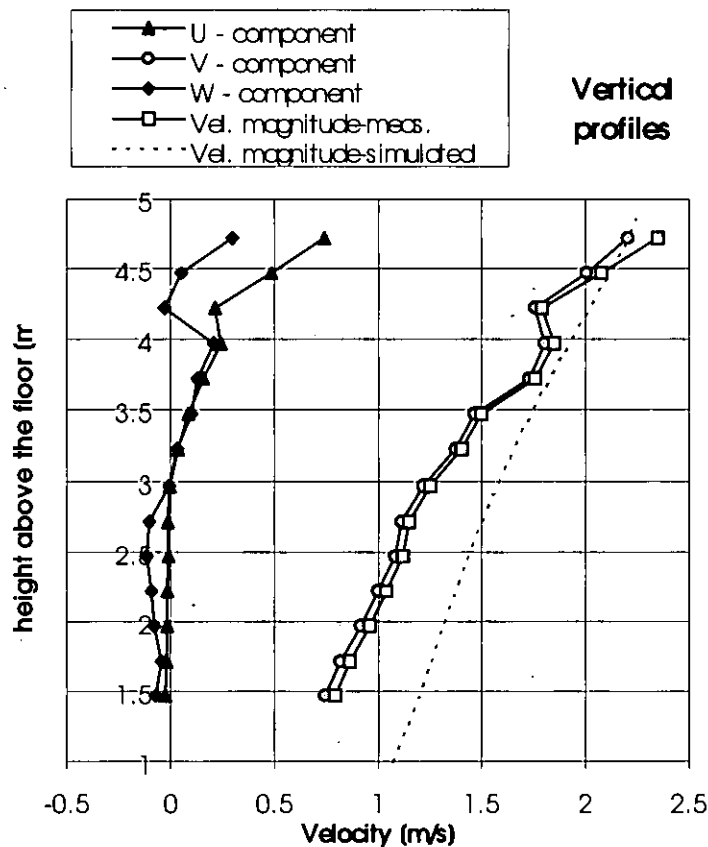


Figure 4.7.6 Velocity profile along the air diffuser axis.

Performance of measurement methods

The IAQ measurements were easy to do, and gave straightforward information on comfort conditions inside the enclosure. These measurements are useful as they link together plant performances and occupation load effects. However, they need to be compared to air flow

rate measurements and, above all, air and ventilation indices in order to provide reproducible results. Both these classes of quantities may be measured by means of tracer gas techniques.

For ventilation flow rate measurement, the tracer technique performs well and its use is, at least in this case, easier and quicker than other methods (such for example velocity profile measurement inside the ducts).

Evaluation of air and ventilation indices requires some caution. The main problems encountered during these measurements were: need of a large number of sampling points, and large amount of tracer gas required to reach measurable concentrations. Moreover the assessment of the air change rates according to the mean age of air at the exhaust is not straightforward when there are more than one exhaust grille.

Our experiences during this experimental campaign point out that step-down and step-up procedures (methods *b* and *d* in Table 4.7.3) are easier to perform than the pulse method and, furthermore, their results appear more reliable. Particularly useful, in order to increase the reliability, is the repetition of sequential step-up and step-down procedures. In this case, however, the measurement period needs to be sufficiently short in order to avoid changes in the boundary or operating conditions.

4.7.3 Analysis Tools

Engineering models: the 'lumped-system model'

In order to evaluate the performance of the engineering models applied to the simulations of large enclosures, the transient history of CO₂ concentration has been investigated with a simple lumped-system model. This is a zero-dimensional model (see Section 2.3.1) derived from the integration over time of the differential equation of CO₂ mass conservation. The time history of CO₂ concentration is given by:

$$C = C_0 \cdot e^{-\varepsilon n(t-t_0)} + \left(C_b + \frac{qN}{\varepsilon \cdot nV} \right) \cdot (1 - e^{-\varepsilon n(t-t_0)}) \quad (4.7.1)$$

The model assumes constant values of n , C_b , q , and N over time. The non-uniform space distribution of CO₂ is taken into account by ventilation efficiency, ε , assumed as a free parameter.

$$\varepsilon = \frac{\langle C \rangle - C_b}{C_{exh} - C_b} \quad (4.7.2)$$

The simulated concentrations, related to case 5, were calculated adopting different values for ventilation efficiencies. The best result was obtained with: $\varepsilon = 0.5$.

The agreement between simulated and experimental results is striking (Figure 4.7.7). It is also interesting to observe how concentrations tend to spread in space during quasi-stationary conditions (from about 09:30 to 10:30), while they tend to converge during the transient decay.

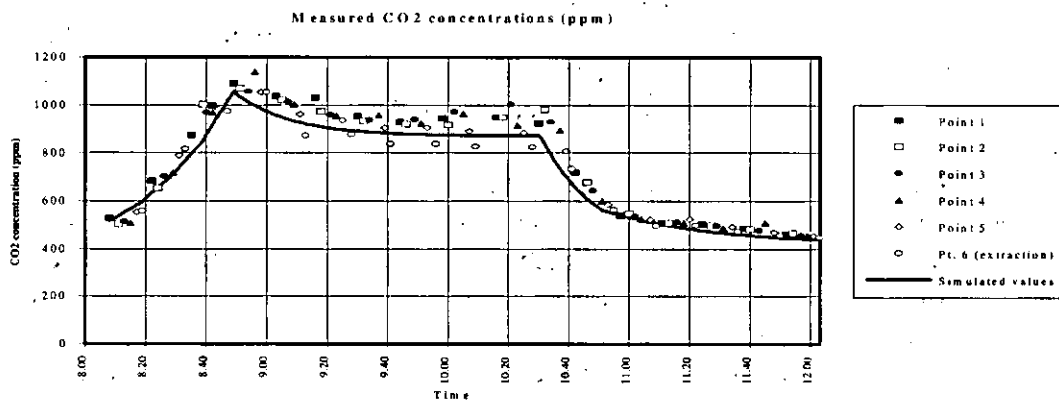


Figure 4.7.7 Measured CO_2 concentrations (ppm).

Field models

A number of simulations were performed using two different commercial codes based on CFD techniques³ (see Section 2.4). Table 4.7.8 summarises all the tested cases, briefly describing the main features of the models and the simulation conditions.

A preliminary set of data was obtained using a simplified 2-D model (cases 1s and 2s). No problems were encountered with the stability of the solution, but convergence was rather slow. Substantial improvements, both in terms of convergence and reliability of results, were obtained during the solution phase, suitably modifying the underrelaxation parameters, the calculation sweeps and the interpolation scheme. A quadratic upwind scheme (QUICK) was adopted in place of Power law (see Section 2.4.2 for more details).

Later on, more realistic 3-D models were implemented (cases 3s, 4s, 5s and 6s), whose further characteristics are briefly listed below. Cases 3s, 6s simulate nominal load and ventilation conditions.

Table 4.7.8 Simulations summary (field-models).

Case	Code	Domain / Turb. model	No. of cells	No. of iterations	Conditions	Notes
1s	Fluent ⁴	2-D std k-ε	196x80 (15680)	5-6000 (35 hours)	Nominal	estimated ach's QUICK
2s	Fluent ⁴	2-D std k-ε	196x80 (15860)	5-6000 (35 hours)	as exp. case 1	estimated ach's QUICK
3s	Fluent ⁴	3-D std k-ε	106x42x14 (62328)	≈ 7000 (156 h)	Nominal	symmetry Power-law
4s	Fluent ⁴	3-D std k-ε	106x42x14 (62328)	≈ 20,000 (≈300 h)	as exp. case 5	symmetry Power-law
5s	Fluent ⁴	3-D std k-ε	106x42x14 (62328)	≈ 20,000 (≈300 h)	as exp. case 5	revised boundary conditions
5s	Phoenics ⁵	3-D std k-ε	80x45x12 (43200)	≈ 6000 (108 h)	Nominal conditions	symmetry

³FLUENT V. 4 and PHOENICS.

⁴running on a HP 9000/720 RISC workstation

⁵running on a VAX 9000 system

Poly-To Model

- Cartesian grid (uniform along x and y , non-uniform along z) (Figure 4.7.8)
- Inlet grilles were simulated as square pipes with equal cross section (0.16 m^2)
- Internal heat and contaminant sources (i.e. people) were modelled by imposing a specific heat flux (75 W per person), a volume flow rate of CO_2 and water vapour (corresponding to 18 l/h per person of CO_2 and 50 g/h of H_2O) on the floor
- Walls were considered adiabatic.
- Volume flow rate of fresh air was $10400 \text{ m}^3/\text{h}$ and the air temperature was 20° C (turbulence intensity: 20%)
- Swirl effect or particular jet-shape due to the inlet diffusers, was not taken into account
- Commercial code: FLUENT

ENEA Model

- Non-uniform Cartesian grid (Figure 4.7.9)
- Inlet grilles were simulated as square pipes with cross section of 0.145 m^2
- Air temperature was 23° C
- Commercial code: PHOENICS

Predicted velocity and CO_2 concentration fields are shown in Figures from 4.7.10 to 4.7.14. The flow fields (Figures 4.7.10 and 4.7.11) show that in the ENEA model, the supply air jets have less penetration than in the TOPO model, and that a stronger upward draught, due to natural convection, takes place. The CO_2 concentration fields (Figures 4.7.12 and 4.7.13) are in rather good agreement, even though the peak values are located slightly more forwards than in the TOPO model.

A comparison between the 2-D and 3-D model results shows that the concentration field in the 2-D model case 1s agrees quite well with the 3-D ENEA model case 6s.

Figure 4.7.14 shows the simulated CO_2 concentrations for actual conditions of occupancy load and ventilation; boundary conditions result from the measurements performed in case 18.

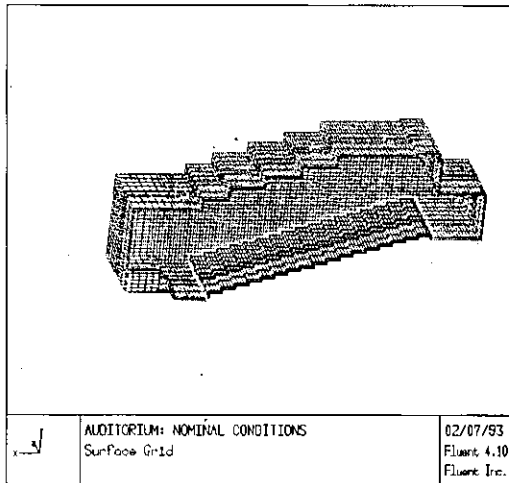


Figure 4.7.8 Surface grid - TOPO Model.

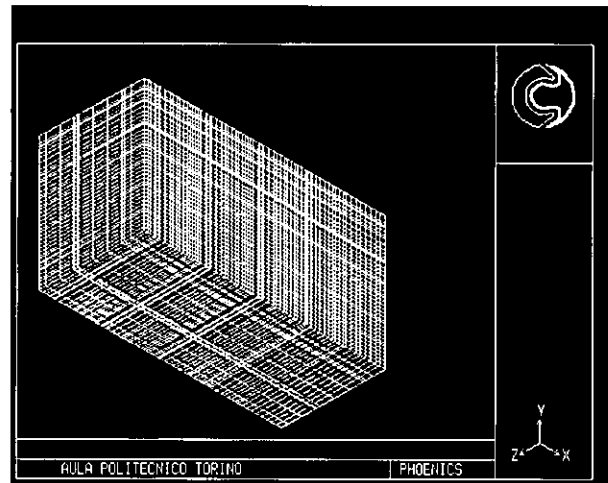


Figure 4.7.9 Grid of ENEA Model.

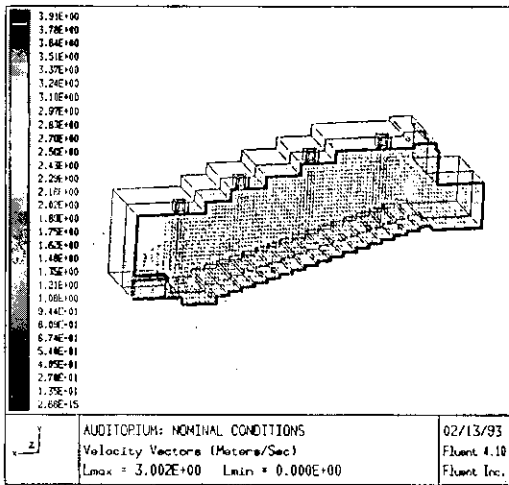


Figure 4.7.10 Flow field (velocity vectors) - Nominal conditions (Case 3s). TOPO Model.

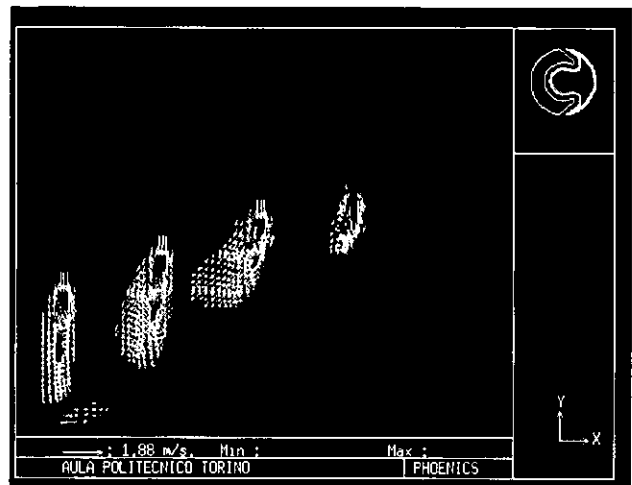


Figure 4.7.11 Flow field (velocity vectors) - Case 6s. ENEA model

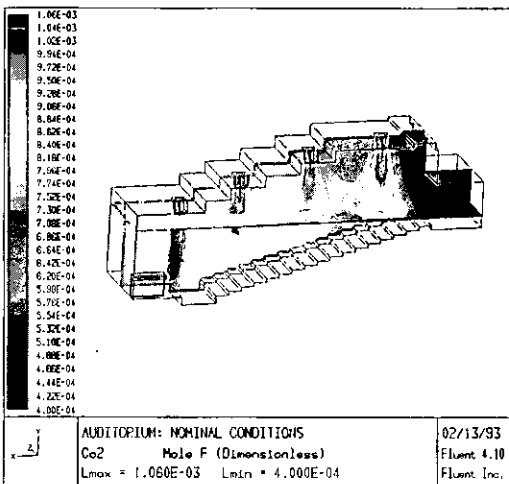


Figure 4.7.12 CO₂ concentration field - Nominal conditions (Case 3s). TOPO Model.

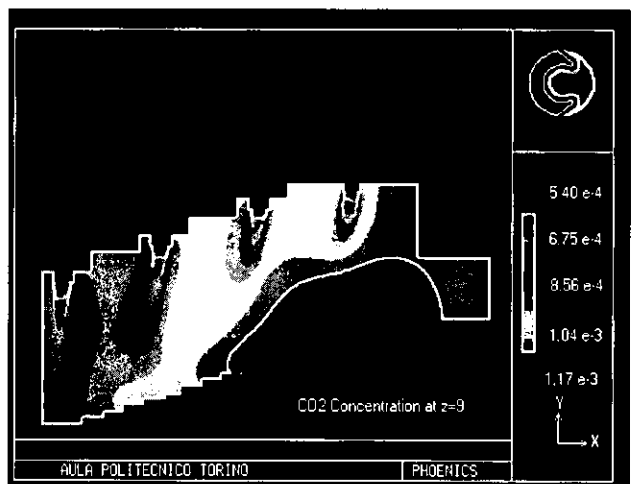


Figure 4.7.13 CO₂ concentration field - Case 6s. ENEA Model.

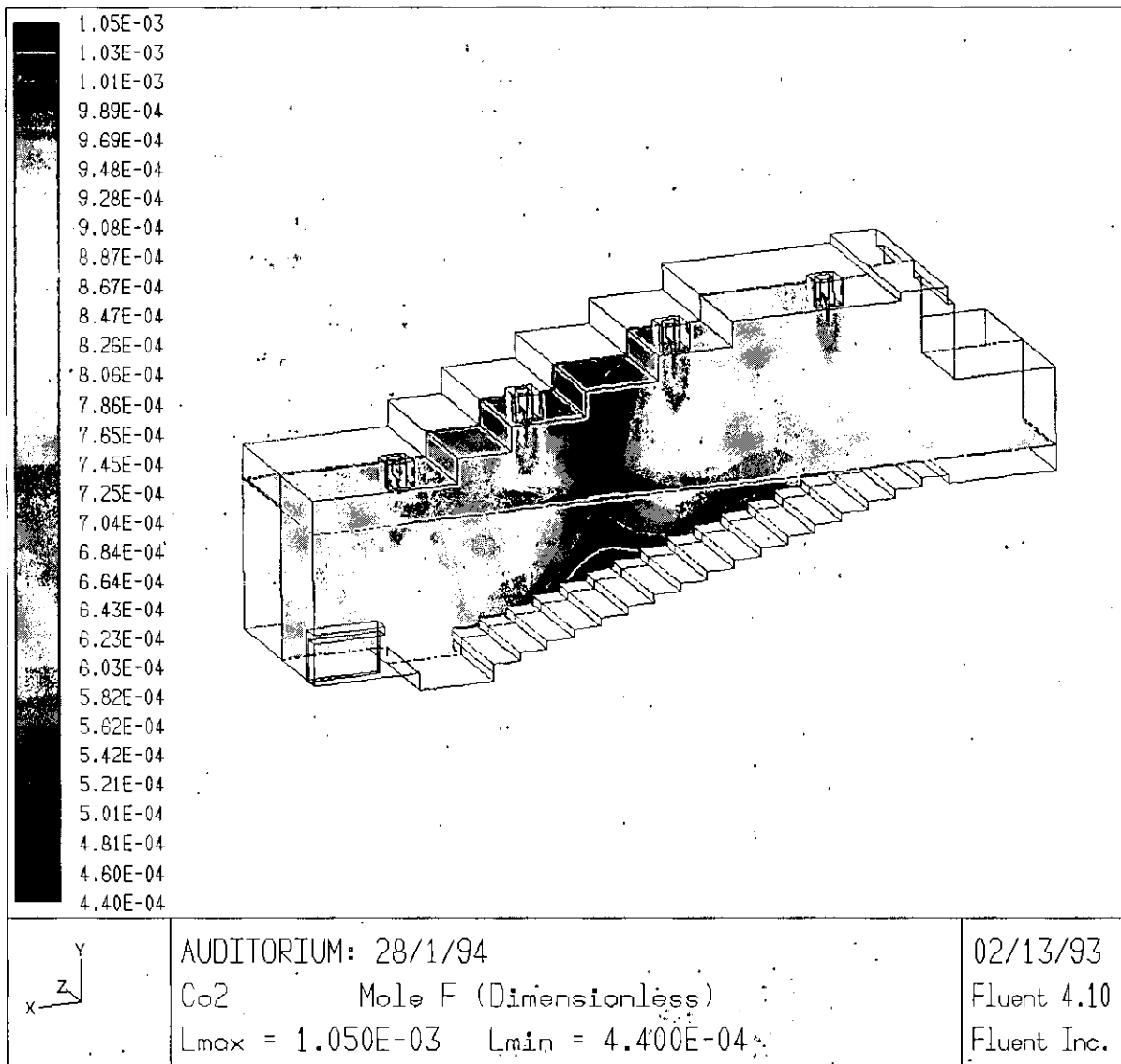


Figure 4.7.14 CO₂ concentration field (Case 5s). TOPO Model.

Performance of analysis tools

Field models

The field models tested here show a general tendency to underestimating the contaminant concentrations (of about 30 to 50%). For example, the *average concentration* of CO₂ in the auditorium, as calculated for the nominal conditions by simply applying continuity, should be of about 1000 ppm, while the numerically calculated fields (Figures 4.7.12 and 4.7.13) exhibit *peak values* of about 1050 ppm (with an average of 600-700 ppm). The uncertainties in pollutant concentration prediction may be due to poor knowledge of boundary conditions (case 4s). Better results (due to the normalisation with the C_p value) usually appear for the air quality index.

The reliability of results grows when the number of sweeps is increased, the under-relaxation parameters for species conservation equations are adjusted, when the total number of iterations is increased, and when the boundary conditions are better known. Case 5s is an

example of this. A detailed comparison of case 5s results, for which a set of measured values is available, shows, in fact, quite good performances of the analysis tools.

Figure 4.7.15 shows the predicted (case 5s) and measured values of CO₂ concentration, the relative errors for concentration evaluation, and the errors between measured and simulated local air quality index (defined as C_{exh}/C_p). The errors are always lower than 10%. However, the computational time required for solving case 5s was quite long: 15 days (using a RISC work-station, HP 9000-720 with 56 Mb of RAM memory). Even in this last simulation, H₂O concentrations and temperatures were underestimated.

The predicted vertical velocity profile along the supply grille axis, are plotted in Figure 4.7.6. It is possible to see that a better agreement between measured and simulated values, is found in the upper part of the jet, while the simulated results show a stronger penetration, with higher velocity values in the lower part of the stream. The uncertainties are mainly due to the fact that the air diffuser is modelled with only few cells (3×3) and that it is not possible to adequately described the real, complex, inlet velocity profiles by means of the boundary conditions. However, the predicted general trend is coherent with experimental data.

Moreover, for all the cases, the local near-wall grid was coarse (see chapter 2.4.5) and the simulation of contaminant release from the human body (see chapter 2.4.4) was probably inadequate.

Engineering models

The only engineering-model tested, agreed satisfactorily with the measured values, but it required prior knowledge of the ventilation efficiency, in the absence of which, the results are limited to mean values and no information is gained about space distribution of the parameters of interest.

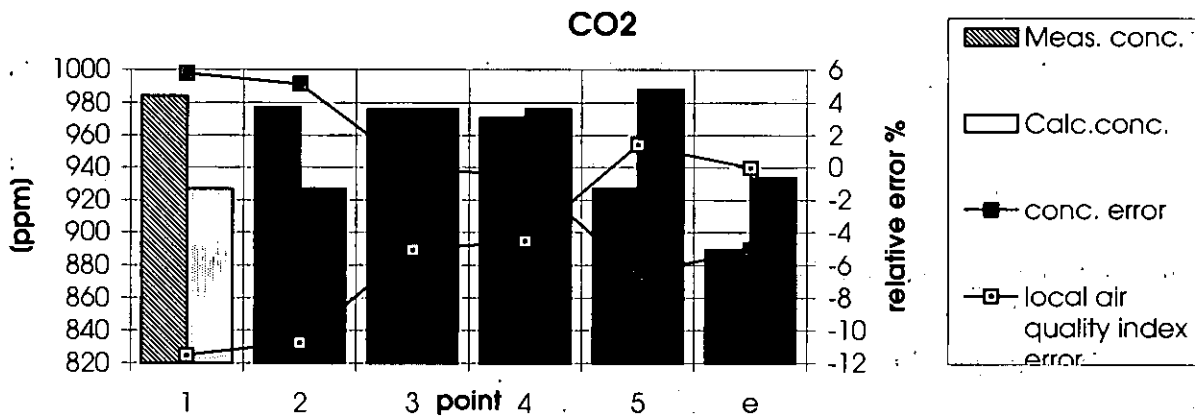


Figure 4.7.15 Relative errors (with reference to measured values) between predicted and measured data - Case 5s.

4.7.4 Conclusions and Recommendations

Experimental tracer-gas techniques are rather effective in characterising the airflow in large enclosures, but some care must be taken. One of the worst disadvantages is the spatial resolution of the results, due to the high cost of having a large number of simultaneous sampling points. A comparison between the different methods showed that the step-up and step-down methods are more reliable than others. When only global values of ventilation indices are required, measurements can easily and quickly be done in the plantroom. The

experimental results confirm that IAQ assessment, for pollution produced by occupants, may be reliably performed using CO₂ as an indicator, because its correlation with TOC content is quite good.

Simple lumped-parameter models are easy to use and quick to develop, but their use should only be limited to first tentative analysis.

In the field models a large number of cells are needed in order to describe the complexity of the enclosure and to minimise the negative effects of the difference in the geometric scales. Therefore long computation times and much memory are required for the simulation. Quantitative results, specially for pollutant concentrations, were systematically underestimated, but qualitative predictions were rather promising. It would not be surprising, therefore, that better performances would be achieved when the predicted parameters were normalised with respect to a concentration value (i.e. C_p or $\langle C \rangle$). The designer should take particular care in employing the models; critical points are the near-wall regions and the simulation of human occupants as a heat and pollutant source. It should also be stressed that the value of normalised residuals (i.e. the residuals in the solution of the conservation equations; see Section 2.4.1 & 2.4.2 for more details) is not always meaningful for evaluating the convergence of the solution. Frequently, even if the species residuals are lower than 10^{-6} , the concentration fields still evolve with further iterations.

References

International Energy Agency

Annex 26

Participating Institutes in Annex 26

REFERENCES

2.1 Introduction

2.2 Flow Element Models

- Akimoto, T.; Nobe, T.; Takebayashi, Y. [1995]: Experimental Study on the Floor-Supply Displacement Ventilation System. *ASHRAE Transactions, Vol 101, Pt. 2.*
- Andersen, K.T. [1996]: SBI Bulletin 112: Cold Down-Draught from Cold Surfaces (in Danish). *Danish Building Research Institute.*
- Beltaos, S. [1976]: Oblique impingement of circular turbulent jets. *Journal of Hydraulic Research, Vol 14, no. 1.*
- Billington, N.S. [1966]: Air Movement over Hot or Cold Surfaces. *Laboratory Report no. 29, HVRA.*
- Blay, D.; Vialle, P. [1996]: Experimental Study of Free Buoyant 3D Jets. Internal Report. *Laboratoire d'Etudes Thermiques, ENSMA, University of Poitiers, France.*
- Cheesewright, R. [1968]: Turbulent Natural Convection from a Vertical Plane Surface. *Journal of Heat Transfer, Vol. 90, pp 1-8.*
- Cheesewright, R.; Ierokipitis, E. [1982]: Velocity Measurements in a Turbulent Natural Convection Boundary Layer. *Int. Heat Transfer Conference, 7, Munich, Vol. 2.*
- Eckert, E.R.G. and Drake, R.M. [1959]: Heat and Mass Transfer. *McGraw-Hill.*
- Eckert, E.R.G.; Jackson, T.W. [1951]: Analysis of Turbulent Free-convection Boundary Layer on Flat Plate. *NACA Report 1015.*
- Grimitlin, M. [1970]: Zuluftverteilung in Räumen, Luft- und Kältetechnik. *No. 5.*
- Guthrie, A.; Ikezawa, H.; Otaka, K. & Yau, R. [1992]: Air Flow Studies in Larger Spaces: A Case Study of Kansai International Airport Passenger Terminal Building, Osaka, Japan. *Proceedings of the International Symposium on Room Air Convection and Ventilation Effectiveness (ISRACVE). Soc.Heat.Air Cond. Sanitary Eng. of Japan (SHASE), Tokyo, Japan. 22-24 July. pp. 674-680.*
- Guthrie, A. [1996]: Designing for Climate Control in Large Volumes. *Proceedings of ROOMVENT'96, 5th Int. Conf. on Air Distribution in Rooms, Yokohama, Vol.1, pp.1-8.*
- Heiselberg, P. [1994a]: Stratified Flow in Rooms with a Cold Vertical Wall. *ASHRAE Transactions, Vol. 100, part 1, pp 1155-1162.*
- Heiselberg, P. [1994b]: Interaction between Flow Elements in Large Enclosures. *Proc. of the Fourth International Conference on Air Distribution in Rooms, ROOMVENT '94, Krakow, Vol. 1, pp 363-376.*
- Heiselberg, P.; Overby, H.; Bjoern, E. [1995]: Energy-Efficient Measures to avoid Downdraft from Large Glazed Facades. *ASHRAE Transactions, Vol. 101, pp*
- Helander, L.; Yen, S.M.; Crank, R.E. [1953]: Maximum Downward Travel of Heated Jets from Standard Long Radius ASME Nozzles. *ASHVE Transactions, No. 1475.*
- Hestad, T. [1976]: Dimensioning of Supply Openings, Cold Downdraught (in Norwegian). *Norsk VVS, No. 6.*

- Holmes, M.J. and Sachariewicz, E. [1973]: The Effect of Ceiling Beams and Light Fittings on Ventilating Jets. *Laboratory Report No. 79, HVRA*.
- Howarth, A.T. et al. [1972]: Air Movement in an Enclosure with a Single Heated Wall. *B.S.E., Vol. 40, pp 149-156*.
- Jackman, P.J. [1970]: Air Movement in Rooms with Sidewall Mounted Grilles - A Design Procedure. *Laboratory Report No. 65, HVRA*.
- Koestel, A. [1955]: Paths of Horizontally Projected Heated and Chilled Air Jets. *ASHRAE Transactions*.
- Koestel., A. [1954]: Computing Temperatures and Velocities in Vertical Jets of Hot or Cold Air. *Heating, Piping & Air Conditioning, June*.
- Kofoed, P.; Nielsen, P.V. [1990]: Thermal Plumes in Ventilated Rooms. *Proc. of the International Conference on Engineering Aero- and Thermodynamics of Ventilated Room, ROOMVENT '90, Oslo*.
- Kofoed, P.; Nielsen, P.V. [1991]: Auftriebsströmungen verschiedener Wärmequellen - Einfluss der umgebenden Wände auf den geförderten Volumenstrom. *DKV-Tagungsbericht, Deutscher Kälte- und Klimatechnischer Verein e.V., Stuttgart*.
- Krause, D. [1972]: Freistrahlen bei der Sonderbewetterung. *Neue Bergbautechnik, 2 Jg, Heft 1*.
- Li, Z.H.; Zhang, J.S.; Zhivov, A.M.; Christianson, L.L. [1993]: Characteristics of Diffuser Air Jets and Airflow in the Occupied Regions of Mechanically Ventilated Rooms - A Literature Review. *ASHRAE Transactions, Vol. 99, part 1, pp 1119-1127*.
- McRee, D.I. and Moses, H.L. [1967]: The Effect of Aspect Ratio and Offset on Nozzle Flow and Jet Reattachment. *Advances in Fluidics, The 1967 Fluidics Symposium, ASME*.
- Milke, J.A. and Mowrer, F.W. [1995]: Computer Aided Design for Smoke Management. *ASHRAE Journal, August 1995*.
- Morton, B.R.; Taylor, G.; Turner, J.S. [1956]: Turbulent Gravitational Convection from Maintained and Instantaneous Sources. *Proc. Royal Soc., Vol. 234A, p. 1*.
- Mundt, E. [1992]: Convection Flows in Rooms with Temperature Gradients - Theory and Measurements. *Proc. of the Third International Conference on Air Distribution in Rooms. ROOMVENT '92, Aalborg*.
- Murakami, S.; Kato, S.; Nakagawa, H. [1991]: Numerical Prediction of Horizontal Nonisothermal 3-d Jet in Room based on the k- ϵ model. *ASHRAE Transaction, Vol. 97, Part 1, pp 96-105*.
- Nielsen, P.V.; Evensen, L.; Grabau, P.; Thulesen-Dahl, J.H. [1987]: Air Distribution in Rooms with Ceiling-Mounted Obstacles and Three-Dimensional Isothermal Flow. *ROOMVENT'87, International Conference on Air Distribution in Ventilated Spaces, Stockholm, 1987*.
- Nielsen, P.V. [1976]: Flow in Air Conditioned Rooms - Model Experiments and Numerical Solution of the Flow Equations. *English translation of Ph.D.-Thesis, Technical University of Denmark, Copenhagen*.
- Nielsen, P.V. [1980]: The Influence of Ceiling-Mounted Obstacles on the Air Flow Pattern in Air-Conditioned Rooms at Different Heat Loads. *Building Service Engineering Research & Technology, Vol. 1, No. 4*.
- Nielsen, P.V. [1983]: Air Diffusion in Rooms with Ceiling-Mounted Obstacles and Two-Dimensional Isothermal Flow. *16th International Congress of Refrigeration, Commission E1, Paris*.

- Nielsen, P.V. [1988]: Personal Communication: *Aalborg University*.
- Nielsen, P.V. [1990]: Air Velocity at the Floor in a Room with Wall Mounted Air Terminal Device and Displacement Ventilation. (in Danish). *Internal Report, Nordic Ventilation Group, ISSN 0902-7513 R9004, Aalborg University, Aalborg*.
- Nielsen, P.V. [1992]: Velocity Distribution in the Flow from a Wall-Mounted Diffuser in Rooms with Displacement Ventilation. *Proc. of the Third International Conference on Air Distribution in Rooms. ROOMVENT '92, Aalborg*.
- Nielsen, P.V. [1994a]: Velocity Distribution in a Room with Displacement Ventilation and Low-Level Diffusers. *Internal IEA-Annex 20 Report, Aalborg University, ISSN 0902-7513 R9403*.
- Nielsen, P.V. [1994b]: Stratified Flow in a Room with Displacement Ventilation and Wall Mounted Air Terminal Devices. *ASHRAE Transactions, Vol. 100, part 1, pp*
- Nielsen, P.V.; Hoff, L.; Pedersen, L.G. [1988]: Displacement Ventilation by Different Types of Diffusers. *9th AIVC Conference on Effective Ventilation, Gent, Belgium*.
- Nielsen, P.V.; Möller, Å.T.A. [1985]: Measurements of the three-dimensional wall jet from different types of air diffusers. *Clima 2000, Copenhagen*.
- Nielsen, P.V.; Möller, Å.T.A. [1987]: Measurements on Buoyant Wall Jet Flows in Air-conditioned Rooms. *ROOMVENT '87, International Conference on Air Distribution in Ventilated Spaces, Stockholm*.
- Nielsen, P.V.; Möller, Å.T.A. [1988]: Measurements on Buoyant Jet Flows from a Ceiling Mounted Slot Diffuser. *Proc. of the 3rd Seminar on "Application of Fluid Mechanics in Environmental Protection - 88", Silesian Technical University*.
- Popiolek, Z. [1996]: Air Volume Flux in Buoyant Plumes. *Silesian Technical University, Gliwice, Poland*.
- Rajaratnam, N. [1976]: Turbulent Jets. *Elsevier, Amsterdam*.
- Regenscheit, B. [1959]: Die Luftbewegung in Klimatisierten Räumen. *Kältetechnik, Heft 1*.
- Regenscheit, B. [1970]: Die Archimedes-zahl. *Gesundheits Ingenieur, Heft 6*.
- Sandberg, M.; Mattsson, M. [1993]: Density Currents created by Supply from Low Velocity Devices. *Research Report TN:44, The National Swedish Institute for Building Research*.
- Schwenke, H. [1975]: Über das Verhalten ebener Horizontaler Zuluftstrahlen im begrenzten Raum. *Luft und Kältetechnik, 1975/5, pp 241-245*.
- Schwenke, H. [1976]: Berechnung Lüftungstechnischer Anlagen. *ILKA Berechnungs-Katalog. Institut für Luft- und Kältetechnik, Dresden*.
- Shillinglaw, J.A. [1977]: Cold Window Surfaces and Discomfort. *BSE, Vol. 45, pp 43-51*.
- Skistad, H. [1993]: Private Communication.
- Skistad, H. [1994]: Displacement Ventilation. *John Wiley & Sons Inc*.
- Skåret, E. [1976]: Air Movement in Ventilated Rooms (in Norwegian). *Institute for VVS, Technical University of Norway, Trondheim*.
- Skåret, E. [1986]: Ventilation by Displacement - Characterisation and Design Implications. *Ventilation '85, edited by H. D. Goodfellow, Elsevier Science Publishers B.V., Amsterdam*.
- Söllner, G. and Klingenberg, K. [1972]: Leuchten als Störkörper im Luftstrom. *HLII, 23, no. 4, 1972*.
- Topp, C.; Heiselberg, P. [1996]: Obstacles - an Energy-Efficient Method to Reduce Downdraught from Large Glazed Surfaces. *Proc. of the Fifth International Conference on Air Distribution in Rooms, ROOMVENT'96, Yokohama, Japan*.

Vialle, P.; Blay, D. [1996]: Decay Laws in the Case of 3D Vertical Free Jets with Positive Buoyancy. ROOMVENT'96, Yokohama, July 17-19, Japan.

Wilkinson, D.L.; Wood, I.R. [1970]: A rapidly varied Flow Phenomenon in a Two-Layer Flow. *J. Fluid Mech.*, Vol. 47, part 2, pp241-256.

2.3 Engineering Models

Aiulfi, D.; Van der Maas J. [1996]: Natural Ventilation in an Auditorium: The Role of Thermal Storage in the Energy Consumption and Comfort of the De Montfort University Auditorium. *Roomvent '96, Yokohama, July 17-19, Japan.*

Allard, F.; Inard, C. [1992]: Natural and mixed convection in rooms. Prediction of thermal stratification and heat transfer by zonal models. *Int. Symposium on Room Air Convection and Ventilation Effectiveness, Invited Paper, Tokyo (Japan).*

Allard, F.; Inard, C.; Simoneau, J.P. [1990]: Phénomènes convectifs intérieurs dans les cellules d'habitation. Approches expérimentales et numériques. *Revue Générale de Thermique, T. 29, n°340, 216-225 pp.*

Arai, Y.; Togari, S.; Miura, K. [1994]: Unsteady-state thermal analysis of a large space with a vertical distribution. *ASHRAE Transactions 100 (2), 396 - 411.*

Baturin, V.V. [1972]: Fundamentals of Industrial Ventilation 3rd Ed. *Pergamon Press Oxford.*

Carslaw and Jaeger. [1959]: Conduction of heat in solids. *Clarendon Press, Oxford.*

Colliver, D.G.; Murphy, W.E.; Sun W. [1994]: Development of a building component air leakage data base. *ASHRAE Transaction Technical paper 3764, Volume 100 (1), pp292 - 305.*

COMIS User Guide, version 1.3 or newer, available from the Lawrence Berkeley Laboratory, Berkeley, USA

Dalcieux, P.; Bouia, H.; Blay, D. [1992]: Simplified modelling of air movements in a room and its first validation with experiments. *Int. Conference on Air Distribution in Rooms, ROOMVENT'92, Aalborg (Denmark).*

Dorer, V.; Weber, A. [1994]: Multizone air flow model Comven-Trnsys, Trnsys Type 57 Documentation. *IEA-ECB Annex 23 technical report, EMPA 175.*

Eckert, E.R.G.; Jackson, B.M. [1951]: Analysis of turbulent free-convection boundary layer on flat plate. *NACA Report 1015.*

Florentzou F.; Van der Maas J.; Roulet, C.-A. [1996]: LESOCOOL 1.0, Thermal Simulation Program for Buildings; A Tool for the Evaluation of the Risk of Overheating and the Potential of Cooling through Ventilation. Available at LESO, EPFL, CH-1015 Lausanne (see Website <http://lesowww.epfl.ch/>)

Idelchik I.E. [1994]: Handbook of hydraulic resistance, *CRC Press, 3rd Ed.*

Inard, C.; Bouia, H.; Dalcieux, P. [1996]: Prediction of air temperature distribution in buildings using a zonal model. *To be published in Energy and Buildings.*

Inard, C.; Doring, H. [1994]: Energy and thermal comfort in buildings: an approach with zonal models. *Int. Conference on Air Distribution in Rooms, ROOMVENT'94, Cracovia (Poland), June 15/17.*

Inard, C.; Meslem, A.; Depecker P. [1996]: Use of a Zonal Model for the Prediction of Air Temperature Distribution in Large Enclosures", *Roomvent '96, Yokohama, July 17-19, Japan.*

Jones, W.P. [1994]: Air Conditioning Engineering. 4Rev.ed., Edward Arnold, London.

- Koestel, A. [1955]: Paths of horizontally projected heated and chilled air jets. *ASHRAE Transactions* 61.
- Kolsaker, K.; Mathisen, H.M. [1992]: Computer Simulation of Energy Use and Thermal Climate in Glazed Spaces. *ROOMVENT'92, Third Int. Conf. Aalborg, Denmark. ISBN 87-982652-6-1. Vol.1, pp.461-472.*
- Kondo, Y.; Miwa, H. [1992]: Numerical study on an atrium by means of macroscopic model and k-e turbulence model. *Proceeding of International Symposium on Room Air Convection and Ventilation Effectiveness (ISRACVE) : pp109-123.*
- Liburdy, J.A.; Faeth, G.M.[1978]: Heat transfer and mean structure of a turbulent thermal plume along a vertical isothermal wall. *J. Heat Transfer, V. 100, n°5, pp177-183.*
- Limb, M.J. [1989]: AIRGUIDE-a guide to the AIVC's AIRBASE. *Coventry, UK : Air Infiltration and Ventilation Centre.*
- Mitalas, G.P.; Arseneault, J.C. [1974]: FortranIV program to Calculate z-Transfer Functions for the Calculation of Transient heat Transfer Through Walls and Roofs, *National Research Council of Canada, Ottawa.*
- Orme, M.; Liddament, M.; Wilson, A. [1994]: An Analysis and Data Summary of the AIVC's Numerical Database. AIVC Technical Note 44, Coventry, Air Infiltration and Ventilation Centre, UK.
- Phaff, J.C.; De Gids, W. F.; Ton, J.A.; van de Ree, D.; van Schijndel, L.L.M. : Investigation of the consequences of opening one window on the internal climate of a room. *Delft IMG-TNO, report C448, March 1980. Airbase #2201.*
- Rajaratnam, N. [1976]: Turbulent jets. *Elsevier Scientific Publishing, New-York.*
- Schaelin, A.; Moser, A.; Van der Maas J.; Aiulfi D. [1996]: Application of Air Flow Models as Design Tools for Atria. *Roomvent '96, Yokohama, July 17-19, Japan.*
- Schild, P.G. [1996]: CFD Analysis of an Atrium, using a Conjugate Heat Transfer Model Incorporating Long-Wave and Solar Radiation. *SINTEF Energy, Report no. STF84-A96208. Norwegian University of Science, & Technology, 7035 Trondheim, Norway. ISBN 82-595-9648-2*
- Seem, J.E. [1987]: Modeling of heat in buildings, *Ph.D. Thesis, Solar Energy Laboratory, University of Wisconsin, Madison.*
- Stephenson, D.G.; Mitalas, B.P. [1971]: Calculation of Heat Conduction Transfer Functions for Multi-Layer Slabs. *ASHRAE Annual Meeting, Washington, D.C., August 22-25, 1971*
- Takemasa, Y.; Togari, S.; Arai, Y. [1996]: Application to an atrium space of an unsteady-state calculation model for predicting vertical temperature distribution. *Technical paper of ASHRAE Winter Meeting, Atlanta, GA.*
- Togari, S.; Arai, Y.; Miura, K. [1993]: A simplified model for predicting vertical temperature distribution in a large space. *ASHRAE Transactions* 99 (1) : 88-99.
- Van der Maas, J.; Kolsaker K. [1996]; Simple Design Tools Applied to an Underground Stadium and Compared with Indoor Climate Measurements. *Roomvent '96, Yokohama, July 17-19, Japan.*
- Van der Maas, J.; Maldonado, E. [1996]: Thermal mass and night ventilation studies in the framework of PASCOOL. *Submitted to International Journal of Solar Energy.*
- Van der Maas, J.; Roulet, C.-A. [1993]: Multizone cooling model for calculating the potential of night time ventilation. *14th AIVC Conference, Copenhagen.*
- Van der Maas, J.; Schaelin, A. [1995]: Application of Air Flow Models to Aircraft Hangers with Very Large Openings. *Proc of the 16th AIVC Conference, Vol. 1, p127-142.*

- Warren, P.R. [1986]: The analysis of single sided ventilation measurements. *Air Infiltration Review*, Vol. 7(2), pp3-5.
- Wurtz, E.; Nataf, J.M. [1994]: Validation des modèles zonaux décrits par l'environnement orienté objet SPARK. *European Conference on Energy Performance and Indoor Climate in Buildings*, Lyon (France), November 24/26.

2.4 Field Models

2.4.1 Introduction to Field Models

- Awbi, H.B. [1989]: Application of computational fluid dynamics in room ventilation. *Building and Environment*, Vol.24, No.1, pp.73-84.
- Awbi, H.B. [1991]: *Ventilation of buildings*. E & FN Spon : London. ISBN 0-419-15690-9.
- Jones, P.J.; Whittle, G.E. [1992]: Computational fluid dynamics for building airflow prediction : current status and capabilities. *Building and Environment*, Vol.27, No.3 (July), pp.321-338.
- Murakami, S.; Kato, S.; Ishida, Y. [1989]: 3-D numerical simulation of turbulent airflow in and around buildings based on the k-eps model with generalized curvilinear coordinates. *ASHRAE Transactions*, Vol.95 Pt.2, pp.30-57.
- Murakami, S.; Kato, S.; Nakagawa, H. [1991]: Numerical prediction of horizontal nonisothermal 3-D jet in room based on k-eps model. *ASHRAE Transactions*, Vol.97 Pt.1, pp.30-57.
- Murakami, S.; Kato, S.; Suyama, Y. [1987]: Three-dimensional numerical simulation of turbulent airflow in a ventilated room by means of a two-equation model. *ASHRAE Transactions*, Vol.93 Pt.2.

2.4.2 Numerical Method

- Caruso, S.C.; Ferziger, J.H.; Oliger, J. [1985]: Adaptive Grid Techniques for Elliptic Fluid-Flow Problems. *Report No.TF-23, Mech.Engrg.Dept., Stanford University*.
- Caruso, S.C.; Ferziger, J.H.; Oliger, J. [1986]: Adaptive Grid Techniques for Elliptic Fluid Flow Problems. *AIAA 24th Aerospace Sciences Meeting, Nevada*.
- Jacobsen, T.V. [1993]: Airflow and temperature distribution in rooms with displacement ventilation. *PhD thesis, Department of Building Technology and Structural Engineering, University of Aalborg, Denmark. ISSN 0902-7513-R9328*.
- Leonard, B.P. [1979]: A stable and accurate convective modelling procedure based on quadratic upstream interpolation. *Computer Methods in Applied Mechanics and Engineering*, Vol.19.
- Leschziner, M.A. [1992]: Turbulence modelling challenges posed by complex flows. *Proc, Roomvent, Vol.1, Aalborg*.
- Matsuo, Y.; Yee, J.; Kurabuchi, T.; Kamata, M. (1992): Highly accurate and non-oscillatory finite difference approximation method for convection diffusion equations. *Proc. Int. Symposium Room Air Convection and Ventilation Effectiveness, Tokyo*.
- Murakami, S.; Kato, S.; Nagano, S. [1988]: Estimation of error caused by coarseness of finite-differencing, Study on diagnostic system for simulation of turbulent flow in room.

- (Part. 1), *J. of Architecture, Planning and Environmental Engineering (Transaction of AIJ)*, No. 385, pp. 9-17.
- Scheuerer, G. [1993]: An overview of the present status of and future requirements for industrial CFD. *SPEEDUP J.*
- Spalding, D.B. [1972]: A novel finite-difference formulation for differential expressions involving first and second derivatives. *Journal of Numerical Methods*, Vol.4.

2.4.4 Relative Performance of Various Turbulence Models

- Chen, Q.; Moser, A.; Huber, A. [1990]: Prediction of buoyant turbulent flow by a low-Reynolds-number k -model. *ASHRAE Transactions, Vol.96, Part.1, pp.564-573.*
- Chikamoto, T.; Murakami, S.; Kato, S. [1992]: Numerical simulation of velocity and temperature fields within atrium based on modified k - model incorporating damping effect due to thermal stratification. *Proc. Int. Symp. Room Air Convection and Vent. Effectiveness : Soc. Heat. Air-Cond. Sanitary Eng. of Japan, Tokyo. 22-24 July. pp.501-509.*
- Deardorff, J.W. [1970]: A numerical study of three-dimensional turbulent channel flow at large Reynolds numbers. *J.Fluid Mech.*, 41(1970)453-480.
- Launder, B.E.; Reece, G.J.; Rodi, W. [1975]: Progress in the development of a Reynolds stress turbulence closure. *J.Fluid Mech.*, 68(1975)537-566.
- Launder, B.E.; Spalding, J.L. [1972]: Mathematical models of turbulence. *Academic Press, New York.*
- Moin, P.; Kim, J. [1982]: Numerical investigation of turbulent channel flow. *J.Fluid, Mech.*, 18(1982)341-377.
- Murakami, S.; Kato, S.; Kondo, Y. [1990]: Examining EVM by means of ASM for a 3-D horizontal buoyant jet in enclosed space. *Engineering Turbulence Modelling and Experiments, Elsevier Science Publishing, 205-214.*
- Murakami, S.; Kato, S.; Ooka, R. [1994]: Computation of numerical predictions of horizontal nonisothermal jet in a room with three turbulence models- k -, EVM, ASM and DSM. *ASHRAE TRANSACTIONS Vol. 100 (1994).*
- Murakami, S.; Kato, S.; Yokoi, M. [1994]: Micro/Macroscopic Analysis of Airmass, Heat and Energy Transport within an Enclosure. *ROOMVENT'94, Krakow, Poland.*
- Murakami, S.; Mochida, A. [1988]: 3D numerical simulation of airflow around a cubic model by means of k - model. *J.Wind Eng.Ind.Aerodyn.*, 31, 283-303.
- Murakami, S.; Mochida, A.; Hayashi, Y. [1991]: Scrutinizing k -, EVM and ASM by means of LES and wind tunnel for flowfield around cube. *Eighth Symposium on Turbulent Shear Flows, Munich (1991.9).*
- Murakami, S.; Mochida, A.; Hibi, K. [1987]: Three-dimensional numerical simulation of airflow around a cubic model by means of large eddy simulation. *J.Wind Eng.Ind.Aerodyn.*, 25(1987)291-305.
- Rodi, W. [1976]: *ZAMM*. 58(1976)T219-T221.
- Schumann, U. [1975]: Subgrid-scale model for finite difference simulation of turbulent flows in plane channels and annuli. *J.Comp.Phys.*, 18(1975)376-404.
- Smagorinsky, J.S. [1963]: General circulation experiments with the primitive equations. *Part1, Basic experiments, Mon. Weather Rev.*, 91(1963)99-164.

2.4.5 Treatment of Openings

- Awbi, H.B. [1991]: Ventilation in buildings. *E & FN Spon : London. ISBN 0-419-15690-9.*
- Nielsen, P.V. [1992]: Description of supply openings in numerical models for room air distribution. *ASHRAE Transactions*, Vol.98, Part.1, pp.963-971.

2.4.6 Treatment of Walls

- Chieng, C.C.; Launder, B.E. [1980]: Numerical Heat Transfer, Vol.3, pp189-207.
- George, W.K.; Capp, S.P. [1979]: A Theory for Natural Convection turbulent Boundary Layer next to Heated Vertical Surfaces. *Int. J. Heat Mass Transfer* 22, pp. 813-826.
- Jones, W.P.; Launder, B.E. [1972]: The Prediction of Laminarization with a Two-Equation Model of Turbulence. *Int. J. of Heat Mass Transfer*, Vol. 15, pp 301 -314.
- Launder, B.E.; Spalding, D.B. [1974]: Computer Methods in Applied mechanics and Engineering. Vol.3,pp269-289.
- Leschnizer, M.A. [1987]: Paper submitted to 7th Open Seminar on Numerical Simulation of Turbulence, IIS, University of Tokyo.
- Murakami, S.; Kato, S.; Chikamoto, T. [1993]: Improvement of Low-Reynolds-Number k -Model. (Part 1), *Annual Meeting of AIJ*, pp. 737 - 738. (in Japanese ??).
- Murakami, S.; Kato, S.; Chikamoto, T. [1994]: New Low-Reynolds-Number k - Model applied to Stratified Flowfield. (Part 2), *Annual Meeting of AIJ*, pp. 19-20. (in Japanese ??).
- Murakami, S.; Kato, S.; Kondo, Y.; Chikamoto, T. [1990]: Numerical Study on Convective Heat Transfer at Wall Boundary. (Parts 1 and 2), *Annual Meeting of AIJ*, pp. 479-482.
- Murakami, S.; Kato, S.; Nagano, S. [1988]: J. of Architecture, Planning and Environmental Engineering (Transaction of AIJ), No. 385, pp. 9-17.
- Murakami, S.; Kato, S.; Suyama, Y. [1985]: Technical Report of Kanto Chapter AIJ, pp. 149-152.
- Neitzke, K-P. [1996]: Investigation of Laminar and Turbulent Flow in Natural Convection. *Technical paper, Institute of Aerospace Engineering, Dresden University of Technology.*
- Patankar, S.V.; Spalding, D.B. [1970]: Heat and Mass transfer in boundary layers. *2nd Edition (IntertextBooks), London.*
- Reynolds, W.C. [1976]: Computation of Turbulent Flows: *Annual Review of Fluid Mechanics*, Vol. 8, pp 183 - 208.
- Sakamoto, Y.; Matsuo, H. [1976]: Annual Meeting of AIJ pp. 177 - 178.
- Spalding, D.B. [1967]: Monograph on Turbulent Boundary Layers. *Imperial College, Mechanical Engineering Department Report, TWF/TN/33.*
- Tsuji, T.; Nagano, Y. [1989]: Velocity and Temperature Measurements in a Natural Convection Boundary Layer along a Vertical Flat Plate. *Experimental Thermal and Fluid Science* 2, pp. 208-215.
- Yuan, X. [1995]: Wall Functions for Numerical Simulation of Natural Convection along Vertical Surfaces. *Dr.Sc.Techn. thesis, Laboratorium für Energiesysteme, ETH Zürich. ISBN 3-260-05370-0.*
- Yuan, X.; Moser, A.; Suter, P. [1993]: Wall Functions for Numerical Simulation of Turbulent Natural Convection along Vertical Plates. *Journal of Heat Mass Transfer.*

Yuan, X.; Moser, A.; Suter, P. [1994]: Application of New Wall Functions in Prediction of Turbulent Natural Convection. *International Symposium on Turbulence, Heat and Mass Transfer*.

2.4.7. Solar Heat Gain Calculation

- Cohen, M.F.; Greenberg, D.P. [1985]: A radiosity solution for complex environments. *Computer Graphics*, vol. 19, No. 3, pp.31-40, 1985.
- Dunne, C.; Reilly, S.; Ward, G.; Winkelmann, F. [1995]: Algorithms for Modelling Secondary Heat Gain. *ASHRAE Transactions*, Vol. 101, Part 2, pp.43-49.
- Duffie, J.A.; Beckman, W.A. [1991]: Solar engineering of thermal processes. 2nd.ed. Wiley : New York. ISBN 0-471-51056-4.
- Emery, A.F.; Johansson, O.; Lobo, M.; Abrous, A. [1991]: A comparative study of methods for computing the diffuse radiation viewfactors for complex structures. *ASME Transactions: Journal of Heat Transfer*, Vol. 113, pp.413-422.
- Gebhart, B.; Ithaca [1959]: A new method for calculating radiant exchange. *ASHRAE Transactions*, Vol. 65.
- Hottel, H.C. [1967]: Radiative transfer. McGraw-Hill, p.86.
- Kato, S.; Murakami, S.; Hanyu, F.; Zeng, J. [1995]: CFD Analysis of Flow and temperature fields in atrium with ceiling height of 130 m. *ASHRAE Annual Meeting, 1995 to be published*.
- Li, Y.; Fuchs, L. [1992]: Prediction of 3D Indoor Airflow- Radiation Interactions by Discrete Transfer Method. *Proceedings of ROOMVENT 92*, Vol. 1, pp. 317-333.
- Murakami, S. [1992]: Prediction, Analysis and Design for Indoor Climate in Large Enclosure. *Proceedings of ROOMVENT 92*, Vol. 1, pp. 1-30.
- Off, F.; Schalin, A.; Moser, A. [1994]: Numerical simulation of air flow and temperature in large enclosures with surface radiation exchange. *Proceeding of ROOMVENT 94*, vol. 1, pp.95-107.
- Omori, T.; Murakami, S.; Kato, S. [1994]: Analysis of indoor heat gain due to solar radiation with composite grid system. *Proc. of annual meeting of the society of heating, air-conditioning and sanitary engineers of Japan*, pp. 265-268, (in Japanese).
- Omori, T.; Taniguch, H.; Kudo, K. [1990]: Prediction method of radiant environment in a room and its application to floor heating. *Transactions of the society of heating, air-conditioning and sanitary engineers of Japan*, Vol. 42; pp.9-18, (in Japanese)
- Ozeki, Y.; Yamamoto, M.; Saito, T.; Ohgaki, S.; Sonda, Y. [1992]: Simulation on temperature and flow field in the atrium. *Proceedings of ROOMVENT 92*, Vol. 2, pp. 307-319.
- Schenker, G.N.; Keller, B. [1995]: Line by line calculations of the absorption of infrared radiation by water vapor in a box shaped enclosure filled with humid air. *J. of Heat Mass Transfer*, to be appear.
- Schild, P.G. [1996]: CFD Analysis of an Atrium, using a Conjugate Heat Transfer Model Incorporating Long-Wave and Solar Radiation. *Proceedings of ROOMVENT'96*, 5th Int. Conf. on Air Distribution in Rooms, Yokohama. Vol.2, pp.185-194.
- Siegel, R.; Howell, J.R. [1992]: Thermal radiation heat transfer. 3rd ed., Hemisphere Publishing Corporation, Washington.

2.4.8 Coupled Analysis of Radiative and Convective Heat Transfer

- Gebhart, B.; Ithaca [1959]: A new method for calculating radiant exchange. *ASHRAE Transactions, Vol. 65*.
- Kondo, Y.; Murakami, S.; Kato, S.; Niwa, K.; Kitamura, N.; Choi, D. [1993]: A study of velocity and temperature fields around seats with supply opening (part 13) : Parametric study of supply and exhaust conditions by 2-D numerical simulation. *SHASEJ Annual Meeting (in Japanese)*.
- Nagase, O.; Kondo, Y.; Matsunawa, K. [1994]: Study of floor-mounted air diffuser system coupled simulation of convection and radiation. *SHASEJ Annual Meeting (in Japanese)*.
- Parthasarathy, G.; Chai, J.C.; Patankar, S.V. [1996]: A Simple Approach to Non-gray Gas Modelling. *Numerical Heat Transfer, Part B, Vol.29, pp.113-123*.

2.4.9 Macro Analysis based on Micro Model Simulation

- Brouns, C.E.; Waters, J.R. [1994]: The Positioning of Tracer Gas Sampling Points in Large Enclosures. *IEA ANNEX26 4th Expert Meeting, Gjovic*.
- Murakami, S.; Kato, S.; Yokoi, M. [1994]: Micro/Macro Analysis of Airmass, Heat and Energy Transport within an Enclosure. *ROOMVENT'94*.

2.4.10 Interactive Analysis of Macro and Micro Models

- Aasem, E.O.; Clarke, J.A.; Hensen, J.L.M.; Kelly, N.J.; MacQueen, J.; Negari, C.O.R. [1994]: Current building systems modelling potential of ESP-r. *System Simulation in Buildings, Proceedings of 4th International Conference, Liège, Belgium, December 5-7*.
- Axley, J.W. [1988]: Integrating Microscopic and Macroscopic Models of Air Movement and Contaminant Dispersion in Building, Building Systems. *Room Air and Air Contaminant Distribution, Edited by Leslie L. Christianson, ASHRAE*.
- Holmes, M.J.; Lam, J.K-W.; Ruddick, K.G.; Whittle, G.E. [1990]: Computation of conduction, convection and radiation in the perimeter zone of an office space. *Proc. Int. Conf. ROOMVENT90, Norway, paper 19*.
- Kato, S.; Murakami, S.; Choi, D. [1990]: Macro-Micro Coupled Model for Numerical Analysis on Velocity-diffusion Field of Indoor-outdoor Spaces. (Part 1), *Summaries of technical papers of annual meeting, Architectural Institute of Japan (in Japanese)*.
- Murakami, S.; Kato, S.; Yokoi, M. [1994]: Micro/Macro Analysis of Airmass, Heat and Energy Transport within an Enclosure. *ROOMVENT'94*.
- Niwa, H.; Kondo, Y. [1992]: Numerical Study on an Atrium by Means of Macroscopic Model and *k*-Turbulence Model. *ISRACVE, Tokyo*.
- Ozeki, Y.; Mikayama, M.; Daito, T.; Ohgaki, S.; Harada, T. 1994. Time-dependent analysis on thermal environment in atrium by numerical simulation. *Roomvent'94, Proceedings of Fourth International Conference, Krakov, Poland, Vol.1, pp.245-258*.

- Peng, X.; van Paassen, A.H.C. [1994]: A type of dynamic simulation of indoor temperature distributions. *System Simulation in Buildings, Proceedings of 4th International Conference, Liège, Belgium, December 5-7.*
- Schalin, A.; Dorer, V.; Van der Maas, J.; Moser, A. [1992]: A New Method For Linking results of Detailed Air Flow Pattern Calculation With Multizone Models. *13th AIVC Conference, Nice.*
- Togari, S.; Arai, Y.; Miura, K. [1993]: A Simplified Model for Predicting Vertical Temperature Distribution in a Large Space. *ASHRAE Transactions, V.99, Pt. 1.*
- ## 2.5 Scale Model Experiments
- Awbi, H.B. [1991]: Ventilation of buildings. *E&FN Spon. London.*
- Baturin, W.W.; Elterman, W.M. [1974]: Natural ventilation of industrial plants. (*In Polish and in Russian*), *Arkady Warszawa.*
- Kato, S.; Murakami, S.; Choi Nam Kong; Nakagawa, H. [1988]: Model Experiment on Indoor Climate and Space Air Distribution in Large-Scale Room. *Proc. of the Intern. Symposium on Scale Modelling, Tokyo.*
- Malmström, T.; Christiansen, B.; Kirkpatrick, A.; Knappmiller, K. [1993]: Low Velocity Air Jets from Round Nozzles. *KTH Installationsteknik, Bulletin no 26.*
- Mierzwinski, S. [1987]: Physical Experiment in Air Distribution Research. *1st Int. Conf. Roomvent '87, Stockholm.*
- Mierzwinski, S.; Nawrocki, W.; Palasz, J.; Piotrowski, J. [1975]: Application of Physical Modelling Methods in Works on Hazard Limitation of Industrial Dust Sources. (*In Polish*) *N.T. w Inz. San. No 6, pp.5-40, Arkady Warszawa.*
- Mierzwinski, S.; Popiolek, Z.; Lipska, B. [1996]: Techniques of scale model experiments. *IEA Annex 26, Project No TO7G00109, Polish State Committee for Scient. Research (KBN).*
- Nerval, D.J.; Probert, S.D. [1977]: Modelling of Air Movements in Rooms. *J. Mech. Eng. Science, vol.19, No 6, pp.264-270.*
- Nielsen, P.V. [1993]: Model Experiments for the Determination of Airflow in Large Spaces. *The 6th Intern. Confer. on Indoor Air Quality, Helsinki.*
- Renz, U.; et. al. [1995]: Demonstration of Tools on Case Study Buildings. Chapter 4.5. Turnhalle München, Germany. *IEA-ECB&CS Programme, Annex 26.*
- Reynolds, A.J. [1974]: Turbulent Flows in Engineering. *J. Wiley & Sons, London.*
- Richter, E.; Müller, H.; Vogel, P.; Rüdiger, F.; Neitzke, K.-P.; Ali, H. [1996]: Untersuchungen zur Modellierung nichtisothermer Raumluftströmungen am Beispiel der luftbeheizten Turnhalle des Karls - Gymnasiums München. *T.U. Dresden.*
- Rollos, M. [1978]: Möglichkeiten der Vorausbestimmung von Strömungs- und Temperaturfeldern in großen Räumen. *HLH Nr 8 p.p. 302-312.*
- Szücs, E. [1980]: Similitude and Modelling. *Akadémiái Kiadó, Budapest.*
- Vogel, P. [1995]: Zum Einfluß der Strömung auf den Wärmeübergang in klimatisierten Räumen bei kleinen Luftwechsein. *Technische Universität Dresden, Fakultät für Maschinenwesen, eingereichte Dissertation.*
- Zhang, J.S.; Christianson, L.L.; Zhang, B. [1992]: Predicting Room Ventilation Flow with Reduced Scale Models. *Proc. Roomvent '92, vol.1, p.p.502-522, Aalborg.*

2.6 Ventilation Efficiency

- Brouns, C. E.; Waters, J. R. [1991]: A guide to contaminant removal effectiveness. *AIVC Technical Note 28.2*.
- Etheridge, D.W.; Sandberg, M. [1996]: Building Ventilation Theory and Measurement. *John Wiley&Sons*.
- Koskela, H.; Niemelä, R.; Hautalampi, T. [1995]: Ventilation Performance and Indoor Climate in a in a Ventilation Duct Factory. *Report 43, Finish Institute Of Occupational Health*.
- Liddament, M. [1993]: A review of ventilation efficiency. *AIVC Technical Note 39*.
- Murakami, S.; Kato, S.; Yokoi, M. [1994]: Micro/Macroscopic Analysis of Airmass, Heat and Energy Transport within an Enclosure. *Proceedings RoomVent'94 Krakow -Polen, June 15-17, 1994 Volume 1*.
- Niemelä, N.; Koskela, H.; Hautalampi, T. [1995]: Ventilation and Indoor Climate in a Manufacturing Plant. *Report 42, Finish Institute Of Occupational Health*.
- Sandberg, M. [1992]: Ventilation Effectiveness and Purging Flow Rate - A Review. *Proc. of Int. Symp. on Room Air Convection and Ventilation Effectiveness, ISRACVE, July 22-24, Tokyo, Japan*.
- Stymne, H.; Boman, C.A.; Kofoed, P.; Böck, O. [1996]: Determination of Air Distribution Patterns in Large Premises - Application Examples of the Homogeneous Emission Tracer Gas Technique. *ROOMVENT '96, Yokohama, July 17-19, Japan*.
- Sutcliffe, H. [1990]: A guide to air change efficiency. *AIVC Technical Note 28*.

3.0 Measurement Techniques

- Alexander, D.K.; Jones, P.J.; Jenkins, H.; Harries, N. [1994]: Tracking Air Movement in Rooms. *15th AIVC Conference, UK*.
- Brouns, C. E.; Waters, J. R. [1991]: A guide to contaminant removal effectiveness. *AIVC Technical Note 28.2*.
- Brouns, C. E.; Waters, J. R. [1994]: The positioning of tracer gas sampling points in large enclosures. *IEA Annex 26, Forum Presentation, 4th Expert Meeting, Gjøvik*.
- Charlesworth, P. [1988]: Ventilation Measurement Techniques. *AIVC Technical Report*.
- Collineau, S.; Slériéys, J. C.; Cunin, J. C. [1995]: Mesures aérauliques dans un atelier de polyester stratifié. *INRS, Vandoeuvres, France*.
- Crommelin, R. D. 6 ; Boeksteijn, P.; Stellingwerf, J.; van Beukering, F. C. [1980]: Schwankungen der Staub- und Fluoridkonzentrationen, Lufttemperaturen und Luftgeschwindigkeiten in einer Fabrikhalle. *Staub-Reinhalt. Luft. 40, 510-514*.
- Crommelin, R. D.; van Beukering, F. C.; Boeksteijn, P.; de Gids, W. F. [1989]: Ausbreitung von Staub- und gasförmigen Luftverunreinigungen in einer Pelletfabrik. *Staub-Reinhalt. Luft. 38*.
- Dittes, W. [1983]: Einsatzmöglichkeiten der Spurengas-Messmethode bei der Untersuchung von Raumluftrömungen. *HLH 34, No 8*.
- Fürbringer, J.-M.; Foradini, F.; Roulet, C.-A. [1994]: Bayesian Method for Estimating Air tightness Coefficients from Pressurisation Measurement. *Building and Environment 29 151-157*.
- Glückert, U. [1992]: Erfassung und Messung von Wärmestrahlung. *Franzis-Verlag*.

- Haberäcker, P. [1991]: Digitale Bildverarbeitung: Grundlagen und Anwendungen. 4. durchges. Aufl., München; Wien: Carl Hanser Verlag.
- Hajakawa, S.; Togari, S. [1990]: Simple Test Method of Evaluating Exterior Tightness of Tall Office Buildings. *Air Change Rate and Air Tightness in Buildings* (M. H. Sherman, Editor) STP 1067, pp 231-248, ASTM, Atlanta.
- Hauf; Grigull; Mayinger [1991]: Optische Meßverfahren in der Wärme- und Stoffübertragung. Springer-Verlag, pp194-225.
- Koskela, H.; Minni, E.; Pekkarinen, J. [1990]: Instrumentation for the measurements of Flow, Temperature and Impurity Concentration Fields. *Roomvent '90, Oslo*.
- Koskela, H. K.; Rolin, I. E.; Norell, L. O. [1992]: Comparison Between Forced-Displacement and Mixing Ventilation in a Garage. *ASHRAE Trans.* 87, part 2, 119-1126.
- Krückels, W. [1969]: Eine Methode zur photometrischen Bestimmung örtlicher Stoffübergangszahlen mit Hilfe chemischer Nachweisreaktionen. *Chemie-Ing.-Techn.* 41, 7, S. 427 - 433.
- Krüger, M. [1984]: Erprobung einer Relativeichmethode für die Analogie Stoff-Wärmeübergang mit NH₃-Tracer-Gas. *TU Dresden, Sektion Energieumwandlung, Beleg GB 643*.
- Liddament, M. [1993]: A review of ventilation efficiency. *AIVC Technical Note 39*.
- Maas, H.G.; Grün A.; Papantoniou D. [1993]: Particle tracking velocimetry in three-dimensional flows. *Experiments in Fluids*, 15.
- Michalski; Eckersdorf; McGhee [1991]: Temperature Measurement. *John Wiley & Sons, pp41-99*.
- Müller; Vogel [1994]: Methods for Investigating Indoor Air Conditions of Ventilated Rooms. *Proceedings of the 15th AIVC Conference, Buxton*.
- Niemelä, R. [1986]: A Tracer Pulse Method for the Assessment of Air Flow Patterns in a Particleboard. *Mill. Scand. J. Work. Environ. Health* 12, 504-511.
- Niemelä, R.; Toppila, E.; Tossavainen, A. [1987]: A Multiple Tracer Gas Technique for the Measurement of Air Flow Patterns in Large Industrial Premises. *Building and Environment*, 22, 61-66.
- Richter; Vogel; Müller; Rüdiger; Neitzke [1994]: Untersuchungen zur Modellierung nichtisothermer Raumluftströmungen am Beispiel der luftbeheizten Turnhalle des Karls-Gymnasium München. *2.Meßbericht, unpublished report*.
- Roulet, C.-A.; Compagnon, R. [1989]: Multizone Tracer Gas Infiltration Measurements - Interpretation Algorithms for Non Isothermal Cases. *Building and Environment* 24, pp221-227.
- Roulet, C. A.; Compagnon, R.; Jakob, M. [1991]: A Simple Method Using Tracer Gas to Identify the Main Air- and Contaminant Paths Within a Room. *Indoor Air* 3 311-322.
- Roulet, C.-A. [1992]: Expérimentation in situ en relation avec les qualités thermiques et aérauliques du bâtiment. *5th J. Cartier Conference, Montréal*.
- Roulet, C.-A.; Vandaele, L. [1992]: Air Flow Patterns Within Buildings - Measurement Techniques. *Tech. Note AIVC 34, Berkshire RG12 4AH, GB*.
- Rüdiger, F.; Vogel, P. [1993]: Ein Bildauswertesystem für die Quantifizierung von NH₃-Stoffübergangsmessungen. *Luft- und Kältetechnik* 29, 3, S. 124-131.
- Scholzen, F.; Moser, A.; Suter, P. [1994]: Particle- Streak-Velocimetry for Room Air Flows. *15th AIVC Conference, Buxton, UK*.
- Seager, A.: Gateway Two. *Draft Report*.

- Sherman, M. H.; Modera, M. P. [1988]: Signal Attenuation Due to Cavity Leakage. *J. Acoust. Soc. Am.* 84 (6), pp 2163-2169.
- Stahl; Miosga [1986]: Infrarottechnik. *Hüthig Verlag.*
- Stymne, H.; Sandberg, M.; Holmgren, O. [1992]: Ventilation Measurements in Large Enclosures. *Roomvent 92. Aalborg.*
- Sutcliffe, H. [1990]: A guide to air change efficiency. *AIVC Technical Note 28.*
- Tamura, G.T.; Wilson, A.G. [1966]: Pressure Differences for Nine-storey Building as a Result of Chimney Effect and Ventilation System Operation. *ASHRAE trans.* 72 pp 180-189.
- Tarantola, A. [1987]: Inverse Problem Theory. *Elsevier, New York.*
- van Beukering, F. C.; Boeksteijn, P.; Crommelin, R. D. [1973]: Die Ausbreitung von Luftverunreinigungen in einer Werkhalle durch Konvektionsströmungen. *Staub-Reinhalt. Luft.* 33, 192-196.
- Van der Maas (editor) [1992]: Air Flow Through Large Openings in Buildings. *IEA-ECB&CS Annex 20 report, LESO.PB, EPFL, CH 1015 Lausanne.*
- Van der Maas, J; Hensen, J. L. M.; Roos, A. [1994]: Ventilation and Energy Flow Through Large Vertical Openings in Buildings. *Proceedings of the 15th AIVC Conference, Buxton.*
- Zamboni, M.; Berchtold, O.; Filleux, Ch.; Krummenacher, S.; Fehlmann, J.; Roulet, C.-A.; Compagnon, R.; Jakob, M.; Fürbringer, J.-M.; Cretton, P. [1992]: Bedarfshabhängige Lüftung in einem Hörsaal. *IEA-ECB Annex 18 Report, Basler & Hofmann, Zürich.*

4.1 Olympic Mountain Hall, Gjøvik, Norway

- Van der Maas, K.; Kolsaker, K. [1996]: Simple Design Tools Applied to an Underground Stadium and Compared with Indoor Climate Measurements, *ROOMVENT '96, Proceedings of 5th Int. Conf., Yokohama, Japan*

4.2 Queens Building, Leicester, United Kingdom

- AIVC [1988]: Air Exchange Rate and Air Tightness Measurement Techniques - An Applications Guide.
- Brouns, C.E.; Waters, J. R. [1994]: The positioning of Tracer Gas Sampling Points in Large Enclosures. *4th Expert Meeting, IEA Annex 26 ("Energy-Efficient Ventilation of Large Enclosures), Leamington-Spa.*
- Clancy, E. M. and Howarth, A. T. [1994]: Measurement of Environmental Conditions in a Naturally Ventilated Lecture Theatre ; Development of Passive Buildings -Future or Folly?. *Seminar at the Institution of Mechanical Engineers.*
- Clancy, E. M. and Howarth, A. T.; Walker, R. [1994]: Assessing Environmental Conditions in a Naturally Ventilated Lecture Theatre. *European Conference on Energy Performance and Indoor Climate in Buildings, Lyon, France.*

4.3 Experimental Atrium, Kanagawa, Japan

- Fischer, V.; Rösler, M. [1995]: Uncoupled and Coupled Simulation of Japanese Experimental Atrium - First Study. *Technical report of Annex26.*

- Fischer, V.; Rösler, M. [1996]: Investigation and Application of Coupled Building and Room Air Flow Simulation. *Proceedings of ROOMVENT'96, 5th Int. Conf. on Air Distribution in Rooms, Yokohama. Vol.2, pp.215-222.*
- Hiramatsu, T.; Harada, T.; Kato, S.; Murakami, S.; Yoshino, H. [1996]: Study of Thermal Environment in Experimental Real-scale Atrium. *Proceedings of ROOMVENT'96, 5th Int. Conf. on Air Distribution in Rooms, Yokohama. Vol.1, pp.523-530.*
- Inard, C. [1996]: Use of a Zonal Model for the Prediction of Air Temperature Distribution in Large Enclosures. *Proceedings of ROOMVENT'96, 5th Int. Conf. on Air Distribution in Rooms, Yokohama, Vol.2, pp.177-184.*
- Nui, J.; van der Kooij, J. [1992]: Grid Optimization for k- ϵ Turbulence Model Simulation of Natural Convection in Rooms. *ROOMVENT'92, Proceedings of 3rd Int. Conf., Aalborg, Denmark. Vol.1, pp.207-223.*
- Neitzke, K-P. [1996]: Investigation of Laminar and Turbulent Flow in Natural Convection. *Technical paper, Institute of Aerospace Engineering, Dresden University of Technology.*
- Off, F.; Moser, A.; Suter, P. [1996]: Transient Numerical Modelling of Heat Transfer by Radiation and Convection in Atrium with Thermal Inertia. *Proceedings of ROOMVENT'96, 5th Int. Conf. on Air Distribution in Rooms, Yokohama. Vol.3, pp.153-162.*
- Ozeki, Y.; Kato, S. [1996]: Numerical Analysis on Flow and Temperature Fields in Experimental Real Scale Atrium. *Proceedings of ROOMVENT'96, 5th Int. Conf. on Air Distribution in Rooms, Yokohama, Vol.3, pp.179-186.*
- Schild, P.G. [1996]: CFD Analysis of an Atrium, Using a Conjugate Heat Transfer Model Incorporating Long-wave and Solar Radiation. *Proceedings of ROOMVENT'96, 5th Int. Conf. on Air Distribution in Rooms, Yokohama. Vol.2, pp.185-194.*
- Yuan, X.; Huber, A.; Schaelin, A.; Hachmann, P.; Moser, A. [1992]: New Wall Functions for the Numerical Simulation of Air Flow Pattern in Rooms. *Proceedings of ROOMVENT'92, 3rd Int. Conf. on Air Distribution in Rooms, Aalborg. Vol.1 pp.75-91.*

4.4 Fibreglass Reinforced Polyester Factory, Caen, France

- Koskela, H.; Niemelä, R.; Collineau, S.; Serieys, J.-C. [1996a]: Experimental Survey of Ventilation in a Reinforced Plastic Factory. *Proceedings of Roomvent 96, Yokohama, July 17-19, Japan.*
- Koskela, H.; Niemela, R.; Hautalampi, T.; Heikkinen, J.; Collineau, S. [1996b]: Use of Ultrasonic Anemometer for Characterising Room Air Flows. *Proceedings of Indoor Air 96, Nagoya, July 21-24, Japan.*

4.5 Turnhalle (Gymnasium) München, Germany

- Jung, A.; Zeller, M. [1994]: An Analysis of Different Tracer Gas Techniques to Determine the Air Exchange Efficiency in a Mechanically Ventilated Room. *Proceedings of Roomvent '94, pt. 2, p. 315-332, Krakow, Poland.*

4.6 Atrium Grafenau, Zug, Switzerland

- Aiulfi, D. [1995]: A Simple Design Tool for the Calculation of the Opening Areas of an Atrium. *IEA Annex 26 Expert Meeting, Dresden, Germany.*
ASHRAE Handbook - 1985 Fundamentals.
- Hajakawa, S.; Togari, S. [1990]: Simple Test Method of Evaluating Exterior Tightness of Tall Office Buildings. *Air Change Rate and Air Tightness in Buildings (M. H. Sherman, Ed.) STP 1067, pp. 231-248, ASTM, Atlanta.*
- Heiselberg, P. [1994]: Draught Risk from Cold Vertical Surfaces. *Building and Environment, Vol. 29, No. 3, pp. 297-301.*
- Heiselberg, P.; Overby, H.; Bjørn, E. [1995]: Energy Efficient Measures to avoid Downdraft from Large Glazed Facades. *ASHRAE Transactions, Vol. 101, part 2.*
- Pauli, E.; Ruch, R. [1994]: Grafenau Zug - Gebäude- und Anlagenbeschrieb. *Interner Bericht, Eicher & Pauli AG, Liestal, Switzerland.*
- Roulet, C.-A.; Müller, D. [1996]: Measurement Techniques for Ventilation of Large Enclosures. *Proceedings of ROOMVENT '96, Yokohama, Japan.*
- Yuan, X.; Moser, A.; Suter, P. [1994]: Application of New Wall Functions in Prediction of Turbulent Natural Convection. *Int. Symp. on Turb. Heat and Mass Transfer, Lisbon.*

INTERNATIONAL ENERGY AGENCY

The International Energy Agency (IEA) was established in 1974 within the framework of the Organization for Economic Co-operation and Development (OECD) to implement an International Energy Programme. A basic aim of the IEA is to foster co-operation among the twenty-one IEA Participating Countries, to increase energy security through energy conservation, development of alternative energy sources and energy research development and demonstration (RD&D). This is achieved in part through a programme of collaborative RD&D consisting of forty-two Implementing Agreements, containing a total of over eighty separate energy RD&D projects. This publication forms one element of this programme.

Energy Conservation in Buildings and Community Systems

The IEA sponsors research and development in a number of areas related to energy. In one of these areas, energy conservation in buildings, the IEA is sponsoring various exercises to predict more accurately the energy use of buildings, including comparison of existing computer programs, building monitoring, comparison of calculation methods, as well as air quality and studies of occupancy. Seventeen countries have elected to participate in this area and have designated contracting parties to the Implementing Agreement covering collaborative research in this area. The designation by governments of a number of private organizations, as well as universities and government laboratories, as contracting parties, has provided a broader range of expertise to tackle the projects in the different technology areas than would have been the case if participation was restricted to governments. The importance of associating industry with government sponsored energy research and development is recognized in the IEA, and every effort is made to encourage this trend.

The Executive Committee

Overall control of the programme is maintained by an Executive Committee, which not only monitors existing projects but identifies new areas where collaborative effort may be beneficial. The Executive Committee ensures that all projects fit into a pre-determined strategy, without unnecessary overlap or duplication but with effective liaison and communication. The Executive Committee has initiated the following projects to date (completed projects are identified by (*).

- Annex 1: Load Energy Determination of Buildings *
- Annex 2: Ekistics & Advanced Community Energy Systems *
- Annex 3: Energy Conservation in Residential Buildings *
- Annex 4: Glasgow Commercial Building Monitoring *
- Annex 5: Air Infiltration and Ventilation Centre
- Annex 6: Energy Systems and Design of Communities *
- Annex 7: Local Government Energy Planning *
- Annex 8: Inhabitant Behaviour with Regard to Ventilation *
- Annex 9: Minimum Ventilation Rates *
- Annex 10: Building HVAC System Simulation *
- Annex 11: Energy Auditing *

ANALYSIS AND PREDICTION TECHNIQUES

- Annex 12: Windows and Fenestration *
 - Annex 13: Energy Management in Hospitals *
 - Annex 14: Condensation *
 - Annex 15: Energy Efficiency in Schools *
 - Annex 16: BEMS-1: Energy Management Procedures *
 - Annex 17: BEMS-2: Evaluation and Emulation Techniques *
 - Annex 18: Demand Controlled Ventilating Systems *
 - Annex 19: Low Slope Roofs Systems *
 - Annex 20: Air Flow Patterns within Buildings *
 - Annex 21: Thermal Modelling *
 - Annex 22: Energy Efficient Communities *
 - Annex 23: Multizone Air Flow Modelling (COMIS) *
 - Annex 24: Heat, Air and Moisture Transfer in Envelopes *
 - Annex 25: Real Time HVAC Simulation *
 - Annex 26: Energy Efficient Ventilation of Large Enclosures *
 - Annex 27: Evaluation and Demonstration of Domestic Ventilation Systems
 - Annex 28: Low Energy Cooling Systems
 - Annex 29: Daylighting in Buildings
 - Annex 30: Bringing Simulation to Application
 - Annex 31: Energy Related Environmental Impact of Buildings
 - Annex 32: Integral Building Envelope Performance Assessment
 - Annex 33: Advanced Local Energy Planning
 - Annex 34: Computer Aided Fault Detection and Diagnosis
 - Annex 35: Hybrid Ventilation in New and Retrofitted Office Buildings
- (* completed Annexes)

ANNEX 26:

ENERGY EFFICIENT VENTILATION OF LARGE ENCLOSURES

“Energy Efficient Ventilation of Large Enclosures”, Annex 26, a task-sharing Annex to the IEA Implementing Agreement on Energy Conservation in Buildings and Community Systems.

- Objectives:** The general objective is to develop methods to minimize energy consumption of large enclosures in the provision of:
- good indoor air quality and comfort
 - the safe removal of airborne contaminants and
 - the satisfactory distribution of fresh air
- The specific objective is to develop the following methods:
- Analysis Methods** to measure or model air motion, thermal stratification, and contaminant spread in given enclosed spaces and to evaluate performance and locate problems. The results are primarily addressed to HVAC specialists and researchers.
- Design Methods** which show how energy-efficient ventilation may be achieved in new designs or in existing buildings (retrofit). These guidelines are primarily aimed at designers and Heating, Ventilation and Air-Conditioning (HVAC) engineers.
- Start:** March 31, 1993
- Duration:** 3 1/3 years
- Completion:** July 31, 1996
- Subtasks:** The work is organized in two parallel subtasks
1. Measurement Techniques and Case Studies
 2. Models
- Participating Countries:** Denmark, Finland, France, Germany, Italy, Japan, The Netherlands, Norway, Poland, Sweden, Switzerland, and United Kingdom.
- Operating Agent:** The Swiss Federal Office of Energy (BEW). Contractor: Alfred Moser, Swiss Fed. Inst. of Technology, ETH, Zürich.
- Subtask Leaders:** Subtask 1: Dr. Robert J. Waters, Coventry University, UK;
Subtask 2: Dr. Per K. Heiselberg, Aalborg University, Denmark.

PARTICIPATING INSTITUTES IN ANNEX 26

Country	Institute	Address	Contact person
Denmark	AAU	Aalborg University Indoor Environmental Technology Sohngaardsholmsvej 57 DK-9000 Aalborg	Dr. Per Heiselberg Phone: +45 98 158 522 Fax: +45 98 148 243 E-mail: i6per@civil.auc.dk
Denmark	DBRI	Danish Building Research Institute Postbox 119 DK-2970 Horsholm	Mr. Karl Terpger Andersen Phone: +45 42 865 533 Fax: +45 42 867 535 E-mail:
Finland	FIOH	Finnish Institute of Occupational Health Laajaniityntie 1 FIN-01620 Vantaa	Dr. Raimo Niemelä Phone: +358 0 47471 Fax: +358 0 890 713 E-mail: rnie@occuphealth.fi
Finland	HUT	Helsinki University of Technology Sahkomiehentie 4 FIN-02150 Espoo	Dr. Markku Lampinen Phone: +358 0 451 3582 Fax: +358 0 451 3419 E-mail: mlampinen@sampo.hut.fi
Finland	VTT	VTT Building Technology P.O.Box 1804 FIN-02044 VTT	Mr. Jorma Heikkinen Phone: +358 0 456 4742 Fax: +358 0 455 2408 E-mail: jorma.heikkinen@vtt.fi
France	INSA	INSA de Lyon Centre de Thermique Bât. 307 20 Avenue Albert Einstein F-69621 Villeurbanne Cedex	Dr. Christian Inard Phone: +33 72 438 462 Fax: +33 72 438 522 E-mail: inard@cethyl.insa-lyon.fr
France	INRS	INRS, Institut National de Recherche et de Sécurité Centre de Recherche Ave. de Bourgogne, B.P. 27 F-54501 Vandoeuvre Cedex	Dr. Jean-Raymond Fontaine Phone: +33 83 502 058 Fax: +33 83 502 184 E-mail: @inrs.fr
France	LET	ENSMA Laboratoire d'Etudes Thermiques BP 109 F-86960 Futuroscope Cedex	Dr. Dominique Blay Phone: +33 49 498 115 Fax: +33 49 498 115 E-mail: blay@let.univ-poitiers.fr

Country	Institute	Address	Contact person
France	CSTB	CSTB 84, Avenue Jean Jaurès Champs-sur-Marne F-77421 Marne-la-Vallee Cedex 2	Dr. Jacques Riberon Phone: +33 1 6468 8308 Fax: +33 1 6468 8350 E-mail:
Germany	IKE	Universität Stuttgart IKE Abt. Heizung, Lüftung, Klima Pfaffenwaldring 35 D-70550 Stuttgart	Dipl.-Ing. Wolfgang Scholer Phone: +49 711 685 2086 Fax: +49 711 685 2096 E-mail:
Germany	RWTH	Lehrstuhl für Wärmeübertragung und Klimatechnik RWTH Aachen Eilfschornsteinstr. 18 D-52056 Aachen	Prof. Ulrich Renz Phone: +49 241 805 400 Fax: +49 241 888 8143 E-mail: renz@wuek.rwth-aachen.de
Germany	TUD	Technische Universität Dresden Inst. für Luft- und Raumfahrttechnik Mommsenstrasse 13 D-01062 Dresden	Prof. Dr-Ing. Roger Grundmann Phone: +49 351 463 8086 Fax: +49 351 463 8087 E-mail: grundman@tfd.mw.tu- dresden.de
Italy	ENEA	ENEA Energy Savings Department ERG SIRE Via Anguillarese, 301 S. Maria di Galeria I-00060 Roma	Dr. Marco Citterio Phone: +39 6 304 833 72 Fax: +39 6 304 863 15 E-mail: citterio_mi@casaccia.enea.it
Italy	TOPO	Politecnico di Torino Dip. di Energetica Corso Duca degli Abruzzi 24 I-10129 Torino	Dr. Gian Vincenzo Fracastoro Phone: +39 11 564 4438 Fax: +39 11 564 4499 E-mail: pfrac@polen2.polito.it
Japan	ASAH	Asahi Glass Co., Ltd Research Center 1150 Hazawa-cho Kanagawa-ku Yokohama-shi Kanagawa 221	Mr. Yoshiichi Ozeki Phone: +81 45 334 6114 Fax: +81 45 334 6187 E-mail: oze@agc.co.jp
Japan	FUJI	Fujita Corporation Technical Research Institute 74 Ohdana-cho Tsuzuki-ku Yokohama-shi 224	Dr. Shinichiro Nagano Phone: +81 45 591 3937 Fax: +81 45 91 2449 E-mail: nagano@giken.fujita.co.jp
Japan	IIS	University of Tokyo Institute of Industrial Science 7-22-1, Roppongi Minato-ku Tokyo 106	Prof. Shuzo Murakami Phone: +81 3 3401 7439 Fax: +81 3 3746 1449 E-mail: murakami@luna.iis.u-tokyo.ac.jp

Country	Institute	Address	Contact person
Japan	MUSA	Musashi Institute of Technology Department of Architecture 28-1 Tamazutsumi 1-Chome Setagaya-ku Tokyo 158	Assoc. Prof. Yasushi Kondo Phone: +81 3 3703 3111 Ext. 3030 Fax: +81 3 5707 2129 E-mail:
Japan	NS	Nikken Sekkei Ltd Tokyo Environmental, M & E Engineering Office 2-1-2 Koraku Bunkyo-ku Tokyo 112	Mr. Shinji Yamamura Phone: +81 3 3813 3361 Fax: +81 3 3818 8238 E-mail:
Japan	SHIM	Shimizu Corporation Institute of Technology 4-17 Etchujima 3-Chome Koto-ku Tokyo 135	Dr. Kazuki Hibi Phone: +81 3 3643 4311 Fax: +81 3 3643 7260 E-mail: hibi@sit.shimz.co.jp
Japan	SINR	Shinryo Corporation Research and Develop Center 41 Wadai Tsukuba-shi Ibaragi 300-42	Mr. Kakuo Ueda Phone: +81 6 344 7571 Fax: +81 6 344 6298 E-mail:
Japan	TAIS	Taisei Corp., M & E Design Dept. 1 Design and Proposal Division 1-25-1 Nishi Shinjuku Shinjuku-ku Tokyo 163-06	Mr. Mutsumi Yokoi Phone: +81 3 5381 5262 Fax: +81 3 3340 1675 E-mail: yokoi@arch.taisei.co.jp
Japan	TOHU	Tohoku University Faculty of Engineering Department of Architecture Sendai 980	Prof. Yoshino Hiroshi Phone: +81 22 217 7883 Fax: +81 22 217 7886 E-mail: yoshino@sabine.archi.tohoku.ac.jp
Nederlands	TNO	TNO Building & Construction Research Dept. of Indoor Environment Building Physics and Systems P.O.Box 29 NL-2600 AA Delft	Ir. Tony Lemaire Phone: +31 2 15 608 492 Fax: +31 2 15 608 432 E-mail: a.lemaire@bouw.tno.nl
Norway	NTNU	Norwegian University of Science and Technology Department of Refrigeration and Air Conditioning N-7034 Trondheim -NTH	Dr. Per Olaf Tjelflaat Phone: +47 73 593 864 Fax: +47 73 593 859 E-mail: per.o.tjelflaat@kkt.unit.no
Norway	SINTEF	SINTEF Division of Applied Thermodynamics N-7034 Trondheim -NTH	Dr. Hans Martin Mathisen Phone: +47 73 593 870 Fax: +47 73 593 859 E-mail: hans.m.mathisen@kkt.sintef.no

Country	Institute	Address	Contact person
Norway	TC	Techno Consult Arnold Haukelands Plass 10 N-1300 Sandvika	Dr. ing. Bent Borresen Phone: +47 67 571 808 Fax: +47 67 571 849 E-mail:
Poland	STU	Silesian Technical University Dept. of Heating, Ventilation and Dust Removal Technology ul. Pstrowskiego 5 PL-44-101 Gliwice	Prof. Zbigniew Popiolek Phone: +48 32 371 280 Fax: +48 32 372 559 E-mail:
Sweden	CTH	Chalmers University of Technology Thermo- and Fluid Dynamics S-412 96 Gothenburg	Prof. Erik Olsson Phone: +46 31 721 401 Fax: +46 31 180 976 E-mail: erik@tfd.chalmers.se
Sweden	KTH	The Royal Institute of Technology Dept. for Built Environment P.O.Box 88 S-801 02 Gävle	Prof. Mats Sandberg Phone: +46 26 147 800 Fax: +46 26 147 801 E-mail: sandberg@bmg.kth.se
Switzerland	EMPA	EMPA Abt. 175 CH-8600 Dübendorf	Dr. Thomas Rüegg Phone: +41 1 823 4721 Fax: +41 1 821 6244 E-mail: rueegg@empa.ch
Switzerland	IET	Air & Climate Research in Building Technology ETH-Zentrum LOW C4 CH-8092 Zürich	Dr. Alfred Moser Phone: +41 1 632 3641 Fax: +41 4 632 1023 E-mail: moser@hbt.arch.ethz.ch
Switzerland	LESO	Laboratoire d'Energie Solaire et de Physique du Batiment École Polytechnique Fédérale de Lausanne CH-1015 Lausanne	Dr. Claude-Alain Roulet Phone: +41 21 693 4557 Fax: +41 21 693 2722 E-mail: claude.roulet@leso.da.epfl.ch
Switzerland	SORANE	Sorane SA Route du Châtelard 52 CH-1018 Lausanne	Dr. Dario Aiulfi Phone: +41 21 647 1175 Fax: +41 21 646 8676 E-mail: sorane@clients.switch.ch
Switzerland	SULZER	Sulzer Innotec AG Fluid Mechanics Laboratory Postfach CH-8401 Winterthur	Dr. Joachim Borth Phone: +41 52 262 4251 Fax: +41 52 262 0154 E-mail: joachim.borth.@sulzer.inet.ch
United Kingdom	BRE	BRE Building Research Establish. Garston Watford, Herts WD2 7JR	Mr. Richard Walker Phone: +44 1923 664 469 Fax: +44 1923 664 095 E-mail: walkerr@bre.co.uk

Country	Institute	Address	Contact person
United Kingdom	COVU	Coventry University School of the Built Environment Priory Street Coventry CV1 5FB	Dr. Robert Waters Phone: +44 1203 838 346 Fax: +44 1203 838 485 E-mail: cbx002@rowan.coventry.ac.uk
United Kingdom	DMU	De Montfort University ECADAP Institute of Energy and Sustainable Development The Gateway Leicester LE1 9BH	Mr. Eoin Clancy Phone: +44 116 257 7417 Fax: +44 116 257 7449 E-mail: emc@de-montfort.ac.uk

This book contains the results of the joint activities in IEA-ECB Annex 26 and it gives an overview of the techniques to analyse, measure and model air flows and ventilation in large enclosures. Advice is given on the application of different analysis methods, on the advantages and disadvantages, on selection and use and on type of results to expect. Many are new methods designed especially for large enclosures or are methods whose application to large enclosures are not well known.

Problems and physical characteristics of large enclosures and what makes them different from small rooms are stated. Several analysis models are described from "easy-to-use" equations for flow elements such as jets, plumes or boundary layer flows, over engineering and zonal models, which include building dynamic models, to complicated computational fluid dynamics models.

Measurements in large enclosures require detailed planning to be successful, and the book introduces a method to plan measurements and gives advice on what to be aware of in particular before and during measurements. Both new techniques developed for large enclosures and application of existing techniques are described.

Working examples of all methods are included, which covers a wide range of large enclosures, such as one industrial hall, two atria, two auditoriums, one stadium and one gymnasium. Both successful and unsuccessful applications are included with comparisons between different models and between models